A Tale of Two Leads: An Investigation into the Development of Theranostic ^{203}Pb and ^{212}Pb Radiopharmaceuticals from Isotope Production to Preclinical Evaluation

by

Brooke McNeil

B.Sc. (Honours), University of Waterloo, 2020

Thesis Submitted in Partial Fulfillment of the
Requirements for the Degree of
Doctor of Philosophy

in the
Department of Chemistry
Faculty of Science

© Brooke McNeil 2025
SIMON FRASER UNIVERSITY
Spring 2025

Copyright in this work is held by the author. Please ensure that any reproduction or re-use is done in accordance with the relevant national copyright legislation.

Declaration of Committee

Name:	**Brooke McNeil**
Degree:	**Doctor of Philosophy (Chemistry)**
Title:	**A Tale of Two Leads: An Investigation into the Development of Theranostic ^{203}Pb and ^{212}Pb Radiopharmaceuticals from Isotope Production to Preclinical Evaluation**
Committee:	**Chair: Loren Kaake** Associate Professor, Chemistry
	Caterina Ramogida Co-supervisor Associate Professor, Chemistry
	Paul Schaffer Co-supervisor Adjunct Professor, Chemistry
	Jeff Warren Committee Member Professor, Chemistry
	Robert Britton Examiner Professor, Chemistry
	Carolyn Anderson External Examiner Professor, Chemistry University of Missouri

Ethics Statement

The author, whose name appears on the title page of this work, has obtained, for the research described in this work, either:

a. human research ethics approval from the Simon Fraser University Office of Research Ethics

or

b. advance approval of the animal care protocol from the University Animal Care Committee of Simon Fraser University

or has conducted the research

c. as a co-investigator, collaborator, or research assistant in a research project approved in advance.

A copy of the approval letter has been filed with the Theses Office of the University Library at the time of submission of this thesis or project.

The original application for approval and letter of approval are filed with the relevant offices. Inquiries may be directed to those authorities.

Simon Fraser University Library
Burnaby, British Columbia, Canada

Update Spring 2016

Abstract

With the potential to determine non-invasively through diag*nostic* imaging if a patient is likely to benefit from a *thera*peutic treatment, *theranostic* radiopharmaceuticals are rapidly gaining clinical attention. These radiopharmaceuticals are composed of a radioactive metal (radiometal) bound by a bifunctional chelator linked to a biological targeting vector that specifically binds to overexpressed biomarkers on cancer cells, allowing for the selective delivery of radiation to cancer cells, sparing healthy surrounding tissues. ^{203}Pb and ^{212}Pb, used respectively for imaging and therapeutic purposes, form an element equivalent theranostic pair that have shown promising results in early clinical trials. However, further advancement of bifunctional chelator-based ^{203}Pb/^{212}Pb radiopharmaceuticals requires optimization and critical evaluation of each component to ensure safety and efficacy. This thesis explores key advancements in ^{203}Pb/^{212}Pb radiopharmaceutical development, with a focus on three essential areas including isotope production, chelator design, and the *in vivo* stability of bioconjugates. A novel purification method combining anion exchange and extraction chromatography, was developed alongside improvements in isotope production, providing a reliable supply of high purity isotopes to support preclinical studies. To expand the portfolio of chelators for lead isotopes, novel chelators were synthesized. Among these, Cyclen-4Py proved to be the most successful with high radiolabeling efficiency and kinetic inertness. An isothiocyanate-based bifunctional analogue of Cyclen-4Py was synthesized and conjugated to fibroblast activation protein inhibitor (FAPI) to evaluate its *in vivo* biodistribution and tumor retention in comparison to the FAPI bioconjugate of the commercial standard, TCMC. Poor initial results led to comparative *in vivo* studies with amide-linked TCMC bioconjugates in small molecule and peptide models that suggested that the thiourea linkage may be unstable. This finding highlights potential limitations of thiourea-based bioconjugation for lead-based radiopharmaceuticals, indicating that amide linkages are a more suitable alternative. This thesis highlights advancements in isotope production, chelator development, and bioconjugate stability, contributing to the improvement of ^{203}Pb/^{212}Pb radiopharmaceuticals for clinical applications.

Keywords: Radiometals; Chelator; Radiopharmaceuticals; Theranostics; Bioconjugation; Biodistribution

Dedication

To all those who have lost their lives to cancer.

Acknowledgements

I am eternally grateful to my co-supervisor, Dr. Caterina Ramogida, for the constant support and encouragement she gave me throughout my doctoral studies. She gave me the freedom to explore my scientific interests and challenged me to go further. Her openness to collaboration fostered new connections and enriched my scientific journey. I also extend my gratitude to my co-supervisor Dr. Paul Schaffer for his mentorship and for supporting the Mitacs Fellowships I completed at ARTMS Inc. that allowed me to look at science from an industrial perspective, one that very few students get to experience in their graduate career. I am deeply grateful to my fellow colleagues, Dr. Anthony McDonagh, Dr. Imma Carbo-Bague, and Dr. Parmissa Randhawa who were always there for me as not only fellow scientists, but also as the dearest of friends. I would also like to thank Dr. Andrew Robertson for taking a chance on me as his co-op student at TRIUMF in 2019 and allowing me to continue and develop the project he started. I am also grateful for my committee member Dr. Jeff Warren for his support and guidance during committee meetings and to my examiners Dr. Robert Britton and Dr. Carolyn Anderson for reviewing my thesis.

At TRIUMF, I give my greatest gratitude to the TR13 Cyclotron Operators David Prevost, Toni Epp, Spencer Staiger, and Ryley Morgan for their constant support, patience, and understanding. I would also like to thank Vicky Hanemaayer for always advocating for myself and fellow graduate students to ensure we always had what we needed in the labs. With immense gratitude, I thank Dr. Hua Yang for her mentorship and and Dr. Luke Wharton for teaching me numerous techniques and encouraging me to always think critically. I would also like to thank Dr. Cristina Rodriguez-Rodriguez and Maryam Osooly at CCM for their assistance and flexibility when conducting our *in vivo* studies.

To my partner Eric Fought, thank you for being with me every step of the way and for your unwavering, eternal support. To Susie and Rob Fought, thank you for welcoming me into your family and supporting my endeavours. To my brother Scott McNeil, I am forever grateful to have been able to experience graduate school with you and have great memories that will last a lifetime. I owe my deepest thanks of all to my parents, John and Kelly McNeil, for always believing in me and for fostering a love of learning at an early age. Thank you for all of the sacrifices you made that allowed me to explore my passions.

Table of Contents

List of Tables

List of Figures

List of Acronyms

%IA/g	Percentage of injected radioactivity per gram of tissue
^{o}C	Degrees Celsius
Å	Angstrom (10^{-10} m)
A	Ampere
ACN	Acetonitrile
AE	Auger electron
AEX	Anion exchange
A_m	Molar activity
ARPIs	Androgen-receptor pathway inhibitors
BFC	Bifunctional chelator
BFC-RP	Bifunctional chelator radiopharmaceutical
Bq	Becquerel
CEX	Cation exchange
CN	Coordination number
Crown-4Py	4,7,13,16-tetrakis(pyridin-2-ylmethyl)-1,10-dioxa-4,7,13,16-tetraazacyclooctadecane
Crypt	Cryptand
Cyclen	1,4,7,10-Tetraazacyclododecane
Cyclen-4Py	1,4,7,10-tetrakis(pyridin-2-ylmethyl)-1,4,7,10-tetraazacyclododecane
CycMSH	Cyclic melanocyte stimulating hormone
CYP	Cytochrome P450
d	Doublet or days
D	Distribution coefficient
Da	Dalton
DIPEA	*N,N*-Diisopropylethylamine
DMF	Dimethylformamide
DMSO	Dimethyl sulfoxide
DNA	Deoxyribonucleic acid
DOTA	1,4,7,10-tetraazacyclododecane-1,4,7,10-tetraacetic acid

DOTA-NCS	S-2-(4-Isothiocyanatobenzyl)-1,4,7,10-tetraazacyclododecane tetraacetic acid
DOTA-TFP	2,2',2''-(10-(2-oxo-2-(2,3,5,6-tetrafluorophenoxy)ethyl)-1,4,7,10-tetraazacyclododecane-1,4,7-triyl)triacetic acid
DOTAGA-NHS-Ester	2,2',2''-(10-(1-carboxy-4-((2,5-dioxopyrrolidin-1-yl)oxy)-4-oxobutyl)-1,4,7,10-tetraazacyclododecane-1,4,7-triyl)triacetic acid
DOTAM	1,4,7,10-Tetrakis(carbamoylmethyl)-1,4,7,10-tetraazacyclododecane
E	Energy
E_{avg}	Average energy
E_{max}	Maximum energy
EC	Electron capture
EDTA	Ethylenediaminetetraacetic acid
EMA	European Medicines Agency
eq	Equivalent
ESI	Electrospray ionization
eV	Electronvolt
EXC	Extraction chromatography
FAP	Fibroblast activation protein
FAPI	Fibroblast activation protein inhibitor
FDA	Food and Drug Administration
g	Gram
GEP-NETs	Gastroenteropancreatic neuroendocrine tumours
h	Hour
HIBA	α-hydroxyisobutyric acid
HOMO	Highest Occupied Molecular Orbital
HPGe	High-purity germanium
HPLC	High performance liquid chromatography
HR-MS	High resolution mass spectrometry
HSAB	Hard-soft acid-base
HSQC	Heteronuclear single quantum coherence
Hz	Hertz

I	Ionic strength
IC_{50}	Half maximal inhibitory concentration
ICP-MS	Inductively coupled plasma mass spectroscopy
ICP-OES	Inductively coupled plasma optical emission spectroscopy
IEC	Ion exchange chromatography
iTLC	Instant thin layer chromatography
J	Coupling constant
K	Degree Kelvin
K_d	Distribution coefficient
LET	Linear energy transfer
LLE	Liquid-liquid extraction
LR-MS	Low resolution mass spectroscopy
LUMO	Lowest Unoccupied Molecular Orbital
M	Molar or mega (10^6)
m	Milli (10^{-3}) or multiplet or meter
m/z	Per unit charge
mAb	Monoclonal antibody
MC1R	Melanocortin-1 receptor
mCRPC	Metastatic castration resistant prostate cancer
min	Minute
MP	Melting point
n	Nano (10^{-9}) or neutron
N_2O_4	1,4,10,13-tetraoxa-7,16-diazacyclooctadecane
N_4O_2	1,10-dioxa-4,7,13,16-tetraazacyclooctadecane
NADPH	Nicotinamide adenine dinucleotide phosphate
nat	Natural
NCS	Isothiocyanate
NET	Neuroendocrine tumour
NHS	*N*-hydroxysuccinimide
NMR	Nuclear magnetic resonance

NOON-2Py	7,16-bis(pyridin-2-ylmethyl)-1,4,10,13-tetraoxa-7,16-diazacyclooctadecane
OAc	Acetate
p	Proton or pico (10^{-12})
p.i.	Post injection
PBS	Phosphate buffered saline
PET	Positron Emission Tomography
pK_a	-log [K_a]
pM	-log [free metal]
PMT	Photomultiplier tube
ppb	Parts per billion
ppm	Parts per million
PSMA	Prostate specific membrane antigen
Py	Pyridine
RCY	Radiochemical yield
R_f	Retention factor
RLY	Radiolabeling yield
RP	Radiopharmaceutical
rpm	Rotations per minute
RPT	Radiopharmaceutical therapy
rt	Room temperature (20 ^oC)
s	Second or singlet
SA	Specific activity or Silicic acid (iTLC)
SFU	Simon Fraser University
SPECT	Single Photon Emission Computed Tomography
SSTR	Somatostatin receptor
SUV	Standardized uptake value
SX	Solvent extraction
T	Temperature
$t_{1/2}$	Half-life
t_R	Retention time

TATE	(Tyr_3-Thr^8)-octreotate
TCMC	1,4,7,10-Tetrakis(carbamoylmethyl)-1,4,7,10-tetraazacyclododecane
TCMC-NCS	2-(4-isothiocyanatobenzyl-1,4,7,10-tetraaza-1,4,7,10-tetra-(2-carbamonylmetyl)-cyclododecane
TEA	Triethylamine
TFA	Trifluoroacetic acid
TLC	Thin layer chromatography
TRT	Targeted radionuclide therapy
UBC	University of British Columbia
UV-Vis	Ultraviolet-visible
XRD	X-ray crystallography
y	Year
α	Alpha particle
β^-	Beta particle
β^+	Positron
γ	Gamma-ray
λ	Wavelength or lamda
μ	Micro (10^{-6})

Preface

Chapter 1 is an adaptation of published work and is reproduced in part, with permission from McNeil, B.L. and Ramogida, C.F. From Cyclotrons to Chromatography and Beyond: A Guide to the Production and Purification of Theranostic Radiometals. *Chemical Society Reviews*. **2024**, *53*(21). https://doi.org/10.1039/D4CS00802B. Copyright 2024 Royal Society of Chemistry. Brooke McNeil wrote the entirety of the manuscript with input and editing from Dr. Caterina Ramogida.

Chapter 2 is an adaptation of published work and is reproduced in part with permission from McNeil, B.L.; Mastroianni, S.; McNeil, S.W.; Zeisler, S.; Kumlin, J.; Borjian, S.; McDonagh, A.W.; Cross, M.; Schaffer, P.; and Ramogida, C.F. Optimized production, purification, and radiolabeling of the ^{203}Pb/^{212}Pb theranostic pair for nuclear medicine. *Scientific Reports* **2024**, *13*, 10623. https://doi.org/10.1038/s41598-023-37313-8. Copyright 2023 Springer Nature. Brooke McNeil developed and optimized the target manufacturing, target recycling, and purification procedures with guidance from Dr. Stefan Zeisler, Joel Kumlin, and Dr. Sogol Borjian. Simona Mastroianni, a fall co-op student, provided assistance with the development process and data collection for ^{212}Pb. Brooke McNeil prepared samples and analyzed the data generated by ICP-MS analysis that was conducted by Scott McNeil. Dr. Anthony McDonagh synthesized and provided Crypt-OH that was used in the radiolabeling studies conducted by Brooke McNeil at TRIUMF. This work was completed as part of a Mitacs Accelerate Fellowship supervised by Dr. Michael Cross, Dr. Paul Schaffer, and Dr. Caterina Ramogida. Brooke McNeil wrote the entirety of the manuscript.

Chapter 3 is an adaptation of published work and is reproduced in part with permission from McNeil, B.L.; Kadassery, K.; McDonagh, A.W.; Zhou, W.; Schaffer, P.; Wilson, J.J.; and Ramogida, C.F. Evaluation of the Effect of Macrocyclic Ring Size on [^{203}Pb]Pb(II) Complex Stability in Pyridyl-Containing Chelators. *Inorganic Chemistry* **2022**, *61*(25), 9638 – 9649. https://doi.org/10.1021/acs.inorgchem.2c01114. Copyright 2022 American Chemical Society. Brooke McNeil performed the synthesis of the chelators and preparation of the Pb^{2+} complexes with assistance from Dr. Anthony McDonagh. Brooke McNeil performed the radiolabeling and kinetic inertness studies at TRIUMF. X-ray crystallography was solved by Dr. Wen Zhou. Potentiometric titrations and data fitting were performed by Dr. Karthika Kadassery. This project was supervised by Dr. Caterina

Ramogida, Dr. Justin Wilson, and Dr. Paul Schaffer. Brooke McNeil wrote the entirety of the manuscript with the exception of the material and methods section on the potentiometric titrations which was written by Dr. Karthika Kadassery.

Chapter 4 is an adaptation of a manuscript in preparation from Brooke L. McNeil, Dr. Luke Wharton, Dr. Chao-Cheng Chen, Helen Merkens, Dr. Milena Colovic, Dr. Cristina Rodriguez-Rodriguez, Dr. John Wilson, Dr. Stefan Mair, Dr. Chengcheng Zhang, Dr. Anthony W. McDonagh, Dr. Kuo-Shyan Lin, Dr. François Bernard, Dr. Frank Wuest, Dr. Paul Schaffer, and Dr. Caterina F. Ramogida. With the exception of Crypt-NCS that was synthesized by Dr. Anthony McDonagh, Brooke McNeil performed the synthesis of the Cyclen-4Py-NXX chelators and all bioconjugates. Brooke McNeil performed the radiolabeling and stability studies alongside the *in vitro* cell studies at TRIUMF. Dr. Milena Colovic provided guidance on the *in vitro* assays. The synthesis of the CycMSH peptide was performed by Dr. Stefan Mair and Dr. Chengcheng Zhang, with supervision from Dr. François Bernard (BC Cancer). Dr. Kuo-Shyan Lin provided the FAPI-04 pharmacophore. Helen Merkens provided the B16F10 cells for *in vitro* assays at TRIUMF and tumour-bearing mice for *in vivo* assays. Dr. Chao-Cheng Chen provided guidance and reagents for the FAPI enzyme inhibition assays. Dr. John Wilson and Dr. Frank Wuest provided ^{203}Pb, which was further purified by Brooke McNeil. Brooke McNeil designed and carried out the *in vivo* studies at the Centre for Comparative Medicine with Dr. Cristina Rodriguez-Rodriguez using the protocol approved by the Institutional Animal Care Committee (IACC) at the University of British Columbia (protocol #A20-0132 (Sossi)) following the Canadian Council on Animal Care Guidelines. Dr. Luke Wharton calculated the standardized uptake values. Dr. Paul Schaffer and Dr. Caterina Ramogida supervised this project. Brooke McNeil wrote the entirety of the manuscript that was edited by Dr. Caterina Ramogida.

Chapter 1.

Introduction: From Cyclotrons to Chromatography and Beyond

1.1. Overview of Nuclear Medicine

Nuclear medicine utilizes radioactive tracers, also known as radiopharmaceuticals (RPs), for both diagnosing and treating disease. In diagnostics, these radioactive tracers enable the visualization of their uptake, providing insights into the physiology and/or functioning of tissues, tumours, and/or organs. For therapeutic purposes, these tracers can administer potent cytotoxic radiation to target diseased cells to induce cell death. With an ever-increasing prevalence of chronic diseases within an aging population[1], the global nuclear medicine market was valued at 8.42 billion USD in 2023 and is anticipated to grow to 29.35 billion USD by 2030.[2]

RPs can be categorized into two main groups: metal-based and nonmetal-based. Nonmetal-based RPs involve the incorporation of nonmetallic radionuclides, such as fluorine-18 (^{18}F, half-life = 109.8 min), nitrogen-13 (^{13}N, half-life = 9.965 min), oxygen-15 (^{15}O, half-life = 122.24 s), carbon-11 (^{11}C, half-life = 20.36 min), and iodine-123 (^{123}I, half-life = 13.22 h), into the radiotracer's structure through the formation of covalent bonds. Most of these isotopes have short half-lives ($t_{1/2}$; time it takes the radioactivity to decrease by half of its original value), necessitating rapid on-site production, chemistry, and quality control in clinics or nearby laboratories. Moreover, many of these nuclides decay in ways suitable only for imaging, limiting the applications of these RPs. In contrast, metallic radioisotopes (radiometals) offer a broader range of half-lives, spanning from minutes to years, and can undergo decay through modes that align with imaging and/or therapeutic applications.

The metal-based radiopharmaceutical category can be further divided into two further subcategories, metal-essential and metal-nonessential, differing by the role of the metal in the targeting process, as shown in **Figure 1.1A** and **1.1B**, respectively.[3] The field of nuclear medicine first started with small molecule metal-essential RPs where a metal, such as technetium-99m (^{99m}Tc; m refers to the metastable state), is coordinated by

ligands and it is the lipophilicity, size, and charge of the overall complex that dictates the *in vivo* biodistribution and targeting ability of the tracer.[4–6] For example, ^{99m}Tc bicisate (Neurolite, **Figure 1.1C**) is a neutral lipophilic complex that facilitates the visualization of cerebral blood flow.[7] If the complexing metal differed, the biodistribution, and thus use of this tracer, would be vastly different. Alternatively, with metal-nonessential RPs, also referred to as bifunctional chelator-based RPs (BFC-RPs, **Figure 1.1B**), tissue targeting is not achieved through the metal coordination environment, but rather through the attachment of a biological targeting vector, such as a peptide, antibody, or small molecule. This vector selectively binds to a cell biomarker that is overexpressed on diseased tissue compared to healthy tissue. As illustrated in **Figure 1.1B** and **1.1D**, via the use of a linker, the targeting vector is attached to the chelator which coordinates and contains the radiometal. Without the radiometal, this structure is often referred to as a bioconjugate. Once the radiometal is coordinated, the bioconjugate is considered radiolabeled and thus a RP. Although the chosen metal can affect the pharmacokinetics of the RP through the charge of the complex and chemical properties of the chelator required for complexation[8], this effect is less profound compared to metal-essential RPs. Unless otherwise noted, RPs mentioned from here on in will be BFC-RPs.

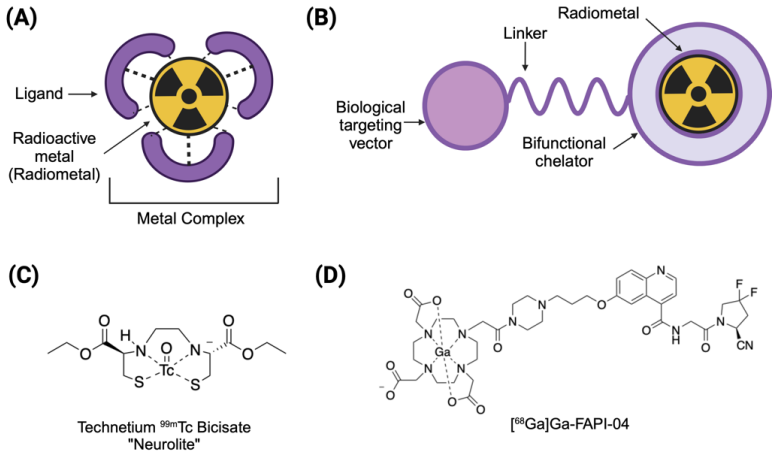

Figure 1.1. General structure of a (A) metal-essential radiopharmaceutical and a (B) metal-nonessential radiopharmaceutical. In a metal-essential radiopharmaceutical, ligand(s)/chelator(s) coordinate the radioactive metal to form a complex, as shown with (C) Neurolite, where the biodistribution is highly affected by the chemical properties of the radiometal. In a metal-nonessential radiopharmaceutical, as shown with (D) [^{68}Ga]Ga-FAPI-04, a bifunctional chelator coordinates the radiometal and is attached to a targeting vector that selectively binds to an overexpressed target on cells and has a greater influence over biodistribution than the radiometal.

The choice of radiometal determines the application of the RP and whether it will be used for imaging, therapy, or a combination of both. This is dependent on both the physical half-life and type of radioactive decay the metal undergoes. Radiometals that undergo positron emission (β^+ decay) or electron capture (EC) release gamma rays (indirectly or directly) that are compatible with medical imaging techniques such as positron emission tomography (PET) or single photon emission computed tomography (SPECT), respectively.[9] Alternatively, radiometals that emit alpha (α) particles, beta (β^-) particles, or Auger electrons (AE) are useful for radiopharmaceutical therapy (RPT) as these particles can induce DNA damage, oxidative stress, membrane damage, and other cytotoxic events that can result in cell death.[10–13]

Diagnostic isotopes are as crucial as therapeutic isotopes in nuclear medicine as they allow for the planning of personalized treatment plans and identification of targetable biomarkers on diseased cells with a minimally invasive approach. For imaging radionuclides, the obtained image quality is greatly affected by: (i) the photon energy (for SPECT) or positron energy (for PET), (ii) the percent abundance of the imaging gamma ray(s) emitted upon radioactive decay and, for positron emitting radiometals, (iii) the positron branching ratio, which refers to the fraction of these atoms that undergo positron decay over other decay modes. When a positron is emitted from the nucleus, depending on its energy, it travels a short distance before it collides with an electron.[14] Upon this collision, annihilation occurs, resulting in the production of two 511 keV gamma photons emitted 180 degrees apart from each other. PET scanners simultaneously detect these two coincident photons and determine the location of the positron annihilation event in the body allowing for visualization of the RP uptake.[14] To improve resolution, it is ideal that the positron travels only a short distance (several mm or less) before annihilation. Compared to PET, SPECT typically has lower spatial resolution as it relies on the emission of a single photon rather than a pair. However, PET imaging tends to be more expensive and less widely available and thus SPECT can be a more practical option. For sufficient SPECT sensitivity and resolution, the useful gamma energy range is typically 30 – 300 keV, with ideal energies between 100 – 250 keV.[15–17] For both PET and SPECT, to minimize the injected dose and patient scan time the positron branching ratio and the abundance of the emitted imageable photon should be high, respectively. **Figure 1.2** shows the differences between PET and SPECT imaging.

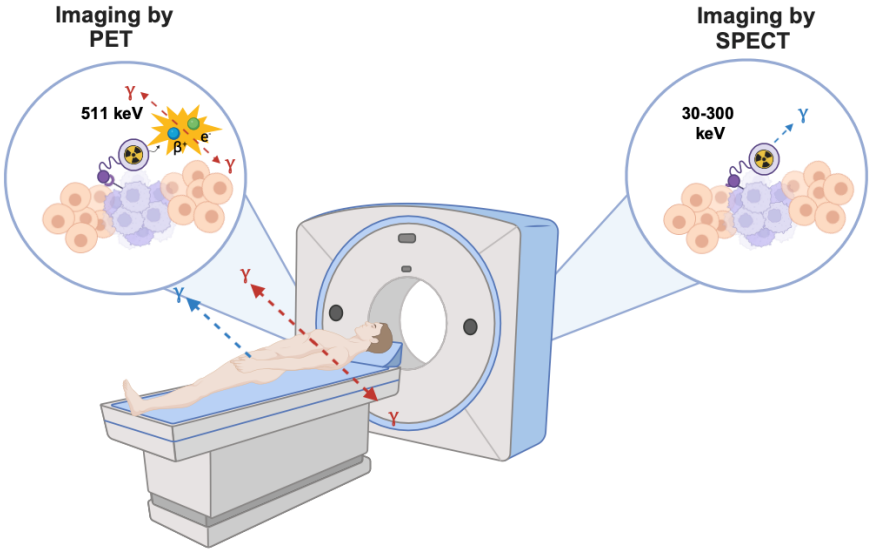

Figure 1.2. Differences between PET imaging, which relies of the simultaneous detection of two 511 keV photons emitted at an angle of 180° to each other post positron annihilation, and SPECT imaging, which detects singular photons.

For therapy, to maximize therapeutic efficacy with RPs, the chosen radiometal should emit a cytotoxic particle whose effective range, pathway, and linear energy transfer (LET; the amount of energy deposited per unit distance travelled), matches the tumour's size, mass, and radiosensitivity. Of the three types of therapeutic emissions employed in radiopharmaceutical therapy, β^- particles, emitted by radiometals undergoing beta decay, have the longest pathlength of up to 12 mm and a low LET (~0.2 keV/μm) making them most compatible for large tumours as they can deliver destructive radiation to several dozen cells in their path.[18] Currently, only ^{177}Lu ($t_{1/2}$ = 6.6 d), a beta-emitting radiometal, has been FDA-approved for use in targeted radiopharmaceutical therapy.[19–23] Due to a lower LET value, beta particles deposit their energy over a long range, leading to less damage per cell, reducing therapeutic effect, and potential off-target effects as surrounding healthy tissues may be affected.[24]

On the other hand, α particles, emitted from radiometals that undergo alpha decay, have a high LET (50 – 250 keV/mm) and shorter path length of approximately 5 – 10 cells, which can produce difficult to repair double stranded DNA breaks and other radiolytic damage to the cell, resulting in apoptosis while minimizing damage to neighbouring healthy cells.[25] As a result, alpha-emitting radiometals for RPT are starting to enter clinical use with dozens of clinical trials in place for a variety of cancer types including, but not

limited to, melanoma, neuroendocrine tumours (NETs), and prostate cancer.[26–29] Xofigo ([^{223}Ra]$RaCl_2$) is currently the only approved alpha-emitting metal-essential radiopharmaceutical intended for use in patients with castration-resistant prostate cancer with symptomatic bone metastases.[30] Although it is not directed to cancer cells using a selective targeting vector like BFC-RPs, ^{223}Ra ($t_{1/2}$ = 11.4 d) in its divalent cation form mimics calcium in the body and accumulates in areas of increased bone turnover, such as bone metastases, where it forms complexes with hydroxyapatite.[30] While Xofigo significantly improved median overall survival, 14 months versus 11.2 months in the placebo group, and enhances quality of life by reducing bone pain in patients with bone metastases, this RP lacks a selective targeting vector and can accumulate in healthy bone tissue, leading to an increased risk of fractures.[30] This emphasizes the need for selectivity, which can be achieved through the use of BFC-RPs.

Although promising, one of the major concerns around the use of alpha emitters for RPT is the recoil effect that occurs during alpha decay. When a high energy alpha particle is emitted from the nucleus, the atom experiences a significant kickback from the recoil force which can cause the radioactive atom to break out of the coordination complex of the chelator releasing the radiometal into the rest of the body which can cause undesirable side effects. The average recoil energy transferred to the daughter nuclide is around 100-200 keV whereas most chemical bonds have binding energies less than 10 eV.[31,32] It is ideal that these RPs are either rapidly internalized into the cell so that daughter radionuclides do not escape or that there are minimal alpha particles emitted in the decay scheme, although this can lead to a lower therapeutic response as there are less cytotoxic particles emitted to damage diseased cells.[33]

Auger electrons have a high LET of 4 – 26 keV/μm and have a short energy deposition range of less than one cell length and thus are most lethal when emitted near the cell nucleus and DNA.[34] AEs can cause double stand breaks in DNA, either by directly damaging DNA or by generating reactive oxygen species.[34] Despite limited clinical studies, early studies have shown promising results.[35–37]

Theranostic radiopharmaceuticals combine diagnostic and therapeutic radionuclides to form theranostic pairs to enable a personalized approach to medicine. Within the pair, the diagnostic component allows visualization of the radiopharmaceutical's uptake in diseased tissue. Based on the findings, if there is sufficient uptake, the

therapeutic component can be administered to facilitate treatment. In theory, this approach provides an opportunity to test the imaging drug prior to administering the therapeutic, allowing for the selection of the most suitable treatment for each patient. Although this approach has great promise, as shown by early clinical trials[29,38,39], the growth and expansion of theranostics is limited by the availability and purity of these medical radionuclides. The preparation of RPs, from isotope production to injection, is shown in **Figure 1.3**.

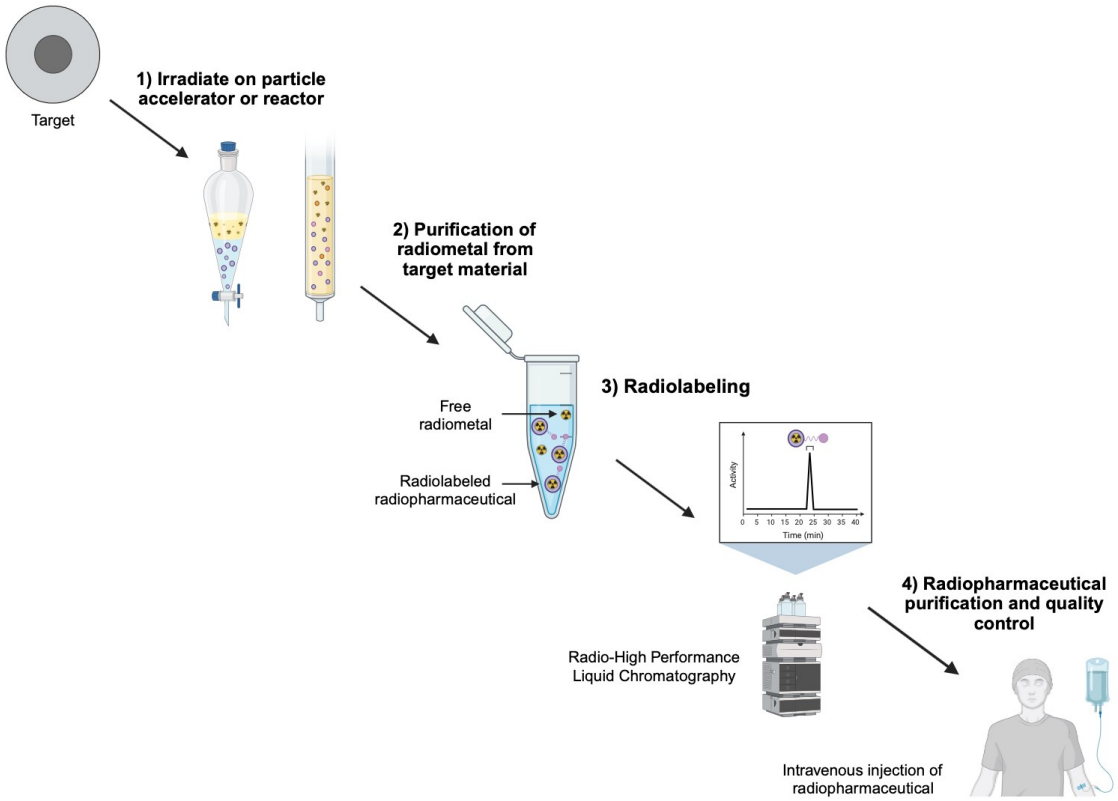

Figure 1.3. Typical stages of radiopharmaceutical production. 1) Target material is irradiated on a particle accelerator or nuclear reactor to produce the radiometal which then must further be 2) separated from the target material using purification techniques. Once purified, the desired bioconjugate is added to the radiometal solution and 3) radiolabeling occurs. 4) The radiopharmaceutical is then purified to remove any non-complexed radiometal and quality control is performed prior to intravenous injection.

Three measures of isotope purity that affect the radiolabeling, which refers to the complexation of a radiometal by a chelator, include chemical purity, radionuclidic purity, and specific activity. Chemical purity refers to the extent of interfering stable chemical impurities (ex: Fe, Ca, etc.) in solution whereas radionuclidic purity refers to the fraction

of the desired radionuclide in a sample relative to all other present radionuclides. Specific activity (SA) refers to the amount of radioactivity per unit mass of the element. For all three measures of purity, it is desirable for the purity to be as high as possible to achieve high radiolabeling yields to improve patient outcomes, as further discussed in the later sections.

To meet the ever-increasing clinical demand and unlock the complete potential of theranostics, continuous improvement of the structure of existing drug designs in addition to the production and development of new radionuclides with diverse therapy or imaging capabilities, is essential. As each component of a BFC-RP is vital to the success of nuclear medicine, this chapter examines the individual components and the optimization required for each to develop a safe and effective BFC-RP. A particular emphasis is placed on covering the fundamentals behind the current radiometal production and purification methods, their limitations, and the necessary advancements required to increase global access to these isotopes as isotope availability is often thought of as the bottleneck point for the future progress of nuclear medicine.

1.2. Chelators

In the context of nuclear medicine, the role of the chelator is to bind and form a stable complex with a radioactive metal ion. A stable complex is required so that upon injection into patients, the radioactivity can be delivered to the tumour site without release of the free radiometal into the body, which could otherwise accumulate in off-target tissues, resulting in undesirable side effects.

The ideal properties of a chelator are that it is able to rapidly and quantitatively complex radiometals under mild conditions (e.g., ambient temperature, <60 min, close to physiological pH) in sub-micromolar concentrations with high thermodynamic stability, kinetic inertness, and high selectivity towards a desired radiometal.[15,40] Thermodynamic stability, measured using potentiometric titration or UV-Vis spectroscopy to yield $\log K_{ML}$ and pM values, quantifies the binding affinity a chelator has towards a select metal where higher values indicate a stronger affinity.[15] Of greater importance than thermodynamic stability is the kinetic inertness of the radiometal complex *in vivo*. Most BFC-RPs are injected intravenously and thus directly enter the bloodstream and circulate throughout the body. In the plasma, there are numerous metal-binding proteins that can compete with the chelator for the radiometal and thus the chelator must be resistant to transchelation.[41–43]

Kinetic inertness is tested *in vitro* with competition assays of radiolabeled complexes incubated in serum to quantify any transchelation or demetallation that may occur in the presence of these proteins.[15] Rapid radiolabeling, which refers to the process by which the chelator complexes the radiometal, under mild, ambient conditions is preferable for heat and pH sensitive biological targeting vectors, such as antibodies, to prevent degradation.

The physical properties of each metal dictate its coordination preferences and to form the most stable complexes, the design of the chelator in a radiopharmaceutical must be tailored to these preferences. The hard-soft acid-base (HSAB) principle provides a framework for understanding metal-chelate complex stability by classifying Lewis acids and bases as either hard, soft, or intermediate based on their properties. Hard Lewis acids and bases have small ionic radii, a high oxidation state, and low polarizability whereas soft Lewis acids and bases have larger ionic radii, low oxidation state, and high polarizability, with intermediate acids and bases falling in between. According to the HSAB principle, hard acids form the most stable complexes with hard bases and soft acids form the most stable complexes with soft bases. As metals act as Lewis acids, chelators should contain Lewis base electron donor groups that complement the metal's hard or soft nature to produce thermodynamically stable complexes that remain intact under physiological conditions. Examples of hard, soft, and intermediate Lewis acids and bases are shown in **Figure 1.4**.

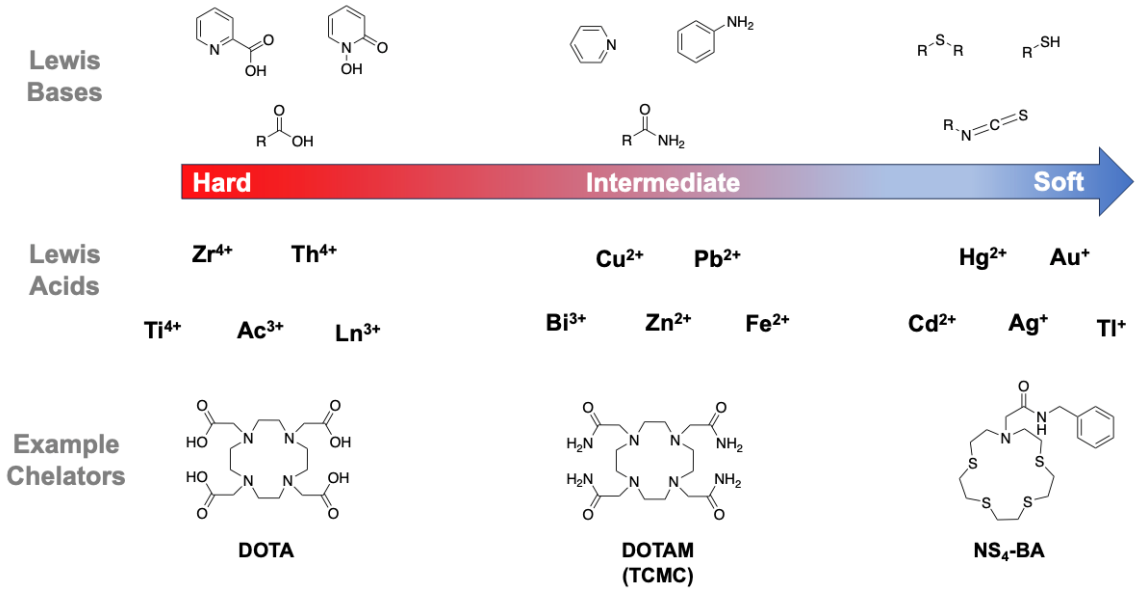

Figure 1.4. Classification of Lewis acids and bases and examples of their incorporation into chelators.

Bifunctional chelators play two roles in BFC-RPs as they coordinate the radiometal and provide an attachment site for the biological targeting vector that give these radiopharmaceuticals their advanced selectivity. To enable this attachment, the BFC must contain a reactive functional group, referred to herein as the bifunctional handle. As most biomolecules contain primary amines and thiols, common bioconjugation strategies involve peptide coupling reactions yielding amide bonds via the use of carboxylic acids or activated esters, isothiocyanates yielding thiourea bonds, or maleimides forming thioether bonds as shown in **Figure 1.5**.[40,44] In pre-targeting approaches, biorthogonal reactions are employed where the biological targeting vector is chemically modified (e.g. with a transcyclooctene group) and administered first. A radiolabeled BFC bearing a complementary reactive group (e.g. a tetrazine) is then introduced, binding selectively *in vivo* to the functional group on the targeting vector and thus localizing the radioactivity at the diseased tissue.[45–48] Ultimately, the chosen conjugation strategy must produce a covalent bond that remains stable under physiological conditions, and attaching the chelator must not compromise the targeting vector's functionality of specificity.

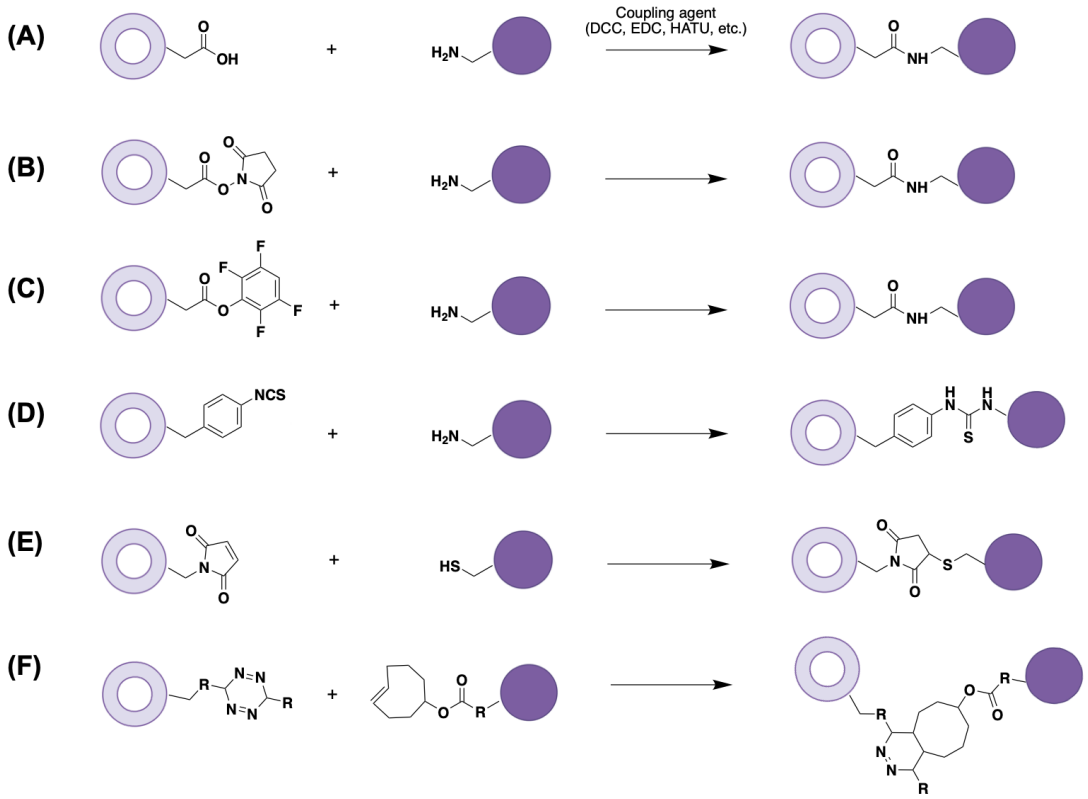

Figure 1.5. Examples of bioconjugation reactions and techniques used for nuclear medicine applications: Peptide coupling of a carboxylic acid and primary amine using (A) a coupling agent and activated ester (B) N-hydroxysuccinimide (NHS) and (C) tetrafluorophenyl (TFP) groups to form amide bonds; (D) coupling of an isothiocyanate to a primary amine to form a thiourea bond; (E) coupling of a maleimide to a thiol to form a thioether bond; (F) strain-promoted Inverse Electron Demand Diels-Alder reaction between a tetrazine and transcyclooctene.

Bifunctional chelators are generally more challenging to synthesize than their non-bifunctional counterparts. Consequently, non-bifunctional chelators are typically prepared first and evaluated for selectivity and stability and if the results are promising, the synthesis of bifunctional analogues is pursued. The major synthetic challenge with BFCs is incorporating the bifunctional handle at a position that will not disrupt the original coordination environment, which can otherwise compromise both radiolabeling efficiency and stability. Common attachment methods include functionalizing the chelator's backbone or replacing or modifying the donor arm with reactive functional groups, with examples shown in **Figure 1.6** for DOTA[49], the most commonly used macrocyclic chelator for BFC-RPs in nuclear medicine. However, replacing a donor arm may change the coordination number, and thus environment. Even if the donor arm remains in place but

is modified (e.g. DOTAGA-NHS-ester[50]), steric hindrance, especially after coupling to the targeting vector, may diminish the group's ability to coordinate the metal effectively. Similarly, amide bond formation, from either activated esters (e.g. DOTA-TFP[51]) or directly from a DOTA carboxylic acid group, may allow coordination from the amide carbonyl group, but likely at a reduced capacity.[40,52] Consequently, functionalizing the backbone, as shown for *p*-SCN-Bn-DOTA[49,53], is often preferable because it preserves the coordination number but this route tends to be more synthetically challenging, and thus costly, compared to other routes.

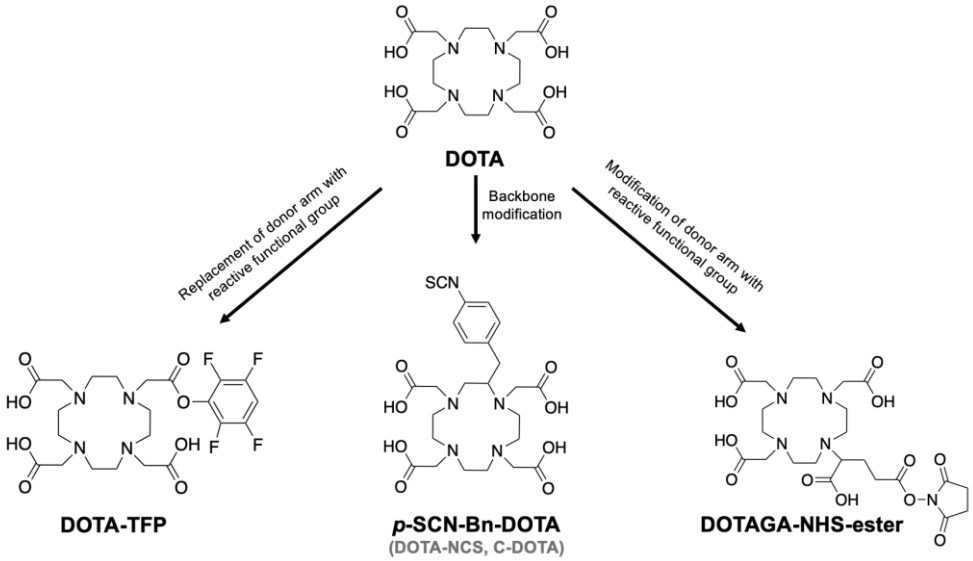

Figure 1.6. Production of bifunctional chelators via replacement[51] and modification[50] of donor arms[51] and functionalization of macrocyclic backbones.[49,53]

Chelators can significantly influence the biodistribution of BFC-RPs *in vivo*, but the extent of this influence depends largely on the type of biological targeting vector being used. A bulky protein, such as a full-size antibody, may overshadow the effects of the chelator, while smaller targeting vectors (e.g., peptides or small molecules) can be more sensitive to variations in chelator structure. Consequently, the choice of both the chelator and targeting vector is guided by the specific disease and molecular target, ensuring that any modifications introduced for radiometal binding do not compromise the targeting vector's ability to localize precisely to cancer cells.

1.3. Biological Targeting Vectors

Biological targeting vectors are the molecules responsible for selectively directing and delivering a bifunctional chelator-based radiopharmaceutical to cancer cells, reducing side effects in surrounding healthy tissues. The choice of targeting vector is essential in designing BFC-RPs as it affects both the pharmacokinetics, how quickly the radiopharmaceutical clears from the bloodstream, and the biological specificity, how effectively and selectively the radiopharmaceutical binds to the target, which further dictates, as described in later sections, the choice of radiometal employed for diagnostic or therapeutic purposes. Three common types of targeting vectors frequently employed in nuclear medicine include antibodies, peptides, and small molecules with each type offering unique advantages and challenges.

1.3.1. Antibodies

Antibodies bind with high affinity and specificity to antigens overexpressed on tumour cells. Fully intact antibodies, such as monoclonal antibodies (mAbs), typically have relatively large molecular weights (~150 kDa) and long circulation times (days) in the bloodstream. This slow clearance can be beneficial for maximizing tumour uptake, but it also necessitates the use of radiometals with longer half-lives so that adequate signal can be detected for imaging and so that sufficient irradiation occurs at the tumour site for therapy. If a radiometal with too short of a half-life is used, the tumour won't be able to be imaged and the majority of the radioactivity will decay before it reaches the tumour, causing irradiation of off-target tissues. Common radionuclides employed for antibody-based radiopharmaceuticals include ^{89}Zr ($t_{1/2}$ = 78.4 h) for immuno-PET imaging, as well as ^{177}Lu ($t_{1/2}$ = 6.7 d) and ^{225}Ac ($t_{1/2}$ = 9.9 d) for therapeutic applications.

Although fully intact antibodies offer unmatched selectivity and affinity towards their antigens, their extended circulation time in the blood exposes blood-rich tissues, like bone marrow, to prolonged radiation. As bone marrow is highly vascularized and contains rapidly dividing precursor cells, it is very sensitive to radiation damage that can result in myelosuppression, reducing blood cell production.[54] Bone marrow toxicity is often the dose-limiting factor in radioimmunotherapy with intact antibodies.[54,55] The use of engineered antibody fragments and modifications maintain selectivity while reducing bone marrow toxicity primarily by shortening systemic circulation time and thus minimizing non-

specific radiation dose to blood-rich tissues. Smaller fragments including, but not limited to, antigen-binding fragments (Fab), single-chain variable fragments (scFv), and nanobodies are cleared from the bloodstream more quickly, thus reducing off-target radiation exposure while still allowing sufficient time to accumulate in the tumour.[56] Additionally, pre-targeting approaches in radioimmunotherapy separate the tumour-targeting step from the radioactive payload step. This first allows for sufficient tumour uptake of the targeting vector to occur before administration of the radiolabeled bifunctional chelator, allowing for greater tolerance of higher doses that could improve therapeutic outcomes with radioimmunotherapy.[57,58]

1.3.2. Peptides

Compared to antibody-based BFC-RPs, peptide-based BFC-RPs typically accumulate at tumours more rapidly with a more uniform intratumoural distribution combined with rapid renal excretion. These properties improve the tumour-to-background contrast, leading to higher-quality diagnostic images.[59] Peptides can also be chemically synthesized, making them easier and less expensive to produce or modify compared to antibodies. However, their rapid renal clearance often makes the kidneys the site of dose-limiting toxicity and peptide-based BFC-RPs tend to have a lower overall tumour uptake, which may require more frequent dosing in clinical applications to achieve a sufficient therapeutic effect.[60] Moreover, native peptides generally have short biological half-lives due to rapid proteolysis by enzymes in the bloodstream, limiting their utility in nuclear medicine. To overcome this, research efforts often focus on prolonging the biological half-life through strategies such as peptide cyclization, the incorporation of unnatural amino acids, addition of albumin-binding moieties, or C- or N-terminus modifications to ensure that peptide-based BFC-RPs remain in circulation long enough to reach their target and be effective for imaging or therapeutic applications.[61–63]

Due to their shorter biological half-lives, radiometals with shorter half-lives, such as ^{68}Ga ($t_{1/2}$ = 68 min) or ^{64}Cu ($t_{1/2}$ = 12.7 h) for imaging and ^{212}Pb ($t_{1/2}$ = 10.6 h) for therapy, are more compatible with peptide-based BFC-RPs. These shorter half-lives are preferrable as they align with the time scale of peptide residency in the tumour tissue, reducing the likelihood of off-target effects that may occur if the half-life is long as this could result in irradiation of healthy organs and tissues during the excretion process. However, if the RP is internalized or the tumour retention period is sufficiently long,

radionuclides with longer half-lives could offer the benefit of prolonged irradiation and therapeutic effects.

1.3.3. Small Molecules

Small molecules used in nuclear medicine are often inhibitors that bind enzymes or receptors overexpressed in cancer cells. This class of BFC-RPs often exhibits very fast pharmacokinetics as their often hydrophilic nature enables rapid tumour penetration but also rapid systemic clearance. Similarly to peptide-based BFC-RPs, small molecule-based counterparts are commonly eliminated renally, making the kidneys the dose limiting organ and thus research efforts often focus on reducing nephrotoxicity while increasing tumour retention.[64] Two common strategies to address the challenges of working with small molecule-based BFC-RPs include a bivalent ligand approach and lipidization.[64] With the bivalent ligand approach, two small molecule pharmacophores are linked together and incorporated into the BFC-RP and the collaborative binding of these two groups enhances binding affinity and thus tumour retention.[64] Lipidization is a chemical approach that involves the attachment of a lipid group to increase the lipophilic nature of the molecule which can enhance permeability across cell membranes and increase circulation time, allowing for greater tumour uptake.[64]

Radionuclides with short half-lives are preferable to match the tumour residency time of the BFC-RP, however, significant therapeutic outcomes have been also observed when using nuclides with longer half-lives, as observed for [^{225}Ac]Ac-PSMA-617 and [^{177}Lu]Lu-PSMA-617, a small molecule-based BFC-RP utilizing DOTA and ^{225}Ac or ^{177}Lu to target prostate-specific membrane antigen overexpressed in prostate cancer.[22,23,39,65] The chemical structures of select peptide and small molecule-based BFC-RPs undergoing clinical trials is shown in **Figure 1.7**.

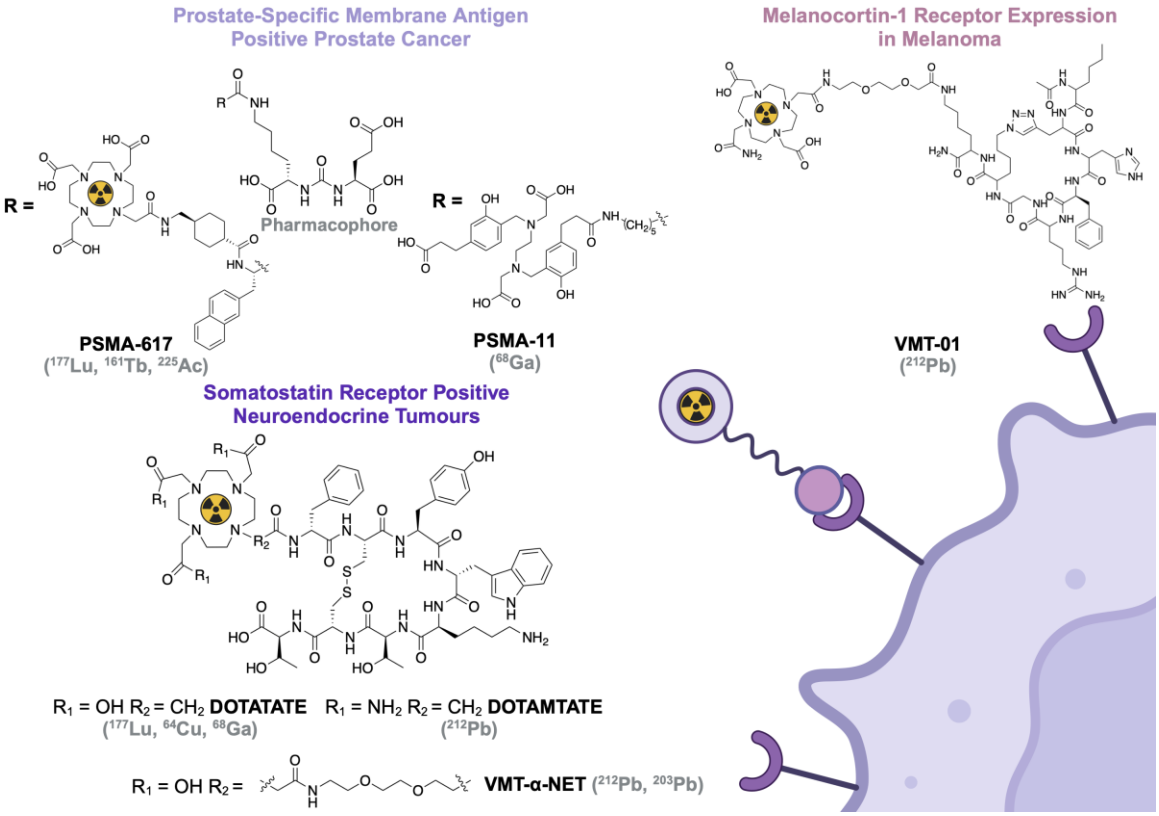

Figure 1.7. Structures and radiometals of select approved and in clinical trials small molecule- and peptide-based BFC-RPs.

1.4. Radiometals

The choice of radiometal profoundly influences the application and success of BFC-RPs. Its decay mode, including Auger electron and beta/alpha particle emission for therapy or gamma/positron emission for imaging, dictates whether the agent is used diagnostically or therapeutically all while its half-life must be compatible with the pharmacokinetics of the targeting vector to ensure optimal tumour uptake and minimal background signal. Although much attention in nuclear medicine focuses on designing the ideal chelator or targeting vector, it is equally critical to recognize that these innovations depend on a reliable supply of radionuclides. Without continued advances in isotope production methods and purification technologies, many promising radiometals would remain impractical for clinical use, limiting the future potential of targeted radionuclide therapy. Consequently, understanding the fundamentals of radionuclide production, and the challenges and costs associated in scaling up, is essential for the ongoing development and success of nuclear medicine.

1.4.1. Production of Metallic Medical Isotopes

While few medical radionuclides, such as ^{212}Pb ($t_{1/2}$ = 10.6 h), may occur naturally as part of the decay chain of long-lived parent nuclides, the production of medical radionuclides in clinically significant quantities requires the use of particle accelerators or nuclear reactors. Using these instruments, high-energy protons, neutrons, alpha particles, or other sub-atomic particles are used to induce nuclear reactions converting a target atomic nucleus into an unstable (radioactive) state that may, if it satisfies certain criteria, be useful for medicinal purposes. In simple terms, the production of both reactor and accelerator-produced isotopes occurs via collision of a high energy particle with a target nucleus to result in the production of a radioactive metal atom.

Even if a nuclide has ideal properties for imaging and/or therapy, if it cannot be produced at clinically significant quantities, the use of this radiometal will be limited. The cost of the target material, which is highly affected by whether or not it must be isotopically enriched, as well as the cross section (σ, the probability that a specific nuclear reaction will occur at a specific particle energy), accessibility to the correct instrument, and the simplicity and capabilities of the purification method to separate the desired isotope from the target material are all factors that need to be taken into consideration before investment in the development of a medical radionuclide. Additionally, if a radionuclide cannot be made on site at the clinic or a facility nearby and if the half-life is too short (minutes to a few hours), it may decay by the time it is purified from the target or parent material, incorporated into a tracer, and sent to the clinic (Process in **Figure 1.3**). On the other hand, if the half-life is too long (weeks to months), the isotope may not significantly decay to release enough cytotoxic particles to observe a therapeutic effect *in vivo,* or it may remain in the body and continue to irradiate the patient for an extended period of time, causing unnecessary dose. Therefore, it is recommended, if possible, to match the radiological half-life of the nuclide to the biological half-life of the radiopharmaceutical.[66]

To better understand the requirements of production, this section will explain the fundamental principles behind the use of particle accelerators and reactors for production of medical radionuclides, targetry requirements, isotope generators, and limitations of each method will be discussed. **Table 1.1** shows a summary of discussed radiometals, their production methods, and their applicable use in nuclear medicine.

Table 1.1. Production methods and clinical applications of discussed radiometals.

Isotope	Half Life	Production Method	Clinical Applicability
^{64}Cu	12.7 h	*Cyclotron:* ^{64}Ni (p,n) ^{64}Cu	PET Imaging (17.9% positron branching ratio)
^{67}Cu	61.8 h	*Linac:* ^{68}Zn (γ,p) ^{67}Cu	Therapy (β^- emission)
^{68}Ga	68 min	*Cyclotron:* ^{68}Zn (p,n) ^{68}Ga *Generator:* ^{68}Ge/^{68}Ga	PET Imaging (89% positron branching ratio)
^{99}Mo	66 h	*Reactor:* ^{235}U (n,f) ^{99}Mo *Linac:* ^{100}Mo (γ,n) ^{99}Mo	Production of ^{99m}Tc
^{99m}Tc	6 h	*Generator:* ^{99}Mo/^{99m}Tc *Cyclotron:* ^{100}Mo (p,2n) ^{99m}Tc	SPECT Imaging (140.5 keV photon at 89% abundance)
^{119}Sb	38.2 h	*Cyclotron:* ^{119}Sn (p,n) ^{119}Sb	Therapy (AE emission)
^{155}Tb	5.3 d	*Cyclotron:* ^{155}Gd (p,n) ^{155}Tb	SPECT Imaging (82 keV and 105 keV photons with abundances of 32% and 25%, respectively)
^{161}Tb	6.9 d	*Reactor:* ^{161}Gd (n,γ) ^{161}Tb	Therapy (β^- and AE emission)
^{165}Er	10.4 h	*Cyclotron:* ^{165}Ho (p,n) ^{165}Er	Therapy (AE emission)
^{177}Lu	6.7 d	*Reactor:* ^{176}Lu (n,γ) ^{177}Lu ^{176}Yb (n,γ) ^{177}Yb$\rightarrow$^{177}Lu	Therapy (β^- emission)
^{203}Pb	51.9 h	*Cyclotron:* ^{203}Tl (p,n) ^{203}Pb ^{205}Tl (p,3n) ^{203}Pb	SPECT Imaging (279 keV photon at 81% abundance)
^{212}Pb	10.6 h	*Generator:* ^{228}Th/^{212}Pb, ^{224}Ra/^{212}Pb	Therapy (α and β^- emission)
^{225}Ra	14.9 d	*Linac:* ^{226}Ra (γ,n) ^{225}Ra *Cyclotron:* ^{232}Th (p,x) ^{225}Ra *Generator:* ^{229}Th/^{225}Ra	Therapy (α and β^- emission)
^{225}Ac	9.9 d	*Cyclotron:* ^{226}Ra (p,2n) ^{225}Ac ^{232}Th (p,x) ^{225}Ac *Generator:* ^{229}Th/^{225}Ac, ^{225}Ra/^{225}Ac	Therapy (α and β^- emission)

It is important to note that during irradiation, only a small fraction, often micrograms to nanograms, of the target material will be converted into the radiometal. However, these often "sub-microgram" masses of nuclide can correspond to several patient doses as radioactivity is measured in units of Becquerel (Bq = 1 disintegration per second) or non-SI units of Curie (1 Ci = 3.7×10^{10} Bq), which can be further converted to number of atoms and thus mass via **Equation 1.1** where A is equal to the activity (Bq), λ is the unique decay constant of the radioisotope ($\lambda = \frac{ln2}{t_{1/2}}$), and N is the number of atoms.

$$A = \lambda N \qquad \textbf{Equation 1.1}$$

1.4.1.1. Nuclear Reactions

Similar to how chemical reactions alter associations of electrons between atoms, nuclear reactions modify the association of nucleons via a binary collision. Upon the collision of a projectile with a target atom, there are several types of possible reaction outcomes. The nucleus may remain unchanged (elastic scattering), be excited to a higher energy state (inelastic scattering), or a new nucleus is formed as nucleons are exchanged or fused (nuclear transmutation).[67] To describe the nature of the target atom, projectile, and products involved in the reactions, they are written in either longhand (**Equation 1.2**) or shorthand (**Equation 1.3**) notation:

$$A + a \rightarrow b + B \qquad \textbf{Equation 1.2}$$

Target nucleus + projectile particle $\rightarrow$ Product nucleus + ejected particle

Example: $^{197}_{79}Au + {}^{1}_{1}p \rightarrow {}^{1}_{0}n + {}^{197}_{80}Hg$

A(a,b)B **Equation 1.3**

Target nucleus (projectile particle, ejected particle) Product nucleus

Example: ^{197}Au(p,n)^{197}Hg

Nuclear reactions must obey the laws of conservation of mass, energy, momentum, charge, and nuclear spin. The mass-energy equivalence equation (**Equation 1.4**) explains the relationship between mass and energy in nuclear reactions as every time there is a change in energy, there is also a change in mass and vice versa. Units

commonly used to quantify energy in a nuclear reaction are joules (J) and megaelectronvolts (MeV) where 1.6022×10^{-13} J = 1 MeV. A proton is 1.00728 atomic mass unit (amu) while a neutron is 1.00866 amu. As per **Equation 1.4**, the energy of 1 amu is 1.4924×10^{-10} J, or 931.5 MeV.

$$E = mc^2 \qquad \textbf{Equation 1.4}$$

The energetics of a nuclear reaction are given by the Q value, which is equal to the difference in the masses (amu) of the reactants and the products of a nuclear reaction, as shown in **Equation 1.5** for the nuclear reaction A(a,b)B. The Q value is representative of the change in kinetic energy during the reaction. If the kinetic energy of the products is higher than that of the reactants, energy is released, the Q value is positive, and the reaction is denoted as exoergic. If the kinetic energy of the products is lower than the reactants, energy is absorbed and the Q value is negative and thus is endoergic; for an endoergic reaction to proceed, energy input is required.

$$Q\ (\text{MeV}) = 931.5\ \Delta M\ (\text{amu}) \qquad \textbf{Equation 1.5}$$

$$\text{Where } \Delta M = (M_{target} + M_{projectile}) - (M_{product} + M_{ejectile})$$

For nuclear reactions to occur with charged particle projectiles (ex: protons, alpha particles, etc.), the Coulomb barrier must be overcome. As both the target nucleus and projectile have a positive charge, they will repel each other unless the projectile has enough kinetic energy to overcome this barrier and then experience the attractive nuclear force. This energy can be supplied by high energy particle accelerators, including cyclotrons. Neutrons, due to their neutral charge, do not face the challenge of the Coulomb barrier. However, charged particles and neutrons both face the centrifugal barrier, which considers that some of the energy of the projectile will be rotational energy and that angular momentum must be conserved for noncentral collisions. The centrifugal and Coulomb barriers are both kinetic factors and can be thought of to affect the nuclear reaction rate in the same way that the transition state energy does for a chemical reaction. The threshold energy is the minimum energy that a particle must possess for an endoergic reaction to occur.

A nuclear cross section (σ) describes the probability of a nuclear reaction to occur. Excitation functions, shown in **Figure 1.8**, plot cross sections, with units in barns (b),

equivalent to 10^{-24} cm^2, as a function of projectile energy. Excitation functions allow for the identification of a projectile energy that will both maximize production of the desired isotope while also minimizing the production of radionuclidic impurities as the excitation functions can show competing reaction channels that can occur over the set energy range with the same target nucleus. For example, in **Figure 1.8**, if one desires to produce ^{203}Pb with a ^{205}Tl target, it is most desirable to use proton energies between 22 – 30 MeV as here, the cross section for the ^{205}Tl (p,3n) ^{203}Pb reaction is high with primarily ^{201}Pb co-produced, but to a lesser extent. If one was to use proton energies of 15 – 20 MeV with the ^{205}Tl target, nearly all the produced activity would be ^{204m}Pb as the cross section for the ^{205}Tl (p,2n) ^{204m}Pb reaction has a maximum probability at this energy, while the probability of the desirable ^{205}Tl (p,3n) ^{203}Pb reaction is low and thus this energy range should not be used. It can also be observed in **Figure 1.8** that reactions that eject more nucleons (e.g. ^{203}Tl (p,3n) ^{201}Pb, σ_{max} = 1200.4 mb at 27 MeV[68]) have their maximum cross sections at higher energies compared to nuclear reactions that eject fewer nucleons (e.g. ^{203}Tl (p,n) ^{203}Pb, σ_{max} = 37.0 mb at 11.0 MeV[69]). This is because for more nucleons to be ejected, a greater nuclear binding energy must be overcome. On high energy (>100 MeV) cyclotrons, spallation reactions may occur where a high energy particle bombards a target nucleus and essentially results in its disintegration as the nucleus breaks up into several constituents, which can include protons, neutrons, and other composite particles.

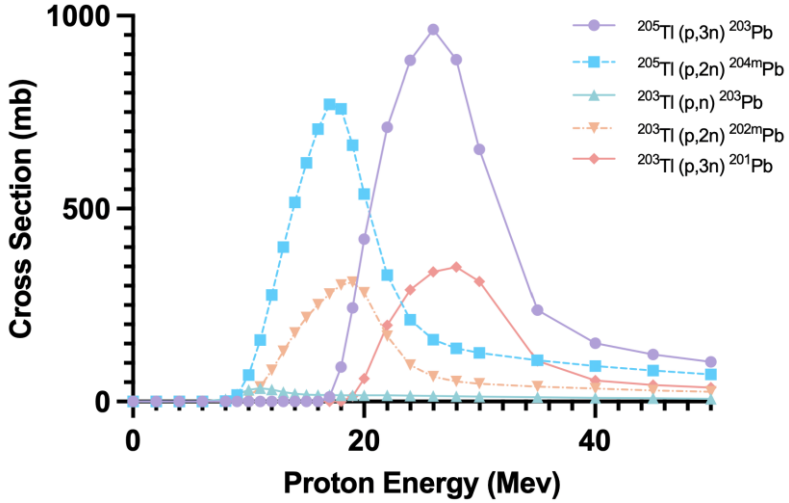

Figure 1.8. Excitation function of proton-induced reactions on natural thallium (Tl) target material; ^{203}Tl = 29.5% abundance, ^{205}Tl = 70.5% abundance.[69]

1.4.1.2. Cyclotrons

Cyclotrons are particle accelerators that use a rapidly alternating electric field and a constant magnetic field to accelerate charged particles along a spiral path. As shown in **Figure 1.9**, they consist of two oppositely charged, semicircular metal cylinders, called dees, placed in a vacuum chamber between the poles of an electromagnet. An ion source injects charged particles into the gap between the dees, where they are accelerated towards the dee of opposite charge by the electric field.[70] Once in the dee, the magnetic field causes the particles to follow a spiral path.[70] When the particles cross back into the gap, the electric field accelerates them again, causing the particles to gain more kinetic energy and travel in larger spiral paths with each cycle.[70] Eventually, the particles exit the cyclotron with a designated energy, dependent on the parameters of the cyclotron, and collide with a target to produce radionuclides. As further discussed later in this section, targets can be solid, liquid, or gas, which can limit the maximum current of particles that can be applied.

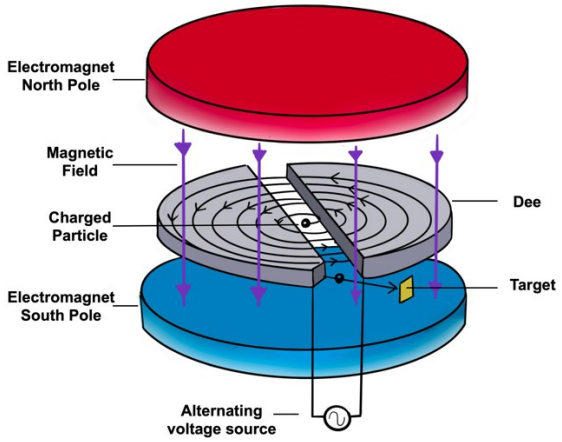

Figure 1.9. The components of a cyclotron.

Cyclotrons are one of the most widely used accelerators in nuclear medicine for isotope production mainly due to the ability to install cyclotrons in hospitals or research facilities which allows for production and use of short-lived isotopes. Cyclotrons are also advantageous as they can produce isotopes with high specific activity as the product radionuclide is often a different element than that of the target material, which also allows for easier separation, as further discussed in **Section 1.4.2**. The energy of the cyclotron's particles can in many models be adjusted to match the peak cross section of the desired reaction, allowing for maximal production of different isotopes.

1.4.1.3. Linear Particle Accelerators "*Linacs*"

Like cyclotrons, linear particle accelerators use a radio frequency alternating voltage source to accelerate electrons.[71] Connected to this voltage source are cylindrical electrodes, called drift tubes, placed in a vacuum chamber and coupled to an ion source.[71] Electrons are accelerated towards a drift tube of opposite charge and maintain a constant velocity inside it.[71] At the end of the tube, the voltage changes, repelling the particles from the exit electrode and attracting them to the next drift tube, increasing their energy.[71,72] This process repeats, with later drift tubes being longer to match the particles' increased velocity at this point. Strong focusing magnets keep the particles on their path, directing them towards a target, also called a converter, of high atomic number material, like tantalum or tungsten, at the end.[71] Upon collision, high-energy X-rays (Bremsstrahlung photons) or electrons are produced.[73] These photons can then further hit another target, of which the material depends on the desired product isotope, to produce radionuclides through photoproton (γ,p) and photoneutron (γ,n) reactions. **Figure 1.10** shows the components of a linear accelerator.

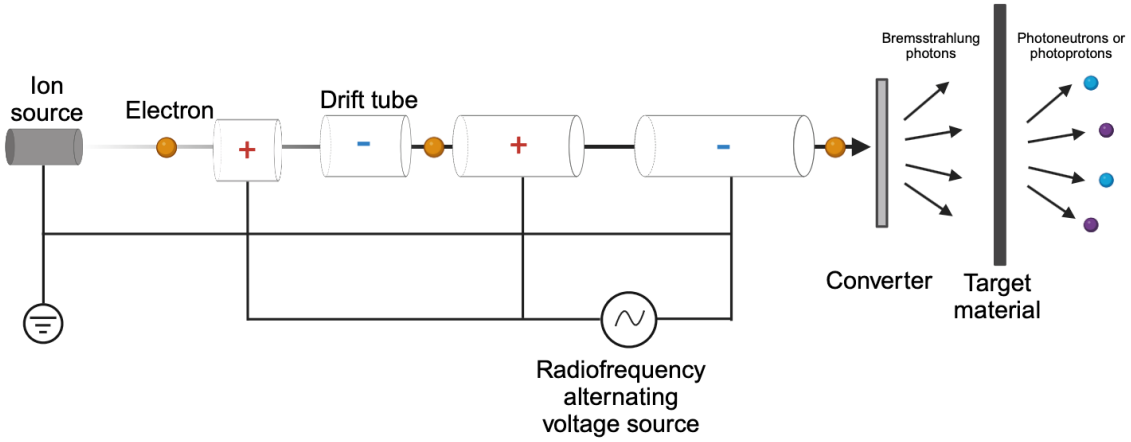

Figure 1.10. Components of a linear accelerator.

One of the benefits of using linear accelerators is that there are fewer possible reaction channels, and thus fewer radionuclidic impurities will be co-produced.[74] However, this can also restrict the possible isotopes that can be produced via this method. Additionally, a challenge of using this method is that photonuclear reactions tend to have smaller cross sections compared to nuclear reactions, limiting the yield of the desired isotope, although this does not apply to all isotopes.[75,76] ^{99}Mo ($t_{1/2}$ = 66 h), the parent of one of the most highly used diagnostic isotopes in nuclear medicine ^{99m}Tc ($t_{1/2}$ = 6 h), and

^{225}Ra; ($t_{1/2}$ = 14.9 d), the parent isotope of the powerful therapeutic isotope ^{225}Ac ($t_{1/2}$ = 9.9 d), can be produced using γ,n reactions on linear accelerators via the ^{100}Mo (γ,n) ^{99}Mo[79,80] and ^{226}Ra (γ,n) ^{225}Ra reaction[79,80], respectively. A discussion on these generators is given in **Section 1.4.1.6**.

Although medical nuclides can be produced directly via γ,n reactions, such as in the case of the ^{65}Cu(γ,n)^{64}Cu reaction[81], it is preferable to produce isotopes via γ,p reactions to ease separation and increase specific activity. This is because in the case of γ,n reactions both the target and product nuclide belong to the same chemical element and thus cannot be chemically separated from each other during the purification process, resulting in low SA. When targets are irradiated on accelerators, only a small fraction, typically micrograms to nanograms, of the target material undergoes nuclear reactions to produce the desired radiometal. As a result, there are typically thousands of times more of the target nuclei compared to product nuclei. If both are the same element, chelators will not distinguish between the isotopes, resulting in reduced radiolabeling yields and low specific activity of the radiotracer. On the other hand, γ,p reactions cause a change in the atomic number from target to product nuclide, thus resulting in different chemical properties, which can more easily be separated from one another. For example, ^{67}Cu can be produced in Curie quantities via irradiation on a 40 MeV linac using ^{68}Zn-enriched targets via the more desirable ^{68}Zn (γ,p) ^{67}Cu reaction with a high radionuclidic purity (>99%) and this has allowed for recent commercial production of this nuclide.[82]

1.4.1.4. Nuclear Reactors

Through neutron capture or neutron-induced fission, nuclear reactors produce neutron-rich isotopes that typically decay via β^- decay as they are neutron-rich. Although most nuclear reactors are used for power generation, research reactors can be used to produce medical isotopes by exposing different target materials to the neutron flux of the reactor core to produce significant quantities of these isotopes.[67]

Nuclear reactors initiate and control fission nuclear chain reactions that start when a heavy fissile nucleus, commonly ^{235}U, captures a neutron and splits into two or more lighter nuclei and in this process, releases kinetic energy, gamma radiation, and on average 2.5 new neutrons[67]. These new neutrons can then go on to induce fission in other ^{235}U nuclei, leading to the production of even more neutrons, resulting in a chain reaction,

as shown in **Figure 1.11**. In the reactor, this reaction is controlled by a moderator, typically water, used to slow down the released high energy neutrons to result in more fission, and control rods, which are made of neutron-absorbing material (ex: Boron) and are inserted or withdrawn to control the rate of the reaction.[67] Neutron reflectors are also added to reduce loss of neutrons from the core, which will allow for a greater production of medical isotopes which is one of the main purposes of research reactors. This results in an environment with a high neutron flux. When target nuclei are placed in this flux, nuclear reactions can be induced to produce new radionuclides.

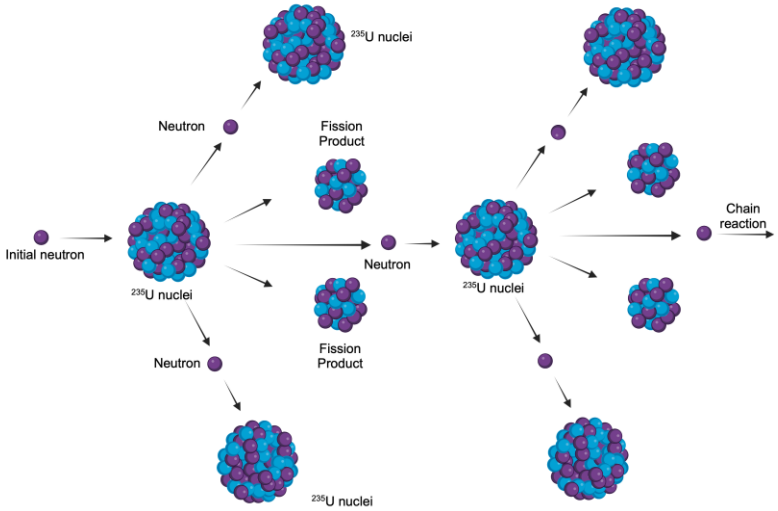

Figure 1.11. Depiction of the chain reaction that occurs in nuclear reactors. An initial neutron is captured by a nucleus of ^{235}U, which subsequently splits into two or more lighter nuclei (fission products) releasing energy and on average 2.5 new neutrons. These newly generated neutrons can be captured by another ^{235}U nucleus, thus perpetuating the nuclear chain reaction.

When a neutron strikes an atom, three general types of reactions may occur: neutron radiative capture (n, γ), neutron capture followed by particle emission ((n,p), (n, α), etc.), and fission (n,f).[67] The most common reaction is neutron radiative capture as it tends to have high cross sections resulting in high yields. However, since both the target and product are the same element, the SA is low. Nevertheless, these reactions can also be used to produce isotopes of different elements if the produced isotope further decays into another element. This occurs with the ^{176}Yb (n,γ) ^{177}Yb reaction, where ^{177}Yb ($t_{1/2}$ = 1.9 h) undergoes beta decay to produce ^{177}Lu, a β^--emitting isotope used in RPT, allowing for separation of the ^{177}Lu from the ^{176}Yb target material.[83–86] This tends to allow for greater

specific activity over the direct production route from the ^{176}Lu (n,γ) ^{177}Lu reaction, although the separation of Yb from Lu has proven possible, yet difficult.[87–91] The direct production route also does not allow for easy recycling of the expensive enriched ^{176}Lu, making indirect production of ^{176}Yb more economically sustainable.

^{99}Mo, which is the parent isotope for ^{99m}Tc, can be produced in two ways on a nuclear reactor: (1) as a product of ^{235}U fission and (2) via neutron radiative capture of ^{98}Mo (^{98}Mo (n,γ) ^{99}Mo). When ^{235}U undergoes fission with thermal neutrons, ^{99}Mo makes up 6.1% of the products, giving a cross section of approximately 37 barns, resulting in extremely high yields.[92] However, this process utilizes highly enriched uranium, which is the same material used in the manufacturing of nuclear weapons and thus is not favourable. Alternatively, the neutron radiative capture reaction of ^{98}Mo, although it has a cross section 300 times less (0.13 barns) than that of the fission process, does not use this regulated material and thus is a promising alternative; however, access to a high flux reactor is required to compensate for the lower cross section.[92]

1.4.1.5. The Isotope Separation On-line (ISOL) Technique

Developed in the 1950s, the ISOL technique was originally developed to produce and separate rare isotopes on the basis of mass. To isolate radionuclides for nuclear medicinal purposes, this technique has 5 main steps: production, thermalization, ionization, mass separation, and implantation.[85] In order to produce the radionuclides, a thick target material (e.g. Ceramic uranium carbide or tantalum foil) is irradiated with high energy protons (~500 MeV – 1.4 GeV), or other particles such as neutrons or deuterons, which results in the production of a wide variety of nuclei via spallation, fragmentation, and induced implantation.[93] In order to produce the radionuclides, a thick target material (e.g. Ceramic uranium carbide or tantalum foil) is irradiated with high energy protons (~500 MeV – 1.4 GeV), or other particles such as neutrons or deuterons, which results in the production of a wide variety of nuclei via spallation, fragmentation, and induced fission reactions.[93,94] After production, the radionuclides are heated, up to ~2000 °C in the case of some solid targets, to extract these isotopes from the target material which are then transported towards the ion source.[93] At the ion source, the radionuclides are ionized by one of many possible mechanisms (e.g. Laser, plasma, electron impact, etc.) so that they can be separated via a magnetic mass separator based on their mass-to-charge ratio.[94,95] The desired ratio (e.g. 225 if ^{225}Ac is to be produced) is selected and the beam is focused

and collected onto an implantation target that is typically a metallic foil or a salt.[96,97] The implantation target can then be collected and isotopes further purified from co-produced isobaric contaminants.

ISOL is a promising and unique technique that enables the production and isolation of isotopes that are challenging or unattainable through other methods. Among others including ^{225}Ac[95,97] and ^{226}Ac[98], ISOL has been particularly useful in the production of terbium radioisotopes.[99–102] Terbium has four isotopes compatible with medical applications including ^{149}Tb ($t_{1/2}$ = 4.1 h) for targeted alpha therapy, ^{152}Tb ($t_{1/2}$ = 17.5 h) for PET imaging, ^{155}Tb ($t_{1/2}$ = 5.3 d) for SPECT imaging, and ^{161}Tb ($t_{1/2}$ = 6.9 d) for SPECT imaging and β-therapy.[99] While ^{161}Tb can be readily produced in a reactor, the production of ^{149}Tb, ^{152}Tb, and to a lesser extent ^{155}Tb, using cyclotron-based approaches is limited by poor cross sections and low natural abundance of target materials, making enrichment difficult and costly.[99] At the CERN-MEDICIS facility, ^{149}Tb, ^{152}Tb, and ^{155}Tb can all be produced via 1.4 GeV proton spallation of Ta-Re targets.[102] Although high quantities of activity (38 GBq of ^{149}Tb, 37 GBq of ^{152}Tb, and 5.3 GBq of ^{155}Tb) can be produced after a typical (12 – 16 hour) irradiation, a low extraction efficiency of 1% limits the activity recovered and thus in order to reliably produce clinical quantities of these isotopes, improvements to extraction efficiency must be made.[99,102]

In addition to low extraction efficiencies, ISOL utilizes high-energy particles to induce nuclear reactions, with spallation reactions as one of the primary production pathways.[94] Although spallation is an excellent technique to produce a wide array of potentially otherwise unattainable isotopes, with so many reaction channels possible, especially in targets with a high atomic number (Z), the overall production cross section for each reaction tends to be low, limiting the yield.[102] Additionally, as such high energy accelerators are required to induce spallation, fragmentation, or induced fission, there are only a few centres globally that have the capability to perform this technique, further limiting the feasibility of producing clinical quantities of isotopes through ISOL. Nevertheless, producing pre-clinical quantities of these isotopes, such as ^{155}Tb[103], with ISOL has enabled researchers to assess the feasibility of using these isotopes for nuclear medicine applications.

1.4.1.6. Isotope Generators

Isotope generators, often referred to as “cows” that are “milked”, allow for the on-site and on-demand production of short-lived medical isotopes that may be impractical to produce off-site and transport to distant facilities. They operate by housing a longer-lived parent isotope that decays into a radioactive daughter isotope, which is often the isotope intended for medical use. To continuously and reliably produce the daughter isotope, radiochemical equilibrium must be reached. Radiochemical equilibrium is achieved when the rate of decay of the parent isotope equals the rate of production of the daughter isotope.[104] Initially, as the parent isotope decays, the daughter will accumulate until its production rate equals its decay rate. At this time, a steady state is achieved resulting in no overall change in the number of daughter atoms/activity, thus allowing for a consistent and reliable extraction of the daughter isotope for diagnostic and/or therapeutic purposes.[104]

There are two types of radiochemical equilibria that can occur between a parent and daughter isotope depending on the differences between their half-lives. Secular equilibrium occurs when the half-life of the parent isotope is much longer (i.e. 10 to more than 100 times greater) than that of the daughter and thus there is no significant decay of the parent isotope over 5 daughter half-lives that pass as the daughter approaches equilibrium. When equilibrium is reached, assuming that the parent decays via a singular mode, the activity of the daughter will be nearly equal to that of the parent, as shown in **Figure 1.12A**. If the parent decays via multiple routes, the maximum daughter activity will be dictated by the parent’s branching ratio. The second type of radiochemical equilibrium is transient equilibrium which occurs when the half-life of the parent isotope is only moderately longer (i.e., $t_{1/2\ (parent)} \lesssim 10 \times t_{1/2\ (daughter)}$) than that of the daughter. As a result, over the time frame of 5 daughter half-lives, there is significant decay of the parent isotope, as shown in **Figure 1.12B**. Examples of isotope generators in transient equilibrium include ^{225}Ra ($t_{1/2}$ = 14.9 d)/^{225}Ac ($t_{1/2}$ = 9.9 d) and ^{99}Mo ($t_{1/2}$ = 66 h)/^{99m}Tc ($t_{1/2}$ = 6 h) generators, while examples of secular equilibrium include ^{68}Ge ($t_{1/2}$ = 271 d)/^{68}Ga ($t_{1/2}$ = 68 min) and ^{228}Th ($t_{1/2}$ = 1.9 y)/^{212}Pb ($t_{1/2}$ = 10.6 h). In both cases, at equilibrium, the maximum activity reached, known as the saturation activity, is dependent on the activity of the parent and this ratio is given by **Equation 1.6**.

$$A_d = A_p \frac{t_p}{t_p - t_d}$$ **Equation 1.6**

The saturation activity of the daughter, A_d, is related to the activity of the parent, A_p, and is dependent on the difference between their half-lives, t_d and t_p, respectively. When t_p is much greater than t_d, as in secular equilibrium, this ratio is nearly equal to one and thus, so long as the parent directly decays to the daughter, $A_d \cong A_p$ at equilibrium. However, as the difference between half-lives reduces, as with transient equilibrium, this ratio increases, and the daughter activity is greater than the parent under equilibrium conditions (assuming the parent produces no other decay products). However, the maximum activity of the daughter nuclide can never be greater than the initial activity of the parent. With secular equilibrium, after 5 daughter half-lives, 96% of the saturation activity is reached. Transient equilibrium is, on average, reached within 4 daughter half-lives.

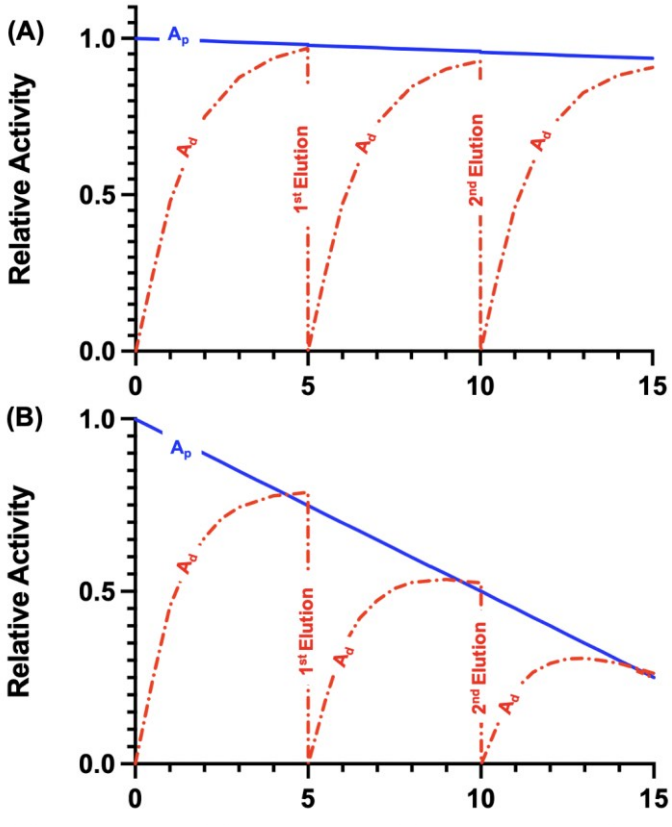

Figure 1.12. Activity time curves for generators that reach (A) secular equilibrium and (B) transient equilibrium. A_d = activity of daughter nuclide, and A_p = activity of parent nuclide, assuming the parent decays solely to the daughter nuclide (Parent nuclide → Daughter nuclide + decay particles).

The parent isotopes of generators may be produced via a variety of the methods previously mentioned. ^{103m}Rh ($t_{1/2}$ = 56.1 m) is an Auger emitter that can be produced from the decay of ^{103}Pd ($t_{1/2}$ = 16.99 d). ^{103}Pd can be produced on a cyclotron via the ^{103g}Rh (p,n) ^{103}Pd reaction, or in much greater amounts via the neutron irradiation of ^{102}Pd.[105] If produced via the ^{102}Pd route, separation of ^{102}Pd target and ^{103}Pd parent material will not be possible and thus the SA of ^{103}Pd will be low. ^{103m}Rh can still be separated from the low SA ^{103}Pd via the use of a chelator-impregnated C18 cartridge[105], but using neutron irradiation to produce generator parent isotopes from target material of the same element can pose chemical challenges.[105] This is because sub-nanograms of daughter material (ex: ^{103m}Rh) will need to be separated from milligram to gram quantities of the parent element (ex: Pd), which can result in breakthrough and thus radionuclidic and chemical impurities in the final product. In general, it is more ideal for the parent isotope to be cyclotron produced. For example, ^{68}Ge ($t_{1/2}$ = 271 d), the parent of ^{68}Ga ($t_{1/2}$ = 68 min), is produced via the ^{69}Ga (p,2n) ^{68}Ge reaction using 15 – 30 MeV protons, with a maximum cross section of 550 mb at approximately 20 MeV.[106,107] The produced ^{68}Ge is first separated from the ^{69}Ga material and then fixed to a chromatographic column where it then produces high specific activity ^{68}Ga.[107]

From a convenience aspect, it is preferable to have the parent isotope fixed to a column so that generator operation merely involves rapid elution of the daughter with a single solution, as shown in **Figure 1.13A**. However, over time, radiolysis of the column material can result in undesired breakthrough of the parent material. This decreases the radionuclidic purity of the daughter isotope and if the parent ends up in the final formulation, this could pose a risk of off-target effects and prolonged irradiation as parent half-lives are longer. To avoid this, “reverse” generators, as shown in **Figure 1.13B**, can be used where the parent isotope solution, in equilibrium with its daughters, is loaded onto the column but only the daughter adsorbs and the parent returns to its initial stock solution. The daughter is eluted from the column for further use. While this decreases column radiolysis, it can make generator operation more laborious and thus it may not be desirable depending on the application.

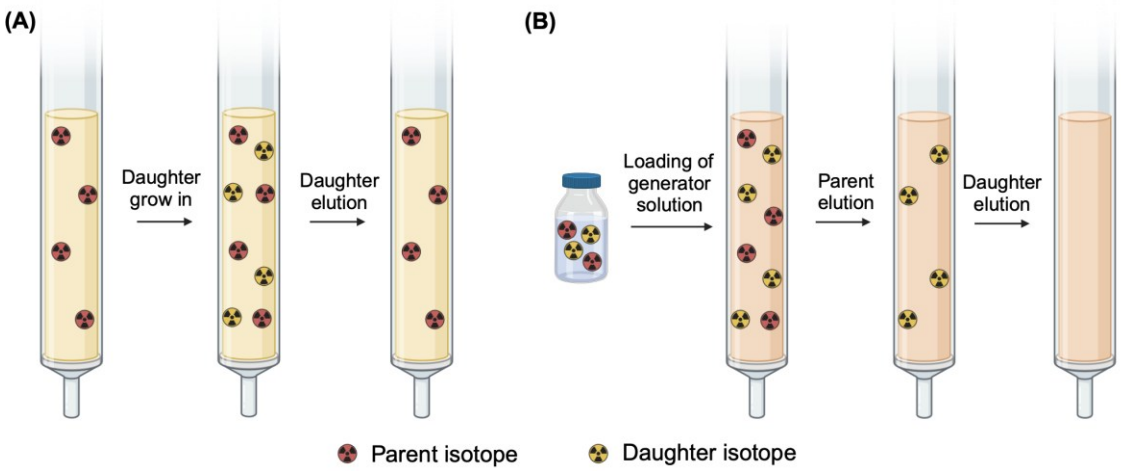

Figure 1.13. Schematic of the use of generators that (A) affix the parent isotope to the column and remove the daughter with each elution compared to (B) reverse generators that load both parent and daughter isotopes onto the column where afterwards the parent is removed before elution of the daughter, resulting in reduced column radiolysis.

1.4.1.7. Production Equations

Regardless of the type of particle accelerator or nuclear reactor used, the production rate is dependent on the flux (number of particles per unit area per unit time) of bombarding particles, the number of target nuclei, and the cross section of the reaction.[108] The factors influencing the rate of production depend on if the reaction is induced by a beam of particles, which occurs with accelerators, or if the target material is immersed in a uniform flux of particles, as is the case for nuclear reactors.[109] The rate of production in nuclear reactors, assuming a thin target where the flux and energy of the projectile does not change as it passes through the target, is given in **Equation 1.7** where R is equal to the rate of nuclei formed per second, φ is the neutron flux (neutrons cm^{-2} s^{-1}), σ is the cross section (cm^2), and N_t is the number of target nuclei within the target. In theory, all target atoms are exposed to the neutron flux and thus target thickness usually does not need to be taken into consideration.[109] The neutron flux is dependent upon location within the reactor and thus optimization can be performed to maximize production yield.

$$R = \varphi\sigma N_t \qquad \textbf{Equation 1.7}$$

However, it must also be considered that upon formation, the product is also undergoing radioactive decay at a decay rate given in **Equation 1.8** where A is the activity

at the given time, A_o is the initial amount of activity, λ is the unique decay constant of the radioisotope ($\lambda = \frac{ln2}{t_{1/2}}$), and t is the amount of time that has passed (i.e. length of the irradiation).

$$A = A_o e^{-\lambda t} \qquad \textbf{Equation 1.8}$$

When this is taken into consideration, the activity produced at the end of bombardment in the reactor is given by **Equation 1.9**.

$$A = \varphi \sigma N_t (1 - e^{-\lambda t}) \qquad \textbf{Equation 1.9}$$

For nuclei produced via target bombardment by a beam of particles, the rate of production (R) in a thin target, whose equation is shown in **Equation 1.10**, is dependent upon reaction cross section (σ), target density (n_t, the number of atoms per cm^2), and particle flux (n_p), which is directly related to the electrical current of the supplied particle beam ($n_p = I/q_e$ where *I* is equal to beam current and q_e is equal to the charge of the particle beam).[109] As a result, the accelerator parameters that can be modified to maximize the rate of production include the particle energy, which determines the cross section, and current as this affects the number of particles (i.e., flux) delivered to the target surface per unit time.

$$R = n_p n_t \sigma \qquad \textbf{Equation 1.10}$$

It is important to note that targets used in accelerators are often considered thick targets as the target materials can significantly attenuate the particle beam and thus the reduction of particle flux needs to be considered for an accurate calculation of produced activity. Like with reactor-produced isotopes, radioactive decay also needs to be accounted for and thus the activity produced at the end of bombardment in an accelerator system is shown in **Equation 1.11**.

$$A = n_p n_t \sigma (1 - e^{-\lambda t}) \qquad \textbf{Equation 1.11}$$

1.4.1.8. Targetry Considerations

In line with accelerators or reactors, target parameters and properties can also be altered to increase the production yield. Targets can be solid, liquid, or gas and amongst

all three, it is the density of target atoms, alongside particle flux, that most greatly affects isotope yield, as shown in **Figure 1.14**. Irradiation of target material generates heat and no matter the target type, all systems must utilize cooling systems to maintain target integrity to avoid contamination. Gas targets are primarily used for production of nonmetallic PET imaging isotopes such as ^{18}F, ^{11}C, ^{15}O, and ^{13}N and contain target material in a gaseous form, for example $^{14}N_2$ gas targets to produce $^{11}CO_2$ or $^{11}CH_4$.[110] Density of the target atoms is increased with higher pressures and thus a robust containment system that can maintain pressure during the irradiation and the radioactive gas product will not escape.[111] With gases having lower density than liquids and solids, the interaction probability to produce isotopes is inherently lower and gases tend to have lower thermal conductivity, making cooling more challenging. Liquid targets employ a salt solution of the target material (i.e. $[^{68}Zn]Zn(NO_3)_2$ solution) and thus a more concentrated solution will result in higher yields.[112] Liquid targets also allow for ease of purification post-irradiation as there is no need for target dissolution, as further discussed in the next section. However, target atom density is lower in solution compared to with solid targets, typically resulting in lower yields in comparison.[111] With high density and thermal conductivity, solid targets can produce the highest yields and dissipate heat most effectively, making them popular for production of radiometals and thus are the focus of this section.

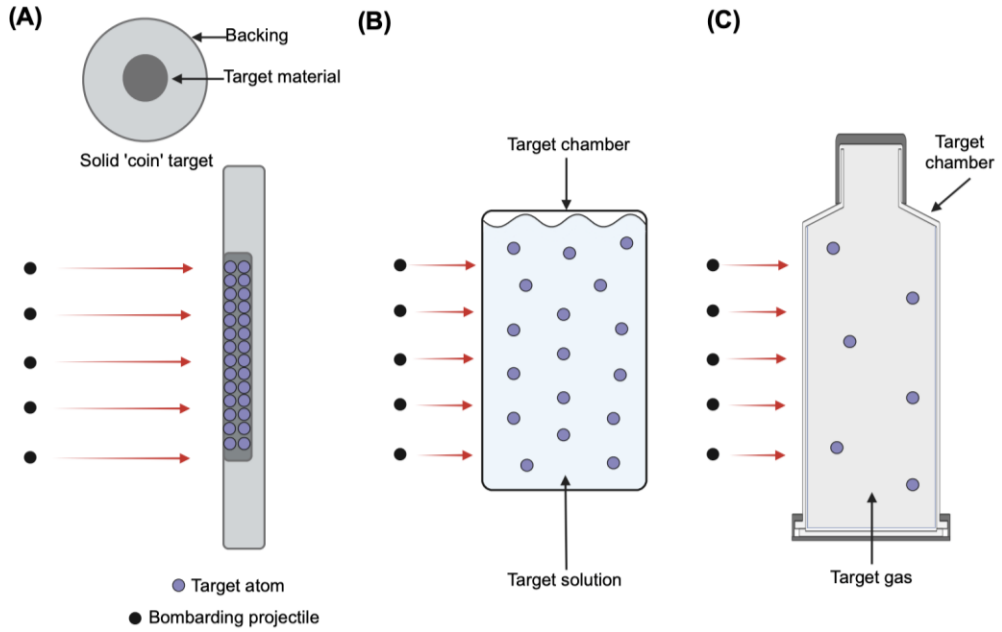

Figure 1.14. Schematics of (A) solid, (B) liquid, and (C) gas targets used for radioisotope production showing the difference in target atom densities between each system, resulting in differing production yields.

Although there are numerous types of solid targets, the two main components are the backing and the target material. The backing of the target provides structural support and plays a large role in the cooling of the target to transfer heat away from the target material, which is of utmost importance when dealing with target materials with low melting points, for example thallium (Melting point (MP) = 304 °C) or tin (MP = 232 °C). Bombardment produces heat and thus materials with high thermal conductivity coefficients, such as silver[113], copper[114], or gold[114], can be useful backing materials. However, high chemical inertness and purity of the backing is also desirable to reduce impurities introduced in the dissolution process post irradiation (see below) and thus if the target material has a high melting point, more inert materials including tantalum[115,116] or aluminum[117] can be used. Target materials for irradiation in nuclear reactors are encapsulated in quartz ampoules and capsules most often made of aluminum due to low neutron absorption and the ability to cold weld the capsule shut to avoid oxidation or decomposition of the target material upon exposure to high temperatures.[118]

Elements in their natural form often contain many isotopes and if the natural material is irradiated, this can lead to a multitude of nuclear reactions occurring with each isotope, producing numerous radionuclides, lowering radionuclidic purity. If the desired

isotope naturally occurs at low levels, this will also lower the yield of the desired product. Radionuclidic impurities can be decreased, and overall production yield increased via the use of isotopically-enriched target materials. Few elements, such as gold (^{197}Au), holmium (^{165}Ho), scandium (^{45}Sc), and yttrium (^{89}Y), are naturally monoisotopic and thus do not need enrichment while other elements, like nickel (^{58}Ni, ^{60}Ni, ^{61}Ni, ^{62}Ni, and ^{64}Ni), have several and thus enrichment of the desired isotope is required. ^{64}Ni, which is used to produce the popular PET nuclide ^{64}Cu ($t_{1/2}$ = 12.7 h) via the ^{64}Ni (p,n) ^{64}Cu reaction, must be enriched to produce clinically relevant quantities of this isotope as its natural abundance is 0.93%[119] and via centrifugation techniques, an abundance up to 99% can be reached.[120] Due to the large amount of material that must be processed to reach high enrichment levels, the cost of enriched materials is high and thus for economic reasons it is desirable for the target material to be recycled and used to produce more targets. Some enriched materials can be purchased in metallic forms while others only as oxides or other salts and thus the preferred target manufacturing method may differ between natural and enriched targets.

The target manufacturing method dictates how the target material is connected to the backing, which affects the heat conduction capability at the target interface. Electrodeposition uses electric current to reduce metal cations to form deposits onto a conductive backing from aqueous or organic solutions.[121] An advantage of this method is that even small amounts of material (<1 mg) can be deposited, which is useful when working with costly enriched or even radioactive materials, such as ^{226}Ra ($t_{1/2}$ =1600 y) which can be electroplated to produce ^{225}Ac.[122] Electrodeposition also leads to higher thermal contact conductance over other methods like pressing, where metal or metal salt/oxide powders are compressed into pellets and further into indents within target backings.[113] Greater thermal conductance allows for higher currents to be applied during irradiation as heat can be more readily dissipated, reducing risk of target failure, thus increasing the production yield making this an attractive method for targets at risk of melting. However, not all target materials can be easily electrodeposited and thus other manufacturing methods, including, but not limited to, mechanical rolling to produce metallic foils[123–125], melting[115,116,126,127], and pressing[128,129] can be used. Unlike with electrodeposition, which can be made more selective towards the desired metal, targets manufactured by these techniques may incorporate all impurities present in the starting

material into the target. Therefore, high isotopic and chemical purity of the utilized target material is essential to avoid radionuclidic and chemical impurities in the final product.

Sealed target systems for accelerators have become more prevalent in the field as they allow for encapsulation of the target material using foils adhered to the target surface. The seal can be applied to targets manufactured by a variety of techniques. Often employing aluminum foil, this type of target is of great use for oxygen sensitive metals, such as barium[130], or low melting point metals, including thallium[131], or to prevent any loss of fragile target material in powder/salt-based targets, which is particularly important for enriched materials which may only be available in salt/oxide form.[117] Additionally, the foil may act as a beam energy degrader as the seal material (e.g. Al) can absorb some of the energy of the beam before it interacts with the target material. This can be ideal for the optimization of the production of specific isotopes. The thickness of the foil can be changed so that it can reduce the beam energy so that the maximum cross section of the reaction can be reached to increase overall yield, or it may be altered to minimize the amount of co-produced radionuclidic impurities due to competing reactions occurring at the same energy. By lowering the incident beam energy, the occurrence of some undesired nuclear reactions may be minimized, improving radionuclidic purity.

1.4.2. Purification of Metallic Medical Isotopes

Although a plethora of radionuclides can be produced using particle accelerators and nuclear reactors, if they cannot be purified from the target material, their application in nuclear medicine is limited. After irradiation, only nanograms of the radiometal is produced from milligrams to grams of target material. The purpose of radiochemical purification is to isolate the desired radiometal from other chemical or radiochemical impurities that may interfere with chelator radiolabeling. In many tumours, there are a limited number of target binding sites on the surface of diseased cells and so to avoid competition between bioconjugate molecules labelled with desired radioactive metal and those labelled with undesired stable atoms, there should be a high abundance of radioactive atoms, and thus high specific activity. As shown in **Figure 1.15A**, if there is a high concentration of chemical and/or radionuclidic impurities, either of different elements or the same element as your radiometal, saturation of the binding sites can occur. Since these metals do not emit radiation compatible with therapy or imaging, there is limited

benefit to this otherwise targeted approach. As a result, the purity of the radiometal solution strongly affects the success of nuclear medicine.

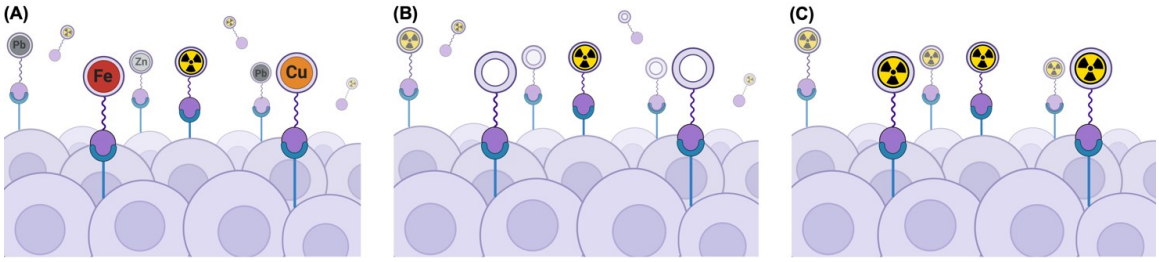

Figure 1.15. Representation of (A) a low radiometal chemical purity and low specific activity for a radiopharmaceutical, (B) a low molar activity radiopharmaceutical, and (C) an ideal high molar activity and radionuclidic and chemical purity radiopharmaceutical *in vivo*. Note that chelators are 'labeled' with non-radioactive metal impurities in addition to the desired radiometal, yet all bioconjugates will bind to the target cell receptor regardless of the metal ion bound to the chelator.

The ideal purification method is high-yielding, rapid, simple, highly reproducible, compatible with automation, avoids evaporation, and allows for recovery of enriched target material. Ideally the final product will be of low volume and low acidity to facilitate easy incorporation of the isotope into a pharmaceutical (via radiolabeling). As most biological targeting vectors are not compatible with acidic pH values and many chelators may not form metallic complexes until a higher pH is reached, buffers are added in RP synthesis to ensure radiolabeling can occur and less acidic radiometal solutions are more easily neutralized by these buffers compared to highly acidic solutions. "Radiolabeling-ready" isotope solutions are composed of buffers of a suitable pH that allow unlabelled chelators or bioconjugates to be directly added without further processing, streamlining the production process; however, careful consideration should be taken when preparing radiometal solutions in buffer to avoid metal hydroxide formation which would render the nuclide unusable. Numerous separation techniques used for other chemical applications can be modified and applied for radiochemical purification including ion exchange chromatography, solvent extraction, extraction chromatography, and precipitation – all of which are discussed in detail below. With solid targets, all of these techniques first require the dissolution of the target material, often in mineral acids such as hydrochloric and nitric acid, rendering the desired metal as an ion in solution. Liquid targets do not require dissolution and can be used immediately.

1.4.2.1. Solvent (Liquid-Liquid) Extraction

Fundamentals and Theory

Solvent extraction (SX), also known as liquid-liquid extraction (LLE), is based on the distribution of a solute between two immiscible phases, often one organic and one aqueous phase. In radiochemistry, SX is used to selectively extract a specific metal ion from an aqueous matrix into the organic phase to isolate the desired metal with high chemical and radiochemical purity. On their own, simple metal salts do not have high solubilities in organic solvents due to their highly ionic nature. In aqueous solutions, the metal ions are solvated by water molecules and coordinating counter ions (ex: nitrate and chloride anions). In order to be soluble in the organic phase, the solvated water and counter ion molecules must be removed to produce an uncharged species that will be soluble in the organic phase. To achieve this, extractants are used. The organic phase may be composed entirely of the extractant, or the extractant may be dissolved in an inert organic diluent. A scheme of how SX works is shown in **Figure 1.16.**

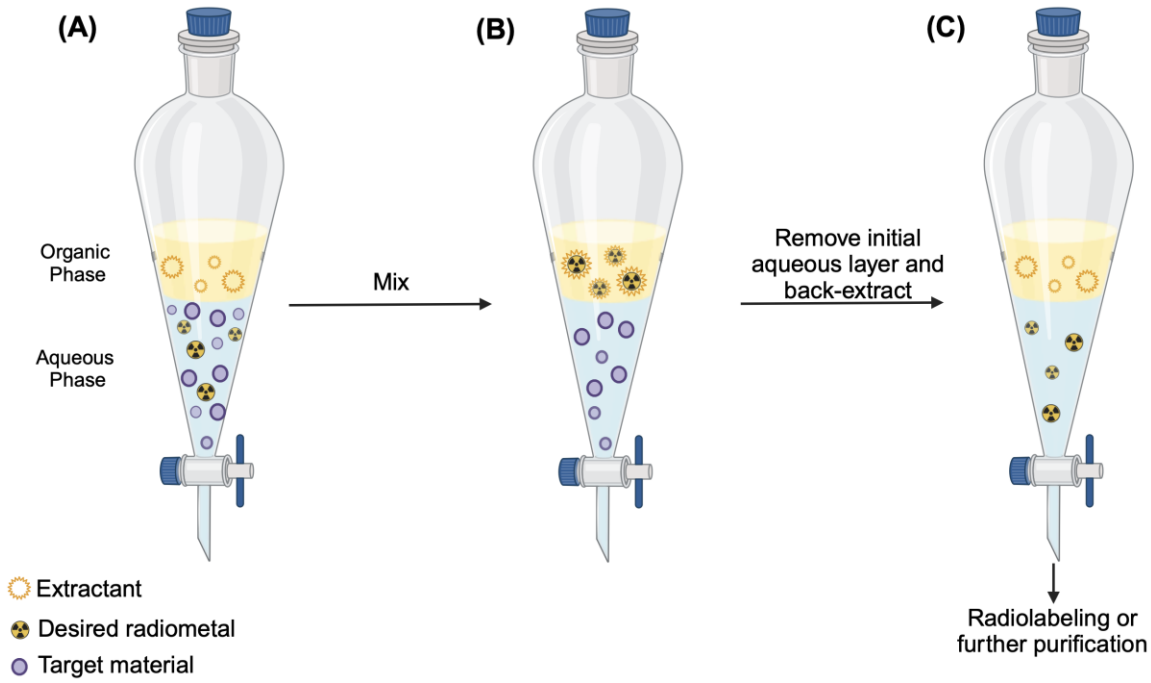

Figure 1.16. Schematic of a simple solvent extraction process in radiochemical separation. (A) The organic phase, containing the extractant in a diluent, is added to the aqueous target solution and mixed. (B) The desired radionuclide is extracted into the organic phase by the extractant while the target material remains in the aqueous phase. The initial aqueous phase is removed and the radiometal is back-extracted into an aqueous phase to make it compatible with radiolabeling or further purification by other methods.

There are four main types of extractants used in SX that differ by the mechanism used to extract metals from the aqueous phase. The mechanisms of extraction by acidic (cation exchangers), neutral (solvating extractants), basic (anion exchangers), and binary (acid-base extractants) extractants are shown in **Equations 1.12** – **1.15**, respectively.[132] Within these equations, M^{n+} is a metal cation, HL is an acidic extractant, a neutral extractant is S, and NR_4 is a basic quaternary amine extractant. The overbar represents that the species is contained in the organic phase.

$$M^{n+} + \mathrm{n}\overline{\mathrm{HL}} \rightleftharpoons \overline{\mathrm{M}L_n} + \mathrm{n}H^+ \qquad \textbf{Equation 1.12}$$

$$M^{n+} + NO_3{}^- + \mathrm{n}\overline{S_x} \rightleftharpoons \overline{M(NO_3)_n \cdot S_x} \qquad \textbf{Equation 1.13}$$

$$M^{n+} + \mathrm{n}Cl^- + \mathrm{x}\overline{\mathrm{N}R_4\mathrm{Cl}} \rightleftharpoons \overline{[\mathrm{N}R_4]_x \cdot [\mathrm{M}Cl_{n+x}]} \qquad \textbf{Equation 1.14}$$

$$M^{n+} + \mathrm{n}Cl^- + \mathrm{n}\overline{\mathrm{N}R_4\mathrm{L}} \rightleftharpoons \overline{ML_n} + \mathrm{n}\overline{NR_4Cl} \qquad \textbf{Equation 1.15}$$

With acidic extractants (**Equation 1.12**), the extent of extraction is highly dependent on the aqueous phase pH whereas for neutral extractants, the concentration of the counterion (NO_3^- for example in **Equation 1.13**) heavily affects the extraction equilibrium.[133] Amines act as basic (anion exchange) extractants and form an ion-pair complex (**Equation 1.14**) where they exchange their initial anion for the anionic metal complex.[133] Binary extractants have both basic and acidic extractant components and extract salts instead of metal cations (**Equation 1.15**).[134] Overall, adjustment of the pH and/or counterion concentration can result in either extraction of the metal into the organic phase or back-extraction of the metal from the organic to the aqueous phase, with the extent depending on both the structure of extractant and diluent, composition of the aqueous phase, and the coordination chemistry of the metal solute itself.

The distribution of the metal solute between the organic and aqueous phase can be described by the distribution coefficient, K_d, and/or the distribution ratio, D, which are given in **Equation 1.16(A)** and **1.16(B)**, respectively respectively.[135] Although very similar and sometimes used interchangeably, the distribution coefficient is used to describe the distribution of a single extractable solute species in the system under equilibrium conditions whereas the distribution ratio refers to ratio of the total concentration of the solute, in all its chemical forms and species, present in each phase.[67] Within this equation, c_{org} refers to the concentration in the organic phase whereas c_{aq} refers to the aqueous phase.

$$\text{(A) } K_d = \frac{c[Single\ species]_{org}}{c[Single\ species]_{aq}} \qquad \text{(B) } D = \frac{c[Total\ solute]_{org}}{c[Total\ solute]_{aq}} \qquad \textbf{Equation 1.16}$$

Overall, the K_d and D can be used to design radiochemical purification systems. For an effective extraction, the distribution ratio/coefficient should be low for impurities and high for the metal of interest. The separation factor (α) is used to compare the distribution ratios of two different metals and to achieve a high decontamination factor it should be as large as possible. Numerous factors can affect the extent of extraction including kinetics, temperature, surface area, extractant concentration, and saturation capacity of the extractant and thus optimization is required.[135]

Use in Literature and Discussion

Before gaining recognition in nuclear medicine, SX was primarily used in the nuclear industry for the reprocessing of nuclear fuels to reduce, recover, and recycle nuclear waste.[136,137] An example of this is the TALSPEAK (Trivalent Actinide Lanthanide Separation with Phosphorus-reagent Extraction from Aqueous Komplexes) process as it was developed in the 1960s to selectively separate trivalent actinide and lanthanide fission products from each other in nuclear fuel reprocessing.[138] Historically this separation was nearly impossible to perform due to the chemical similarities of these elements but due to the selectivity of the developed extractants and rigid pH control in the SX process, radioactivity levels in nuclear waste could be reduced.[138] Due to its ability to separate isotopes with high chemical and radiochemical purity, multiple SX processes have been developed for nuclear medicine to separate radiometals from target materials for subsequent use for radiolabeling. An ideal separation will employ a “radiolabeling ready” back-extraction solution, require no further chromatographic purification, and is compatible with automation modules.

Although rapid and selective, one of the main drawbacks that limited the use of SX in nuclear medicine was its presumed difficulty to automate and large product volumes. For example, ^{119}Sb ($t_{1/2}$ = 38.2 h), an Auger emitter, can be produced via the irradiation of tin targets via the ^{119}Sn (p,n) ^{119}Sb reaction and purified by SX.[139] Once the target is dissolved in 12 M HCl and oxidized with H_2O_2, dibutyl ether selectively extracts [^{119}Sb]Sb(V), reducing tin content by 99.95% after back-extraction with 0.1 M sodium citrate (pH 5.5).[139] Despite the sodium citrate solution potentially leading to a radiolabeling ready solution, the final volume is 8 mL which makes the activity concentration prohibitively low, making radiolabeling studies difficult as larger volumes reduce the likelihood of interactions that result in complexation.[139]

The choice of back-extraction solution and its concentration can have a large impact on the success of downstream radiolabeling. ^{47}Sc ($t_{1/2}$ = 3.35 d) is a radiometal compatible with both therapy (via β^- emission) and imaging (via emission of SPECT-compatible 159 keV gamma ray).[140] ^{47}Sc is a daughter of ^{47}Ca ($t_{1/2}$ = 4.7 d), which itself can be produced via the neutron bombardment of Ca and Ti targets via the ^{46}Ca (n,γ) ^{47}Ca and ^{47}Ti (n,p) ^{47}Ca reactions, respectively[141], to produce a generator system in transient equilibrium. ^{47}Sc can be purified from ^{47}Ca using SX but the pH of the aqueous phase must be kept at pH 1.8 to minimize Ca^{2+} co-extraction into the organic phase.[141] This strict pH control can pose difficulty when automating this procedure. A high extraction efficiency

of 99.2% can be reached but the ^{47}Sc is back-extracted to the aqueous phase with a high concentration (0.4 M) of oxalic acid to reach these quantitative levels.[141] The high concentration of acid will require post-purification neutralization of the product, increasing handling of the product and the high oxalate counterion concentration can interfere with radiolabeling of some chelators, making this separation less ideal.

Despite lower production yields given their reduced target density[142,143], liquid targets are most compatible with automated SX systems, especially if the aqueous phase containing target material can be reused in subsequent irradiations without reprocessing. This can lead to direct reuse of the target solution, minimizing loss of enriched material that often comes with target recycling and no dissolution step. Natural and enriched (^{68}Zn) zinc nitrate[144,145] or chloride[146] solutions in nitric acid or hydrochloric acid, respectively, act as liquid targets to produce ^{68}Ga. The SX can use various extractants in halogenated solvents to extract ^{68}Ga from the target solution and then back-extract with high yields (80 - >95%) using 0.1 – 2 M HCl in membrane separator-based systems.[144–146] These extractions are rapid (<20 minutes) and do not require manual manipulation during purification. Automation increases reproducibility and reduces the possibility of human error; however, the membranes used to separate the organic and aqueous phases in these systems are prone to radiolysis[145], which may be a limiting factor for these methods. Advances in the automation of in-flow extraction and microfluidic systems hold great promise for the future of SX purification in nuclear medicine.

Overall, SX is a rapid and selective purification technique that historically, and currently, holds great importance in nuclear medicine. Expansion of the field and applications of microfluidics will allow for easier implementation of SX purification and motivation to use liquid targets over solid targets, if applicable, to simplify recycling and automation methods. However, resin-based chromatographic purification techniques (discussed below) remain, and likely will remain, the most prevalent due to their inexpensive set up and ease to operate and automate. The mechanisms by which the resin-based separations work, including ion exchange and extraction chromatography, are similar to that of solvent extraction.

1.4.2.2. Extraction Chromatography

Fundamentals and Theory

Extraction chromatography (EXC) is a separation technique that combines the selectivity of solvent extraction with the convenience of column chromatography. As shown in **Figure 1.17A**, EXC resins are composed of acrylic, macroporous inert support beads and within the pores of these beads, extractants are adsorbed via physisorption (a weak process governed by Van der Waals interactions).[147] The extractants, which form the stationary phase, typically have a hydrophilic component that interacts with the metal ions and a lipophilic portion that interacts with the support beads. Although not required, the extractants can be dissolved in diluents and the choice of diluent can affect selectivity as it can either reduce or promote interactions in the organic stationary phase, help solubilize the extractant, or increase the hydrophobicity of the stationary phase.[148–152] As these extractants are not covalently bound, organic solvents cannot be used in purification processes or extractant leaching will occur. As shown in **Figure 1.17B**, metals and radiometals are separated by a series of washes and elutions with mineral acids, commonly nitric and hydrochloric acid. When designing a separation scheme, it is pertinent to know the behaviour of the metal on this resin as a function of acid type and concentration as the retention of the metal complex varies with these conditions. Similar to how the distribution ratio in solvent extraction (SX) indicates the extent of extraction into the organic phase, the capacity factor (k') and the distribution coefficient (K_d) are commonly used in EXC to describe how effectively the metal is retained by the stationary phase.[153] The weight distribution ratio (D_w) (**Equation 1.17**) is used to calculate the capacity factor (**Equation 1.18**); this is like the distribution ratio in SX, but it takes into account the masses of the resin (m_r), volume of the aqueous phase (V_a), volume of resin (V_r) and the activity of the radiometal tracer on the resin (A_r) and in the aqueous phase (A_a).[154]

$$D_w = \frac{A_r \cdot V_a}{A_a \cdot m_r} \qquad \textbf{Equation 1.17}$$

$$k' = D_w \cdot \frac{V_r}{V_a} \qquad \textbf{Equation 1.18}$$

The capacity factor (k') for a particular (radio)metal is often plotted as a function of acid concentration (**Figure 1.17C**), and these plots can be used to design appropriate separation strategies. During the loading and washing steps, as shown in **Figure 1.17B** and **1.17C**, conditions should be selected so that the radiometal has a high capacity factor such that it remains on the column while the target material and other impurities have a

low capacity factor to allow for effective removal and separation. During the elution step, conditions should be selected so that the desired radiometal has a low k' to facilitate recovery from the column. This sequential adjustment of conditions and capacity factors maximizes the purity and yield of the radiometal.

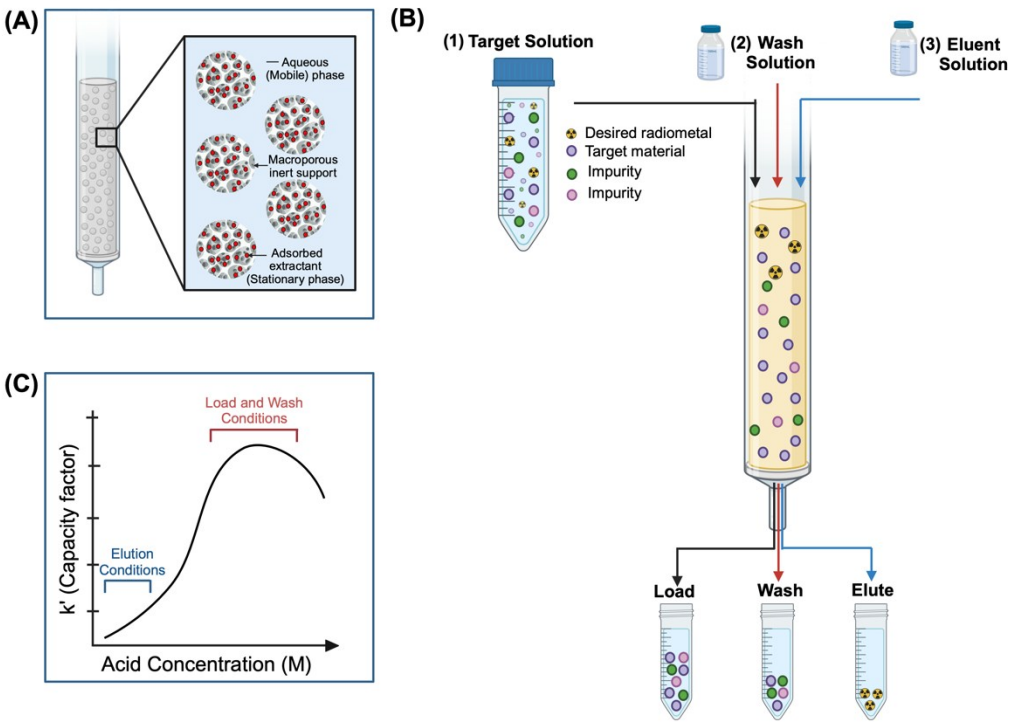

Figure 1.17. (A) Composition of extraction chromatographic resin. (B) Schematic of a resin-based purification process. C) Capacity factor plot of the desired radiometal as a function of acid concentration.

Due to their high selectivity and ease of use, extraction chromatography is extremely common in radiochemistry as over a dozen different resins exist, giving them a wide variety of applications, with a select few shown in **Table 1.2**.

Table 1.2. Summary of selected extraction chromatography resins used in nuclear medicine.

Resin Name	Structure of Extractant[155]	Applications

Pb resin	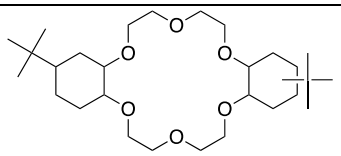	Separation of Pb, Sr, and Po.[113,114,131,156]
DGA resin	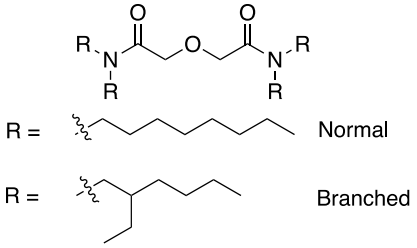	Americium separation, Ra/Ac/La separation, Y/Sr separation.[97,130,157,158]
TRU resin	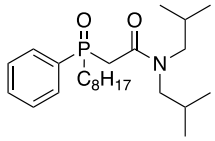	Separation of actinides[159,160]
LN resin	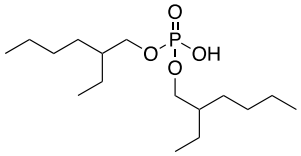	Separation of radium and light rare earth elements (ex: La, Ce, Pr, Nd, Sm, Eu)[161,162]
TEVA	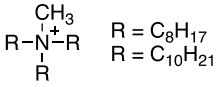	Analysis of technetium, separation of actinides and lanthanides[159,163]
UTEVA	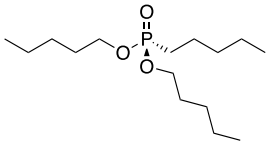	Separation of uranium and other tetravalent actinides (Ex: Np, Th, and Pu)[159,163]
TK221	Structure undisclosed – Mixture of diglycoamide and phosphine oxide with long-chained alcohols.	Separation of lanthanides and actinides[164–166]
TK211/212/213	Structure undisclosed – Mixture of organophosphoric, orthophosphinic, and orthophosphonic acids	Complex lanthanide separations[165,166]

Use in Literature and Discussion

With their high selectivity, EXC resins can be of great use for initial target material debulking in solid target purification methods or for separation of the desired daughter isotope in low specific activity generators, as shown with Pb resin for the purification of ^{203}Pb from ^{203}Tl/^{205}Tl targets[113,114,131,156] and use in ^{228}Th/^{212}Pb generators.[113,156] Low specific activity ^{228}Th/^{212}Pb generators source ^{228}Th as a by-product of ^{232}Th target spallation on high energy (ex: 500 MeV) cyclotrons but since ^{232}Th and ^{228}Th cannot be separated, the specific activity of ^{228}Th is low.[113,156] Pb resin is composed of an 18-crown-

6 derivative that exhibits high retention (k' >100) of Pb^{2+} in 0.1 – 10 M HNO_3 to allow for loading and washing without significant Pb losses.[149] Pb^{2+} also exhibits low retention in HCl at concentrations over 6 M HCl and with buffer solutions (e.g. sodium/ammonium acetate or citrate) to allow for effective elution.[149] In HNO_3, Tl can have over a 100-fold lower capacity factor than Pb while ^{228}Th and its daughters are not retained by this resin and thus in load and wash steps, the majority of these impurities are removed while $^{203/212}$Pb remains bound to the column; this can result in impressive separation factors up to 10^5.[113,149,156] Despite these high separation factors, one limitation of extraction chromatographic resins is their limited capacity as these resins can become oversaturated if large (milligram to gram) quantities of material are passed through. This can affect the uptake, chemical purity, and radiochemical purity of radiolead, as shown by high Tl and Th concentrations in the ^{203}Pb or ^{212}Pb product after the use of a single Pb resin column after loading 320 – 350 mg of Tl[113,156] and 8 – 10 grams of ^{232}Th, respectively.[113,156] High concentrations of target or parent material in the elute can negatively affect radiolabeling yields[113] and thus the use of secondary columns after EXC are common.[113,114,131] Overall, Pb resin is of particular value for the ^{203}Pb/^{212}Pb theranostic pair, but the solutions required for elution may require a secondary column to be employed.

EXC resins are not only useful when the chemical properties of the desired metal are considerably different from the target/parent material but also when they are extremely similar. Historically, separating lanthanides and actinides, both within and between these groups, has been challenging. This process typically required large ion exchange resins, which led to substantial volumes of eluate and waste. As a result, EXC resins such as the DGA, Ln, and TK2XX series have become increasingly popular for radiometal purification. DGA resin is composed of tetraalkyldiglycoamides that act as neutral, solvating extractants and it comes in two different forms, either normal, which contains N,N,N',N'-tetra-n-octyldiglycolamide, or branched, which contains N,N,N',N'-tetra-2-ethylhexyldiglycolamide which has lower capacity factors overall to allow for easier elution of the desired radiometals.[167] The trivalent lanthanides and actinides have high affinity for this resin in nitric acid while common impurities, like Fe^{3+}, do not, allowing for effective decontamination.[167,168] This resin is heavily used in the purification of ^{225}Ac from both direct production from ^{232}Th spallation targets[157,168] or ^{226}Ra targets[122] or indirect production with ^{225}Ra/^{225}Ac generators as ^{225}Ra will not adhere to the column, allowing for further washing and purification of ^{225}Ac.[97,155,157] DGA resin is an ideal resin for purification of ^{225}Ac

produced from a ^{232}Th spallation process, which produces nearly all nuclides with atomic masses less than ^{232}Th as the co-production of radiolanthanides and radioactinides poses a challenge for purification due to chemical similarities. However, Ca^{2+} and Ac^{3+} have similar capacity factors on this resin and Ca^{2+} contamination, which can negatively affect radiolabeling[97,157], can be difficult to reduce without other resins or techniques applied.

TK2XX resins, which include TK211, TK212, TK213, and TK221 are of particular use for the separation of the lanthanide series, which is of particular benefit for the purification of the ^{155}Tb ($t_{1/2}$ = 5.3 d) /^{161}Tb ($t_{1/2}$ = 6.9 d) theranostic pair.[166] The TK21X resins have high affinity for the lanthanides in dilute HNO_3 and HCl with drastic changes occurring from small changes in acid concentration, for example on TK212 resin, the K_D of Gd^{3+} at 0.05 M HNO_3 is approximately 1000 but rapidly drops to less than 10 at 0.2 M HNO_3.[166] With this resin, neighbouring lanthanide Tb^{3+} has a higher K_D of 100 at 0.2 M HNO_3 and thus TK212, as well as TK211 and TK213, are excellent resins to separate the lanthanides.[166] In HNO_3 concentrations greater than 0.1 M, TK221 shows very high retention of the lanthanides and very low retention with dilute HCl, making TK221 an ideal finishing resin at the end of a purification series.[166] This results in concentrated activity with high chemical and radionuclidic purity, as well as specific activity, with an acid concentration that is easily neutralized to allow for simple RP synthesis. Although it is beneficial that the separation can occur with dilute acids from a waste and resin stability aspect, as shown by McNeil *et al*. the large changes in K_D values with small changes to acid concentration can lead to challenges with establishing a highly reproducible automated procedure.[166] With automated systems, it is not uncommon to have dead volumes in the tubing and syringes leading to mixing of reagents in the lines, which can affect procedures sensitive to acid concentration and lead to lower and more variable yields and thus optimization is required.

EXC offers one of the highest degrees of selectivity for radiometals that may only be possible with other techniques by using large amounts of solvent/acids or long columns that are difficult to operate or automate. However, due to their limited capacity, breakthrough of target material in elutes is not uncommon and thus these columns may find greatest use in a series as an initial debulking column or as a final column used to concentrate the activity into a produce with smaller volume, preferably with a low acid concentration.

1.4.2.3. Ion Exchange Chromatography

Fundamentals and Theory

Ion exchange chromatography (IEC) is often used in conjunction with EXC to separate radiometals based on differences in charge. Ion exchange resins are composed of crosslinked polystyrene beads with covalently bonded, charged functional groups. IEC resins are either cation exchangers, where the functional groups are negatively charged to exchange cations, or anion exchangers, where the functional groups are positively charged to exchange anions. Examples of cation exchange (CEX) functional groups include sulfonic acid and carboxylic acids for strong and weak acidic CEX resins, respectively. Anion exchange (AEX) functional groups include quaternary amino groups and primary/second/tertiary amino groups for strong and weakly basic AEX resins, respectively. In these systems, the resin acts as the stationary phase and the aqueous solution, typically mineral acids like HCl or HNO_3, is the mobile phase. Distribution coefficients (K_D) and ratios (D) represent the distribution of the metal cation between the two phases as a function of concentration of acid or other eluent.

Although IEC separates on the basis of charge, metals with identical charges may interact differently with the same resin due to differences in chemical properties such as hydration number, hydration energy, electronegativity, charge density, and ionic radius.[169–172] Acid concentration in the mobile phase can affect the extent of metal ion hydration, the extent of metal complex formation with acid anions (NO_3^-, Cl^-,etc.), and the overall charge of the formed complex, which can affect the interaction of the metal with the resin.[169–172] The distribution coefficients of nearly the entire periodic table on common CEX and AEX resins for nitric, hydrochloric, and perchloric acid have been determined and are an excellent resource for planning a radiochemical separation.[170,171,173–176] Although mineral acids are the most common mobile phases, chelating/complexing agents (e.g. Ammonium acetate[177], oxalic acid[178], α-hydroxyisobutyric acid[179,180]) and organic solvent mixtures (ex: HCl-acetone[181], HNO_3-methanol[182]) may also be used.

Use in Literature and Discussion

Due to their increased metal capacity over EXC resins (20 to >200 mg/g vs 10 to 50 mg/g, respectively), IEC resins can be used to separate both macro and tracer quantities of material, making them well suited for applications in radiochemistry. As previously discussed, it is possible for extraction chromatography to be used as the sole purification technique to separate radiometals from a target. However, this only works well if the K_D values of the target material are sufficiently lower than that of the desired radiometal to allow for the target material to be removed in load and wash steps. If the K_D values of the target material are always higher than the desired radiometal, EXC can be the sole purification method used but a large (containing several grams of resin), costly column would be required, and there is a greater chance of breakthrough of the target material into the radiometal elute. In this situation, the use of IEC, particularly CEX for the separation of radiolanthanides from lanthanide targets, with its higher capacity can be employed.

Lanthanides, due to their similar chemical properties and trivalent charge, are not easily separated from each other via CEX. However, the chelating agent α-hydroxyisobutyric acid (HIBA) can be employed to form complexes with the lanthanides.[180] When lanthanides form complexes with HIBA, this lowers the affinity of the lanthanide for the resin.[180] Later lanthanides tend to form stronger complexes with HIBA than earlier lanthanides and thus tend to elute from the resin first.[180] However, pH and HIBA concentration also have an effect on complex stability and thus conditions must be optimized.[180] CEX and ammonium α-hydroxybutyrate (70 mM, pH 4.75), the ammonium salt of HIBA, were used in a purification method used to separate ^{165}Er ($t_{1/2}$ = 10.4 h), a therapeutic Auger electron emitting radiometal, produced via the proton bombardment of ^{165}Ho via the ^{165}Ho (p,n) ^{165}Er reaction, from ^{165}Ho. Ho, as an earlier lanthanide, was retained on the resin while Er was eluted.[165] In this method, ~200 nanograms of [^{165}Er]Er^{3+} was separated from ~200 mg of [^{165}Ho]Ho^{3+} via the use of CEX chromatography for general debulking of the Ho material.[165] Although this column was an excellent debulking step, the chemical purity, due to milligram breakthrough of ^{165}Ho in the elute, and large (~250 mL) elute volume, were incompatible with radiolabeling and thus additional EXC resins were required to further purify and concentrate the activity.[165]

IEC is not beneficial only for debulking, but it can also be useful as a concentrating and finishing column to remove trace impurities and to make the elute solution composition

more compatible with radiolabeling. For example, as shown with ^{203}Pb,[113,114] EXC Pb resin was first used to remove bulk thallium and other impurities and ^{203}Pb was then eluted with 8 M HCl[113] or sodium acetate (1 M, pH 5.5). [114] 8 M HCl is not directly compatible with radiolabeling and the use of sodium acetate leads to a large (5 mL) elute volume. To avoid evaporation and concentrate the activity, CEX[114] and AEX[113] were used as the Pb resin elutes could be loaded either directly (CEX) or after a simple dilution to 2 M HCl (AEX) to allow for elution with less than 2 mL of 1 or 0.01 M HCl, respectively. Typically, it is most ideal for a purification procedure to be composed of a single column to simplify automation and minimize loss of material that may occur during transfer. However, if the utilization of a second column can avoid evaporation, reduce acid concentration and/or elute volume, and greatly improve chemical and/or radiochemical purity, it should be implemented.

IEC has also been used to produce isotope generators for radiometals such as ^{212}Pb. ^{212}Pb is a daughter of ^{224}Ra ($t_{1/2}$ = 3.6 d) which further is a daughter of ^{228}Th ($t_{1/2}$ = 1.9 y). ^{224}Ra/^{212}Pb generators, where the ^{224}Ra is fixed to AGMP-50 CEX resin, are commercially available and allow for daily elution of ^{212}Pb using 2 M HCl as ^{224}Ra and ^{212}Pb reach transient equilibrium.[183] This system allows for easier automation and collection of the ^{212}Pb with minimal operator dose during its elution. Although it would be most ideal to fix both ^{228}Th and ^{224}Ra to the resin to extend the useful lifetime of the generator, any resin, whether IEC or EXC, would undergo significant radiolysis due to the prolonged irradiation of the resin by the parent nuclide during decay. Over time, this can result in breakthrough of the parent material, reducing radiochemical purity. To prolong the lifetime of a generator with a long-lived parent, generator systems that do not affix the parent to resin should be used to maintain performance over time.[184]

Despite not having the selectivity of EXC, IEC is still an extremely useful technique with great prevalence in the field of nuclear medicine today. Due to its high capacity, IEC can be an excellent debulking step but can also be useful to change the elute composition from previous steps. Although IEC can handle both macro and tracer levels of material, there can often be significant breakthrough and thus other methods, such as precipitation, can be useful when dealing with large quantities of material.

1.4.2.4. Precipitation

Precipitation techniques take advantage of differences in solubility between the target and radionuclide material. In most cases, precipitation is the one of the first steps in a purification process and acts to reduce the burden of large quantities of target material to allow for superior separation and reduction of breakthrough in subsequent steps. In the 500 MeV proton spallation of ^{232}Th to produce ^{225}Ac, Robertson *et al* precipitated out 99.95% of the thorium in the 8 – 10 g thorium target as thorium peroxide to allow efficient separation of other radiometals in subsequent steps.[157] ^{68}Ga can be separated from Zn[185] and ^{44g}Sc from Ca[186] by precipitation with sodium hydroxide. Although nearly all metal nitrates are soluble in water, ^{132}La/^{135}La can be separated from Ba[187] and ^{203}Pb from Tl[113] by precipitation of the nitrate species through adjustment of nitrate concentration, volume, and temperature. Although in most cases chromatography is used afterwards to remove traces of target material, the level of decontamination that precipitation allows for would not be possible with traditional chromatographic techniques that, at this scale, would be difficult to both construct and automate.

1.4.2.5. Application of Analytical and Radioanalytical Chemistry Techniques for Quality Control

Overall, the goal of a radiochemist is to produce a radiometal solution with a high radiochemical and chemical purity in high yield and low volume using a simple, rapid, and reliable purification technique composed of one or a combination of the methods discussed in this section. To determine if this has been accomplished, analytical and radioanalytical techniques need to be applied. To determine the concentration of any metal impurities in the radiometal product, inductively coupled plasma mass spectrometry (ICP-MS) or inductively coupled plasma optical emission spectroscopy (ICP-OES) can be employed. ICP-MS is a more sensitive technique, with limits of detection down to parts per trillion, which is useful for metals with low regulatory limits. ICP-OES can be useful if all concentrations are above 10 ppb and if the sample contains a high concentration of total dissolved solids. To quantify the activity in solution, gamma spectroscopy can be used to identify and quantify radionuclides that emit gamma radiation. Some radionuclides do not emit gamma radiation at a high abundance and thus to quantify their activity, one can wait for the grow-in of a daughter that emits gamma radiation or, if they emit alpha particles, alpha spectroscopy can be used. Much like how gamma spectrometers measure the energy and quantity of emitted gamma radiation, alpha spectrometers measure the energy of the emitted alpha particle. As emitted alpha particles are mono-energetic, the

identity of the radionuclide can be determined. For applicable isotopes, the detection limit of alpha spectroscopy can be 100 – 1000 times lower than that of gamma spectroscopy[190] but the sample preparation is more difficult and thus gamma spectroscopy is used when possible.

Radiolabeling studies measure the radiolabeling yield (RLY), which is the extent to which a BFC-RP or chelator alone complexes a radiometal, and these studies are a critical quality control measure for radiometals. Radiolabeling can be affected by chemical purity, radionuclidic purity, and specific activity of the added radiometals, alongside other experimental conditions including temperature, pH, buffer concentration, chelator concentration, and reaction volume. When a radiometal is of high purity, more of the BFC-RP or chelator molecules added to the reaction will complex the radiometal and thus the molar activity (A_m), which is a measure of the radioactivity complexed per mole of the BFC-RP or chelator, typically expressed in units of becquerels (Bq)/mol, is higher. A high molar activity indicates a high ratio of radioactively labelled to unlabelled molecules. This is ideal and important when *in vivo* target sites are limited to prevent oversaturation of the receptors with 'unlabeled' drug to ensure high quality images and to elicit a therapeutic effect. **Figure 1.15B and 1.15C** shows the difference between a radiopharmaceutical with low molar activity compared to one with high molar activity, respectively. An ideal radiometal purification procedure will result in a radiometal product with high, reproducible radiolabeling yields and high molar activities of BFC-RPs or chelators can be reached. Radiochemical yield (RCY) is closely related to radiolabeling yield, but also takes into account the final yield obtained after both labelling and purifying the radiopharmaceutical. This value reflects the quality of both the radiometal and radiopharmaceutical purification methods.

A large library of chelators has been developed and are in development for the ever-expanding radiometal toolbox in nuclear medicine.[15,40,191–193] DOTA (1,4,7,10-Tetraazacyclododecane-1,4,7,10-tetraacetic acid, **Figure 1.18A**) is considered the commercial standard chelator for many radiometals including, but not limited to, ^{225}Ac and ^{177}Lu. As DOTA can coordinate many different metals, its RLY can be highly affected by isotope purity. DOTAM (TCMC or 1,4,7,10-tetraazacyclododecane-1,4,7,10-tetrayl)tetraacetamide, **Figure 1.18B**) is considered the commercial standard for the chelation of ^{203}Pb and ^{212}Pb.

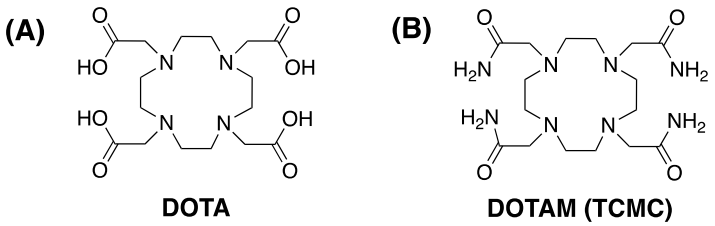

Figure 1.18. The chemical structure of (A) DOTA and (B) DOTAM (TCMC).

In a radiolabeling study, as shown in **Figure 1.19A**, radiometal (often in dilute acid) is added to a solution containing chelator in buffer at an appropriate pH to promote radiometal complexation. The reaction mixture is then incubated at a set temperature and after a set period of time has elapsed, an aliquot is removed to determine the RLY. Quantification of the RLY requires that the free/noncomplexed activity is separated from complexed activity and this can be performed using radio-instant thin layer chromatography (iTLC) or radio-high performance liquid chromatography (HPLC), which separate components based on the extent of interaction with the stationary phase and the mobile phase. iTLC quantifies RLYs based on differences in retention factors (R_f) and HPLC by retention times of the free and complexed activity. As shown in **Figure 1.19B**, for iTLC, aliquots of the reaction are spotted onto chromatographic paper or silica plates and developed using a mobile phase, typically a pH-adjusted chelating solution such as EDTA or citrate. This mobile phase forms a soluble complex with the radiometals that remain unchelated in the reaction. As the plate develops, the more hydrophilic EDTA or citrate complexes of the “unbound” activity migrates further up the plate with the solvent front (Rf ≅ 1), while the radiometal complexed with the BFC-RP remains behind (Rf < 1). This separation allows for quantification of the percentage of the radiometal successfully incorporated into the BFC-RP in the reaction.

iTLC plate readers determine the RLY of the reaction by measuring the radioactivity as a function of distance along the plate. The majority of iTLC plate readers use gas-filled proportional counters as their detectors. The detection chamber of these detectors is filled with a gas mixture, commonly 90% argon and 10% methane (P-10 gas), and as ionizing radiation enters the detector, it ionizes the gas atoms generating free electrons and positive ions. The free electrons are accelerated towards the positively charged anode of the detector and as they move, they produce secondary ionization events that produce a cascade effect. The number of secondary ionizations produced is proportional to the activity of the sample at the measured location on the TLC plate. The

area under the curve at each location is integrated and the RLY is quantified, as shown in **Figure 1.19B**.

In radioHPLC, as shown **in Figure 1.19C,** detectors, often sodium iodide (NaI) scintillation detectors, are used to create radiochromatograms that plot measured radioactivity against retention time. When ionizing radiation enters the NaI crystal, it excites the atoms, causing them to emit visible light as they return to their ground state. This process, known as scintillation, generates photons which then strike the photocathode of a photomultiplier tube (PMT). The PMT amplifies the signal by releasing additional electrons through the photoelectric effect, creating an electron cascade that corresponds to the energy and intensity of the incoming radiation. This amplified signal allows for quantification of the radioactivity present. Typically with reverse-phase radioHPLC where hydrophobic C18 columns are often used, free activity has a shorter retention time than the BFC-RP or chelator complex as it does not interact strongly due to its high hydrophilicity.

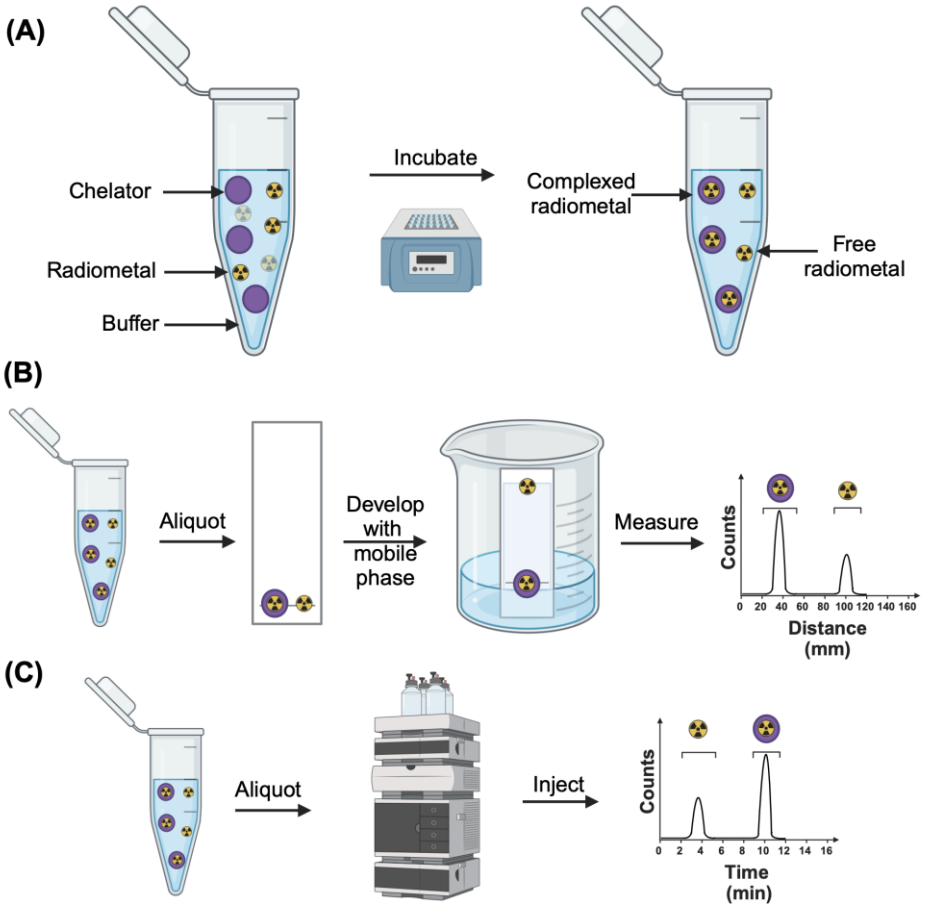

Figure 1.19. (A) Components of a radiolabeling reaction. Typically, to a solution containing sub-micromolar concentration of chelator or bioconjugate in buffer is added the radiometal. The reaction mixture is allowed to react at prescribed time or temperature. The resultant reaction mixture is then analysed using (B) radio-iTLC and/or (C) radioHPLC. In both chromatographic techniques, any "unchelated" or "free" radiometal must be resolved from the radiometal-complex to determine the percent radiolabeling yield (%RLY)/radiochemical yield (%RCY) by integrating peaks in the (radio)chromatograms.

If a radiometal solution has low chemical or radionuclidic purity, other competing cations (Fe^{3+}, Ca^{2+}, etc.) or radionuclides may be complexed instead of the desired radiometal, lowering the RLY and thus A_m, which is less than desirable for *in vivo* studies and treatments. Therefore, before a radiometal can move onto clinical trials to expand the bright future of nuclear medicine, it must 1) be able to be produced in clinical quantities, of which the value differs depending on the nature of the isotope, and 2) must be able to be reproducibly purified to give high chemical and radionuclidic purity to result in high RLYs that allow for the synthesis of BFC-RPs to be used in clinical settings.

1.4.3. Trends and Future Outlook on Isotope Use, Production, and Purification

Advances in the capabilities to both produce and purify radiometals with decay properties suitable for targeted imaging and/or therapy has significantly advanced the potential for personalized medicine by increasing the number of treatment options available with potentially reduced side effects. Consequently, numerous radiopharmaceuticals have received approval from the United States Food and Drug Administration (FDA) and European Medicines Agency (EMA), and many others are currently undergoing clinical trials with early results showing promise for improving patient outcomes. This section highlights currently approved RPs, RPs in clinical trials, production methods for these radiometals, and challenges associated with scaling up these radiopharmaceuticals to meet clinical demand. **Figure 1.7** displays the structures of select approved and in trial BFC-RPs.

1.4.3.1. ^{68}Ga

^{68}Ga is a diagnostic isotope as it undergoes decay via positron emission, making it compatible with PET imaging. The average positron range for ^{68}Ga in tissue is 3.5 mm[189], allowing for high resolution images to be obtained, making ^{68}Ga an attractive diagnostic radiometal. The utility of ^{68}Ga is demonstrated by the FDA approval of several ^{68}Ga-based imaging agents for clinical use, including both [^{68}Ga]Ga-DOTATATE (Netspot, approved in 2016) and [^{68}Ga]Ga-DOTATOC (Somakit, approved in 2019)[190] for the localization of somatostatin receptor (SSTR)-positive NETs, and [^{68}Ga]Ga-PSMA-11 (Illucix/Locametz, approved in 2020) for the localization of prostate specific membrane antigen (PSMA, also sometimes denoted as PSA)-positive prostate cancer.[191] These agents are often paired with their ^{177}Lu counterparts, Lutathera for neuroendocrine tumours (NETs) and Pluvicto for metastatic castration resistant prostate cancer (mCRPC), respectively, to act as a theranostic pair to identify patients who may benefit most from these targeted treatments and to monitor their response over the treatment course. However, these radiometals are not isotopes of the same element, nor are they composed of the same targeting vector if [^{68}Ga]Ga-PSMA-11 is used for mCRPC scans, and thus the diagnostic ^{68}Ga RP may not accurately predict the biodistribution of its therapeutic Lu counterpart, but these mixed pairs can still be useful for tumour biochemical profiling and visualization of tumour burden.

As clinical trials continue to show the benefits of the ^{68}Ga/^{177}Lu theranostic pair and other ^{68}Ga RPs, the isotope supply of ^{68}Ga must be able to meet the increased demand. ^{68}Ga can be produced directly on a cyclotron from enriched ^{68}Zn targets via the ^{68}Zn (p,n) ^{68}Ga reaction or from a ^{68}Ge/^{68}Ga generator.[192] With a half-life of 271 days, a ^{68}Ge/^{68}Ga generator can last for a year, rapidly supplying up to 3.7 GBq (100 mCi) of ^{68}Ga allowing for approximately 20 patient doses, although this yield reduces over the generator's lifetime and the number of patient doses depends on the tracer employed.[193] Generators are straightforward to use and can supply ^{68}Ga without the need for an expensive cyclotron, making them a convenient option for many medical facilities. However, generators produce far less activity than the solid target cyclotron production method as a two-hour irradiation (80 μA, 13 MeV) can produce more than 370 GBq (>10 Ci) at the end of bombardment and 194 GBq (5.2 Ci) at the end of a 35-minute automated purification[194]. This represents a 52-times increase in the available activity and maximum possible patient doses available (>500) compared to a generator, which is useful in the cases of high clinic demand.[194] Nevertheless, this substantial increase in activity brings with it costly infrastructure requirements to safely handle these doses. Overall, the choice of the isotope production method is dependent on the specific needs, resources, and capabilities of the medical facility. In the future, greater interest in the procurement of cyclotron-produced ^{68}Ga over generator-produced ^{68}Ga is anticipated as more ^{68}Ga RPs receive FDA approval. This is due to the higher yield achievable with cyclotron production, which will enable distribution to more facilities while still maintaining higher activity levels than what can be produced by generators. Although expensive (~$5/mg), currently the supply of ^{68}Zn is stable and thus there are minimal concerns with regards to future isotope availability.

1.4.3.2. ^{64}Cu

^{64}Cu is a unique radiometal as it can decay either by positron emission (17.9%), electron capture (43.1%) or via beta decay (39.0%) theoretically making it compatible with both imaging and therapy and thus compatible with theranostics. Compared to ^{68}Ga, ^{64}Cu has a lower maximal positron energy (0.65 vs 1.90 MeV) and thus a lower positron range (0.56 vs 3.5 mm) that should result in superior resolution and image quality.[189] A comparison between imaging of SSTR-bearing tumours with [^{68}Ga]Ga- and [^{64}Cu]Cu-DOTATATE is shown in **Figure 1.20**. However, in these studies there was no clear advantage of using ^{64}Cu over ^{68}Ga. ^{64}Cu has a lower positron yield (17% vs 88%) and thus

should require more activity to be injected to achieve the same number of counts as ^{68}Ga. However, it was found that 148 MBq (4 mCi) was sufficient to obtain suitable images whereas up to 200 MBq (5.4 mCi) is recommended with ^{68}Ga.[195] The longer half-life of ^{64}Cu (12.7 h vs 68 min for ^{68}Ga) allows for imaging at later time points post injection to allow for superior tumour-to-background ratios to be obtained and easier coordination of the time from radiochemical production to patient injection.[195] As a result of copper's ideal decay properties, in 2020, [^{64}Cu]Cu-DOTATATE (Detectnet) was FDA approved for the imaging of SSTR-positive NETs in adult patients.

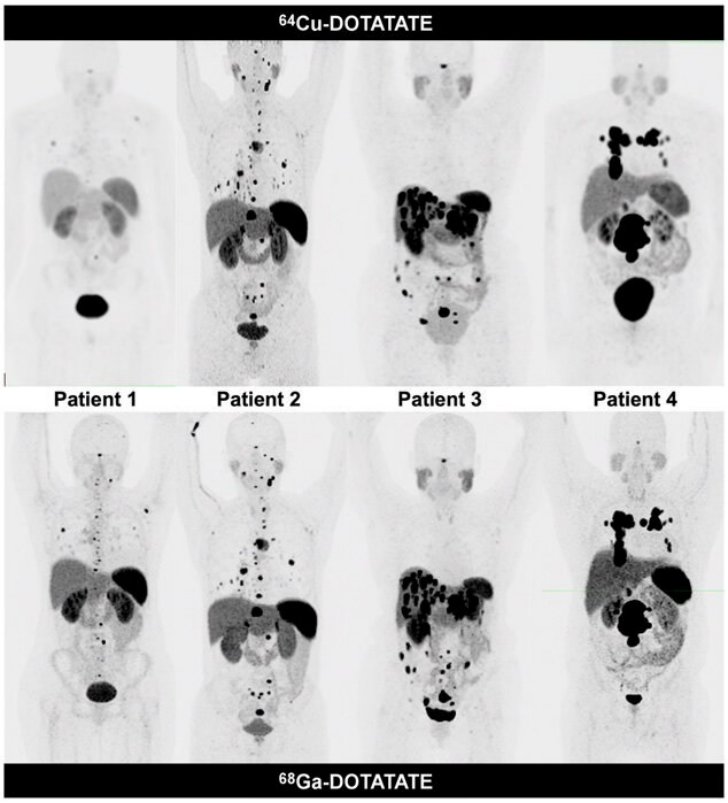

Figure 1.20. Comparative PET/CT imaging of SSTR in 4 patients with [^{64}Cu]Cu-DOTATATE and [^{68}Ga]Ga-DOTATATE.194

This figure was originally published in the Journal of Nuclear Medicine and is reproduced with permission. Jha, A. et al. Choice Is Good at Times: The Emergence of [^{64}Cu]Cu-DOTATATE–Based Somatostatin Receptor Imaging in the Era of [^{68}Ga]Ga-DOTATATE. J Nucl Med. 2022, 63(9): 1300 – 1301.

Although ^{64}Cu exhibits several superior decay properties compared to ^{68}Ga for imaging purposes, it cannot be generator produced, which poses a significant barrier to its use in remote facilities and those without cyclotron access. ^{64}Cu can be produced with the highest yield and specific activity via the ^{64}Ni (p,n) ^{64}Cu reaction with the maximum cross section occurring at 10.5 MeV to yield several GBq (100s of mCi) of ^{64}Cu, allowing

for scans of over a dozen patients per irradiation.[196–198] In addition to yielding less activity than the cyclotron production of ^{68}Ga, the ^{64}Ni target is also much pricier at ~$50/mg compared to ~$5/mg of ^{68}Zn.[199] If higher energy (>20 MeV) cyclotrons are available, ^{64}Cu can be produced with the ^{68}Zn target via the ^{68}Zn (p,nα) ^{64}Cu reaction to utilize the less expensive target material.[200] However, a lower yield of ^{64}Cu is obtained with lower radionuclidic purity due to the co-production of ^{68}Ga, ^{67}Ga, and ^{67}Cu making this route less likely to be pursued unless a facility has financial restrictions.[200]

Even though ^{64}Cu, due to its more ideal decay properties, should theoretically result in images of higher quality, the available comparison data with ^{68}Ga is not conclusive. These isotopes cannot necessarily be used interchangeably due to chemical differences between divalent copper and trivalent gallium that can result in differences in the biodistribution of radiopharmaceuticals. Until data showing a significant improvement of one over the other is available, the choice of employing ^{64}Cu or ^{68}Ga will likely depend on isotope availability.[189]

1.4.3.3. ^{177}Lu

^{177}Lu is a β^--emitting radiolanthanide primarily used for therapeutic purposes. However, it can also be utilized for SPECT imaging due to its 208 keV (11% abundance) gamma emission. This gives the potential for intercycle monitoring of disease progression without the need to administer an additional diagnostic radiopharmaceutical.[201–203] Nevertheless, this approach is not common as diagnostic isotopes are typically employed first to confirm biomarker expression and perform dosimetry calculations to evaluate suitability of this treatment option for patients prior to administration of a cytotoxic therapeutic agent that may not always be ideal.[204] Diagnostic agents that employ ^{68}Ga tend to have higher detection rates and thus at this time ^{177}Lu BFC-RPs are primarily used for therapeutic purposes.[204,205]

Currently, two ^{177}Lu BFC-RPs, Lutathera ([^{177}Lu]Lu-DOTATATE)[20] and Pluvicto ([^{177}Lu]Lu-PSMA-617), are FDA and EMA approved for the treatment of somatostatin positive gastroenteropancreatic neuroendocrine tumours (GEP-NETs) and prostate specific-membrane antigen (PSMA, also sometimes denoted as PSA)-positive metastatic castration resistant prostate cancer (mCRPC), respectively. **Figure 1.21** shows PET imaging of a patient with mCRPC with [^{68}Ga]Ga-PSMA-11, an imaging agent further

discussed below, before and after two treatment cycles of Pluvicto, showing nearly a complete response and thus the potential of this RPT.

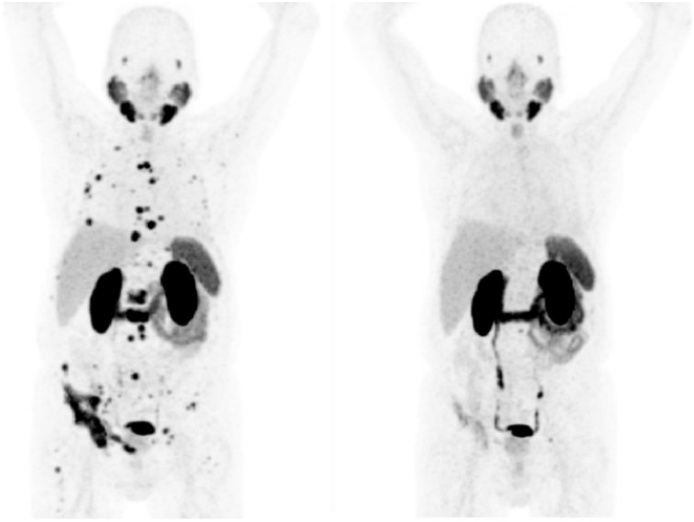

Figure 1.21. Maximal intensity projection of [^{68}Ga]Ga-PSMA-11 PET images obtained of a patient with mCRPC before (left) and after (right) two cycles with [^{177}Lu]Lu-PSMA-617.[23]
This figure was originally published in BMC Cancer and reproduced with permission. van der Sar, E. et al. Tolerability of concurrent external beam radiotherapy and [^{177}Lu]Lu-PSMA-617 for node-positive prostate cancer in treatment naïve patients, phase I study (PROQURE-I trial). BMC Cancer. 2023, 23(1): 268.

Lutathera, approved by the FDA for use in adults in 2018, uses a somatostatin analog (DOTATATE) to bind to somatostatin receptors (SSTRs), which can be overexpressed on neuroendocrine tumour cells, at a dose of 7.4 GBq every 8 weeks for up to 4 doses, or until disease progression.[206] The two major clinical trials that focused on the use of Lutathera in NETs are the NETTER-1 (Phase 3 completed in 2015) and NETTER-2 (Phase 3 completed in 2023).[19,207] In the NETTER-1 study, Lutathera was investigated in patients with progressive disease who had already undergone other treatments[19,206,208] and in the NETTER-2 study, Lutathera was used as the initial treatment option.[207] At 20 months into the NETTER-1 study, the objective response rate (ORR) in the Lutathera group was 18% compared to 3% in the control group, which were only given octreotide, another non-radioactive somatostatin analog.[19] Meanwhile in NETTER-2, the ORR was 43.0% in the Lutathera group compared to 9.3% in the control (octreotride) group, demonstrating that this RPT may act as a promising initial treatment option even with more aggressive tumours. Patients in the NETTER-1 trial were followed for 5 years post treatment and the Lutathera treatment resulted in a clinically and statistically

significant improvement in progression free survival (PFS) and an improvement in overall survival (OS) by 11.7 months compared to the control group, showing the powerful potential of this RPT.[20,208]

Pluvicto, approved by the FDA for use in adults in 2022, uses a PSMA inhibitor (PSMA-617) to target PSMA, which can be highly overexpressed in mCRPC.[209] The first study with Pluvicto was the VISION trial, completed in 2021, to evaluate the efficacy of Pluvicto in patients previously treated with androgen-receptor pathway inhibitors (ARPIs) and taxane-based chemotherapy.[21] Every 6 weeks for 4 – 6 cycles, 7.4 GBq of Pluvicto was administered and results were compared to the control group that received standard care treatments.[21] The median OS was 15.3 months in the Pluvicto group compared to 11.3 months of the control group and PFS was 8.4 months over 3.4 months with the control.[21] The PSMAfore trial was completed in 2022 and evaluated the efficacy of Pluvicto in patients with PSMA-positive mCRPC who had only been previously treated with ARPI to evaluate the efficacy of Pluvicto as a new standard treatment for this cancer.[22] Similarly to the VISION trial, there was an improvement in PFS of 12.0 months in the Pluvicto group compared to 5.6 months in the control group.[22]

The expansion of the use of Pluvicto and Lutathera will improve the treatment options for patients with mCRPC and SSTR-positive NETs, respectively, but will only be able to do so if there is sufficient access to ^{177}Lu, which is dictated by the limitations of both production and purification methods. As previously discussed, ^{177}Lu can be directly produced via a carrier added method with the neutron irradiation of ^{176}Lu (^{176}Lu (n,γ) ^{177}Lu)92 or indirectly with a no-carrier added method via the beta decay of ^{177}Yb, produced via the neutron irradiation of ^{176}Yb (^{176}Yb (n,γ) ^{177}Yb; ^{177}Yb $\rightarrow$ ^{177}Lu).[86,90] For radiolabeling purposes, a no-carrier added method is preferable as there is less competition for complexation, typically resulting in higher RLYs and A_m, making synthesis of the RPs easier. Additionally, the carrier added method co-produces ^{177m}Lu, a beta emitting isotope with a half-life of 160 days that decreases radionuclidic purity and creates challenges with waste management in clinics.[210] However, in the case of ^{177}Lu, the over 1000 times greater cross section and reduced cost of target material for the carrier-added method must be considered. To produce 50 patient doses, only 1 milligram of enriched ^{176}Lu is required whereas 1 gram of enriched ^{176}Yb is needed for the no-carrier added route.[210] Currently, Russia's Electrokhimprebor is the principal supplier of ^{176}Yb and can produce 700 grams per year at a cost of $16,000 USD/gram.[211] With an expected future demand

of 100,000 patients/year, 3 kilograms of ^{176}Yb would be required annually and thus for the no-carrier added approach to be feasible, there must be other facilities built to produce the isotope.[211] To maximize yields to keep up with increasing demand as more patients become eligible for treatment with new clinical trials, consistent access to high neutron flux reactors will be critical to the isotope supply chain. Downtime at these reactors is not unexpected due to their increasing age, but would risk isotope shortage and patient access to life-saving treatments and thus there must be continued investments into the construction of more reactors to ensure supply stability.

1.4.3.4. ^{161}Tb

^{161}Tb is a promising radiolanthanide in the early stages of human testing with similar chemical and decay properties to ^{177}Lu. Both radiometals undergo beta decay with half-lives of 6.95 days (^{161}Tb) and 6.65 days (^{177}Lu) and average β^- particle energies of 154 keV and 134 keV, respectively and thus ^{161}Tb is being explored as a therapeutic option for prostate cancer and NETs.[217,218] Unlike ^{177}Lu, ^{161}Tb also emits conversion and Auger electrons which may make ^{161}Tb a more effective therapeutic option than ^{177}Lu[214], although comparative studies have not yet been performed. Additionally, ^{161}Tb emits two gamma photons with energies of 48.9 keV (Abundance = 17%) and 74.5 keV (Abundance = 10.2%) that have recently been used to obtain SPECT images with 5.5 GBq of [^{161}Tb]Tb-PSMA-617 administered for RPT. However, due to the low abundance of these photons, more activity is needed, compared to other imaging isotopes, to visualize the *in vivo* biodistribution. ^{155}Tb, which decays via electron capture releasing photons with SPECT-compatible energies of 87 keV (32%) and 105 keV (25%), can be used alongside ^{161}Tb as an element equivalent theranostic pair to allow for pre-treatment imaging and planning, making ^{161}Tb an attractive option for TRT.[215]

In 2023, a patient with mCRPC, who had disease progression after 8 treatment cycles of [^{177}Lu]Lu-PSMA-617, was given a single dose of 6.5 GBq of [^{161}Tb]Tb-PSMA-617 that resulted in a 53.4% decline in prostate specific antigen levels and tumour burden, showing evidence of the power of ^{161}Tb RPs.[216] With such early success, it is important that the isotope supply chain remains stable in order to advance the use of this radiometal. The production of ^{161}Tb occurs through the neutron irradiation of ^{160}Gd via the ^{160}Gd (n,γ) ^{161}Gd reaction where ^{161}Gd undergoes beta decay to produce up to 20 GBq of no-carrier-added ^{161}Tb. [166,217] Efforts to increase the production yield are in place but the high cost of

^{160}Gd (>$750/mg) limits the number of facilities with sufficient funding to produce this isotope.[199] However, if there is significant benefit over ^{177}Lu, which will only be revealed through future publications and clinical trials, demand will increase and there will be increased economic incentive to produce ^{160}Gd in a more cost effective manner. Like with ^{177}Lu and other reactor-produced radionuclides, any downtime or access disruption to high flux reactors will affect isotope supply; thus to ensure stability, investments in maintaining existing infrastructure while also investing in new reactors should be a priority.

1.4.3.5. ^{212}Pb

With a 10.6-hour half-life, single alpha emission, and short-lived (<60.6 min) daughters, ^{212}Pb is an ideal isotope to introduce alpha emitters into the world of RPT as these decay characteristics minimize concerns about the recoil effect and subsequent redistribution of daughter nuclides in the body. ^{212}Pb undergoes beta decay as per the decay scheme in **Figure 1.22** and can act as an *in vivo* generator of alpha particles.

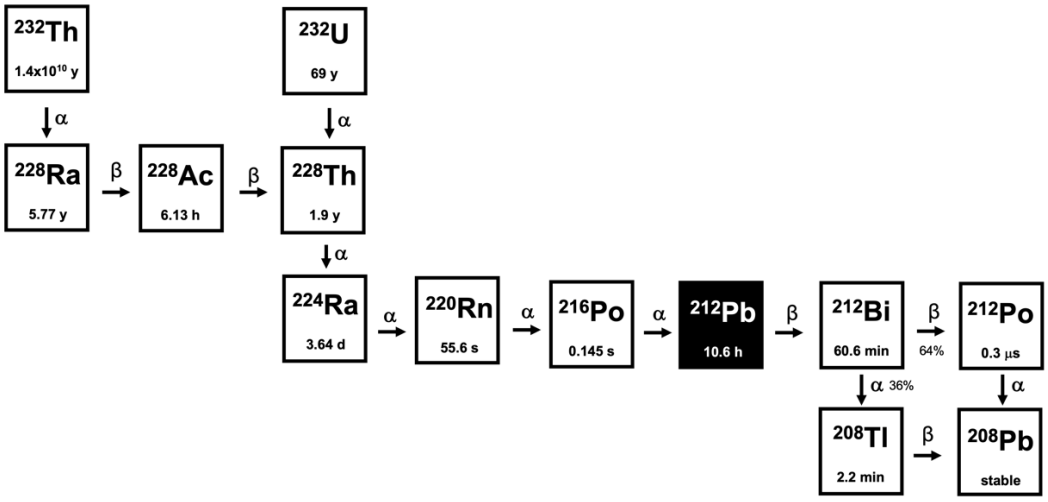

Figure 1.22. Decay chain of ^{232}Th and ^{232}U, which decay to ^{212}Pb.

Although ^{212}Bi is the first alpha emitter in the decay chain and could be isolated for RPT, administering a ^{212}Pb therapeutic RP is preferable over a ^{212}Bi RP as a longer half-life allows for more time for the preparation and injection of the RP, making it easier to manage logistically in clinical settings. ^{212}Pb has been involved in a number of clinical trials including the evaluation of [^{212}Pb]Pb-DOTAMTATE (AlphaMedix), shown in **Figure 1.23**, in patients with GEP-NETs where the phase 2 trial received FDA breakthrough designation due to a high (80%) objective response rate in patients.[29] This is a drastic

improvement over the 13% ORR with [^{177}Lu]Lu-DOTATATE, which itself is an improvement over conventional treatment with octeotride (ORR of 4%).[218] Perspective Therapeutics has both [^{212}Pb]Pb-VMT-α-NET[219] and [^{212}Pb]Pb-VMT-01[28] in phase I/IIa clinical trials for the treatment of SSTR-positive NETs and melanocortin-1 receptor (MC1R)-positive melanoma, respectively.

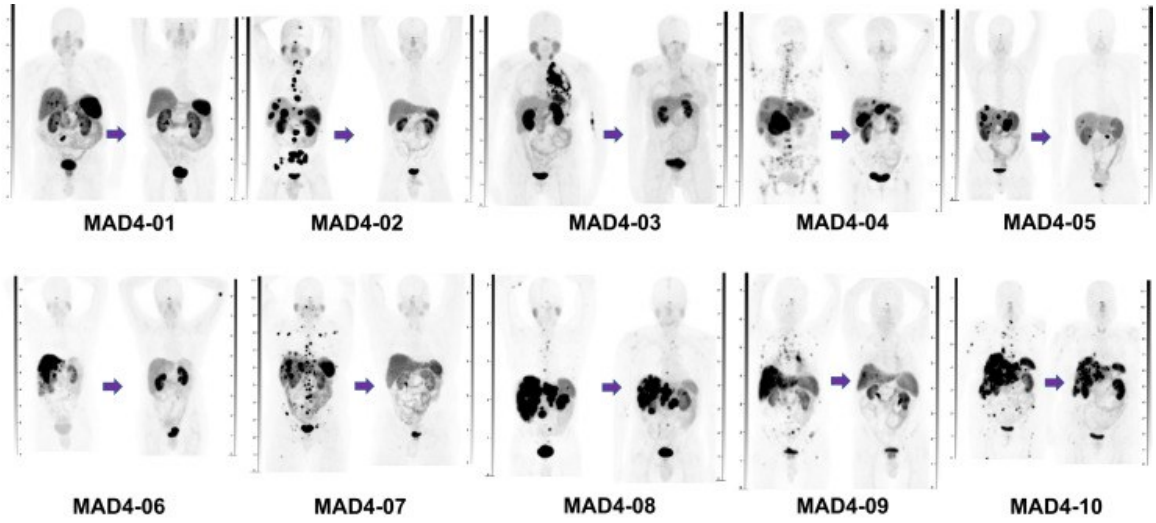

Figure 1.23. Images of [^{68}Ga]Ga-DOTATATE PET/CT scans of 10 patients before and after treatment administration of 4 cycles of 2.50 MBq/kg (67.6 μCi/kg) of [^{212}Pb]Pb-DOTAMTATE.[29]
This figure was originally published in the Journal of Nuclear Medicine and is reproduced with permission. Delpassand, E. et al. Targeted α-Emitter Therapy with ^{212}Pb-DOTAMTATE for the Treatment of Metastatic SSTR-Expressing Neuroendocrine Tumors: First-in-Humans Dose-Escalation Clinical Trial. J Nucl Med. 2022, 63(9):1326 – 1333.

^{212}Pb can also be used for SPECT imaging with the 238.6 keV (Abundance = 43.6%) and 75-91 keV emissions (Abundance ranges from 5.75 –16.8%), as has been done to image mCRPC.[220] Although possible, the high energy 2.6 MeV gamma photon emitted by daughter ^{208}Tl can cause significant scattering and thus high levels of noise that make obtaining high quality images useful enough for treatment planning and progress evaluation difficult. Luckily, ^{212}Pb has a diagnostic counterpart, ^{203}Pb ($t_{1/2}$ = 51.9 h), that decays via electron capture and emits a 279 keV photon (Abundance = 81%) compatible with SPECT imaging. By first employing ^{203}Pb, physicians can observe and quantify tumour uptake to determine if treatment with ^{212}Pb would be beneficial for the patient as the biodistribution of the ^{203}Pb RP should be nearly identical to that of its ^{212}Pb counterpart as they are both the same element and thus have identical chemical properties. This is a distinct advantage over the use of mixed theranostic pairs (ex: ^{68}Ga

and ^{177}Lu) where the biodistribution can be drastically different between the two members due to the use of two different metals or even different targeting vectors. An element-equivalent theranostic approach minimizes radiation exposure, especially if it is determined that this treatment would not be suitable for this patient, compared to directly injecting and imaging with ^{212}Pb. With such great potential, the next few years will be pivotal to understand the power that alpha emitters like ^{212}Pb hold and how revolutionary they could be for RPT, so long as there is sufficient supply available.

As a generator produced isotope, the supply of ^{212}Pb is dictated by the supply of its parent ^{228}Th. There are several methods to produce ^{228}Th for RPT, such as via ^{232}Th high energy proton energy spallation[156], neutron irradiation of ^{226}Ra[221,222], and extraction from naturally occurring ^{232}Th ores or reactor produced ^{232}U.[223] When ^{228}Th is produced via spallation of multi-gram quantities of ^{232}Th on high energy (>100 MeV) cyclotrons, one of the major challenges associated with such method is the inability to isolate ^{228}Th from ^{232}Th due to identical chemical behaviour. Although ^{224}Ra could be separated from the ^{228}Th and ^{232}Th to produce a ^{224}Ra/^{212}Pb generator, separating nanograms of ^{224}Ra from 10 grams of ^{232}Th is challenging and there will very likely be breakthrough in the ^{224}Ra fractions. However, this method can reliably produce preclinical ^{228}Th/^{212}Pb generators that can be used to further explore ^{212}Pb radiochemistry before application in clinical studies.[113,156]

^{228}Th can also be produced through neutron irradiation of ^{226}Ra on Oak Ridge National Laboratory's High Flux Isotope Reactor.[222] ^{226}Ra is irradiated to produce ^{227}Ra (via ^{226}Ra (n,γ)^{227}Ra) that further undergoes beta decay to ^{227}Ac, which further can be irradiated to produce ^{228}Ac (via ^{227}Ac (n,γ) ^{228}Ac), which undergoes beta decay to produce ^{228}Th, as summarized in **Figure 1.24**.[222] The feasibility of this production method is dependent on uncompromised access to few costly, highly complex high flux reactors and ^{226}Ra, which is only available in limited quantities at a high cost due to the complexity of extracting this isotope from uranium ores. Even with access to these facilities and materials, ^{229}Th can be co-produced if ^{228}Th further captures a neutron via the ^{228}Th (n, γ) ^{229}Th reaction, reducing radionuclidic purity as ^{229}Th will decay to produce ^{225}Ra and all of its subsequential daughters including ^{225}Ac and ^{213}Bi.[222] If a purification method can be established to separate the produced ^{212}Pb from ^{225}Ac, this issue can be minimized, but this can make construction of generators more complicated. Reactors can also, typically as a by-product of nuclear processes involving the use of ^{232}Th or ^{233}U, produce ^{232}U ($t_{1/2}$

= 69 y) which undergoes alpha decay to produce ^{228}Th. Using anion exchange chromatography, ^{228}Th is separated from ^{232}U and further processed to isolate ^{224}Ra to construct ^{224}Ra/^{212}Pb generators.[224] Using this method, a 16 mCi (592 MBq) ^{224}Ra/^{212}Pb generator is available every month.[224]

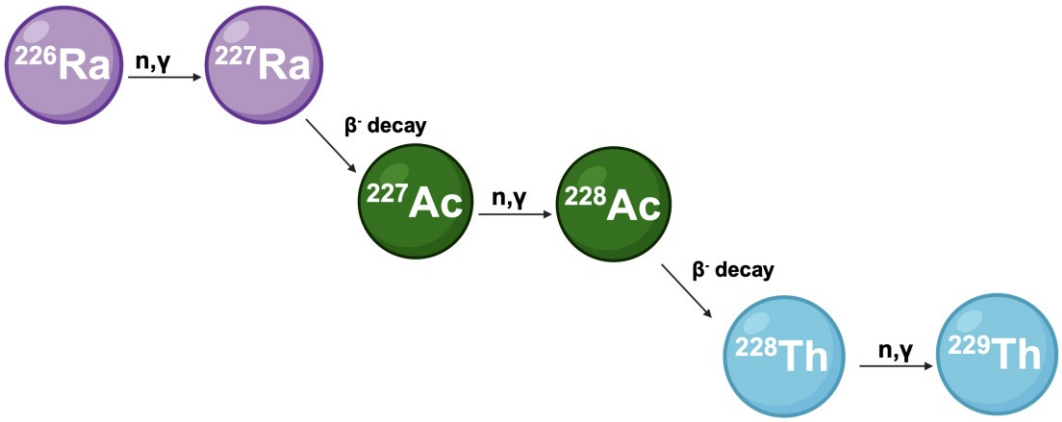

Figure 1.24. Production pathway for therapeutic radiometals from ^{226}Ra and daughter targets on a high flux reactor.[222]

With ^{228}Th being a part of the decay chain of naturally occurring ^{232}Th, it can be purified from thorium ores. As shown in **Figure 1.22**, ^{232}Th decays to ^{228}Ra ($t_{1/2}$ = 5.75 y) which can be purified from the ^{232}Th which can then be further used to produce ^{228}Th without interference from ^{232}Th. However due to a long half-life of 14 billion years, the specific activity of ^{232}Th is low at 4 MBq/kg and thus hundreds of thousands of kilograms of ^{232}Th would need to be processed and purified to reach clinical requirements. As this is a natural ore, attaining this is possible but production facilities must have state of the art processes and equipment to be able to separate out micrograms to nanograms of ^{228}Ra from thousands of kilograms of ^{232}Th. Although this may be challenging, this method currently supplies a large percentage of the world's ^{228}Th, alongside reactor-produced ^{228}Th, to continue to provide ^{212}Pb for clinical trials.

1.4.3.6. ^{225}Ac

With a half-life of 9.9 days and a yield of four alpha particles in its decay chain with energies between 5.8 – 8.4 MeV, as shown in **Figure 1.25**, ^{225}Ac is a potent alpha-emitter that has attracted significant clinical interest for RPT. When multiple alpha particles are emitted, more dose is delivered to the tumour as more ionization events and cell damage occur, resulting in a higher therapeutic effect compared to decay chains with fewer

emissions.[33] However, as previously discussed, the challenge with these radiometals is the recoil effect which essentially, if the RP has not been internalized, makes the therapy no longer targeted. Ultimately there should be a balance between the increased therapeutic effect from multiple emissions and potential off-target effects from the recoil experienced upon decay.

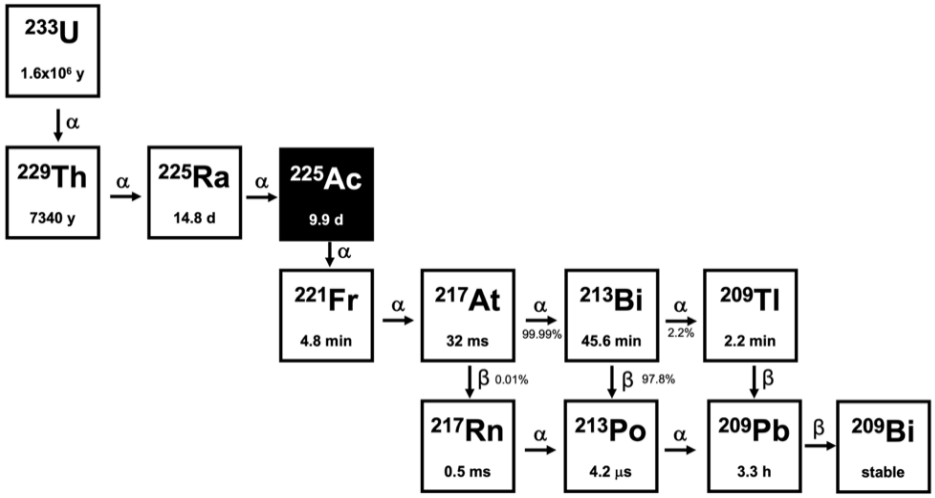

Figure 1.25. Decay chain of ^{233}U, which decays to ^{225}Ac.

Unlike with lead, there are no actinium isotopes that offer imaging capabilities without also emitting therapeutic alpha particles, which complicates treatment planning with this isotope. Although not as ideal as an element-equivalent theranostic pair, diagnostic radiolanthanides, such as ^{155}Tb or ^{133}La, or even ^{68}Ga, can be used as an imaging surrogate for ^{225}Ac. Via the 440 keV (Abundance = 11.44%) and 218 keV (Abundance = 25.9%) gamma ray emissions from ^{221}Fr and ^{213}Bi, respectively, some studies suggest that it may be one day possible to image ^{225}Ac directly with SPECT using high energy collimators.[225,226] However, high noise levels and activity requirements for quantitative imaging pose the greatest challenge as too high of a dose may result in toxicity for patients and until these issues are resolved, other diagnostic isotopes will be used instead.[227]

^{225}Ac has shown promising pre-clinical and clinical results for RPT and as a result, ^{225}Ac-based RPs are involved in several clinical trials. A phase 1 dose escalation trial is underway with ^{225}Ac-labelled antibody JNJ-69086420 for treatment of mCRPC by targeting human kallikrein 2 (hK2), which is similar to PSMA with minimal expression in non-prostate tissue.[228] In this study, treatment was escalated from 50 μCi (1.85 MBq) to

400 μCi (14.8 MBq) every 8 to 12 weeks.[228] Remarkably, 44% of patients in this trial had a PSA reduction of at least 50% in the 250 μCi cumulative dose group.[229] However, although it was important to do this dose escalation study to determine safe levels, treatment emergent adverse events (TEAEs) were seen in 96% of patients with the most common being thrombocytopenia, a condition classified by low platelet levels, at 58.7%.[229] Two dose related deaths occurred at cumulative doses of 600 μCi (22.2 MBq) or greater, showing that this powerful isotope has the power to both heal and harm and thus dosimetry calculations and treatment planning are crucial.[229] This study is one of the first that utilized a fully intact antibody labelled with ^{225}Ac. It is commonly thought that using isotopes, like ^{225}Ac, with long half-lives may be better matched with studies with antibodies due to their longer circulation times in the body before they reach the tumour site. However, as shown from the results of this clinical trial, further studies that focus on the effects of increased circulation time of a powerful alpha emitter in the body are needed to learn how to negate them. It may be that pre-targeted approaches or the use of antibody fragments may be more suitable for antibody-based treatments with ^{225}Ac.

Nevertheless, ^{225}Ac has also been employed in peptide-based studies and clinical trials and has shown revolutionary results, as shown in **Figure 1.26** with [^{225}Ac]Ac-PSMA-617 in the first-in-human treatment with an alpha emitter-labelled PSMA RPT.[39] This patient had disease progression after 2 cycles with [^{177}Lu]Lu-PSMA-617 and after a total of three cycles with ^{225}Ac at a dose of 100 kBq/kg (2.7 μCi/kg), PSA could not be detected as the patient showed a complete response.[39] Other pilot studies with this RPT led to a >90% reduction in PSA levels in 82% (14/17) of patients with 41% (7/17) showing a complete response for at least 12 months after therapy.[230] The most common side effect was xerostomia (dry mouth) which was due, in part, to the off-target expression of PSA on the salivary glands, causing irradiation and damage of these tissues.[230] As a result of the remarkable responses, the AcTION study, which is a phase I trial with [^{225}Ac]Ac-PSMA-617 in men with PSA-positive mCRPC, is underway.

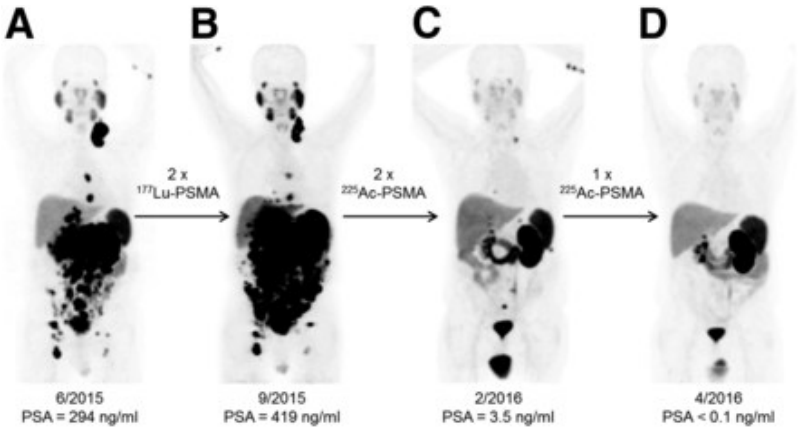

Figure 1.26. PET/CT scans of [^{68}Ga]Ga-PSMA-11 in a patient (A) initially and (B) after 2 treatment cycles with [^{177}Lu]Lu-PSMA-617. Subsequentially after disease progression, the patient was imaged again after (C) two treatment cycles and (D) three treatment cycle with [^{225}Ac]Ac-PSMA-617.[39]

This figure was originally published in the Journal of Nuclear Medicine and is reproduced with permission. Kratochwil, C. et al. ^{225}Ac-PSMA-617 for PSMA-Targeted-α-Radiation Therapy of Metastatic Castration-Resistant Prostate Cancer. J Nucl Med. 2016, 57(12): 1941 – 1944.

Despite the promise that ^{225}Ac holds, its use and advancement in clinical trials is severely limited by its availability and thus numerous techniques have been used to produce this rare isotope. The largest source of ^{225}Ac comes from ^{229}Th ($t_{1/2}$ = 7880 y) produced through the decay of ^{233}U that was originally intended for use in nuclear weapons and reactors (**Figure 1.25**).[231] This ^{229}Th can be used to produce either ^{229}Th/^{225}Ac or ^{225}Ra/^{225}Ac generators that produce 63 GBq (1.7 Ci) of high radionuclidic purity ^{225}Ac anually.[232] However, this quantity is not sufficient to support preclinical research, clinical trials, and one day approved RPs and it has been estimated that the annual demand could reach 1.85 TBq (50 Ci).[232,233] To address this gap, ^{225}Ac can be produced via several methods including from ^{232}Th spallation[157], cyclotron[122] and neutron irradiation[222] of ^{226}Ra, and via linear accelerators with ^{226}Ra targets.[234] Although useful for producing preclinical quantities of ^{225}Ac from uranium carbide targets, at the current time of writing ISOL is not capable of reliably providing clinical quantities of ^{225}Ac and thus is not a focus in this section.[97]

Through proton spallation of ^{232}Th, ^{225}Ac can be directly produced or the co-produced ^{225}Ra can be purified to serve as a generator for ^{225}Ac.[157] Theoretically, with a 500 MeV proton beam with a current of 120 μA, which can be found at TRIUMF in Vancouver, BC, 3 TBq (82 Ci) of ^{225}Ac could be directly produced monthly, already meeting the projected demand.[232] However, co-produced ^{227}Ac ($t_{1/2}$ = 21.8 y), despite only

accounting for 0.15% of the Ac produced[157], can cause extended radiotoxicity and poses a challenge for waste disposal due to its long half-life. However, if ^{225}Ra is harvested and used as a generator, the quantity of ^{227}Ac can be reduced to less than 7.5×10^{-5}%, making it useful for clinical trials, despite the comparatively reduced (5-fold lower) yield of ^{225}Ra.[157] One additional challenge with this method is that it generates a significant amount of radioactive waste, including long-lived isotopes that can make disposal challenging. Yet it can also act as a source of potentially useful co-produced isotopes such as ^{228}Th.[156] Although this method poses its own challenges, if it can provide such significant quantities of ^{225}Ac, further development of the methodology to enable this should be prioritized.

Using ^{226}Ra targets, cyclotrons and reactors can be used to directly or indirectly produce ^{225}Ac, respectively. With a large cross section of 710 mb at 16.8 MeV, the ^{226}Ra (p,2n) ^{225}Ac reaction has the potential to reach expected demand for ^{225}Ac with a single irradiation of a 1 gram target with 20 MeV protons as an irradiation at a current of 500 μA could produce up to 4 TBq (108 Ci) of ^{225}Ac.[232] Although ^{226}Ac is also co-produced, with a shorter half-life of 29.4 hours, the radionuclidic purity can be increased by allowing the isotope to decay. However, the high cost of this target material, due to its scarcity and that 3.9 tonnes of uranium ore are required to produce a 1 g ^{226}Ra target[232], and the special infrastructure required to deal with the ^{222}Rn ($t_{1/2}$ = 3.8 d) gas emitted from the target may limit its widespread use. Through the pathways shown in **Figure 1.24**, scarce ^{226}Ra targets on a high flux reactor can produce 74.0 ± 7.4 MBq/g of ^{229}Th which, through its decay, can produce ^{225}Ac, respectively.[222] Although the yields are lower, by producing ^{229}Th, the production of ^{225}Ac is extended compared to cyclotron approaches due to its long half-life. Additionally, co-produced ^{227}Ac, ^{228}Ac, and ^{228}Th can be harvested to prepare generators of ^{227}Th, ^{228}Th, and ^{224}Ra or ^{212}Pb, respectively.[222]

One of the most promising routes to produce ^{225}Ac is via the use of electron linear accelerators to produce the parent ^{225}Ra via the ^{226}Ra (γ,n) ^{225}Ra reaction.[235] While ^{224}Ra can be co-produced via the (γ,2n) reaction, this production method does not produce any other actinium isotopes and so this ^{225}Ac is considered to be no carrier added, which makes regulatory approval and waste management easier for implementation in clinics. Despite the high cost of the ^{226}Ra target, using an IBA TT300 HE electron accelerator, which can produce a beam up to 245 kW, NorthStar Medical Radioisotopes has claimed that they will be able to produce up to 7400 MBq (200 Ci) of ^{225}Ac per year per accelerator

employed[236], surpassing the expected clinical demand to allow for even more research to be conducted with this powerful isotope without worry about supply. **Table 1.3** summarizes the different production routes for ^{225}Ac along with the respective pros and cons of each method.

Table 1.3. Summary of discussed production routes for ^{225}Ac production.

Production Method	Pros	Cons
^{229}Th/^{225}Ac generators	• Free of long-lived ($t_{1/2}$ = 21.8 y) ^{227}Ac contaminants • Long half-life of ^{229}Th ($t_{1/2}$ = 7880 y) allows for ^{225}Ra/^{225}Ac generators to be produced reliably for decades to come • Established and reliable separation chemistry	• Sourced from extremely limited ^{233}U originally produced for use in nuclear weapons material, raising concerns over handling • Only able to produce 63 GBq (1.7 Ci) annually which is insufficient to meet forecasted clinical demands
^{232}Th spallation	• ^{232}Th target material is naturally occurring • ^{225}Ac with a 7.5x10^{-5}% ^{227}Ac content can be produced via isolation of the ^{225}Ra parent from spallation mixture • The process is scalable and can produce up to 3 TBq (82 Ci) monthly at maximum capacity • A multitude of other isotopes useful for nuclear medicinal purposes are co-produced and can be isolated (e.g. ^{228}Th for ^{212}Pb production	• ^{232}Th is a fissionable material and thus is safeguarded, limiting access to this target material • Requires access to high energy accelerators which are located at only a few sites globally • Co-production of long-lived radionuclidic impurities in the spallation process can lead to difficulties with waste disposal • ^{225}Ac directly produced from the spallation reaction contains ^{227}Ac, which may limit its clinical use due to radiotoxicity concerns
Neutron irradiation of ^{226}Ra	• Production of ^{229}Th parent isotope will allow for reliable production of ^{225}Ra/^{225}Ac generators for decades to come	• Utilizes scarce and expensive ^{226}Ra as the target material making recycling required • ^{226}Ra releases ^{222}Rn in its decay which requires specialized facilities to prevent release of this radioactive gas

	• Co-produced ^{227}Ac, ^{228}Ac, and ^{228}Th can be harvested to prepare generators of ^{227}Th, ^{228}Th and ^{224}Ra/^{212}Pb, respectively, making the process more economically feasible	• Only 74.0 ± 7.4 MBq of ^{229}Th is produced per gram of ^{226}Ra, making this method unlikely to produce clinical quantities in the near future • ^{228}Th is co-produced and separation of ^{229}Th and ^{228}Th is not possible • The number of suitable high flux reactors that can produce the ^{229}Th is extremely limited
Cyclotron production from ^{226}Ra	• With a peak cross section (710 mb) occurring at 16.8 MeV, many existing low energy medical cyclotrons could be used for ^{225}Ac production, allowing for onsite production • No long-lived co-produced Ac isotopes • Minimal competing reaction channels • A single irradiation could produce up to 4 TBq (108 Ci) of ^{225}Ac	• Utilizes scarce and expensive ^{226}Ra as the target material making recycling required • ^{226}Ra releases ^{222}Rn in its decay which requires specialized facilities to prevent release of this radioactive gas • Potential co-production of ^{226}Ac from the ^{226}Ra (p,n) ^{226}Ac reaction • Large target masses needed to reach production potential
Production of ^{225}Ra/^{225}Ac generators on linear accelerators	• Produces parent isotope ^{225}Ra to allow for construction of ^{225}Ra/^{225}Ac generators to extend the availability of ^{225}Ac • Does not co-produce any Ac impurities • It is claimed that up to 7400 MBq (200 Ci) of ^{225}Ac will be produced annually	• Utilizes scarce and expensive ^{226}Ra as the target material making recycling required • ^{226}Ra releases ^{222}Rn in its decay which requires specialized facilities to prevent release of this radioactive gas • High operational cost of linacs • Limited high energy linacs available

1.5. Concluding Remarks

The success of nuclear medicine is dependent on all aspects of RP design. The choice of radiometal determines the diagnostic or therapeutic abilities, the chelator affects radiolabeling ability and *in vivo* stability, and the targeting vector delivers the selective aspect that sets RPT apart from other traditional medical approaches. However, without the ability to produce and separate clinical quantities of these radionuclides, research will never extend beyond the pre-clinical level, hindering the advancement of such a promising field. The continued research and development of new nuclides, purification methods, chelators, and targeting vectors is key to new breakthroughs and revolutions in cancer diagnosis and treatment.

1.6. Thesis Overview and Aims

Within this work, I aimed to create a foundation for the development of ^{203}Pb/^{212}Pb-based radiopharmaceuticals at TRIUMF by exploring and developing nearly all aspects of radiopharmaceutical development including isotope production and purification, chelator (bifunctional and non-bifunctional) and radiopharmaceutical synthesis, and *in vitro* and *in vivo* evaluation of these radiopharmaceuticals in cell and murine models, respectively. Herein, the aims of this work were to:

- Develop a reproducible isotope production and purification method amenable to both ^{203}Pb and ^{212}Pb to ensure a stable supply of these isotopes.
- Synthesize, characterize, and evaluate novel chelators to identify a promising candidate for *in vivo* studies with ^{203}Pb and ^{212}Pb.
    - Perform radiolabeling studies and competition assays to evaluate their radiolabeling efficiencies and kinetic inertness *in vitro*.
- Synthesize the bifunctional analogue of the most promising chelator candidate and conjugate to a biological targeting vector
    - Perform radiolabeling studies, serum stability studies, and cell-based studies to evaluate if bioconjugation has affected the coordination capabilities and stability of the chelator and to determine the half maximal inhibitory concentration values of the bioconjugates to ensure conjugation has not strongly affected binding affinity.
- Evaluate the radiopharmaceuticals *in vivo* in tumour-bearing mouse models.

- Identify the most promising candidate from which future work should improve upon.

Chapter 2 outlines the isotope production and purification method development for both ^{203}Pb and ^{212}Pb in order to establish a reliable supply of high purity isotopes. The optimized methods developed in Chapter 2 enable all further studies in this thesis and the broad TRIUMF community, including international and industrial collaborators. Chapter 3 explores the effect of macrocyclic ring size on [^{203}Pb]Pb^{2+} complex stability in pyridyl-containing chelators, and identifies a promising cyclen-based candidate, Cyclen-4Py, to move forward towards bifunctionalization. Chapter 4 investigates the effect of the bioconjugation bond type and stability on the *in vivo* biodistribution of fibroblast activation protein inhibitor (FAPI)-based and cyclic melanocyte stimulating hormone(CycMSH)-based bioconjugates with ^{203}Pb and ^{212}Pb. Lastly, Chapter 5 summarizes and concludes all the work presented here and suggests potential future projects to continue to expand the research platform for ^{203}Pb and ^{212}Pb explored in this thesis.

Chapter 2.

Optimized Production, Purification, and Radiolabeling of the $^{203}Pb/^{212}Pb$ Theranostic Pair for Nuclear Medicine

2.1. Introduction

Within the field of nuclear medicine, *theranostic* radiopharmaceuticals (TRPs), where *theranostic* refers to the combination of a therapeutic and diagnostic agent, enable diagnostic imaging and therapy to be conducted simultaneously, or sequentially, to allow for the development of image-guided, personalized cancer treatment plans.[237] Overall, the goal of *theranostics* is to identify the most compatible treatment option for patients to improve clinical outcome.[237] Bifunctional-chelator (BFC)-based radiopharmaceuticals for *theranostics* are composed of a radioactive metal coordinated to a bifunctional chelator attached, via a linker, to a biological targeting vector.[238,239] The vector selectively seeks out and binds to unique cell biomarkers on cancer cells to directly and selectively deliver a radioactive payload, compatible with either imaging techniques or therapy dependent on the type of radioactive decay the radiometal undergoes, to cancer cells.[238,239]

Recent successes in clinical trials with therapeutic isotope lead-212 (^{212}Pb)-labeled radiopharmaceuticals is sparking significant interest in the potential of the element-equivalent $^{203}Pb/^{212}Pb$ theranostic pair as a means to develop image-guided, personalized cancer treatment plans for patients.[29] ^{203}Pb is a diagnostic isotope that decays via electron capture, releasing a 279 keV photon (81%) compatible with single photon emission computed tomography (SPECT).[240] ^{212}Pb acts as a therapeutic isotope in this pair. Despite ^{212}Pb being a pure β^- emitter, it is used for targeted alpha therapy as it acts as an *in vivo* generator of its alpha emitting daughters ^{212}Bi ($t_{1/2}$ = 60.5 min, $E_{\alpha\ avg}$ = 6.2 MeV, 36%) and ^{212}Po ($t_{1/2}$ = 0.3 μs, $E_{\alpha\ avg}$ = 8.9 MeV, **Figure 2.1**).[239,241] Due to its longer half-life compared to its daughters, the use of ^{212}Pb allows for increased radiopharmaceutical preparation time.

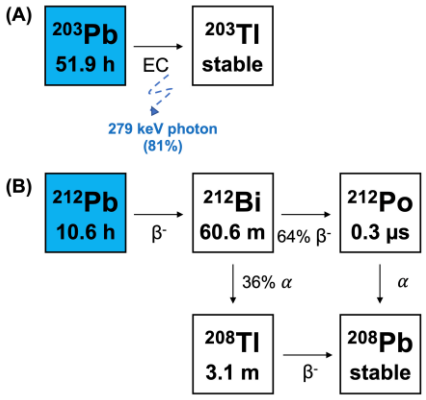

Figure 2.1. Decay scheme of (A) ^{203}Pb and (B) ^{212}Pb.

Although all components of BFC-based radiopharmaceuticals affect the success of TRPs, the importance of the specific activity of the radiometal, which refers to the amount of measured activity per unit mass of compound, is often overlooked.[242] Stable (non-radioactive) metal impurities in the radiometal solution can interfere with radiolabeling and, depending on the selectivity of the chelator, may be coordinated by the chelator. Competition with the radiometal can lower radiochemical yields (RCYs) and thus apparent molar activity (A_m) of the radiopharmaceutical. A low A_m can affect kinetics and uptake at the tumour site and can lead to poor scan quality or low therapeutic effect.[243] Therefore, improving the chemical purity of the radiometal solution, and thus increasing the specific activity, is critical for advancement of TRPs. For cyclotron produced isotopes, for example ^{203}Pb, the greatest chemical impurity is often the target material[156], mandating effective separation chemistry.

In an ideal purification procedure, one should avoid the use of several columns and evaporation steps to help simplify automation and reduce risk of material loss, while utilizing a column that will remove the bulk contaminant while the isotope of interest remains bound until elution. The desired radiometal should then be eluted in a small volume of dilute acid or buffer solution to help minimize the mass of radiopharmaceutical precursor needed for labeling. In the case of cyclotron produced isotopes, it is also ideal to enable recycling of the expensive enriched target material included in the purification process to reduce costs.

^{203}Pb production, particularly on a 13 MeV cyclotron like at TRIUMF, poses many challenges. ^{203}Pb is produced from the proton bombardment of Tl targets. At low proton energies (i.e. 13 MeV), ^{203}Pb is produced via the ^{203}Tl (p,n) ^{203}Pb reaction, while at higher

proton energies (i.e. 24 MeV), ^{203}Pb is produced via the ^{205}Tl (p,3n) ^{203}Pb reaction.[244,245] At 13 MeV the cross section of the ^{203}Tl (p,n) ^{203}Pb reaction is low at 37.4 mb[246], limiting the amount of activity produced at the end of bombardment (EOB). Using natural Tl target, EOB yields are further limited by the lower natural abundance of ^{203}Tl (29.5%) compared to ^{205}Tl (70.5%)[247]. Additional complications include the low melting point of Tl (304 ºC), which can cause issues with thermal stability of targets at higher currents; along with safety and contamination risks that need to be considered when using a highly toxic element such as Tl.

In our previous work on the production, purification, and radiolabeling of the ^{203}Pb/^{212}Pb theranostic pair, the production of ^{203}Pb was limited by low thermal stability of the Tl targets, leading to a maximum allowable current of 8 μA.[156] Our previously-reported one-column purification approach, which employed extraction chromatographic PB resin, was rapid, simple, compatible with both isotopes, and eluted $^{203/212}$Pb in 1 M NH_4OAc (pH 7, 3 mL), making the elute directly compatible with radiolabeling.[156] However, Tl and ^{232}Th were present in the ^{203}Pb and ^{212}Pb elutes at concentrations of 58.2 ± 35.4 ppm and 24.3 ± 16.2 ppm, respectively. In the ^{203}Pb elute, stable Pb was present at a concentration greater than 400 ppb.[156] The high concentrations of these metal impurities directly interfered with radiolabeling and contributed to the low specific activity and chemical purity that prevented, in conjunction with limitations to ^{203}Pb production due to thermal instability, *in vivo* pre-clinical studies.[156] As a result, we focused on improving the manufacturing of the thallium target to allow for increased beam current to be applied during irradiation and on developing a novel, simple purification method that will improve the specific activity and chemical purity of the $^{203/212}$Pb elute that would enable (pre-)clinical use of the theranostic pair.

In this work, we describe the development of a novel target manufacturing method modified from a literature electroplating procedure[248]. These silver-backed electroplated targets have extremely high thermal stability, allowing us to produce pre-clinical amounts of ^{203}Pb for imaging studies. Additionally, we have developed a novel, high-yielding purification method compatible with both ^{203}Pb and ^{212}Pb. This method uses selective Tl precipitation for ^{203}Pb, requires minimal columns, and minimal amounts of acid. It avoids evaporation and elutes $^{203/212}$Pb in just 2 mL of dilute HCl. This method has also resulted in $^{203/212}$Pb elutes with lower concentrations of stable metal impurities compared to other methods found in literature.[131,156,249,250] This method is also directly compatible with Tl

recycling, a rare but desirable feature that will decrease the cost of using enriched Tl targets. Optimization of the chemical purity and specific activity of $^{203/212}$Pb gave improved radiochemical yields (RCYs) of Pb^{2+} chelators. We anticipate this will improve the outcomes of imaging and therapy studies to come.

2.2. Materials and methods

2.2.1. Chemicals

All reagents used were purchased from commercial suppliers (Sigma Aldrich, Fisher Scientific, VWR) and were used as received, unless otherwise noted. Ultrapure hydrochloric acid (TraceSELECT), sodium hydroxide (99.99% trace metal grade), and ammonium acetate (Trace metal grade 99.99%), and Dowex-1X8 anion exchange resin (200-400 mesh, Cl form) were purchased from Fisher Scientific (Pittsburgh, PA). Ultrapure nitric acid (Environmental grade) was purchased from VWR (Radnor, PA). EDTA (99.995% trace metals basis), BRIJ-35, hydrazine hydrate (reagent grade 50-60%), thallium (I) nitrate (99.999% trace metals basis), thallium (I) sulphate (99.99% trace metals basis), 3-methyl-2-benzothiazolinonehydrazone hydrochloride (MBTH), N-(1-naphthyl)-ethylenediaminedihydrochloride (NEDA), orthophosphoric acid (ACS grade), phenol, sodium bromide, and hydrogen peroxide (30% w/w) were purchased from Millipore Sigma (St. Louis, MO). Silver sheets (14 gauge, 99.999, ¼ hard) were obtained from RioGrande (Albuquerque, NM). PB resin (Di-t-butylcyclohexano 18-crown-6, 100–150µm particle size) was obtained from Eichrom Technologies (Lisle, IL). 1 mL poly-propylene cartridges and 1/8″ polyethylene frits were purchased from United Chemical Technologies (Lewistown, PA). Natural Tl (99.99% metals basis) was purchased from Alfa Aesar (Tewksbury, MA). S-2-(4-Isothiocyanatobenzyl)-1,4,7,10-tetraaza-1,4,7,10-tetra(2-carbamoylmethyl)cyclododecane (herein referred to as TCMC) was purchased from Macrocyclics (Plano, TX) and the cryptand (Herein referred to as Crypt-OH) was synthesized as previously described.[251] Silicic acid impregnated instant thin layer chromatography paper (iTLC-SA) was purchased from Agilent Technologies (Santa Clara, CA). Deionized water was prepared on site using a MilliporeDirect-Q® 3UV water purification system.

2.2.2. Instrumentation

All radioactivity measurements were performed using gamma ray spectroscopy on an N-type co-axial high purity germanium (HPGe) gamma spectrometer (Canberra Industries) that has been calibrated with a 20 mL ^{152}Eu and ^{133}Ba source. Aliquots (5-200 µL) were removed from the samples and diluted to 20 mL for measurement at a minimum distance of 5 cm above the detector until the uncertainty of the peak area was below 5% with the dead time also kept below 5%. Analysis was performed with the Genie 2000 software package (Canberra Industries) using the 279 keV and 401 keV gamma lines for ^{203}Pb measurement, and the 238 keV and 300 keV gamma lines for ^{212}Pb measurement. Non-radioactive impurities in the ^{203}Pb and ^{212}Pb elutes were quantified using inductively coupled plasma mass spectrometry (ICP-MS) using an 8900 ICP-MS Triple Quad with a SPS 4 autosampler (Agilent Technologies, Santa Clara, CA) calibrated with calibration standards (10 ppt to 1 ppm) prepared from multi-element calibration standard 1 and 2A (Agilent Technologies, Santa Clara, CA). RadioTLC was performed using an AR-2000 TLC Scanner (Eckert and Ziegler, Valencia, CA) and radiochemical yields quantified using WinScan V3 software (Academic Software Inc.). The electroplating apparatus was obtained from ARTMS Inc. (Burnaby, BC). The set-up of the plating cell used has been previously described.[119] Spectrophotometric studies were performed using a Cary 100 UV-Visible spectrophotometer. For electroplating, the power supply used was BK Precision 9174B (B&K Precision, Yorba Linda, CA).

2.2.3. Thallium targetry and cyclotron irradiation

The target disc was manufactured from a sheet of fine silver with a diameter of 28 mm and thickness of 1.5 mm and included a recess diameter of 10 mm and depth of 0.55 mm. The silver discs were polished using diamond paste (Ted Pella, Redding, CA) until a mirror finished was achieved and cleaned with water and acetone prior to plating.

The constant current electroplating method used to produce the silver backed thallium targets was based on a literature method with minor deviations.[248] The plating bath was an alkaline (pH >12.5) EDTA (0.5 M) bath with 1% hydrazine hydrate and 0.2% BRIJ-35.[248] To prepare a 100 mL plating bath, in the first beaker, 21 g of ethylenediamine tetraacetic acid (EDTA) and 5 g of sodium hydroxide were dissolved in 90 mL of deionized water and stirred until completely dissolved. Once dissolved, 2.53 mL of hydrazine hydrate

and 250 μL of BRIJ-35 were added. To a second beaker, 8.475 g of natural Tl_2SO_4 or 8.949 g of $TlNO_3$ was added and the contents of beaker 1 were transferred at a rate of 10 mL/min; once the transfer was complete, an additional 250 μL of hydrazine hydrate was added. To the plating chamber, approximately 6 mL of the plating solution was added, and electroplating occurred at a current density of 2.3 $mA \cdot cm^{-2}$ in constant current mode for 24 hours. The target was rinsed with deionized water, dried, weighed, and vacuum sealed until installation.

The Tl target was installed into a quick release solid target holder[252] on TRIUMF's TR13 (13 MeV) cyclotron[253] where the 13 MeV protons are degraded to approximately 12.8 MeV by an aluminum foil (25 μm thick) used to separate the targetry system from the vacuum. Targets were irradiated at 20 μA for 2-4 hours and after EOB, the target remained in the target holder for a minimum of 18 hours to allow for the decay of co-produced ^{202m}Pb ($t_{1/2}$ = 3.6 h).

2.2.4. Radiochemical separation of ^{203}Pb

Irradiated targets were dissolved in 4 mL of 2 M HNO_3 on a hot plate at 150 ºC. As soon as the dissolution of the thallium was complete, the solution was removed to reduce the dissolution of the silver target backing. The solution was then placed in a beaker of ice to precipitate Tl as $TlNO_3$ by taking advantage of the difference in the solubility of $TlNO_3$ in water at 100 ºC (414 g/100 mL)[254], 25 ºC (9.55 g/100 mL)[254], and 0 ºC (3.90 g/100 mL)[254]. A PB resin column, composed of 60 mg of PB resin packed into a 1 mL polypropylene cartridge, was conditioned with 5 mL of deionized water followed by 5 mL of 2 M HNO_3. The supernatant was loaded onto the PB resin column by gravity and washed with 10 mL of 2 M HNO_3 at a flow rate of 1 mL/minute to remove residual Tl and other metal impurities. The ^{203}Pb was eluted from the column with 2 mL of 8 M HCl into 4, 0.5 mL fractions at a flow rate of 1.5 mL/min. The first 1 mL of eluate was diluted to 2 M HCl with 3 mL of deionized water before loading onto a second column. The diluted elute was then loaded onto a second column composed of 500 mg of Dowex-1X8 anion exchange resin (200 – 400 mesh, Cl form), preconditioned with 10 mL of MilliQ water followed by 10 mL of 2 M HCl. The column was washed with 0.5 mL of 1 M HCl by gravity before eluting with 0.01 M HCl at a flow rate of 1.5 mL/min into 4, 0.5 mL fractions (See **Figure 2.2**). The yield and radionuclidic purity of the ^{203}Pb in the load, wash, and elute fractions for each column were

assessed via gamma spectroscopy. The chemical purity of the ^{203}Pb elutes was assessed via ICP-MS to quantify the concentration of stable metal impurities.

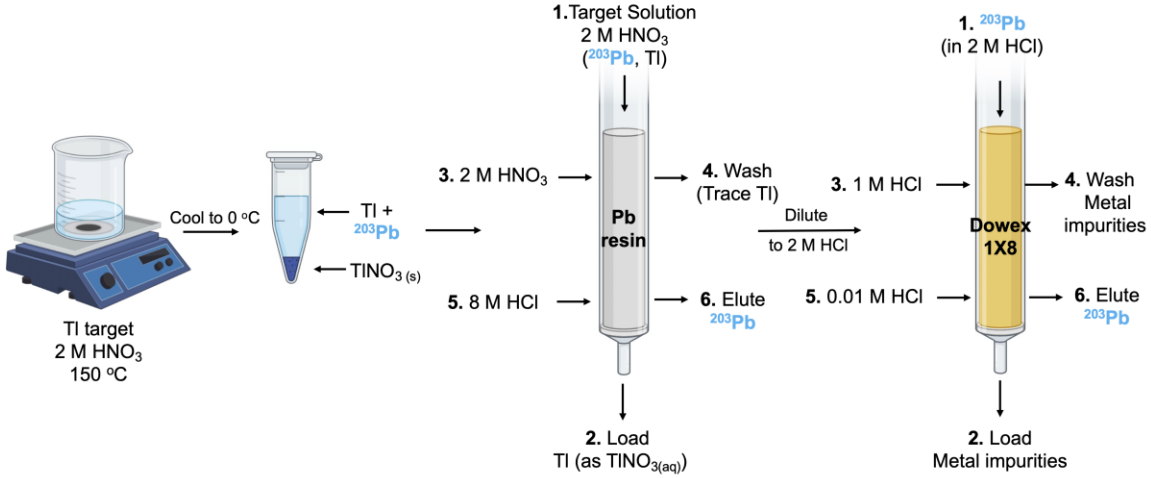

Figure 2.2. A novel ^{203}Pb purification method employing selective precipitation of thallium nitrate prior to extraction via anion exchange chromatography.

2.2.5. Recycling of Tl targets

To recycle the Tl target material, the load and wash fractions from the PB resin column of the ^{203}Pb purification step were evaporated to dryness and combined with the dried thallium (I) nitrate precipitate of the thallium precipitation step. The recovered Tl (I) nitrate was then added to a plating bath solution and was used for target plating. The oxidation state and yield of the recovered thallium was determined via colorimetry.[255] Briefly, this method is based on the *in-situ* generation of a diazonium cation of MBTH by Tl^{3+}, which reacts with NEDA to produce a blue-coloured product, whose absorbance at 590 nm is dependent on the concentration of Tl^{3+}. Samples with Tl^{+} will not produce the blue product, but the Tl in these samples can still be quantified when oxidized with bromine water to oxidize the Tl^{+} to Tl^{3+}.

2.2.6. Preparation of ^{228}Th/^{212}Pb generator stock solution and radiochemical separation of ^{212}Pb

A ^{228}Th/^{212}Pb generator stock solution was prepared as previously described.[156] Briefly, thorium peroxide, precipitated out from irradiated thorium targets, was dissolved in 200 mL of 10 M HCl before loading onto a 10 mL Dowex-1X8 column.[156] The column

was subsequently washed with 60 mL of 10 M HCl and then the load and wash fractions were collected and evaporated to dryness and exchanged three times with 10 M HNO_3 before redissolving in 30 mL of 2 M HNO_3.[156] The radiochemical separation of ^{212}Pb from the $^{228}Th/^{212}Pb$ generator and the characterization of the elute product was identical to that of ^{203}Pb with minor exceptions: 1) The exclusion of the thallium precipitation step and 2) that the generator stock solution was loaded onto the PB resin column at a flow rate of 1 mL/minute instead of by gravity (See **Figure 2.3**).

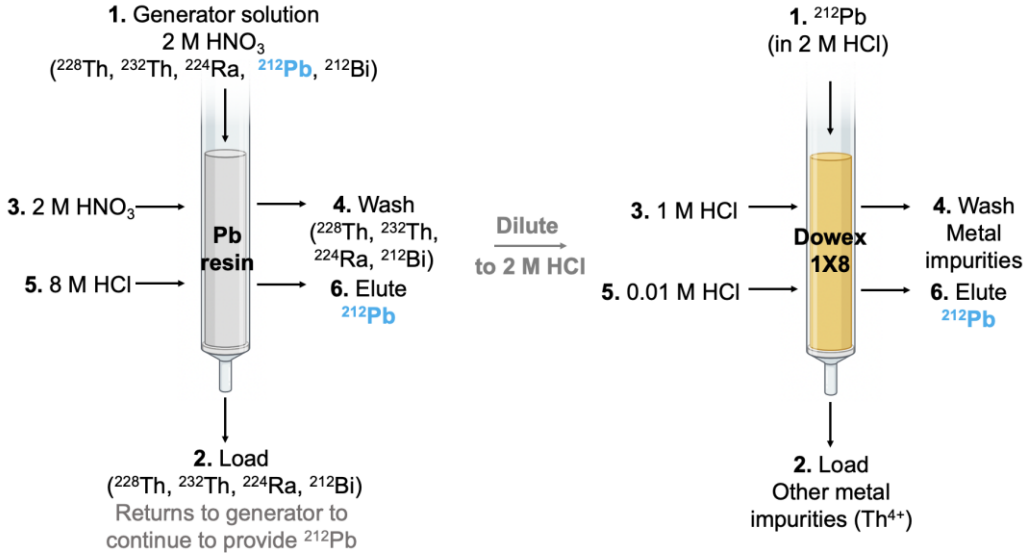

Figure 2.3. **^{212}Pb purification method employing extraction and anion exchange chromatography.**

2.2.7. Radiolabeling

Chelators TCMC and Crypt-OH were dissolved in deionized water to give stock solutions (10^{-2} M), from which serial dilutions were made to prepare chelator solutions at concentrations from 10^{-3} to 10^{-8} M. The radiolabeling reactions consisted of 10 μL of the respective chelator solution, 10 μL of 1 M NH_4OAc (pH 7), 2 μL (for ^{203}Pb, 85 kBq) to 5 μL (for ^{212}Pb, 100 kBq) of the elute solution, and 78-75 μL of deionized water for a final reaction volume of 100 μL. These differences in required activity volume reflect the lower kBq/μL concentration of ^{212}Pb over ^{203}Pb. These reactions were all performed at ambient temperature in triplicate. Radiochemical conversion was established using iTLC-SA plates developed using EDTA (50 mM, pH 5.0). Under these conditions, the Pb^{2+} complexes remain at the baseline (R_f = 0) and "free"/non-complexed Pb^{2+} migrates with the solvent line ($R_f \cong 1$). At 60 minutes, 10 μL aliquots were removed from each reaction mixture and

analyzed. To allow for the decay of ^{212}Bi ($t_{1/2}$ = 60.6 minutes), plates containing ^{212}Pb were measured a minimum of 10 hours after development. ^{203}Pb plates were measured immediately.

2.2.8. ICP-MS Analysis

For determination of the concentration of the stable metal impurities that may interfere with radiolabeling in the ^{212}Pb and ^{203}Pb elutes after the PB resin and Dowex-1X8 columns, 50 μL and 2 mL aliquots were removed, respectively, and diluted to 10 mL using 2% w/w HNO_3.

2.3. Results

2.3.1. Targetry and cyclotron irradiation

347.6 ± 11.7 mg (n = 7) of Tl was plated onto the silver backings after 24 hours at a current density of 2.3 mA·cm^{-2}. In an attempt to demonstrate the utility of recycled $TlNO_3$, 346.1 ± 8.7 mg (n = 4) of Tl was plated under identical conditions. The deposits were occlusion- and dendrite-free mitigating the need for mechanical pressing post plating. Prior to irradiation with higher currents, test irradiations were first performed with ^{nat}Tl targets using beam currents between 5 and 20 μA, for 2 to 4 hours to investigate thermal stability of the target. No signs of melting were observed over this range.

2.3.2. ^{203}Pb Isotope Production and Radiochemical Separation

On average (n = 4), 4-hour 12.8 MeV proton irradiations of ^{nat}Tl targets at 20 μA produced 131.8 ± 4.6 MBq of ^{203}Pb at the EOB. Under the same conditions, recycled ^{nat}Tl targets produced 138.7 ± 5.1 MBq (n = 3), as determined by gamma spectroscopy. The thallium metal of the target was completely dissolved after approximately 1 minute, and after cooling to 0 ºC, 81.0 ± 4.5% (n = 4) of the Tl metal precipitated out as solid thallium (I) nitrate; with negligible ^{203}Pb in the precipitate. The load (0-4 mL) and wash (4-14 mL) fractions of the PB resin column contained 1.5 ± 0.3% and 2.7 ± 0.5% of the initial ^{203}Pb activity (n = 4), respectively. These fractions were evaporated to dryness and, in combination with the mass of the $TlNO_3$ precipitate, 94.8 ± 1.0% (n = 4) of the initial Tl

was recovered as $TlNO_3$ to be reused in the plating baths for target manufacturing. With the first PB resin column, 95.4 ± 3.0% (n = 4) of the initial ^{203}Pb activity was recovered in the elute with 2 mL of 8 M HCl (14-16 mL). The elution profile of ^{203}Pb on the PB resin column is shown in **Figure 2.4a**. The first 1 mL of 8 M HCl (Vol 14-15mL), which contained 90.0 ± 2.4% (n = 4) of the initial ^{203}Pb, was collected and diluted to 2 M HCl and loaded onto the Dowex-1X8 anion exchange resin where 94.8 ± 2.7% (n = 4) was eluted in 4x0.5 mL of 0.01 M HCl (Vol 4.5-6.5 mL), with minimal losses in the load (2.1 ± 1.3%, vol 0-4 mL) and wash (4.3 ± 0.5%, vol 4-4.5 mL), as shown in **Figure 2.4b**. 83.3 ± 4.1% (n = 4) of the initial activity was found in the second 0.5 mL fraction (Vol 5.5 mL).

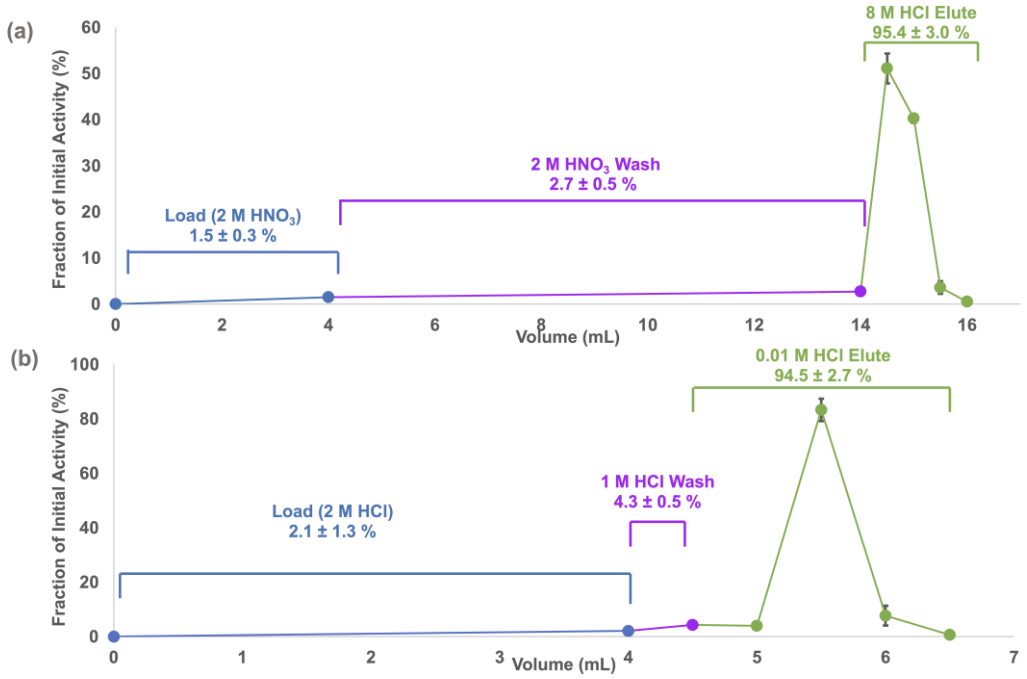

Figure 2.4. Representative elution profile of ^{203}Pb purification on (a) PB resin (extraction chromatography) and (b) Dowex-1X8 resin (anion exchange chromatography) (n = 4).

The ^{203}Pb was determined to be radionuclidically pure via gamma spectroscopy (**Figure A.1**). The chemical purity was assessed via ICP-MS, as shown in **Table 2.1**, with the concentrations (ppb) and masses (ng) of metal impurities in the Dowex-1X8 elute. Select metal concentrations and masses from the PB resin elute in parentheses, obtained via this method are compared to values from our previously reported one-column method.[156]

Table 2.1. Metal content of ^{203}Pb elute fractions in ppb (µg/L) and ng as determined by ICP-MS (n=3).

Metal	Al	Ag	Ca	Fe	Cu	Zn	Pb	Tl
ppb (µg/L)								
One-column method [156]	168 ± 152	N.S.	568 ± 263	18 ± 11	2.7 ± 1.8	21 ± 4	495 ± 218	58,220 ± 35,392
This work	100 ± 51	1.4 ± 0.3 (In 8 M HCl elute: 3,353 ± 287)	N.S.	29 ± 9	N.S.	14 ± 4	34 ± 6	26 ± 3 (In 8 M HCl elute: 2,236 ± 483)
This work – Recycled ^{nat}Tl	N.S.	1.8 ± 0.2	N.S.	18 ± 1	N.S.	26 ± 5	25 ± 8	28 ± 14
ng								
One-column method [156]	504 ± 456	N.S.	1,704 ± 789	54 ± 33	8.1 ± 5.4	63 ± 12	1,485 ± 654	174,660 ± 106,176
This work	200 ± 102	2.8 ± 0.6 (In 8 M HCl elute: 6,706 ± 574)	N.S.	58 ± 18	N.S.	28 ± 8	68 ± 12	52 ± 6 (In 8 M HCl elute: 4,472 ± 966)
This work - Recycled ^{nat}Tl	N.S.	3.6 ± 0.4	N.S.	36 ± 2	N.S.	52 ± 10	50 ± 16	56 ± 28

N.S. = not significant

2.3.3. ^{212}Pb Radiochemical Separation

The ^{228}Th/^{212}Pb generator stock solution, prepared from a 12,500 μA·h irradiation of 8 g of ^{232}Th, initially contained 22.80 ± 0.03 MBq of ^{228}Th when it was processed ten months post EOB. A 30 mL generator stock solution was first passed through the PB resin column (**Figure 2.3**) and the load (0-30 mL) is recovered to serve as a source of ^{212}Pb after equilibrium is established after approximately two days. Washing the PB resin with 10 mL of 2 M HNO_3 (Vol 30-40 mL) resulted in the loss of 3.2 ± 0.5% (n = 4) of the initial ^{212}Pb activity, while 94.9 ± 0.8% was eluted in 2 mL of 8 M HCl (40-42 mL, see **Figure 2.5a**). The first 1 mL (40-41 mL) of the PB resin elute contained 89.0 ± 1.6% (n = 4) of the initial ^{212}Pb activity and was loaded onto the Dowex-1X8 resin (**Figure 2.5b**) where a minimal amount (0.4 ± 0.1%, n = 4) of the activity was lost in the load (Vol 0-4 mL), along with 0.8 ± 0.4% (n = 4) in the 1 M HCl wash (4-4.5 mL). The entire 2 mL 0.01 M HCl elute (4.5-6.5 mL) contained 96.8 ± 2.9% (n = 4) of the initial activity, with 81.9 ± 2.0% found in the second, 0.5 mL fraction (5-5.5 mL).

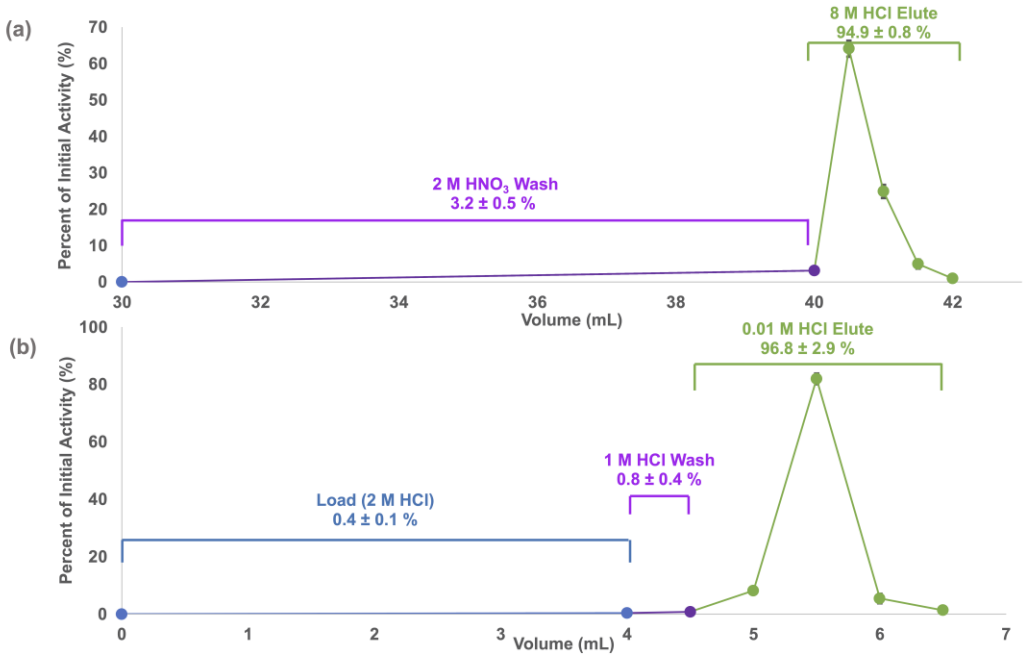

Figure 2.5. Representative elution profile of ^{212}Pb purification on (a) PB resin (extraction chromatography) and (b) Dowex-1X8 resin (anion exchange chromatography) (n = 4)

Similarly to ^{203}Pb, ^{212}Pb was determined to be radionuclidically pure (>99.9%) via gamma spectroscopy (**Figure A.2**). The chemical purity was assessed via ICP-MS, as

shown in **Table 2.2,** and compared to the metal concentrations and masses found in the elute of the previous one-column ^{212}Pb purification method.[156]

Table 2.2. Metal contents in ^{212}Pb elute fractions in ppb (µg/L) and ng as determined by ICP-MS (n=3).

Metal	Al	Mg	Ca	Ti	Fe	Co	Ni	Cu	Zn	Pb	Th
ppb (µg/L)											
One-column method [156]	22 ± 9	612 ± 226	N.S.	354 ± 168	N.S.	26 ± 11	N.S.	3 ± 2	N.S.	2 ± 2	24,352 ± 16,227
This work	2 ± 3	15 ± 7	15 ± 5	N.S.	N.S.	0.3 ± 0.2	N.S.	4 ± 2	N.S.	4 ± 2	291 ± 56 (In 8 M HCl elute: 37,650 ± 3,195)
ng											
One-column method [156]	66 ± 27	1,836 ± 678	N.S.	1,062 ± 504	N.S.	78 ± 33	N.S.	9 ± 6	N.S.	6 ± 6	73,056 ± 48,681
This work	4 ± 6	30 ± 14	30 ± 10	N.S.	N.S.	0.6 ± 0.4	N.S.	8 ± 4	N.S.	8 ± 4	582 ± 112 (In 8 M HCl elute: 112,950 ± 9,585)

N.S. = not significant

2.3.4. Radiolabeling

Comparative radiolabeling studies were performed to determine if there were any differences in the RCYs of chelators TCMC and Crypt-OH (See chemical structures in **Figure 2.6a** and **Figure 2.6b**, respectively) when labeled with ^{203}Pb or ^{212}Pb purified using the two different methods: the previous one-column procedure[156] and the novel procedure described above. For ^{203}Pb radiolabeling, the reactions were performed in triplicate at pH 7 and room temperature and the RCY (%) was determined by radio-iTLC at one hour. Using ^{203}Pb isolated via the one-column method[156], the RCYs (n = 3) of the TCMC at chelator concentrations of 10^{-4} to 10^{-5} M were quantitative and at concentrations of 10^{-6} to 10^{-8} M were 51.5 $\pm$ 8.8%, 8.5 $\pm$ 5.3%, and 0%, respectively. With the ^{203}Pb isolated via the novel two-column method, quantitative RCYs were obtained at TCMC concentrations of 10^{-4} to 10^{-6} M, and were 86.7 $\pm$ 2.4% and 22.8 $\pm$ 6.9% at 10^{-7} and 10^{-8} M, respectively. By using the novel, two-column procedure, the results suggest that the A_m of [^{203}Pb][Pb(TCMC)]$^{2+}$ increased from 437.9 $\pm$ 38.0 MBq/μmol to 7.4 $\pm$ 0.2 GBq/μmol. For Crypt-OH, with the one-column ^{203}Pb[156], quantitative RCYs (n = 3) were achieved at concentrations of 10^{-4} and 10^{-5} M and then from 10^{-6} to 10^{-8} M, the RCYs decreased to 88.6 $\pm$ 6.0%, 13.6 $\pm$ 3.0%, and 0%, respectively. However, with the ^{203}Pb obtained via the two-column method, quantitative RCYs were obtained at concentrations from 10^{-4} to 10^{-6} M and at 10^{-7} and 10^{-8} M, RCYs of 82.7 $\pm$ 1.6% and 0%, respectively, were obtained. The improvements in RCYs, as shown in **Figure 2.6c**, suggest the A_m of [^{203}Pb][Pb(Crypt-OH)]$^{2+}$ increased from 753.1 $\pm$ 45.2 MBq/μmol to 7.0 $\pm$ 0.1 GBq/μmol.

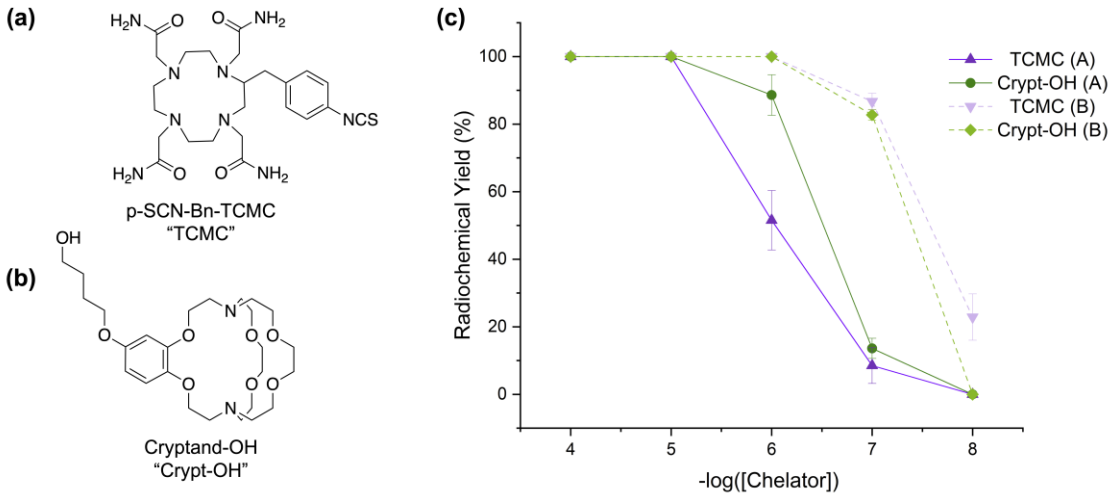

Figure 2.6. Chemical structures of (a) TCMC and (b) Crypt-OH and (c) radiochemical yields (%) for ^{203}Pb (85 kBq) labeling reactions at pH 7 (0.1 M NH_4OAc), room temperature, and 1 h at chelator concentrations of 10^{-4} to 10^{-8} M using ^{203}Pb produced via the previous one-column (A)[156] and new (B) method. (n = 3)

With ^{212}Pb, at ambient temperature RCYs for Crypt-OH were not quantitative at any concentration for either Pb-purification method. However, ^{212}Pb isolated via the previously-reported one-column method saw improved RCYs (n = 3) at 80 °C between chelate concentrations of 10^{-4} to 10^{-8} M, with yields of 64.9 ± 10.7%, 36.2 ± 5.7,% 8.7 ± 1.7%, 0 %, and 0%, respectively. With ^{212}Pb isolated using the two-column method reported here, the RCYs increased to 100 ± 0%, 94.8 ± 4.6,% 84.3 ± 3.0,% 35.7 ± 3.8%, and 3.0 ± 0.7%, respectively. This resulted in the A_m of $[^{212}Pb][Pb(Crypt\text{-}OH)]^{2+}$ increasing from 13.2 ± 1.3 MBq/μmol to 1.7 ± 0.05 GBq/μmol.

With TCMC, radiolabeling was observed at both ambient temperature and 80 °C for both methods. At ambient temperature, with the one-column method, quantitative ^{212}Pb RCYs were obtained for chelator concentrations of 10^{-4} and 10^{-5} M, dropping to 90.0 ± 1.6%, 48.7 ± 10.0%, and 0% between 10^{-6} to 10^{-8} M, respectively. With the two-column method, quantitative RCYs were obtained for concentrations from 10^{-4} to 10^{-6} M and yields of 50.7 ± 7.2% and 0% at chelator concentrations of 10^{-7} and 10^{-8} M, respectively, as shown in **Figure A.8**. At ambient temperature, the apparent molar activities of $[^{212}Pb][Pb(TCMC)]^{2+}$ were 9.7 ± 1.0 GBq/μmol and 10.1 ± 0.7 GBq/μmol when ^{212}Pb was purified using the previous one- and novel two-column purification methods, respectively.

At 80°C, with ^{212}Pb from both methods, quantitative RCYs were obtained at chelator concentrations of 10^{-4} to 10^{-6} M. At concentrations of 10^{-7} and 10^{-8} M, the RCYs with the one-column ^{212}Pb decreased to 88.8 ± 5.5% and 9.8 ± 1.5%, while with the two-column ^{212}Pb, the RCYs decreased to 82.6 ± 6.7% and 1.7 ± 1.5%, respectively, as shown in **Figure 2.7**. At 80 °C, the A_m of $[^{212}Pb][Pb(TCMC)]^{2+}$ was 16.5 ± 1.1 GBq/μmol and 17.8 ± 1.0 GBq/μmol when using ^{212}Pb purified via the previous one- and novel two-column methods, respectively.

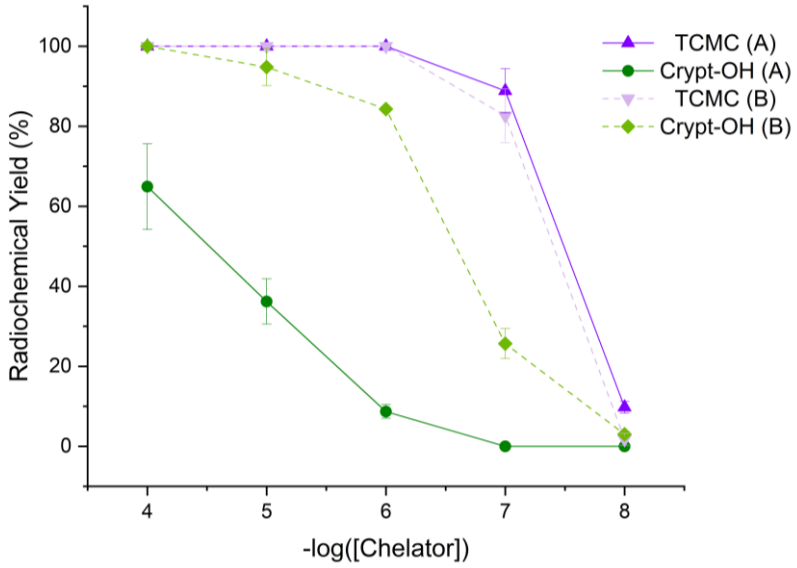

Figure 2.7. Radiochemical yields (%) for ^{212}Pb (100 kBq) labeling reactions at pH 7 (0.1 M NH_4OAc), 80 °C, and 1 h at chelator concentrations of 10^{-4} to 10^{-8} M using ^{212}Pb produced via the previous one-column[156] (A) and new (B) method. (n = 3)

2.4. Discussion

In our previous work, thallium targets prepared by mechanically pressing metallic Tl into aluminum backings were only able to withstand currents up to 8 μA and ^{203}Pb elutes were found to contain a stable Pb concentration greater than 400 ppb.[156] Together, these factors contributed to the low specific activity of the ^{203}Pb product, which could only be overcome by modifying the target manufacturing procedure to increase thermal stability and produce more ^{203}Pb at EOB. In the previous one-column purification procedure, the irradiated Tl targets were dissolved in 20 mL of 2 M HNO_3 at 125 °C and after cooling, the target solution was loaded onto a single extraction chromatographic resin (PB resin), followed by washing with 2 M HNO_3 (5 mL), and eluting with 1 M NH_4OAc (pH 7, 3 mL).[156]

This method was attractive as it was rapid, simple, and also compatible with ^{212}Pb purification from a ^{228}Th/^{212}Pb generator; the ^{228}Th was purified from the Th waste of a ^{232}Th proton spallation process on TRIUMF's 500 MeV cyclotron used to produce ^{225}Ac.[156,157] Although this purification process was rapid and simple, Tl and ^{232}Th were present in the ^{203}Pb and ^{212}Pb elutes at high concentrations of 58.2 ± 35.4 ppm and 24.3 ± 16.2 ppm, respectively[156], and thus there was a great need for the development of a new purification procedure that would reduce metal impurities in the $^{203/212}$Pb eluate(s).

To improve the thermal contact conductance of the thallium with the backing material, targets were manufactured via electroplating onto silver backings. Previous reports employed copper as the backing material [248]; however, given its higher thermal conductivity, silver was chosen for this work. Furthermore, the electroplating method selectively deposits Tl, which minimizes the amount of stable Pb incorporated into the deposit. This is in contrast to the pressing of Tl metal, where existing impurities are incorporated into the target, posing greater challenges during target processing and purification. Using constant current electrolysis, a maximum current density of 2.3 mA·cm^{-2} was employed to minimize dendrite formation. The silver-backed electroplated targets have been successfully irradiated at currents up to 20 μA, 2.5 times greater than the previous maximum current, and will be tested with higher currents and enriched ^{203}Tl targets in future studies.

Despite the capacity factor (k') of Pb^{2+} on PB resin being nearly 100 times greater than the k' of Tl^{+} in 2 M nitric acid[149], with approximately 350 mg of Tl in each target, extraction chromatographic resins, including PB resin, can be overloaded beyond their capacity, which can result in variability and breakthrough. In our previous method, 320-330 mg of thallium metal was dissolved in 2 M HNO_3 and passed through 60 mg of resin, yielding a thallium concentration of 58.2 ± 35.4 ppm in the eluate.[156] This high Tl burden resulted in variable Tl concentrations between batches, ultimately affecting the reproducibility of radiolabeling yields, particularly for chelators sensitive to competing non-radioactive metal impurities. In order to reduce the Tl concentration of the elute, we exploited differences in the solubility of $TlNO_3$ at different temperatures to precipitate the majority (81.0 ± 4.5%, n = 4) of the thallium by cooling the target solution to 0 ºC prior to loading on the first PB resin column. As a result, in combination with an additional 5 mL of 2 M HNO_3 in the PB resin wash, the Tl concentration in the 8 M HCl elute was reduced to 2.2 ± 0.5 ppm (n = 3), which correlates to over a twenty six-fold decrease in concentration.

In addition to reducing Tl burden, the precipitated $TlNO_3$ can be collected, and the Tl recycled, which is of great importance when using costly enriched materials. To further improve recycling yield, the load and wash of the PB resin can be evaporated which results in a Tl recovery of 94.8 ± 1.0% (n = 4). The recovered Tl was confirmed to be in the +1 oxidation state as $TlNO_3$ by using a colorimetric method.[255] The recovered $TlNO_3$ was successfully electroplated, with the resulting targets showing no statistical difference in final target mass, or ^{203}Pb produced at EOB, compared to non-recycled $TlNO_3$ or Tl_2SO_4.

Ideal radiochemical separations involve the use of a minimal number of columns and no evaporation which would complicate automation and minimize potential losses. Additionally, it can be most beneficial when testing a wide range of chelators for the activity to be eluted in an easily neutralized medium, so that optimization can be performed for each chelator. For the first (PB) column, it was still most ideal to use a nitric acid medium to separate the ^{203}Pb or ^{212}Pb from Tl and Th, respectively, as Pb^{2+} has high k'_{Pb} at all nitric acid concentrations. Initially studies utilized an eluate composed of 0.01 M HNO_3, [149]. However, this resulted in a large elution volume and thus was not further investigated. 8 M hydrochloric acid can be an effective desorption agent from PB resin as the k'_{Pb} is less than 10 at higher acid concentrations.[149] This resulted in 94.8 ± 2.7% and 94.9 ± 0.8% (n = 4) of the ^{203}Pb and ^{212}Pb to be eluted from this resin in 2 mL of 8 M HCl, respectively. However, 8 M HCl is not easily compatible with radiolabeling and there were still high concentrations of Tl (2.2 ± 0.5 ppm, ^{203}Pb), Ag (3.3 ± 0.3 ppm, ^{203}Pb), and Th (37.7 ± 3.2 ppm, ^{212}Pb) present, and as such, the use of a second column to improve chemical purity and reduce acid concentration was required.

To eliminate the need for acid exchange (e.g. HNO_3) and evaporation of the 8 M HCl eluate before loading the second column, we searched for distribution coefficients (D) of Pb^{2+} with HCl on strong base type I anion exchange resins[169,171,174]. Through method development studies (see Supporting Information), Dowex-1X8 resin was chosen as the resin for the second column. The adsorption of Pb^{2+} is low in dilute HCl (D = 1 in 0.05 M HCl), reaches a maximum at 1.5 M HCl (D = 25), and decreases such that there is minimal adsorption (D < 1) at concentrations greater than 8 M HCl.[169,171,174] As a result, $^{203/212}Pb$ can be loaded and washed in 1-2 M HCl and eluted in 0.01 M HCl. Additionally, there is little to no adsorption of Th^{4+} and Tl^{+} under these conditions and a higher adsorption of Ag^{+} over Pb^{2+}, which should result in decreases of these main contaminants.[174] Despite the difference in D at varying HCl concentrations, these values are still relatively low and

thus it was critical to optimize the loading and wash volumes to reduce the breakthrough of ^{203}Pb and ^{212}Pb. As a result, only the first 1 mL of the 8 M HCl elute, which contained 90.0 ± 2.4% and 89.0 ± 1.6% of the initial ^{203}Pb and ^{212}Pb, respectively, was taken and diluted to 2 M HCl rather than to 1.25 M, at which the D is the highest, to minimize the loading volume while still maintaining sufficient adsorption to the resin. The resin was then washed in 1 M HCl to further remove metal impurities and reduce the acid concentration in the final elute as the ^{203}Pb/^{212}Pb is eluted with 0.01 M HCl to allow for easier neutralization by radiolabeling buffers. The flow rate was also found to be critical to the successful use of the Dowex-1X8 resin, as high flow rates (>0.5 mL/min) would cause activity breakthrough. To minimize losses, the column was loaded and washed by gravity. Despite this limitation, the low volume of the load and wash allows for the entire purification procedure, for either ^{203}Pb or ^{212}Pb, to be completed in two hours.

The most important benefit of this novel method over the previous one-column method is the reduction in the mass and concentrations of Tl and Th contaminants in the ^{203}Pb and ^{212}Pb elutes, respectively. With the previous method, the Tl separation factor was 1.86×10^3, whereas with the novel method, a separation efficiency of 6.68×10^6 was achieved, leading to a Tl:^{203}Pb ratio of 122:1. Therefore, compared to the previous method, the optimized method reduced the Tl mass content 3.59×10^3-fold and the Tl concentration by 2.24×10^3-fold. To the best of our knowledge, this is the lowest Tl concentration in ^{203}Pb reported in the literature[131,156,250]. Additionally, given the selectivity of the electroplating procedure towards Tl, reduced stable Pb concentrations of 34 ± 6 ppb were detected in the ^{203}Pb elute, compared to 495 ± 218 ppb from our previously reported method. For a two hour irradiation of a natural Tl target at maximum current (8 μA[156] vs 20 μA), the ^{203}Pb specific activity increased from 18.3 ± 8.6 MBq/μg[156] to 969.1 ± 173.9 MBq/μg (n = 3) for the previous one- and novel two-column method, respectively. This resulted in an average stable Pb:^{203}Pb ratio of 6:1 which can be further reduced as (i) irradiation currents increase, (ii) enriched targets are employed, and (iii) the ^{205}Tl (p, 3n) ^{203}Pb reaction is utilized at higher proton energies.

For ^{212}Pb, the greatest benefit of the novel two-column method over the previously employed one-column method was a one hundred and twenty six-fold greater reduction in Th content. Previously with one column, the Th separation factor was 1.10×10^5, which resulted in a final elute concentration of 24.3 ± 16.2 ppm (n =3).[156] With the two-column

method, a separation factor of $1.37x10^7$ was achieved to give a final Th^{4+} concentration of 291 $\pm$ 56 ppb (n = 3), which is nearly an eighty four-fold decrease in ^{232}Th concentration in the final elute. Concentrations of previous contaminants Mg, Al, Co, and Ti, decreased even further to 15 $\pm$ 7 ppb, 2 $\pm$ 3 ppb, 0.3 $\pm$ 0.2 ppb, and 0 ppb (N.S.), respectively, thus improving the chemical purity of the ^{212}Pb product. The stable Pb^{2+} concentration did not significantly differ. This has led to a ^{232}Th:^{212}Pb ratio of 1203:1 in the Dowex elute compared to the initial ratio of $1.65x10^{10}$:1 in the generator stock solution. This reduction in ^{232}Th in the elute may explain the dramatic improvement in the ^{212}Pb RCYs of Crypt-OH.

The significance and impact of the optimizations achieved through the novel method are demonstrated by the corresponding improvements in the RCYs of Pb^{2+} chelators TCMC and Crypt-OH. With a lower Tl and stable Pb content, the A_m of $[^{203}Pb][Pb(TCMC)]^{2+}$ and $[^{203}Pb][Pb(Crypt\text{-}OH)]^{2+}$ increased by a factor of seventeen and nine at ambient temperature, respectively, showing that improvements in ^{203}Pb specific activity and chemical purity translated directly into improved RCYs. For ^{212}Pb, there were no substantial changes to the RCYs of TCMC at room temperature or at 80 °C. This is most likely because the stable Pb concentration did not significantly change and TCMC is more selective towards $Pb^{2+}$and not affected drastically by Th^{4+}. With the previous one-column method, the average Th concentration was 24.3 $\pm$ 16.2 ppm, which led to a ^{232}Th:^{212}Pb of $1.5x10^5$:1, which decreased to 1203:1 with the novel, two-column method. Interestingly, in the case of Crypt-OH, no radiolabeling was observed with ^{212}Pb from either method at room temperature, despite the successful quantitative radiolabeling with ^{203}Pb. This suggests that the cryptand is highly sensitive to the concentration of Th^{4+}. However, moderate radiolabeling yields were observed at 80 °C with the novel, two-column method, suggesting that the ^{212}Pb radiolabeling may be kinetically driven, but this is beyond the scope of this paper and will be a focus of later studies. With a one hundred and twenty six-fold decrease in the ^{232}Th:^{212}Pb ratio, a one hundred and twenty nine-fold improvement in the A_m of $[^{212}Pb][Pb(Crypt\text{-}OH)]^{2+}$ was observed at 80 °C, demonstrating the importance of the chemical purity of ^{212}Pb for this chelator.

2.5. Conclusions

We have developed a target manufacturing method that involves electroplating thallium onto silver. This resulted in a target with high thermal stability, one capable of withstanding higher irradiation currents, and leading to a significant increase in ^{203}Pb production when irradiated with a 13 MeV cyclotron. These improvements to the target manufacturing procedure, due to higher allowable current and lower stable Pb content, have resulted in a nearly fifty three-fold increase in the specific activity of ^{203}Pb. Additionally, we have developed a novel purification procedure that, to the best of our knowledge, has produced ^{203}Pb/^{212}Pb of the highest chemical purity reported to date from an academic laboratory. The specific activity and ^{203}Pb: stable Pb ratio are expected to improve in future studies as enriched targets are manufactured and irradiated with high proton energies and currents towards a maximum of 26.5 MeV; this will allow production of ^{203}Pb at a level suitable for clinical use. Further, as ^{232}Th irradiations are conducted at higher currents and for longer durations, this purification procedure will allow researchers to easily produce high specific activity ^{212}Pb for pre-clinical purposes to meet the growing demand and interest in this theranostic pair that is seeing increasing clinical use.

Chapter 3.

Evaluation of the Effect of Macrocyclic Ring Size on [^{203}Pb]Pb(II) Complex Stability in Pyridyl-Containing Chelators

3.1. Introduction

The bifunctional chelator (BFC) approach is a common strategy employed in the development of novel radiopharmaceuticals.[256] More specifically, the BFC approach in the field of radiopharmaceutical development involves tissue-specific delivery of a radioactive payload through the use of a chelator coordinating a radioactive metal (radiometal) which is attached via a linker to a biological targeting vector. This vector-chelate-isotope complex is then injected to selectively seek out and bind its cancer biomarker. In the context of radionuclide therapy, this highly selective and direct delivery of radiation allows for reduced side effects on healthy cells compared to existing methods.[257] This technique is also intriguing as it enables a personalized approach to healthcare by pairing both photon- and particle-emitting isotopes, which in turn allow clinicians to assess radiopharmaceutical uptake via imaging prior to therapy. Use of radiometals that emit cytotoxic alpha (α) particles, beta (β^-) particles, or Meitner-Auger electrons (MAEs) are compatible with therapy, while those that emit photons, through decay processes such as electron capture (EC) or positron emission (β^+ decay), are compatible with imaging techniques single-photon emission computed tomography (SPECT) and positron emission tomography (PET), respectively. The combination of both *thera*peutic and diag*nostic* forms of a radiopharmaceutical is referred to as *theranostics*.

In order to realize the full potential of *theranostic* radiopharmaceuticals, the biodistribution and chemical properties of the isotope pair being used must be very similar, if not identical. If the biodistribution of the imaging radiopharmaceutical differs greatly from the therapeutic, an inappropriate treatment method may be chosen with which there can be adverse effects.[258] Chemically matched, or element-equivalent, theranostic isotope pairs, which are composed of isotopes of the same element, are ideal as the chemical properties of the isotopes are essentially identical and thus should have identical biodistribution.[259,260] In this regard, lead-203 (^{203}Pb, $t_{1/2}$ = 51.9 h) and lead-212 (^{212}Pb, $t_{1/2}$

= 10.6 h) are a promising element-equivalent theranostic pair that is currently being explored for clinical use.[261] ^{203}Pb decays via electron capture and releases a 279 keV photon with an abundance of 81%, making it compatible with SPECT imaging. ^{212}Pb emits both beta- and alpha particles (via its daughter ^{212}Bi), making it compatible with therapy.

Diagnostic and therapeutic radiopharmaceuticals utilizing matched theranostic pairs can have nearly identical biodistribution as they are able to utilize identical chelators. This results in the same molecular properties such as overall charge, hydrophilicity, and same chemical properties for both imaging and therapeutic drug forms. In addition, the thermodynamic stability of the complex and its kinetic inertness are critical to the success of the BFC approach. Chelates can have a significant effect on the pharmacokinetic properties of a radiopharmaceutical, and in order for one to be effective at coordinating and containing the radiometal, its design must be tailored to the metal's chemical properties.[40,262] In general, there are two broad chelator categories: acyclic and macrocyclic, both of which have two main components: i) a backbone which serves as an anchor to connect ii) pendant functional arms containing electron donor moieties for metal coordination. Macrocyclic chelators have constricted geometries as their rigid backbones form a pre-organized metal ion binding site resulting in a decreased entropic penalty and thus an increased thermodynamic favourability towards complexation when compared to their acyclic counterparts.[263] This phenomenon is commonly referred to as the macrocycle effect.[263] However, macrocycles tend to have slower reaction kinetics requiring elevated temperatures to induce complexation, which can be detrimental when handling a heat or pH-sensitive targeting vector and thus the choice of chelator type can depend on the reaction environment.[40]

The choice of chelating moieties is often based on the hard-soft acid-base (HSAB) theory, which matches harder (non-polarizable) acids with harder bases and softer (more-polarizable) acids with softer bases to result in the most stable coordination complexes.[264–266] Pb^{2+} is considered an intermediate Lewis acid and thus should form the most stable complexes with intermediate Lewis bases, including pyridine and amides. For example, the structure of the current commercial standard for lead chelation, TCMC, also known as DOTAM, (1,4,7,10-tetrakis(carbamoylmethyl)-1,4,7,10-tetraazacyclododecane) employs four pendant amides where the carbonyl oxygen acts as an electron donor.[265,267]

In addition to choice of donor moieties, the macrocyclic ring size can greatly affect complex stability and metal selectivity.[263] Crown- and aza-crown ethers are attractive backbones for the design of macrocyclic chelators for radiopharmaceuticals due to their ease of functionalization and wide variety of potential ring-sizes. With a judicious choice of donor atoms and ring size, one can design macrocyclic chelates with enhanced selectivity toward specific metals. Despite this, the understanding of the relationship between structure, metal selectivity, and complex stability is often limited to the idea of size-match selectivity, although this has been contested.[263] However, these trends often do not translate when donor arms are introduced and can be unpredictable, especially with bulky donor groups, like pyridine, where steric strain can have a large role in complex formation[263]; thus these relationships should be studied on a case-by-case basis. A further understanding of this relationship can advance not only metal-based radiopharmaceutical development but also the design of antibiotics[268], ion exchange resins[269], and metal intoxication treatments[270], among others.

The focus of this study is to investigate the effect of macrocyclic backbone size in pyridyl-containing chelators to identify optimal chelators for [$^{203/212}$Pb]Pb^{2+} radiopharmaceuticals. The optimal chelator will complex ^{203}Pb at a low chelator:metal ratio with fast kinetics, and be thermodynamically stable and kinetically inert to prevent transchelation with endogenous metal-seeking biomolecules *in vivo*. We hypothesized pyridyl, an intermediate Lewis base, will form stable complexes with Pb^{2+}, an intermediate Lewis acid. The outcome of this study provides insights into the ideal backbone size required for minimal steric strain, which should increase the thermodynamic favourability of complexation, and be reflected by higher radio-lead incorporation yields. Results of concentration-dependent ^{203}Pb radiolabeling, kinetic inertness, and serum stability studies with a panel of pyridyl-containing chelators have been rationalized based on the solid state Pb-complex structures (elucidated via X-ray diffraction), solution structures (via ^{1}H nuclear magnetic resonance (NMR) spectroscopy), and thermodynamic stability constants (determined via potentiometric titrations). The pyridyl-containing chelators and commercial standards investigated in this study are shown in **Figure 3.1**. The 18-membered macrocycles, NOON-2Py (7,16-bis(pyridin-2-ylmethyl)-1,4,10,13-tetraoxa-7,16-diazacyclooctadecane) and crown-4Py (4,7,13,16-tetrakis(pyridin-2-ylmethyl)-1,10-dioxa-4,7,13,16-tetraazacyclooctadecane) have been investigated previously for use as a lead detoxifying agent[271], and as a biomimetic model of the methane monooxygenase

enzyme for alkane functionalization when complexed to manganese,[272] respectively. The 12-membered macrocycle cyclen-4Py (1,4,7,10-tetrakis(pyridin-2-ylmethyl)-1,4,7,10-tetraazacyclododecane) was synthesized previously to investigate its coordination of copper, bismuth, and lanthanum[273–276]. These pyridyl-containing macrocycles were compared to commercial standard chelators TCMC and DOTA (1,4,7,10-tetraazacyclododecane-1,4,7,10-tetraacetic acid).

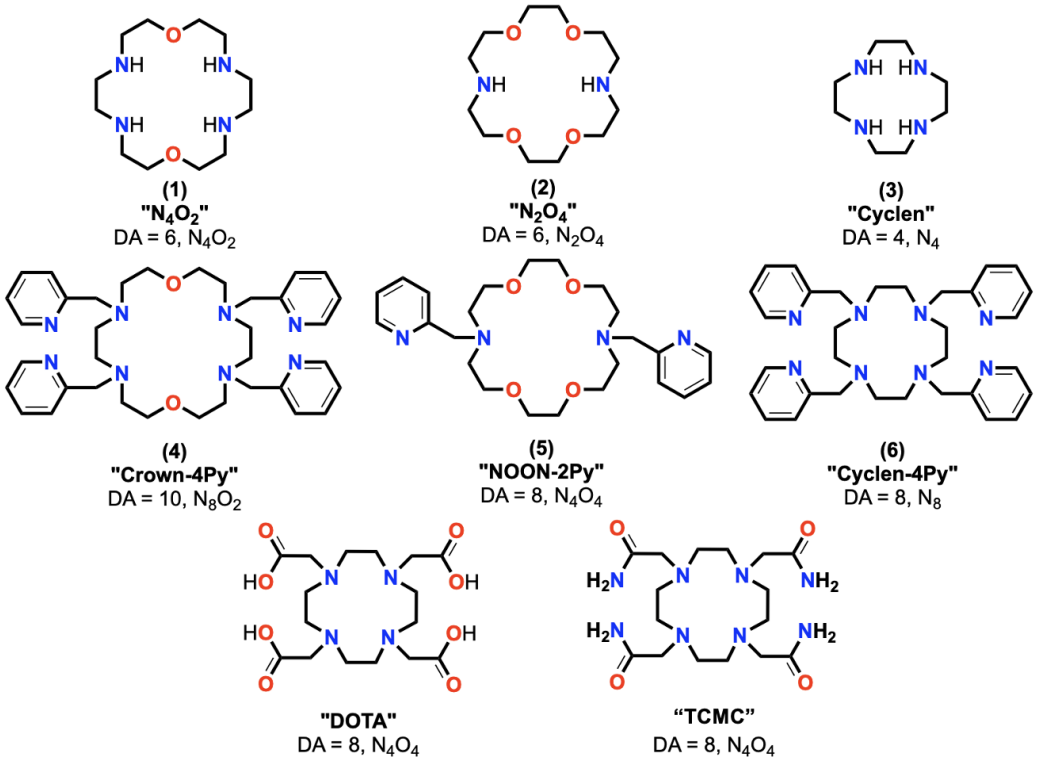

Figure 3.1. Core macrocyclic structures (top row), macrocyclic pyridyl-containing chelators (middle row), and commercially available chelators of interest (bottom row) investigated in this study.
DA = donor atoms

3.2. Experimental

3.2.1. General

All chemicals were purchased from commercial suppliers and used without further purification. The eighteen membered backbone, 1,10-dioxa-4,7,13,16-tetraazacyclooctadecane (N_4O_2, (1)) was synthesized as previously described with no deviations.[277] The eighteen membered backbone, 1,4,10,13-tetraoxa-7,16-

diazacyclooctadecane (N_2O_4, (2)) was purchased from VWR (Radnor, PA). The backbone 1,4,7,10-tetraazacyclododecane (Cyclen,(3)), was purchased from TCI. Commercial chelators DOTA (1,4,7,10-Tetraazacyclododecane-1,4,7,10-tetraacetic acid) and TCMC (1,4,7,10-Tetrakis(carbamoylmethyl)-1,4,7,10-tetraazacyclododecane) were purchased from Macrocyclics Inc. (Plano, TX). Anhydrous solvents were obtained following storage over 3 Å molecular sieves activated under heat. Water was purified using a MilliQ purification system. NMR spectra were obtained using a Bruker 400 (400 MHz), Bruker 500 (500 MHz), or a Bruker 600 (600 MHz) (Billerica, MA) with signals measured relative to the signal of the solvent. Mass spectrometry was performed using either an Agilent (Santa Clara, CA) 6210 TOF LC/MS or Advion expression LC-MS (Ithaca, NY) equipped with an electrospray source. The ^{203}Pb utilized for radiolabeling studies was produced as previously described and received as [^{203}Pb]Pb$(OAc)_2$ in 1 M ammonium acetate (NH_4OAc).[156] Quantification of ^{203}Pb activity per reaction was quantified using gamma ray spectroscopy on an N-type co-axial high purity germanium (HPGe) gamma spectrometer from Canberra Industries (Meridan, CT). The gamma spectrometer was calibrated with a 20 mL ^{152}Eu and ^{133}Ba source.

3.2.2. Chelator Synthesis

The synthetic scheme can be found in the supporting information (**Scheme B.1**).

General procedure

To a stirred suspension of the respective macrocyclic backbone (1 equiv.) and K_2CO_3 (5 equiv.) in 10 mL of anhydrous acetonitrile, a 10 mL solution of 2-(bromomethyl)pyridine hydrobromide (4.5 equiv.) was added dropwise at room temperature over the course of 10 minutes and left to react for 48 hours. After 48 hours, the K_2CO_3 was filtered off and the solvent removed by rotary evaporation. The crude red oil was redissolved in dichloromethane and washed at least three times, or until the aqueous phase was no longer pink, with equal volumes of saturated sodium bicarbonate. The organic layers were combined and the solvent removed by rotary evaporation. Further purification, if necessary, as determined by quality of the ^{1}H NMR spectrum, is described below.

4,7,13,16-tetrakis(pyridin-2-ylmethyl)-1,10-dioxa-4,7,13,16-tetraazacyclooctadecane (Crown-4Py,*(4)*): The recovered oil was further purified by reverse phase semi-preparative high performance liquid chromatography using a Phenomenex Luna C18 (250 mm× 100 mm) column at 3 mL/min with the following method: A: H_2O with 0.1% TFA, B: Acetonitrile (CH_3CN) with 0.1% TFA; 0-5 min 10% B; 5-20 min 10-100% B, 20-25 min 100% B. The fraction at 11.8 minutes was collected and lyophilized to yield crown-4Py as a yellow powder (56.9 mg, 48%). ^{1}H NMR (500 MHz, CD_2Cl_2) δ 8.44 (d, J = 4.76 Hz, 4H), 7.58 (td, J = 7.7, 1.8 Hz, 4 H), 7.46 (d, J = 7.83 Hz, 4 H), 7.11 (m, 4H), 3.72 (s, 8 H), 3.53 (t, J = 5.6 Hz, 8 H), 2.79 (s, 8 H), 2.77 (t, J = 5.8 Hz, 8 H). ^{13}C NMR (125 MHz, CD_2Cl_2) δ 160.6, 148.7, 136.1, 122.7, 121.6, 69.92, 61.49, 53.2. HR-MS calculated for $[C_{36}H_{48}N_8O_2 + H]^+$: 625.3978; found 625.3979.

7,16-bis(pyridin-2-ylmethyl)-1,4,10,13-tetraoxa-7,16-diazacyclooctadecane (NOON-2Py, *(5)*): Further purification by HPLC was not required and so a light-yellow powder was yielded (103.0 mg, 61% yield). ^{1}H NMR (400 MHz, CD_2Cl_2) δ 8.47 (d, J = 5.0 Hz, 2 H), 7.64 (dd, J = 7.8, 1.8 Hz, 2 H), 7.53 (d, J = 7.7 Hz, 2 H), 7.13 (dd, J = 7.1, 5.1 Hz, 2 H), 3.80 (s, 4 H), 3.59 (t, J = 5.8 Hz, 8 H), 3.56 (s, 8 H), 2.82 (t, J = 5.8 Hz, 8 H). ^{13}C NMR (100 MHz, DMSO-d_6) δ 159.9, 148.8, 136.6, 122.8, 122.1, 69.8, 69.0, 60.9, 53.9. HR-MS calculated for $[C_{24}H_{36}N_4O_4 + H]^+$: 445.2815; found 445.2824.

1,4,7,10-tetrakis(pyridin-2-ylmethyl)-1,4,7,10-tetraazacyclododecane (Cyclen-4Py, *(6)*): The recovered oil was further purified by reverse phase semi preparative high performance liquid chromatography using a Phenomenex Luna C18 (250 mm × 100 mm) column at 3 mL/min with the following method: A: H_2O with 0.1% TFA, B: Acetonitrile (CH_3CN) with 0.1% TFA; 0-5 min 10% B; 5-20 min 10-100% B, 20-25 min 100% B. The fraction at 12.6 minutes was collected and lyophilized to yield cyclen-4Py as a light-yellow powder (322.5 mg, 69%). ^{1}H NMR (400 MHz, CD_3CN) δ 8.35 (d, J = 5.1 Hz, 4H), 7.87 (td, J = 7.8, 1.8 Hz, 4H), 7.47 (d, J = 1.2 Hz, 4H), 7.41 (m, 4H), 4.30 (s, 8H), 3.33 (s, 16H). ^{13}C NMR (100 MHz, CD_3CN) δ 151.63, 147.81, 139.47, 125.07, 124.43, 56.20, 49.47. HR-MS calculated for $[C_{32}H_{40}N_8 + H]^+$: 537.3454; found 537.3450.

3.2.3. Synthesis of Pb Complexes

**Caution: Perchlorate salts are considered potentially explosive and should be handled with care.

[Pb(Cyclen-4Py)]$^{2+}$

To a solution of cyclen-4Py in methanol (1 mL, 22.4 mg, 41.7 μmol), a methanolic solution of $Pb(ClO_4)_2 \cdot 3H_2O$ (19.2 mg, 41.7 μmol) was added. A yellow solid immediately precipitated out of solution. The solid was placed in a centrifuge at 10,000 rpm for 2 minutes and the supernatant removed. This process was repeated three times (3 x 500 μL) with methanol, followed by washing with diethyl ether (3 x 500 μL) before drying under vacuum (18.3 mg, 59.0%). An aliquot was taken for NMR studies and dissolved in deuterated acetonitrile. The complex was redissolved in dimethylformamide (1 mL) and via vapour diffusion of tetrahydrofuran, single crystals suitable for X-ray diffraction analyses were obtained. ^{1}H NMR (500 MHz, CD_3CN) δ 7.90 (s, 4H), 7.65 (s, 4H), 7.42 (d, J = 7.7 Hz, 4H), 7.25 (s, 4H), 4.19 (d, J = 15.9 Hz, 4H), 4.01 (d, J = 15.5 Hz, 4H), 3.55 (t, J = 14.1 Hz, 4H), 3.09 (t, J = 13.8 Hz, 4 H), 2.80 (m, 8 H). NMR spectrum found in supplementary information (**Figures B.7-B.10**) HR-MS calculated for $[C_{32}H_{40}N_8 + Pb]^{2+}$: 372.1571; found 372.1578.

[Pb(Crown-4Py)]$^{2+}$

To a solution of crown-4Py in methanol (1 mL, 15.2 mg, 24.3 μmol) a methanolic solution of $Pb(ClO_4)_2 \cdot 3\ H_2O$ (11.2 mg 24.3 μmol) was added. Immediately, a yellow solid precipitated out of solution. The washing procedure for this solid was identical to that described for [Pb(Cyclen-4Py)]$^{2+}$ and the solid was dried under vacuum (20.2 mg, 99.0 %). An aliquot was taken for NMR studies and dissolved in deuterated acetonitrile. The complex was redissolved in acetonitrile (1 mL) and via vapour diffusion of diethyl ether, single crystals suitable for X-ray diffraction analyses were obtained. Multiple isomers were found in solution. NMR spectrum found in supplementary information (**Figures B.11-B.14**). HR-MS calculated for $[C_{36}H_{48}N_8O_2 + Pb]^{2+}$: 416.1834; found 416.1834.

[Pb(NOON-2Py)]$^{2+}$

To a solution of NOON-2Py in methanol (1 mL, 24.4 mg, 54.39 μmol) a methanolic solution of $Pb(ClO_4)_2 \cdot 3\ H_2O$ (27.5 mg 59.8 μmol) was added. Unlike the previous two complexes, a solid did not precipitate. To this, a solution of NH_4PF_6 (21.1 mg, 129.5 μmol) in deionized water was added to exchange the perchlorate counterions for hexafluorophosphate as numerous attempts to form crystals with the perchlorate

counterion failed. The solvent was removed under a steady stream of nitrogen to give a pale yellow solid which was washed three times with diethyl ether and then dried under vacuum (17.8 mg, 50.2%). An aliquot was taken for NMR studies and dissolved in deuterated DMSO. The complex was redissolved in dimethylformamide (1 mL) and via vapour diffusion of tetrahydrofuran, single crystals suitable for X-ray diffraction analyses were obtained. Multiple isomers were found in solution. NMR spectrum found in supplementary information (**Figures B.15-B.18**). HR-MS calculated for [$C_{24}H_{36}N_4O_4$ + acetate ($C_2H_3O_2$) + Pb]$^+$: 711.2641; found 711.2638.

3.2.4. X-ray crystallography

All crystals were mounted on a 150 mm MiTeGen Dual-Thickness MicroMount using Paratone oil and measurements were made on a Bruker Photon II diffractometer with TRIUMPH-monochromated Mo Kα radiation (sealed tube) or Cu Kα radiation (Cu-micro source). The data were collected at a temperature of 298 K in a series of scans in 0.50º oscillations. Data were collected and integrated using the Bruker SAINT software package (Version 7.46A) and were corrected for absorption effects using the multi-scan technique (SADABS) or (TWINABS). All structures were solved by direct methods.[278,279] All non-hydrogen atoms were refined anisotropically. All hydrogen atoms were placed in calculated positions but not refined. All refinements were performed using the SHELXTL crystallographic software package of Bruker-AXS (Version 5.1). The molecular drawings were generated by the use of POV.[280] Additional crystallographic information can be found in Appendix B.

3.2.5. pH Potentiometry

Potentiometric titrations were carried out using a Metrohm Titrando 888 titrator controlled by *Tiamo 2.5* software and equipped with a Ross Orion combination electrode (8103BN, ThermoFisher Scientific) and a Metrohm 806 exchange unit with an automatic burette (10 mL). The titration vessel was fitted into a removable glass cell (≈ 70 mL) maintained at 25 °C (pK_w = 13.78)[281] using a Thermomix 1442D circulating water bath. CO_2 was excluded from the setup using a positive pressure of argon, which was passed through an aqueous 30 wt% KOH solution. Aqueous KOH (0.1 M, BDH Chemicals, Radnor, PA) and aqueous HCl (0.1 M, J.T. Baker, Phillipsburg, NJ) commercially obtained were standardized by potentiometric titration against potassium hydrogen phthalate or

TRIS base, respectively. The glass electrode was calibrated before each titration by titrating a solution of standardized HCl (5 or 10 mM) with standardized KOH. The data were analyzed using the program *Glee*[282] (version 3.0.21) to obtain the standard electrode potential, slope, and slope factor. The ionic strength of the titration solutions was maintained at 0.1 M using KCl (>99.5%, BioUltra, Sigma-Aldrich), and the titration solutions were allowed to equilibrate for 15 min prior to addition of titrant. Chelator stock solutions were prepared by dissolving HCl salts of the chelators in pure water and their exact concentrations were determined based on the end points of the potentiometric titration curves obtained during the protonation constant measurements. Inductively coupled plasma (ICP) standard solutions (VWR BDH Aristar) of lead (10,000 µg/mL) in nitric acid (0.5% v/v) were employed as the source of metal ions in the titrations.

Protonation constant measurements were carried out by titrating an aqueous solution (~ 15 mL) of free chelator (~ 1 mM) and HCl (~ 10 mM) with standardized KOH (0.1 M). The ionic strength of the solution was maintained at 0.1 M using KCl. The titration method employed a 0.1 mV/min drift limit with a minimum and maximum wait time of 0 s and 180 s respectively between addition of KOH aliquots (0.020 mL volume increments). The titration data within the pH range of 2.2-11.3 were analyzed using *Hyperquad2013* software.[283] The protonation constants were calculated from the average of three independent titrations. Stability constant measurements were carried out by titrating an aqueous solution (~ 15 mL) of chelator (~ 1 mM), metal (~1 mM), and HCl (~ 10 mM) with standardized KOH (0.1 M). The ionic strength of the solution was maintained at 0.1 M using KCl. The titration method employed a 0.1 mV/min drift limit with a minimum and maximum wait time of 0 s and 300 s respectively between addition of KOH aliquots (0.015 mL volume increments). No metal hydroxide precipitation was observed within the pH range and concentration employed. The titration data within the pH range of 2.2-11.3 were analyzed using *Hyperquad2013* software. The stability constants were calculated from the average of three independent titrations.

3.2.6. Radiolabeling

**Caution: ^{203}Pb emits ionizing radiation and should only be used in a facility designed in accordance with appropriate safety controls.

The chelators DOTA, TCMC, crown-4Py, NOON-2Py, and cyclen-4Py were dissolved in deionized water to give 10^{-3} M stock solutions from which serial dilution was used to prepare chelator solutions from 10^{-4} M – 10^{-6} M. A 10 μL aliquot of the respective chelator, or deionized water as a negative control, was further diluted with 80 μL of deionized water and for ^{203}Pb labeling studies, [^{203}Pb]Pb(OAc)$_2$ (85 kBq, 10 μL, 1 M NH_4OAc, pH 7) was added and mixed at ambient temperature to begin the reaction. The instant thin layer chromatography (iTLC) plate system used to separate the "free/uncomplexed" ^{203}Pb from the complexed ^{203}Pb was iTLC-SA (iTLC paper impregnated with silicic acid) plates (1.5 x 10 cm, baseline at 1.5 cm; Agilent Technologies) developed with 50 mM EDTA (pH 5.0). With this system, the complexed $^{203}Pb^{2+}$ remained at the baseline (R_f = 0) and the free $^{203}Pb^{2+}$ migrated with the solvent front (R_f ~ 1). At 60 minutes, 10 μL aliquots were spotted onto the plates and developed. Once dried, radiochemical yields (RCYs) were measured using a BioScan System 200 Scanner (Washington, DC) and quantified with WinScan software.

3.2.7. Human Serum Stability

The serum stability of the [$^{203}Pb^{2+}$][Pb(DOTA)]$^{2-}$ and [$^{203}Pb^{2+}$][Pb(TCMC)]$^{2+}$ complexes were previously evaluated.[156] To perform serum stability studies with the cyclen-4Py complex, a 10 μL aliquot of the 10^{-4} M chelator solution was added to 80 μL of deionized water and 10 μL of [^{203}Pb]Pb(OAc)$_2$ (85 kBq,1 M NH_4OAc, pH 7). To ensure prior to the start of the study that the RCY was 100%, a 10 μL aliquot was removed at 60 minutes. Once a quantitative yield was confirmed as previously described, human serum (90 μL) was added and incubated at 37ºC. At 24-, 48-, and 72-hour time points, an aliquot (10 μL) of the mixture was removed and spotted onto the iTLC-SA plates, developed, and measured as previously described to determine the amount of complex intact.

3.2.8. EDTA and Pb Challenge Studies

A stock solution of 20 mM EDTA) was prepared in H_2O and the pH was adjusted to 7.0 using aqueous sodium hydroxide. A stock solution of 20 mM lead (II) acetate was prepared in H_2O. Preformed [^{203}Pb]Pb^{2+} complexes, prepared as described above at a chelator concentration of 10^{-4} M and RCY >99% after 1 hour post ^{203}Pb addition at ambient temperature, were challenged with 20-fold excess EDTA and non-radioactive Pb. To the

complex solution, an aliquot (10 μL) of the EDTA or Pb solution was added. At 0.5-, 24-, 48-, and 72-hour time points, an aliquot (10 μL) of the mixture was removed and spotted onto the iTLC-SA plates, developed, and measured as previously described to evaluate the kinetic inertness of the complex.

3.3. Results and Discussion

Depending on the radius of the metal cation and macrocycle cavity, three main types of complexes are formed.[284] If the metal cation is of an appropriate size to fit within the cavity, encapsulating meridional complexes typically result.[284] If the metal cation is too large to be encapsulated, the metal will sit above the cavity and form either a facial or sandwich complex; with facial complexes forming when the metal is coordinated above the cavity of a single chelator, while sandwich complexes occur when a single metal atom is complexed between two individual chelators.[284] The radii of the cavity of relevant crown ethers in this study and Pb^{2+} ionic radii as a function of coordination number (CN), are listed in **Table 3.1**.

Table 3.1. Relevant crown ether cavity and Pb^{2+} ionic radii.

Crown ether	Cavity size[285]	Pb^{2+} CN	Pb^{2+} ionic radius[286]
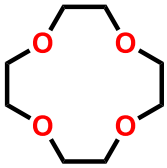 12-crown-4	r = 0.6 – 0.75 Å d = 1.2 – 1.5 Å	4	0.98
		6	1.19
		7	1.23
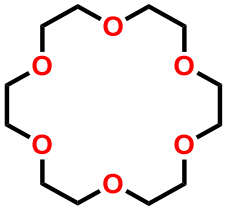 18-crown-6	r = 1.3 – 1.6 Å d = 2.6 – 3.2 Å	8	1.29
		9	1.35
		10	1.40

Although the structures shown in **Table 3.1** are of the oxygen-rich crown ethers, the radii of the aza-derivatives of interest to this study should be nearly equivalent as the covalent radii of oxygen and nitrogen are 0.66 Å and 0.70 Å, respectively.[287] From this table, one can observe that with a CN of 8, the maximum potential CN found in cyclen-

4Py, with an ionic radius of 1.29 Å, Pb^{2+} is too large to form meridional complexes with the chelator and thus should form a facial complex where the Pb^{2+} sits above the cavity. With crown-4Py and a possible maximum CN of 10, with an ionic radius of 1.40 Å, the Pb^{2+} should be fully encapsulated in a meridional complex.

With these two pyridyl-containing chelators expected to form two different types of complexes with Pb^{2+} due to their backbone size, the effect of the size difference of these macrocycles on their radiolabeling ability was investigated. The ^{203}Pb radiolabeling was performed in 0.1 M NH_4OAc at pH 7 and at ambient temperatures, as these mild conditions are ideal when working with heat-sensitive biomolecules, including antibodies. The RCYs were compared to that of DOTA and TCMC, both commercially available standards, with TCMC being widely regarded as the gold standard for lead chelation. Our initial hypothesis was that crown-4Py would have superior selectivity and metal incorporation ability, and therefore greater RCYs, over cyclen-4Py due to the larger and more similar cavity size of the former when compared to the ionic radius of Pb^{2+}.

A summary of RCYs is illustrated in **Figure 3.2**. The RCYs for crown-4Py at concentrations between 10^{-4} and 10^{-7} M were 85.5 ± 5.0%, 45.3 ± 1.4%, 2.0 ± 3.5%, and 0%, respectively. RCYs for cyclen-4Py at the same concentrations were 99.7 ± 0.2 %, 92.8 ± 2.5%, 40.8 ± 2.0%, and 8.0 ± 2.3%, respectively. For DOTA, the RCYs were 99.4 ± 0.4%, 98.6 ± 0.3%, 10.8 ± 1.8%, and 2.5 ± 0.3%, respectively. For the commercial standard TCMC, RCYs of 99.7 ± 0.2%, 99.5 ± 0.4%, 51.5 ± 8.8%, and 18.5 ± 0.1% were observed. Although it was unsurprising that TCMC demonstrated the highest RCYs, what was surprising was the overall low yields for crown-4Py based on our initial hypothesis. At no concentration tested was the yield quantitative, making it difficult to justify pursuing this chelator in a clinical setting for either ^{203}Pb or ^{212}Pb. Serum stability, EDTA challenge, and Pb challenge studies with cyclen-4Py showed that after 72 hours, 97.0 ± 2.8%, 98.1 $\pm$ 0.5%, 98.0 $\pm$ 0.4 % of the complex remained intact, respectively, indicating that $[^{203}Pb][Pb(Cyclen\text{-}4Py)]^{2+}$ is a highly inert complex compatible with radiopharmaceutical applications (**Tables B.1-B.3**).

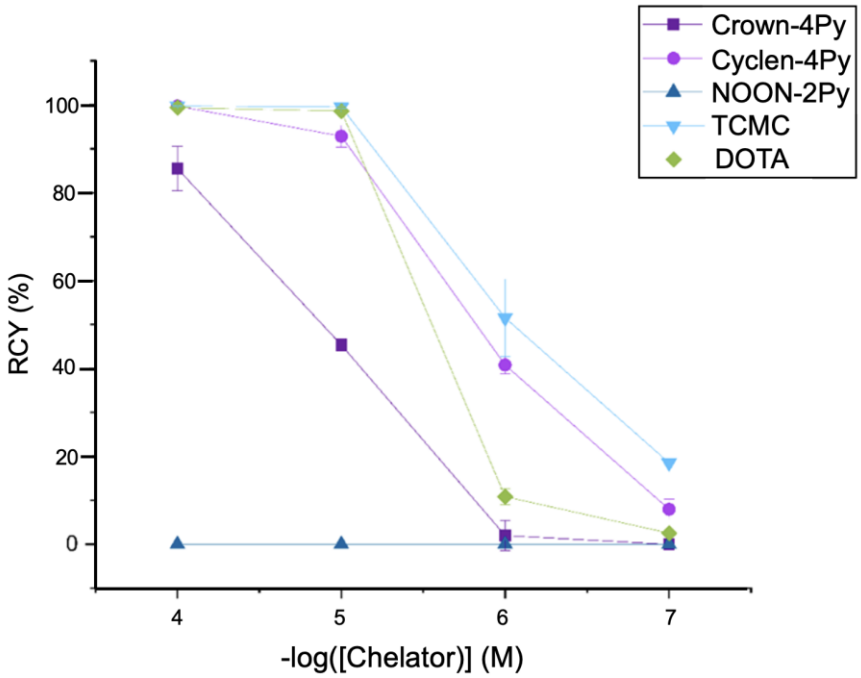

Figure 3.2. Radiochemical yields (RCY, %) for ^{203}Pb radiolabeling reactions. *(Conditions = 1 hr, ambient temperature, and chelator concentrations between 10^{-4} and 10^{-7} M) (n = 3 each data point).*

Aiming to rationalize the RCYs and understand the structure-radiolabeling ability relationship of Pb^{2+}-chelators with bulky pyridyl donor groups, the complexes were also studied by ^{1}H NMR, X-ray diffraction, and potentiometry to determine the thermodynamic stability and protonation constants. The ability to study Pb complexes with these techniques is another benefit of this theranostic pair as, unlike an emerging alpha-emitter, actinium-225 (^{225}Ac), stable isotopes of this element exist, including ^{207}Pb, which is NMR active.

The solid-state structures of the Pb^{2+} complexes of cyclen-4Py and crown-4Py, shown in **Figure 3.3,** as well as the Pb^{2+} complexes of their respective cyclen and N_4O_2 backbones (**Figure B.23**), were determined by X-ray diffraction. Select interatomic distances and angles of the metal coordination environment are given in **Table 3.2 and 3.3**, respectively.

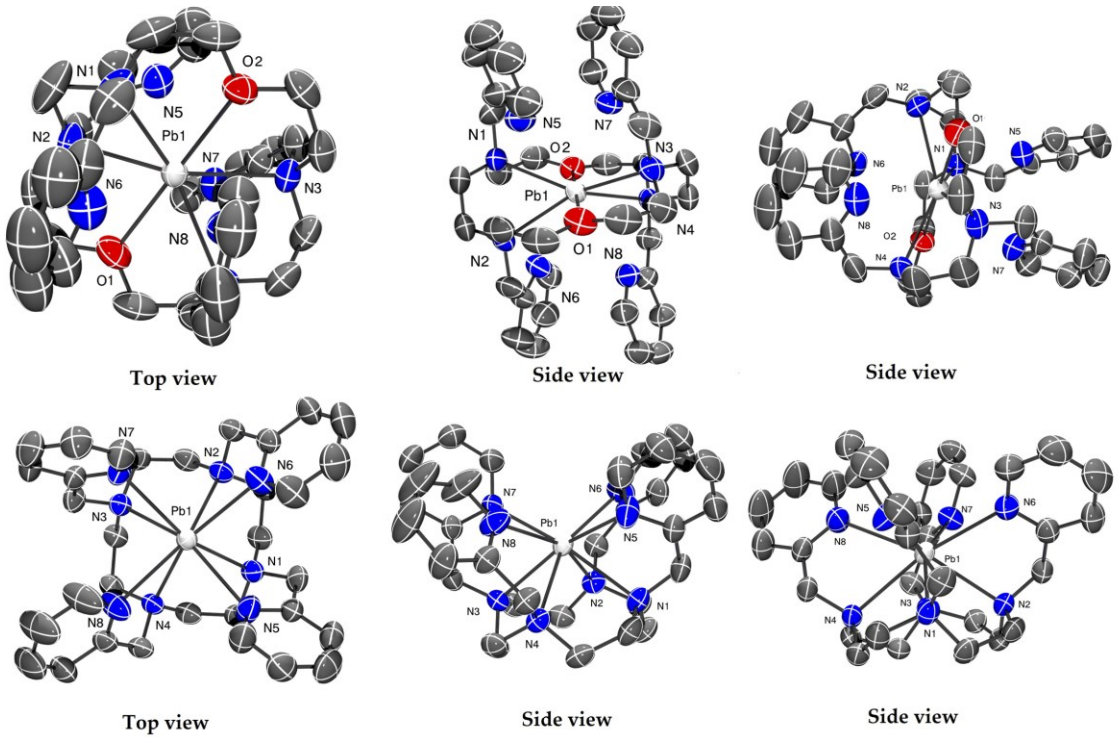

Figure 3.3. X-ray crystal structures of $[Pb(Crown\text{-}4Py)]^{2+}$ (top) and $[Pb(Cyclen\text{-}4Py)]^{2+}$ (bottom) complexes with labeled atoms.
Hydrogen atoms and counter anions were omitted for clarity. Ellipsoids drawn at 50% probability level.

Table 3.2. Select Interatomic Distances (Å) in the Metal Coordination Environment in $[Pb(Cyclen\text{-}4Py)]^{2+}$ and $[Pb(Crown\text{-}4Py)]^{2+}$ Complexes

	$[Pb(Cyclen\text{-}4Py)]^{2+}$	$[Pb(Crown\text{-}4Py)]^{2+}$
Pb(1) – N(1)	2.630(2)	2.806(3)
Pb(1) – N(2)	2.652(2)	2.769(3)
Pb(1) – O(1)	n/a	2.613(3)
Pb(1) – O(2)	n/a	2.604(3)
Pb(1) – N(5)	2.712(3)	3.113
Pb(1) – N(6)	2.776(3)	2.995
Pb(1) – N(7)	2.781(2)	2.924
Pb(1) – N(8)	2.823(2)	3.026

As shown in the crystal structure, the crown-4Py complex presents a staggered conformation with adjacent pyridyl groups nearly 180° to each other while with the Pb^{2+} complex of cyclen-4Py presents a *syn* conformation with all four of the pyridyl arms on the same side of the complex. As expected, crown-4Py formed a meridional complex with

Pb^{2+} coordinated within the ring and cyclen-4Py formed a facial complex with the Pb^{2+} situated above the ring.

The maximum interatomic distance for a Pb-N interaction to be considered coordinating is approximately 2.9 Å.[286] In each of the complexes, both the Pb-O and Pb-N bonds in the macrocyclic backbone meet this requirement. The shorter average Pb-O interatomic distance (2.609(3) Å) in the crown-4Py N_4O_2 backbone, is reflective of the harder nature of the oxygen donor compared to its nitrogen counterpart, with an average backbone Pb-N interatomic distance of 2.770(3) Å. Interestingly, the Pb-N bonds in the cyclen-4Py backbone exhibited an average distance of 2.641(2) Å, while the average Pb-N_{pyr} (pyridine group nitrogen) distance was 2.773(3) Å; both substantially shorter than the same associations observed in the crown-4Py complex, which maintained an average interatomic distance of 3.015 Å. With Pb^{2+} sitting deeper in the macrocyclic cavity of crown-4Py, this likely negatively affects the accessibility of the lead ion by the pyridine nitrogen atoms, resulting in longer associations that make coordination less favourable by these bulky donor groups, and potentially explaining the lower radiochemical yields. With Pb^{2+} coordinated to cyclen-4Py in an exocyclic manner, the Pb^{2+} sits above the cyclen backbone, making it more accessible to the bulkier pyridyl groups.

The thermodynamic favourability of cyclen-4Py over crown-4Py Pb-complex formation is further evinced by the bond angles observed in the five membered ring which form between the backbone nitrogen atoms, lead, and pyridine nitrogens (N-Pb-N_{pyr}). These angles are summarized in **Table 3.3**. To reduce steric strain and consequently increase thermodynamic favourability, the ideal bond angle of these five membered rings should be ~69°, of which any deviation suggests an increase in steric strain.[288] The average N-Pb-N_{pyr} bond angles for $[Pb(Crown\text{-}4Py)]^{2+}$ and $[Pb(Cyclen\text{-}4Py)]^{2+}$ are 56.91° and 62.90°, respectively. The larger deviation from the ideal bond angle in the crown-4Py complex (~12°) compared to the cyclen-4Py complex (~7°) indicates a larger strain energy in the former compared to the latter, reducing the Pb-complex thermodynamic favourability and potentially explaining crown-4Py's poor metal incorporation ability.

Table 3.3. Select N-Pb-N Bond Angles (°) in the Metal Coordination Environment in $[Pb(Cyclen\text{-}4Py)]^{2+}$ and $[Pb(Crown\text{-}4Py)]^{2+}$ Complexes

	$[Pb(Cyclen\text{-}4Py)]^{2+}$	$[Pb(Crown\text{-}4Py)]^{2+}$
N(1) – Pb(1) – N(5)	63.14(8)	55.8(1)
N(2) – Pb(1) – N(6)	64.10(8)	56.72(9)
N(3) – Pb(1) – N(7)	60.90(7)	58.0(1)
N(4) – Pb(1) – N(8)	63.41(7)	57.10(9)
N(1) – Pb(1) – N(4)	68.95(7)	n/a
N(2) – Pb(1) – N(3)	69.55(7)	n/a
N(1) – Pb(1) – N(2)	68.87(7)	66.8(1)
N(3) – Pb(1) – N(4)	67.74(7)	67.05(9)

Given the inability of the four pyridyl groups to coordinate Pb in the crown-4Py complex, it was hypothesized that reducing the number of pyridyl groups from four to two would reduce both steric strain and the loss of entropy the chelator experiences during complex formation. As such, the 18-membered N_2O_4 backbone chelator NOON-2Py (**Figure 3.1**) was studied. This backbone cavity still possesses approximately the same diameter as Pb^{2+} at a coordination number of 8, presumably conserving size selectivity. Surprisingly, macrocyclic NOON-2Py was not able to incorporate the radio-lead under any condition tested. Investigation into the coordination chemistry was also performed with X-ray diffraction studies, with the crystal structure shown in **Figure 3.4**.

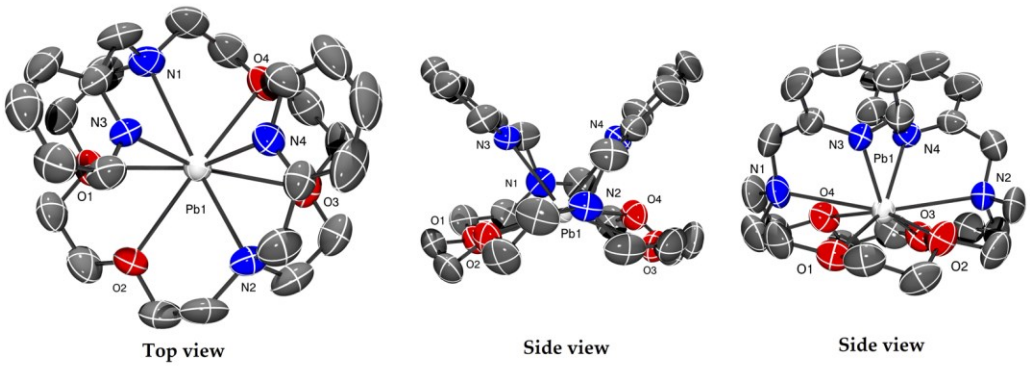

Figure 3.4. X-ray crystal structure of $[Pb(NOON\text{-}2Py)]^{2+}$ complex with labeled atoms.
Hydrogens and counter anions were omitted for clarity. Ellipsoids drawn at 50% probability level.

In literature, steric strain is minimized when the lone pairs of nitrogen atoms in a five-membered coordination ring are situated so as to produce a M-N association distance of 2.5 Å.[288] For $[Pb(NOON\text{-}2Py)]^{2+}$, it was found that the average Pb-N_{pyr} interatomic distance was 2.587(4) Å and average N-Pb-N_{pyr} angle of 65.0(1)°, the closest of all the

macrocyclic pyridyl chelators investigated to the ideal literature values, which should suggest that there is minimal steric strain energy involved in complexation. On this basis alone, one would have expected NOON-2Py to give rise to the highest ^{203}Pb incorporation yields, however, no incorporation was observed. Given these results, other aspects of the structure, as well as the difference between experiments performed at the tracer level versus the macroscopic scale must be considered to provide insight into these results.

Due to its electron configuration of $[Xe]4f^{14}5d^{10}6s^2$, Pb^{2+} exhibits an inert-pair effect as the outermost electrons of Pb^{2+} are not involved in bond formation.[289] This inert lone pair of electrons can thus cause a non-spherical distribution of the donating electrons around the Pb^{2+} and, depending on the chelator, can form a distinct void in the coordination sphere.[289] In this situation, the lone pair is designated as stereochemically active with this type of geometry referred to as hemidirected.[289] When the donating arms are located evenly throughout the coordination sphere, it is referred to as holodirected coordination.[289] The nature of the coordination is determined heavily by the coordination number and geometry of the chelator itself. With CNs from 2-5, all complex geometries are hemidirected and from 9-10, all are holodirected, but from 6-8, both geometries are possible.

With a possible CN of 8 for NOON-2Py, holo- or hemidirected coordination is possible for $[Pb(NOON\text{-}2Py)]^{2+}$. With both pyridyl groups located on the same side of the complex, it takes on a *syn*-like conformation. This *syn*-like conformation may be due to the presence of a stereochemically active lone pair that results in hemidirected geometry, causing a large void in the coordination sphere. A large void in a coordination complex can be an issue for radiopharmaceuticals as it can allow for coordination by a competing, metal-seeking endogenous protein or biomolecule *in vivo*.[290] However, the thermodynamic favourability of complexation in the solution state cannot be determined from the crystal structure and although mass spectrometry has been utilized and can provide information on the composition of the coordination complex, it cannot provide any information on stability or how the complex acts in solution. Therefore, investigation by solution state NMR and potentiometry was necessary.

Literature precedence suggests that in solution, macrocyclic complexes, particularly polyether complexes, can exhibit dynamic and fluxional behaviour that can make analysis of NMR spectroscopic data difficult, limiting its utility.[284] This fluxional nature

was apparent in the spectrum of the Pb^{2+} complexes of crown-4Py and NOON-2Py, as shown in **Figure 3.5** and **3.6**, respectively. In the ^1H NMR spectrum of $[Pb(Crown\text{-}4Py)]^{2+}$, the broadening of the peaks correlating to both the backbone and pyridine groups indicates that complexes form multiple isomers in solution, suggesting fluxional coordination which can cause incompatibility *in vivo*. However with $[Pb(NOON\text{-}2Py)]^{2+}$, this behaviour is only evident for the hydrogen atoms belonging to the backbone (H_f, H_g, H_h), suggesting that the macrocycle undergoes dynamic changes at the NMR timescale while the coordinating pyridine moieties do not. For the cyclen-4Py complex, one highly symmetric isomer is observed in solution. All methylene hydrogens (H_e and H_f), shown in **Figure 3.7,** are no longer equivalent and are diastereotopic as they exist in different chemical environments due to the formation of this complex. A single isomer in solution is advantageous as these complexes tend to be more stable *in vivo*, although this is not a reliable measure of absolute stability. A single isomer will lower the entropic penalty that the chelators face upon complexation as reorganization is not continually occurring. Although these NMR studies give insight into what is occurring in the solution state, the thermodynamic stability in solution can be quantitatively determined by potentiometry.

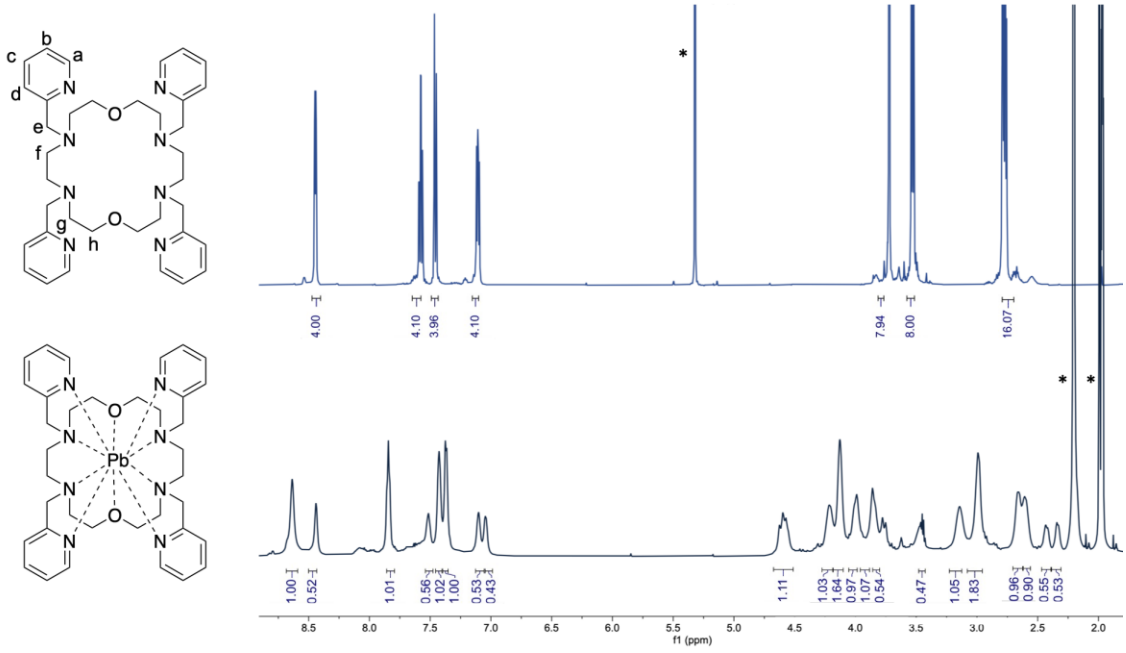

Figure 3.5. ^1H NMR spectra at 25°C of Crown-4Py showing changes upon Pb^{2+}complexation.
*Top: Crown-4Py (500 MHz, CD_2Cl_2-d_2). Bottom: $[Pb(Crown\text{-}4Py)]^{2+}$ (600 MHz, CD_3CN-d_3). *Residual solvent peak.*

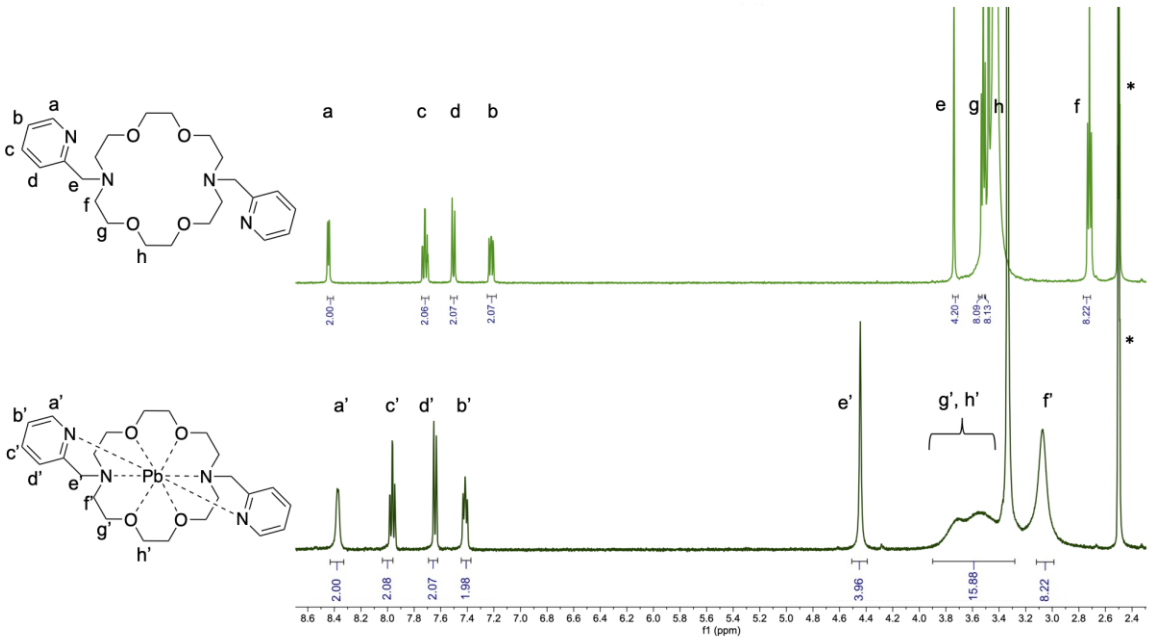

Figure 3.6. ^{1}H NMR spectra at 25°C of NOON-2Py showing changes upon Pb^{2+}complexation.

*Top: NOON-2Py (400 MHz, DMSO-d_6). Bottom: $[Pb(NOON\text{-}2Py)]^{2+}$ (500 MHz, DMSO-d6). *Residual solvent peak.*

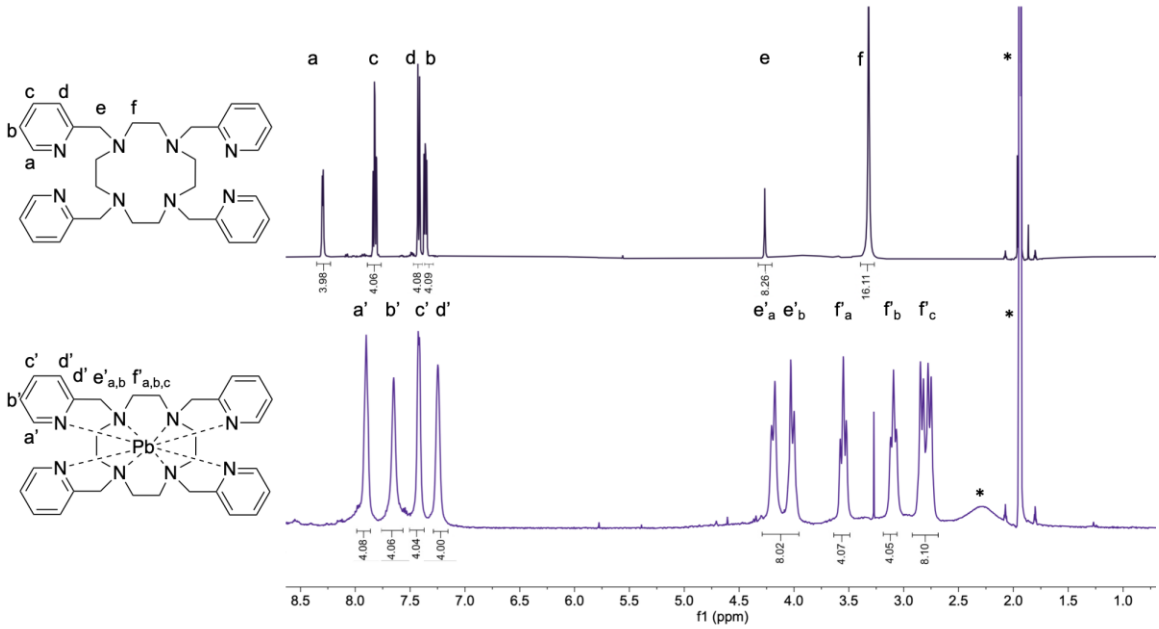

Figure 3.7. ^{1}H NMR spectra at 25°C of Cyclen-4Py showing changes upon Pb^{2+}complexation.

*Top: Cyclen-4Py (400 MHz, CD_3CN-d_3). Bottom: $[Pb(Cyclen\text{-}4Py)]^{2+}$ (500 MHz, CD_3CN-d_3). *Residual solvent peak and water.*

The protonation constants (log K_a) of the pyridyl chelators and the thermodynamic stability constants (log K_{ML}) of the Pb^{2+} complexes were determined by potentiometric titration in 0.1 M KCl, as shown in **Table 3.4** and in **Figures B.20-B.23**. However, thermodynamic stability constants alone are not adequate to predict and compare the stability of the complexes under physiological conditions, and so the more representative conditional stability constant (log K'_{Pb}) and pM values were determined at pH 7.4 and 25°C. The pM values were calculated at a metal concentration of 1 μM and chelator concentration of 10 μM.

Of the pyridyl chelators tested, cyclen-4Py has the largest log K_{ML} and pM value of 19.95(3) and 17.88, respectively. Both the NMR spectrum, that showed one highly symmetric isomer in solution, and the solid-state structure, that showed Pb^{2+} was easily accessed by the pyridyl donor groups, can explain the high ^{203}Pb RCY with cyclen-4Py, suggesting that the smaller cyclen backbone is ideal when incorporating bulky donor groups into the design of a tailored lead(II) chelator. These constants and speciation diagrams can be of great use to predict the ideal pH for radiolabeling and the suitability of a chelator for a given metal; however, it is important to note that differences can arise at the tracer level used for radiopharmaceuticals, which may explain why TCMC had a greater RCY than cyclen-4Py, but DOTA did not. At the tracer level, the chelator is in excess by orders of magnitude compared to the radiometal whereas in these studies, the metal:chelator ratio is either 1:1 or 1:10, a ratio unlikely to be reached with radiolabeling.

Table 3.4. Chelator Protonation Constants and Thermodynamic Stability Constants of Pb^{2+} Complexes.

	DOTA[38]	NOON-2Py[271]	Crown-4Py	Cyclen-4Py	TCMC[291]
log K_1	12.09	7.44	7.91(4)	10.05(4)	7.70(1)
log K_2	9.76	6.26	7.33(4)	7.53(2)	6.21(1)
log K_3	4.559	1.38	4.64(1)	3.54(7)	-
log K_4	4.09	-	4.00(6)	2.23(6)	-
log K_{PbL}	25.3(1)[292]	11.67	13.29(5)	19.95(3)	>19
log K_{PbHL}	-	-	5.22(1)	2.06(9)	-
log K_{PbH2L}	-	-	3.50(8)	-	-
log K'_{Pb}*	15.64	11.33	12.45	16.93	-
pPb**	20[292]	12.29	13.40	17.88	-

*I = 0.1 M KCl for NOON-2Py, Crown-4Py, and Cyclen-4Py; I = 0.1 M $NaNO_3$ for TCMC, 0.1 M Me_4NNO_3[293] or 0.1 M NaCl[292] for DOTA. *Conditional stability constants (log K'_{Pb}) at pH 7.4, 25 °C, and I = 0.1 M. **pPb values calculated from $-\log [Pb]_{free}$ ($[Pb]_{tot} = 10^{-6}$ M, $[L]_{tot} = 10^{-5}$ M, pH 7.4, 25 °C, and I = 0.1 M)*

Given that this structure-activity relationship study was meant to advance the use of $^{203}Pb/^{212}Pb$ radiopharmaceuticals, it would be of great interest to explore if this trend extends to bismuth (Bi^{3+}) as ^{212}Bi ($t_{1/2}$ = 60.55 min) is the alpha-emitting daughter of ^{212}Pb. Additionally, non-radioactive Bi^{3+} complexes of cyclen-4Py have been shown to possess anti-cancer activity *in vitro*[294]; Bi^{3+} complexation[274,276] and [^{213}Bi]Bi^{3+} radiolabeling studies[276] have been previously conducted with this chelator and results indicate that further investigation with this element is justified. Most of all, Bi^{3+}, like Pb^{2+}, has the potential to possess a stereochemically active lone pair. Additionally, future studies to observe if these findings can be extrapolated to intermediate Lewis bases with a smaller ionic radius, like Cu^{2+}, could provide insight on how to optimize chelator design in radiopharmaceuticals to improve metal selectivity and complex stability.

3.4. Conclusion

In summary, this study has demonstrated that when incorporating sterically hindered donor groups, pyridines in this study, the presence and size of the macrocyclic backbone has a significant effect on complex stability and feasibility for use in lead(II)

radiopharmaceuticals. Through XRD, NMR spectroscopy, and potentiometric titration studies, it was found that, at room temperature, Pb-complexation with smaller backbones (i.e. cyclen) cause the formation of facial-complexes which are more favourable allowing the metal to be more available for exocyclic coordination by the bulky donor groups, reducing conformational flexibility and increasing the thermodynamic favourability of complexation compared to larger backbones with endocyclic coordination. With larger backbones (i.e. N_2O_4), reducing the number of bulky donor groups can improve accessibility to the metal, but the $6s^2$ lone pair belonging to lead, if stereochemically active, can cause a void in the coordination sphere which can make the chelator incompatible with radiopharmaceutical applications. This work demonstrates the challenges associated with designing chelators for Pb-based radiopharmaceuticals and that cyclen-4Py holds the most promise of these pyridyl-containing chelators for future studies.

Chapter 4.

Is Thiourea the Weak Link? An Investigation of the *In Vitro* and *In Vivo* Destabilization of [^{203}Pb]- and [^{212}Pb]Pb^{2+} Thiourea-Based Bioconjugates

4.1. Introduction

With the incidence of cancer continuing to increase, more research than ever is needed to develop safe, personalized, and effective diagnostic and therapeutic agents with minimal side effects. Bifunctional chelator-based radiopharmaceuticals (BFC-RPs) have gained significant attention over the past few years with the approval of both diagnostic[190,191] and therapeutic[295,296] agents composed of four main components. This includes 1) a radioactive metal (radiometal) coordinated by 2) a chelator attached via 3) a linker to 4) a biological targeting vector, as shown in **Figure 4.1**.[297,298] This targeting vector seeks out and binds to biomolecules overexpressed on cancer cell surfaces allowing for direct delivery of a radioactive payload specifically to these cells. This spares healthy surrounding tissues to reduce side-effects compared to many traditional chemotherapeutic approaches. Increasingly, these radiopharmaceuticals are being used in *theranostic* applications—an approach that guides decisions on therapeutic approaches using the results of preliminary diagnostic imaging using these BFC-RPs.[299–301]

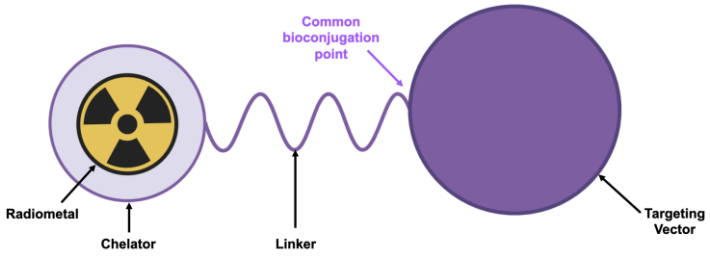

Figure 4.1. Structure of a bifunctional chelator-based radiopharmaceutical.

The success and selectivity of BFC-RPs hinges on the careful optimization of each component to ensure clinical safety and efficacy. The choice of radiometal is key as its mode of radioactive decay determines its application as radiometals emitting gamma rays of select energies can be used for imaging, while those releasing alpha particles, beta particles, or Auger electrons may be suitable for therapeutic purposes.[302–305] Increasingly,

BFC-RPs are designed as theranostic pairs and thus the choice of radiometal(s) incorporated in the drug design is such that one radiometal, the diagnostic agent, will allow for imaging while the other, the therapeutic agent, will allow for therapy. If the same element, such as with the lead-203 (^{203}Pb, $t_{1/2}$ = 51.9 h) / lead-212 (^{212}Pb, $t_{1/2}$ = 10.6 h) theranostic pair, is employed for each agent, the biodistribution of the imaging counterpart should match that of the therapeutic counterpart allowing for visualization of projected therapeutic uptake and thus identification of an ideal treatment regimen.[306,307] Even with an exceptional radiometal, if it is not bound stably by an optimized chelator, the radiometal may release *in vivo*, which can result in off-target accumulation and undesirable side effects.[308,309] The targeting vector, responsible for recognizing and binding to cancer-specific molecules, heavily influences the selectivity, binding affinity, and efficacy of the radiopharmaceutical.[298] Common targeting vectors include antibodies, peptides, and small molecules. Often underappreciated, however, is the linker that connects the radiometal-chelator complex to the targeting vector. Linker structures can range from an existent donor arm on a chelator to elaborate structures with the addition of various chemical modifications and additions designed to moderate the *in vivo* biodistribution of the radiopharmaceutical.[297,310,311]

Bioconjugation is the process of linking the chelator-linker to the targeting vector. The bioconjugation method chosen dictates the type of covalent bond formed between these two groups which directly impacts the stability, pharmacokinetics, and efficacy of the radiopharmaceutical.[312–314] Bioconjugation occurs via a reaction between a functional group on the linker and a complementary group on the targeting vector. A wide variety of bioconjugation methods exist and common bioconjugation methods include, but are not limited to, amide coupling, thiourea linkage, thiosuccinimide linkages, and click chemistry. Each method offers distinct advantages and disadvantages depending on its application as the bonds formed have different chemical stabilities and resistance to biological degradation. For example, thiosuccinimide linkages, which are formed between maleimides and the sulfhydryl groups of cysteines of protein-based biomolecules, allow for site-selective addition but are prone to retro-Michael additions and other thiol exchange reactions *in vivo* which can cause cleavage of the thiosuccinimide group which can lead to an untargeted delivery of radiation to tissues in the body if used in BFC-RPs, making these groups clinically undesirable.[315]

Amide and thiourea-based conjugations are two of the most widely used bioconjugation methods to develop BFC-RPs. Amide coupling involves a reaction between a carboxylic acid and an amine to form a stable amide bond. To facilitate this reaction, carboxylic acids are often activated with groups like N-hydroxysuccinimide (NHS) esters (as shown in **Figure 4.2A**), to increase their reactivity towards a nucleophilic attack from an amine, resulting in amide-coupled BFC-RPs.[316] Amide bonds are highly stable *in vivo*, except in the presence of peptidases, proteases, and related enzymes, making them a highly attractive option for bioconjugation. On the other hand, thiourea-based conjugation is achieved through a reaction between an isothiocyanate and an amine, as shown in **Figure 4.2B**. This reaction occurs under mild conditions and is highly selective, reducing possible side reactions and side products. Additionally, there are a wide variety of commercially available isothiocyanate-functionalized chelators and modifiable backbones available, making the synthesis of thiourea-based bioconjugates readily accessible. However, recent studies in literature have suggested that the thiourea bond may not be as stable *in vivo* as previously thought potentially due to increased susceptibility to radiolysis[317] or enzymatic degradation[318,319], which was further investigated in this study.

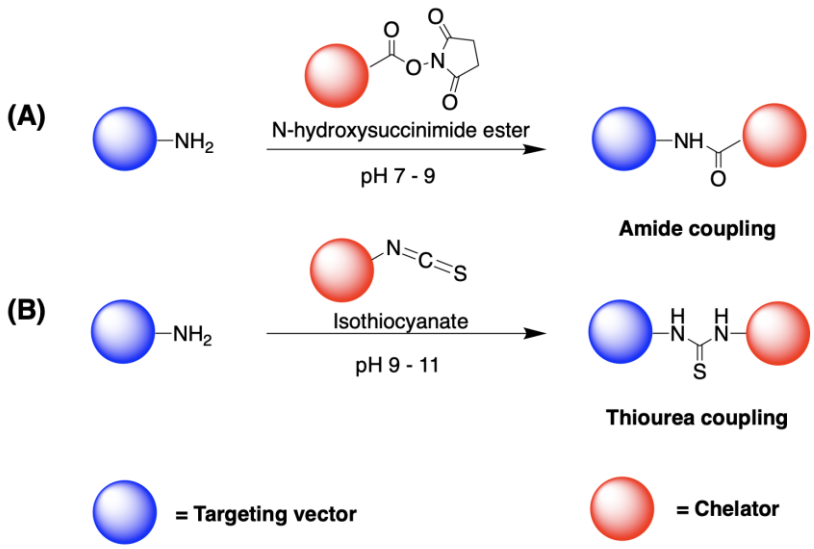

Figure 4.2. General reaction schemes for and (A) amide coupling using a N-hydroxysuccinimide activated carboxylic acid-functionalized chelator and (B) thiourea coupling using isothiocyanate-functionalized chelators to an amine on a biological targeting vector.

When this study was initially conceptualized, the purpose was to evaluate the effect of different chelators on the biodistribution of ^{203}Pb/^{212}Pb-labeled fibroblast activation

protein inhibitor (FAPI)-based bioconjugates, which targets fibroblast activation protein (FAP) overexpressed in over 90% of epithelial carcinomas.[320] Similar to many other small molecule-based bioconjugates, FAPI BFC-RPs rapidly accumulate in tumors but exhibit low tumour retention times and fast renal clearance, which limits their effectiveness for therapeutic applications.[321–325] Peptide-based bioconjugates, such as cyclic melanocyte stimulating hormone (CycMSH) targeting the melanocortin-1 receptor (MC1R) overexpressed on melanoma cells, also suffer from these limitations, although to a lesser extent.[326–330] It was hypothesized that a change in chelator structure, which often affects hydrophilicity of the RP, may improve tumour retention.[331–334]

The commercially available bifunctional chelator TCMC-NCS, also commonly referred to as DOTAM, was compared against cryptand-NCS, a bifunctional chelator previously developed in-house[251], and newly synthesized Cyclen-4Py-NCS, conjugated to FAPI via a thiourea bond, as shown in **Figure 4.3**. Initial *in vitro* stability studies with human serum suggested that these ^{203}Pb/^{212}Pb-labeled bioconjugates were stable when analyzed via instant thin layer chromatography (iTLC). However, suboptimal *in vivo* biodistribution results suggested that these thiourea-based bioconjugates may be subject to extensive degradation and aggregation *in vivo*. To study this potential phenomenon, a side-by-side comparison of the thiourea- and amide-based ^{203}Pb/^{212}Pb FAPI and CycMSH bioconjugates using TCMC was conducted *in vitro* and *in vivo*. This study investigates how the chelator and type of bioconjugation affects the *in vitro* and *in vivo* stability of ^{203}Pb/^{212}Pb-based BFC-RPs, aiming to highlight potential limitations of thiourea-based bioconjugation in small molecule and peptide-based models with this theranostic pair in future applications.

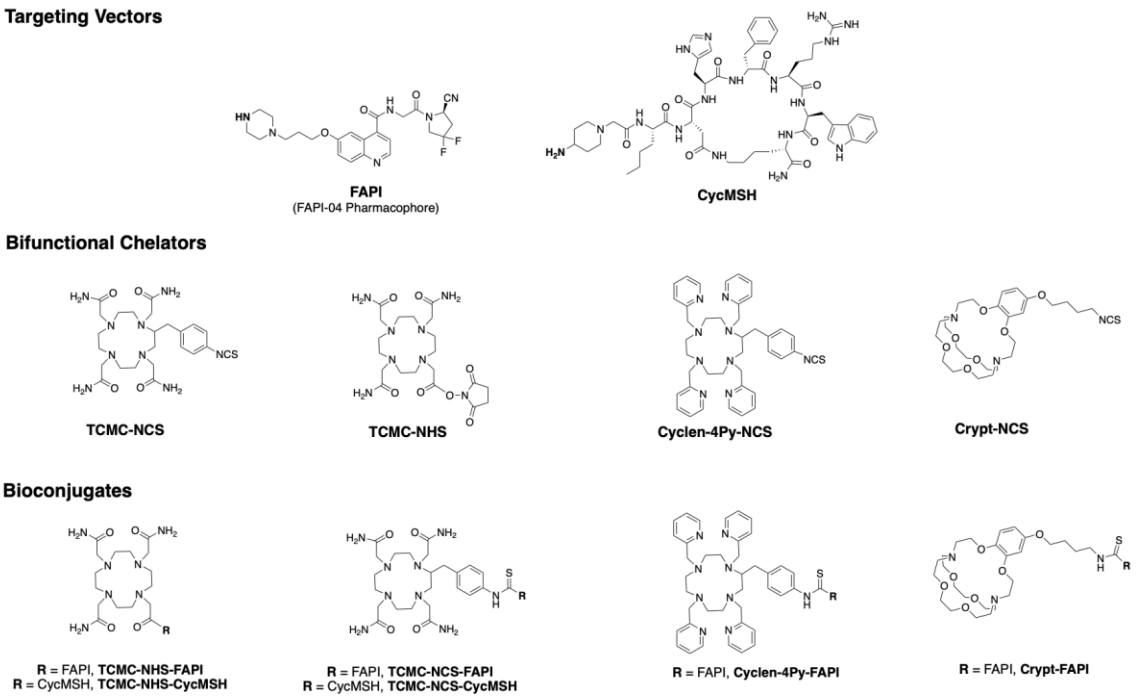

Figure 4.3. The structures of all targeting vectors, bifunctional chelators, and bioconjugates investigated in this study.

4.2. Materials and Methods

4.2.1. General

All solvents and reagents used in this study were purchased from commercial suppliers and used directly without further purification. Anhydrous solvents were obtained via storage over 3 Å molecular sieves that were activated with heat. Water was purified using a MilliQ purification system to give what is further referred to in this text as MQ H_2O. Ultrapure water, Optima™ hydrochloric acid, and Optima™ nitric acid were purchased from Fisher Scientific (Waltham, MA). Ammonium acetate (NH_4OAc; 99.99% trace metals basis), sodium hydroxide (99.99% trace metals basis), ethylenediaminetetraacetic acid (EDTA) disodium salt (ACS grade), human serum (Male AB plasma), mouse serum, saline, phosphate buffered saline (PBS), and PBS 0.05% Tween-20 were purchased from Millipore Sigma (Burlington, MA). Instant thin layer chromatography paper impregnated with silicic acid (iTLC-SA) was purchased from Agilent Technologies (Santa Clara, CA). S-2-(4-Nitrobenzyl)-1,4,7,10-tetraazacyclododecane (p-NO_2-Bn-Cyclen), S-2-(4-Isothiocyanatobenzyl)-1,4,7,10-tetraaza-1,4,7,10-tetra(2-

carbamoylmethyl)cyclododecane (TCMC-NCS), and 1-acetic acid mono(N-hydroxysuccinimidyl ester)-4,7,10-Tris(acetamido)-1,4,7,10-tetraazacyclododecane (TCMC-NHS) were purchased from Macrocyclics Inc. (Plano, TX). Pb resin was purchased from Eichrom Technologies (Lisle, IL). Human FAP was purchased from Biolegend (San Diego, CA) and Suc-Gly-Pro-AMC substrate from Bachem (Torrance, CA).

Nuclear magnetic resonance (NMR) spectra were obtained using a Bruker 400 (400 MHz) or a Bruker500 (500 MHz) (Billerica, MA) with signals measured relative to the signal of the solvent. Mass spectrometry was performed using either an Agilent (Santa Clara, CA) 6210 TOF LC/MS, Bruker Maxis Impact Q-TOF LC/MS/MS or Advion expression LC-MS (Ithaca, NY) equipped with an electrospray source. Synthetic purification was performed using a reverse phase HPLC system consisting of an Agilent 1100 series HPLC module using a semipreparative Phenomenex Luna C18 (250 mm × 100 mm) column. All RadioHPLC experiments were performed using a system consisting of an Agilent 1260 Infinity II Quaternary Pump, Agilent 1260 autosampler, Raytest Gabi Star NaI (Tl) radiation detector, Agilent 1260 variable wavelength detector with a Phenomenex Luna 5 µm C18 100 Å liquid chromatography analytical column (250 × 4.6mm). Unless otherwise stated, the gradient used was 100% A to 100% B over 20 minutes at 1 mL/min where A = 0.1% TFA in water and B = 0.1% TFA in acetonitrile. Radiolabeling or radiochemical yields were determined by iTLC and analyzed on an AR-200 TLC Scanner (Eckert and Ziegler, Valencia, California) with WinScan software V3 software (Academic Software Inc.). SPECT/CT studies were performed using a calibrated multimodal VECTor/CT system (MILabs, Netherlands) with an ultra-high sensitivity 2-mm pinhole collimator. Image analysis was performed using AMIDE software (V. 1.0.5).

4.2.2. Production of ^{203}Pb and ^{212}Pb

^{212}Pb was produced as previously described[156] with a deviation. Instead of constructing the ^{228}Th/^{212}Pb from the thorium waste of one target, the generator used in this study was produced from the pooled thorium waste of two targets, giving rise to approximately 16 g of ^{232}Th material in the generator stock solution (30 mL, 2 M HNO_3). Despite this, the activity was purified as previously described with a singular Pb resin column.[156] ^{203}Pb was either sourced from TRIUMF's TR13 (13 MeV) cyclotron via a ^{203}Tl (p,n) ^{203}Pb reaction or from the University of Alberta's TR24 (24 MeV) cyclotron via a ^{205}Tl

(p,3n) ^{203}Pb reaction. When ^{203}Pb was produced at TRIUMF, the ^{203}Pb was purified by extraction chromatography (EXC) followed by anion exchange chromatography (AEX), as described in literature.[113] When produced at the University of Alberta, the ^{203}Pb was purified using EXC, as described by Nelson *et al.*[131] and shipped to TRIUMF as [^{203}Pb]$PbCl_2$ in 8 M HCl. Upon receipt at TRIUMF, the solution was diluted with ultrapure water to 2 M HCl and then purified via AEX as per literature methods.[113] Measurements of ^{203}Pb radioactivity were performed with a Capintec-55tR or CRC-15 Dose Calibrator on setting #344 or with gamma ray spectroscopy with a co-axial high purity germanium (HPGe) gamma spectrometer (N-type, Canberra Industries, Meriden, CT). This gamma spectrometer was calibrated with a 20 mL ^{152}Eu and ^{133}Ba source and samples were measured at a minimum distance of 5 cm above the detector with a dead time kept below 5%. Samples were counted until the uncertainty in measurement was below 5%. ^{212}Pb was quantified only via the use of gamma spectroscopy.

4.2.3. Synthesis

The synthesis of (S)-2-(4-isothiocyanatobenzyl)-1,4,7,10-tetrakis(pyridin-2-ylmethyl)-1,4,7,10-tetraazacyclododecane (Cyclen-4Py-NCS) from S-2-(4-Nitrobenzyl)-1,4,7,10-tetraazacyclododecane (p-NO_2-Bn-Cyclen), is described in detail in the Supplementary Information and summarized in **Scheme C.1**. The cyclic melanocyte stimulating hormone derivative, “CycMSH”, was synthesized and purified as previously described.[327] The FAPI-04 pharmacophore, “FAPI”, was synthesized and purified as described in the literature.[335,336] The synthetic scheme for the production of all CycMSH and FAPI bioconjugates is shown in **Scheme 4.1** and **Scheme 4.2**, respectively. Details on the synthetic and purification procedures are described in the Supplementary Information. As all of these bioconjugates were purified using HPLC systems employing water with 0.1% trifluoroacetic acid (TFA) and acetonitrile with 0.1% TFA as the mobile phases, in order to accurately prepare a stock solution, the concentration, or mass percentage, of TFA in each isolate bioconjugate had to be determined. The TFA content was measured using ^{19}F NMR spectroscopy as described in literature with a deviation that instead of using DMSO-d_6 to prepare calibration standards and samples, D_2O was used.[337] Briefly, 600 μL TFA calibration standards at concentrations from 0.48 mM to 9.8 mM were prepared in D_2O and with these standards, ^{19}F NMR spectra were obtained to form a calibration curve. This calibration curve was used to determine the TFA content in 0.5 – 1

mg samples of the purified bioconjugate to allow for a more accurate determination of the bioconjugate mass and yield post-HPLC purification.

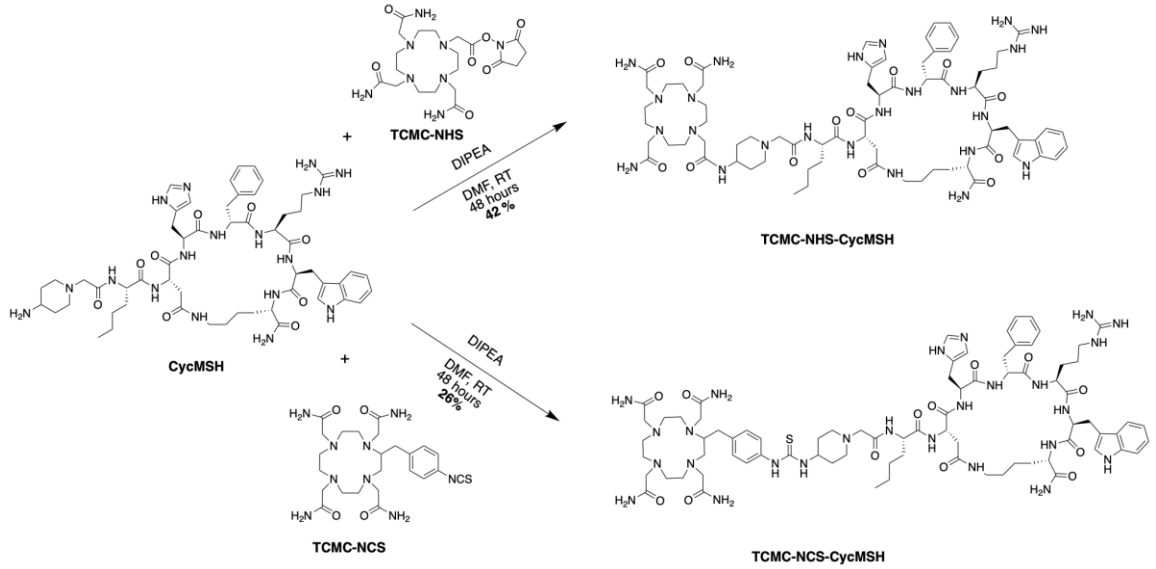

Scheme 4.1. Synthesis of CycMSH-based bioconjugates TCMC-NHS-CycMSH and TCMC-NCS-CycMSH used in this study.

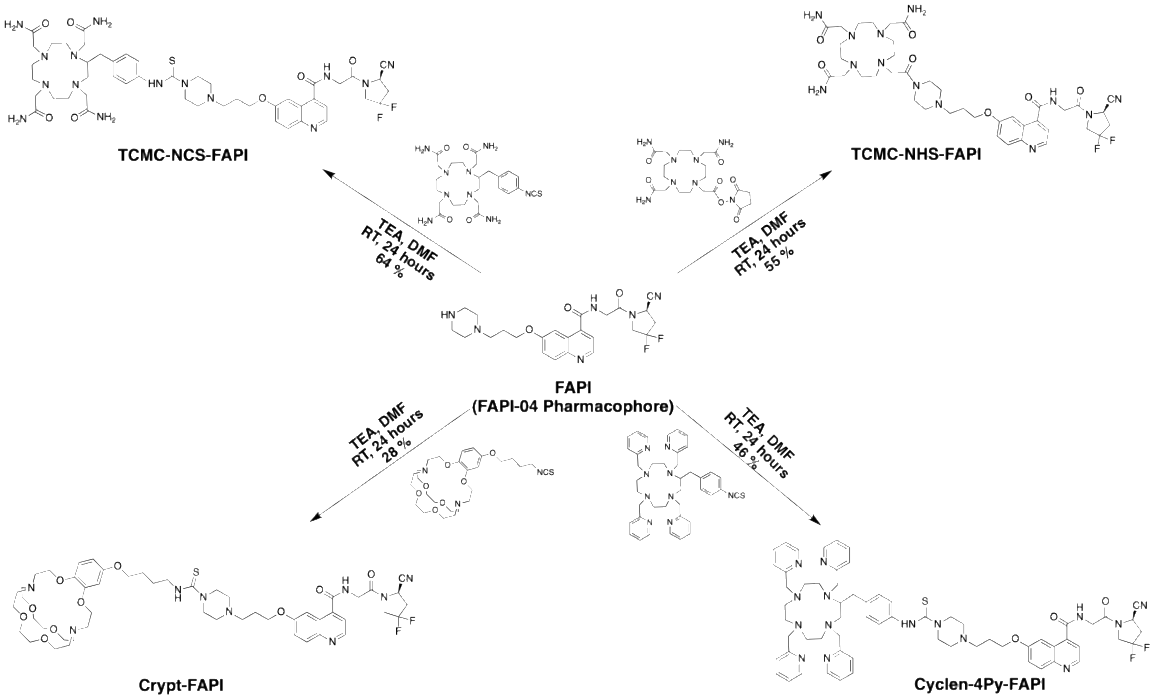

Scheme 4.2. Synthesis of FAPI-based bioconjugates TCMC-NCS-FAPI, TCMC-NHS-FAPI, Crypt-FAPI, and Cyclen-4Py-FAPI used in this study.

4.2.4. Radiolabeling

For concentration dependent radiolabeling studies, [^{203}Pb]$PbCl_2$ (200 kBq, 2 μL) in ~ 0.05 M HCl was added to 5 μL of 1 M NH_4OAc (pH 7), 38 μL of MQ H_2O, and 5 μL of a bioconjugate solution (10^{-3} to 10^{-6} M). With ^{212}Pb, [^{212}Pb]$Pb(OAc)_2$ (200 kBq, 5 μL) in 1 M NH_4OAc (pH 7) was added to 40 μL of MQ H_2O and 5 μL of a bioconjugate solution (10^{-3} – 10^{-6} M). For the negative controls, the bioconjugate solutions were replaced with MQ H_2O. The reactions were incubated at either room temperature or 80 °C and 2-5 μL aliquots were removed from each solution at 30 minutes and 60 minutes and spotted onto an iTLC-SA plate and developed with 50 mM EDTA (pH 5). Using this mobile system, any free/non-complexed radiolead is complexed by EDTA and this EDTA complex moves with the solvent front (R_f = 1) while activity complexed by the bioconjugates remains at the baseline (R_f = 0). Plates containing ^{203}Pb were measured immediately whereas for ^{212}Pb were measured after at least 5 hours to allow for the decay of free short-lived daughter products. All experiments were performed in triplicate.

4.2.5. $LogD_{7.4}$

To a microcentrifuge tube containing quantitively labeled ^{203}Pb radiolabeling solutions (~50 μL), prepared and quantified as described in the previous section, 550 μL of PBS and 600 μL of n-octanol was added and the mixture was vortexed for 3 minutes. The mixture was then centrifuged at 1000 rpm for 30 seconds to improve the separation between the organic and aqueous layer. Aliquots (200 μL) of each phase were collected, in triplicate, and measured using a Hidex AMG gamma counter (Hidex, Mainz, Germany). $LogD_{7.4}$ was defined as:

$$logD_{7.4} = log \frac{Activity_{organic\ phase}}{Activity_{aqueous\ phase}} \qquad \textbf{Equation 4.1}$$

4.2.6. Serum and Saline Stability Studies

To prepare [^{203}Pb]Pb^{2+} complexes for serum stability studies, 5 μL of the 10^{-3} M bioconjugate solution was added to 5 μL of 1 M NH_4OAc (pH 7), 35 μL of deionized water, and 3 μL of [^{203}Pb]$PbCl_2$ (1 MBq). For the negative control, water was added in place of the bioconjugate solution. The reactions were incubated at room temperature for 1 hour

and the RCY confirmed to be quantitative by iTLC prior to dilution with serum. After confirmation, 100 μL of human serum or 1 mL of saline was added, and the reaction was incubated at 37 °C over a course of 72 hours. Aliquots were removed at 0 h, 24 h, 48 h, and 72 h and the stability of the complex was evaluated using iTLC and radioHPLC using a Phenomenex Luna 5 μm C18 100 Å analytical (250 × 4.6mm) column. For HPLC analysis, a 20 μL aliquot was removed and 60 μL of acetonitrile was added to precipitate the serum proteins. The tubes were centrifuged at 14,000 rpm for 20 minutes. The supernatant was removed and diluted with 420 μL of water and the species present were analyzed using radioHPLC where the gradient used was 100% A to 100% B over 20 minutes at 1 mL/min where A = 0.1% TFA in water and B = 0.1% TFA in acetonitrile. For saline studies, the samples were directly injected. ^{203}Pb complexes were used for this study instead of ^{212}Pb to simplify the radioHPLC trace obtained.

4.2.7. Cell Culture

The B16F10 murine melanoma cell line used in the tumour model and *in vitro* assays for CycMSH studies was obtained commercially from ATTC (CRL-6475). The cells were cultured in Dulbecco's Modified Eagle Medium (DMEM) supplemented with 10% fetal bovine serum (FBS), penicillin (100 U/mL), and streptomycin (100 μg/mL) in a humidified incubator containing 5% CO_2 at 37 °C. The HEK293T:hFAP cells, generated as described in literature[336], used in the tumour model for FAPI studies, were cultured in DMEM GlutaMAX™ medium that was supplemented with 10% FBS, penicillin (100 U/mL), and streptomycin (100 μg/mL) in a humidified incubator containing 5% CO_2 at 37 °C. For both cell lines, cells were grown until approximately 90% confluence and washed with sterile 1X PBS (pH 7.4) followed by trypsinization. The cell concentration was counted using an Invitrogen Countess 3 FL automated cell counter (Invitrogen, Carlsbad, CA).

4.2.8. *In vitro* FAP Fluorescence Assay

The half maximal inhibitory concentration (IC_{50}) values of the bioconjugates for FAP were measured using an *in vitro* enzymatic assay based on literature methods.[338] The recombinant human FAP (0.22 ng/μL, 50 μL) was added to a 96-well plate. Afterwards, 100 μL of the tested nonradioactive Pb-complexed bioconjugates (0.1 μM to 1 pM in PBS) were added to each well (n = 3) and then incubated for 30 minutes at 37 °C.

After incubation, 50 μL of the Suc-Gly-Pro-AMC (2 mM in PBS) was added to each well and incubation continued at 37 °C. The fluorescent signals (Excitation wavelength = 380 nm, emission wavelength= 460 nm) were acquired at 30 minutes using a Varioskan LUX multimode reader (Thermo Scientific, Waltham, MA) with Thermo Scientific SkanIt Software. IC_{50} values were calculated using the non-linear fit model on GraphPad Prism 10.2.3 software.

4.2.9. Competitive Receptor Binding Assays – CycMSH Bioconjugates

The *in vitro* competitive binding assays were performed using B16F10 cells. 150,000 cells were suspended in 300 μL of reaction buffer (20 mM HEPES with 2 mg/mL BSA) and incubated at 37 °C for 1 hour. After incubation, non-radioactive Pb-labeled TCMC-NCS-CycMSH or TCMC-NHS-CycMSH bioconjugates, at concentrations from 0.5 pM to 5 μM, were added along with 50,000 cpm of ^{125}I-[Nle^4, D-Phe^7]-alpha-MSH (Revvity, Boston, MA). The binding of the radioiodine-labeled peptide was competed with by increasing concentrations of the complexed TCMC-NHS- or NCS- bioconjugates (n = 3). The tubes were incubated at 25 °C with gentle agitation at 40 rpm for 1 hour. After incubation, the cells were centrifuged at 1300 rpm for 6 minutes and then the supernatant was removed. The cells were then washed with ice-cold PBS and centrifuged again followed by removal of the wash. The cells were then lysed with 1 M NaOH for 5 minutes and then the ^{125}I radioactivity in each fraction was measured on a Hidex AMG gamma counter (Hidex, Mainz, Germany). The IC_{50} of each bioconjugate was calculated using a non-linear fit model on GraphPad Prism 10.2.3 software.

4.2.10. *Ex Vivo* Biodistribution and SPECT/CT Imaging Studies

For FAPI bioconjugate studies, male NOD.Cg-Rag1tm1Mom Il2rgtm1Wjl/SzJ (NRG) mice were used whereas for the CycMSH bioconjugate or free activity studies, male C57BL/6J mice were used. The experiments were conducted according to guidelines established by the Canadian Council on Animal Care and these studies were approved by the Animal Ethics Committee of the University of British Columbia. For tumour inoculation, the mice were briefly sedated via inhalation of 2.5% isoflurane in oxygen and then HEK293T:hFAP (10×10^6 cells) or B16F10 (5×10^6 cells) were inoculated subcutaneously behind the left shoulder. B16F10 tumours grew to 8-10 mm in diameter in

10 days whereas the HEK293T:hFAP tumours grew to 6-9 mm in diameter over 4-5 weeks and once these diameters were reached, the mice were used for SPECT/CT imaging and biodistribution studies.

Both ^{203}Pb and ^{212}Pb bioconjugate complexes, FAPI and CycMSH-based, were prepared by adding the [^{203}Pb]$PbCl_2$ or [^{212}Pb]$Pb(OAc)_2$ to a solution of 1 M NH_4OAc pH 7 with the respective bioconjugate. TCMC-N**X**S-CycMSH (X = H or C) radiolabeling reactions were prepared such that each subject, whether for imaging or biocondistribution studies, would be administered with 20 pmol of tracer. The FAPI bioconjugate reactions were prepared so that each subject, again either for imaging or biodistribution studies, would be administered with 100 pmol of tracer. For blocking studies with [^{203}Pb][Pb(TCMC-NHS-FAPI)]$^{2+}$, 50 nmol of tracer was administered. The choice of quantity of tracer administered was based on results in literature that suggest that these values do not oversaturate the target sites on the cell surface.[327,336,338] All reactions were carried out at 80 ^{o}C for 30 minutes and the reaction was monitored by iTLC.

If quantitative (>99% RCY) radiolabeling was not achieved, the reaction was diluted to 1 mL with saline and loaded onto a C18 SepPak (C18 SepPak Plus Light, Waters, Mississauga, ON) cartridge preconditioned with 5 mL of anhydrous ethanol followed by 5 mL of saline. On this cartridge, the tracer is retained during the load and wash (2 mL of saline) while free activity is removed. The tracer was eluted with a total of 1 mL of anhydrous ethanol, collected into 4, ~250 μL aliquots. iTLC was used to determine the radiochemical purity of each fraction and only the aliquots with >99% RCYs were combined and the ethanol was blown off using nitrogen. Once all of the ethanol was removed, 1X PBS Tween-20 (0.05%) with 50 mM sodium ascorbate was added for CycMSH-based bioconjugates and saline with 50 mM sodium ascorbate for FAPI-based bioconjugates so that each mouse would receive a 110-125 μL injection. If SepPak purification was not required, reactions were diluted using their respective solutions to obtain this same injection volume. The apparent molar activities achieved for each tracer in each study are listed in **Table C.3**. For ^{203}Pb imaging studies, injected activity ranged from 2.55 MBq up to 6.01 MBq. For biodistribution studies, on average 100 – 240 kBq of ^{203}Pb-labeled tracers and 60 – 280 kBq of ^{212}Pb-labeled tracers were administered. For the free ^{203}Pb imaging and biodistribution study, 8.98 MBq of ^{203}Pb in 1X PBS Tween-20 was used for imaging and 147-234 kBq for biodistribution.

The tracers were administered via the tail vein of the mice. After administration, the mice used for biodistribution studies were allowed to move freely in their cages with unlimited access to food and water. Mice used for imaging were kept under isoflurane for the duration of the study. At either the 1 hour (FAPI bioconjugates) or 2 hours (CycMSH bioconjugates or free ^{203}Pb) post injection, the mice were euthanized by CO_2 asphyxiation under isoflurane anesthesia. Blood was collected by a cardiac puncture and the organs were removed, cleaned from blood, and weighed before the activity was measured using a calibrated Packard Cobra II auto-gamma counter (Perkin Elmer, Waltham, MA). The two energy windows used for ^{203}Pb were 50 – 110 keV and 240 – 320 keV while for ^{212}Pb they were 55 – 110 keV and 200 – 270 keV. The full biodistribution results can be found in the supplementary information in **Tables C.4 – C.6**. To analyze images, AMIDE software (v. 1.0.5) was used. Standardized uptake values (SUV) were extracted from the regions of interest in the SPECT scans and were used to construct decay-corrected time-activity curves over the course of the scan. The SUV values obtained from the quantitative SPECT studies were consistent with the values obtained in the biodistribution studies.

4.2.11. Urine analysis

To determine urine metabolites, urine was collected directly from the bladder of mice post euthanasia and diluted 10-fold with MQ water before injection. The metabolites were analyzed using a linear gradient of 100% A to 100% B over 20 minutes at 1 mL/min, where A = 0.1% TFA in water and B = 0.1% TFA in acetonitrile, using a Phenomenex Luna 5 µm C18 100 Å analytical (250 × 4.6mm) column.

4.2.12. Statistical Analysis

The data was analyzed using GraphPad Prism (Version 10.2.3). Unpaired two-tailed t tests were performed for IC_{50} values and all organs in the biodistribution studies. A difference was considered statistically significant when the p value was less than 0.05.

4.3. Results and Discussion

4.3.1. Chelator and Bioconjugate Synthesis

DOTA (1,4,7,10-Tetraazacyclododecane-1,4,7,10-tetraacetic acid), is the most commonly used chelator in the design of BFC-RPs. DOTA is composed of a 12-membered macrocycle backbone (1,4,7,10-tetraazacyclododecane), commonly referred to as cyclen, and utilizes four carboxylic acid groups as electron donor arms to form coordination complexes. Carboxylic acids are typically categorized as hard Lewis bases and as per the hard-soft acid-base theory, which states that highly-charged, hard Lewis acids (metals) form the most stable complexes with highly-charged hard Lewis bases, DOTA is heavily employed for chelation of the lanthanides, actinides, and early transition metals. However, as an intermediate Lewis acid, Pb^{2+} is most stably complexed by intermediate Lewis bases which include amides, amines, pyridines, and many more functional groups containing nitrogen, oxygen, and sulphur as electron donors. TCMC, also commonly known as DOTAM, utilizes amides in place of carboxylic acids and is currently recognized as the gold standard for lead chelation as it forms thermodynamically stable and kinetically inert complexes with ^{203}Pb and ^{212}Pb. TCMC is readily commercially available in its bifunctional form with an isothiocyanate handle (TCMC-NCS) or *N*-hydroxysuccinimide ester (TCMC-NHS). As a result of these factors, in this study TCMC was used as a benchmark to compare the other bioconjugates to.

When designing a bifunctional chelator based on a non-bifunctional version, it is preferable to introduce minimal structural changes to maintain the same coordination number and environment about the metal centre. Bifunctional handles are often attached in one of three ways: 1) Via replacement of a donor arm, 2) off of the backbone for a macrocyclic chelator, or 3) off of a donor arm. By attaching the handle to the backbone, in most cases, the coordination environment is minimally affected and thus this route is ideal and was desired for this study. Cyclen-based macrocyclic chelators can be made bifunctional by synthesizing the chelator using commercially available (S)-2-(4-nitrobenzyl)-1,4,7,10-tetraazacyclododecane (Cyclen-NO_2) as the backbone, making this a synthetically attractive bifunctionalization route.

Cyclen-4Py, a cyclen-based macrocyclic chelator bearing four pyridine donor arms previously synthesized and studied with ^{203}Pb in our lab[339], was an ideal chelator to

integrate into a BFC-RP as its ^{203}Pb complex was shown to be kinetically inert and stable in human serum. To synthesize the bifunctional version of this chelator, which is described further in the supplementary information, the secondary amines of the cyclen-NO_2 backbone were directly alkylated using 2-(bromomethyl)pyridine under mildly basic conditions, as shown in **Scheme 4.3**, to yield (S)-2-(4-nitrobenzyl)-1,4,7,10-tetrakis(pyridin-2-ylmethyl)-1,4,7,10-tetraazacyclododecane (Cyclen-4Py-NO_2 (***1***), 97%). Cyclen-4Py-NO_2 was hydrogenated using palladium on carbon as a catalyst to produce (S)-4-((1,4,7,10-tetrakis(pyridin-2-ylmethyl)-1,4,7,10-tetraazacyclododecan-2-yl)methyl)aniline (Cyclen-4Py-NH_2, (***2***), 69%). The last step of the synthesis used thiophosgene to convert the primary amine to an isothiocyanate, (S)-2-(4-isothiocyanatobenzyl)-1,4,7,10-tetrakis(pyridin-2-ylmethyl)-1,4,7,10-tetraazacyclododecane (Cyclen-4Py-NCS, (***3***), 77%).

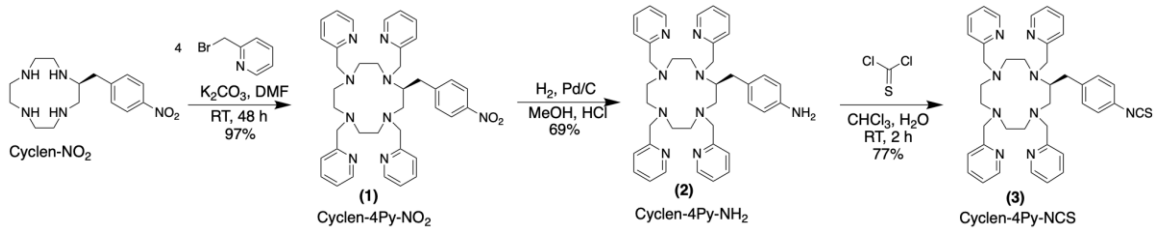

Scheme 4.3. Synthesis of Cyclen-4Py-NCS from Cyclen-4Py-NO_2.

With four pyridine groups, it was hypothesized that Cyclen-4Py-NCS bioconjugates would form more lipophilic radiolead complexes than those produced with TCMC-NCS. This increased hydrophobicity could slow the clearance of the FAPI bioconjugate, making it more ideal for therapeutic studies. Crypt-NCS, a bifunctional [2.2.2]-cryptand previously synthesized in our lab, showed high selectivity towards ^{203}Pb.[251] Unlike TCMC-NCS and Cyclen-4Py-NCS, which both employ a benzyl isothiocyanate handle, Crypt-NCS utilizes an isothiocyanate handle incorporating both an aromatic and alkyl component. It was hypothesized that the inclusion of both elements may further increase the hydrophobicity of the bioconjugate complexes, making Crypt-NCS an excellent addition to this comparative study. As shown in **Scheme 4.2**, the isothiocyanate chelators were incorporated into thiourea-based FAPI bioconjugates under basic conditions at room temperature over 24 hours. In contrast, TCMC-NHS is a bifunctional chelator that uses an N-hydroxysuccinimide ester group to form an amide bond in its bioconjugate rather than a thiourea bond. The decision to include this

bifunctional chelator in the study was made when initial results with the thiourea-based bioconjugates, as described in later sections, called the stability of the thiourea bond into question. The use of this chelator permitted a comparison of differences in both *in vitro* and *in vivo* stability, as well as *in vivo* biodistribution, arising from the bioconjugation method. Although these chelators are not perfectly comparable as they have slightly different coordination environments as a donor arm of TCMC-NHS also acts as a bifunctional handle, their similarity is sufficient for a proof-of-principle comparison.

After initial studies with FAPI bioconjugates suggested instability of the thiourea bond both *in vitro* and *in vivo*, as discussed in later sections, attention turned to a peptide model, specifically CycMSH bioconjugates, to observe if this phenomenon occurred in peptide-based BFC-RPs as well. These CycMSH bioconjugates were synthesized using TCMC-NCS and TCMC-NHS, the same chelators used for FAPI studies, allowing a simpler comparison to be made. It was decided to use TCMC as the base chelator for the CycMSH bioconjugates over the other chelators in this study because of the low expression levels of the melanocortin-1 receptor (MC1R), which CycMSH binds to, on melanoma cells. Some human melanoma cell lines express only about 400–1,600 MC1R receptors per cell[326] while the B16F10 murine melanoma cell line expresses roughly 3,000 receptors per cell[340]. This is significantly reduced expression than with other cancer cell lines such as LNCaP (Human prostate cancer), which have approximately 190,000 prostate specific membrane antigen (PSMA) receptors per cell.[341] With such low receptor density, it is necessary to inject only a small amount of tracer to avoid oversaturating the limited binding sites. At the same time, to achieve reliable tumor imaging, the tracer must have a high molar activity, where molar activity refers to the amount of activity per mole of tracer. Achieving high molar activity requires a chelator capable of high radiolabeling yields at low concentrations. Since TCMC is considered the gold standard for lead chelation, it was employed in CycMSH studies where maximizing molar activity was critical. As shown in **Scheme 4.1**, the chelators were added to a solution the CycMSH peptide in basic conditions to yield TCMC-NCS-CycMSH and TCMC-NHS-CycMSH.

4.3.2. Radiolabeling

To compare radiolabeling abilities between chelators, concentration dependent radiolabeling studies were performed at both room temperature and 80 °C. **Figure 4.4** shows the results of ^{203}Pb radiolabeling comparing the CycMSH (A) and FAPI

bioconjugates (B and C) at both room temperature or 80 °C at 30 minutes. Other temperatures, time points, and results of ^{212}Pb radiolabeling studies are given in the supplementary information (**Figures C.20 – C.25**).

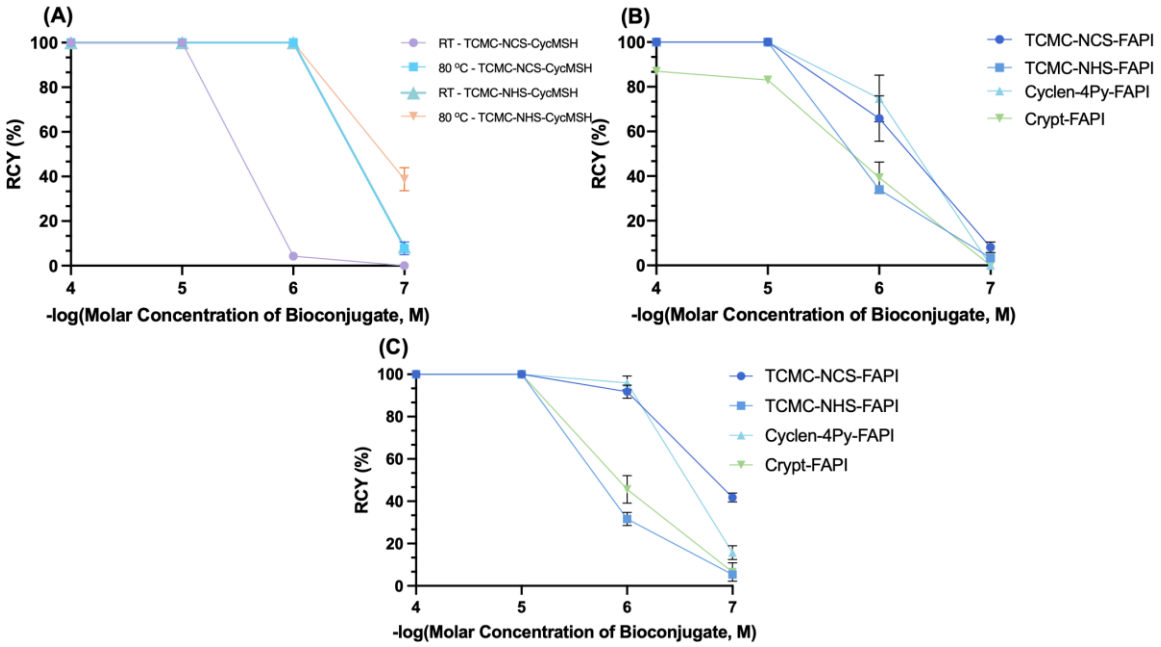

Figure 4.4. Radiochemical yields (RCY, %) for ^{203}Pb (200 kBq) radiolabeling reactions with (A) CycMSH bioconjugates at room temperature and 80 °C and FAPI bioconjugates at (B) room temperature and (C) 80 °C (n = 3 for each data point) at 30 minutes in 0.1 M NH_4OAc (pH 7).

Initially, it was hypothesized that TCMC-NCS bioconjugates would have superior radiolabeling capabilities compared to TCMC-NHS bioconjugates based on the reduced disruption to the Pb^{2+} coordination environment. Surprisingly, with CycMSH bioconjugates labeled with both ^{203}Pb and ^{212}Pb, TCMC-NHS-CycMSH outperformed its NCS counterpart at both temperatures tested. At 80 °C and a concentration of 10^{-7} M, TCMC-NHS-CycMSH achieved a ^{203}Pb RCY of 38.8 ± 5.2%, whereas TCMC-NCS-CycMSH only reached 7.8 ± 2.9% (n = 3). At room temperature, the difference was even more pronounced as at a concentration of 10^{-6} M, TCMC-NHS-CycMSH was able to be labeled quantitatively (>99%) compared to 8.5 ± 2.0% for TCMC-NCS-CycMSH (n = 3). It is hypothesized that the amide bond may still contribute to coordination, which may explain why the RCYs were not drastically diminished. However, the reverse trend was observed with the FAPI bioconjugates where TCMC-NCS-FAPI generally achieved higher RCYs at lower concentrations, with the exception of room temperature at 30 minutes. As a result,

the effect of the bifunctional handle on the coordination behaviour of TCMC must be evaluated on a case-by-case basis. A table of all the radiolabeling data generated in this study can be found in the supplementary information in **Tables C.1** and **C.2**.

Cyclen-4Py-FAPI, tested with both ^{203}Pb and ^{212}Pb, exhibited superior radiolabeling capabilities compared to TCMC-NHS at both temperatures. However, it was either inferior (at 80 ^{o}C) or on par with TCMC-NCS-FAPI (at room temperature), depending on the conditions. For Crypt-FAPI, quantitative complexation at 10^{-4} and 10^{-5} M could not be reached at room temperature and required heating to 80 °C. Under heated conditions (80 °C, 10^{-6} M) at 30 minutes, Crypt-FAPI reached a RCY of 45.7 ± 6.5%, whereas TCMC-NHS-FAPI reached 31.6 ± 3.1% (n = 3). After 60 minutes at 80 °C, TCMC-NHS-FAPI improved to 51.0 ± 3.5%, while Crypt-FAPI remained at 45.4 ± 6.3%. This suggests that the complexation kinetics of Crypt-FAPI are more rapid than that of TCMC-NHS-FAPI, but ultimately it does not surpass this chelator in terms in complexation yield. Crypt-FAPI was not evaluated with ^{212}Pb under these conditions because reproducible data could not be obtained due to high thorium contamination in the ^{212}Pb produced by the newly employed ^{228}Th/^{212}Pb generator. This newer generator contained two ^{232}Th targets (16 g total) compared to the previous system's single target (8 g), which had previously afforded reproducible radiolabeling with the Crypt chelator.[113]

4.3.3. *In Vitro* Binding Affinity Studies

To ensure that the inclusion of the bifunctional chelator did not disrupt the targeting ability of the biological targeting vectors, the binding affinities of the stable lead complexes of the bioconjugates were measured using a competitive receptor binding assay and enzyme inhibition assay for CycMSH and FAPI bioconjugates, respectively. As per **Table 4.1** and **Figure 4.5**, all bioconjugates tested showed IC_{50} values in the nanomolar range, as expected for these pharmacophores[327,336], and the response was dose-dependent. The IC_{50} values of [^{nat}Pb(TCMC-NCS-CycMSH)]$^{2+}$ and [^{nat}Pb(TCMC-NHS-CycMSH)]$^{2+}$ were not significantly different ($p = 0.0596$), suggesting with the peptide, a larger targeting vector, the chelator had no significant effect on binding. However, with the FAPI bioconjugates, where the targeting vector is a small molecule, the choice of bifunctional chelator had a greater impact on the targeting vectors inhibitive properties.

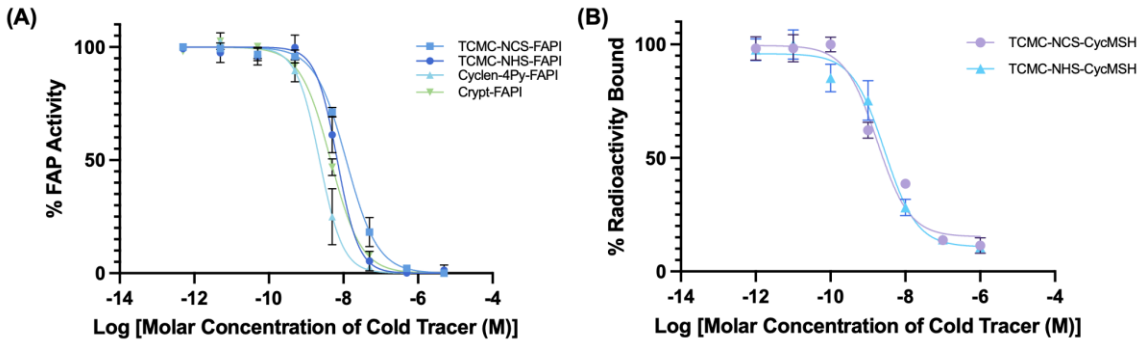

Figure 4.5. IC_{50} determination of (A) FAPI bioconjugates using an in vitro FAP enzymatic activity assay and (B) CycMSH bioconjugates using an in vitro competitive binding assay using natural lead-labeled tracers. All values were obtained in triplicate.

While all tested FAPI bioconjugates displayed nanomolar-range IC_{50} values, confirming strong target binding, significant differences were observed. Among the TCMC-based compounds, $[^{nat}Pb(TCMC\text{-}NCS\text{-}FAPI)]^{2+}$ was significantly less potent ($p = 0.0008$) with an IC_{50} of 11.9 ± 0.20 nM compared to its amide analogue ($IC_{50} = 6.81 \pm 0.96$ nM), suggesting that the bulky benzyl thiourea group may hinder FAP inhibition. However, $[^{nat}Pb(Cyclen\text{-}4Py\text{-}FAPI)]^{2+}$, which features an even more sterically hindered coordination environment with four additional pyridyl groups in addition to the benzyl thiourea, achieved the lowest IC_{50} value (2.29 ± 0.48 nM) of all bioconjugates tested. This suggested that the reduced inhibitory effect observed with $[^{nat}Pb(TCMC\text{-}NCS\text{-}FAPI)]^{2+}$ was likely not solely due to the benzyl thiourea moiety. $[^{nat}Pb(Crypt\text{-}FAPI)]^{2+}$ contained an alkyl thiourea handle and while this did not compromise potency ($IC_{50} = 4.53 \pm 0.49$ nM), it was still a less potent inhibitor than $[^{nat}Pb(Cyclen\text{-}4Py\text{-}FAPI)]^{2+}$. Overall, all bioconjugates synthesized showed sufficient inhibitory potency to proceed with further studies.

Table 4.1. Summary of *in vitro* study results for tested bioconjugates.

Bioconjugate	IC_{50} (nM)	$LogD_{7.4}$	*In vitro* human serum stability at 72 h (iTLC)	*In vitro* mouse serum stability at 72 h (iTLC)
TCMC-NCS-FAPI	11.9 ± 0.20	-2.42 ± 0.17	100%	100%
TCMC-NHS-FAPI	6.81 ± 0.96	-2.95 ± 0.10	100%	100%
Cyclen-4Py-FAPI	2.29 ± 0.48	-0.76 ± 0.03	100%	100%
Crypt-FAPI	4.53 ± 0.49	0.072 ± 0.011	$83.8 \pm 4.0\%$	$86.2 \pm 1.6\%$

TCMC-NCS-CycMSH	1.76 ± 0.59	-2.16 ± 0.11	100%	100%
TCMC-NHS-CycMSH	2.77 ± 0.32	-2.43 ± 0.26	100%	100%

For all data points, n = 3. For $logD_{7.4}$ and serum stability studies, ^{203}Pb-labeled bioconjugates were used whereas for IC_{50} studies, natural lead-labeled bioconjugates were used.

4.3.4. $LogD_{7.4}$

The lipophilicity of the ^{203}Pb complexes of the bioconjugates were estimated by measuring $logD_{7.4}$ values using the shake flask method with phosphate buffered saline (pH 7.4) and n-octanol (**Table 4.1**). In the case of the CycMSH bioconjugates, [^{203}Pb][Pb(TCMC-NCS-CycMSH)]$^{2+}$ ($logD_{7.4}$ = -2.16 ± 0.11) and [^{203}Pb][Pb(TCMC-NHS-CycMSH)]^{2} ($logD_{7.4}$ = -2.43 ± 0.26) were similarly hydrophilic, with no statistically significant difference observed between them (p = 0.2064). Although the incorporation of the benzyl moiety was expected to increase hydrophobicity, this was not observed for these bioconjugates, likely because the peptide scaffold exerts a stronger influence over the overall complex lipophilicity than the chelator modifications.

In contrast, the FAPI bioconjugates showed a clearer correlation between chelator structure and lipophilicity. Compared to [^{203}Pb][Pb(TCMC-NHS-FAPI)]$^{2+}$ ($logD_{7.4}$ = -2.95 ± 0.10), [^{203}Pb][Pb(TCMC-NCS-FAPI)]$^{2+}$ ($logD_{7.4}$ = -2.42 ± 0.17) was significantly more hydrophobic (p = 0.016), consistent with the aromatic group increasing lipophilicity. However, these were not the most lipophilic species tested. Both [^{203}Pb][Pb(Cyclen-4Py-FAPI)]$^{2+}$ ($logD_{7.4}$ = -0.76 ± 0.03) and [^{203}Pb][Pb(Crypt-FAPI)]$^{2+}$ ($logD_{7.4}$ = 0.072 ± 0.011) exhibited greater lipophilicity than either TCMC-based derivative. Despite having fewer aromatic groups, the Crypt-based complex was moderately lipophilic, suggesting that the propyl ether bifunctional handle likely strongly contributed to its increased hydrophobicity.

[^{68}Ga][Ga-FAPI-04], a clinically utilized imaging agent, has a reported $logD_{7.4}$ value of -1.02 ± 0.35.[336] This complex clears rapidly from circulation, providing high tumour-to-background contrast. Given that more hydrophilic complexes typically clear even faster, it was predicted, based on the results of the $logD_{7.4}$ values alone, that [^{203}Pb]Pb(TCMC-NHS-FAPI)]$^{2+}$ and [^{203}Pb]Pb(TCMC-NCS-FAPI)]$^{2+}$ would yield excellent image contrast results. However, their rapid clearance could limit tumour retention, reducing their therapeutic utility. In comparison, [^{203}Pb][Pb(Cyclen-4Py-FAPI)]$^{2+}$, with a $logD_{7.4}$ value not significantly different than that of [^{68}Ga][Ga-FAPI-04] (p = 0.3268), may behave more

similarly to the clinical agent. However, the pyridyl groups of the chelator may change the *in vivo* metabolic routing of the complex. The more lipophilic [^{203}Pb][Pb(Crypt-FAPI)]$^{2+}$ may clear more slowly and exhibit prolonged circulation and tumour retention. However, log$D_{7.4}$ values alone do not provide insight into a compound's *in vivo* stability or metabolic activity. These factors are more accurately assessed using *in vitro* serum stability assays in addition to biodistribution and imaging studies *in vivo*.

4.3.5. Serum Stability Studies – iTLC Measurement

Serum stability studies are performed to quantitatively evaluate how well radiometal-labeled bioconjugates retain their metal ions under physiological conditions. The radiometal complexes are incubated in serum where abundant proteins, such as transferrin and albumin, may compete with the chelator for the radiometal ion. This can result in transchelation and loss of the radiometal from the bioconjugate complex which can reduce imaging and/or therapeutic efficacy and deliver an off-target dose of radiation to healthy tissues. Serum stability assays measure the percentage of intact radiometal complex versus free radiometal at various time points. The extent of this release can be measured using instant thin layer chromatography (iTLC) where an aliquot is spotted onto chromatography paper and the intact bioconjugate is separated, often using a chelating mobile phase, from the free radiometal released into serum and the activity measured. The results of this assay are shown in **Table 4.1** where it can be observed that all bioconjugate complexes were resistant to transchelation over 72 hours as all complexes, with the exception of [^{203}Pb][Pb(Crypt-FAPI)]$^{2+}$ (83.8 $\pm$ 4.0% intact in human serum and 86.2 $\pm$ 1.6% in mouse serum), remained completely (>99%) intact and no free radiometal was lost in either mouse or human serum. As these results were promising, these bioconjugates were tested *in vivo* in tumour-bearing mice models.

4.3.6. *In Vivo* Biodistribution and Imaging Studies – Thiourea Group

Quantitative SPECT/CT scans were performed in male B16F10 tumour-bearing C57BL/6J mice over 2 hours for the CycMSH and free activity group and in male HEK293T:hFAP tumour-bearing NRG mice over 1 hour for the FAPI group using ^{203}Pb labeled bioconjugates. When the study first commenced, only thiourea FAPI

bioconjugates had been prepared due to the commercial availability of the Cyclen-NO_2 backbone allowing for a direct bifunctionalization of the Cyclen-4Py chelator.

When evaluated at one hour, $[^{203}Pb][Pb(Crypt\text{-}FAPI)]^{2+}$ showed significant uptake in the kidneys, liver, and bones, suggesting that the radiometal-chelate complex was not stable *in vivo*, releasing free ^{203}Pb (**Figure 4.6**). To provide a benchmark for comparison, a study with free, unchelated $[^{203}Pb]PbCl_2$ was performed over 2 hours (**Figure 4.6**). This study was performed in C57BL/6J mice rather than with NRG mice used for FAPI studies due to the reduced cost and increased availability of this mouse strain at the facility. The two-hour timeframe also allowed for imaging data to be obtained that could be directly compared if the CycMSH studies were to reveal potential instability.

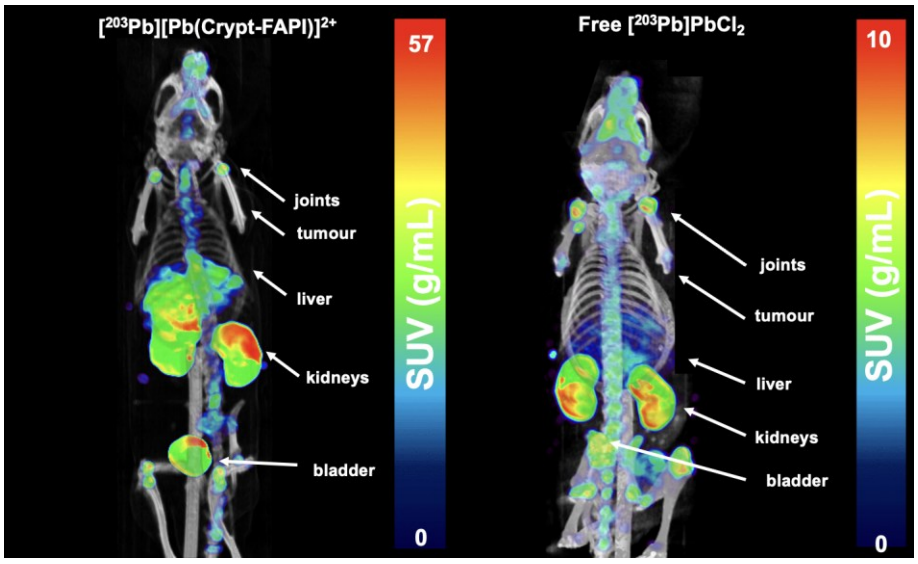

Figure 4.6. Coronal SPECT images of $[^{203}Pb][Pb(Crypt\text{-}FAPI)]^{2+}$ (left) at 50 minutes and free, unchelated ^{203}Pb at 47 minutes post injection (right) in HEK293T:hFAP (NRG) and B16F10 (C57BL/6J) tumour-bearing mice, respectively.

Like with $[^{203}Pb][Pb(Crypt\text{-}FAPI)]^{2+}$, in the free ^{203}Pb group, significant accumulation in the kidneys, liver, and bones was observed. The decay-corrected time-activity curves in **Figure 4.7** show similar trends in kidney, liver, and tumor uptake between the two subjects, but notable differences in bladder and bone uptake. Specifically, the $[^{203}Pb][Pb(Crypt\text{-}FAPI)]^{2+}$ group exhibited higher bladder uptake (SUV = 15.90 g/mL vs. 4.85 g/mL), while the free ^{203}Pb group showed greater bone uptake (SUV = 10.58 g/mL vs. 4.24 g/mL). These differences may be attributed to the different mouse strains used in the study as strain-specific variations in physiology and metabolism can influence how

free ^{203}Pb is distributed throughout the body, or possibly not all of the complex was unstable and there may be residual intact [^{203}Pb][Pb(Crypt-FAPI)]$^{2+}$ circulating *in vivo* at early time points. To test this, future investigations should include free ^{203}Pb studies in NRG mice to determine if the change in mouse strain is the cause of this difference.

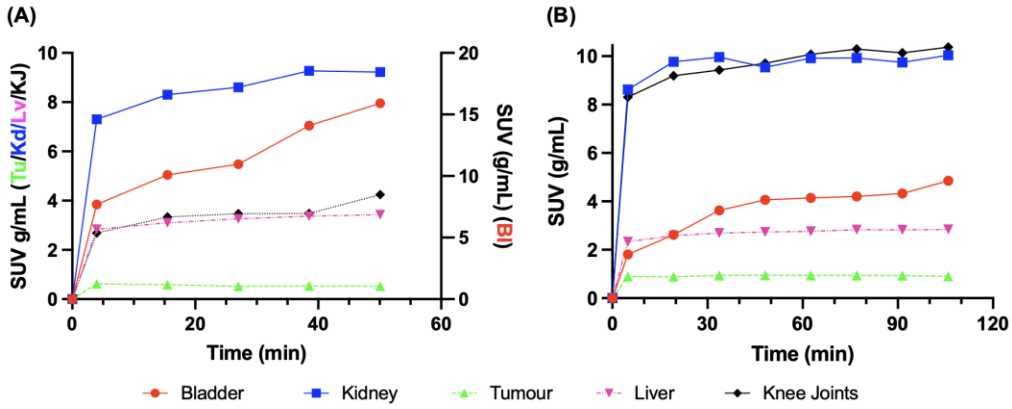

Figure 4.7. Representative standardized-uptake time-activity curves of (A) [^{203}Pb][Pb(Crypt-FAPI)]$^{2+}$ over 1 hour and (B) free, unchelated ^{203}Pb over 2 hours in HEK293T:hFAP (NRG) and B16F10 (C57BL/6J) tumour-bearing mice, respectively. (n = 1)

To further confirm that the [^{203}Pb][Pb(Crypt-FAPI)]$^{2+}$ was unstable *in vivo*, as shown in **Figure 4.8**, the urine of the imaging mouse was collected and analyzed via reverse phase, radioHPLC and compared to the trace of the [^{203}Pb][Pb(Crypt-FAPI)]$^{2+}$ prior to injection and free ^{203}Pb. The similarity in retention times between the urine metabolites and free ^{203}Pb indicate that this radiometal complex is unstable *in vivo* and thus further investigation with this chelator and theranostic pair should not continue.

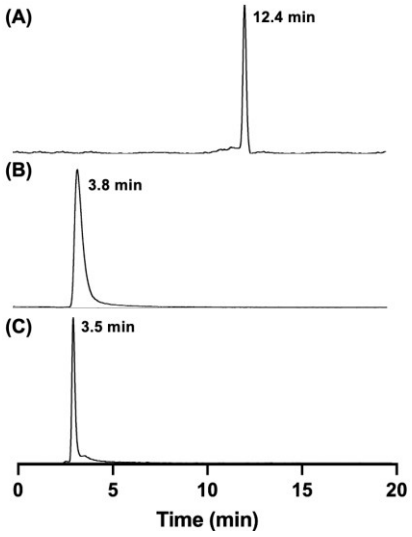

Figure 4.8. RadioHPLC traces of (A) [^{203}Pb][Pb(Crypt-FAPI)]$^{2+}$ prior to animal injection, (B) free, unchelated ^{203}Pb (negative control), and (C) the urine metabolites collected from the imaging mouse from the [^{203}Pb][Pb(Crypt-FAPI)]$^{2+}$ study 50 minutes post injection.

The HPLC method was A: H_2O with 0.1% TFA, B: Acetonitrile (CH_3CN/ACN) with 0.1% TFA; 0 – 100 % B over 20 minutes at 1 mL/min.

[^{203}Pb][Pb(TCMC-NCS-FAPI)]$^{2+}$, the most hydrophilic of the thiourea-based bioconjugates, was also evaluated over one hour. As shown in **Figure 4.9**, this tracer underwent rapid renal clearance and was almost entirely found in the urine. Initially, it was hypothesized that this tracer may be too hydrophilic, resulting in rapid clearance without any significant tumour uptake, as shown in the time-activity curve in **Figure 4.9B**.

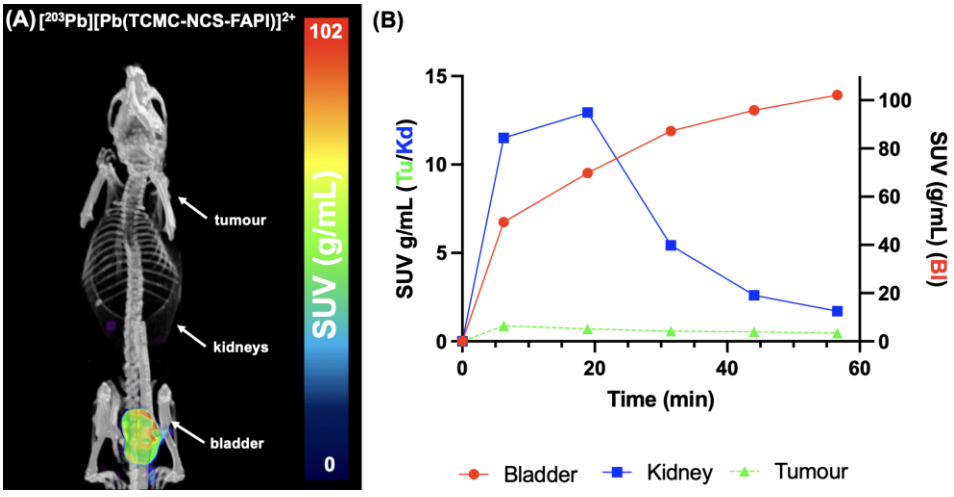

Figure 4.9. (A) Coronal SPECT/CT image and (B) standardized-uptake time-activity curve of [^{203}Pb][Pb(TCMC-NCS-FAPI)]$^{2+}$ at and over the course of 1 hour, respectively, in a HEK293T:hFAP (NRG) tumour-bearing mouse.

When tracers are injected into the tail vein of a mouse, they directly enter the bloodstream, allowing for rapid distribution throughout the body, bypassing potential absorption barriers and the first-pass effect of the liver that can occur with other administration methods.[342] Hydrophilic tracers generally remain in the blood plasma before filtration by the kidneys where they are excreted into the urine with minimal metabolic modification. If this was the case for $[^{203}Pb][Pb(TCMC\text{-}NCS\text{-}FAPI)]^{2+}$, one would expect the HPLC trace of the urine metabolites to show minimal metabolic activity. The radioHPLC trace of $[^{203}Pb][Pb(TCMC\text{-}NCS\text{-}FAPI)]^{2+}$ prior to injection, its urine metabolites, and a trace of a mixture of $[^{203}Pb][Pb(TCMC\text{-}NCS)]^{2+}$ and $[^{203}Pb][Pb(TCMC\text{-}NH_2)]^{2+}$ for comparison purposes are shown in **Figure 4.10**.

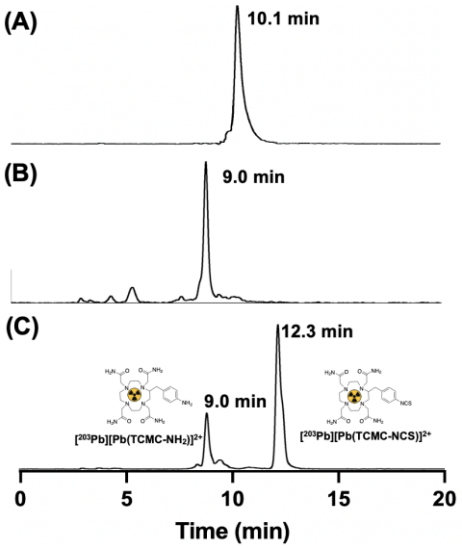

Figure 4.10. RadioHPLC traces of $[^{203}Pb][Pb(TCMC\text{-}NCS\text{-}FAPI)]^{2+}$ (A) prior to animal injection and its (B) urine metabolites collected at one hour post-injection compared to (C) a chromatogram of $[^{203}Pb][Pb(TCMC\text{-}NCS)]^{2+}$ and $[^{203}Pb][Pb(TCMC\text{-}NH_2)]^{2+}$.
The HPLC method used was 0 – 100% B over 20 minutes at 1 mL/min. A: H_2O (0.1% TFA), B: ACN (0.1% TFA).

Based on the urine metabolite radioHPLC trace, $[^{203}Pb][Pb(TCMC\text{-}NCS\text{-}FAPI)]^{2+}$ appeared to have completely degraded, as indicated by a shift in retention time from 10.1 minutes to 9.0 minutes, which is suggestive of the formation of a more polar species. The retention time of the metabolite also matched that of $[^{203}Pb][Pb(TCMC\text{-}NH_2)]^{2+}$, suggesting that the observed metabolite could either be $[^{203}Pb][Pb(TCMC\text{-}NH_2)]^{2+}$ itself or a similarly polar derivative. If the FAPI targeting vector was cleaved from the bifunctional chelator in the bloodstream, as indicated by the radioHPLC trace, there would be no targeted delivery

to the tumour, explaining the very low tumour uptake observed in this study. Although thiourea-containing compounds are often metabolized in the liver by flavin-containing monooxygenases and cytochrome P450s, previous reports also indicate instability in serum, suggesting serum components may also contribute to this degradation.[318,319,343,344]

With $[^{203}Pb][Pb(TCMC\text{-}NCS\text{-}FAPI)]^{2+}$ having completely degraded *in vivo*, it was of interest to observe if a similar phenomenon would occur with $[^{203}Pb][Pb(Cyclen\text{-}4Py\text{-}FAPI)]^{2+}$ as it also employs the thiourea bond. With a $logD_{7.4}$ of -0.76 ± 0.03, compared to -2.42 ± 0.17 of $[^{203}Pb][Pb(TCMC\text{-}NCS\text{-}FAPI)]^{2+}$, this complex is more hydrophobic and should exhibit a different pharmacokinetic profile. As shown in **Figure 4.11**, rapid liver uptake with very minimal tumour accumulation was observed.

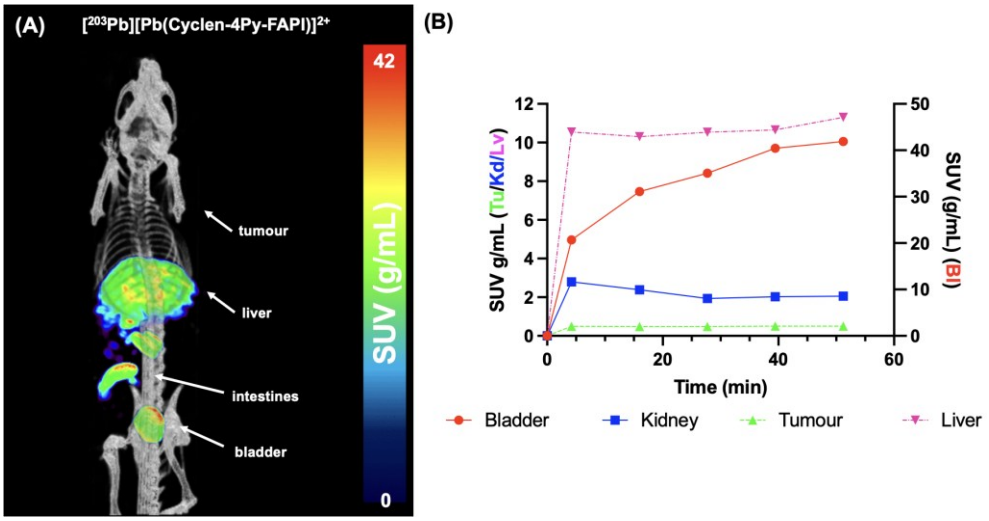

Figure 4.11. (A) Coronal SPECT/CT images and (B) standardized-uptake time-activity curves of $[^{203}Pb][Pb(Cyclen\text{-}4Py\text{-}FAPI)]^{2+}$ at and over the course of 1 hour, respectively, in a HEK293T:hFAP (NRG) tumour-bearing mouse.

Interestingly, the liver uptake remained relatively stable throughout the one-hour study whereas bladder uptake increased. This suggests that the complex may undergo both renal and hepatic clearance. Pyridine itself is largely metabolized in the liver via oxidative metabolism by cytochrome P450 enzymes to produce more polar metabolites that can then be excreted in the urine.[345] To determine whether the degradation observed in the urine metabolites of $[^{203}Pb][Pb(TCMC\text{-}NCS\text{-}FAPI)]^{2+}$ also occurred with $[^{203}Pb][Pb(Cyclen\text{-}4Py\text{-}FAPI)]^{2+}$, the urine was collected and analyzed via radioHPLC. The results are shown in **Figure 4.12** with comparison to $[^{203}Pb][Pb(Cyclen\text{-}4Py\text{-}NH_2)]^{2+}$.

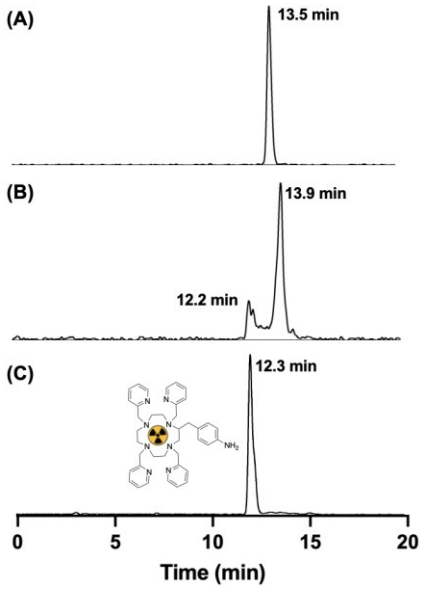

Figure 4.12. RadioHPLC traces of [^{203}Pb][Pb(Cyclen-4Py-FAPI)]$^{2+}$ (A) prior to animal injection and its (B) urine metabolites collected at one hour post-injection compared to (C) a chromatogram of [^{203}Pb][Pb(Cyclen-4Py-NH2)]$^{2+}$.
The HPLC method used was 0 – 100% B over 20 minutes at 1 mL/min. A: H2O (0.1% TFA), B: ACN (0.1% TFA).

The radioHPLC trace of the urine metabolites indicates that only a small portion of [^{203}Pb][Pb(Cyclen-4Py-FAPI)]$^{2+}$ underwent a degradation pathway similar to that of [^{203}Pb][Pb(TCMC-NCS-FAPI)]$^{2+}$ where the retention time of the urine metabolite (t_r = 12.2 min) matched the retention time of the amine-functionalized bifunctional chelate (t_r = 12.3 min). Notably, the main peak's retention time shifted from 13.5 minutes before injection to 13.9 minutes in the urine sample. If this peak is the intact complex, the shift may be due to the urine matrix or it may be a different metabolite. A potential cause for the reduced degradation is the substantial steric hindrance provided by the four bulky pyridyl groups as the chelator's donor arms. In the non-bifunctional form, a facial complex is formed where the Pb^{2+} is positioned above the macrocycle in a syn conformation, with all four pyridyl arms on the same side of the complex.[339] This configuration may shield the thiourea group from degradation enzymes, thereby minimizing cleavage. If so, the same steric protection could make the thiourea bioconjugation approach still suitable for attaching chelators to sterically hindered antibodies or sterically hindered chelators to targeting vectors. However this would have to be balanced with the potential for increased liver uptake with increased hydrophobicity as observed with [^{203}Pb][Pb(Cyclen-4Py-FAPI)]$^{2+}$.

The biodistribution studies were repeated with [^{212}Pb][Pb(TCMC-NCS-FAPI)]$^{2+}$ to observe if the low tumour accumulation occurs with the ^{212}Pb-labeled bioconjugate as well. The biodistribution (% IA/g) of select organs/tissues with the thiourea-based FAPI bioconjugates is shown in **Figure 4.13**. The biodistribution in all organs/tissues is given in the supplementary information in **Tables C.5** and **C.6**.

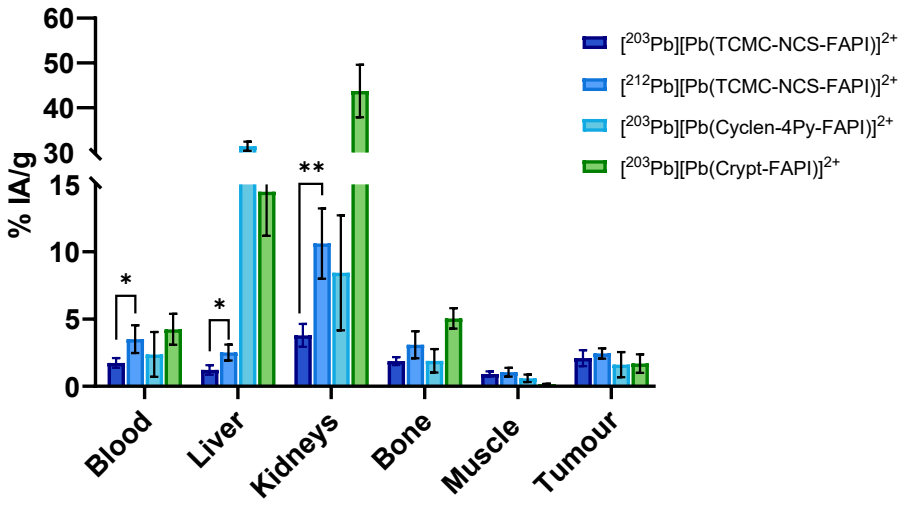

Figure 4.13. Biodistribution of the ^{203}Pb and ^{212}Pb-labeled thiourea-based FAPI bioconjugates at 1 hour-post injection in male, HEK293T:hFAP (NRG) tumour-bearing mice (n = 4) in select organs and tissues.
*Statistical significance was calculated using unpaired two-tailed t-test with the Holm–Sidak method. * $p < 0.05$, ** $p < 0.01$.*

Overall, the [^{212}Pb][Pb(TCMC-NCS-FAPI)]$^{2+}$ followed the same general trend as [^{203}Pb][Pb(TCMC-NCS-FAPI)]$^{2+}$ with the majority found in the urine at values of 312.52 ± 164.27% IA/g versus 231.10 ± 99.49% IA/g for the ^{203}Pb and ^{212}Pb labeled bioconjugates, respectively. The large standard deviation is likely due to differences in urination time between the mice used in this study. Some significant differences were observed between uptake in the ^{203}Pb and ^{212}Pb-labeled counterparts in the blood (1.74 ± 0.36 vs 3.51 ± 1.03% IA/g , $p = 0.035$), liver (1.21 ± 0.36 vs 2.51 ± 0.59% IA/g, $p = 0.013$) and kidneys (3.79 ± 0.85 vs 10.61 ± 2.61% IA/g, $p = 0.0098$). With the exception of the kidneys, all of the other differences between organs, although significant, were small showing that in general ^{203}Pb is able to predict the biodistribution of its ^{212}Pb-labeled counterpart. The difference in kidney uptake may be due to increased radiolysis that the tracer solution may have encountered between its final quality control and injection into the mouse as the time

between these two events was approximately one hour due to logistics of the facility. Future studies should shorten this time frame or add a higher concentration of radiolytic protectant to the formulation solution.

To observe if this degradation that limits tumour accumulation with the thiourea bioconjugation occurs with peptide-based BFC-RPs as well, [^{203}Pb][Pb(TCMC-NCS-CycMSH)]$^{2+}$ was evaluated in B16F10 tumour-bearing C57BL/6J mice over 2 hours, as shown in **Figure 4.14**.

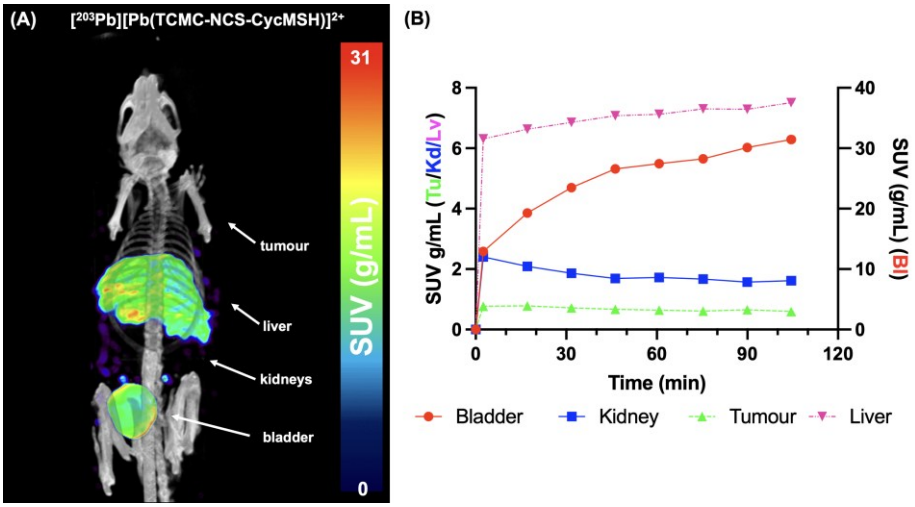

Figure 4.14. A) Coronal SPECT/CT images and (B) standardized-uptake time-activity curves of [^{203}Pb][Pb(TCMC-NCS-CycMSH)]$^{2+}$ at and over the course of 2 hours, respectively, in a C57BL/J6 B16F10 tumour-bearing mouse.

It can be observed that significant liver uptake occurs almost immediately while simultaneous renal clearance leads to accumulation in the bladder. This suggests that the complex undergoes both hepatic and renal clearance. Although the $logD_{7.4}$ of [^{203}Pb][Pb(TCMC-NCS-CycMSH)]$^{2+}$ (-2.16 $\pm$ 0.11) is not significantly different ($p = 0.102$) from that of [^{203}Pb][Pb(TCMC-NCS-FAPI)]$^{2+}$ (-2.42 $\pm$ 0.17), the larger, cyclic peptide may cause routing to the liver that the small-molecule was not subjected to. The high retention of the complex in the liver over 2 hours may be due to aggregation or the thiourea metabolism by flavin-containing monooxygenases and cytochrome P450s contained in the liver. Thioureas can be metabolized to sulfenic, sulfinic, or sulfonic acids that can alkylate other liver macromolecules, including other metabolism enzymes such as glutathione-S-transferase and cytochrome P450 1A1.[318,319] This alkylation contributes to

the pulmonary and hepatoxicity in other thiourea-containing drugs and may be the cause for retention observed in this study.[318,319] As with [^{203}Pb][Pb(TCMC-NCS-FAPI)]$^{2+}$, no substantial accumulation was observed in the tumour, suggesting again that the complex may degrade in the bloodstream before reaching it. Urine was collected and analyzed via radioHPLC, as shown in **Figure 4.15**.

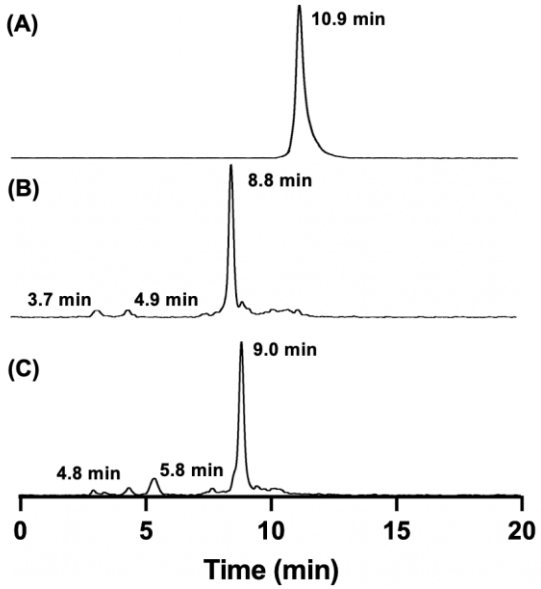

Figure 4.15. RadioHPLC traces of [^{203}Pb][Pb(TCMC-NCS-CycMSH)]$^{2+}$ (A) prior to animal injection and its (B) urine metabolites collected at two hours post-injection compared to (C) the urine [^{203}Pb][Pb(TCMC-NCS-FAPI)]$^{2+}$.
The HPLC method used was 0 – 100% B over 20 minutes at 1 mL/min. A: H2O (0.1% TFA), B: ACN (0.1% TFA).

Like with [^{203}Pb][Pb(TCMC-NCS-FAPI)]$^{2+}$, it was observed that [^{203}Pb][Pb(TCMC-NCS-CycMSH)]$^{2+}$ undergoes the same complete degradation to produce a urine metabolite with the same retention time of its amine-functionalized bifunctional chelate, demonstrating that this phenomenon can occur with both a small molecule and peptide-based BFC-RPs. With the thiourea bond suspected to be the cause of the instability, the amide versions of the bioconjugates, TCMC-NHS-CycMSH and TCMC-NHS-FAPI, were synthesized and tested *in vivo* with both ^{203}Pb and ^{212}Pb.

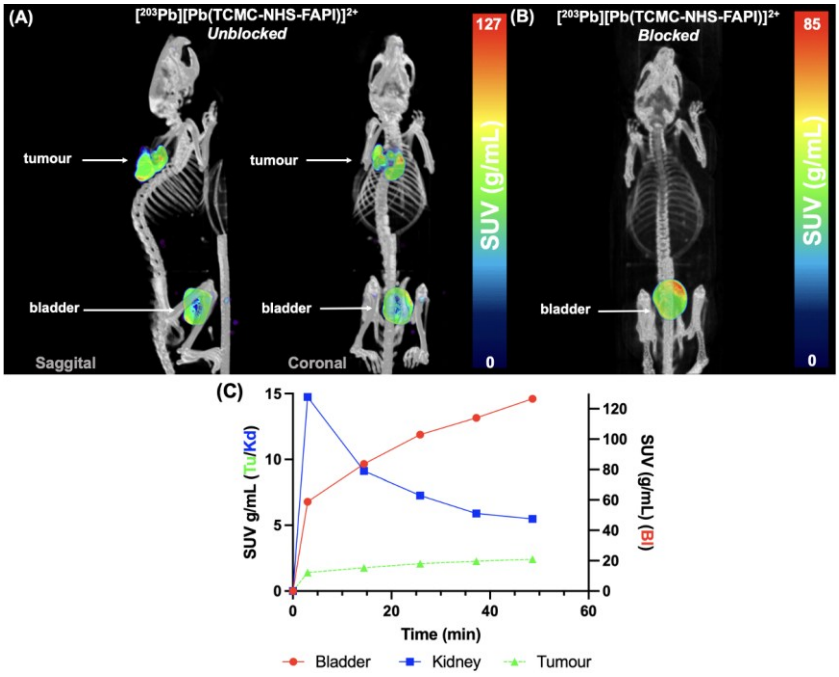

Figure 4.16. (A) Coronal and saggital SPECT/CT images of unblocked and (B) blocked uptake of [^{203}Pb][Pb(TCMC-NHS-FAPI)]$^{2+}$ at one hour post-injection with a (C) standardized-uptake time-activity curves of unblocked [^{203}Pb][Pb(TCMC-NHS-FAPI)]$^{2+}$ over the course of 1 hour, respectively, in a HEK293T:hFAP (NRG) tumour-bearing mouse.

As demonstrated in **Figure 4.16**, with the substitution of the thiourea bond with an amide bond, there was significant accumulation of the tracer in the tumour with a high tumour-to-background contrast, likely due to a $logD_{7.4}$ of -2.95 ± 0.10 that resulted in rapid clearance from the blood. The tracer underwent renal clearance, indicated by an average bladder uptake of 291.34 ± 114.41 % IA/g (n = 4). The decrease in tumour uptake from 8.62 ± 1.32% IA/g to 1.22 ± 0.22 % IA/g (n = 4) in the non-blocking to the blocking study, which employed 100 pmol and 50 nmol of radiolabeled tracer, respectively, confirms that the tumour uptake of this tracer is FAP mediated. The non-blocking study was repeated with ^{212}Pb and the biodistribution of select organs and tissues, in comparison to the unblocked and blocked ^{203}Pb study, are shown in **Figure 4.17**. A complete list of all measured organs and tissues for these tracers is given in the supplementary information in **Table C.5**.

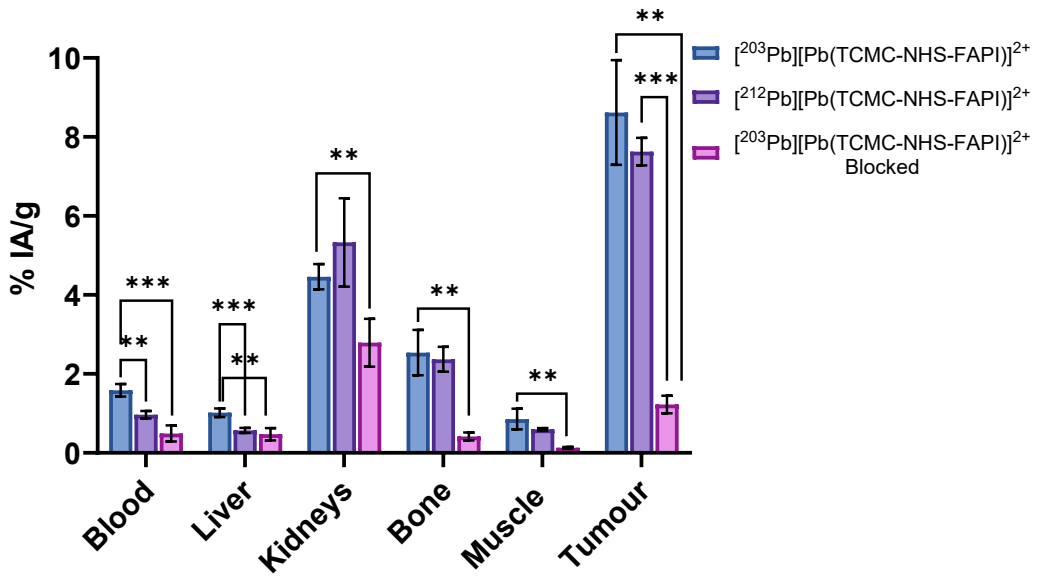

Figure 4.17. Biodistribution of the ^{203}Pb and ^{212}Pb-labeled amide-based FAPI bioconjugates at 1 hour-post injection in male, HEK293T:hFAP (NRG) tumour-bearing mice (n = 4) in select organs and tissues.
*Statistical significance was calculated using unpaired two-tailed t-test with the Holm–Sidak method. * p < 0.05, ** p < 0.01, *** p < 0.001.*

For the majority of organs and tissues, the biodistribution of [^{203}Pb][Pb(TCMC-NHS-FAPI)]$^{2+}$ did not significantly differ from that of [^{212}Pb][Pb(TCMC-NHS-FAPI)]$^{2+}$ with the exception of blood (1.59 ± 0.16 versus 0.97 ± 0.10% IA/g, p = 0.0012) and the liver (1.02 ± 0.11 versus 0.47 ± 0.16% IA/g, p = 0.00097). However, the uptake in these organs/tissues are low and thus differences are not of concern and thus ^{203}Pb can accurately predict the biodistribution of its ^{212}Pb counterpart. To test if the amide bond offered superior stability *in vivo*, the urine was collected and the metabolites were analyzed via radioHPLC, as shown in **Figure 4.18** below.

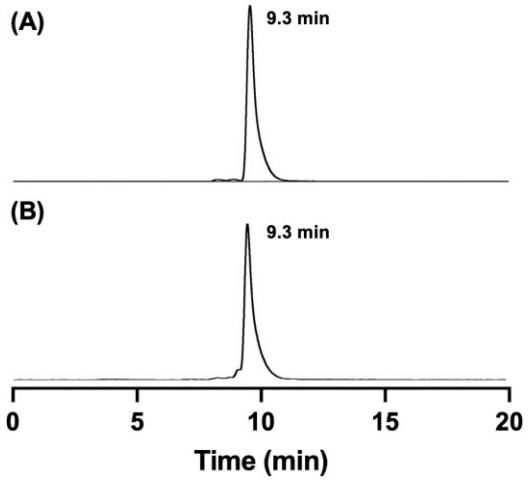

Figure 4.18. RadioHPLC traces of [^{203}Pb][Pb(TCMC-NHS-FAPI)]$^{2+}$ (A) prior to injection and its (B) urine metabolites collected at one hour post-injection.
The HPLC method used was 0 – 100% B over 20 minutes at 1 mL/min. A: H2O (0.1% TFA), B: ACN (0.1% TFA).

The identical retention times of the urine metabolite and the tracer prior to injection show that the tracer remained intact *in vivo*, suggesting that the amide bond effectively shields the tracer from the same degradation pathway observed with the thiourea bond. It is unlikely that this effect is merely due to an increase in the hydrophilicity of this tracer over its thiourea counterpart as previous studies with [^{68}Ga]Ga-FAPI-04, which employs the DOTA chelator with the same pharmacophore and amide bond as the bioconjugates in this study, found this tracer to have a $logD_{7.4}$ of -1.02 ± 0.35 and it still exhibits a high tumour-to-background ratio with minimal liver uptake.[336] To observe if the amide bond improves tumour uptake and *in vivo* stability in a peptide model, imaging (**Figure 4.19**) and biodistribution studies (**Figure 4.21**) were conducted with [^{203}Pb][Pb(TCMC-NHS-CycMSH)]$^{2+}$ and [^{212}Pb][Pb(TCMC-NHS-CycMSH)]$^{2+}$ (biodistribution only) in comparison to their thiourea counterparts.

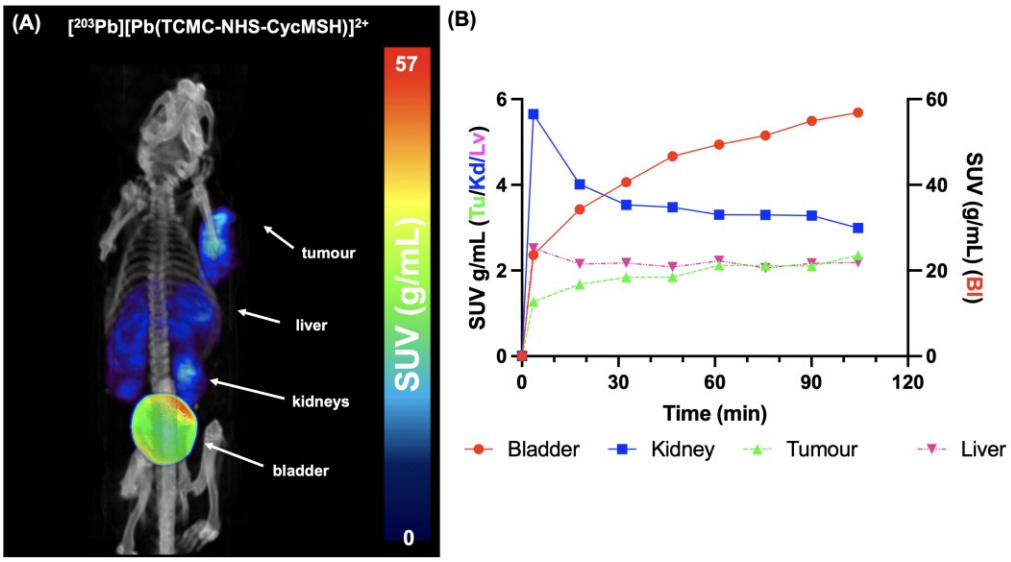

Figure 4.19. (A) Coronal SPECT/CT images and (B) standardized-uptake time-activity curves of $[^{203}Pb][Pb(TCMC\text{-}NHS\text{-}CycMSH)]^{2+}$ at and over the course of 2 hours, respectively, in a C57BL/J6 B16F10 tumour-bearing mouse.

By replacing the thiourea bond with an amide bond in this peptide model, the tumor uptake (SUV_{mean} value) at 2 hours increased substantially from 0.60 to 2.35 g/mL, respectively, representing a 3.9-fold improvement. This enhanced tumor accumulation appears to stem, at least in part, from a 3.7-fold reduction in liver uptake as the SUV_{mean} decreased from 7.51 to 2.02 g/mL, which allows more tracer to localize in the tumor. Although the amide tracer still shows some liver accumulation, potentially due to aggregation, its $logD_{7.4}$ value (-2.43 ± 0.26) does not differ significantly ($p = 0.2064$) from that of the thiourea analogue (-2.16 ± 0.11), indicating that increased hydrophilicity is not the main cause of the improved biodistribution. Instead, the amide bond appears to provide greater overall stability *in vivo* in both of these peptide and small molecule models. This conclusion is further supported by the urine metabolite radioHPLC analysis shown in **Figure 4.20**.

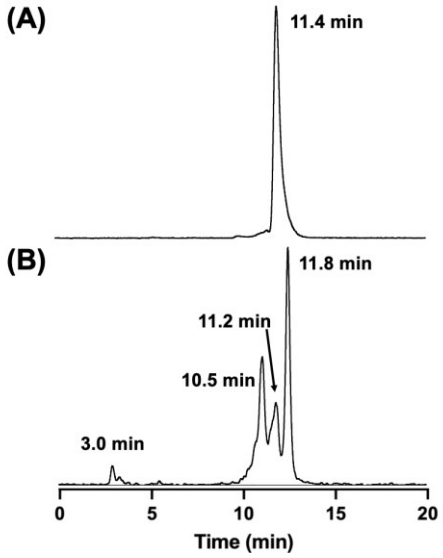

Figure 4.20. RadioHPLC traces of [^{203}Pb][Pb(TCMC-NHS-CycMSH)]$^{2+}$ (A) prior to animal injection and its (B) urine metabolites collected at two hours post-injection. *The HPLC method used was 0 – 100% B over 20 minutes at 1 mL/min. A: H_2O (0.1% TFA), B: ACN (0.1% TFA).*

The radioHPLC analysis of urine metabolites showed partial tracer degradation, which is not unexpected given the known *in vivo* instability of melanocyte stimulating hormone (MSH) peptides.[346,347] The peaks at 11.2 and 10.5 minutes may reflect proteolytic fragments. While native MSH is prone to rapid breakdown, the unnatural amino acid substitutions, truncation, and cyclization used in the peptide employed in this study increase its stability. Still, these modifications do not fully prevent degradation as a study by *Zhang et al.* using this same peptide, with the difference of using DOTA instead of TCMC and ^{68}Ga instead of ^{203}Pb/^{212}Pb, only 34.0 ± 10.4% of the tracer remained intact in urine after 1 hour and thus these additional peaks are not unexpected.[346] It is hypothesized that the 11.8-minute peak corresponds to intact tracer, whereas the 3.0-minute peak likely represents free radioactivity, although the urine matrix may have shifted retention times.

Importantly, this radioHPLC trace contrasts sharply with the thiourea-based analogue, which underwent complete degradation to a single peak, which we hypothesize is likely the unconjugated chelator radiometal complex due to the instability of the thiourea bond *in vivo*. To further investigate, biodistribution studies were repeated for both bioconjugates using ^{212}Pb. This allowed for assessment of both the suitability of ^{203}Pb as a diagnostic match for ^{212}Pb and for confirmation that these findings could be reproduced with another isotope. Select results are shown in **Figure 4.21** and a detailed table of the biodistribution (% IA/g) of all measured organs and tissues are given in the supplementary

information in **Table C.4**. For clarity, statistical significance is shown only for comparisons between the thiourea and amide groups of the same isotope.

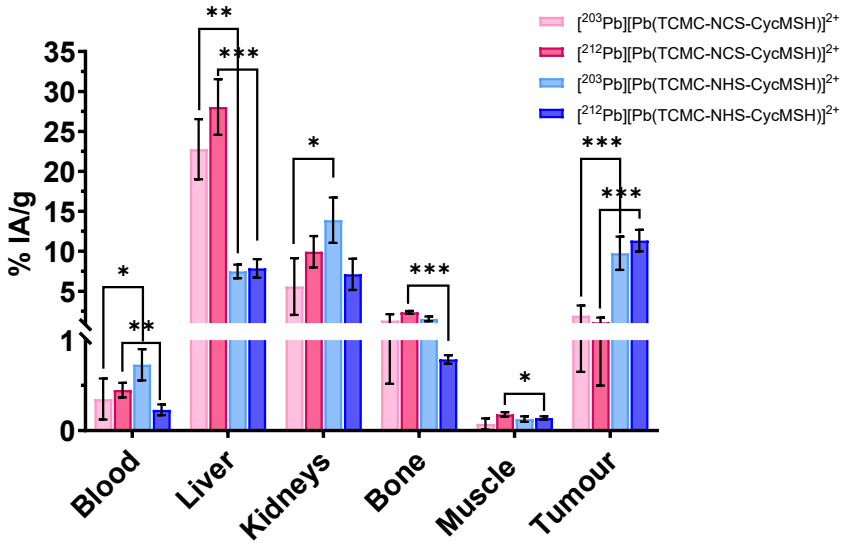

Figure 4.21. Biodistribution of the ^{203}Pb and ^{212}Pb-labeled CycMSH bioconjugates at 2 hours-post injection in male, B16F10 tumour-bearing C57BLJ/6 mice (n = 4) in select organs and tissues.
*Statistical significance was calculated using unpaired two-tailed t-test with the Holm–Sidak method. * p < 0.05, ** p < 0.01, *** p < 0.001.*

Overall, similar trends were observed within the thiourea and amide groups with both ^{203}Pb and ^{212}Pb and the *ex vivo* biodistribution results were in agreement with the SPECT/CT studies. With both isotopes, TCMC-NHS-CycMSH complexes showed lower liver uptake ($p = 0.0029$ for ^{203}Pb and $p = 0.0006$ for ^{212}Pb) and higher tumour uptake ($p = 0.0014$ for ^{203}Pb and $p = 0.00012$ for ^{212}Pb) than the TCMC-NCS-CycMSH complexes. Some differences were observed between the tracers in kidney uptake as [^{203}Pb][Pb(TCMC-NHS-CycMSH)]$^{2+}$ showed higher kidney uptake than [^{203}Pb][Pb(TCMC-NCS-CycMSH)]$^{2+}$ ($p = 0.012$) while [^{212}Pb][Pb(TCMC-NCS-CycMSH)]$^{2+}$ showed higher bone ($p = 0.0002$) and muscle ($p = 0.049$) uptake than [^{212}Pb][Pb(TCMC-NHS-CycMSH)]$^{2+}$.

Within the thiourea and amide groups themselves, comparisons could also be made between the uptakes of the ^{203}Pb and ^{212}Pb labeled bioconjugates to evaluate how well ^{203}Pb can predict the biodistribution of its ^{212}Pb counterpart in this peptide model. Within the thiourea group, the only significant difference between the ^{203}Pb and ^{212}Pb groups was in muscle uptake ($p = 0.036$) and even then, both uptake values were very

low at 0.07 ± 0.06 and 0.18 ± 0.03 % IA/g, respectively, and thus these differences would be unlikely to have a significant impact. However, TCMC-NHS-CycMSH displayed more isotope-dependent differences with statistically significant differences in the blood ($p = 0.0068$), kidneys ($p = 0.0097$), and bone ($p = 0.012$). Although the blood uptake remained under 1% IA/g for both isotopes and therefore may not be highly consequential, the ^{203}Pb-labeled version had roughly twice the uptake in both the kidneys (13.89 ± 2.84% IA/g) and bone (1.54 ± 0.30% IA/g) compared with its ^{212}Pb-labeled counterpart (7.11 ± 1.96% IA/g for kidneys and 0.79 ± 0.05 % IA/g for bone). These isotope-dependent differences may be due to radiolysis as the powerful emissions of ^{212}Pb and its daughters may produce radiolytic products that can be excreted through the kidneys at different rates than the metabolites of the intact tracer. Nevertheless, this study suggests that amide-based bioconjugation methods are more favourable for ^{203}Pb/^{212}Pb BFC-RPs, based on the results with these peptide and small molecule models.

4.3.7. Serum Stability Studies – radioHPLC Measurement

Prior to conducting *in vivo* studies, the serum stability of each bioconjugate was assessed using radio-instant thin-layer chromatography (iTLC). This method quantifies the extent of the release of the radiometal from its chelator in the presence of serum proteins. This is accomplished by utilizing chromatography paper and a chelating mobile solution to separate unchelated and chelated activity, which are then further quantified using a TLC scanner that determines the amount of activity in the given area on the chromatography paper.[305] However, one limitation of this technique, as observed herein, is that this study only reveals whether the radiometal-chelate complex remains intact. If the radiometal remains bound to its chelate, the analysis may indicate that the bioconjugate complex is stable, even if the rest of the bioconjugate undergoes degradation in the serum.

To determine the stability of a bioconjugate complex in serum, radioHPLC is a superior technique as it can use reverse-phase chromatography, or size exclusion chromatography depending on the application, to separate and identify different radiolabeled species that may be produced after incubation in serum over time. Reverse phase radioHPLC, employed in this study, separates compounds based on differences in hydrophobicity. As we saw in the urine metabolites, the thiourea compounds mainly

produce a singular metabolite with a retention time around 8.8 – 9.0 minutes. With the retention time of free ^{203}Pb being approximately 3.5 minutes, it is evident that the ^{203}Pb is still chelated in this metabolite, explaining why it appeared that the bioconjugates were stable in serum *in vitro* via iTLC prior to the studies *in vivo*. To determine if the degradation observed *in vivo* was at least to some extent caused by serum proteins, the radiolabeled bioconjugates were incubated in serum, both human and mouse, over 72 hours and then analyzed via radioHPLC. To ensure that any observed degradation was not due merely to radiolysis, the complexes were also incubated in saline. Only ^{203}Pb was used to allow for simpler interpretation of the radioHPLC chromatograms and the longer half-life allowed (51.9 hours versus 10.6 hours for ^{212}Pb) for a longer study period. **Table 4.2** and **Table 4.3** show the radioHPLC traces of the tested FAPI and CycMSH bioconjugates, respectively, over the course of 72 hours after incubation in serum and saline.

Table 4.2. Serum (mouse and human) and saline stability of tested ^{203}Pb-labeled FAPI bioconjugate complexes as measured via radioHPLC.

Bioconjugate	Time	Saline	Mouse Serum	Human Serum
TCMC-NCS-FAPI	0 h	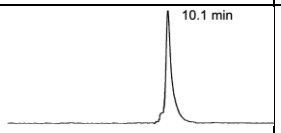	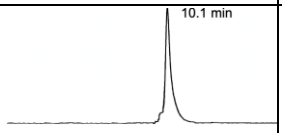	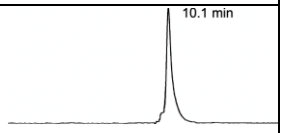
	24 h	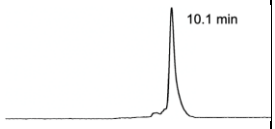	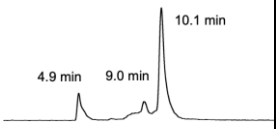	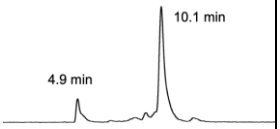
	48 h	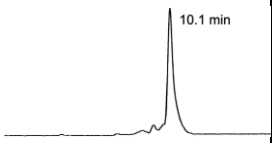	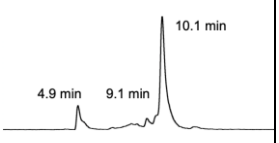	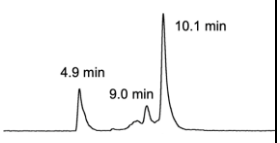
	72 h	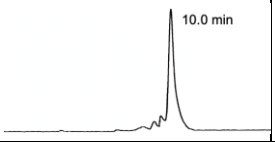	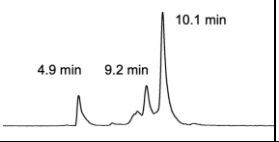	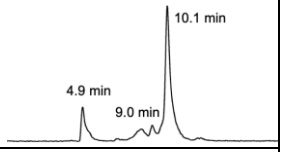
TCMC-NHS-FAPI	0 h	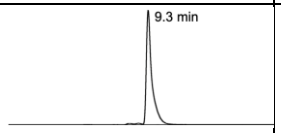	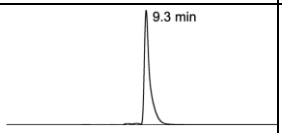	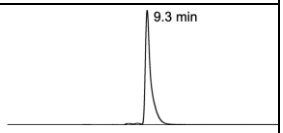
	24 h	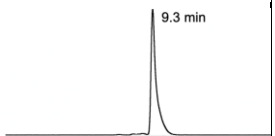	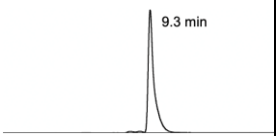	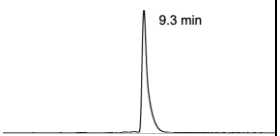
	48 h	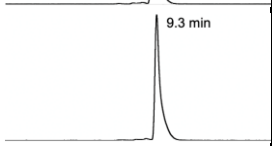	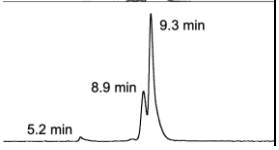	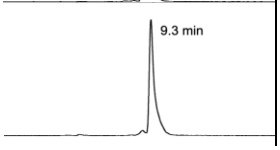

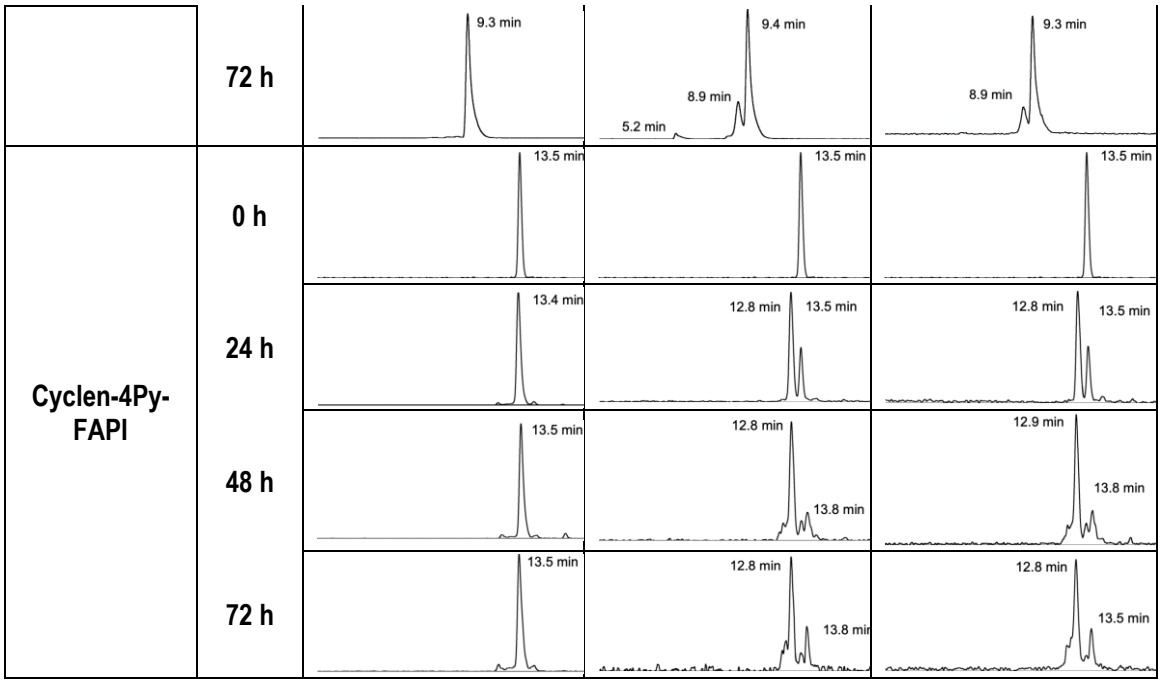

The HPLC method used was 0 – 100% B over 20 minutes at 1 mL/min. A: H2O (0.1% TFA), B: ACN (0.1% TFA).

As expected due to its exceptional stability *in vivo*, $[^{203}Pb][Pb(TCMC\text{-}NHS\text{-}FAPI)]^{2+}$ remained nearly completely intact over 72 hours with only a small peak at 8.9 minutes growing in starting at 48 hours in serum. No significant radiolysis was observed for any of the FAPI-based bioconjugates, suggesting that the degradation observed in serum was not due to radiolysis. With $[^{203}Pb][Pb(TCMC\text{-}NCS\text{-}FAPI)]^{2+}$, two additional peaks developed over time at approximately 4.9 and 9.0 minutes. The 9.0 minute peak matches the retention time of the metabolite found in the urine of mice injected with this tracer, suggesting that the serum could be responsible for the degradation observed *in vivo*. The identity of the peak at 4.9 minutes is unknown but as the retention time is greater than 3.5 minutes, the retention time of unchelated ^{203}Pb, the radiolead is still chelated. *In vivo*, after one hour the entire tracer was degraded to a single species. In this serum study, the majority of the tracer was still intact. For this study, an equal volume of serum was added to the reaction buffer to initiate the study. To make the reaction conditions more similar to *in vivo*, future studies should repeat this experiment with a greater serum to buffer ratio to observe if more of these products are produced.

With $[^{203}Pb][Pb(Cyclen\text{-}4Py\text{-}FAPI)]^{2+}$, by 24 hours in both human and mouse serum, a second peak at 12.8 minutes was present. Initially, the retention time of the tracer was 13.5 minutes but individual variance of the run, and potentially a matrix effect, may

have resulted in the shift observed at 48 hours to 13.8 minutes. In the urine metabolites (**Figure 4.12**), the main product had a retention time of 13.8 minutes while there was a minor peak at 12.2 minutes that matched the retention time of $[^{203}Pb][Pb(Cyclen\text{-}4Py\text{-}NH_2)]^{2+}$. This suggested that the majority of the complex may have remained intact due to the steric hindrance of the four pyridyl groups, which contradicts the result obtained from this serum stability study experiment. However, *in vivo* and *in vitro* conditions vary drastically, and the *in vitro* assay does not account for the significant liver uptake of this tracer (31.42 ± 1.02% IA/g) observed in **Figures 4.11** and **4.13** that may have subjected it to less serum degradation compared to the *in vitro* study.

Table 4.3. Serum (mouse and human) and saline stability of tested ^{203}Pb-labeled CycMSH bioconjugate complexes as measured via radioHPLC.

Bioconjugate	Time	Saline	Mouse Serum	Human Serum
TCMC-NCS-CycMSH	0 h	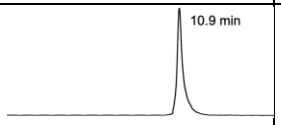	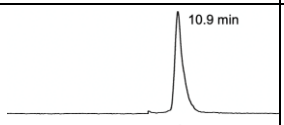	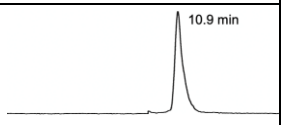
	24 h	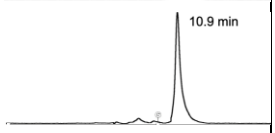	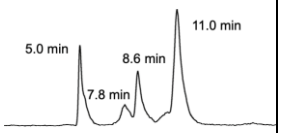	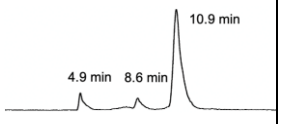
	48 h	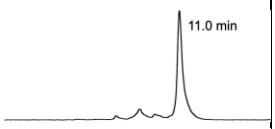	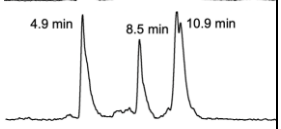	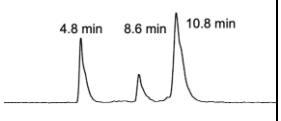
	72 h	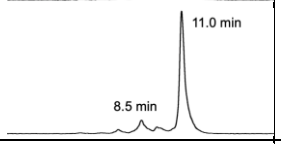	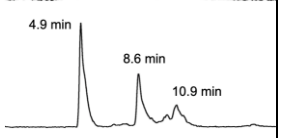	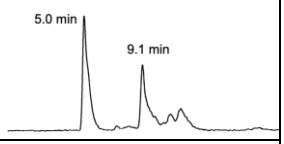
TCMC-NHS-CycMSH	0 h	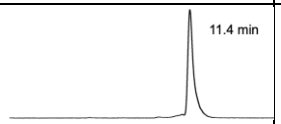	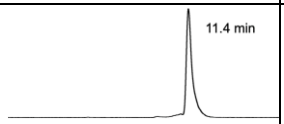	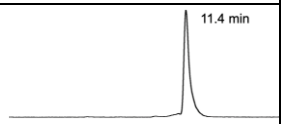
	24 h	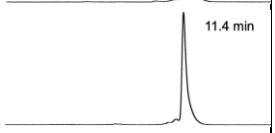	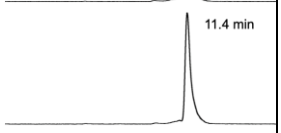	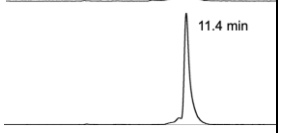
	48 h	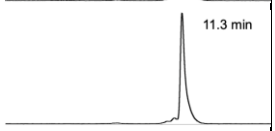	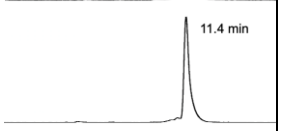	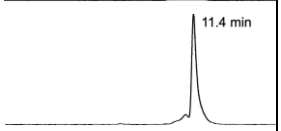
	72 h	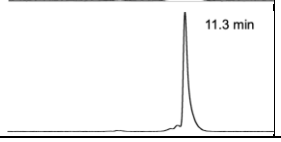	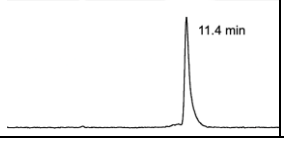	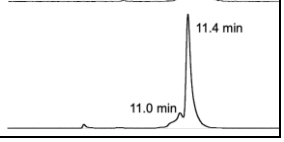

The HPLC method used was 0 – 100% B over 20 minutes at 1 mL/min. A: H_2O (0.1% TFA), B: ACN (0.1% TFA).

As with [^{203}Pb][Pb(TCMC-NHS-FAPI)]$^{2+}$, [^{203}Pb][Pb(TCMC-NHS-CycMSH)]$^{2+}$ was highly resistant to radiolysis and degradation in both types of serum. The urine metabolites (**Figure 4.20**) showed more degradation than what was observed in the *in vitro* serum study, but this may be because the serum used lacks the proteases found *in vivo* that are likely the cause of the degradation of this tracer.

However, with [^{203}Pb][Pb(TCMC-NCS-CycMSH)]$^{2+}$, significant degradation was observed as the singular peak at 10.9 minutes became three peaks at 4.9, 8.6, and 10.9 minutes in both human and mouse serum, similar to what was observed with [^{203}Pb][Pb(TCMC-NCS-FAPI]$^{2+}$ in **Table 4.2**. This is not unexpected as both of these tracers use the same chelator and if degradation was occurring at the bioconjugation point, it would be expected to obtain similar radiolabeled products. The extent of degradation is greater with [^{203}Pb][Pb(TCMC-NCS-CycMSH)]$^{2+}$ over [^{203}Pb][Pb(TCMC-NCS-FAPI]$^{2+}$ and this may be because the CycMSH version contains a secondary amine in its structure compared to a tertiary amine in the FAPI version at the bioconjugation point which can affect enzyme activity. However, both of these compounds degrade completely to the same metabolite *in vivo*, suggesting that this is not of significant practical importance. The 8.6-minute peak is likely the same product obtained in the urine metabolites (**Figure 4.15**, retention time = 9.0 minutes). If this product is the radiometal-chelator complex no longer conjugated to its targeting vector due to degradation by a protein in the serum at the thiourea bond site, this may explain the poor tumour uptake *in vivo*.

Attempts to repeat this serum study with stable lead in place of radiolead to identify the products produced via mass spectrometry were unsuccessful as we wanted to keep the tracers at the same scale used for radiochemistry experiments to be representative of what could occur *in vivo*, but this was below the limit of detection of the mass spectrometer after protein precipitation and sample filtration. Future studies that incubate these complexes separately with specific serum proteins or metabolic enzymes may help to identify the cause of this degradation so that in the future, bioconjugates can be designed to be resistant to its degradation.

4.4. Conclusion

In conclusion, three thiourea-based FAPI- and one CycMSH bioconjugates were synthesized and evaluated with ^{212}Pb and/or ^{203}Pb and were found to be unstable *in vivo*.

Amide derivatives of these bioconjugates were synthesized and found to improve *in vivo* stability and tumour uptake. This study emphasized the importance of using radioHPLC instead of radioTLC for evaluation of serum stability of radiolabeled bioconjugate complexes as radioTLC can fail to detect partial or complete degradation of the bioconjugate if the radiometal-chelate complex still remains intact. Additionally, our findings suggest that thiourea-based bioconjugation is not suitable for the FAPI small molecule or CycMSH peptide models and potentially other models, although further research is required to determine exactly what causes the instability of this bond and how it can be prevented.

Chapter 5.

Conclusion and Future Work

5.1. Thesis Conclusions

The work presented in this thesis focuses on laying a foundation for the development and expansion of radiopharmaceuticals based on ^{203}Pb and ^{212}Pb. At the beginning of my Ph.D., my primary goal was to improve the production of both ^{203}Pb and ^{212}Pb and to improve their chemical purity and specific activity. To achieve this, I developed a novel purification method compatible with both isotopes, as detailed in Chapter 2. Establishing a reliable supply of high-purity isotopes was essential for conducting reproducible, large-scale experiments, which formed the basis for the research explored in Chapters 3 and 4 that were focused on the development and evaluation of ^{203}Pb/^{212}Pb chelators and bioconjugates, respectively. Overall, I have synthesized, characterized, and evaluated three pyridyl-based chelators and six bioconjugates for which coordination chemistry, radiolabeling, stability, *in vitro*, and *in vivo* studies were performed. The findings of these studies had important implications for the future design of ^{203}Pb/^{212}Pb-based radiopharmaceuticals.

Chapter 2 focused on improving the production and purification methods for ^{203}Pb and ^{212}Pb with the ultimate goal of being able to produce enough high purity radioactivity to perform *in vivo* imaging and biodistribution studies with lead-based radiopharmaceuticals. By optimizing an electroplating method to allow thallium to be electroplated onto silver, the thermal stability improved, increasing the maximal allowable proton current from 8 μA to 20 μA, resulting in a nearly three-fold increase in ^{203}Pb produced. A novel purification method that combined precipitation (^{203}Pb only), extraction chromatography, and anion exchange chromatography was developed, resulting in a 2.24 x 10^3-fold and 84-fold decrease in the concentration of Tl and Th in ^{203}Pb and ^{212}Pb, respectively. With fewer impurities, the apparent molar activities of both TCMC and Crypt-OH significantly improved, demonstrating the importance of a reproducible, effective purification procedure on preparing high molar activity radiopharmaceuticals. The work I undertook to establish ^{203}Pb and ^{212}Pb production at TRIUMF has proven to be highly significant and impactful for our research community. Beyond advancing my own research

efforts, this foundational work enabled me to contribute to over a dozen collaborations within my group and other local and international collaborators.

Chapter 3 investigated the effect of macrocyclic ring size on the stability of [^{203}Pb]Pb^{2+} complexes in pyridyl-containing chelators, including Cyclen-4Py, Crown-4Py, and NOON-2Py. The stability of the metal complexes were investigated with ^{203}Pb radiolabeling studies,^{1}H NMR spectroscopy, X-ray crystallography, and potentiometry. With the shortest average Pb-N pyridine interatomic distances, the highest radiolabeling yields, and the formation of one highly symmetric isomer in solution, Cyclen-4Py was shown to be the most promising chelator due to the cyclen backbone producing a facial complex with Pb^{2+}, allowing for effective coordination by the bulky electron donor groups. This study emphasized the importance of macrocyclic backbone size in the design of Pb^{2+} chelators and suggested future studies should employ the N_4 cyclen group over the N_4O_2 and N_2O_4 rings also investigated in this study.

In Chapter 4, Cyclen-4Py was made bifunctional by introducing an isothiocyanate handle off of the cyclen backbone. With this chelator, alongside TCMC-NCS and Crypt-NCS, thiourea-based FAPI bioconjugates were synthesized to investigate the effect of the chelator on tumour retention with FAPI bioconjugates. Initial *in vivo* studies and urine analysis indicated *in vivo* instability that was further replicated in a peptide model using thiourea-based TCMC-NCS-CycMSH. Amide bond coupled bioconjugates TCMC-NHS-FAPI and TCMC-NHS-CycMSH were synthesized using TCMC-NHS, which utilizes an *N*-hydroxysuccinimide group for coupling. The amide-based bioconjugates showed superior stability *in vivo* and further HPLC analysis of serum stability studies suggested the instability of the thiourea bond was due to a serum component. The observation that the thiourea bond was unstable *in vivo* in these small molecule and peptide-based ^{203}Pb/^{212}Pb radiopharmaceuticals has important implications for the future design of Pb-based radiopharmaceuticals as isothiocyanate-functionalized chelators should be avoided for these types of bioconjugates.

5.2. Thesis Outlook and Future Directions

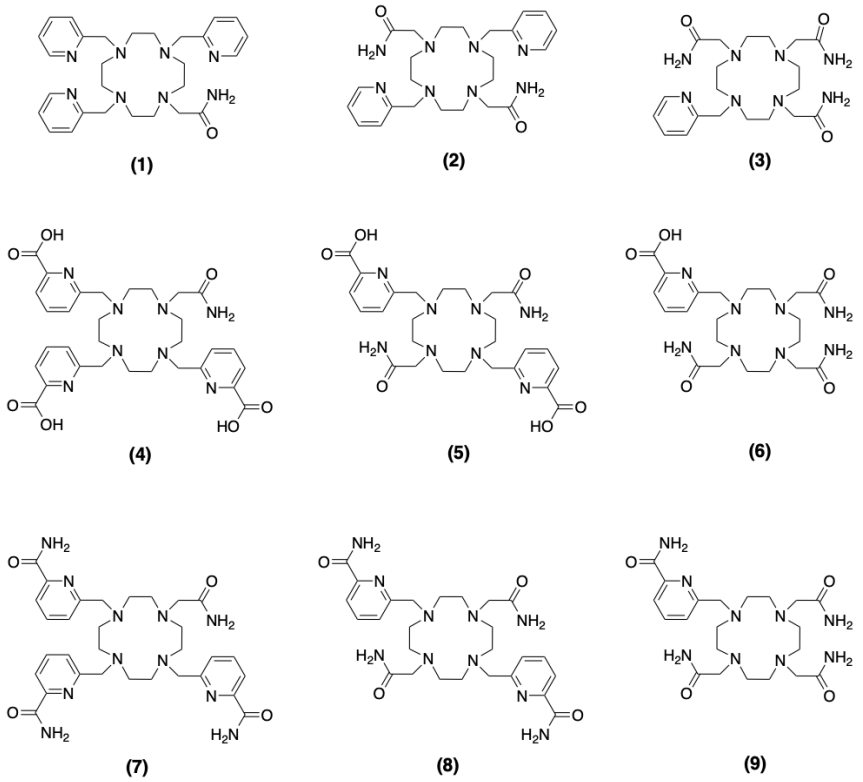

Figure 5.1. Structures of proposed chelators for future studies with ^{203}Pb and ^{212}Pb.

With *in vivo* instability observed with thiourea-based bioconjugates, it is recommended that small molecule and peptide-based ^{203}Pb/^{212}Pb bioconjugates be synthesized with an amide bond using bifunctional chelators containing carboxylic acids or activated esters as their bifunctional handles. To achieve this, a donor arm of the chelator can be sacrificed. If bifunctionalization through the macrocyclic backbone is desired to maintain the coordination environment, the commercially available Cyclen-NO_2 backbone, used in Chapter 4 for the synthesis of Cyclen-4Py-NCS to produce Cyclen-4Py-FAPI, can be derivatized via many possible routes, as shown in **Figure 5.2**.

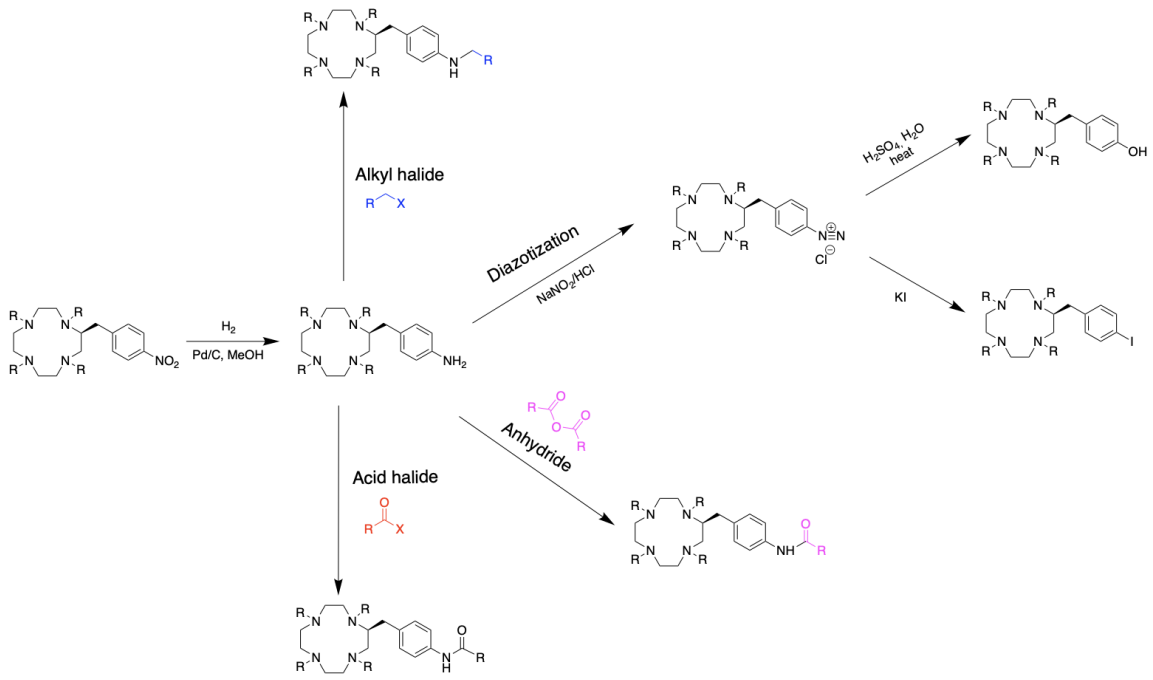

Figure 5.2. Possible bifunctionalization routes starting with the Cyclen-NO_2 backbone.

As shown in **Figure 1.5**, peptide coupling reactions occur between a carboxylic acid or activated ester with an amine. **Figure 5.3** shows two possible ways in which a carboxylic acid could be obtained. However, the researcher should evaluate if the donor arms should be first added onto the backbone before or after these steps and what choice of protecting groups is required to maintain the structural integrity of the chelator throughout the synthesis. It should also be noted that small changes in the linker structure may have a large effect on the pharmacokinetics of the tracer[327] and as so, the design of the bifunctional handle must be chosen carefully.

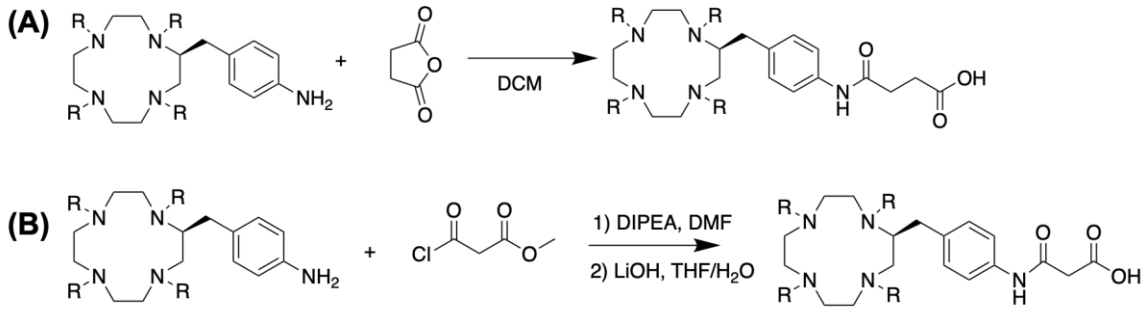

Figure 5.3. Addition of a carboxylic acid group using (A) methyl malonyl chloride and (B) succinic anhydride.

As this work did not investigate the effect of the thiourea bond in antibody-based bioconjugates, the instability of the thiourea bond in these BFC-RPs is unknown and should be investigated. Additionally, the studies should be repeated in the CycMSH and FAPI models with another non-Pb isotope to observe if this effect may be in part caused by the lead ion. However, the chelator may need to be changed from TCMC to DOTA or another chelator to be compatible with the chemical preference of the studied radiometal. ^{111}In or ^{155}Tb/^{161}Tb may be of interest to investigate as they are imageable and have abundant gamma emissions with simple decay schemes that can make radioHPLC analysis more straightforward.[103,348,349] To maintain the TCMC chelator, ^{213}Bi could be used, though a short half-life of 45.6 minutes would make studies challenging to execute.

In order to further reduce the number of candidates prior to *in vivo* studies and to better understand structure-stability relationships with BFC-RPs, metabolic studies can be conducted. Understanding the metabolic fate of BFC-RPs is essential in order to correctly interpret PET/SPECT images. The inability of these imaging techniques to directly differentiate between the intact radiolabeled compound and its metabolites can lead to incorrect conclusions about a BFC-RP's utility. As cytochrome P450 (CYP) enzymes, found primarily in the liver, play a significant role in mammalian drug metabolism, analysis of this enzyme's activity towards a radiolabeled BFC-RP can provide insight on any metabolic weak spots that may cause uptake of the tracer metabolites in undesirable locations.[350]

Although it would be more desirable to use human hepatocytes for these studies from a translatability perspective, the restricted availability of liver tissue, in combination with the difficulty of culturing and maintaining these cells *in vitro*, limits their use.[350] Liver microsomes are derived from the smooth endoplasmic reticulum of cells from liver tissue using differential ultracentrifugation.[351] Liver microsomes derived from numerous species, including humans, can be purchased commercially and stored at -80 ºC for years with little to no loss of activity.[350] Liver microsomes contain primarily phase 1 and drug metabolizing enzymes, including CYPs and glucoronosyltransferase.[350] To perform these assays, the co-factor nicotinamide adenine dinucleotide phosphate (NADPH) is added to a solution of liver microsomes with the test compound at 37 ºC and at set time points, the reaction is quenched with an organic solvent, followed by centrifugation to precipitate out the microsomes so that the supernatant can be analyzed by radioHPLC, as shown in **Figure 5.4**.[352] Changes to the percentage of intact tracer and metabolic half-life can be quantified

and determined. Identification of metabolites using radioHPLC can be performed via the co-injection of radiolabeled standards. Heavily metabolized compounds may be less stable *in vivo*; however, this is an *in vitro* assay and not necessarily representative of *in vivo* conditions.

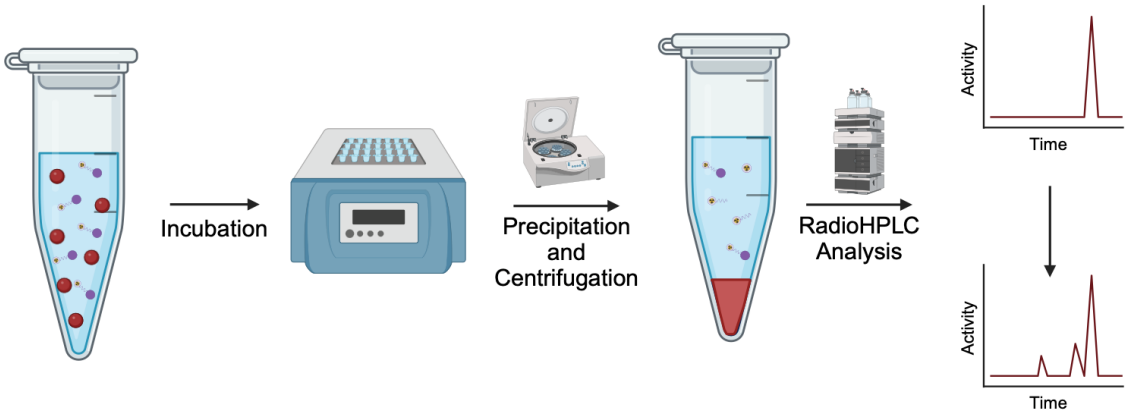

Figure 5.4. Overview of a liver microsome metabolic assay using BFC-RPs.

In addition to metabolic assays, if the targeting vector of choice can undergo internalization, cellular internalization assays can help determine if changes in chelator, linker, or targeting vector structure affects cell uptake, which can further effect tumour uptake and retention.[353] These assays are generally performed by incubating the cells with the radiolabeled tracer in reaction buffer and at given time points, the buffer is removed and the cells are washed with an acidic solution to quantify surface bound activity, followed by lysis with trypsin or sodium hydroxide to quantify internalized activity using a gamma counter.[327,353–355] Conducting internalization assays prior to *in vivo* evaluation allows for the identification of structural issues within the BFC-RP that may hinder efficient internalization into tumour cells. By eliminating candidates early with *in vitro* assays, only the most promising candidates are selected for further evaluation. This approach improves the likelihood of success in subsequent *in vivo* studies and increases the likelihood of advancing the safety and development of radiopharmaceuticals for the diagnosis and treatment of cancer.

References

(1) Siegel, R. L.; Miller, K. D.; Wagle, N. S.; Jemal, A. Cancer Statistics, 2023. *CA Cancer J Clin* **2023**, *73* (1), 17–48. https://doi.org/10.3322/caac.21763.

(2) *Nuclear Medicine Market Size, Share & COVID-19 Impact Analysis, By Type (Diagnostic and Therapeutic), By Application (Neurology, Cardiology, Oncology, and Others), By End-user (Hospitals & Clinics, Diagnostic Centers, and Others), and Regional Forecast, 2023-2030*. Fortune Business Insights. https://www.fortunebusinessinsights.com/industry-reports/infographics/nuclear-medicine-radiopharmaceuticals-market-101812.

(3) Kostelnik, T. I.; Orvig, C. Radioactive Main Group and Rare Earth Metals for Imaging and Therapy. *Chem Rev* **2019**, *119* (2), 902–956. https://doi.org/10.1021/acs.chemrev.8b00294.

(4) Kim, Y. S.; He, Z.; Hsieh, W. Y.; Liu, S. Impact of Bidentate Chelators on Lipophilicity, Stability and Biodistribution Characteristics of Cationic ^{99m}Tc-Nitrido Complexes. *Bioconjug Chem* **2007**, *18* (3), 929–936. https://doi.org/10.1021/bc0603182.

(5) Liu, S. The Role of Coordination Chemistry in the Development of Target-Specific Radiopharmaceuticals. *Chem Soc Rev* **2004**, *33* (7), 445–461. https://doi.org/10.1039/b309961j.

(6) Storr, T.; Thompson, K. H.; Orvig, C. Design of Targeting Ligands in Medicinal Inorganic Chemistry. *Chem Soc Rev* **2006**, *35* (6), 534–544. https://doi.org/10.1039/b514859f.

(7) Lever, S. Z.; Fan, K. H.; Lever, J. R. Tactics for Preclinical Validation of Receptor-Binding Radiotracers. *Nucl Med Biol* **2017**, *44*, 4–30. https://doi.org/10.1016/j.nucmedbio.2016.08.015.

(8) Lin, M.; Welch, M. J.; Lapi, S. E. Effects of Chelator Modifications on ^{68}Ga-Labeled [Tyr$_3$]Octreotide Conjugates. *Mol Imaging Biol* **2013**, *15* (5), 606–613. https://doi.org/10.1007/s11307-013-0627-x.

(9) Crișan, G.; Moldovean-Cioroianu, N. S.; Timaru, D. G.; Andrieș, G.; Căinap, C.; Chiș, V. Radiopharmaceuticals for PET and SPECT Imaging: A Literature Review over the Last Decade. *Int J Mol Sci* **2022**, *23*, 1–52. https://doi.org/10.3390/ijms23095023.

(10) Little, J. B. Principal Cellular and Tissue Effects of Radiation. In *Holland-Frei Cancer Medicine*; BC Decker: Hamilton, ON, 2003.

(11) Pouget, J. P.; Constanzo, J. Revisiting the Radiobiology of Targeted Alpha Therapy. *Front Med (Lausanne)* **2021**, *8*, 1–11. https://doi.org/10.3389/fmed.2021.692436.

(12) Eriksson, D.; Stigbrand, T. Radiation-Induced Cell Death Mechanisms. *Tumor Biology* **2010**, *31* (4), 363–372. https://doi.org/10.1007/s13277-010-0042-8/.

(13) Ku, A.; Facca, V. J.; Cai, Z.; Reilly, R. M. Auger Electrons for Cancer Therapy – a Review. *EJNMMI Radiopharm Chem* **2019**, *4* (1), 1–36. https://doi.org/10.1186/s41181-019-0075-2.

(14) Berger, A. How Does It Work? Positron Emission Tomography. *Br Med J* **2003**, *326* (7404), 1449. https://doi.org/10.1136/bmj.326.7404.1449.

(15) Ramogida, C. F.; Orvig, C. Tumour Targeting with Radiometals for Diagnosis and Therapy. *Chemical Communications* **2013**, *49* (42), 4720–4739. https://doi.org/10.1039/c3cc41554f.

(16) Peterson, T. E.; Furenlid, L. R. SPECT Detectors: The Anger Camera and Beyond. *Phys Med Biol* **2011**, *56* (17), 145–182. https://doi.org/10.1088/0031-9155/56/17/r01.

(17) Wadas, T. J.; Wong, E. H.; Weisman, G. R.; Anderson, C. J. Coordinating Radiometals of Copper, Gallium, Indium, Yttrium, and Zirconium for PET and SPECT Imaging of Disease. *Chem Rev* **2010**, *110* (5), 2858–2902. https://doi.org/10.1021/cr900325h.

(18) Poty, S.; Francesconi, L. C.; McDevitt, M. R.; Morris, M. J.; Lewis, J. S. α-Emitters for Radiotherapy: From Basic Radiochemistry to Clinical Studies—Part 1. *Journal of Nuclear Medicine* **2018**, *59* (6), 878–884. https://doi.org/10.2967/jnumed.116.186338.

(19) Strosberg, J.; El-Haddad, G.; Wolin, E.; Hendifar, A.; Yao, J.; Chasen, B.; Mittra, E.; Kunz, P. L.; Kulke, M. H.; Jacene, H.; Bushnell, D.; O'Dorisio, T. M.; Baum, R. P.; Kulkarni, H. R.; Caplin, M.; Lebtahi, R.; Hobday, T.; Delpassand, E.; Van Cutsem, E.; Benson, A.; Srirajaskanthan, R.; Pavel, M.; Mora, J.; Berlin, J.; Grande, E.; Reed, N.; Seregni, E.; Öberg, K.; Lopera Sierra, M.; Santoro, P.; Thevenet, T.; Erion, J. L.; Ruszniewski, P.; Kwekkeboom, D.; Krenning, E. Phase 3 Trial of ^{177}Lu-Dotatate for Midgut Neuroendocrine Tumors. *N Engl J Med* **2017**, *376* (2), 125–135. https://doi.org/10.1056/nejmoa1607427.

(20) Strosberg, J. R.; Caplin, M. E.; Kunz, P. L.; Ruszniewski, P. B.; Bodei, L.; Hendifar, A. E.; Mittra, E.; Wolin, E. M.; Yao, J. C.; Pavel, M. E.; Grande, E.; Cutsem, E. Van; Seregni, E.; Duarte, H.; Gericke, G.; Bartalotta, A.; Demange, A.; Mutevelic, S.; Krenning, E.; group, on behalf of the N.-1 study. Final Overall Survival in the Phase 3 NETTER-1 Study of Lutetium-177-DOTATATE in Patients with Midgut Neuroendocrine Tumors. *Journal of Clinical Oncology* **2021**, *39* (Suppl. 15), 4112. https://doi.org/10.1200/jco.2021.39.15_suppl.4112.

(21) Rohith, G. VISION Trial: ^{177}Lu-PSMA-617 for Progressive Metastatic Castration-Resistant Prostate Cancer. *Indian Journal of Urology* **2021**, *37* (4), 372–373. https://doi.org/10.4103/iju.iju_292_21.

(22) Sartor, O.; Castellano Gauna, D.; Herrmann, K.; de Bono, J. S. .; Shore, N. D. .; Chi, K. N. N.; Crosby, M.; Piulats, J. M.; Flechon, A.; Wei, X. X.; Mahammedi, H.; Roubaud, G.; Studentova, H.; Ghebremariam, S.; Kpamegan, E.; Kriesl, T. N.; Delgoshale, N.; Lehnoff, K.; Morris, M. J.; Fizazi, K. LBA13 - Phase III Trial of [^{177}Lu]Lu-PSMA-617 in Taxane-Naive Patients with Metastatic Castration-Resistant Prostate Cancer (PSMAfore). *Annals of Oncology* **2023**, *34* (Suppl. 2), S1324–S1325.

(23) van der Sar, E. C. A.; Braat, A. J. A. T.; van der Voort- van Zyp, J. R. N.; van der Veen, B. S.; van Leeuwen, P. J.; de Vries-Huizing, D. M. V.; Hendrikx, J. M. A.; Lam, M. G. E. H.; Vogel, W. V. Tolerability of Concurrent External Beam Radiotherapy and [^{177}Lu]Lu-PSMA-617 for Node-Positive Prostate Cancer in Treatment Naïve Patients, Phase I Study (PROQURE-I Trial). *BMC Cancer* **2023**, *23* (1), 1–13. https://doi.org/10.1186/s12885-023-10725-5/.

(24) Abdollahi, H.; Uribe, C.; Rahmim, A.; Saboury, B. Radiobiology of Alpha and Beta Particles in Radiopharmaceutical Therapy: What to Unlearn from External Beam Radiotherapy. *Journal of Nuclear Medicine* **2023**, *64* (Suppl. 1), P1468.

(25) Song, H.; Senthamizhchelvan, S.; Hobbs, R. F.; Sgouros, G. Alpha Particle Emitter Radiolabeled Antibody for Metastatic Cancer: What Can We Learn from Heavy Ion Beam Radiobiology? *Antibodies* **2012**, *1* (2), 124–148. https://doi.org/10.3390/antib1020124.

(26) *A Phase I/II, Open-label, Multi-center Study of [225Ac]Ac-PSMA-R2 in Men With PSMA-positive Prostate Cancer With or Without Prior 177Lu-PSMA Radioligand Therapy.* Novartis. https://www.novartis.com/clinicaltrials/study/nct05983198.

(27) Morris, M. J.; Wong, J. Y. C.; Nordquist, L.; Szmulewitz, R. Z.; Agarwal, N.; Attiyeh, E. F.; Max, S. I.; Divgi, C. R.; Patricia, D.; Cao, Y.; Li, X.; Yu, A.; Urtishak, K.; Lauring, J. D.; Sartor, O. A Phase 1 Study of JNJ-69086420 (JNJ-6420), an Actinium-225 (^{225}Ac) - Labeled Antibody Targeting Human Kallikrein 2 (HK2), for Metastatic Castration-Resistant Prostate Cancer (MCRPC). *Journal of Clinical Oncology* **2024**, *42* (Suppl. 16), 5010. https://doi.org/10.1200/jco.2024.42.16_suppl.5010.

(28) Morris, Z. S.; Puhlmann, M.; Johnson, F.; Hanna, A.; Cho, S. Y. A Phase I/IIa of [^{212}Pb]VMT01 Targeted a-Particle Therapy for Unresectable or Metastatic Melanoma. *Journal of Clinical Oncology* **2024**, *42* (Suppl. 16), TPS9610. https://doi.org/10.1200/jco.2024.42.16_suppl.tps9610.

(29) Delpassand, E. S.; Tworowska, I.; Esfandiari, R.; Torgue, J.; Hurt, J.; Shafie, A.; Núñez, R. Targeted α -Emitter Therapy with ^{212}Pb-DOTAMTATE for the Treatment of Metastatic SSTR-Expressing Neuroendocrine Tumors: First-in-Humans Dose-Escalation Clinical Trial. *Journal of Nuclear Medicine* **2022**, *63* (9), 1326–1333. https://doi.org/10.2967/jnumed.121.263230.

(30) Kluetz, P. G.; Pierce, W.; Maher, V. E.; Zhang, H.; Tang, S.; Song, P.; Liu, Q.; Haber, M. T.; Leutzinger, E. E.; Al-Hakim, A.; Chen, W.; Palmby, T.; Alebachew, E.; Sridhara, R.; Ibrahim, A.; Justice, R.; Pazdur, R. Radium Ra-223 Dichloride Injection: U.S. Food and Drug Administration Drug Approval Summary. *Clin Cancer Res* **2014**, *20* (1), 9–14. https://doi.org/10.1158/1078-0432.ccr-13-2665.

(31) Kozempel, J.; Mokhodoeva, O.; Vlk, M. Progress in Targeted Alpha-Particle Therapy. What We Learned about Recoils Release from In Vivo Generators. *Molecules* **2018**, *23* (3), 1–18. https://doi.org/10.3390/molecules23030581.

(32) Roscher, M.; Bakos, G.; Benešová, M. Atomic Nanogenerators in Targeted Alpha Therapies: Curie's Legacy in Modern Cancer Management. *Pharmaceuticals* **2020**, *13* (4), 1–21. https://doi.org/10.3390/ph13040076.

(33) Pallares, R. M.; Abergel, R. J. Development of Radiopharmaceuticals for Targeted Alpha Therapy: Where Do We Stand? *Front Med (Lausanne)* **2022**, *9*, 1–16. https://doi.org/10.3389/fmed.2022.1020188/.

(34) Ku, A.; Facca, V. J.; Cai, Z.; Reilly, R. M. Auger Electrons for Cancer Therapy – a Review. *EJNMMI Radiopharm Chem* **2019**, *4* (1), 1–36. https://doi.org/10.1186/s41181-019-0075-2.

(35) Valkema, R.; De Jong, M.; Bakker, W. H.; Breeman, W. A. P.; Kooij, P. P. M.; Lugtenburg, P. J.; De Jong, F. H.; Christiansen, A.; Kam, B. L. R.; De Herder, W. W.; Stridsberg, M.; Lindemans, J.; Ensing, G.; Krenning, E. P. Phase I Study of Peptide Receptor Radionuclide Therapy with [^{111}In-DTPA]Octreotide: The Rotterdam Experience. *Semin Nucl Med* **2002**, *32* (2), 110–122. https://doi.org/10.1053/snuc/2002.31025.

(36) Limouris, G. S.; Chatziioannou, A.; Kontogeorgakos, D.; Mourikis, D.; Lyra, M.; Dimitriou, P.; Stavraka, A.; Gouliamos, A.; Vlahos, L. Selective Hepatic Arterial Infusion of In-111-DTPA-Phe1- Octreotide in Neuroendocrine Liver Metastases. *Eur J Nucl Med Mol Imaging* **2008**, *35* (10), 1827–1837. https://doi.org/10.1007/s00259-008-0779-0/.

(37) Vallis, K. A.; Reilly, R. M.; Scollard, D.; Merante, P.; Brade, A.; Velauthapillai, S.; Caldwell, C.; Chan, I.; Freeman, M.; Lockwood, G.; Miller, N. A.; Cornelissen, B.; Petronis, J.; Sabate, K. Phase I Trial to Evaluate the Tumor and Normal Tissue Uptake, Radiation Dosimetry and Safety of ^{111}In-DTPA-Human Epidermal Growth Factor in Patients with Metastatic EGFR-Positive Breast Cancer. *Am J Nucl Med Mol Imaging* **2014**, *4* (2), 181–192.

(38) Sartor, O.; de Bono, J.; Chi, K. N.; Fizazi, K.; Herrmann, K.; Rahbar, K.; Tagawa, S. T.; Nordquist, L. T.; Vaishampayan, N.; El-Haddad, G.; Park, C. H.; Beer, T. M.; Armour, A.; Pérez-Contreras, W. J.; DeSilvio, M.; Kpamegan, E.; Gericke, G.; Messmann, R. A.; Morris, M. J.; Krause, B. J. Lutetium-177–PSMA-617 for Metastatic Castration-Resistant Prostate Cancer. *New England Journal of Medicine* **2021**, *385* (12), 1091–1103. https://doi.org/10.1056/nejmoa2107322/.

(39) Kratochwil, C.; Bruchertseifer, F.; Giesel, F. L.; Weis, M.; Verburg, F. A.; Mottaghy, F.; Kopka, K.; Apostolidis, C.; Haberkorn, U.; Morgenstern, A. ^{225}Ac-PSMA-617 for PSMA-Targeted a-Radiation Therapy of Metastatic Castration-Resistant Prostate Cancer. *Journal of Nuclear Medicine* **2016**, *57* (12), 1941–1944. https://doi.org/10.2967/jnumed.116.178673.

(40) Price, E. W.; Orvig, C. Matching Chelators to Radiometals for Radiopharmaceuticals. *Chem Soc Rev* **2014**, *43* (1), 260–290. https://doi.org/10.1039/c3cs60304k.

(41) Permyakov, E. A.; Gonçalves, A. M. M. Metal Binding Proteins. *Encyclopedia* **2021**, *1* (1), 261–292. https://doi.org/10.3390/encyclopedia1010024.

(42) Scott, B. J.; Bradwell, A. R. Identification of the Serum Binding Proteins for Iron, Zinc, Cadmium, Nickel, and Calcium. *Clin Chem* **1983**, *29* (4), 629–633. https://doi.org/10.1093/clinchem/29.4.629.

(43) Bal, W.; Christodoulou, J.; Sadler, P. J.; Tucker, A. Multi-Metal Binding Site of Serum Albumin. *J Inorg Biochem* **1998**, *70* (1), 33–39. https://doi.org/10.1016/s0162-0134(98)00010-5.

(44) Zeglis, B. M.; Lewis, J. S. A Practical Guide to the Construction of Radiometallated Bioconjugates for Positron Emission Tomography. *Dalton Transactions* **2011**, *40* (23), 6168–6195. https://doi.org/10.1039/c0dt01595d.

(45) Bird, R. E.; Lemmel, S. A.; Yu, X.; Zhou, Q. A. Bioorthogonal Chemistry and Its Applications. *Bioconjug Chem* **2021**, *32* (12), 2457–2479. https://doi.org/10.1021/acs.bioconjchem.1c00461/.

(46) Mitry, M. M. A.; Greco, F.; Osborn, H. M. I. *In Vivo* Applications of Bioorthogonal Reactions: Chemistry and Targeting Mechanisms. *Chemistry – A European Journal* **2023**, *29* (20), 1–24. https://doi.org/10.1002/chem.202203942.

(47) Zeglis, B. M.; Sevak, K. K.; Reiner, T.; Mohindra, P.; Carlin, S. D.; Zanzonico, P.; Weissleder, R.; Lewis, J. S. A Pretargeted PET Imaging Strategy Based on Bioorthogonal Diels–Alder Click Chemistry. *Journal of Nuclear Medicine* **2013**, *54* (8), 1389–1396. https://doi.org/10.2967/jnumed.112.115840.

(48) Tomarchio, E. G.; Turnaturi, R.; Saccullo, E.; Patamia, V.; Floresta, G.; Zagni, C.; Rescifina, A. Tetrazine–Trans-Cyclooctene Ligation: Unveiling the Chemistry and Applications within the Human Body. *Bioorg Chem* **2024**, *150*, 1–12. https://doi.org/10.1016/j.bioorg.2024.107573.

(49) Chappell, L. L.; Ma, D.; Milenic, D. E.; Garmestani, K.; Venditto, V.; Beitzel, M. P.; Brechbiel, M. W. Synthesis and Evaluation of Novel Bifunctional Chelating Agents Based on 1,4,7,10-Tetraazacyclododecane-N,N′,N″,N‴-Tetraacetic Acid for Radiolabeling Proteins. *Nucl Med Biol* **2003**, *30* (6), 581–595. https://doi.org/10.1016/s0969-8051(03)00033-7.

(50) Eisenwiener, K. P.; Powell, P.; Mäcke, H. R. A Convenient Synthesis of Novel Bifunctional Prochelators for Coupling to Bioactive Peptides for Radiometal Labelling. *Bioorg Med Chem Lett* **2000**, *10* (18), 2133–2135. https://doi.org/10.1016/s0960-894X(00)00413-3.

(51) Mier, W.; Hoffend, J.; Krämer, S.; Schuhmacher, J.; Hull, W. E.; Eisenhut, M.; Haberkorn, U. Conjugation of DOTA Using Isolated Phenolic Active Esters: The Labeling and Biodistribution of Albumin as Blood Pool Marker. *Bioconjug Chem* **2004**, *16* (1), 237–240. https://doi.org/10.1021/bc034216c.

(52) Liu, S.; Edwards, S. D. Bifunctional Chelators for Therapeutic Lanthanide Radiopharmaceuticals. *Bioconjug Chem* **2001**, *12* (1), 7–34. https://doi.org/10.1021/bc000070v.

(53) McMurry, T. J.; Brechbiel, M.; Kumar, K.; Gansow, O. A. Convenient Synthesis of Bifunctional Tetraaza Macrocycles. *Bioconjug Chem* **1992**, *3* (2), 108–117. https://doi.org/10.1021/bc00014a004.

(54) Vallabhajosula, S.; Goldsmith, S. J.; Hamacher, K. A.; Kostakoglu, L.; Konishi, S.; Milowski, M. I.; Nanus, D. M.; Bander, N. H. Prediction of Myelotoxicity Based on Bone Marrow Radiation-Absorbed Dose: Radioimmunotherapy Studies Using ^{90}Y- and ^{177}Lu-Labeled J591 Antibodies Specific for Prostate-Specific Membrane Antigen. *Journal of Nuclear Medicine* **2005**, *46* (5), 850–858.

(55) Vallabhajosula, S.; Tagawa, S.; Osborne, J.; Nauseef, J.; Ricaurte Fajardo, A.; Castellanos, S.; Davidson, Z.; Bander, N. H. Actinium (Ac-225) Rosopatamab Tetraxetan (Ac-RT) Therapy in Metastatic Castration Resistant Prostate Cancer (MCRPC); Radiation Dosimetry, Hematological Toxicity, and Dose-Limiting Toxicity (DLT). *Journal of Nuclear Medicine* **2024**, *65* (Suppl. 2), 241342.

(56) Nelson, A. L. Antibody Fragments: Hope and Hype. *MAbs* **2010**, *2* (1), 77–83. https://doi.org/10.4161/mabs.2.1.10786.

(57) Verhoeven, M.; Seimbille, Y.; Dalm, S. U. Therapeutic Applications of Pretargeting. *Pharmaceutics* **2019**, *11* (9), 1–25. https://doi.org/10.3390/pharmaceutics11090434.

(58) Cheal, S. M.; Chung, S. K.; Vaughn, B. A.; Cheung, N. K. V.; Larson, S. M. Pretargeting: A Path Forward for Radioimmunotherapy. *Journal of Nuclear Medicine* **2022**, *63* (9), 1302–1315. https://doi.org/10.2967/jnumed.121.262186.

(59) Lewis, M. R.; Cutler, C. S.; Jurisson, S. S. Targeted Antibodies and Peptides. In *Molecular Imaging: Principles and Practice*; Ross, B., Gambhir, S., Eds.; Academic Press, 2021; 531–546. https://doi.org/10.1016/b978-0-12-816386-3.00022-3.

(60) Vegt, E.; Jong, M. De; Wetzels, J. F. M.; Masereeuw, R.; Melis, M.; Oyen, W. J. G.; Gotthardt, M.; Boerman, O. C. Renal Toxicity of Radiolabeled Peptides and Antibody Fragments: Mechanisms, Impact on Radionuclide Therapy, and Strategies for Prevention. *Journal of Nuclear Medicine* **2010**, *51* (7), 1049–1058. https://doi.org/10.2967/jnumed.110.075101.

(61) Zaman, R.; Islam, R. A.; Ibnat, N.; Othman, I.; Zaini, A.; Lee, C. Y.; Chowdhury, E. H. Current Strategies in Extending Half-Lives of Therapeutic Proteins. *Journal of Controlled Release* **2019**, *301*, 176–189. https://doi.org/10.1016/j.jconrel.2019.02.016.

(62) Musaimi, A.; Lombardi, O.; Williams, L.; Albericio, D. R.; Al Musaimi, O.; Lombardi, L.; Williams, D. R.; Albericio, F. Strategies for Improving Peptide Stability and Delivery. *Pharmaceuticals* **2022**, *15* (10), 1–33. https://doi.org/10.3390/ph15101283.

(63) Wang, L.; Wang, N.; Zhang, W.; Cheng, X.; Yan, Z.; Shao, G.; Wang, X.; Wang, R.; Fu, C. Therapeutic Peptides: Current Applications and Future Directions. *Signal Transduct Target Ther* **2022**, *7* (48), 1–27. https://doi.org/10.1038/s41392-022-00904-4.

(64) Chaturvedi, S.; Mishra, A. K. Small Molecule Radiopharmaceuticals - A Review of Current Approaches. *Front Med (Lausanne)* **2016**, *3* (5), 1–18. https://doi.org/10.3389/fmed.2016.00005.

(65) Alam, M. R.; Singh, S. B.; Thapaliya, S.; Shrestha, S.; Deo, S.; Khanal, K. A Review of ^{177}Lutetium-PSMA and ^{225}Actinium-PSMA as Emerging Theranostic Agents in Prostate Cancer. *Cureus* **2022**, *14* (9), 1–0. https://doi.org/10.7759/cureus.29369.

(66) Kassis, A. I. Therapeutic Radionuclides: Biophysical and Radiobiologic Principles. *Semin Nucl Med* **2008**, *38* (5), 358–366. https://doi.org/10.1053/j.semnuclmed.2008.05.002.

(67) Choppin, G.; Liljenzin, J.-O.; Rydberg, J.; Ekberg, C. *Radiochemistry and Nuclear Chemistry* , 4th ed.; Elsevier: Amsterdam, Netherlands, 2013.

(68) Karpuz, N.; Mavi, B. Theoretical Production of Radiopharmaceuticals Used in Mycardial Perfusion Scintigraphy. *Acta Phys Pol A* **2016**, *130* (1), 304–305. https://doi.org/10.12693/aphyspola.130.304.

(69) Rochman, D.; Koning, A. J.; Sublet, J. C.; Fleming, M.; Bauge, E.; Hilaire, S.; Romain, P.; Morillon, B.; Duarte, H.; Goriely, S.; Van Der Marck, S. C.; Sjöstrand, H.; Pomp, S.; Dzysiuk, N.; Cabellos, O.; Ferroukhi, H.; Vasiliev, A. The TENDL Library: Hope, Reality and Future. *EPJ Web Conf* **2017**, *146*, 1–5. https://doi.org/10.1051/epjconf/201714602006.

(70) Cohen, B. L. Cyclotrons and Synchrocyclotrons. In *Creutz, E. (eds) Nuclear Instrumentation I / Instrumentelle Hilfsmittel der Kernphysik I. Encyclopedia of Physics / Handbuch der Physik*; Springer: Berlin, 1959; Vol. 8, 105–169. https://doi.org/10.1007/978-3-642-45926-9_3.

(71) Conte, M.; MacKay, W. *An Introduction to the Physics of Particle Accelerators*, 2nd ed.; World Scientific: Hackensack, New Jersey, 2008. https://doi.org/10.1142/6683.

(72) Vretenar, M. Linear Accelerators. In *CAS-CERN Accelerator School*; Herr, W., Ed.; Trondheim, Norway, 2013; 295–329. https://doi.org/10.5170/cern-2014-009.295.

(73) Rotsch, D. A.; Alford, K.; Bailey, J. L.; Bowers, D. L.; Brossard, T.; Brown, M. A.; Chemerisov, S. D.; Ehst, D.; Greene, J.; Gromov, R. G.; Grudzinski, J. J.; Hafenrichter, L.; Hebden, A. S.; Henning, W.; Heltemes, T. A.; Jerden, J.; Jonah, C. D.; Kalensky, M.; Krebs, J. F.; Makarashvili, V.; Micklich, B.; Nolen, J.; Quigley, K. J.; Schneider, J. F.; Smith, N. A.; Stepinski, D. C.; Sun, Z.; Tkac, P.; Vandegrift, G. F.; Virgo, M. J.; Wesolowski, K. A.; Youker, A. J. Production of Medical Isotopes with Electron Linacs. In *Proceedings of NAPAC2016*; Chicago, IL, 2016; 1091–1095.

(74) Starovoitova, V. N.; Tchelidze, L.; Wells, D. P. Production of Medical Radioisotopes with Linear Accelerators. *Applied Radiation and Isotopes* **2014**, *85*, 39–44. https://doi.org/10.1016/j.apradiso.2013.11.122.

(75) Konefał, A.; Orlef, A.; Sokół, M. Application of Therapeutic Linear Accelerators for the Production of Radioisotopes Used in Nuclear Medicine. *Polish Journal of Medical Physics and Engineering* **2022**, *28* (3), 107–116. https://doi.org/10.2478/pjmpe-2022-0013.

(76) Danagulyan, A. S.; Hovhannisyan, G. H.; Bakhshiyan, T. M.; Avagyan, R. H.; Avetisyan, A. E.; Kerobyan, I. A.; Dallakyan, R. K. Formation of Medical Radioisotopes ^{111}In, ^{117m}Sn, ^{124}Sb, and ^{177}Lu in Photonuclear Reactions. *Physics of Atomic Nuclei* **2015**, *78* (4), 447–452. https://doi.org/10.1134/s1063778815030035.

(77) Jang, J.; Kumakura, Y.; Tatenuma, K.; Ozeki, A. N.; Wada, Y.; Akimitsu, N.; Tsuguchi, A.; Kikunaga, H.; Higaki, S.; Uesaka, M. A Preliminary Biodistribution Study of [^{99m}Tc]Sodium Pertechnetate Prepared from an Electron Linear Accelerator and Activated Carbon-Based ^{99m}Tc Generator. *Nucl Med Biol* **2022**, *110*, 1–9. https://doi.org/10.1016/j.nucmedbio.2022.03.002.

(78) Avagyan, R.; Avetisyan, A.; Kerobyan, I.; Dallakyan, R.; Alikhanyan, ∗ A I. Photo-Production of ^{99}Mo/^{99m}Tc with Electron Linear Accelerator Beam. *Nucl Med Biol* **2014**, *41* (8), 705–709. https://doi.org/10.1016/j.nucmedbio.2014.04.132.

(79) Maeda, M.; Tadokoro, T.; Ueno, Y.; Kani, Y.; Nishida, K.; Koiwai, T.; Sasaki, T.; Watanabe, T.; Yoshimoto, M.; Ohnuki, K.; Fujii, H.; Kikunaga, H.; Kashiwagi, S.; Shirasaki, K.; Sekimoto, S.; Ohtsuki, T.; Inagaki, M.; Fukutani, S.; Shibahara, Y. Experimental Production of Ac-225 Using an Electron Linear Accelerator: Scaling up the Production to MBq Level and Improving the Quality. *Journal of Nuclear Medicine* **2023**, *64* (Suppl. 1), P24.

(80) Maslov, O. D.; Sabel'nikov, A. V.; Dmitriev, S. N. Preparation of ^{225}Ac by ^{226}Ra(γ,n) Photonuclear Reaction on an Electron Accelerator, MT-25 Microtron. *Radiochemistry* **2006**, *48* (2), 195–197. https://doi.org/10.1134/s1066362206020184.

(81) Gopalakrishna, A.; Suryanarayana, S. V.; Naik, H.; Nayak, B. K.; Patil, B. J.; Devraju, S.; Upreti, R. R.; Kinhikar, R.; Deshpande, D. D.; Maletha, P.; Kamaldeep; Banerjee, S.; Saxena, A. Production of ^{99}Mo and ^{64}Cu in a Mixed Field of Photons and Neutrons in a Clinical Electron Linear Accelerator. *J Radioanal Nucl Chem* **2018**, *317* (3), 1409–1417. https://doi.org/10.1007/s10967-018-6016-9.

(82) Merrick, M. J.; Rotsch, D. A.; Tiwari, A.; Nolen, J.; Brossard, T.; Song, J.; Wadas, T. J.; Sunderland, J. J.; Graves, S. A. Imaging and Dosimetric Characteristics of ^{67}Cu. *Phys Med Biol* **2021**, *66* (3), 1. https://doi.org/10.1088/1361-6560/abca52.

(83) Kabanov, D. V; Zukau, V. V; Timchenko, S. N.; Ushakov, I. A. Capability Assessment of Production of n.c.a. Isotope ^{177}Lu on the Average Flux Reactor IRT-T. *J Phys Conf Ser* **2022**, *2147*, 1–7. https://doi.org/10.1088/1742-6596/2147/1/012019.

(84) Vimalnath, K. V.; Shetty, P.; Lohar, S. P.; Adya, V. C.; Thulasidas, S. K.; Chakraborty, S.; Dash, A. Aspects of Yield and Specific Activity of (n,γ) Produced ^{177}Lu Used in Targeted Radionuclide Therapy. *J Radioanal Nucl Chem* **2014**, *302* (2), 809–812. https://doi.org/10.1007/s10967-014-3240-9.

(85) Chakraborty, S.; Vimalnath, K. V.; Lohar, S. P.; Shetty, P.; Dash, A. On the Practical Aspects of Large-Scale Production Of ^{177}Lu for Peptide Receptor Radionuclide Therapy Using Direct Neutron Activation Of ^{176}Lu in a Medium Flux Research Reactor: The Indian Experience. *J Radioanal Nucl Chem* **2014**, *302* (1), 233–243. https://doi.org/10.1007/s10967-014-3169-z.

(86) Tarasov, V.; Andreev, O.; Romanov, E.; Kuznetsov, R.; Kupriyanov, V.; Tselishchev, I. Production of No-Carrier Added Lutetium-177 by Irradiation of Enriched Ytterbium-176. *Curr Radiopharm* **2015**, *8* (2), 95–106. https://doi.org/10.2174/1874471008666150312160855.

(87) Horwitz, E. P.; Mcalister, D. R.; Bond, A. H.; Barrans, R. E.; Williamson, J. M. A Process for the Separation of ^{177}Lu from Neutron Irradiated ^{176}Yb Targets. *Applied Radiation and Isotopes* **2005**, *63* (1), 23–36. https://doi.org/10.1016/j.apradiso.2005.02.005.

(88) Alekseev, I. E.; Krotov, S. A. Preparation of ^{177}Lu Using Vacuum Sublimation Technology. *Radiochemistry* **2023**, *65* (2), 198–204. https://doi.org/10.1134/s1066362223020066s.

(89) Van So, L.; Morcos, N.; Zaw, M.; Pellegrini, P.; Greguric, I.; Nevissi, A. Alternative Chromatographic Processes for No-Carrier Added ^{177}Lu Radioisotope Separation: Part II. The Conventional Column Chromatographic Separation Combined with HPLC for High Purity. *J Radioanal Nucl Chem* **2008**, *277* (3), 675–683. https://doi.org/10.1007/s10967-007-7130-2.

(90) Dash, A.; Chakravarty, R.; (Russ) Knapp, F.; Pillai, A. Indirect Production of No Carrier Added (NCA) ^{177}Lu from Irradiation of Enriched ^{176}Yb: Options for Ytterbium/Lutetium Separation. *Curr Radiopharm* **2015**, *8* (2), 107–118. https://doi.org/10.2174/1874471008666150312161942.

(91) Cáceres-Rivero, C.; Ramos-Trujillo, B. J.; Farfán, Y.; Solis, J. L.; Bedregal, P. The Role of PH in the Separation of Lu and Yb by Ion-Exchange Explained by Novel Chemical Structures of Lanthanide Complexes. *Results Chem* **2022**, *4*, 1–7. https://doi.org/10.1016/j.rechem.2022.100514.

(92) National Research Council. *Medical Isotope Production Without Highly Enriched Uranium*; The National Academies Press : Washington, DC, 2009.

(93) Van Duppen, P. Isotope Separation On Line and Post Acceleration. In *The Euroschool Lectures on Physics with Exotic Beams, Vol. II. Lecture Notes in Physics*; Al-Khalili, J., Roeckl, E., Eds.; Springer, Berlin, Heidelberg, 2006; Vol. 700, 37–77. https://doi.org/10.1007/3-540-33787-3_2.

(94) Laxdal, R.; Morton, C.; Schaffer, P. Radioactive Ion Beams and Radiopharmaceuticals. *Reviews of Accelerator Science and Technology* **2014**, *6*, 37–57. https://doi.org/10.1142/s179362681330003X.

(95) Dockx, K.; Elias Cocolios, T.; Stora, T. ISOL Technique for the Production of ^{225}Ac at CERN-MEDICIS. *J Med Imaging Radiat Sci* **2019**, *50* (4), S92. https://doi.org/10.1016/j.jmir.2019.11.077.

(96) Ballan, M.; Vettorato, E.; Morselli, L.; Tosato, M.; Nardella, S.; Borgna, F.; Corradetti, S.; Monetti, A.; Lunardon, M.; Zenoni, A.; Di Marco, V.; Realdon, N.; Andrighetto, A. Development of Implantation Substrates for the Collection of Radionuclides of Medical Interest Produced via ISOL Technique at INFN-LNL. *Applied Radiation and Isotopes* **2021**, *175*, 1. https://doi.org/10.1016/j.apradiso.2021.109795.

(97) Ramogida, C. F.; Robertson, A. K. H.; Jermilova, U.; Zhang, C.; Yang, H.; Kunz, P.; Lassen, J.; Bratanovic, I.; Brown, V.; Southcott, L.; Rodríguez-Rodríguez, C.; Radchenko, V.; Bénard, F.; Orvig, C.; Schaffer, P. Evaluation of Polydentate Picolinic Acid Chelating Ligands and an α-Melanocyte-Stimulating Hormone Derivative for Targeted Alpha Therapy Using ISOL-Produced ^{225}Ac. *EJNMMI Radiopharm Chem* **2019**, *4* (1), 1–20. https://doi.org/10.1186/s41181-019-0072-5.

(98) Koniar, H.; Wharton, L.; Ingham, A.; Rodríguez-Rodríguez, C.; Kunz, P.; Radchenko, V.; Yang, H.; Rahmim, A.; Uribe, C.; Schaffer, P. *In Vivo* Quantitative SPECT Imaging of Actinium-226: Feasibility and Proof-of-Concept. *Phys Med Biol* **2024**, *69* (15), 1–12. https://doi.org/10.1088/1361-6560/ad5c37.

(99) Naskar, N.; Lahiri, S. Theranostic Terbium Radioisotopes: Challenges in Production for Clinical Application. *Front Med (Lausanne)* **2021**, *8*, 1–11. https://doi.org/10.3389/fmed.2021.675014.

(100) Allen, B. J.; Goozee, G.; Sarkar, S.; Beyer, G.; Morel, C.; Byrne, A. P. Production of Terbium-152 by Heavy Ion Reactions and Proton Induced Spallation. *Applied Radiation and Isotopes* **2001**, *54* (1), 53–58. https://doi.org/10.1016/s0969-8043(00)00164-0.

(101) Favaretto, C.; Grundler, P. V.; Talip, Z.; Köster, U.; Johnston, K.; Busslinger, S. D.; Sprung, P.; Hillhouse, C. C.; Eichler, R.; Schibli, R.; Müller, C.; van der Meulen, N. P. Terbium-149 Production: A Focus on Yield and Quality Improvement towards Preclinical Application. *Sci Rep* **2024**, *14* (1), 1–12. https://doi.org/10.1038/s41598-024-53610-2.

(102) Duchemin, C.; Cocolios, T. E.; Dockx, K.; Farooq-Smith, G. J.; Felden, O.; Formento-Cavaier, R.; Gebel, R.; Köster, U.; Neumaier, B.; Scholten, B.; Spahn, I.; Spellerberg, S.; Stamati, M. E.; Stegemann, S.; Verhoeven, H. Production Cross-Section Measurements for Terbium Radionuclides of Medical Interest Produced in Tantalum Targets Irradiated by 0.3 to 1.7 GeV Protons and Corresponding Thick Target Yield Calculations. *Front Med (Lausanne)* **2021**, *8*, 1–11. https://doi.org/10.3389/fmed.2021.625561.

(103) Wharton, L.; McNeil, S. W.; Merkens, H.; Yuan, Z.; Van de Voorde, M.; Engudar, G.; Ingham, A.; Koniar, H.; Rodríguez-Rodríguez, C.; Radchenko, V.; Ooms, M.; Kunz, P.; Bénard, F.; Schaffer, P.; Yang, H. Preclinical Evaluation of [$^{155/161}$Tb]Tb-Crown-TATE—A Novel SPECT Imaging Theranostic Agent Targeting Neuroendocrine Tumours. *Molecules* **2023**, *28* (7), 1–16. https://doi.org/10.3390/molecules28073155.

(104) Prince, J. Comments on Equilibrium, Transient Equilibrium, and Secular Equilibrium in Serial Radioactive Decay. *Journal of Nuclear Medicine* **1979**, *20* (2), 162–164.

(105) Jensen, A. I.; Zhuravlev, F.; Severin, G.; Magnus, C. B.; Fonslet, J.; Köster, U.; Jensen, M. A Solid Support Generator of the Auger Electron Emitter Rhodium-103m from [^{103}Pd]Palladium. *Applied Radiation and Isotopes* **2020**, *156*, 1–7. https://doi.org/10.1016/j.apradiso.2019.108985.

(106) Sounalet, T.; Michel, N.; Alliot, C.; Audouin, A.; Barbet, J.; Bonraisin, A. C.; Bortoli, Y.; Bossé, V.; Bourdeau, C.; Bouvet, G.; Buhour, J. M.; Cadiou, A.; Fresneau, S.; Guillamet, M.; Haddad, F.; Laizé, J.; Milleto, T.; Milon, F.; Mokili, M.; Montavon, G. Strontium-82 and Future Germanium-68 Production at the ARRONAX Facility. *Nuclear Data Sheets* **2014**, *119*, 261–266. https://doi.org/10.1016/j.nds.2014.08.072.

(107) Kambali, I.; Wibowo, F. A. Comparison of Gallium-68 Production Yields from (p,2n), (α,2n) and (p,n) Nuclear Reactions Applicable for Cancer Diagnosis. *J Phys Conf Ser* **2019**, *1198*, 1–10. https://doi.org/10.1088/1742-6596/1198/2/022003.

(108) Ruth, T. J. The Uses of Radiotracers in the Life Sciences. *Reports on Progress in Physics* **2009**, *72* (1), 1–23. https://doi.org/10.1088/0034-4885/72/1/016701.

(109) *Handbook of Nuclear Chemistry*; Vértes, A., Nagy, S., Klencsár, Z., Lovas, R. G., Rösch, F., Eds.; Springer US: Boston, MA, 2011. https://doi.org/10.1007/978-1-4419-0720-2.

(110) Christman, D. R.; Finn, R. D.; Karlstrom, K. I.; Wolf, A. P. The Production of Ultra High Activity ^{11}C-Labeled Hydrogen Cyanide, Carbon Dioxide, Carbon Monoxide and Methane via the ^{14}N(p,α)^{11}C Reaction. *Int J Appl Radiat Isot* **1975**, *26* (8), 435–442. https://doi.org/10.1016/0020-708x(75)90057-5.

(111) Steinbach, J. The Gas Target Technique for Radionuclide Production with Small Accelerators. *Isotopenpraxis Isotopes in Environmental and Health Studies* **1990**, *26* (3), 102–106. https://doi.org/10.1080/10256019008624242.

(112) do Carmo, S. J. C.; Scott, P. J. H.; Alves, F. Production of Radiometals in Liquid Targets. *EJNMMI Radiopharm Chem* **2020**, *5* (1), 1–21. https://doi.org/10.1186/s41181-019-0088-x.

(113) McNeil, B. L.; Mastroianni, S. A.; McNeil, S. W.; Zeisler, S.; Kumlin, J.; Borjian, S.; McDonagh, A. W.; Cross, M.; Schaffer, P.; Ramogida, C. F. Optimized Production, Purification, and Radiolabeling of the ^{203}Pb/^{212}Pb Theranostic Pair for Nuclear Medicine. *Sci Rep* **2023**, *13* (1), 1–12. https://doi.org/10.1038/s41598-023-37313-8.

(114) Saini, S.; Bartels, J. L.; Appiah, J.-P. K.; Rider, J. H.; Baumhover, N.; Schultz, M. K.; Lapi, S. E. Optimized Methods for the Production of High-Purity ^{203}Pb Using Electroplated Thallium Targets. *Journal of Nuclear Medicine* **2023**, *64*, 1–7. https://doi.org/10.2967/jnumed.123.265976.

(115) Saghez, B. S.; Yang, H.; Radchenko, V. High Separation Factor, High Molar Activity, and Inexpensive Purification Method for the Production of Pure ^{165}Er. *Inorg Chem* **2024**, *63* (12), 5330–5340. https://doi.org/10.1021/acs.inorgchem.3c03166.

(116) Chen, S.; Bas, M.; Happel, S.; Randhawa, P.; McNeil, S.; Kurakina, E.; Zeisler, S.; Maskell, K.; Hoehr, C.; Ramogida, C. F.; Radchenko, V. Determination of Distribution Coefficients of Mercury and Gold on Selected Extraction Chromatographic Resins - towards an Improved Separation Method of Mercury-197 from Proton-Irradiated Gold Targets. *J Chromatogr A* **2023**, *1688*, 1. https://doi.org/10.1016/j.chroma.2022.463717.

(117) Nelson, B. J. B.; Ferguson, S.; Wuest, M.; Wilson, J.; John, M.; Duke, M.; Richter, S.; Soenke-Jans, H.; Andersson, J. D.; Juengling, F.; Wuest, F. First In Vivo and Phantom Imaging of Cyclotron-Produced ^{133}La as a Theranostic Radionuclide for ^{225}Ac and ^{135}La. *Journal of Nuclear Medicine* **2022**, *63* (4), 584–590. https://doi.org/10.2967/jnumed.121.262459.

(118) IAEA. *Manual for Reactor Produced Radioisotopes*; 2003. https://www-pub.iaea.org/MTCD/Publications/PDF/te_1340_web.pdf.

(119) McCarthy, D. W.; Shefer, R. E.; Klinkow, R. E.; Bass, L. A.; Margeneau, W. H.; Cutler, C. S.; Anderson, C. J.; Welch, M. J. Efficient Production of High Specific Activity ^{64}Cu Using A Biomedical Cyclotron. *Nucl Med Biol* **1997**, *24* (1), 35–43. https://doi.org/10.1016/s0969-8051(96)00157-6.

(120) Cheltsov, A. N.; Sosnin, L. Y.; Khamylov, V. K. Centrifugal Enrichment of Nickel Isotopes and Their Application to the Development of New Technologies. *J Radioanal Nucl Chem* **2014**, *299* (2), 981–987. https://doi.org/10.1007/s10967-013-2755-9.

(121) Stolarz, A. Target Preparation for Research with Charged Projectiles. *J Radioanal Nucl Chem* **2014**, *299* (2), 913–931. https://doi.org/10.1007/s10967-013-2652-2.

(122) Nagatsu, K.; Suzuki, H.; Fukada, M.; Ito, T.; Ichinose, J.; Honda, Y.; Minegishi, K.; Higashi, T.; Zhang, M. R. Cyclotron Production of ^{225}Ac from an Electroplated ^{226}Ra Target. *Eur J Nucl Med Mol Imaging* **2021**, *49* (1), 279–289. https://doi.org/10.1007/s00259-021-05460-7.

(123) Müller, C.; Zhernosekov, K.; Köster, U.; Johnston, K.; Dorrer, H.; Hohn, A.; Van Der Walt, N. T.; Türler, A.; Schibli, R. A Unique Matched Quadruplet of Terbium Radioisotopes for PET and SPECT and for α- and B−-Radionuclide Therapy: An In Vivo Proof-of-Concept Study with a New Receptor-Targeted Folate Derivative. *Journal of Nuclear Medicine* **2012**, *53* (12), 1951–1959. https://doi.org/10.2967/jnumed.112.107540.

(124) Durazzo, M.; Souza, J. A. B.; Ianelli, R. F.; Takara, E. M.; Neto, J. S. G.; Saliba-Silva, A. M.; Urano De Carvalho, E. F. Manufacturing LEU-Foil Annular Target in Brazil. *Annals of Nuclear Energy* **2021**, *165*, 1–16. https://doi.org/10.1016/j.anucene.2021.108646.

(125) Ianelli, R. F.; Saliba-Silva, A. M.; Takara, E. M.; Neto, J. G.; Souza, J. A. B.; Urano de Carvalho, E. F.; Durazzo, M. Nickel Electrodeposition in LEU Metal Foil Annular Targets to Produce Mo-99. *Mater Chem Phys* **2022**, *290*, 1–12. https://doi.org/10.1016/j.matchemphys.2022.126620.

(126) Walther, M.; Preusche, S.; Bartel, S.; Wunderlich, G.; Freudenberg, R.; Steinbach, J.; Pietzsch, H.-J. Theranostic Mercury: $^{197(m)}$Hg with High Specific Activity for Imaging and Therapy. *Applied Radiation and Isotopes* **2015**, *97*, 177–181. https://doi.org/10.1016/j.apradiso.2015.01.001.

(127) Bzowski, P.; Borys, D.; Gorczewski, K.; Chmura, A.; Daszewska, K.; Gorczewska, I.; Kastelik-Hryniewiecka, A.; Szydło, M.; d'Amico, A.; Sokół, M. Efficiency of ^{124}I Radioisotope Production from Natural and Enriched Tellurium Dioxide Using ^{124}Te(p,xn)^{124}I Reaction. *EJNMMI Phys* **2022**, *9* (41), 1–24. https://doi.org/10.1186/s40658-022-00471-1.

(128) Alnahwi, A. H.; Tremblay, S.; Guérin, B. Comparative Study with ^{89}Y-Foil and ^{89}Y-Pressed Targets for the Production of ^{89}Zr. *Applied Sciences* **2018**, *8* (9), 1–13. https://doi.org/10.3390/app8091579.

(129) Gagnon, K.; Risler, R.; Pal, S.; Hamlin, D.; Orzechowski, J.; Pavan, R.; Zeisler, S.; Wilbur, D. S. Design and Evaluation of an External High-Current Target for Production of ^{211}At. *J Labelled Comp Radiopharm* **2012**, *55* (12), 436–440. https://doi.org/10.1002/jlcr.2968.

(130) Nelson, B. J. B.; Wilson, J.; Andersson, J. D.; Wuest, F. High Yield Cyclotron Production of a Novel $^{133/135}$La Theranostic Pair for Nuclear Medicine. *Sci Rep* **2020**, *10* (1), 1–10. https://doi.org/10.1038/s41598-020-79198-x.

(131) Nelson, B. J. B.; Wilson, J.; Schultz, M. K.; Andersson, J. D.; Wuest, F. High-Yield Cyclotron Production of ^{203}Pb Using a Sealed ^{205}Tl Solid Target. *Nucl Med Biol* **2023**, *116*, 1–13. https://doi.org/10.1016/j.nucmedbio.2023.108314.

(132) Li, Z.; Dewulf, B.; Binnemans, K. Nonaqueous Solvent Extraction for Enhanced Metal Separations: Concept, Systems, and Mechanisms. *Ind Eng Chem Res* **2021**, *60* (48), 17285–17302. https://doi.org/10.1021/acs.iecr.1c02287.

(133) Wilson, A. M.; Bailey, P. J.; Tasker, P. A.; Turkington, J. R.; Grant, R. A.; Love, J. B. Solvent Extraction: The Coordination Chemistry behind Extractive Metallurgy. *Chem Soc Rev* **2013**, *43* (1), 123–134. https://doi.org/10.1039/c3cs60275c.

(134) Eyal, A. M.; Bressler, E.; Bloch, R.; Kazan, B. Extraction of Metal Salts by Mixtures of Water-Immiscible Amines and Organic Acids (Acid-Base Couple Extractants). 1. A Review of Distribution and Spectroscopic Data and of Proposed Extraction Mechanisms. *Ind Eng Chem Res* **1994**, *33* (5), 1067–1075. https://doi.org/10.1021/ie00029a001.

(135) Stary, J. *The Solvent Extraction of Metal Chelates*; Irving, H., Ed.; Pergamon Press : London, 1964. https://doi.org/10.1016/c2013-0-01830-0.

(136) Narbutt, J. Solvent Extraction for Nuclear Power. In *Handbooks in Separation Science*; Poole, C. F., Ed.; Elsevier, 2020; 725–744. https://doi.org/10.1016/b978-0-12-816911-7.00024-4.

(137) Lyseid Authen, T.; Adnet, J. M.; Bourg, S.; Carrott, M.; Ekberg, C.; Galán, H.; Geist, A.; Guilbaud, P.; Miguirditchian, M.; Modolo, G.; Rhodes, C.; Wilden, A.; Taylor, R. An Overview of Solvent Extraction Processes Developed in Europe for Advanced Nuclear Fuel Recycling, Part 2 — Homogeneous Recycling. *Sep Sci Technol* **2022**, *57* (11), 1724–1744. https://doi.org/10.1080/01496395.2021.2001531.

(138) Nash, K. The Chemistry of TALSPEAK: A Review of the Science. *Solvent Extraction and Ion Exchange* **2014**, *33* (1), 1–55. https://doi.org/10.1080/07366299.2014.985912.

(139) Kostelnik, T. I.; Olson, A. P.; Grundmane, A.; Ellison, P. A.; Mynerich, J.; Chen, S.; Marinova, A.; Randhawa, P.; Karaivanov, D.; Aluicio-Sarduy, E.; Barnhart, T. E.; Orvig, C.; Ramogida, C. F.; Hoehr, C.; Filosofov, D.; Engle, J. W.; Radchenko, V. Production and Radiochemistry of Antimony-120m: Efforts toward Auger Electron Therapy with ^{119}Sb. *Nucl Med Biol* **2023**, *122*, 1–5. https://doi.org/10.1016/j.nucmedbio.2023.108352.

(140) Domnanich, K. A.; Müller, C.; Benešová, M.; Dressler, R.; Haller, S.; Köster, U.; Ponsard, B.; Schibli, R.; Türler, A.; van der Meulen, N. P. ^{47}Sc as Useful β–-Emitter for the Radiotheragnostic Paradigm: A Comparative Study of Feasible Production Routes. *EJNMMI Radiopharm Chem* **2017**, *2* (1), 1–17. https://doi.org/10.1186/s41181-017-0024-x.

(141) Shahr El-Din, A. M.; Rizk, H. E.; Attallah, M. F. Purification of Carrier-Free ^{47}Sc of Biomedical Interest: Selective Separation Study from NatCa(n,γ). *Separations* **2022**, *10* (1), 1–1. https://doi.org/10.3390/separations10010008.

(142) Pandey, M. K.; Degrado, T. R. Cyclotron Production of PET Radiometals in Liquid Targets. *Curr Radiopharm* **2021**, *14*, 325–339. https://doi.org/10.2174/1874471013999200820165734.

(143) Krol, V.; Koers, L. M. gennant; McNeil, S.; Hoehr, C.; Radchenko, V. Cyclotron Production of ^{103}Pd Using a Liquid Target. *Nucl Med Biol* **2023**, *118*, 1–8. https://doi.org/10.1016/j.nucmedbio.2023.108328.

(144) Zhuravlev, F.; Gulzar, A.; Falborg, L. Recovery of Gallium-68 and Zinc from HNO_3-Based Solution by Liquid–Liquid Extraction with Arylamino Phosphonates. *Molecules* **2022**, *27* (23), 1–4. https://doi.org/10.3390/molecules2723837.

(145) Trapp, S.; Lammers, T.; Engudar, G.; Hoehr, C.; Denkova, A. G.; Paulssen, E.; de Kruijff, R. M. Membrane-Based Microfluidic Solvent Extraction of Ga-68 from Aqueous Zn Solutions: Towards an Automated Cyclotron Production Loop. *EJNMMI Radiopharm Chem* **2023**, *8* (1), 1–14. https://doi.org/10.1186/s41181-023-00195-2.

(146) Pedersen, K. S.; Nielsen, K. M.; Fonslet, J.; Jensen, M.; Zhuravlev, F. Separation of Radiogallium from Zinc Using Membrane-Based Liquid-Liquid Extraction in Flow: Experimental and COSMO-RS Studies. *Solvent Extraction and Ion Exchange* **2019**, *37* (5), 376–391. https://doi.org/10.1080/07366299.2019.1646982.

(147) Sanku, M. G.; Forsberg, K.; Svärd, M. Impregnation of Preparative High-Performance Solid Phase Extraction Chromatography Columns by Organophosphorus Acid Compounds. *J Chromatogr A* **2022**, *1676*, 1–9. https://doi.org/10.1016/j.chroma.2022.463278.

(148) McAlister, D. R.; Kurosaki, H.; Happel, S.; Philip Horwitz, E. *Development of Extraction Chromatography Resins for Metal Ion Separations in Analytical Radiochemistry*. https://www.osti.gov/servlets/purl/1607048.

(149) Philip Horwitz, E.; Dietz, M. L.; Rhoads, S.; Felinto, C.; Gale, N. H.; Houghton, J. A Lead-Selective Extraction Chromatographic Resin and Its Application to the Isolation of Lead from Geological Samples. *Anal Chim Acta* **1994**, *292* (3), 263–273. https://doi.org/10.1016/0003-2670(94)00068-9.

(150) Kajan, I.; Florianova, M.; Ekberg, C.; Matyskin, A. V. Effect of Diluent on the Extraction of Europium(III) and Americium(III) with N,N,N′,N′-Tetraoctyl Diglycolamide (TODGA). *RSC Adv* **2021**, *11* (58), 36707–36718. https://doi.org/10.1039/d1ra07534a.

(151) Batchu, N. K.; Binnemans, K. Effect of the Diluent on the Solvent Extraction of Neodymium(III) by Bis(2-Ethylhexyl)Phosphoric Acid (D2EHPA). *Hydrometallurgy* **2018**, *177*, 146–151. https://doi.org/10.1016/j.hydromet.2018.03.012.

(152) Ying, Z.; Liu, S.; Li, G.; Wei, Q.; Ren, X. The Effect of Diluent on the Extraction: Amide Extracting Chromium (VI) as an Example. *J Mol Liq* **2023**, *384*, 1–10. https://doi.org/10.1016/j.molliq.2023.122205.

(153) Mendes, M.; Aupiais, J.; Jutier, C.; Pointurier, F. Determination of Weight Distribution Ratios of Pa(V) and Np(V) with Some Extraction Chromatography Resins and the AG1-X8 Resin. *Anal Chim Acta* **2013**, *780*, 110–116. https://doi.org/10.1016/j.aca.2013.04.019.

(154) Philip Horwitz, E.; Chiarizia, R.; Dietz, M. L. A Novel Strontium-Selective Extraction Chromatographic Resin. *Solvent Extraction and Ion Exchange* **1992**, *10* (2), 313–336. https://doi.org/10.1080/07366299208918107.

(155) TRISKEM. *Extraction Chromatography Technical Documentation-All Resins*. https://www.triskem-international.com/scripts/files/5ee8cbaf847631.58650092/technical-doc-all-resins-en-online.pdf.

(156) McNeil, B. L.; Robertson, A. K. H.; Fu, W.; Yang, H.; Hoehr, C.; Ramogida, C. F.; Schaffer, P. Production, Purification, and Radiolabeling of the ^{203}Pb/^{212}Pb Theranostic Pair. *EJNMMI Radiopharm Chem* **2021**, *6*, 1–18. https://doi.org/10.1186/s41181-021-00121-4.

(157) Robertson, A. K. H.; McNeil, B. L.; Yang, H.; Gendron, D.; Perron, R.; Radchenko, V.; Zeisler, S.; Causey, P.; Scha, P. ^{232}Th-Spallation-Produced ^{225}Ac with Reduced ^{227}Ac Content. **2020**, *59* (17), 12156–12165. https://doi.org/10.1021/acs.inorgchem.0c01081.

(158) Aluicio-Sarduy, E.; Hernandez, R.; Olson, A. P.; Barnhart, T. E.; Cai, W.; Ellison, P. A.; Engle, J. W. Production and *In Vivo* PET/CT Imaging of the Theranostic Pair $^{132/135}$La. *Sci Rep* **2019**, *9* (1), 1–6. https://doi.org/10.1038/s41598-019-47137-0.

(159) Ermolaev, S. V.; Skasyrskaya, A. K.; Vasiliev, A. N. Rapid Elution of ^{226}Th from a Two-Column ^{230}U/^{226}Th Generator with Diluted and Buffer Solutions. *Molecules* **2023**, *28* (8), 1–17. https://doi.org/10.3390/molecules28083548.

(160) Peterson, D.; Montoya, V. Separation of Actinides Using Capillary Extraction Chromatography - Inductively Coupled Plasma Mass Spectrometry. *J Chromatogr Sci* **2009**, *47* (7), 545–548. https://doi.org/10.1093/chromsci/47.7.545.

(161) Chiera Id, N. M.; Talip, Z.; Fankhauser, A.; Schumann, D. Separation and Recovery of Exotic Radiolanthanides from Irradiated Tantalum Targets for Half-Life Measurements. *PLoS One* **2020**, *15* (7), 1–19. https://doi.org/10.1371/journal.pone.0235711.

(162) Arrigo, L. M.; Jiang, J.; Finch, Z. S.; Bowen, J. M.; Beck, C. L.; Friese, J. I.; Greenwood, L. R.; Seiner, B. N. Development of a Separation Method for Rare Earth Elements Using LN Resin. *J Radioanal Nucl Chem* **2021**, *327*, 457–463. https://doi.org/10.1007/s10967-020-07488-9.

(163) Maillard, C.; Maloubier, D.; Boulay, O.; Savigny, V.; Quemet, A. U and Pu Separation with U/TEVA Resin: Influence of Some Parameters on Chromatographic Cycle Performances. *J Radioanal Nucl Chem* **2021**, *330* (3), 579–587. https://doi.org/10.1007/s10967-021-07986-4.

(164) Papp, I.; Vajda, N.; Happel, S. An Improved Rapid Method for the Determination of Actinides in Water. *J Radioanal Nucl Chem* **2022**, *331* (9), 3835–3846. https://doi.org/10.1007/s10967-022-08389-9.

(165) Saghez, B. S.; Yang, H.; Radchenko, V. High Separation Factor, High Molar Activity, and Inexpensive Purification Method for the Production of Pure ^{165}Er. *Inorg Chem* **2024**, *63* (12), 5330–5340. https://doi.org/10.1021/acs.inorgchem.3c03166.

(166) McNeil, S. W.; Van de Voorde, M.; Zhang, C.; Ooms, M.; Bénard, F.; Radchenko, V.; Yang, H. A Simple and Automated Method for ^{161}Tb Purification and ICP-MS Analysis of ^{161}Tb. *EJNMMI Radiopharm Chem* **2022**, *7* (31), 1–17. https://doi.org/10.1186/s41181-022-00183-y.

(167) Horwitz, E. P.; McAlister, D. R.; Bond, A. H.; Barrans, E. Novel Extraction of Chromatographic Resins Based on Tetraalkyldiglycolamides: Characterization and Potential Applications. *Solvent Extraction and Ion Exchange* **2005**, *23* (3), 319–344. https://doi.org/10.1081/sei-200049898.

(168) Radchenko, V.; Mastren, T.; Meyer, C. A. L.; Ivanov, A. S.; Bryantsev, V. S.; Copping, R.; Denton, D.; Engle, J. W.; Griswold, J. R.; Murphy, K.; Wilson, J. J.; Owens, A.; Wyant, L.; Birnbaum, E. R.; Fitzsimmons, J.; Medvedev, D.; Cutler, C. S.; Mausner, L. F.; Nortier, M. F.; John, K. D.; Mirzadeh, S.; Fassbender, M. E. Radiometric Evaluation of Diglycolamide Resins for the Chromatographic Separation of Actinium from Fission Product Lanthanides. *Talanta* **2017**, *175*, 318–324. https://doi.org/10.1016/j.talanta.2017.07.057.

(169) Nelson, F.; Kraus, K. A. Anion-Exchange Studies. XI. Lead (II) and Bismuth (III) in Chloride and Nitrate Solutions. *J Am Chem Soc* **1954**, *76* (23), 5916–5920. https://doi.org/https://doi.org/10.1021/ja01652a006.

(170) Nelson, F.; Kraus, K. A. Ion Exchange Procedures 1. Cation Exchange in Concentrated HCl and $HClO_4$ Solutions. *J Chromatogr A* **1964**, *13*, 503–535. https://doi.org/https://doi.org/10.1016/s0021-9673(01)95146-5.

(171) Kraus, K. A.; Nelson, F. Anion Exchange Studies XXII. Metal Separations by Anion Exchange. *American Society for Testing and Materials* **1958**, *195*, 27–59. https://doi.org/https://doi.org/10.1520/stp44180s.

(172) Grzybkowski, W. Nature and Properties of Metal Cations in Aqueous Solutions. *Pol J Environ Stud* **2006**, *15* (4), 655–663.

(173) Kraus, K. A.; Nelson, F.; Smith, G. W. Anion-Exchange Studies. IX. Adsorbability of a Number of Metals in Hydrochloric Acid Solutions. *Journal of Physical Chemistry* **1954**, *58* (1), 11–17. https://doi.org/https://doi.org/10.1021/j150511a003.

(174) Marsh, S. F.; Alarid, J. E.; Hammond, C. F.; Mcleod, M. J.; Roensch, F. R.; Rein, J. E. *Anion Exchange of 58 Elements in Hydrobromic Acid and in Hydriodic Acid*; Los Alamos, 1978.

(175) Marsh, S. F.; Alarid, J. E.; Hammond, C. F.; Mcleod, M. J.; Roensch, F. R.; Rein, J. E. *Cation Exchange of 53 Elements in Nitric Acid*; Los Alamos, New Mexico, 1978.

(176) Strelow, F. W.; Von S. Toerien, F. Separation of Lead(II) from Bismuth(III), Thallium(III), Cadmium(II), Mercury(II), Gold(II), Platinum(IV), Palladium(II) and Other Elements by Anion Exchange Chromatography. *Anal Chem* **1966**, *38* (4), 545–548. https://doi.org/10.1021/ac60236a006.

(177) Eusebius, L. C. T.; Ghose, A. K.; Dey, A. K. Cation Exchange Column Chromatography in Aqueous Ammonium Acetate: Separation of U(VI), Al(III), Sr(II), Ba(II) and Hg(II) from Other Metal Ions. *Mikrochim Acta* **1985**, *85*, 365–373. https://doi.org/10.1007/bf01201531.

(178) de Corte, F.; van Den Winkel, P.; Speecke, A.; Hoste, J. Distribution Coefficients for Twelve Elements in Oxalic Acid Medium on a Strong Anion-Exchange Resin. *Anal Chim Acta* **1968**, *42*, 67–77. https://doi.org/10.1016/s0003-2670)(01)80270-1.

(179) Li, H.; Tissot, F. L. H.; Lee, S. G.; Hyung, E.; Dauphas, N. Distribution Coefficients of the REEs, Sr, Y, Ba, Th, and U between α-HIBA and AG50W-X8 Resin. *ACS Earth Space Chem* **2021**, *5* (1), 55–65. https://doi.org/10.1021/acsearthspacechem.0c00273.

(180) Nash, K. L.; Jensen, M. P. Analytical Separations of the Lanthanides: Basic Chemistry and Methods. In *Handbook on the Physics and Chemistry of Rare Earths*; Gschneidner, K., Eyring, L., Eds.; Elsevier, 2000; Vol. 28, pp 311–371. https://doi.org/10.1016/s0168-1273(00)28008-2.

(181) Strelow, F. W. E. Distribution Coefficients and Ion-Exchange Selectivities for 46 Elements with a Macroporous Cation-Exchange Resin in Hydrochloric Acid-Acetone Medium. *Talanta* **1988**, *35* (5), 385–395. https://doi.org/10.1016/0039-9140(88)80032-8.

(182) Strelow, F. W. E.; Weinert, C. H. S. W.; Van Der Walt, T. N. Separation of Lithium from Sodium, Beryllium and Other Elements by Cation-Exchange Chromatography in Nitric Acid-Methanol. *Anal Chim Acta* **1974**, *71* (1), 123–132. https://doi.org/10.1016/s0003-2670(01)82877-4.

(183) Atcher, R. W.; Friedman, A. M.; Hines, J. J. An Improved Generator for the Production of ^{212}Pb and ^{212}Bi from ^{224}Ra. *Int. J. Radiat. Appl. Instrum. Part A* **1988**, *39* (4), 283–286. https://doi.org/10.1016/0883-2889(88)90016-0.

(184) McAlister, D. R.; Horwitz, E. P. Chromatographic Generator Systems for the Actinides and Natural Decay Series Elements. *Radiochim Acta* **2011**, *99* (3), 151–159. https://doi.org/10.1524/ract.2011.1804.

(185) Sadeghi, M.; Mokhtari, L. Rapid Separation of ^{67,68}Ga from ^{68}Zn Target Using Precipitation Technique. *J Radioanal Nucl Chem* **2010**, *284* (2), 471–473. https://doi.org/10.1007/s10967-010-0500-1.

(186) Severin, G. W.; Engle, J. W.; Valdovinos, H. F.; Barnhart, T. E.; Nickles, R. J. Cyclotron Produced ^{44g}Sc from Natural Calcium. *Applied Radiation and Isotopes* **2012**, *70* (8), 1526–1530. https://doi.org/10.1016/j.apradiso.2012.04.030.

(187) Aluicio-Sarduy, E.; Barnhart, T. E.; Weichert, J.; Hernandez, R.; Engle, J. W. Cyclotron-Produced ^{132}La as a PET Imaging Surrogate for Therapeutic ^{225}Ac. *Journal of Nuclear Medicine* **2021**, *62* (7), 1012–1015. https://doi.org/10.2967/jnumed.120.255794.

(188) Vukanac, I.; Šešlak, B.; Kandić, A.; Čeliković, I.; Nikolić, N. M.; Milanović, T.; Obradović, Z.; Đurašević, M. A Comparison of Alpha-Particle and Gamma-Ray Spectrometry Methods for Determination of ^{235}U, ^{238}U and ^{226}Ra Activity Concentration in Samples of Coal, Slag and Fly-Ash. *Radiation Physics and Chemistry* **2022**, *193*, 1–7. https://doi.org/10.1016/j.radphyschem.2021.109933.

(189) Jha, A.; Patel, M.; Carrasquillo, J. A.; Chen, C. C.; Millo, C.; Maass-Moreno, R.; Ling, A.; Lin, F. I.; Lechan, R. M.; Hope, T. A.; Taïeb, D.; Civelek, A. C.; Pacak, K. Choice Is Good at Times: The Emergence of [^{64}Cu]Cu-DOTATATE–Based Somatostatin Receptor Imaging in the Era of [^{68}Ga]Ga-DOTATATE. *Journal of Nuclear Medicine* **2022**, *63* (9), 1300–1301. https://doi.org/10.2967/jnumed.122.264183.

(190) Hennrich, U.; Benešová, M. [^{68}Ga]Ga-DOTA-TOC: The First FDA-Approved ^{68}Ga-Radiopharmaceutical for PET Imaging. *Pharmaceuticals* **2020**, *13* (3), 1–12. https://doi.org/10.3390/ph13030038.

(191) Hennrich, U.; Eder, M. [^{68}Ga]Ga-PSMA-11: The First FDA-Approved ^{68}Ga-Radiopharmaceutical for PET Imaging of Prostate Cancer. *Pharmaceuticals* **2021**, *14* (8), 1–12. https://doi.org/10.3390/ph14080713.

(192) Ashhar, Z.; Ahmad Fadzil, M. F.; Othman, M. F.; Yusof, N. A.; Abdul Onny, M. A.; Mat Ail, N.; Abd Rahman, S. F. Cyclotron Production of Gallium-68 Radiopharmaceuticals Using the ^{68}Zn(p,n)^{68}Ga Reaction and Their Regulatory Aspects. *Pharmaceutics* **2022**, *15* (1), 1–21. https://doi.org/10.3390/pharmaceutics15010070.

(193) Kumar, K. The Current Status of the Production and Supply of Gallium-68. *Cancer Biother Radiopharm* **2020**, *35* (3), 163–166. https://doi.org/10.1089/cbr.2019.3301.

(194) Thisgaard, H.; Kumlin, J.; Langkjær, N.; Chua, J.; Hook, B.; Jensen, M.; Kassaian, A.; Zeisler, S.; Borjian, S.; Cross, M.; Schaffer, P.; Dam, J. H. Multi-Curie Production of Gallium-68 on a Biomedical Cyclotron and Automated Radiolabelling of PSMA-11 and DOTATATE. *EJNMMI Radiopharm Chem* **2021**, *6* (1), 1–11. https://doi.org/10.1186/s41181-020-00114-9.

(195) Delpassand, E. S.; Ranganathan, D.; Wagh, N.; Shafie, A.; Gaber, A.; Abbasi, A.; Kjaer, A.; Tworowska, I.; Núñez, R. 64Cu-DOTATATE PET/CT for Imaging Patients with Known or Suspected Somatostatin Receptor–Positive Neuroendocrine Tumors: Results of the First U.S. Prospective, Reader-Masked Clinical Trial. *Journal of Nuclear Medicine* **2020**, *61* (6), 890–896. https://doi.org/10.2967/jnumed.119.236091.

(196) Liu, T.; Redalen, K. R.; Karlsen, M. Development of an Automated Production Process of [^{64}Cu][Cu (ATSM)] for Positron Emission Tomography Imaging and Theranostic Applications. *J Labelled Comp Radiopharm* **2022**, *65* (7), 191–202. https://doi.org/10.1002/jlcr.3973.

(197) Jauregui-Osoro, M.; De Robertis, S.; Halsted, P.; Gould, S. M.; Yu, Z.; Paul, R. L.; Marsden, P. K.; Gee, A. D.; Fenwick, A.; Blower, P. J. Production of Copper-64 Using a Hospital Cyclotron: Targetry, Purification and Quality Analysis. *Nucl Med Commun* **2021**, *42* (9), 1024–1038. https://doi.org/10.1097/mnm.0000000000001422.

(198) Aslam, M. N.; Sudár, S.; Hussain, M.; Malik, A. A.; Shah, H. A.; Qaim, S. M. Charged Particle Induced Reaction Cross Section Data for Production of the Emerging Medically Important Positron Emitter ^{64}Cu: A Comprehensive Evaluation. *Radiochim Acta* **2009**, *97* (12), 669–686. https://doi.org/10.1524/ract.2009.1670.

(199) *Stable Isotope Prices | Institute for Rare Earths and Metals*. https://en.institut-seltene-erden.de/unser-service-2/metall-preise/preise-fuer-stabile-isotope/.

(200) Nelson, B. J. B.; Leier, S.; Wilson, J.; Wuest, M.; Doupe, J.; Andersson, J. D.; Wuest, F. ^{64}Cu Production via the ^{68}Zn(p,α)^{64}Cu Nuclear Reaction: An Untapped, Cost-Effective and High Energy Production Route. *Nucl Med Biol* **2024**, *128*, 1–12. https://doi.org/10.1016/j.nucmedbio2024.108875.

(201) Meyer, C.; Szidonya, L.; Winters, C.; Mench, A.; Mallak, N.; Mittra, E. Quantitative Imaging for ^{177}Lu-PSMA Treatment Response Monitoring and Dosimetry. *Frontiers in Nuclear Medicine* **2023**, *3*, 1–8. https://doi.org/10.3389/fnume.2023.1291253.

(202) Jung, N.; Aga, N.; Lu, M.; Uribe, C.; Colpo, N. Whole Body and SPECT/CT Imaging for Dosimetry of ^{177}Lu-Labeled Radiopharmaceutical Therapies: A Technologist's Perspective. *Journal of Nuclear Medicine* **2022**, *63* (Suppl. 2), 4103.

(203) Toderas, L.; Chen, D.; Iravani, A.; Scherzer, Z.; Erickson, M.; Miyaoka, R. Clinical Implementation of Lu-177 PSMA Therapy, Including SPECT/CT Imaging Post Therapy. *Journal of Nuclear Medicine* **2023**, *64* (Suppl. 1), T56.

(204) Peters, S. M. B.; Hofferber, R.; Privé, B. M.; de Bakker, M.; Gotthardt, M.; Janssen, M.; de Lange, F.; Muselaers, C. H. J.; Mehra, N.; Witjes, J. A.; Costa, P. F.; Nagarajah, J.; Konijnenberg, M. W.; Jentzen, W. [^{68}Ga]Ga-PSMA-11 PET Imaging as a Predictor for Absorbed Doses in Organs at Risk and Small Lesions in [^{177}Lu]Lu-PSMA-617 Treatment. *Eur J Nucl Med Mol Imaging* **2022**, *49* (4), 1101–1112. https://doi.org/10.1007/s00259-021-05538-2.

(205) Ghodsirad, M. A.; Pirayesh, E.; Akbarian, R.; Javanmard, B.; Kaghazchi, F.; Tavakoli, M.; Fattahi, K. Diagnostic Utility of Lutetium-177 (Lu-177) Prostate-Specific Membrane Antigen (PSMA) Scintigraphy In Prostate Cancer Patients With PSA Rise And Negative Conventional Imaging. *Urol J* **2020**, *17* (4), 374–378. https://doi.org/10.22037/uj.v0i0.5451.

(206) Mejia, A.; Vivian, E.; Nwogu, C.; Shah, J.; Longoria, R.; Vo, A.; Shahin, I.; Verma, J.; Bageac, A. Peptide Receptor Radionuclide Therapy Implementation and Results in a Predominantly Gastrointestinal Neuroendocrine Tumor Population. *Medicine* **2022**, *101* (9), 1–8. https://doi.org/10.1097/md.0000000000028970.

(207) Singh, S.; Halperin, D. M.; Myrehaug, S.; Herrmann, K.; Pavel, M.; Kunz, P. L.; Chasen, B.; Capdevila, J.; Tafuto, S.; Oh, D.-Y.; Yoo, C.; Falk, S.; Halfdanarson, T. R.; Folitar, I.; Zhang, Y.; Santoro, P.; Aimone, P.; de Herder, W. W.; Ferone, D. [^{177}Lu]Lu-DOTA-TATE plus Long-Acting Octreotide versus High-dose Long-Acting Octreotide for the Treatment of Newly Diagnosed, Advanced Grade 2–3, Well-Differentiated, Gastroenteropancreatic Neuroendocrine Tumours (NETTER-2): An Open-Label, Randomised, Phase 3 Study. *The Lancet* **2024**, *403* (10446), 2807–2817. https://doi.org/10.1016/s0140-6736(24)00701-3.

(208) Strosberg, J. R.; Caplin, M. E.; Kunz, P. L.; Ruszniewski, P. B.; Bodei, L.; Hendifar, A.; Mittra, E.; Wolin, E. M.; Yao, J. C.; Pavel, M. E.; Grande, E.; Van Cutsem, E.; Seregni, E.; Duarte, H.; Gericke, G.; Bartalotta, A.; Mariani, M. F.; Demange, A.; Mutevelic, S.; Krenning, E. P. ^{177}Lu-Dotatate plus Long-Acting Octreotide versus High-dose Long-Acting Octreotide in Patients with Midgut Neuroendocrine Tumours (NETTER-1): Final Overall Survival and Long-Term Safety Results from an Open-Label, Randomised, Controlled, Phase 3 Trial. *Lancet Oncol* **2021**, *22* (12), 1752–1763. https://doi.org/10.1016/s1470-2045(21)00572-6.

(209) Felber, V. B.; Valentin, M. A.; Wester, H. J. Design of PSMA Ligands with Modifications at the Inhibitor Part: An Approach to Reduce the Salivary Gland Uptake of Radiolabeled PSMA Inhibitors? *EJNMMI Radiopharm Chem* **2021**, *6* (1), 1–24. https://doi.org/10.1186/s41181-021-00124-1.

(210) Vogel, W. V.; van der Marck, S. C.; Versleijen, M. W. J. Challenges and Future Options for the Production of Lutetium-177. *Eur J Nucl Med Mol Imaging* **2021**, *48* (8), 2329–2335. https://doi.org/10.1007/s00259-021-05392-2.

(211) Mario, N.; Kolmayer, A.; Turquet, G.; Vallee, A.; Goethals, P. E. *Co-Ordinated Approach to the Development and Supply of Radionuclides in the EU : Final Report.*; Publications Office of the European Union: Luxembourg, 2021. https://doi.org/10.2833/120792.

(212) Baum, R. P.; Singh, A.; Kulkarni, H. R.; Bernhardt, P.; Rydén, T.; Schuchardt, C.; Gracheva, N.; Grundler, P. V.; Köster, U.; Müller, D.; Pröhl, M.; Zeevaart, J. R.; Schibli, R.; van der Meulen, N. P.; Müller, C. First-in-Humans Application of ^{161}Tb: A Feasibility Study Using ^{161}Tb-DOTATOC. *Journal of Nuclear Medicine* **2021**, *62* (10), 1391–1397. https://doi.org/10.2967/jnumed.120.258376.

(213) Al-Ibraheem, A.; Doudeen, R. M.; Juaidi, D.; Abufara, A.; Maus, S. ^{161}Tb-PSMA Radioligand Therapy: First-in-Humans SPECT/CT Imaging. *Journal of Nuclear Medicine* **2023**, *64* (8), 1322–1323. https://doi.org/10.2967/jnumed.122.265291.

(214) Bernhardt, P.; Svensson, J.; Hemmingsson, J.; van der Meulen, N. P.; Zeevaart, J. R.; Konijnenberg, M. W.; Müller, C.; Kindblom, J. Dosimetric Analysis of the Short-Ranged Particle Emitter ^{161}Tb for Radionuclide Therapy of Metastatic Prostate Cancer. *Cancers (Basel)* **2021**, *13* (9), 1–13. https://doi.org/10.3390/cancers13092011.

(215) Favaretto, C.; Talip, Z.; Borgna, F.; Grundler, P. V.; Dellepiane, G.; Sommerhalder, A.; Zhang, H.; Schibli, R.; Braccini, S.; Müller, C.; van der Meulen, N. P. Cyclotron Production and Radiochemical Purification of Terbium-155 for SPECT Imaging. *EJNMMI Radiopharm Chem* **2021**, *6* (37), 1–17. https://doi.org/10.1186/s41181-021-00153-w.

(216) Rosar, F.; Maus, S.; Schaefer-Schuler, A.; Burgard, C.; Khreish, F.; Ezziddin, S. New Horizons in Radioligand Therapy: ^{161}Tb-PSMA-617 in Advanced MCRPC. *Clin Nucl Med* **2023**, *48* (5), 433–434. https://doi.org/10.1097/rlu.0000000000004589.

(217) Gracheva, N.; Müller, C.; Talip, Z.; Heinitz, S.; Köster, U.; Zeevaart, J. R.; Vögele, A.; Schibli, R.; van der Meulen, N. P. Production and Characterization of No-Carrier-Added ^{161}Tb as an Alternative to the Clinically-Applied ^{177}Lu for Radionuclide Therapy. *EJNMMI Radiopharm Chem* **2019**, *4* (12), 1–16. https://doi.org/10.1186/s41181-019-0063-6.

(218) Mittra, E. S. Neuroendocrine Tumor Therapy: ^{177}Lu-DOTATATE. *American Journal of Roentgenology* **2018**, *211* (2), 278–285. https://doi.org/10.2214/ajr.18.19953.

(219) Prasad, V.; Trikalinos, N.; Hanna, A.; Johnson, F.; Puhlmann, M.; Wahl, R. A Phase I/IIa of [^{212}Pb]VMT-a-NET Targeted Alpha-Particle Therapy for Advanced SSTR2 Positive Neuroendocrine Tumors. *Journal of Nuclear Medicine* **2024**, *65* (Suppl. 2).

(220) Griffiths, M. R.; Pattison, D. A.; Latter, M.; Kuan, K.; Taylor, S.; Tieu, W.; Kryza, T.; Meyrick, D.; Quan Lee, B.; Hansen, A.; Rose, S. E.; Puttick, S. G.; Rose, S. First-in-Human ^{212}Pb-PSMA-Targeted a-Therapy SPECT/CT Imaging in a Patient with Metastatic Castration-Resistant Prostate Cancer. *Journal of Nuclear Medicine* **2024**, *65* (4), 664. https://doi.org/10.2967/jnumed.123.267189.

(221) Kukleva, E.; Kozempel, J.; Vlk, M.; Mičolová, P.; Vopálka, D. Preparation of ^{227}Ac/^{223}Ra by Neutron Irradiation of ^{226}Ra. *J Radioanal Nucl Chem* **2015**, *304* (1), 263–266. https://doi.org/10.1007/s10967-014-3432-3.

(222) Hogle, S.; Boll, R. A.; Murphy, K.; Denton, D.; Owens, A.; Haverlock, T. J.; Garland, M.; Mirzadeh, S. Reactor Production of Thorium-229. *Applied Radiation and Isotopes* **2016**, *114*, 19–27. https://doi.org/10.1016/j.apradiso.2016.05.002.

(223) Andreoletti, G.; Belieres, M.; Nardoux, P.; Moulin, J.-P.; Montaletang, A.; Bourdet, P. Production of Thorium-228 Starting from a Natural Thorium Salt. US 8,221,520B2, July 17, 2012. https://patents.google.com/patent/US8221520B2/en.

(224) *DOE Isotope Program Announces Availability of Radium-224/Lead-212 Generators | NIDC: National Isotope Development Center*. https://www.isotopes.gov/node/123.

(225) Kamaleshwaran, K.; Suneelkumar, M.; Madhusairam, R.; Radhakrishnan, E.; Arunpandiyan, S.; Arnold, V. Whole-Body and Single-Photon Emission Computed Tomography/Computed Tomography Postpeptide Receptor Alpha Radionuclide Therapy Images of Actinium-225-Tetraazacyclododecanetetraacetic Acid–Octreotide as a Primary Modality of Treatment in a Patient with Advanced Rectal Neuroendocrine Tumor with Metastases. *Indian Journal of Nuclear Medicine* **2020**, *35* (3), 226–228. https://doi.org/10.4103/ijnm.ijnm_58_20.

(226) Tulik, M.; Kuliński, R.; Tabor, Z.; Brzozowska, B.; Łaba, P.; Bruchertseifer, F.; Morgenstern, A.; Królicki, L.; Kunikowska, J. Quantitative SPECT/CT Imaging of Actinium-225 for Targeted Alpha Therapy of Glioblastomas. *EJNMMI Phys* **2024**, *11* (41), 1–17. https://doi.org/10.1186/s40658-024-00635-1.

(227) Robertson, A. K. H.; Ramogida, C. F.; Rodríguez-Rodríguez, C.; Blinder, S.; Kunz, P.; Sossi, V.; Schaffer, P. Multi-Isotope SPECT Imaging of the ^{225}Ac Decay Chain: Feasibility Studies. *Phys Med Biol* **2017**, *62* (11), 4406–4420. https://doi.org/10.1088/1361-6560/aa6a99.

(228) Morris, M. J.; Sartor, A. O.; Wong, J. Y. C.; Max, S. I.; Xie, H.; Russell, M.; Divgi, C. R.; Patricia, D.; Avadhani, A. N.; Nordquist, L. T. Phase 1 Study of JNJ-69086420, an Actinium-225-Labeled Antibody Targeting Human Kallikrein-2, for Advanced Prostate Cancer. *Journal of Clinical Oncology* **2022**, *40* (Suppl. 6). https://doi.org/10.1200/jco.2022.40.6_suppl.tps206.

(229) Sava, J. *JNJ-6420 Shows Early Signs of Efficacy With Safety Considerations in mCRPC*. https://www.targetedonc.com/view/jnj-6420-shows-early-signs-of-efficacy-with-safety-considerations-in-mcrpc.

(230) Sathekge, M.; Bruchertseifer, F.; Knoesen, O.; Reyneke, F.; Lawal, I.; Lengana, T.; Davis, C.; Mahapane, J.; Corbett, C.; Vorster, M.; Morgenstern, A. ^{225}Ac-PSMA-617 in Chemotherapy-Naive Patients with Advanced Prostate Cancer: A Pilot Study. *Eur J Nucl Med Mol Imaging* **2019**, *46*, 129–138. https://doi.org/10.1007/s00259-018-4167-0.

(231) Alvarez, R. Managing the Uranium-233 Stockpile of the United States. *Science & Global Security* **2013**, *21* (1), 53–69. https://doi.org/10.1080/08929882.2013.754311.

(232) Robertson, A. K. H.; Ramogida, C. F.; Schaffer, P.; Radchenko, V. Current Radiopharmaceuticals Development of ^{225}Ac Radiopharmaceuticals: TRIUMF Perspectives and Experiences. *Curr Radiopharm* **2018**, *11* (3), 156–172. https://doi.org/10.2174/1874471011666180416161908.

(233) *Multiple Production Methods Underway to Provide Actinium-225 | NIDC: National Isotope Development Center*. https://www.isotopes.gov/information/actinium-225.

(234) Grimm, T.; Grimm, A.; Peters, W.; Zamiara, M. High-Purity Actinium-225 Production from Radium-226 Using a Superconducting Electron Linac. *J Med Imaging Radiat Sci* **2019**, *50* (1), 12–13. https://doi.org/10.1016/j.jmir.2019.11.045.

(235) Melville, G.; J Allen, B. Cyclotron and Linac Production of Ac-225. *Applied Radiation and Isotopes* **2009**, *67* (4), 549–555. https://doi.org/10.1016/j.apradiso.2008.11.012.

(236) *Actinium-225 | NorthStar Medical Radioisotopes, LLC*. https://www.northstarnm.com/radiopharmaceutical-therapy/actinium-225/.

(237) Barca, C.; Griessinger, C. M.; Faust, A.; Depke, D.; Essler, M.; Windhorst, A. D.; Devoogdt, N.; Brindle, K. M.; Schäfers, M.; Zinnhardt, B.; Jacobs, A. H. Expanding Theranostic Radiopharmaceuticals for Tumor Diagnosis and Therapy. *Pharmaceuticals* **2022**, *15* (13), 1–20. https://doi.org/10.3390/ph15010013.

(238) Price, E. W.; Orvig, C. Matching Chelators to Radiometals for Radiopharmaceuticals. *Chem Soc Rev* **2014**, *43* (1), 260–290. https://doi.org/10.1039/c3cs60304k.

(239) Carbo-Bague, I.; Ramogida, C. F. Emerging Therapeutic Radiopharmaceuticals and Their Theranostic Pairs. *Encyclopedia of Inorganic and Bioinorganic Chemistry* **2021**, 1–34. https://doi.org/10.1002/9781119951438.eibc2763.

(240) National Nuclear Data Center. *Nudat 2.8*. Nuclear Structure and Decay Data. https://www.nndc.bnl.gov/nudat3/chartNuc.jsp.

(241) Yong, K.; Brechbiel, M. Application of ^{212}Pb for Targeted α-Particle Therapy (TAT): Pre-Clinical and Mechanistic Understanding through to Clinical Translation. *AIMS Med Sci* **2015**, *2* (3), 228–245. https://doi.org/10.3934/medsci.2015.3.228.

(242) Coenen, H. H.; Gee, A. D.; Adam, M.; Antoni, G.; Cutler, C. S.; Fujibayashi, Y.; Jeong, J. M.; Mach, R. H.; Mindt, T. L.; Pike, V. W.; Windhorst, A. D. Open Letter to Journal Editors on: International Consensus Radiochemistry Nomenclature Guidelines. *Ann Nucl Med* **2018**, *32* (3), 236–238. https://doi.org/10.1007/s12149-018-1238-z.

(243) Luurtsema, G.; Pichler, V.; Bongarzone, S.; Seimbille, Y.; Elsinga, P.; Gee, A.; Vercouillie, J. EANM Guideline for Harmonisation on Molar Activity or Specific Activity of Radiopharmaceuticals: Impact on Safety and Imaging Quality. *EJNMMI Radiopharm Chem* **2021**, *6* (34), 1–16. https://doi.org/10.1186/s41181-021-00149-6.

(244) Al-Saleh, F. S.; Al-Harbi, A. A.; Azzam, A. Yield and Excitation Function Measurements of Some Nuclear Reactions on Natural Thallium Induced by Protons Leading to the Production of Medical Radioisotopes 201Tl and 203Pb. *Radiochim Acta* **2007**, *95* (3), 127–132. https://doi.org/10.1524/ract.2007.95.3.127.

(245) Qaim, S. M.; Weinreich, R.; Ollig, H. Production of Thallium-201 and Lead-203 via Proton Induced Nuclear Reactions on Natural Thallium. *International Journal of Applied Radiation and Isotopes* **1979**, *30* (2), 85–95. https://doi.org/10.1016/0020-708x(79)90138-8.

(246) Azzam, A.; Said, S. A.; Al-abyad, M. Evaluation of Different Production Routes for the Radio Medical Isotope ^{203}Pb Using TALYS 1.4 and EMPIRE 3.1 Code Calculations. *Applied Radiation and Isotopes* **2014**, *91*, 109–113. https://doi.org/10.1016/j.apradiso.2014.05.009.

(247) Prohaska, T.; Irrgeher, J.; Benefield, J.; Böhlke, J. K.; Chesson, L. A.; Coplen, T. B.; Ding, T.; Dunn, P. J. H.; Gröning, M.; Holden, N. E.; Meijer, H. A. J.; Moossen, H.; Possolo, A.; Takahashi, Y.; Vogl, J.; Walczyk, T.; Wang, J.; Wieser, M. E.; Yoneda, S.; Zhu, X. K.; Meija, J. Standard Atomic Weights of the Elements 2021 (IUPAC Technical Report). *Pure and Applied Chemistry* **2022**, *94* (5), 573–600. https://doi.org/10.1515/pac-2019-0603.

(248) Winkel, P.; De Vis, L.; Vreese, M.; Wageneer, R.; Schrijver, A.; Arzumanov, A.; Gorodiskaya, N.; Zheltov, P. *Standardized High Current Solid Targets for Cyclotron Production of Diagnostic And Therapeutic Radionuclides: Technical Reports No. 432*; 2005.

(249) Li, M., Zhang, X., Quinn, T., Lee, D., Liu, D., Kunkel, F., Zimmerman, B., McAlister, D., Olewein, K., Menda, Y., Mirzadeh, S., Copping, R., Johnson, F., Schultz, M. Automated Cassette-Based Production of High Specific Activity [$^{203/212}$Pb] Peptide-Based Theranostic Radiopharmaceuticals for Image-Guided Radionuclide Therapy for Cancer. *Applied Radiation and Isotopes* **2017**, *127*, 52–60. https://doi.org/10.1016/j.apradiso.2017.05.006.

(250) Máthé, D.; Szigeti, K.; Hegedűs, N.; Horváth, I.; Veres, D. S.; Kovács, B.; Szűcs, Z. Production and in Vivo Imaging of 203Pb as a Surrogate Isotope for *In Vivo* ^{212}Pb Internal Absorbed Dose Studies. *Applied Radiation and Isotopes* **2016**, *114*, 1–6. https://doi.org/10.1016/j.apradiso.2016.04.015.

(251) McDonagh, A. W.; McNeil, B. L.; Patrick, B. O.; Ramogida, C. F. Synthesis and Evaluation of Bifunctional [2.2.2]-Cryptands for Nuclear Medicine Applications. *Inorg Chem* **2021**, *60* (13), 10030–10037. https://doi.org/10.1021/acs.inorgchem.1c01274.

(252) Zeisler, S.; Clarke, B.; Kumlin, J.; Hook, B.; Varah, S.; Hoehr, C. A Compact Quick-Release Solid Target System for the TRIUMF TR13 Cyclotron. *Instruments* **2019**, *3* (1), 1–8. https://doi.org/10.3390/instruments3010016.

(253) Laxdal, R. E.; Altman, A.; Kuo, T. Beam Measurements on a Small Commercial Cyclotron. In *European Particle Accelerator Conference*; London, 1994; pp 545–547.

(254) *Chemical Book Thallium (I) Nitrate*. https://www.chemicalbook.com/ChemicalProductProperty_EN_CB6111526.htm.

(255) Nagaraja, P.; Al-Tayar, N. G. S.; Kumar, A. S. Development of a Selective and Sensitive Spectrophotometric Method for the Trace Determination of Thallium(III) Using 3-Methyl-2-Benzothiazolinone Hydrazone Hydrochloride and N-(1-Naphthyl)-Ethylenediamine Dihydrochloride. *J AOAC Int* **2008**, *91* (5), 1116–1123. https://doi.org/10.1093/jaoac/91.5.1116.

(256) Okoye, N. C.; Baumeister, J. E.; Khosroshahi, F. N.; Hennkens, H. M.; Jurisson, S. S. Chelators and Metal Complex Stability for Radiopharmaceutical Applications. *Radiochim Acta* **2019**, *107* (9), 1087–1120. https://doi.org/10.1515/ract-2018-3090.

(257) Zukotynski, K.; Jadvar, H.; Capala, J.; Fahey, F. Targeted Radionuclide Therapy: Practical Applications and Future Prospects. *Biomark Cancer* **2016**, *8* (Suppl. 2), 35–38. https://doi.org/10.4137/bic.s31804.

(258) Miller, C.; Rousseau, J.; Ramogida, C. F.; Celler, A.; Rahmim, A.; Uribe, C. F. Implications of Physics, Chemistry and Biology for Dosimetry Calculations Using Theranostic Pairs. *Theranostics* **2022**, *12* (1), 232–259. https://doi.org/10.7150/thno.62851.

(259) Ballinger, J. R. Theranostic Radiopharmaceuticals: Established Agents in Current Use. *British Journal of Radiology* **2018**, *91*, 1–8. https://doi.org/10.1259/bjr.20170969.

(260) Rösch, F.; Herzog, H.; Qaim, S. M. The Beginning and Development of the Theranostic Approach in Nuclear Medicine, as Exemplified by the Radionuclide Pair ^{86}Y and ^{90}Y. *Pharmaceuticals* **2017**, *10* (2), 1–28. https://doi.org/10.3390/ph10020056.

(261) Delpassand, E. S.; Tworowska, I.; Esfandiari, R.; Torgue, J.; Hurt, J.; Shafie, A.; Núñez, R. Targeted Alpha-Emitter Therapy With ^{212}Pb-DOTAMTATE for the Treatment of Metastatic SSTR-Expressing Neuroendocrine Tumors: First-in-Human, Dose-Escalation Clinical Trial. *Journal of Nuclear Medicine* **2022**, *63* (9), 1326–1333. https://doi.org/10.2967/jnumed.121.263230.

(262) Banerjee, S. R.; Pullambhatla, M.; Foss, C. A.; Falk, A.; Byun, Y.; Nimmagadda, S.; Mease, R. C.; Pomper, M. G. Effect of Chelators on the Pharmacokinetics of ^{99m}Tc-Labeled Imaging Agents for the Prostate-Specific Membrane Antigen (PSMA). *J Med Chem* **2013**, *56* (15), 6108–6121. https://doi.org/10.1021/jm400823w.

(263) Hancock, R. D.; Martell, A. E. Ligand Design for Selective Complexation of Metal Ions in Aqueous Solution. *Chem. Rev* **1989**, *89* (8), 1875–1914. https://doi.org/10.1021/cr00098a011.

(264) Pearson, R. G. Hard and Soft Acids and Bases. *J Am Chem Soc* **1963**, *85* (22), 3533–3539. https://doi.org/10.1021/ja00905a001.

(265) Pearson, R. G. Hard and Soft Acids and Bases, HSAB, Part I: Fundamental Principles. *J Chem Educ* **1968**, *45* (9), 581–587. https://doi.org/10.1021/ed045p581.

(266) Pearson, R. G. Hard and Soft Acids and Bases, HSAB, Part II: Underlying Theories. *J Chem Educ* **1968**, *45* (10), 643–648. https://doi.org/10.1021/ed045p643.

(267) Chappell, L. L.; Dadachova, E.; Milenic, D. E.; Garmestani, K.; Wu, C.; Brechbiel, M. W. Synthesis, Characterization, and Evaluation of a Novel Bifunctional Chelating Agent for the Lead Isotopes ^{203}Pb and ^{212}Pb. *Nucl Med Biol* **2000**, *27* (1), 93–100. https://doi.org/10.1016/s0969-8051(99)00086-4.

(268) Holbein, B. E.; Ang, M. T. C.; Allan, D. S.; Chen, W.; Lehmann, C. Iron-Withdrawing Anti-Infectives for New Host-Directed Therapies Based on Iron Dependence, the Achilles' Heel of Antibiotic-Resistant Microbes. *Environ Chem Lett* **2021**, *19* (4), 2789–2808. https://doi.org/10.1007/s10311-021-01242-7.

(269) Gode, F.; Pehlivan, E. A Comparative Study of Two Chelating Ion-Exchange Resins for the Removal of Chromium(III) from Aqueous Solution. *J Hazard Mater* **2003**, *100* (1), 231–243. https://doi.org/10.1016/s0304-3894(03)00110-9.

(270) Ferreirós-Martínez, R.; Esteban-Gómez, D.; Tóth, E.; De Blas, A.; Platas-Iglesias, C.; Rodríguez-Blas, T. Macrocyclic Receptor Showing Extremely High Sr(II)/Ca(II) and Pb(II)/ Ca(II) Selectivities with Potential Application in Chelation Treatment of Metal Intoxication. *Inorg Chem* **2011**, *50* (8), 3772–3784. https://doi.org/10.1021/ic200182e.

(271) Damu, K. V.; Shaikjee, M. S.; Michael, J. P.; Howard, A. S.; Hancock, R. D. Control of Metal Ion Selectivity in Ligands Containing Neutral Oxygen and Pyridyl Groups. *Inorg Chem* **1986**, *25* (22), 3879–3883. https://doi.org/10.1021/ic00242a010.

(272) Tétard, D.; Rabion, A.; Verlhac, J. B.; Guilhem, J. Alkane Hydroxylation by a Manganese Analogue of the Iron Core from Methane Monooxygenase. *J Chem Soc Chem Commun* **1995**, No. 5, 531–532. https://doi.org/10.1039/c39950000531.

(273) Bu, X.-H.; Cao, X.-C.; Zhang, W.-Q.; Zhang, R.-H. A New Tetraazamacrocycle Functionalized with Pendant Pyridyl Groups : Synthesis and Crystal Structure of a Copper (II) Complex Of. *Transition Metal Chemistry* **1997**, *22*, 513–515. https://doi.org/10.1023/a:1018527716715.

(274) Morfin, J. F.; Tripier, R.; Baccon, M. Le; Handel, H. Bismuth(III) Complexes with Tetra-Pyridylmethyl-Cyclen. *Inorganica Chim Acta* **2009**, *362* (6), 1781–1786. https://doi.org/10.1016/j.ica.2008.08.013.

(275) Wilson, J. J.; Birnbaum, E. R.; Batista, E. R.; Martin, R. L.; John, K. D. Synthesis and Characterization of Nitrogen-Rich Macrocyclic Ligands and an Investigation of Their Coordination Chemistry with Lanthanum(III). *Inorg Chem* **2015**, *54* (1), 97–109. https://doi.org/10.1021/ic501843c.

(276) Wilson, J. J.; Ferrier, M.; Radchenko, V.; Maassen, J. R.; Engle, J. W.; Batista, E. R.; Martin, R. L.; Nortier, F. M.; Fassbender, M. E.; John, K. D.; Birnbaum, E. R. Evaluation of Nitrogen-Rich Macrocyclic Ligands for the Chelation of Therapeutic Bismuth Radioisotopes. *Nucl Med Biol* **2015**, *42* (5), 428–438. https://doi.org/10.1016/j.nucmedbio.2014.12.007.

(277) Yang, H.; Zhang, C.; Yuan, Z.; Rodriguez-Rodriguez, C.; Robertson, A.; Radchenko, V.; Perron, R.; Gendron, D.; Causey, P.; Gao, F.; Bénard, F.; Schaffer, P. Synthesis and Evaluation of a Macrocyclic Actinium-225 Chelator, Quality Control and In Vivo Evaluation of ^{225}Ac-Crown-AMSH Peptide. *Chemistry - A European Journal* **2020**, *26* (50), 11435–11440. https://doi.org/10.1002/chem.202002999.

(278) Altomare, A.; Cascarano, G.; Giacovazzo, C.; Guagliardi, A. Completion and Refinement of Crystal Structures with SIR92. *J Appl Crystallogr* **1993**, *26* (3), 343–350. https://doi.org/10.1107/s0021889892010331.

(279) Altomare, A.; Burla, M. C.; Camalli, M.; Cascarano, G. L.; Giacovazzo, C.; Guagliardi, A.; Moliterni, A. G. G.; Polidori, G.; Spagna, R. SIR97: A New Tool for Crystal Structure Determination and Refinement. *J Appl Crystallogr* **1999**, *32* (1), 115–119. https://doi.org/10.1107/s0021889898007717.

(280) Farrugia, L. J. WinGX Suite for Small-Molecule Single-Crystal Crystallography. *J Appl Crystallogr* **1999**, *32* (4), 837–838. https://doi.org/10.1107/s0021889899006020.

(281) Sweeton, F. H.; Mesmer, R. E.; Baes, C. F. Acidity Measurements at Elevated Temperatures. VII. Dissociation of Water. *J Solution Chem* **1974**, *3*, 191–214. https://doi.org/10.1007/bf00645633.

(282) Gans, P.; O'Sullivan, B. GLEE, a New Computer Program for Glass Electrode Calibration. *Talanta* **2000**, *51* (1), 33–37. https://doi.org/10.1016/s0039-9140(99)00245-3.

(283) Gans, P.; Sabatini, A.; Vacca, A. Investigation of Equilibria in Solution. Determination of Equilibrium Constants with the HYPERQUAD Suite of Programs. *Talanta* **1996**, *43* (10), 1739–1753. https://doi.org/https://doi.org/10.1016/0039-9140(96)01958-3.

(284) Swidan, A.; Macdonald, C. L. B. Polyether Complexes of Groups 13 and 14. *Chem Soc Rev* **2016**, *45* (14), 3883–3915. https://doi.org/10.1039/c5cs00934k.

(285) Steed, J. W. First- and Second-Sphere Coordination Chemistry of Alkali Metal Crown Ether Complexes. *Coord Chem Rev* **2001**, *215* (1), 171–221. https://doi.org/10.1016/s0010-8545(01)00317-4.

(286) Shannon, R. D. Revised Effective Ionic Radii and Systematic Studies of Interatomie Distances in Halides and Chaleogenides. *Acta Cryst* **1976**, *32*, 751–767. https://doi.org/10.1107/S0567739476001551.

(287) Bird, C. W.; Cheeseman, G. W. H. Structure of Five-Membered Rings with One Heteroatom. *Comprehensive Heterocyclic Chemistry* **1984**, *4*, 1–38. https://doi.org/10.1016/b978-008096519-2.00051-5.

(288) Hancock, R. D. Chelate Ring Size and Metal Ion Selection: The Basis of Selectivity for Metal Ions in Open-Chain Ligands and Macrocycles. *J Chem Educ* **1992**, *69* (8), 615–621. https://doi.org/10.1021/ed069p615.

(289) Shimoni-Livny, L.; Glusker, J. P.; Bock, C. W. Lone Pair Functionality in Divalent Lead Compounds. *Inorg Chem* **1998**, *37* (8), 1853–1867. https://doi.org/10.1021/ic970909r.

(290) Ingham, A.; Kostelnik, T. I.; McNeil, B. L.; Patrick, B. O.; Choudhary, N.; Jaraquemada-Peláez, M. de G.; Orvig, C. Getting a Lead on Pb^{2+}-Amide Chelators for $^{203/212}Pb$ Radiopharmaceuticals. *Dalton Transactions* **2021**, *50* (33), 11579–11595. https://doi.org/10.1039/d1dt01653a.

(291) Maumela, H.; Hancock, R. D.; Carlton, L.; Reibenspies, J. H.; Wainwright, K. P. The Amide Oxygen as a Donor Group. Metal Ion Complexing Properties of Tetra-A-Acetamide Substituted Cyclen: A Crystallographic, NMR, Molecular Mechanics, and Thermodynamic Study. *J Am Chem Soc* **1995**, *117* (25), 6698–6707. https://doi.org/10.1021/ja00130a008.

(292) Tosato, M.; Lazzari, L.; Marco, V. Di. Revisiting Lead(II)-1,4,7,10-Tetraazacyclododecane-1,4,7,10-Tetraacetic Acid Coordination Chemistry in Aqueous Solutions: Evidence of an Underestimated Thermodynamic Stability. *ACS Omega* **2022**, *7* (18), 15596–15602. https://doi.org/10.1021/acsomega.2c00387.

(293) Chaves, S.; Delgado, R.; Da Silva, J. J. R. F. The Stability of the Metal Complexes of Cyclic Tetra-Aza Tetra-Acetic Acids. *Talanta* **1992**, *39* (3), 249–254. https://doi.org/10.1016/0039-9140(92)80028-C.

(294) Wang, X.; Zhang, X.; Lin, J.; Chen, J.; Xu, Q.; Guo, Z. DNA-Binding Property and Antitumor Activity of Bismuth(III) Complex with 1,4,7,10-Tetrakis(2-Pyridylmethyl)-1,4,7,10-Tetraazacyclododecane. *Dalton Transactions* **2003**, No. 12, 2379–2380. https://doi.org/10.1039/b305290g.

(295) Fallah, J.; Agrawal, S.; Gittleman, H.; Fiero, M. H.; Subramaniam, S.; John, C.; Chen, W.; Ricks, T. K.; Niu, G.; Fotenos, A.; Wang, M.; Chiang, K.; Pierce, W. F.; Suzman, D. L.; Tang, S.; Pazdur, R.; Amiri-Kordestani, L.; Ibrahim, A.; Kluetz, P. G. FDA Approval Summary: Lutetium Lu-177 Vipivotide Tetraxetan for Patients with Metastatic Castration-Resistant Prostate Cancer. *Clin Cancer Res* **2023**, *29* (9), 1651–1657. https://doi.org/10.1158/1078-0432.ccr-22-2875.

(296) *FDA approves lutetium Lu 177 dotatate for pediatric patients 12 years and older with GEP-NETS | FDA*. https://www.fda.gov/drugs/resources-information-approved-drugs/fda-approves-lutetium-lu-177-dotatate-pediatric-patients-12-years-and-older-gep-nets.

(297) Holik, H. A.; Ibrahim, F. M.; Elaine, A. A.; Putra, B. D.; Achmad, A.; Kartamihardja, A. H. S. The Chemical Scaffold of Theranostic Radiopharmaceuticals: Radionuclide, Bifunctional Chelator, and Pharmacokinetics Modifying Linker. *Molecules* **2022**, *27* (10), 1–34. https://doi.org/10.3390/molecules27103062.

(298) Chaturvedi, S.; Mishra, A. K. Vectors for the Delivery of Radiopharmaceuticals in Cancer Therapeutics. *Ther Deliv* **2014**, *5* (8), 893–912. https://doi.org/10.4155/tde.14.57.

(299) Miller, C.; Rousseau, J.; Ramogida, C. F.; Celler, A.; Rahmim, A.; Uribe, C. F. Implications of Physics, Chemistry and Biology for Dosimetry Calculations Using Theranostic Pairs. *Theranostics* **2022**, *12* (1), 232–259. https://doi.org/10.7150/thno.62851.

(300) Burkett, B. J.; Bartlett, D. J.; McGarrah, P. W.; Lewis, A. R.; Johnson, D. R.; Berberoğlu, K.; Pandey, M. K.; Packard, A. T.; Halfdanarson, T. R.; Hruska, C. B.; Johnson, G. B.; Kendi, A. T. A Review of Theranostics: Perspectives on Emerging Approaches and Clinical Advancements. *Radiol Imaging Cancer* **2023**, *5* (4), 1–16. https://doi.org/10.1148/rycan.220157.

(301) Carbo-Bague, I.; Ramogida, C. F. Emerging Therapeutic Radiopharmaceuticals and Their Theranostic Pairs. *Encyclopedia of Inorganic and Bioinorganic Chemistry* **2021**, 1–34. https://doi.org/10.1002/9781119951438.eibc2763.

(302) Ramogida, C. F.; Orvig, C. Tumour Targeting with Radiometals for Diagnosis and Therapy. *Chemical Communications* **2013**, *49* (42), 4720–4739. https://doi.org/10.1039/c3cc41554f.

(303) Sharma, S.; Pandey, M. K. Radiometals in Imaging and Therapy: Highlighting Two Decades of Research. *Pharmaceuticals* **2023**, *16* (10), 1–44. https://doi.org/10.3390/ph16101460.

(304) Hernandez, R.; Aluicio-Sarduy, E.; Grudzinski, J.; Pinchuk, A.; Engle, J.; Weichert, J. Choice of Radiometal Influences the Tumor Targeting and Biodistribution Properties of Theranostic Alkylphosphocholine Chelates in Vivo. *Journal of Nuclear Medicine* **2018**, *59* (Suppl. 1), 533.

(305) McNeil, B. L.; Ramogida, C. F. From Cyclotrons to Chromatography and Beyond: A Guide to the Production and Purification of Theranostic Radiometals. *Chem Soc Rev* **2024**, *53* (21), 10409–10449. https://doi.org/10.1039/d4cs00802b.

(306) Bauer, D.; Carter, L. M.; Atmane, M. I.; De Gregorio, R.; Michel, A.; Kaminsky, S.; Monette, S.; Li, M.; Schultz, M. K.; Lewis, J. S. ^{212}Pb-Pretargeted Theranostics for Pancreatic Cancer. *J Nucl Med* **2024**, *65*, 109–116. https://doi.org/10.2967/jnumed.123.266388.

(307) Li, M.; Sagastume, E. E.; Lee, D.; Mcalister, D.; Degraffenreid, A. J.; Olewine, K. R.; Graves, S.; Copping, R.; Mirzadeh, S.; Zimmerman, B. E.; Larsen, R.; Johnson, F. L.; Schultz, M. K. $^{203/212}$Pb Theranostic Radiopharmaceuticals for Image-Guided Radionuclide Therapy for Cancer. *Curr Med Chem* **2020**, *27* (41), 7003–7031. https://doi.org/10.2174/0929867327999200727190423.

(308) Abou, D. S.; Thiele, N. A.; Gutsche, N. T.; Villmer, A.; Zhang, H.; Woods, J. J.; Baidoo, K. E.; Escorcia, F. E.; Wilson, J. J.; Thorek, D. L. J. Towards the Stable Chelation of Radium for Biomedical Applications with an 18-Membered Macrocyclic Ligand. *Chem Sci* **2021**, *12* (10), 3733–3742. https://doi.org/10.1039/d0sc06867e.

(309) Raavé, R.; Sandker, G.; Adumeau, P.; Jacobsen, C. B.; Mangin, F.; Meyer, M.; Moreau, M.; Bernhard, C.; Da Costa, L.; Dubois, A.; Goncalves, V.; Gustafsson, M.; Rijpkema, M.; Boerman, O.; Chambron, J. C.; Heskamp, S.; Denat, F. Direct Comparison of the *in Vitro* and *in Vivo* Stability of DFO, DFO* and DFOcyclo* for ^{89}Zr-ImmunoPET. *Eur J Nucl Med Mol Imaging* **2019**, *46* (9), 1966–1977. https://doi.org/10.1007/s00259-019-04343-2.

(310) Eder, A. C.; Schäfer, M.; Schmidt, J.; Bauder-Wüst, U.; Roscher, M.; Leotta, K.; Haberkorn, U.; Kopka, K.; Eder, M. Rational Linker Design to Accelerate Excretion and Reduce Background Uptake of Peptidomimetic PSMA-Targeting Hybrid Molecules. *Journal of Nuclear Medicine* **2021**, *62* (10), 1461–1467. https://doi.org/10.2967/jnumed.120.248443.

(311) Kazuta, N.; Nakashima, K.; Watanabe, H.; Ono, M. Effect of Linker Entities on Pharmacokinetics of ^{111}In-Labeled Prostate-Specific Membrane Antigen-Targeting Ligands with an Albumin Binder. *ACS Pharmacol Transl Sci* **2024**, *7* (8), 2401–2413. https://doi.org/10.1021/acsptsci.4c00257.

(312) Dudchak, R.; Podolak, M.; Holota, S.; Szewczyk-Roszczenko, O.; Roszczenko, P.; Bielawska, A.; Lesyk, R.; Bielawski, K. Click Chemistry in the Synthesis of Antibody-Drug Conjugates. *Bioorg Chem* **2024**, *143*, 1–16. https://doi.org/10.1016/j.bioorg.2023.106982.

(313) Stephanopoulos, N.; Francis, M. B. Choosing an Effective Protein Bioconjugation Strategy. *Nat Chem Biol* **2011**, *7* (12), 876–884. https://doi.org/10.1038/nchembio.720.

(314) Kalia, J.; Raines, R. T. Advances in Bioconjugation. *Curr Org Chem* **2009**, *14* (2), 138–147. https://doi.org/10.2174/138527210790069839.

(315) Ravasco, J. M. J. M.; Faustino, H.; Trindade, A.; Gois, P. M. P. Bioconjugation with Maleimides: A Useful Tool for Chemical Biology. *Chemistry: A European Journal* **2019**, *25* (1), 43–59. https://doi.org/10.1002/chem.201803174.

(316) Fan, J.; Toth, I.; Stephenson, R. J. Bioconjugated Materials in the Development of Subunit Vaccines. In *Comprehensive Analytical Chemistry*; Verma, S., Das, A., Eds.; Elsevier, 2023; Vol. 103, pp 59–103. https://doi.org/10.1016/bs.coac.2023.02.005.

(317) Vizier, R.; Adumeau, P.; Moreau, M.; Goncalves, V.; Denat, F. Moving Beyond Isothiocyanates: A Look at the Stability of Conjugation Links Toward Radiolysis in ^{89}Zr-Labeled Immunoconjugates. *Bioconjug Chem* **2024**, *35* (5), 633–637. https://doi.org/10.1021/acs.bioconjchem.4c00105.

(318) Onderwater, R. C. A.; Commandeur, J. N. M.; Menge, W. M. P. B.; Vermeulen, N. P. E. Activation of Microsomal Glutathione S-Transferase and Inhibition of Cytochrome P450 1A1 Activity as a Model System for Detecting Protein Alkylation by Thiourea-Containing Compounds in Rat Liver Microsomes. *Chem Res Toxicol* **1999**, *12* (5), 396–402. https://doi.org/10.1021/tx980198p.

(319) Samuelsson, K.; Bergström, M. A.; Jonsson, C. A.; Westman, G.; Karlberg, A.-T. Diphenylthiourea, a Common Rubber Chemical, Is Bioactivated to Potent Skin Sensitizers. *Chem Res Toxicol* **2011**, *24* (1), 35–44. https://doi.org/10.1021/tx100241z.

(320) Mhawech-Fauceglia, P.; Yan, L.; Sharifian, M.; Ren, X.; Liu, S.; Kim, G.; Gayther, S. A.; Pejovic, T.; Lawrenson, K. Stromal Expression of Fibroblast Activation Protein Alpha (FAP) Predicts Platinum Resistance and Shorter Recurrence in Patients with Epithelial Ovarian Cancer. *Cancer Microenvironment* **2014**, *8* (1), 23–31. https://doi.org/10.1007/s12307-014-0153-7.

(321) Kessler, L.; Ferdinandus, J.; Hirmas, N.; Zarrad, F.; Nader, M.; Kersting, D.; Weber, M.; Kazek, S.; Sraieb, M.; Hamacher, R.; Lueckerath, K.; Umutlu, L.; Fendler, W. P.; Rischpler, C. Pitfalls and Common Findings in ^{68}Ga-FAPI PET: A Pictorial Analysis. *Journal of Nuclear Medicine* **2022**, *63* (6), 890–896. https://doi.org/10.2967/jnumed.121.262808.

(322) Al-Ibraheem, A.; Abdlkadir, A. S.; Alalawi, H.; Badarneh, M. ^{68}Ga-FAPI PET/CT Imaging: Unveiling the Hidden Pitfalls. *Clin Nucl Med* **2023**, *48* (11), 965–966. https://doi.org/10.1097/rlu.0000000000004802.

(323) Al-Ibraheem, A. Fibroblast Activation Protein Inhibitor Theranostics: A Huge Opportunity with Its Fair Share of Oncological Pitfalls. *World J Nucl Med* **2024**, *23* (2), 71–72. https://doi.org/10.1055/s-0044-1787886.

(324) Giesel, F. L.; Kratochwil, C.; Schlittenhardt, J.; Dendl, K.; Eiber, M.; Staudinger, F.; Kessler, L.; Fendler, W. P.; Lindner, T.; Koerber, S. A.; Cardinale, J.; Sennung, D.; Roehrich, M.; Debus, J.; Sathekge, M.; Haberkorn, U.; Calais, J.; Serfling, S.; Buck, A. L. Head-to-Head Intra-Individual Comparison of Biodistribution and Tumor Uptake of ^{68}Ga-FAPI and ^{18}F-FDG PET/CT in Cancer Patients. *Eur J Nucl Med Mol Imaging* **2021**, *48* (13), 4377–4385. https://doi.org/10.1007/s00259-021-05307-1.

(325) Martin, M.; Ballal, S.; Yadav, M. P.; Bal, C.; Van Rymenant, Y.; De Loose, J.; Verhulst, E.; De Meester, I.; Van Der Veken, P.; Roesch, F. Novel Generation of FAP Inhibitor-Based Homodimers for Improved Application in Radiotheranostics. *Cancers (Basel)* **2023**, *15* (6), 1–24. https://doi.org/10.3390/cancers15061889.

(326) Siegrist, W.; Solca, F.; Stutz, S.; Giuffrè, L.; Carrel, S.; Girard, J.; Eberle, A. N. Characterization of Receptors for α-Melanocyte-Stimulating Hormone on Human Melanoma Cells. *Cancer Res* **1989**, *49* (22), 6352–6358.

(327) Zhang, C.; Zhang, Z.; Lin, K.-S.; Pan, J.; Dude, I.; Hundal-Jabal, N.; Colpo, N.; Bénard, F. Preclinical Melanoma Imaging with ^{68}Ga-Labeled α-Melanocyte-Stimulating Hormone Derivatives Using PET. *Theranostics* **2017**, *7* (4), 805–813. https://doi.org/10.7150/thno.17117.

(328) Angell, Y.; Holford, M.; Moos, W. H. Building on Success: A Bright Future for Peptide Therapeutics. *Protein Pept Lett* **2018**, *25* (12), 1044–1050. https://doi.org/10.2174/0929866525666181114155542.

(329) Marqus, S.; Pirogova, E.; Piva, T. J. Evaluation of the Use of Therapeutic Peptides for Cancer Treatment. *J Biomed Sci* **2017**, *24* (1), 1–15. https://doi.org/10.1186/s12929-017-0328-x.

(330) Miao, Y.; Whitener, D.; Feng, W.; Owen, N. K.; Chen, J.; Quinn, T. P. Evaluation of the Human Melanoma Targeting Properties of Radiolabeled α-Melanocyte Stimulating Hormone Peptide Analogues. *Bioconjug Chem* **2003**, *14* (6), 1177–1184. https://doi.org/10.1021/bc034069i.

(331) Westerlund, K.; Honarvar, H.; Norrström, E.; Strand, J.; Mitran, B.; Orlova, A.; Eriksson Karlström, A.; Tolmachev, V. Increasing the Net Negative Charge by Replacement of DOTA Chelator with DOTAGA Improves the Biodistribution of Radiolabeled Second-Generation Synthetic Affibody Molecules. *Mol Pharm* **2016**, *13* (5), 1668–1678. https://doi.org/10.1021/acs.pharmaceut.6b00089.

(332) Jain, A.; Chakraborty, S.; Sarma, H. D.; Dash, A. A Systematic Comparative Evaluation of ^{68}Ga-Labeled RGD Peptides Conjugated with Different Chelators. *Nucl Med Mol Imaging* **2017**, *52* (2), 125–134. https://doi.org/10.1007/s13139-017-0499-0.

(333) Banerjee, S. R.; Pullambhatla, M.; Foss, C. A.; Falk, A.; Byun, Y.; Nimmagadda, S.; Mease, R. C.; Pomper, M. G. Effect of Chelators on the Pharmacokinetics of ^{99m}Tc-Labeled Imaging Agents for the Prostate-Specific Membrane Antigen (PSMA). *J Med Chem* **2013**, *56* (15), 6108–6121. https://doi.org/10.1021/jm400823w.

(334) Krutzek, F.; Donat, C. K.; Stadlbauer, S. Chelator Impact: Investigating the Pharmacokinetic Behavior of Copper-64 Labeled PD-L1 Radioligands. *EJNMMI Radiopharm Chem* **2024**, *9* (1), 1–24. https://doi.org/10.1186/s41181-024-00243-5.

(335) Lindner, T.; Loktev, A.; Altmann, A.; Giesel, F.; Kratochwil, C.; Debus, J.; Jäger, D.; Mier, W.; Haberkorn, U. Development of Quinoline-Based Theranostic Ligands for the Targeting of Fibroblast Activation Protein. *Journal of Nuclear Medicine* **2018**, *59* (9), 1415–1422. https://doi.org/10.2967/jnumed.118.210443.

(336) Verena, A.; Zhang, Z.; Kuo, H. T.; Merkens, H.; Zeisler, J.; Wilson, R.; Bendre, S.; Wong, A. A. W. L.; Bénard, F.; Lin, K. S. Synthesis and Preclinical Evaluation of Three Novel ^{68}Ga-Labeled Bispecific PSMA/FAP-Targeting Tracers for Prostate Cancer Imaging. *Molecules* **2023**, *28* (3), 1–17. https://doi.org/10.3390/molecules28031088.

(337) Little, M. J.; Aubry, N.; Beaudoin, M. E.; Goudreau, N.; LaPlante, S. R. Quantifying Trifluoroacetic Acid as a Counterion in Drug Discovery by ^{19}F NMR and Capillary Electrophoresis. *J Pharm Biomed Anal* **2007**, *43* (4), 1324–1330. https://doi.org/10.1016/j.jpba.2006.10.039.

(338) Verena, A.; Kuo, H. T.; Merkens, H.; Zeisler, J.; Bendre, S.; Wong, A. A. W. L.; Bénard, F.; Lin, K. S. Novel ^{68}Ga-Labeled Pyridine-Based Fibroblast Activation Protein-Targeted Tracers with High Tumor-to-Background Contrast. *Pharmaceuticals* **2023**, *16* (3), 1–13. https://doi.org/10.3390/ph16030449.

(339) McNeil, B. L.; Kadassery, K. J.; McDonagh, A. W.; Zhou, W.; Schaffer, P.; Wilson, J. J.; Ramogida, C. F. Evaluation of the Effect of Macrocyclic Ring Size on [^{203}Pb]Pb(II) Complex Stability in Pyridyl-Containing Chelators. *Inorg Chem* **2022**. https://doi.org/10.1021/acs.inorgchem.2c01114.

(340) Guo, H.; Shenoy, N.; Gershman, B. M.; Yang, J.; Sklar, L. A.; Miao, Y. Metastatic Melanoma Imaging with an ^{111}In-Labeled Lactam Bridge-Cyclized α-Melanocyte-Stimulating Hormone Peptide. *Nucl Med Biol* **2009**, *36* (3), 267–276. https://doi.org/10.1016/j.nucmedbio.2009.01.003.

(341) Lückerath, K.; Stuparu, A. D.; Wei, L.; Kim, W.; Radu, C. G.; Mona, C. E.; Calais, J.; Rettig, M.; Reiter, R. E.; Czernin, J.; Slavik, R.; Herrmann, K.; Eiber, M.; Fendler, W. P. Detection Threshold and Reproducibility of ^{68}Ga-PSMA11 PET/CT in a Mouse Model of Prostate Cancer. *Journal of Nuclear Medicine* **2018**, *59* (9), 1392–1397. https://doi.org/10.2967/jnumed.118.207704.

(342) Claasen, V. Intravenous Drug Administration. In *Techniques in the Behavioural and Neural Sciences*; Elsevier: Amsterdam, 1994; Vol. 12, 5–22. https://doi.org/10.1016/b978-0-444-81871-3.50007-2.

(343) Henderson, M. C.; Krueger, S. K.; Stevens, J. F.; Williams, D. E. Human Flavin-Containing Monooxygenase Form 2 S-Oxygenation: Sulfenic Acid Formation from Thioureas and Oxidation of Glutathione. *Chem Res Toxicol* **2004**, *17* (5), 633–640. https://doi.org/10.1021/tx034253s.

(344) Chapeau, D.; Koustoulidou, S.; Handula, M.; Beekman, S.; de Ridder, C.; Stuurman, D.; de Blois, E.; Buchatskaya, Y.; van der Schilden, K.; de Jong, M.; Konijnenberg, M. W.; Seimbille, Y. [^{212}Pb]Pb-ESOMA-01: A Promising Radioligand for Targeted Alpha Therapy of Neuroendocrine Tumors. *Pharmaceuticals* **2023**, *16* (7), 1–19. https://doi.org/10.3390/ph16070985.

(345) Wilke, T. J.; Jondorf, W. R.; Powis, G. Oxidative Metabolism of ^{14}C-Pyridine by Human and Rat Tissue Subcellular Fractions. *Xenobiotica* **1989**, *19* (9), 1013–1022. https://doi.org/10.3109/00498258909043158.

(346) Guo, H.; Miao, Y. Melanoma Targeting Property of a Lu-177-Labeled Lactam Bridge-Cyclized Alpha-MSH Peptide. *Bioorg Med Chem Lett* **2013**, *23* (8), 2319–2323. https://doi.org/10.1016/j.bmcl.2013.02.069.

(347) Zhang, C.; Zhang, Z.; Zeisler, J.; Colpo, N.; Lin, K. S.; Bénard, F. Selective Cyclized α-Melanocyte-Stimulating Hormone Derivative with Multiple N-Methylations for Melanoma Imaging with Positron Emission Tomography. *ACS Omega* **2020**, *5* (19), 10767–10773. https://doi.org/10.1021/acsomega.0c00310.

(348) Wharton, L.; Jaraquemada-Peláez, M. D. G.; Zhang, C.; Zeisler, J.; Rodríguez-Rodríguez, C.; Osooly, M.; Radchenko, V.; Yang, H.; Lin, K. S.; Bénard, F.; Schaffer, P.; Orvig, C. H4picoopa─Robust Chelate for ^{225}Ac/^{111}In Theranostics. *Bioconjug Chem* **2022**, *33* (10), 1900–1921. https://doi.org/10.1021/acs.bioconjchem.2c00364.

(349) Wharton, L.; Zhang, C.; Yang, H.; Zeisler, J.; Radchenko, V.; Rodríguez-Rodríguez, C.; Osooly, M.; Patrick, B. O.; Lin, K. S.; Bénard, F.; Schaffer, P.; Orvig, C. [^{213}Bi]Bi^{3+}/[^{111}In]In^{3+}-Neunpa-CycMSH: Theranostic Radiopharmaceutical Targeting Melanoma-Structural, Radiochemical, and Biological Evaluation. *Bioconjug Chem* **2022**, *33* (3), 505–522. https://doi.org/10.1021/acs.bioconjchem.2c00038.

(350) Giron, M. C.; Portolan, S.; Bin, A.; Mazzi, U.; Cutler, C. S. Cytochrome P450 and Radiopharmaceutical Metabolism. *Quarterly Journal of Nuclear Medicine and Molecular Imaging* **2008**, *52* (3), 254–266.

(351) Boobis, A. R.; McKillop, D.; Robinson, D. T.; Adams, D. A.; McCormick, D. J. Interlaboratory Comparison of the Assessment of P450 Activities in Human Hepatic Microsomal Samples. *Xenobiotica* **1998**, *28* (5), 493–506. https://doi.org/10.1080/004982598239416.

(352) Knights, K. M.; Stresser, D. M.; Miners, J. O.; Crespi, C. L. *In Vitro* Drug Metabolism Using Liver Microsomes. *Curr Protoc Pharmacol* **2016**, *7* (8), 1–24. https://doi.org/10.1002/CPPH.9.

(353) Navqi, S.; Sosabowski, J. K.; Ahamad Nagra, S.; Ishfaq, M. M.; Mather, S. J.; Matzow, T. Radiopeptide Internalisation and Externalisation Assays: Cell Viability and Radioligand Integrity. *Applied Radiation and Isotopes* **2011**, *69* (1), 68–74. https://doi.org/10.1016/j.apradiso.2010.09.005.

(354) Winter, G.; Vogt, A.; Begum, N.; Solbach, C.; Beer, A.; Glatting, G.; Kletting, P. Determination of the Internalization Rate of Radiolabeled Ligands by Mathematical Modeling. *Journal of Nuclear Medicine* **2018**, *59* (Suppl. 1), 1294.

(355) Loktev, A.; Lindner, T.; Burger, E. M.; Altmann, A.; Giesel, F.; Kratochwil, C.; Debus, J.; Marmé, F.; Jäger, D.; Mier, W.; Haberkorn, U. Development of Fibroblast Activation Protein–Targeted Radiotracers with Improved Tumor Retention. *Journal of Nuclear Medicine* **2019**, *60* (10), 1421–1429. https://doi.org/10.2967/jnumed.118.224469.

Appendix A.

Supplementary Information for Chapter 2

Gamma-ray spectra

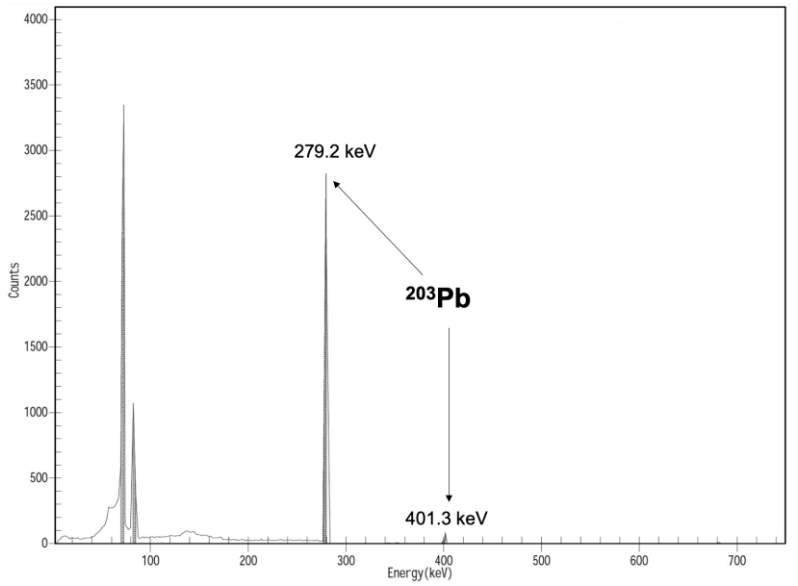

Figure A.1. Gamma-ray spectrum of the ^{203}Pb Dowex-1x8 elute.

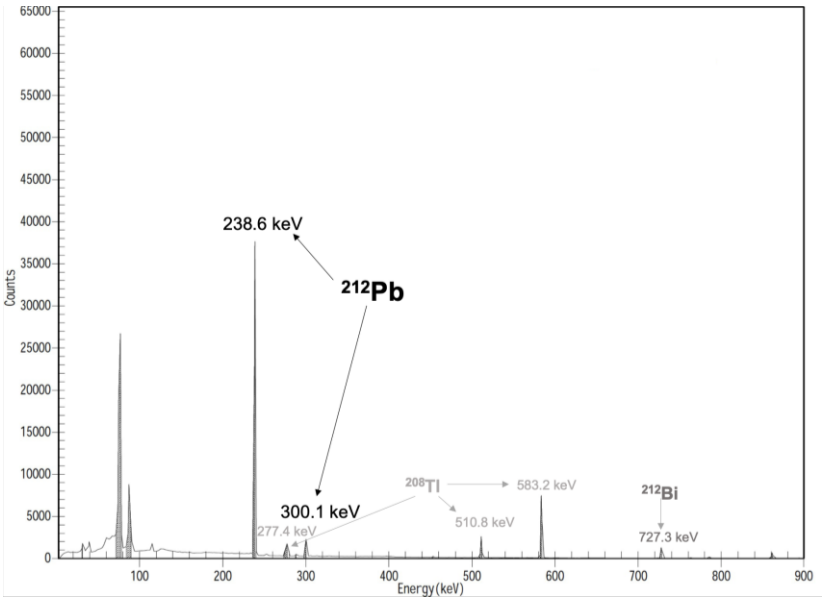

Figure A.2. Gamma-ray spectrum of the ^{212}Pb Dowex-1x8 elute.

Dowex-1X8 Resin - Method Development

When anion exchange resins were being considered for use as a second column in our two-column purification procedure, we evaluated both Dowex-1X8 (200-400 mesh, Cl form, Pittsburgh, PA) and AG-1X8 (50-100 mesh, Cl form, Biorad, Mississauga, ON) resins. AG-1X8 and Dowex-1X8 resins share the same structure (type I, strong base anion exchangers with quaternary amine functional groups on styrene divinyl benzene polymeric beads), but AG-1X8 is an analytical grade resin, whereas Dowex-1X8 is not. Analytical grade resins typically contain less metal contaminants and have a more narrow particle size distribution that can lead to superior resolution, which could result in smaller elute volumes, ideal for radiochemical separation. However, this resin is nearly twice the price of Dowex-1X8.

In order to determine which resin was more useful for our applications, and what column volume should be used for a loading volume of at least 4 mL, 100 mg of each resin (column volume of ~100 μL) was first used. The resin was packed as a slurry in deionized water into a 1 mL polypropylene cartridge and preconditioned with 5 mL of deionized water and 5 mL of 2 M HCl. The loading solution containing the diluted Pb^{TM} resin elute (in 2 M HCl) was loaded onto the column by gravity before eluting with 0.01 M HCl at 1.5 mL/min. Gamma spectroscopy was used to quantify the ^{203}Pb in the load and elute fractions as at this point in the investigative process, the 1 M HCl wash was not yet employed, as shown in **Figure A.3**.

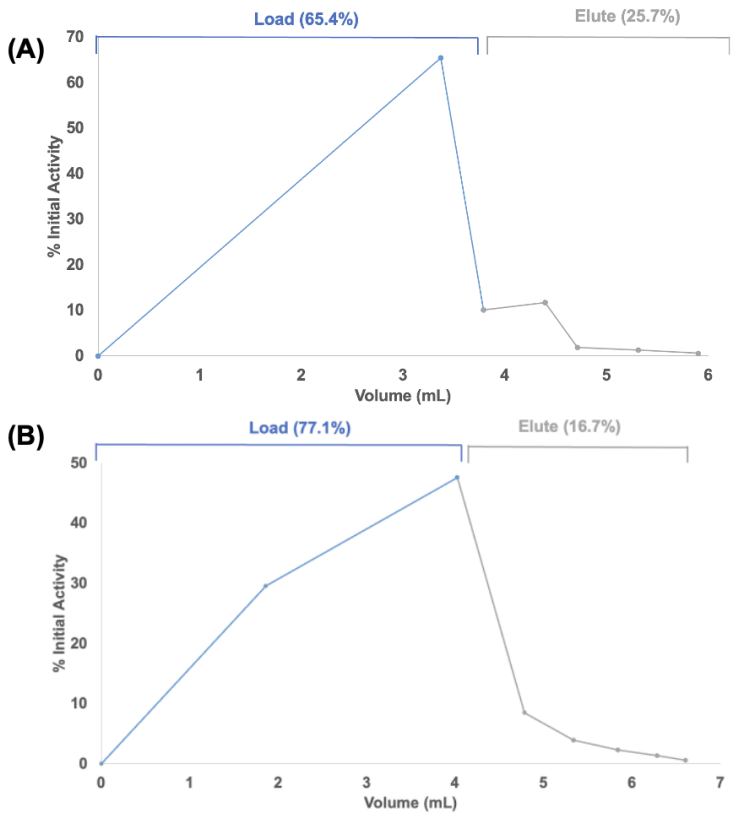

Figure A.3. Average elution profile of ^{203}Pb (~4 mL in 2 M HCl) purification on (A) 100 mg of Dowex-1X8 resin and (B) 100 mg of AG-1X8 resin (n=1).

Despite this only being one replicate, it was clear that this column volume was too small and thus had to be increased. For the next set of experiments, 500 mg of resin (column volume ~530 μL) was packed as a slurry into a 1 mL polypropylene cartridge and preconditioned with 10 mL of deionized water and 10 mL of 2 M HCl. The columns were loaded by gravity and eluted with 0.01 M HCl at 1.5 mL/min, with the elution profiles shown in **Figure A.4**.

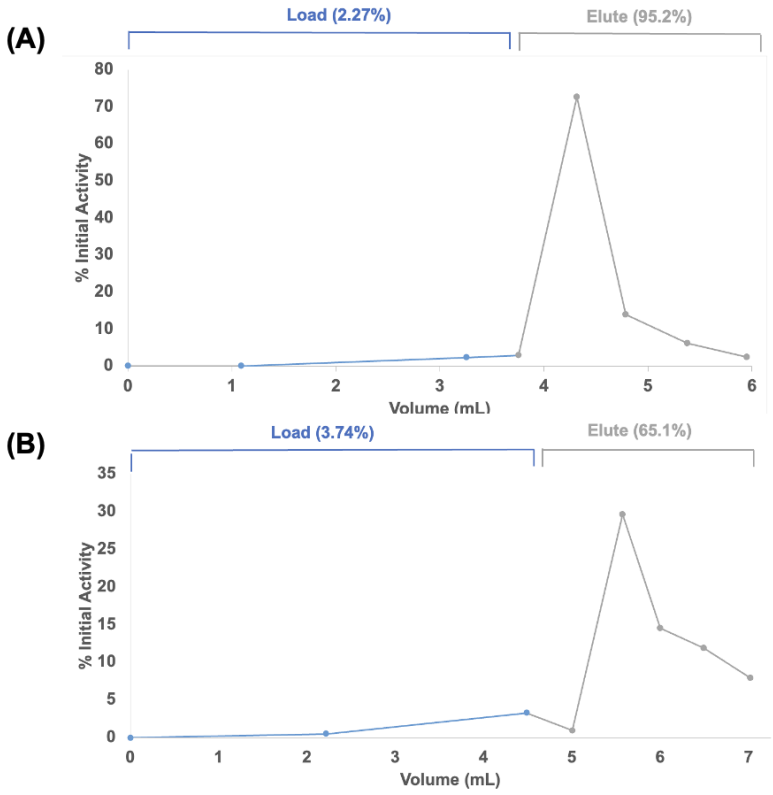

Figure A.4. Average elution profile of ^{203}Pb (~4 mL in 2 M HCl) purification on (A) 500 mg of Dowex-1X8 resin and (B) 500 mg of AG-1X8 resin (n=1).

Initially, it was expected that the elution profiles would be opposite as AG-1X8 should offer greater resolution. However, due to the drastic, unexpected difference in the elution profiles in **Figure A.4**, and the lower cost, it was decided to proceed with Dowex-1X8 as the resin of choice. To further determine if the ^{203}Pb lost in the load could be further reduced, 1000 mg of Dowex-1X8 resin was prepared as previously described and identical loading and elution conditions were used.

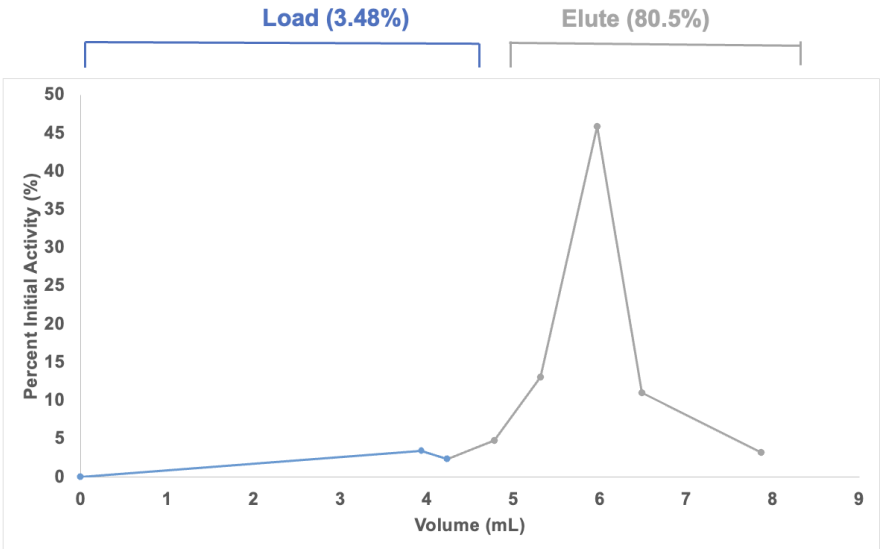

Figure A.5. Average elution profile of ^{203}Pb (~4 mL in 2 M HCl) purification on 1000 mg of Dowex-1X8 resin. (n=1)

With a 1000 mg column, the ^{203}Pb in the load did not decrease and the elution volume and profile began to broaden as more 0.01 M HCl was required to elute the ^{203}Pb from the larger column, as expected. Since it is desirable for the elute volume to be as low as possible, 500 mg was the finalized column volume used in this novel purification procedure.

Representative iTLCs

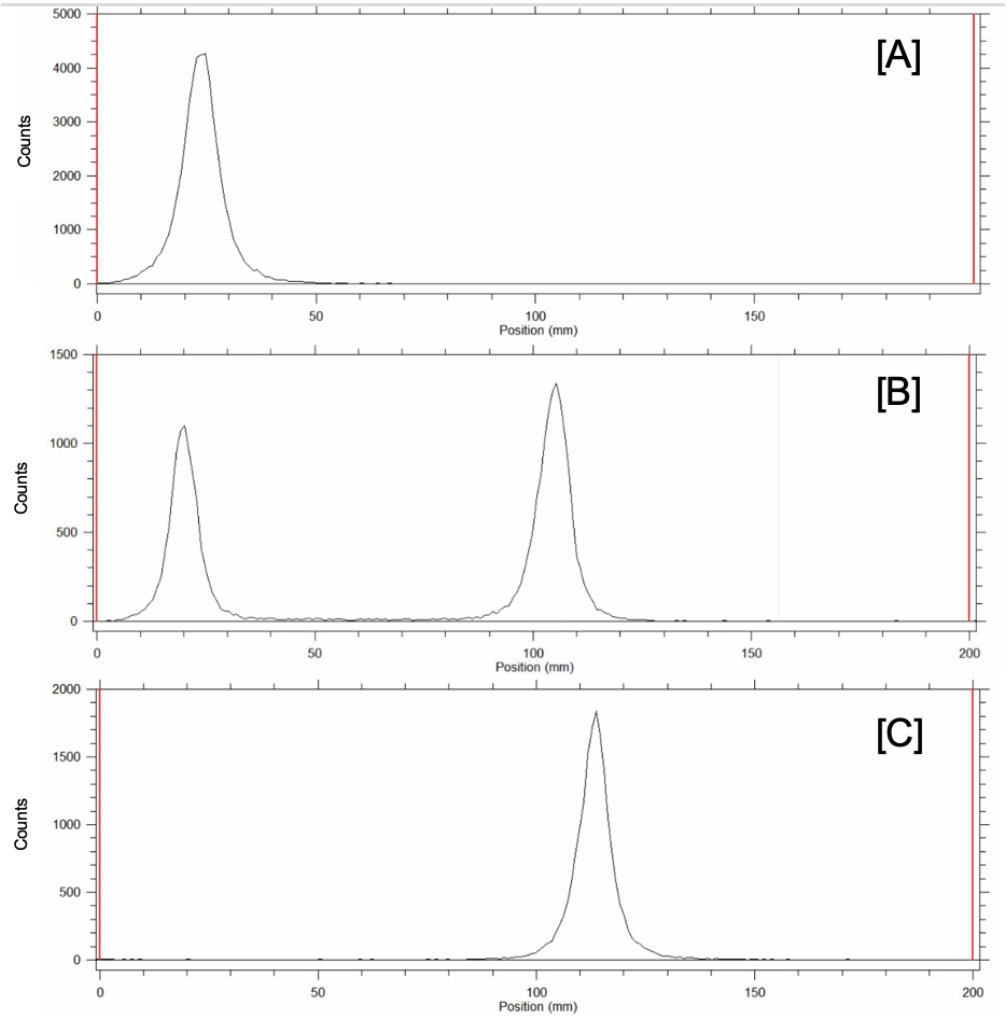

Figure A.6. Representative iTLC radio-chromatograms for ^{212}Pb radiolabelling. [A] 10^{-6} M TCMC labelled with 100 kBq ^{212}Pb at room temperature (0.1 M NH_4OAc, pH 7, 1 h), [B] 10^{-7} M TCMC labelled with 100 kBq ^{212}Pb at room temperature (0.1 M NH_4OAc, pH 7, 1 h), and [C] unlabelled ^{203}Pb (negative control) 1 h aliquot spotted onto SA iTLC plates, developed using EDTA (50 mM, pH 5.0) as the mobile phase.

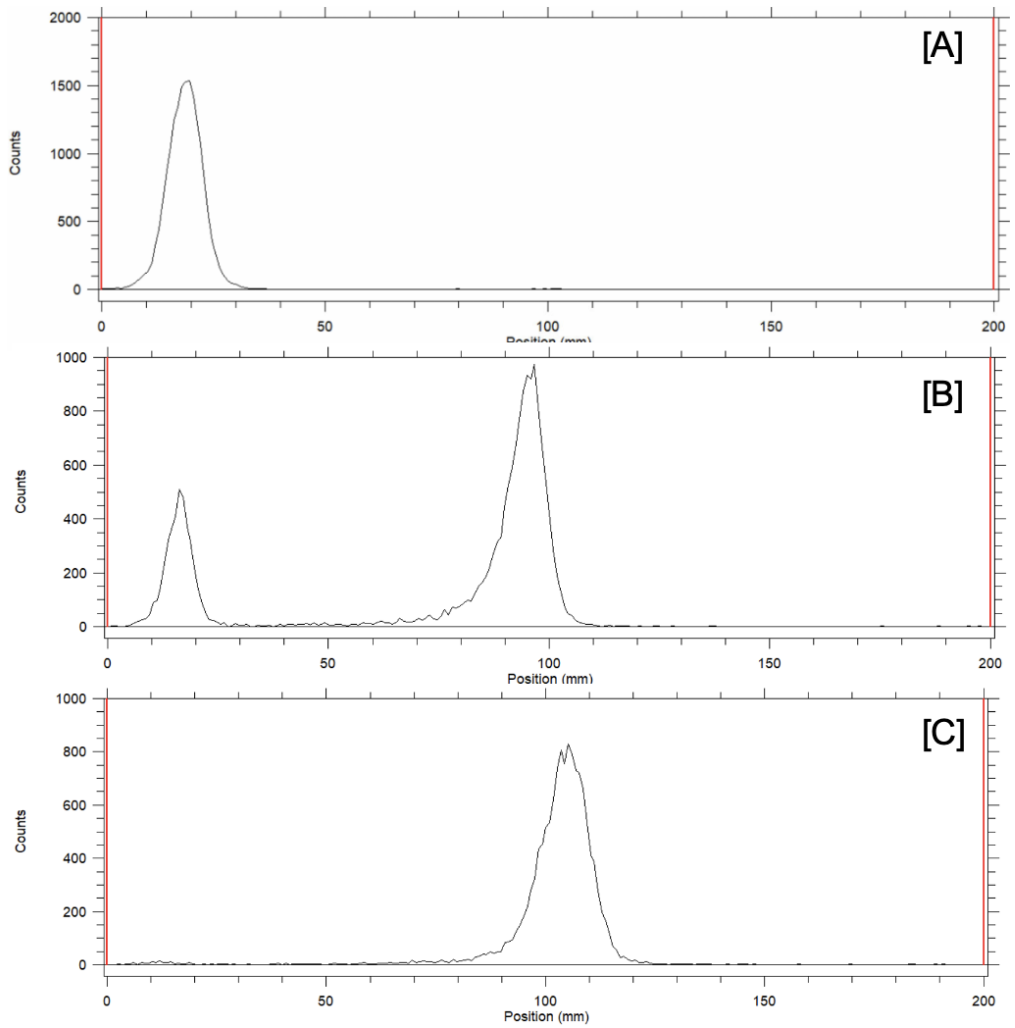

Figure A.7. Representative iTLC radio-chromatograms for ^{203}Pb radiolabelling. [A] 10^{-6} M TCMC labelled with 85 kBq ^{203}Pb at room temperature (0.1 M NH_4OAc, pH 7, 1 h), [B] 10^{-8} M TCMC labelled with 85 kBq ^{203}Pb at room temperature (0.1 M NH_4OAc, pH 7, 1 h), and [C] unlabelled ^{203}Pb (negative control) 1 h aliquot spotted onto SA iTLC plates, developed using EDTA (50 mM, pH 5.0) as the mobile phase.

^{212}Pb Radiolabeling

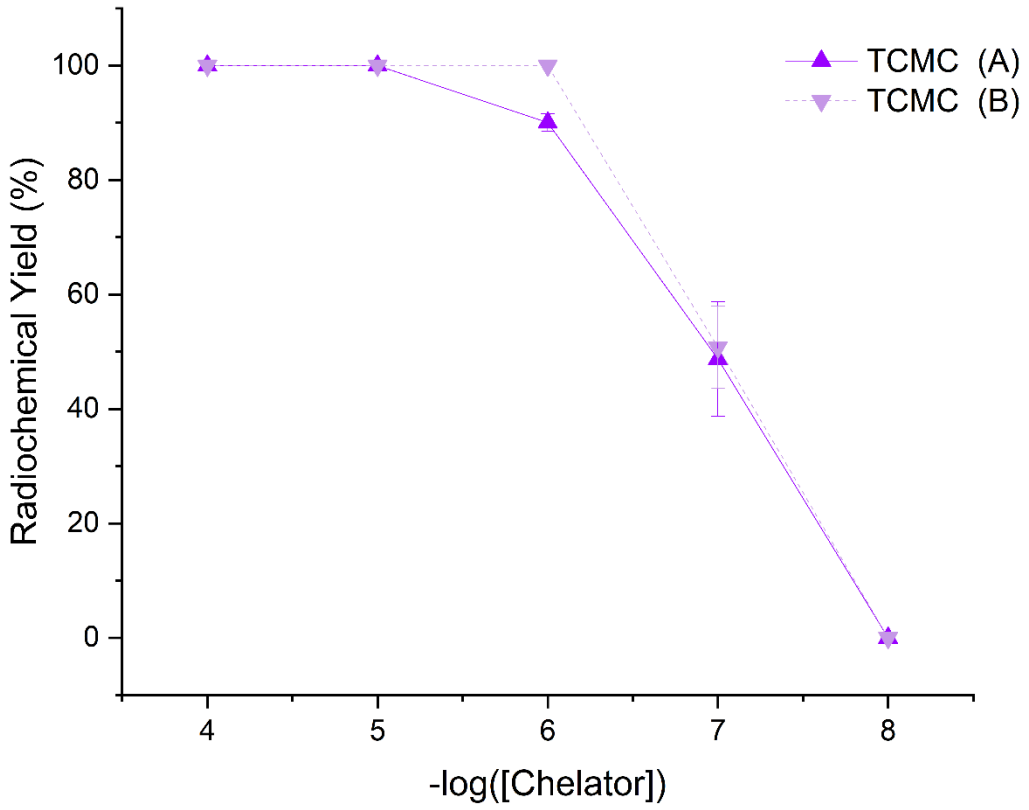

Figure A.8. Radiochemical yields (%) for ^{212}Pb (100 kBq) labeling reactions at pH 7 (0.1 M NH_4OAc), room tempeature, and 1 h at chelator concentrations of 10^{-4} to 10^{-8} M using ^{212}Pb produced via the one-column[156] (A) and two-column (B) method. (n = 3)

Photograph of Average Electroplated Tl Target

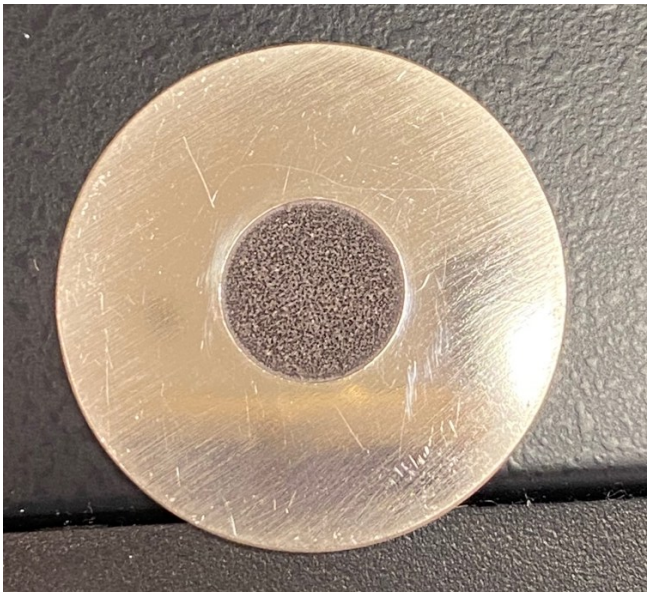

Figure A.9. Photograph of a representative silver-backed, electroplated ^{nat}Tl target.

Appendix B.

Supplementary Information for Chapter 3

Synthesis and Characterization of Chelators and Pb^{2+} Complexes

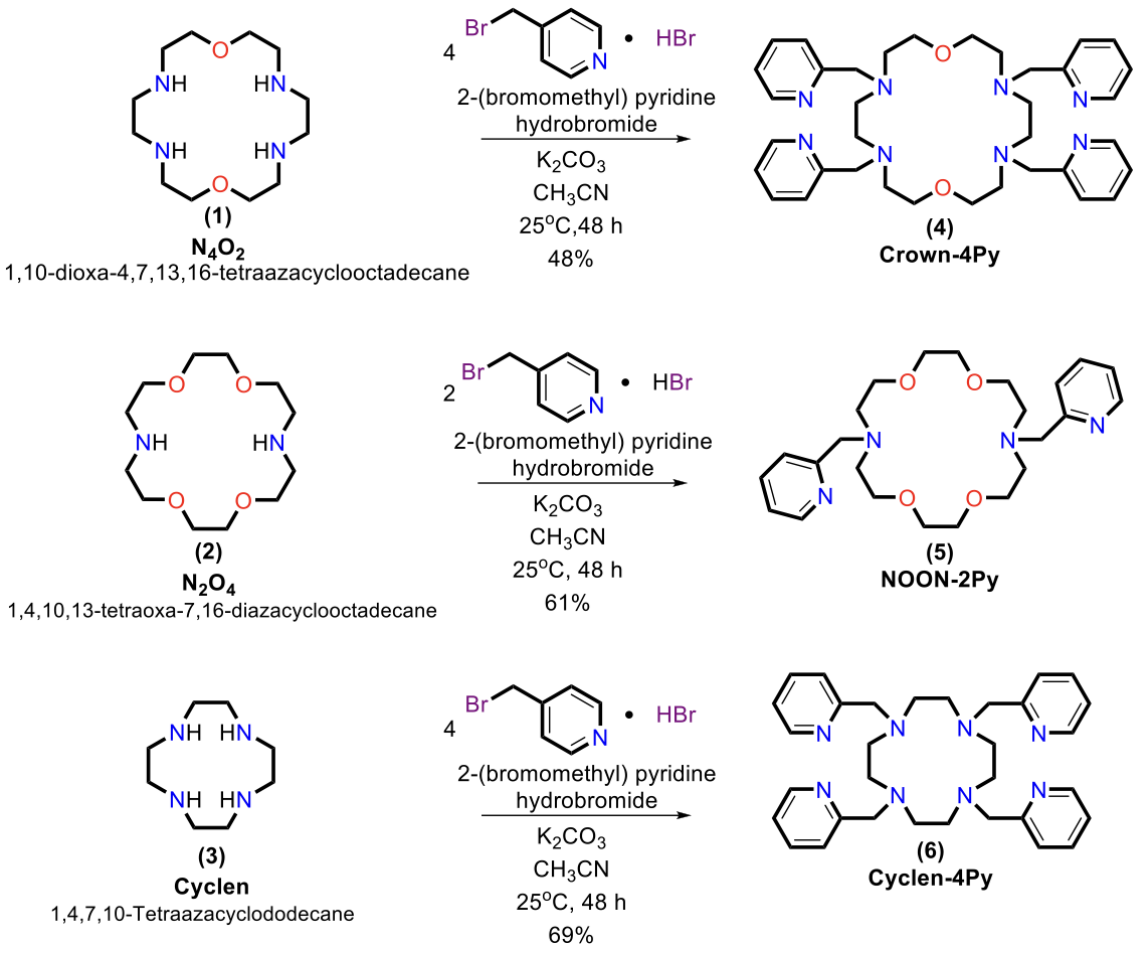

Scheme B.1. Synthesis of pyridyl-containing chelators in this study.

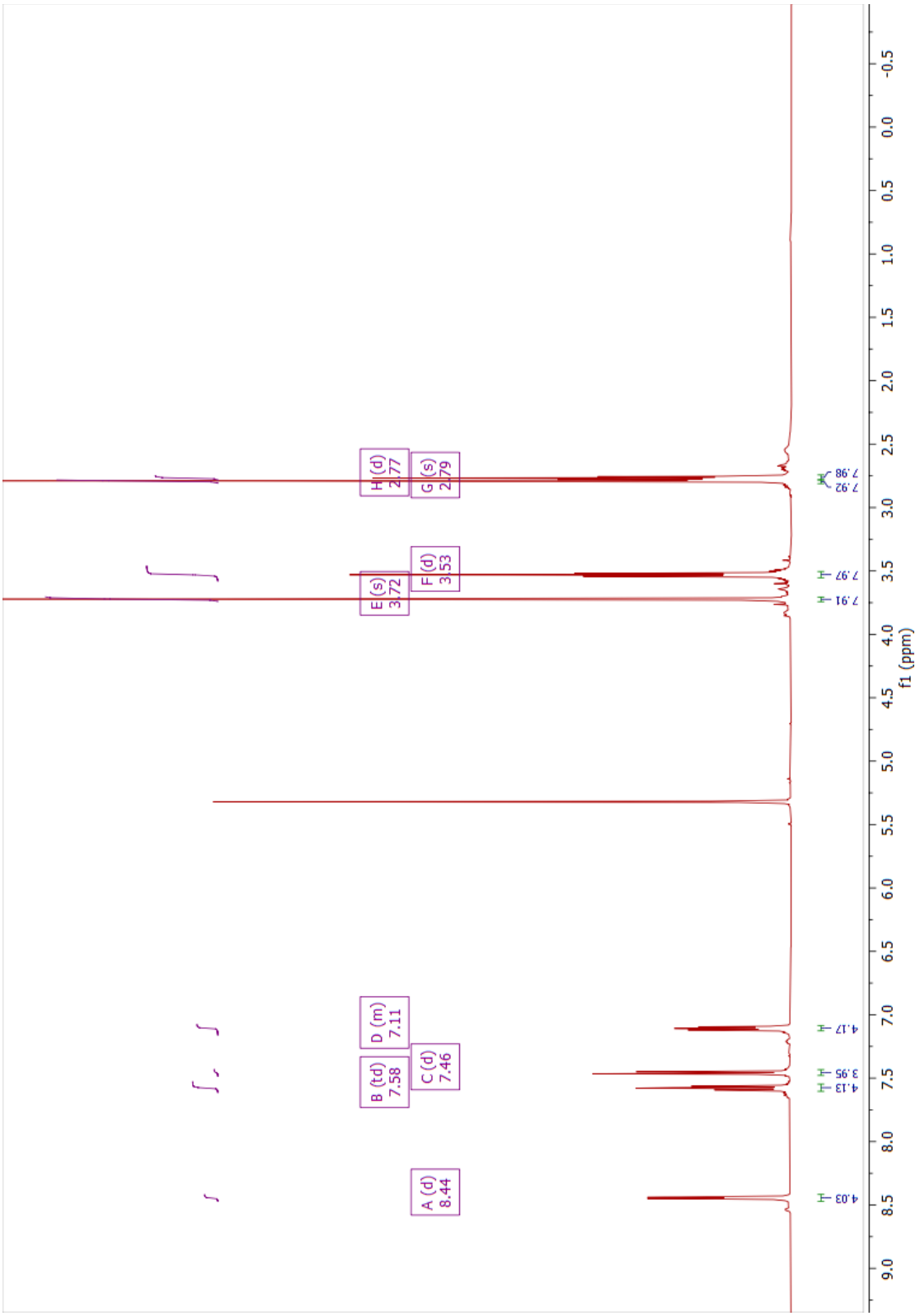

Figure B.1. ^{1}H NMR spectrum of Crown-4Py (500 MHz, CD_2Cl_2, 25 °C)

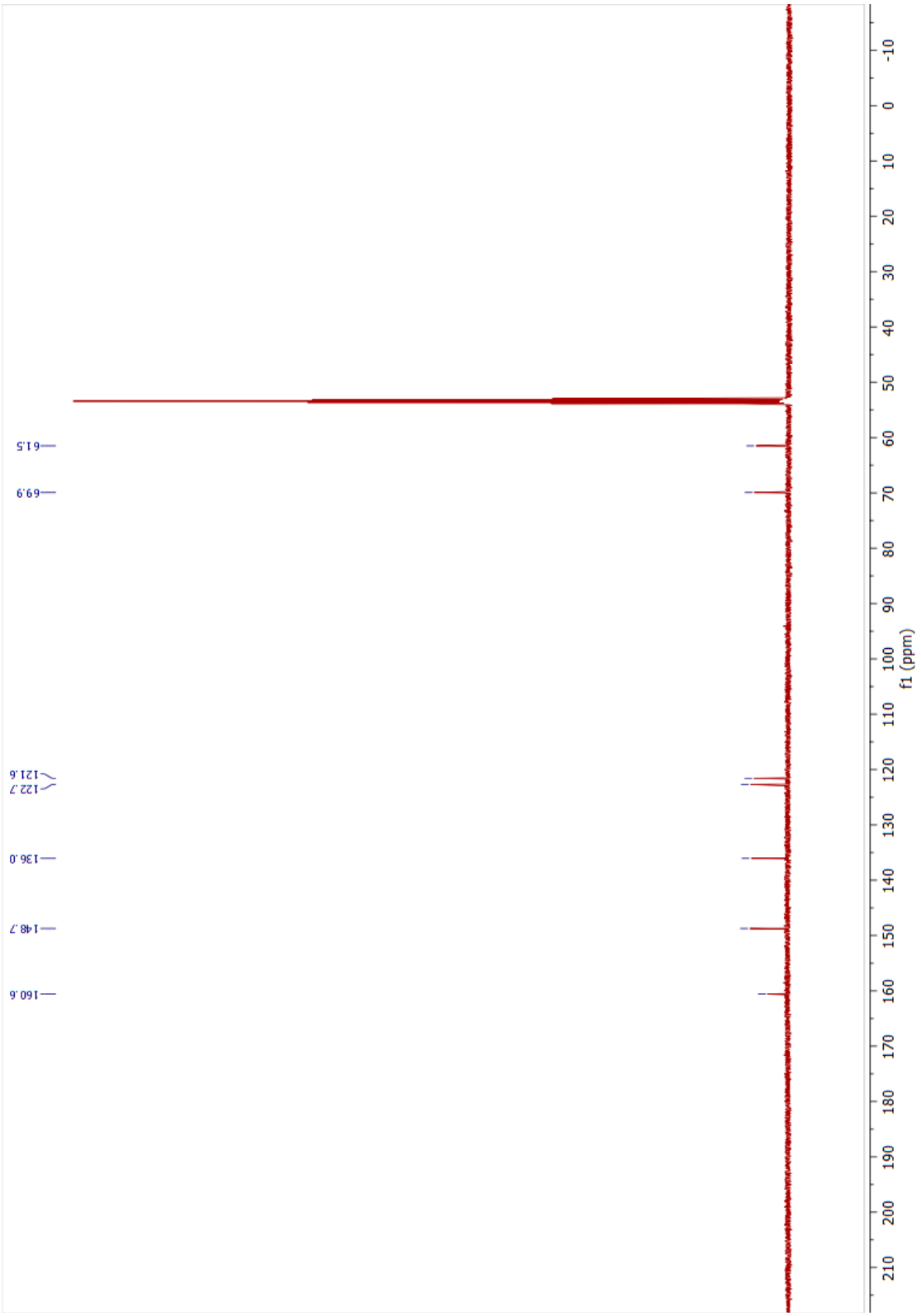

Figure B.2. ^{13}C NMR spectrum of Crown-4Py (125 MHz, CD_2Cl_2, 25 °C)

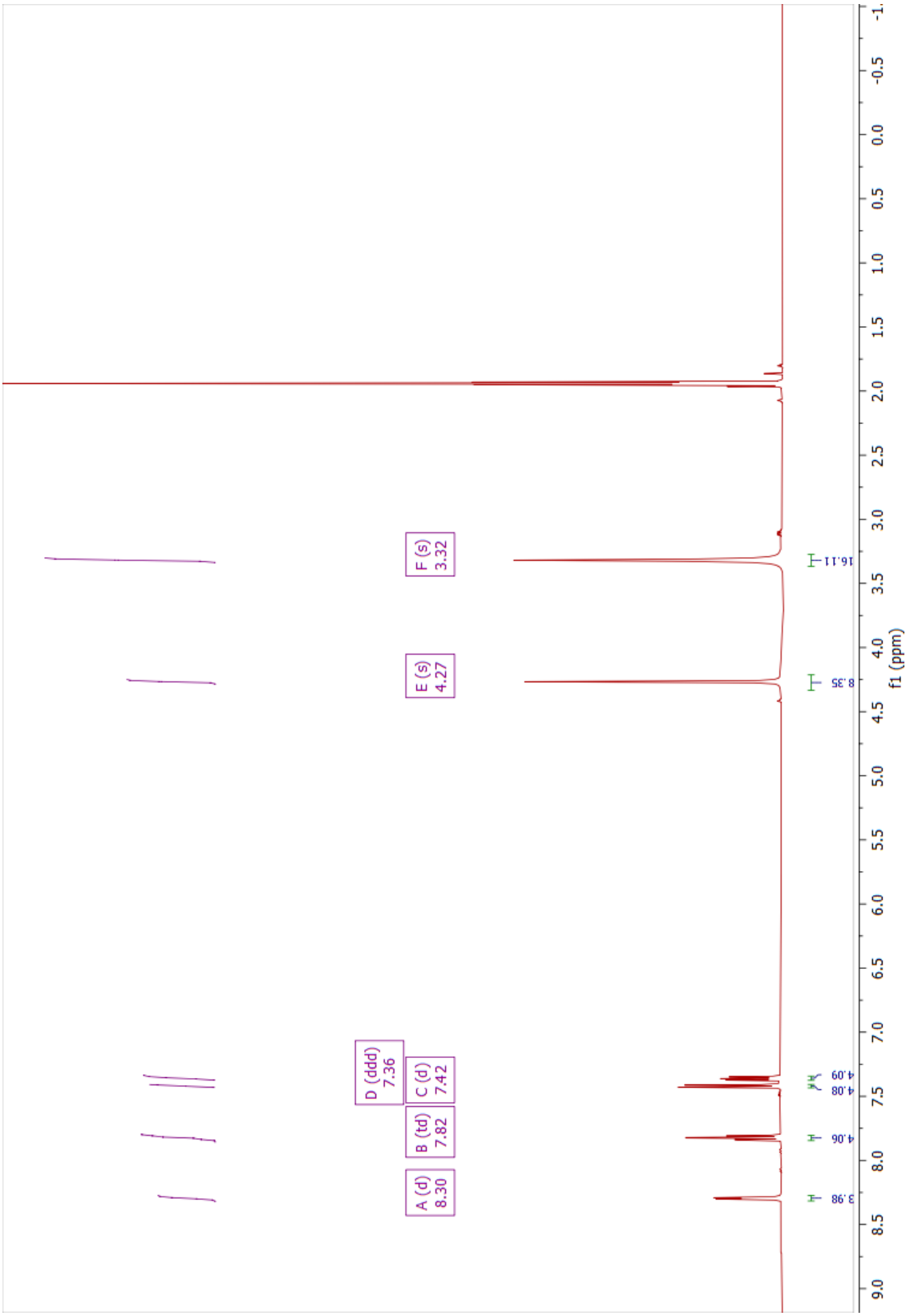

Figure B.3. ^{1}H NMR spectrum of Cyclen-4Py (400 MHz, CD_3CN, 25 °C)

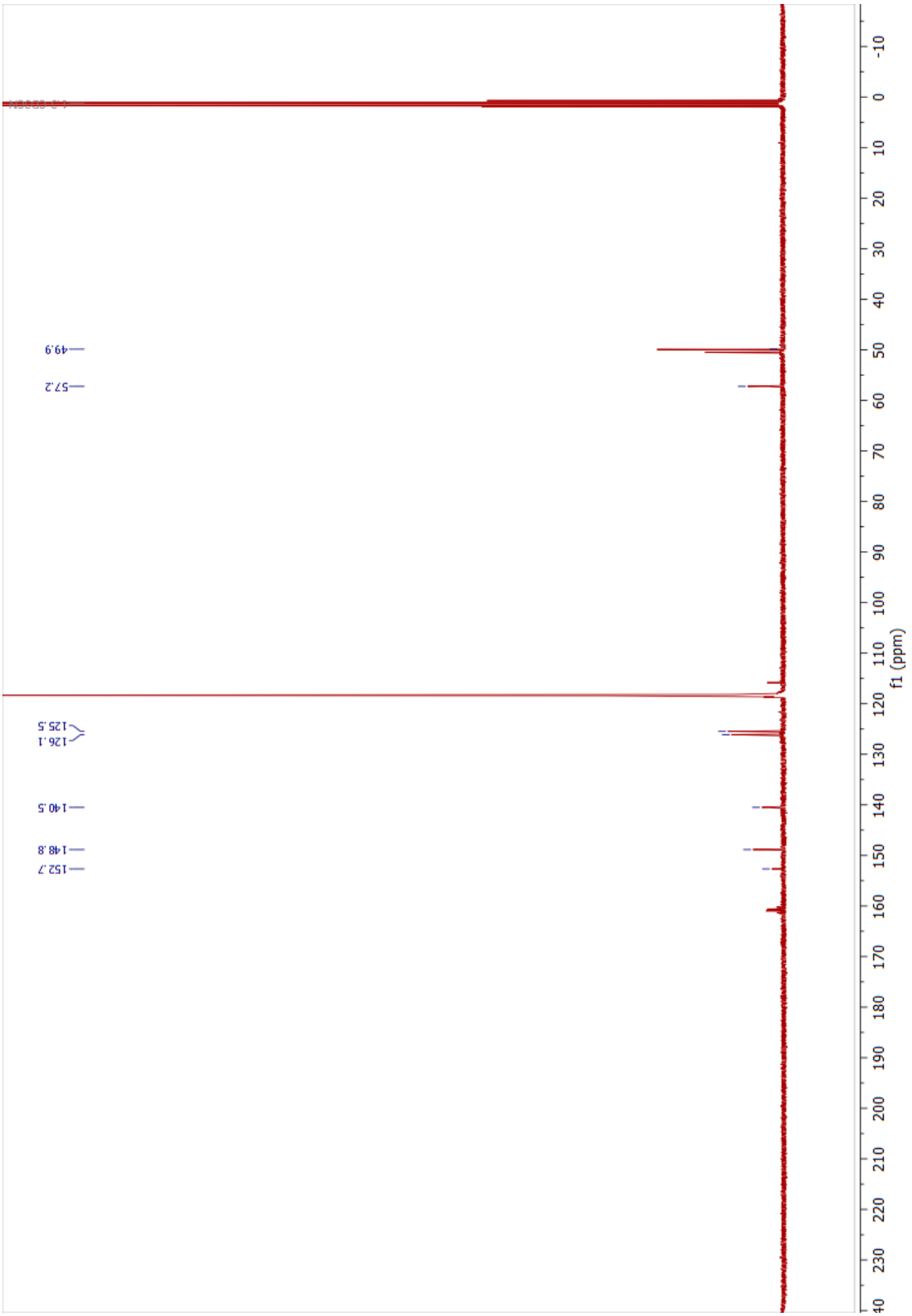

Figure B.4. ^{13}C NMR spectrum of Cyclen-4Py (100 MHz, CD_3CN, 25 °C)

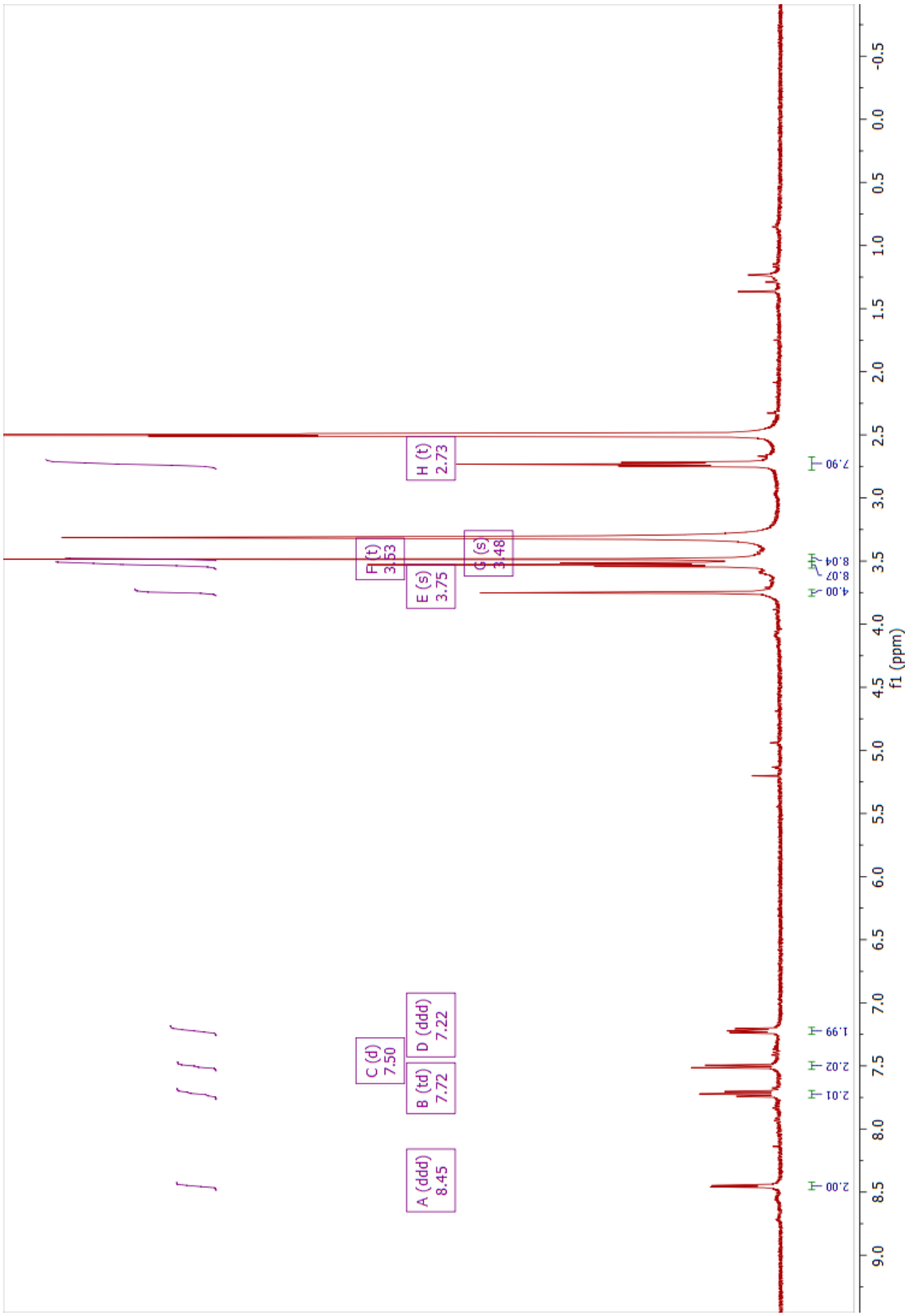

Figure B.5. ^{1}H NMR spectrum of NOON-2Py (400 MHz, DMSO-d_6, 25°C)

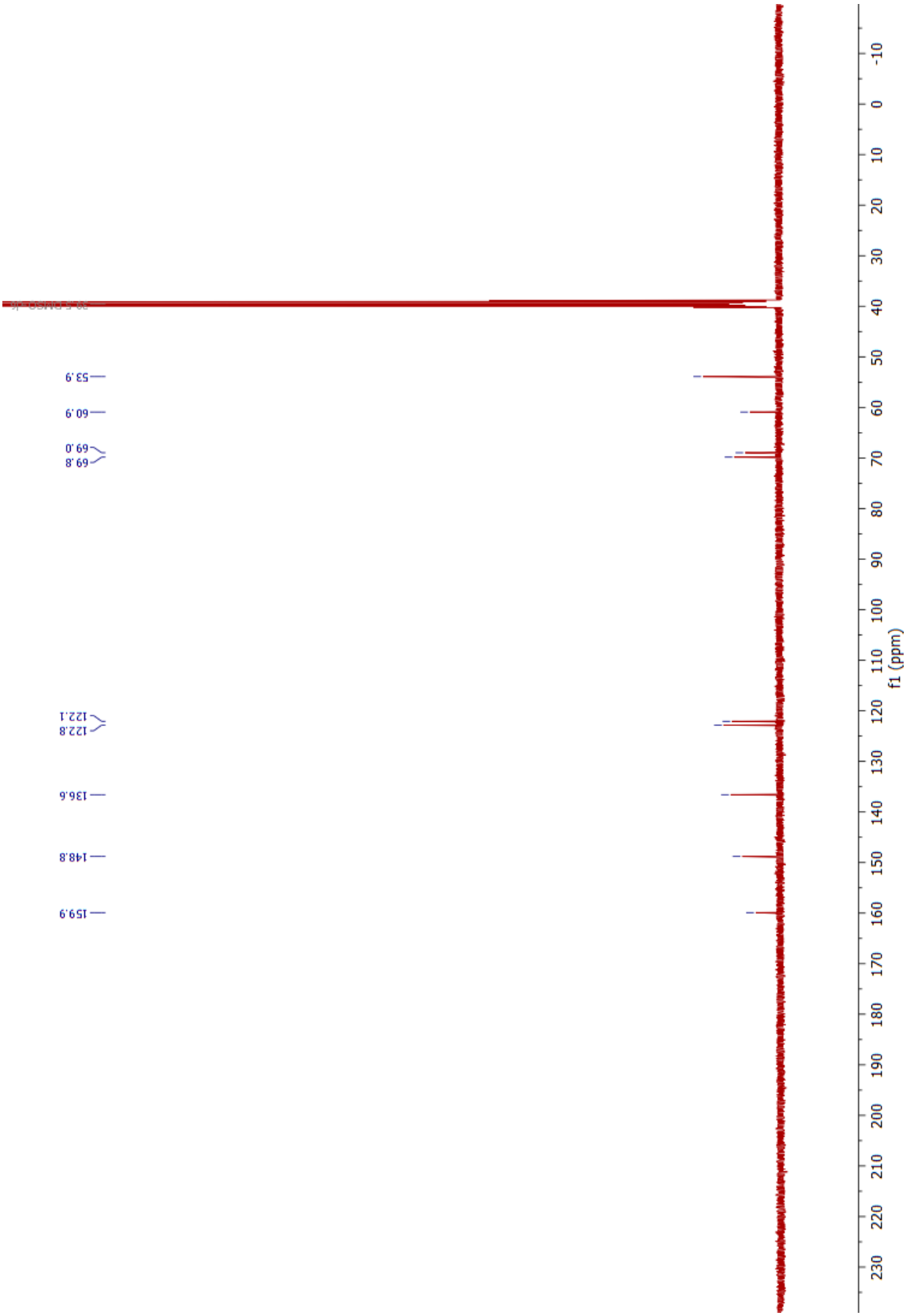

Figure B.6. ^{13}C NMR spectrum of NOON-2Py (100 MHz, DMSO-d6, 25 °C)

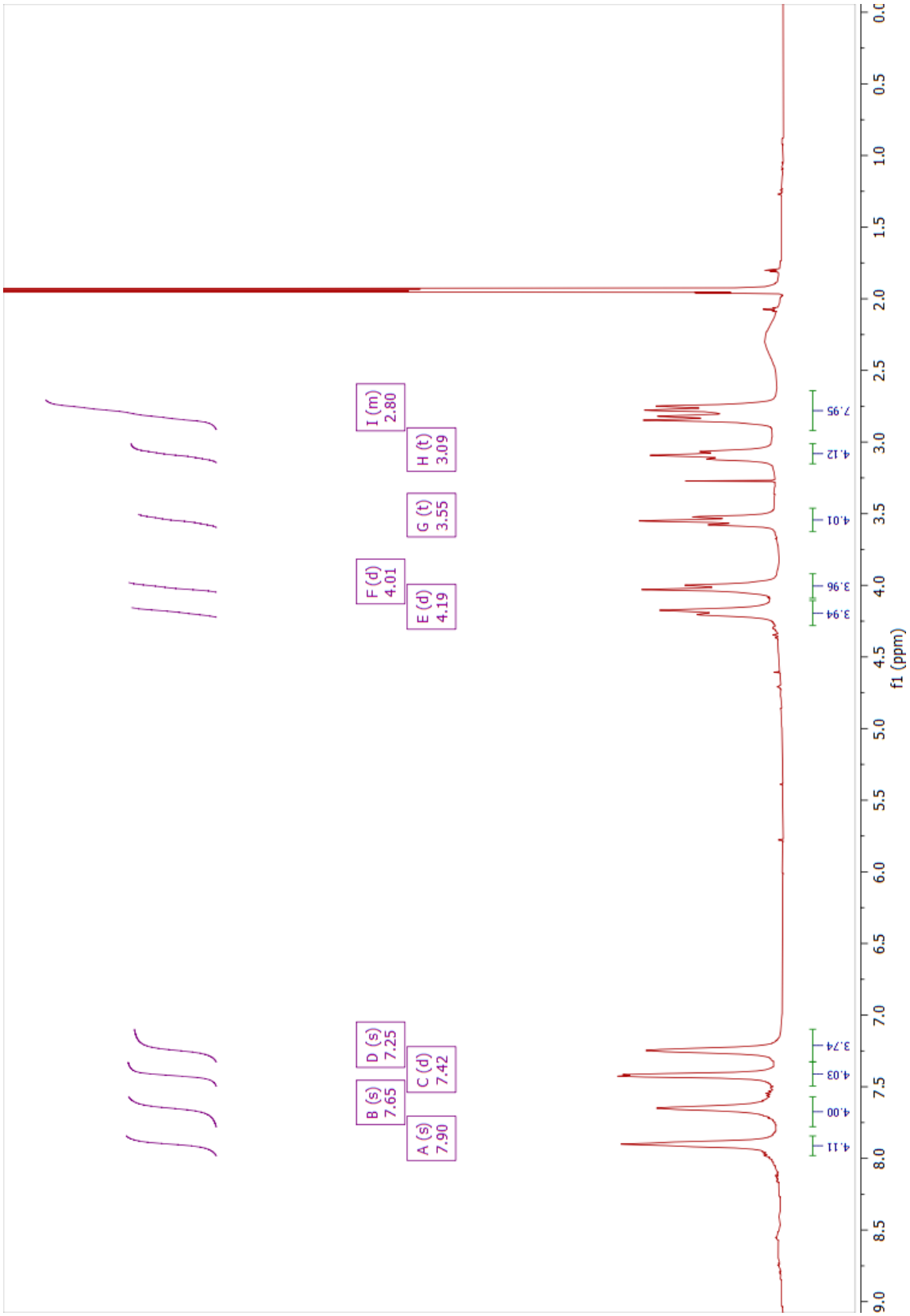

Figure B.7. ^{1}H NMR spectrum of $[Pb(Cyclen\text{-}4Py)]^{2+}$ (500 MHz, CD_3CN, 25 °C)

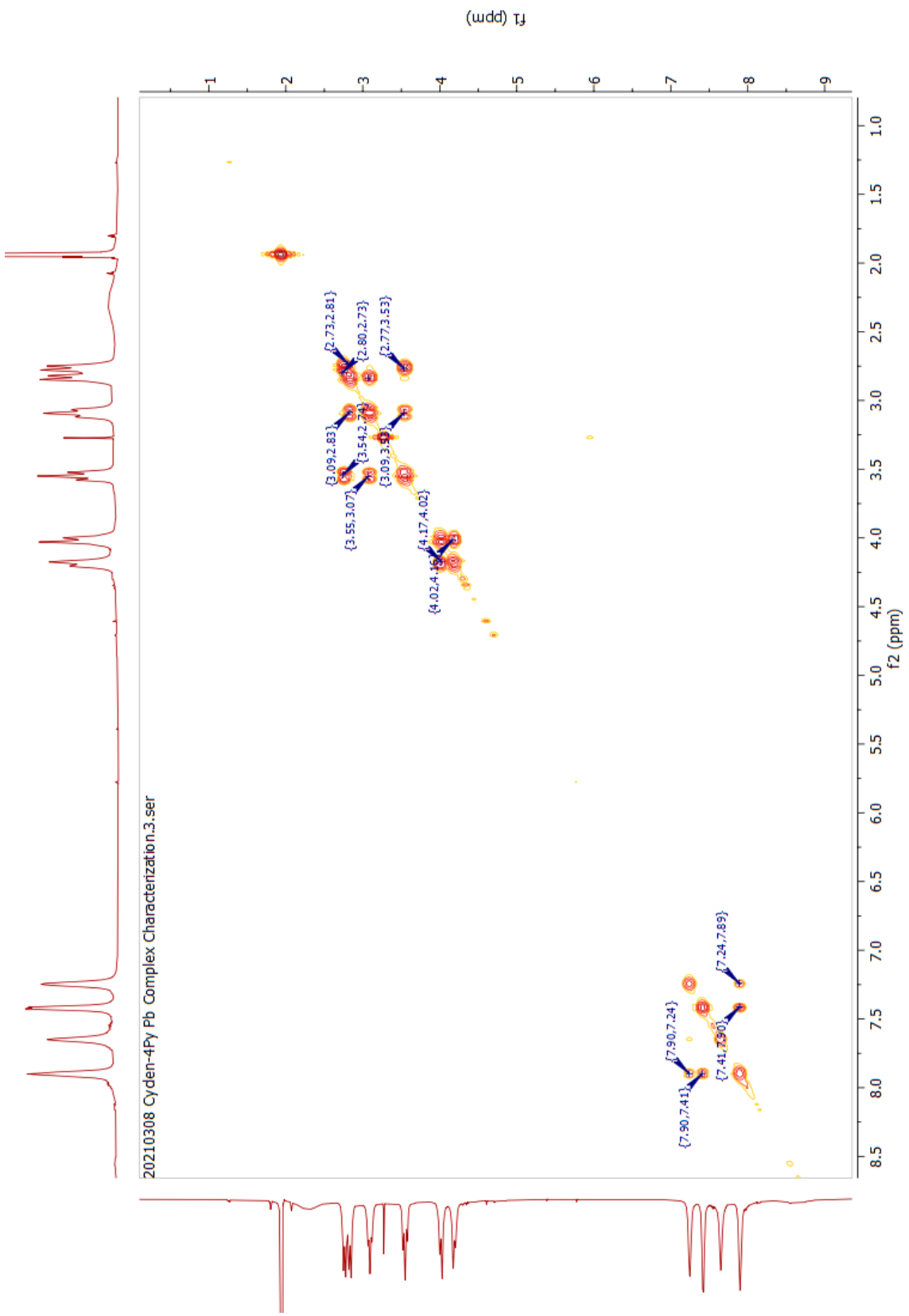

Figure B.8. ^{1}H-^{1}H COSY NMR spectrum of $[Pb(Cyclen\text{-}4Py)]^{2+}$ (500 MHz, CD_3CN, 25 °C)

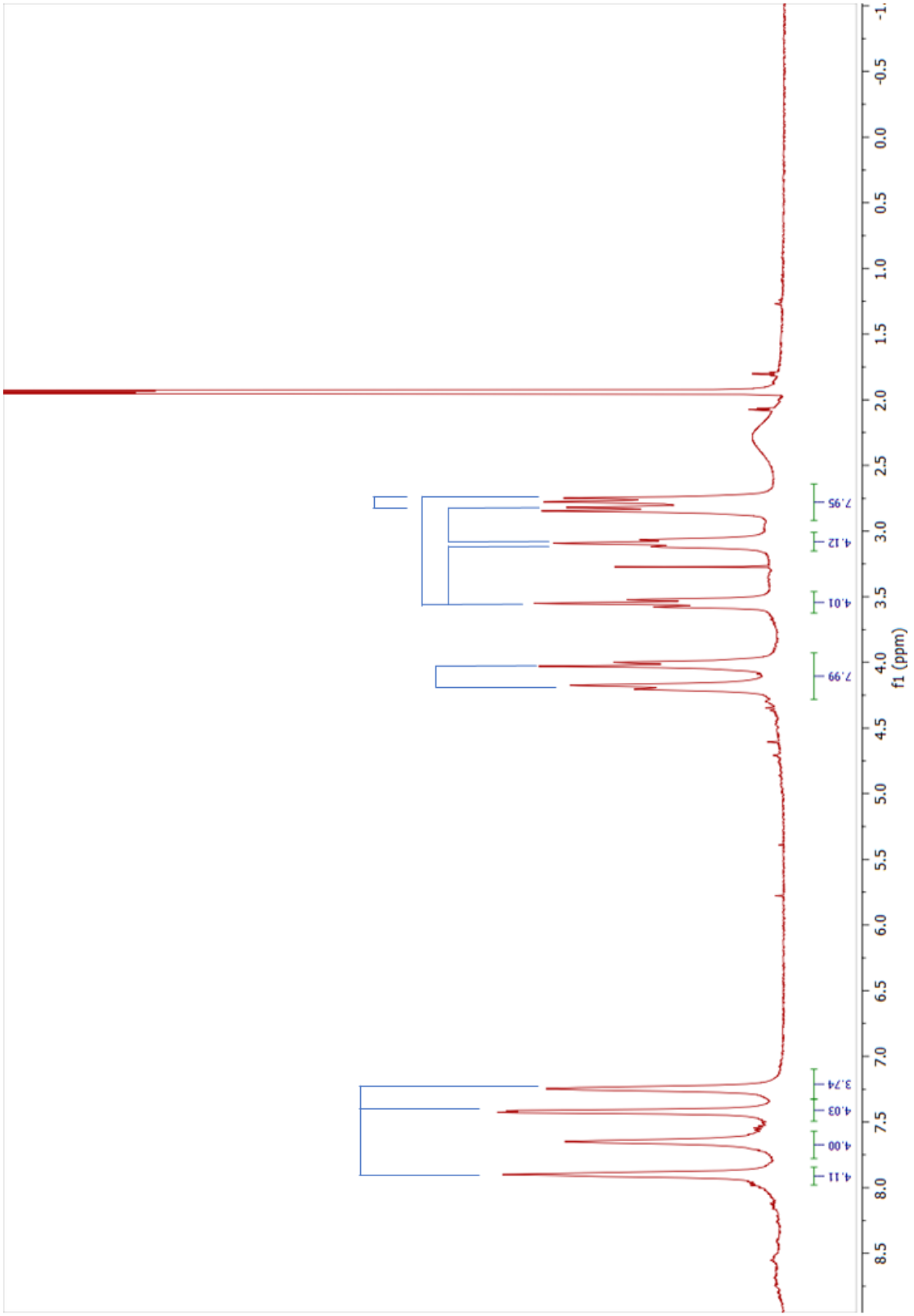

Figure B.9. ^{1}H NMR spectrum of $[Pb(Cyclen\text{-}4Py)]^{2+}$ (500 MHz, CD_3CN, 25 °C) showing ^{1}H-^{1}H correlations obtained from 2D COSY.

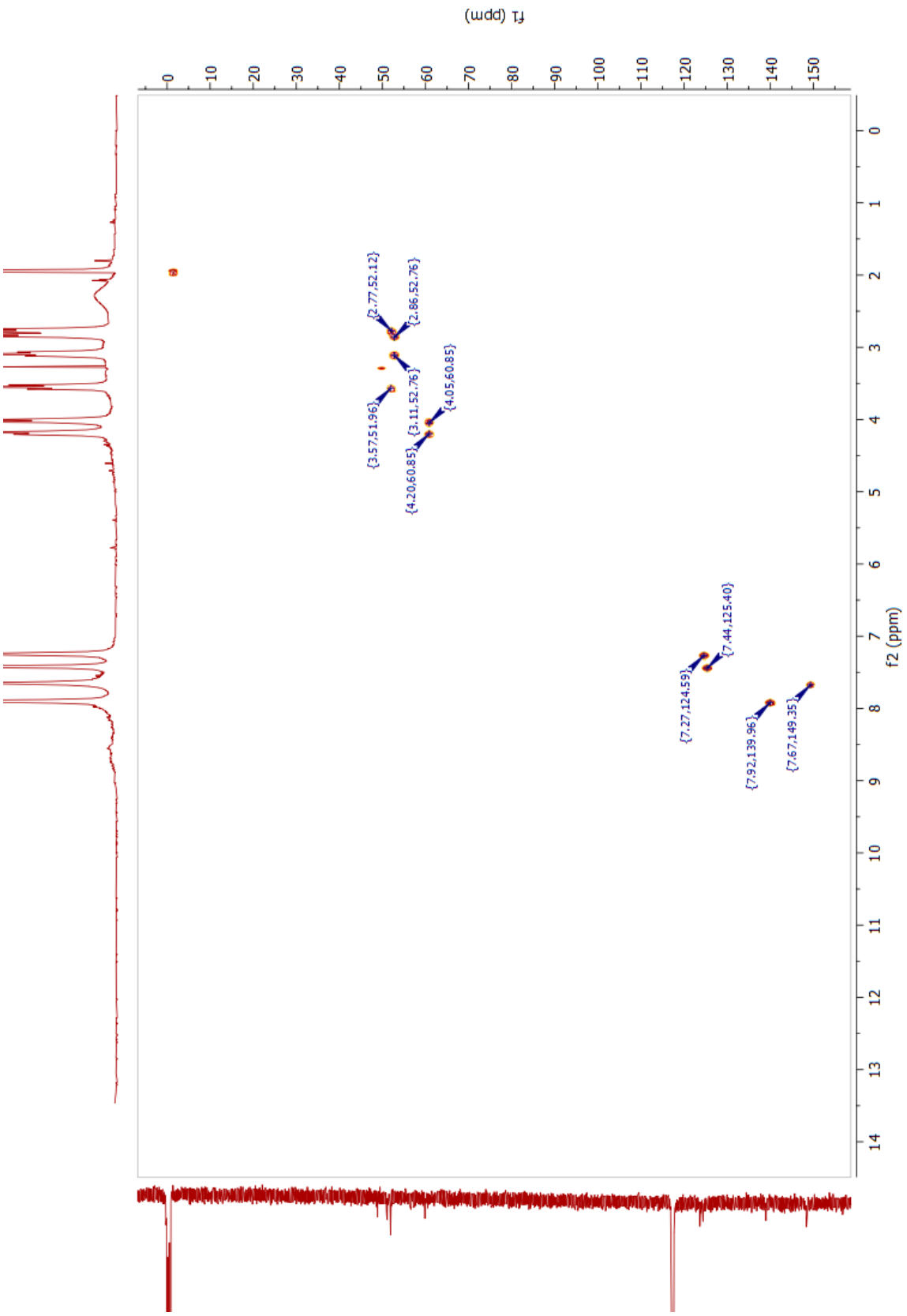

Figure B.10. HSQC NMR spectrum of $[Pb(Cyclen\text{-}4Py)]^{2+}$ (500 MHz, CD_3CN, 25 °C)

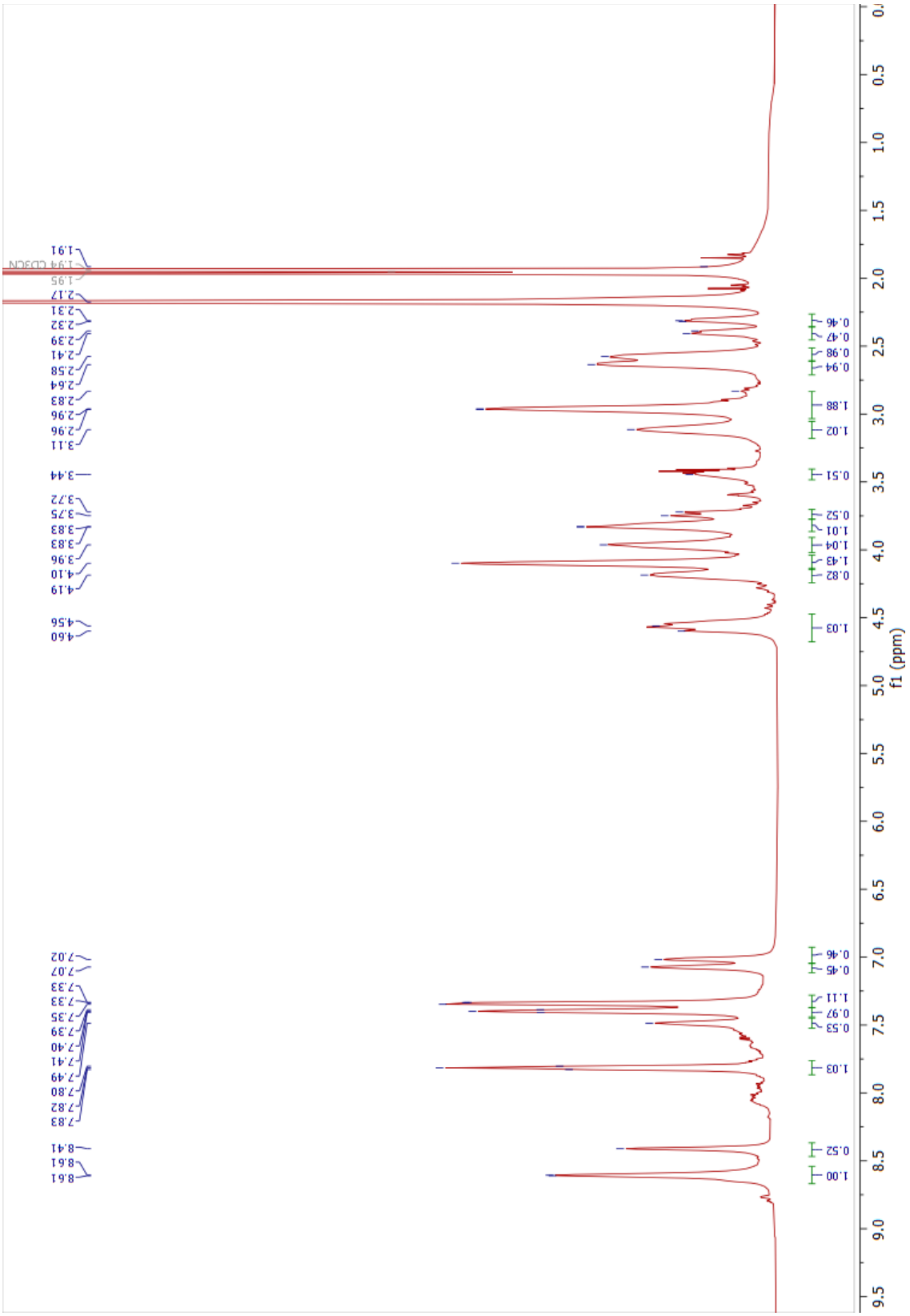

Figure B.11. ^{1}H NMR spectrum of $[Pb(Crown\text{-}4Py)]^{2+}$ (600 MHz, CD_3CN, 25 °C)

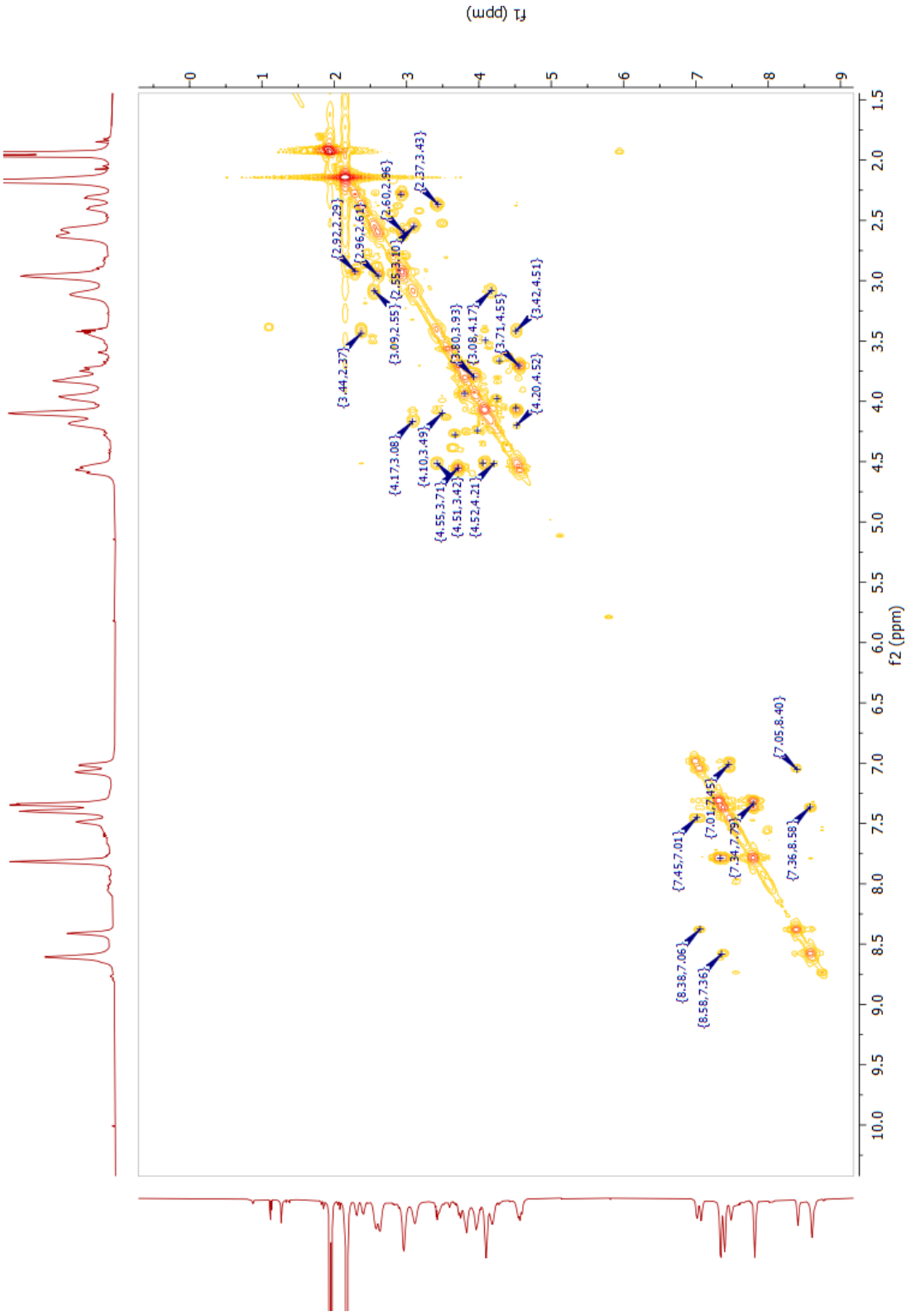

Figure B.12. ^{1}H-^{1}H COSY NMR spectrum of $[Pb(Crown\text{-}4Py)]^{2+}$ (600 MHz, CD_3CN, 25 °C)

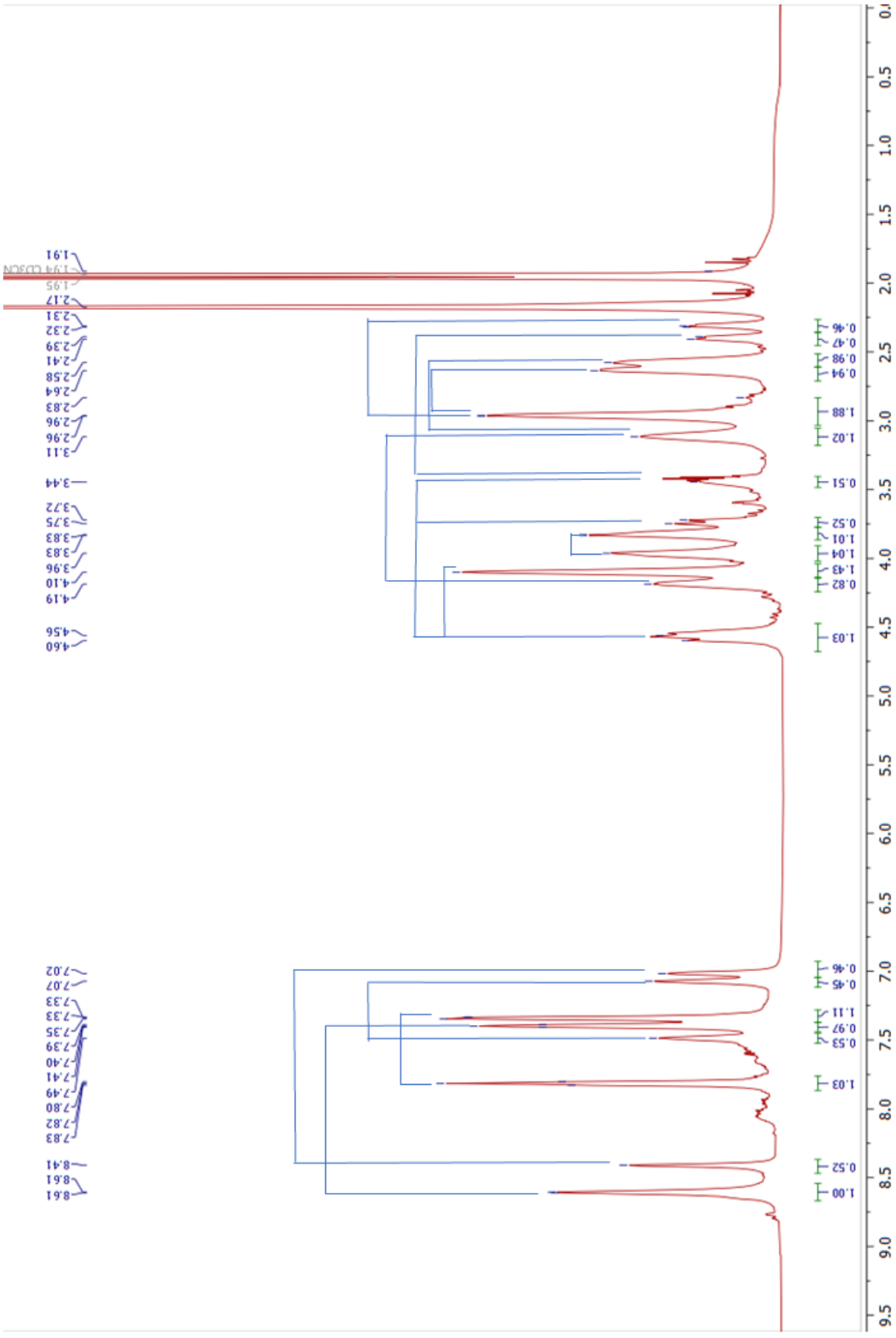

Figure B.13. ^{1}H NMR spectrum of $[Pb(Crown\text{-}4Py)]^{2+}$ (600 MHz, CD_3CN, 25 °C) showing ^{1}H-^{1}H correlations obtained from 2D COSY.

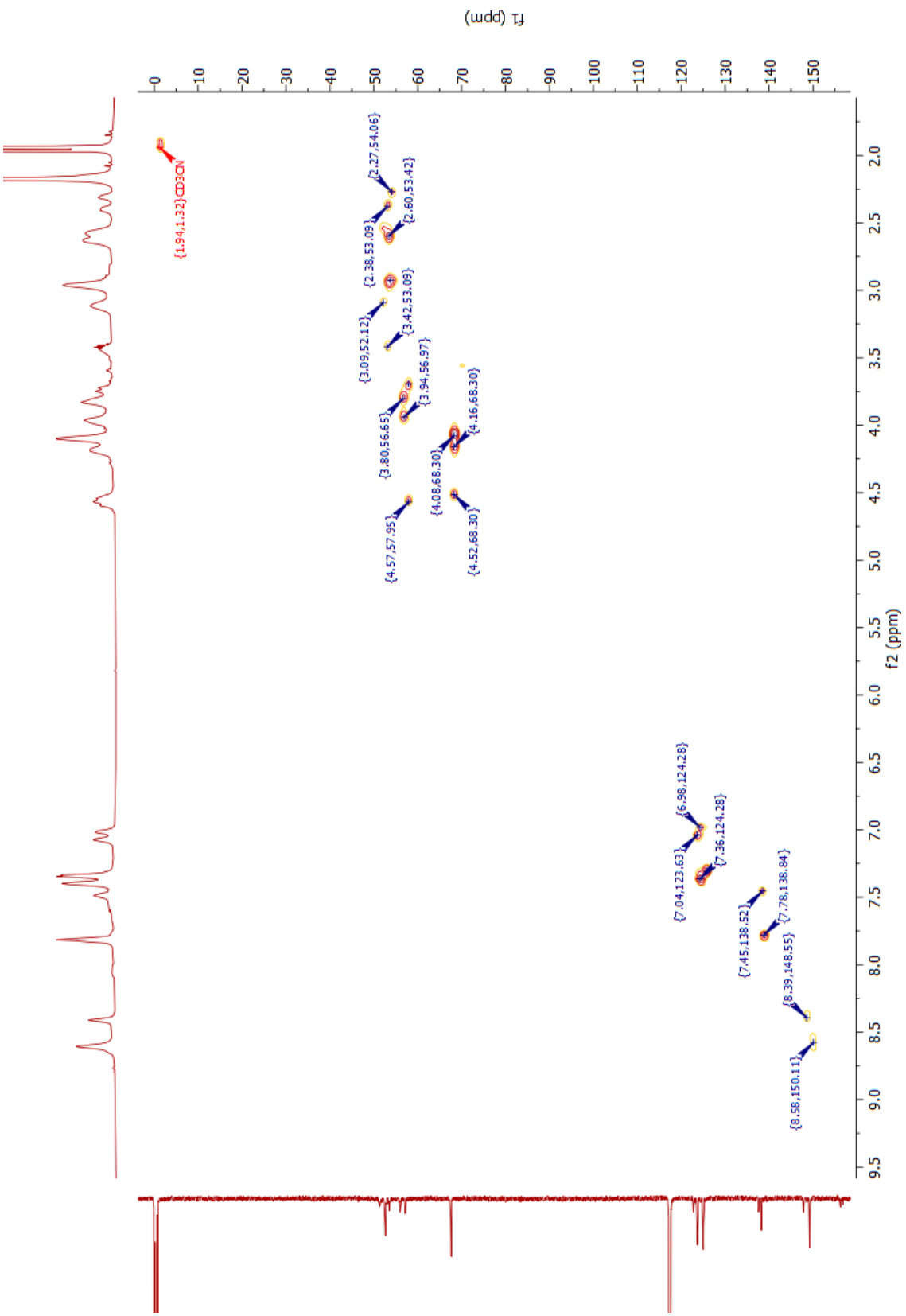

Figure B.14. HSQC NMR spectrum of $[Pb(Crown\text{-}4Py)]^{2+}$ (600 MHz, CD_3CN, 25 °C)

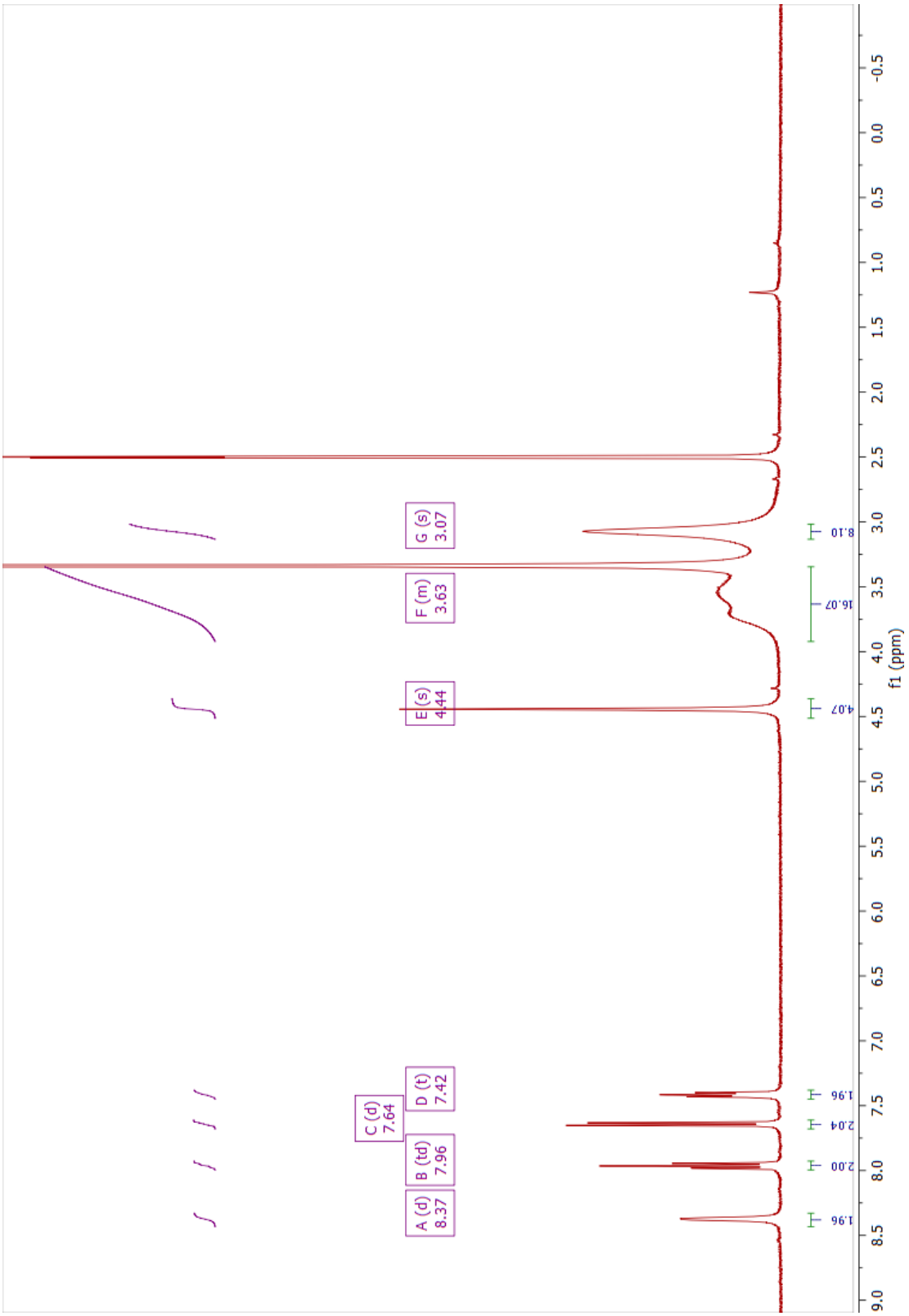

Figure B.15. ^{1}H NMR spectrum of $[Pb(NOON\text{-}2Py)]^{2+}$ (400 MHz, DMSO-d_6, 25 °C)

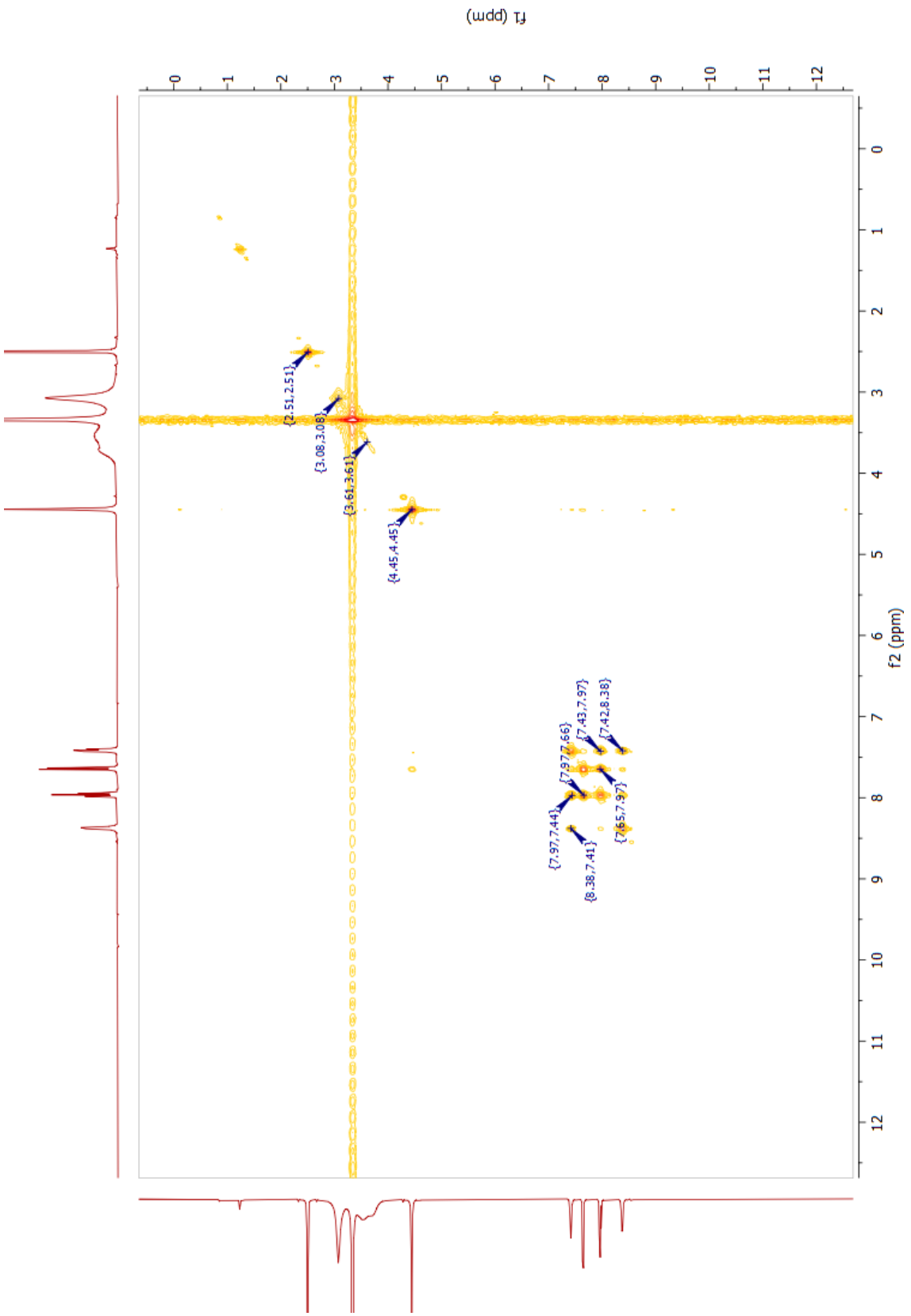

Figure B.16. ^{1}H-^{1}H COSY NMR spectrum of $[Pb(NOON\text{-}2Py)]^{2+}$ (400 MHz, DMSO-d6, 25 °C)

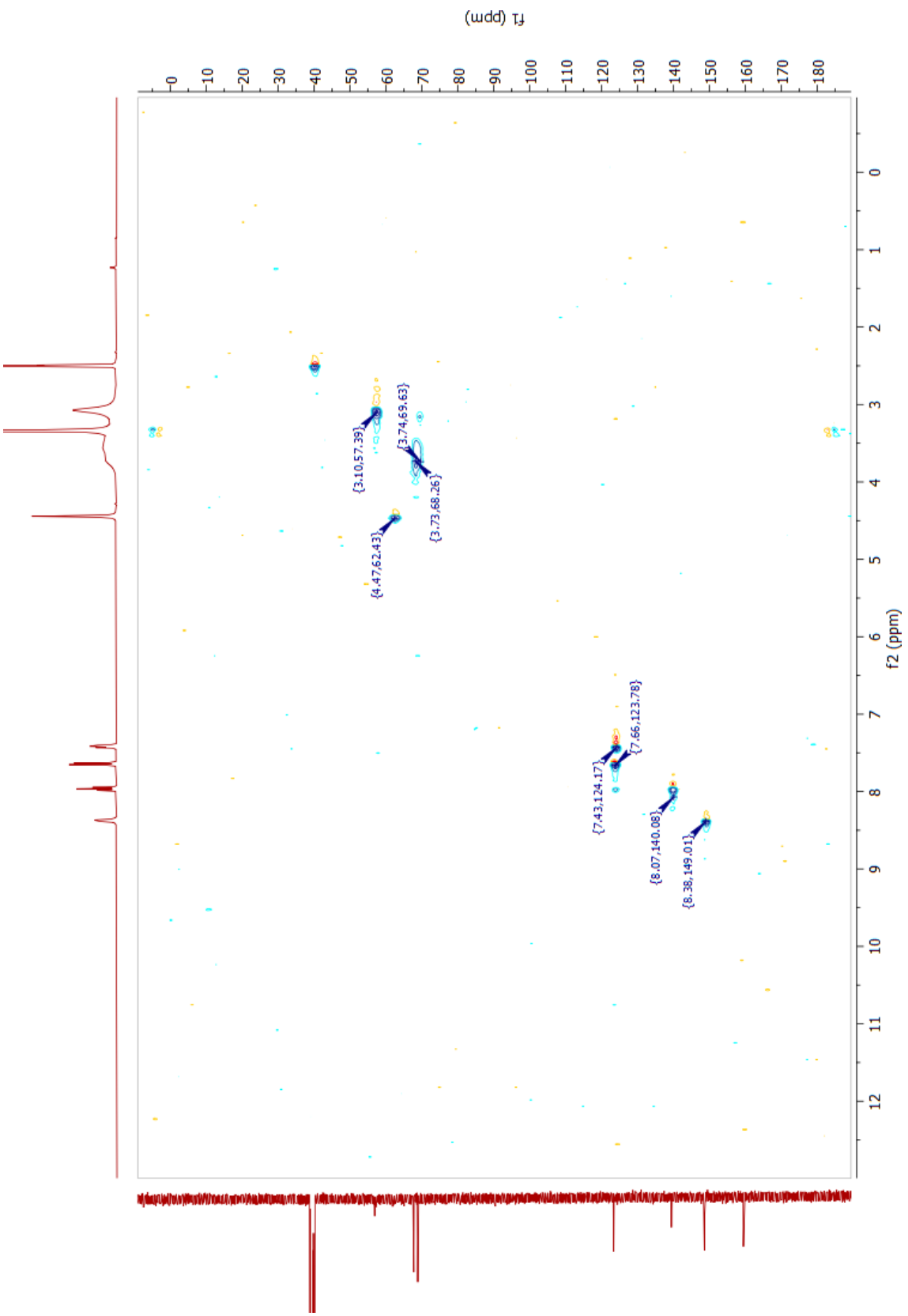

Figure B.17. HSQC NMR spectrum of $[Pb(NOON\text{-}2Py)]^{2+}$ (400 MHz, DMSO-d_6, 25 °C)

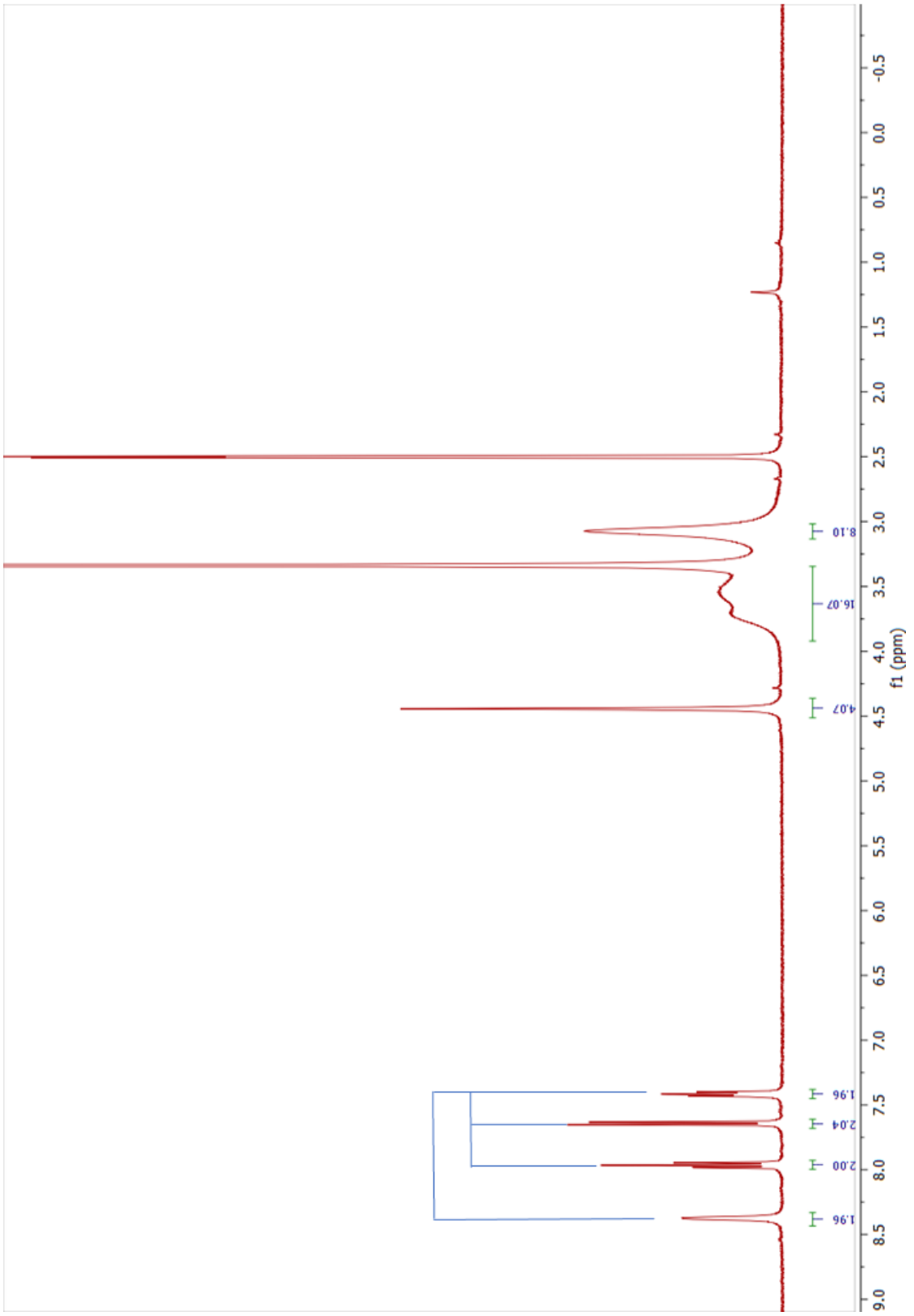

Figure B.18. ^{1}H NMR spectrum of $[Pb(NOON\text{-}2Py)]^{2+}$ (400 MHz, DMSO-d6, 25 °C) showing ^{1}H-^{1}H correlations obtained from 2D COSY.

Kinetic Inertness Studies

Table B.1. *In vitro* stability of ^{203}Pb-labeled chelators at 37 °C in human serum (n = 3)

^{203}Pb complex % intact	Time Point		
	24 h	48 h	72h
$[^{203}Pb][Pb(TCMC)]^{2+}$	98.1 ± 0.2%	98.2 ± 0.3%	97.2 ± 0.7%
$[^{203}Pb][Pb(DOTA)]^{2-}$	97.3 ± 0.6%	98.1 ± 0.2%	97.4 ± 0.5%
$[^{203}Pb][Pb(Cyclen\text{-}4Py)]^{2+}$	96.3 ± 5.5%	99.0 ± 1.1%	97.0 ± 2.8

The data from DOTA and TCMC were reproduced from reference 156.

Table B.2. Stability of ^{203}Pb-labeled chelators in a 20-fold excess EDTA (n = 3)

^{203}Pb complex % intact	Time Point			
	0.5 h	24 h	48 h	72h
$[^{203}Pb][Pb(TCMC)]^{2+}$	99.5 + 0.1%	98.1 + 1.6%	98.1 + 1.3%	97.5 + 2.8%
$[^{203}Pb][Pb(DOTA)]^{2-}$	99.0 + 0.3%	99.3 + 0.4%	99.4 + 0.1%	98.9 + 0.4%
$[^{203}Pb][Pb(Cyclen\text{-}4Py)]^{2+}$	98.8 + 0.8%	97.7 + 1.7%	97.5 + 1.2%	98.1 + 0.5%

Table B.3. Stability of ^{203}Pb-labeled chelators in a 20-fold excess Pb^{2+} (n = 3)

^{203}Pb complex % intact	Time Point			
	0.5 h	24 h	48 h	72h
$[^{203}Pb][Pb(TCMC)]^{2+}$	99.4 ± 0.1%	97.9 ± 2.1%	99.4 ± 0.1%	97.8 ± 2.0%
$[^{203}Pb][Pb(DOTA)]^{2-}$	99.2 ± 0.3%	99.2 ± 0.3%	99.1 ± 0.2%	98.7 ± 0.5%
$[^{203}Pb][Pb(Cyclen\text{-}4Py)]^{2+}$	98.6 ± 0.3%	98.5 ± 0.6%	97.5 ± 0.3%	98.0 ± 0.4%

Synthesis of Macrocyclic Backbone Pb Complexes

$[Pb(Cyclen)]^{2+}$

To a solution of cyclen in methanol (1 mL, 24.6 mg, 142.8 μmol) a methanolic solution of $Pb(ClO_4)_2 \cdot 3\ H_2O$ (65.7 mg, 142.8 μmol) was added. A white precipitate crashed out of solution. The washing procedure for this solid was identical to that described for $[Pb(Cyclen\text{-}4Py)]^{2+}$ and the solid was dried under vacuum. The complex was redissolved in acetonitrile and via vapour diffusion of diethyl ether, single colourless crystals suitable for X-ray diffraction analyses were obtained.

$[Pb(N_2O_4)]^{2+}$

To a solution of N_2O_4 in methanol (1 mL, 13.7 mg, 52.2 μmol a methanolic solution of $Pb(ClO_4)_2 \cdot 3\ H_2O$ (26.4 mg, 57.4 μmol) was added. No precipitate crashed out of solution and via vapour diffusion of diethyl ether into the methanol solution was used to obtain white, single crystals suitable for X-ray diffraction analyses.

$[Pb(N_4O_2)]^{2+}$

To a solution of N_4O_2 in methanol (1 mL, 11.0 mg , 42.2 μmol) a methanolic solution of $Pb(ClO_4)_2 \cdot 3\ H_2O$ (21.4 mg, 46.5 μmol) was added. Immediately, a white solid crashed out of solution. The washing procedure for this solid was identical to that described for $[Pb(Cyclen\text{-}4Py)]^{2+}$ and the solid was dried under vacuum. The complex was redissolved in acetonitrile (1 mL) and via vapour diffusion of diethyl ether, single crystals suitable for X-ray diffraction analyses were obtained.

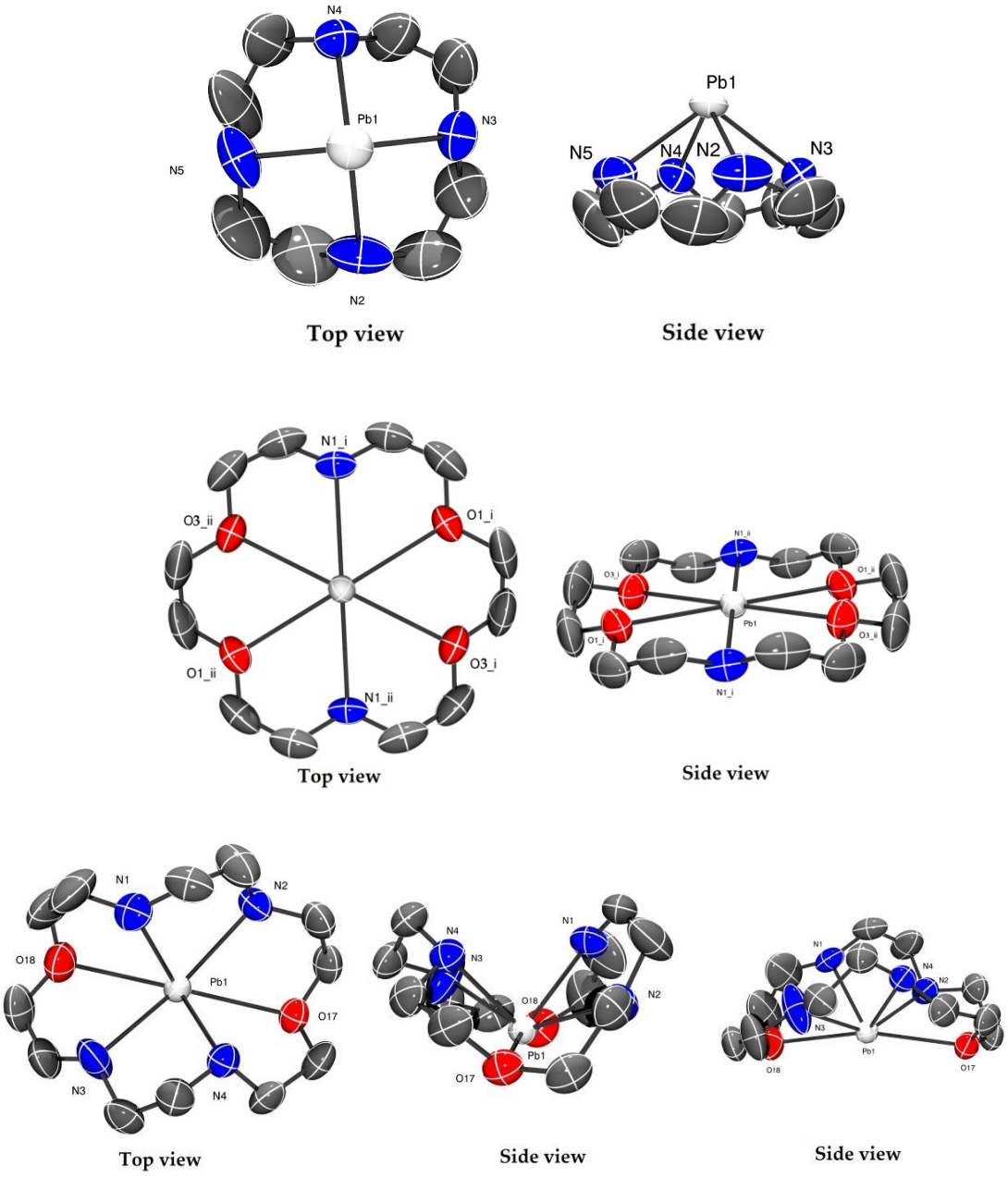

Figure B.19. X-ray crystal structures of $[Pb(Cyclen)]^{2+}$ (top), $[Pb(N_2O_4)]^{2+}$ (middle), and $[Pb(N_4O_2)]^{2+}$ (bottom) complexes with labeled atoms; hydrogens and counter anions were omitted for clarity. Ellipsoids drawn at 50% probability level.

X-ray Crystallography

Complexes $[Pb(NOON\text{-}2Py)]^{2+}$ and $[Pb(N_4O_2)]^{2+}$ crystallize with one independent molecule in the asymmetric unit. Complex $[Pb(Cyclen)]^{2+}$ crystallizes with one molecule in the asymmetric unit; in addition, the nitrogen groups are disordered and were modeled in two orientations. All the crystal structures containing ClO_4^- anions are disordered and were modeled in two orientations. Complex $[Pb(N_2O_4)]^{2+}$ crystallizes with half of the molecule residing on the inversion center.

Crystal data and structure refinement for Crystal structure $[Pb(Crown\text{-}4Py)]^{2+}$

Identification code	Crystal Structure $[Pb(Crown\text{-}4Py)]^{2+}$
Empirical formula	$C_{38}H_{51}N_9PbCl_2O_{10}$
Formula weight	1071.96
Temperature/K	296(2)
Crystal system	monoclinic
Space group	$P2_1/n$
a/Å	14.8512(16)
b/Å	15.4178(15)
c/Å	19.2200(19)
α /°	90
β /°	100.990(4)
γ /°	90
Volume/Å^3	4320.1(8)
Z	4
ρ_{calc}g/cm^3	1.648
μ /mm^{-1}	4.095
F(000)	2152.0
Crystal size/mm^3	0.612 × 0.378 × 0.34
Radiation	MoKα (λ = 0.71073)
2Θ range for data collection/°	3.412 to 58.312
Index ranges	-20 ≤ h ≤ 20, -20 ≤ k ≤ 21, -25 ≤ l ≤ 26
Reflections collected	129718
Independent reflections	11646 [R_{int} = 0.0428, R_{sigma} = 0.0236]
Data/restraints/parameters	11646/986/542
Goodness-of-fit on F^2	1.032

Final R indexes [I>=2 σ (I)]	R_1 = 0.0316, wR_2 = 0.0806
Final R indexes [all data]	R_1 = 0.0454, wR_2 = 0.0882
Largest diff. peak/hole / e Å^{-3}	0.91/-0.66

Bond Lengths for Crystal Structure of $[Pb(Crown\text{-}4Py)]^{2+}$						
Atom	**Atom**	**Length/Å**		**Atom**	**Atom**	**Length/Å**
Pb1	O1	2.613(3)		N4	C27	1.488(5)
Pb1	O2	2.604(3)		C4	C5	1.408(9)
Pb1	N2	2.769(3)		N5	C5	1.327(7)
Pb1	N3	2.742(3)		N6	C10	1.322(5)
Pb1	N4	2.764(3)		N6	C14	1.328(6)
Cl1	O7	1.329(6)		C6	C32	1.503(6)
Cl1	O8	1.378(7)		N7	C32	1.339(5)
Cl1	O9	1.254(6)		N7	C36	1.340(6)
Cl1	O10	1.250(8)		C7	C8	1.470(7)
O1	C16	1.426(6)		N8	C22	1.333(5)
O1	C17	1.434(6)		N8	C26	1.337(5)
N1	C7	1.501(6)		N9	C37	1.111(9)
N1	C30	1.473(6)		C9	C10	1.497(6)
N1	C31	1.463(6)		C10	C11	1.370(6)
C1	C2	1.392(7)		C11	C12	1.371(8)
C1	N5	1.344(7)		C12	C13	1.341(8)
C1	C31	1.504(8)		C13	C14	1.361(7)
Cl2	O3	1.388(5)		C15	C16	1.491(8)
Cl2	O4	1.422(4)		C17	C18	1.523(8)
Cl2	O5	1.353(5)		C19	C20	1.510(7)
Cl2	O6	1.393(6)		C21	C22	1.510(5)
O2	C28	1.417(5)		C22	C23	1.375(5)
O2	C29	1.428(5)		C23	C24	1.373(7)
N2	C8	1.480(6)		C24	C25	1.369(7)
N2	C9	1.467(5)		C25	C26	1.362(7)
N2	C15	1.488(6)		C27	C28	1.505(7)
C2	C3	1.357(10)		C29	C30	1.507(7)
N3	C6	1.471(5)		C32	C33	1.381(6)
N3	C18	1.479(6)		C33	C34	1.361(8)
N3	C19	1.478(6)		C34	C35	1.353(8)
C3	C4	1.341(11)		C35	C36	1.381(7)
N4	C20	1.473(5)		C37	C38	1.445(11)
N4	C21	1.473(5)				

Bond Angles for Crystal Structure of $[Pb(Crown\text{-}4Py)]^{2+}$							
Atom	**Atom**	**Atom**	**Angle/˚**	**Atom**	**Atom**	**Atom**	**Angle/˚**
O1	Pb1	N2	63.11(11)	C20	N4	C27	111.6(3)
O1	Pb1	N3	63.24(10)	C21	N4	Pb1	111.5(2)
O1	Pb1	N4	115.86(10)	C21	N4	C20	108.9(3)
O2	Pb1	O1	178.39(9)	C21	N4	C27	109.6(3)
O2	Pb1	N2	116.65(10)	C27	N4	Pb1	104.8(2)
O2	Pb1	N3	117.02(10)	C3	C4	C5	118.6(7)
O2	Pb1	N4	63.27(9)	C5	N5	C1	116.8(5)
N3	Pb1	N2	126.33(11)	N5	C5	C4	123.2(7)
N3	Pb1	N4	67.05(10)	C10	N6	C14	117.5(4)
N4	Pb1	N2	142.97(9)	N3	C6	C32	113.7(3)
O7	Cl1	O8	106.5(6)	C32	N7	C36	117.2(4)
O9	Cl1	O7	106.4(6)	C8	C7	N1	116.0(4)
O9	Cl1	O8	115.2(7)	C22	N8	C26	117.1(4)
O10	Cl1	O7	102.9(8)	C7	C8	N2	115.9(4)
O10	Cl1	O8	109.0(6)	N2	C9	C10	113.7(4)
O10	Cl1	O9	115.6(8)	N6	C10	C9	117.9(3)
C16	O1	Pb1	122.7(3)	N6	C10	C11	122.4(5)
C16	O1	C17	114.5(4)	C11	C10	C9	119.7(4)
C17	O1	Pb1	122.8(3)	C10	C11	C12	118.8(5)
C30	N1	C7	112.9(4)	C13	C12	C11	119.2(5)
C31	N1	C7	107.0(4)	C12	C13	C14	118.9(5)
C31	N1	C30	111.6(4)	N6	C14	C13	123.2(5)
C2	C1	C31	120.6(5)	N2	C15	C16	114.4(4)
N5	C1	C2	122.3(6)	O1	C16	C15	109.5(4)
N5	C1	C31	117.1(4)	O1	C17	C18	109.3(3)
O3	Cl2	O4	114.0(3)	N3	C18	C17	113.8(4)
O3	Cl2	O6	104.6(5)	N3	C19	C20	114.7(3)
O5	Cl2	O3	112.9(5)	N4	C20	C19	114.7(3)
O5	Cl2	O4	112.5(4)	N4	C21	C22	113.1(3)
O5	Cl2	O6	104.6(6)	N8	C22	C21	117.9(3)
O6	Cl2	O4	107.2(4)	N8	C22	C23	122.5(4)
C28	O2	Pb1	123.4(2)	C23	C22	C21	119.5(4)
C28	O2	C29	113.8(3)	C24	C23	C22	119.0(5)
C29	O2	Pb1	122.7(3)	C25	C24	C23	119.0(4)
C8	N2	Pb1	110.2(2)	C26	C25	C24	118.4(4)
C8	N2	C15	113.0(4)	N8	C26	C25	123.8(5)
C9	N2	Pb1	111.3(2)	N4	C27	C28	114.4(3)

C9	N2	C8	107.7(4)		O2	C28	C27	109.2(3)
C9	N2	C15	110.5(3)		O2	C29	C30	109.3(4)
C15	N2	Pb1	104.2(2)		N1	C30	C29	115.4(4)
C3	C2	C1	119.5(7)		N1	C31	C1	114.8(4)
C6	N3	Pb1	109.8(3)		N7	C32	C6	118.2(4)
C6	N3	C18	111.5(3)		N7	C32	C33	122.0(5)
C6	N3	C19	108.4(4)		C33	C32	C6	119.8(4)
C18	N3	Pb1	106.1(2)		C34	C33	C32	119.4(5)
C19	N3	Pb1	110.2(2)		C35	C34	C33	119.6(5)
C19	N3	C18	110.8(4)		C34	C35	C36	118.5(5)
C4	C3	C2	119.6(6)		N7	C36	C35	123.2(5)
C20	N4	Pb1	110.4(2)		N9	C37	C38	173.7(12)

Crystal data and structure refinement for Crystal structure $[Pb(Cyclen\text{-}4Py)]^{2+}$

Identification code	Crystal structure $[Pb(Cyclen\text{-}4Py)]^{2+}$
Empirical formula	$C_{32}H_{40}N_8PbCl_2O_8$
Formula weight	942.81
Temperature/K	296(2)
Crystal system	triclinic
Space group	P-1
a/Å	8.9974(13)
b/Å	10.9577(18)
c/Å	19.929(3)
α/°	81.901(6)
β/°	77.037(5)
γ/°	72.741(6)
Volume/Å^3	1822.7(5)
Z	2
ρ_{calc}g/cm^3	1.718
μ/mm^{-1}	4.835
F(000)	936.0
Crystal size/mm^3	0.356 × 0.234 × 0.212
Radiation	MoKα (λ = 0.71073)
2Θ range for data collection/°	3.904 to 61.002
Index ranges	-12 ≤ h ≤ 12, -15 ≤ k ≤ 15, -28 ≤ l ≤ 27
Reflections collected	36513

Independent reflections	11077 [R_{int} = 0.0450, R_{sigma} = 0.0403]
Data/restraints/parameters	11077/554/497
Goodness-of-fit on F^2	1.044
Final R indexes [I>=2σ (I)]	R_1 = 0.0262, wR_2 = 0.0605
Final R indexes [all data]	R_1 = 0.0355, wR_2 = 0.0638
Largest diff. peak/hole / e $Å^{-3}$	0.76/-0.69

Bond Lengths for Crystal structure $[Pb(Cyclen\text{-}4Py)]^{2+}$						
Atom	**Atom**	**Length/Å**		**Atom**	**Atom**	**Length/Å**
Pb1	N1	2.630(2)		N4	C27	1.481(3)
Pb1	N2	2.652(2)		O6	O7	1.75(5)
Pb1	N3	2.695(2)		N5	C10	1.333(4)
Pb1	N4	2.710(2)		N5	C14	1.346(4)
Pb1	N5	2.712(3)		C5	C6	1.527(4)
Pb1	N6	2.776(3)		N6	C16	1.324(4)
Pb1	N7	2.781(2)		N6	C20	1.347(5)
Cl1	O1	1.407(4)		N7	C22	1.332(3)
Cl1	O2	1.414(3)		N7	C26	1.344(4)
Cl1	O3	1.378(3)		C7	C8	1.507(4)
Cl1	O4	1.400(3)		N8	C28	1.336(4)
N1	C1	1.480(4)		N8	C32	1.333(4)
N1	C8	1.490(4)		C9	C10	1.514(4)
N1	C9	1.477(4)		C10	C11	1.366(4)
C1	C2	1.517(4)		C11	C12	1.375(5)
Cl2	O5	1.34(2)		C12	C13	1.354(5)
Cl2	O6	1.39(2)		C13	C14	1.366(5)
Cl2	O7	1.524(18)		C15	C16	1.511(4)
Cl2	O8	1.283(14)		C16	C17	1.371(4)
Cl2	O9	1.426(8)		C17	C18	1.377(5)
Cl2	O10	1.392(8)		C18	C19	1.353(6)
Cl2	O11	1.383(4)		C19	C20	1.369(5)
Cl2	O12	1.409(5)		C21	C22	1.519(4)
N2	C2	1.486(4)		C22	C23	1.379(4)
N2	C3	1.486(4)		C23	C24	1.371(5)
N2	C15	1.485(4)		C24	C25	1.356(5)
N3	C4	1.486(3)		C25	C26	1.376(5)
N3	C5	1.477(3)		C27	C28	1.496(4)
N3	C21	1.468(4)		C28	C29	1.371(4)
C3	C4	1.504(4)		C29	C30	1.368(5)
N4	C6	1.475(4)		C30	C31	1.361(6)
N4	C7	1.481(3)		C31	C32	1.355(6)

Bond Angles for Crystal structure $[Pb(Cyclen\text{-}4Py)]^{2+}$							
Atom	**Atom**	**Atom**	**Angle/°**		**Atom**	**Atom**	**Atom**	**Angle/°**
N1	Pb1	N2	68.87(7)		C21	N3	C5	109.8(2)
N1	Pb1	N3	106.07(7)		N2	C3	C4	114.1(2)
N1	Pb1	N4	68.95(7)		C6	N4	Pb1	110.50(15)
N1	Pb1	N5	63.14(8)		C6	N4	C7	110.1(2)
N1	Pb1	N6	87.38(8)		C6	N4	C27	109.7(2)
N1	Pb1	N7	157.30(8)		C7	N4	Pb1	109.10(15)
N2	Pb1	N3	69.55(7)		C7	N4	C27	110.3(2)
N2	Pb1	N4	105.97(7)		C27	N4	Pb1	107.02(16)
N2	Pb1	N5	119.95(7)		N3	C4	C3	114.0(2)
N2	Pb1	N6	64.10(8)		Cl2	O6	O7	56.5(16)
N2	Pb1	N7	88.66(8)		Cl2	O7	O6	49.6(11)
N3	Pb1	N4	67.74(7)		C10	N5	Pb1	114.87(19)
N3	Pb1	N5	156.39(9)		C10	N5	C14	117.8(3)
N3	Pb1	N6	122.48(7)		C14	N5	Pb1	125.4(2)
N3	Pb1	N7	60.90(7)		N3	C5	C6	112.6(2)
N4	Pb1	N5	88.65(8)		C16	N6	Pb1	114.43(19)
N4	Pb1	N6	156.31(8)		C16	N6	C20	118.0(3)
N4	Pb1	N7	116.75(7)		C20	N6	Pb1	126.5(2)
N5	Pb1	N6	79.48(9)		N4	C6	C5	113.0(2)
N5	Pb1	N7	135.92(8)		C22	N7	Pb1	113.10(18)
N6	Pb1	N7	85.46(8)		C22	N7	C26	117.6(3)
O1	Cl1	O2	108.0(3)		C26	N7	Pb1	119.34(19)
O3	Cl1	O1	107.1(3)		N4	C7	C8	113.6(2)
O3	Cl1	O2	108.4(2)		C32	N8	C28	118.3(3)
O3	Cl1	O4	114.2(3)		N1	C8	C7	113.2(2)
O4	Cl1	O1	107.6(2)		N1	C9	C10	113.7(2)
O4	Cl1	O2	111.2(2)		N5	C10	C9	117.7(3)
C1	N1	Pb1	110.17(16)		N5	C10	C11	121.7(3)
C1	N1	C8	110.1(2)		C11	C10	C9	120.6(3)
C8	N1	Pb1	109.09(15)		C10	C11	C12	119.5(3)
C9	N1	Pb1	107.74(17)		C13	C12	C11	119.6(3)
C9	N1	C1	110.1(2)		C12	C13	C14	118.2(3)
C9	N1	C8	109.6(2)		N5	C14	C13	123.1(3)
N1	C1	C2	113.2(2)		N2	C15	C16	112.6(2)
O5	Cl2	O6	92(2)		N6	C16	C15	115.9(2)
O5	Cl2	O7	88.9(18)		N6	C16	C17	122.4(3)

O6	Cl2	O7	74(2)
O8	Cl2	O5	130.5(17)
O8	Cl2	O6	137.7(14)
O8	Cl2	O7	104.3(14)
O10	Cl2	O9	117.6(7)
O10	Cl2	O12	95.5(8)
O11	Cl2	O9	113.5(5)
O11	Cl2	O10	116.1(5)
O11	Cl2	O12	108.1(4)
O12	Cl2	O9	103.0(6)
C2	N2	Pb1	110.62(16)
C3	N2	Pb1	110.08(16)
C3	N2	C2	109.9(2)
C15	N2	Pb1	105.74(17)
C15	N2	C2	110.2(2)
C15	N2	C3	110.2(2)
N2	C2	C1	112.1(2)
C4	N3	Pb1	106.22(15)
C5	N3	Pb1	109.70(16)
C5	N3	C4	110.8(2)
C21	N3	Pb1	110.29(16)
C21	N3	C4	109.9(2)

C17	C16	C15	121.6(3)
C16	C17	C18	118.9(3)
C19	C18	C17	119.2(3)
C18	C19	C20	119.2(4)
N6	C20	C19	122.2(4)
N3	C21	C22	115.2(2)
N7	C22	C21	117.8(2)
N7	C22	C23	122.7(3)
C23	C22	C21	119.4(3)
C24	C23	C22	118.3(3)
C25	C24	C23	120.1(3)
C24	C25	C26	118.6(3)
N7	C26	C25	122.6(3)
N4	C27	C28	113.7(2)
N8	C28	C27	116.3(2)
N8	C28	C29	121.9(3)
C29	C28	C27	121.8(3)
C30	C29	C28	118.8(3)
C31	C30	C29	119.3(3)
C32	C31	C30	119.1(4)
N8	C32	C31	122.5(4)

Crystal data and structure refinement for Crystal structure $[Pb(NOON\text{-}2Py)]^{2+}$

Identification code	Crystal structure $[Pb(NOON\text{-}2Py)]^{2+}$
Empirical formula	$C_{48}H_{72}ClN_8O_9Pb_2P_4F_{24}$
Formula weight	1899.39
Temperature/K	299(2)
Crystal system	triclinic
Space group	P-1
a/Å	10.8986(12)
b/Å	17.928(2)
c/Å	19.422(2)
α /°	65.923(4)
β /°	86.744(4)
γ /°	75.221(4)
Volume/Å^3	3345.2(6)
Z	2
ρ_{calc} g/cm^3	1.886
μ /mm^{-1}	5.245
F(000)	1856.0
Crystal size/mm^3	0.523 × 0.368 × 0.18
Radiation	MoKα (λ = 0.71073)
2Θ range for data collection/°	3.87 to 56.624
Index ranges	$-14 \le h \le 14$, $-23 \le k \le 23$, $-25 \le l \le 25$
Reflections collected	54204
Independent reflections	16637 [R_{int} = 0.0342, R_{sigma} = 0.0403]
Data/restraints/parameters	16637/0/875
Goodness-of-fit on F^2	1.047
Final R indexes [I>=2σ (I)]	R_1 = 0.0334, wR_2 = 0.0811
Final R indexes [all data]	R_1 = 0.0485, wR_2 = 0.0875
Largest diff. peak/hole / e Å^{-3}	1.25/-1.03

Bond Lengths for Crystal structure $[Pb(NOON\text{-}2Py)]^{2+}$						
Atom	**Atom**	**Length/Å**		**Atom**	**Atom**	**Length/Å**
Pb1	N1	2.776(3)		P4	F26	1.547(4)
Pb1	O2	2.718(3)		N4	C20	1.345(5)
Pb1	N2	2.716(3)		N4	C24	1.331(6)
Pb1	O3	2.717(3)		O5	C34	1.403(7)
Pb1	N3	2.598(3)		O5	C35	1.416(7)
Pb1	O4	2.754(3)		N5	C30	1.485(8)
Pb1	N4	2.575(3)		N5	C31	1.484(7)
P1	F1	1.590(4)		N5	C43	1.475(7)
P1	F2	1.584(3)		C5	C6	1.485(7)
P1	F3	1.598(3)		O6	C32	1.406(7)
P1	F4	1.582(4)		O6	C33	1.424(8)
P1	F5	1.587(3)		N6	C25	1.514(7)
P1	F6	1.561(3)		N6	C36	1.474(7)
O1	C10	1.431(6)		N6	C37	1.481(7)
O1	C11	1.429(6)		O7	C28	1.427(7)
N1	C1	1.486(6)		O7	C29	1.422(7)
N1	C12	1.490(6)		N7	C38	1.317(7)
N1	C13	1.477(6)		N7	C42	1.348(7)
C1	C2	1.500(7)		C7	C8	1.496(7)
Pb2	O5	2.741(4)		O8	C26	1.414(7)
Pb2	N6	2.686(4)		O8	C27	1.430(7)
Pb2	N7	2.550(4)		N8	C44	1.333(6)
Pb2	O8	2.670(3)		N8	C48	1.345(6)
Pb2	N8	2.537(4)		C9	C10	1.477(8)
P2	F7	1.521(5)		C11	C12	1.495(7)
P2	F8	1.589(4)		F13	F14	1.608(14)
P2	F9	1.527(5)		C13	C14	1.501(6)
P2	F10	1.541(5)		C14	C15	1.382(6)
P2	F11	1.542(4)		C15	C16	1.366(7)
P2	F12	1.526(5)		F16	F17	1.610(15)
O2	C8	1.429(6)		C16	C17	1.370(7)
O2	C9	1.439(6)		F17	F20	1.766(12)
N2	C6	1.493(6)		C17	C18	1.376(7)
N2	C7	1.481(6)		F15	F20	1.714(15)
N2	C19	1.476(5)		C19	C20	1.498(6)
C2	O4	1.433(5)		C20	C21	1.388(6)

P3	F13	1.484(7)		C21	C22	1.362(8)
P3	F16	1.488(7)		C22	C23	1.381(7)
P3	F14	1.546(7)		C23	C24	1.369(6)
P3	F17	1.481(7)		C25	C26	1.471(9)
P3	F18	1.544(9)		C27	C28	1.485(9)
P3	F15	1.577(9)		C29	C30	1.491(9)
P3	F19	1.539(6)		C31	C32	1.495(9)
P3	F20	1.485(6)		C33	C34	1.486(9)
O3	C4	1.418(6)		C35	C36	1.490(9)
O3	C5	1.429(5)		C37	C38	1.497(8)
N3	C14	1.343(5)		C38	C39	1.382(8)
N3	C18	1.340(6)		C39	C40	1.363(11)
C3	O4	1.426(6)		C40	C41	1.363(11)
C3	C4	1.480(7)		C41	C42	1.359(8)
P4	F21	1.555(4)		C43	C44	1.496(8)
P4	F22	1.575(3)		C44	C45	1.380(8)
P4	F23	1.545(5)		C45	C46	1.377(9)
P4	F24	1.567(4)		C46	C47	1.327(9)
P4	F25	1.591(3)		C47	C48	1.354(7)
Pb1	N1	2.776(3)		P4	F26	1.547(4)
Pb1	O2	2.718(3)		N4	C20	1.345(5)
Pb1	N2	2.716(3)		N4	C24	1.331(6)

Bond Angles for Crystal Structure $[Pb(NOON\text{-}2Py)]^{2+}$								
Atom	Atom	Atom	Angle/°		Atom	Atom	Atom	Angle/°
O2	Pb1	N1	120.50(10)		C18	N3	C14	117.6(4)
O2	Pb1	O4	156.35(10)		O4	C3	C4	108.5(4)
N2	Pb1	N1	155.12(10)		F21	P4	F22	90.8(2)
N2	Pb1	O2	64.73(11)		F21	P4	F24	179.6(4)
N2	Pb1	O3	65.76(10)		F21	P4	F25	90.6(2)
N2	Pb1	O4	121.90(10)		F22	P4	F25	178.0(3)
O3	Pb1	N1	124.23(10)		F23	P4	F21	88.8(4)
O3	Pb1	O2	112.03(10)		F23	P4	F22	89.2(3)
O3	Pb1	O4	60.01(9)		F23	P4	F24	90.7(4)
N3	Pb1	N1	64.69(11)		F23	P4	F25	89.4(2)
N3	Pb1	O2	78.85(11)		F23	P4	F26	174.8(4)
N3	Pb1	N2	94.84(11)		F24	P4	F22	89.2(2)
N3	Pb1	O3	147.48(10)		F24	P4	F25	89.5(2)
N3	Pb1	O4	120.45(10)		F26	P4	F21	96.4(4)
O4	Pb1	N1	64.36(10)		F26	P4	F22	90.9(2)
N4	Pb1	N1	95.03(10)		F26	P4	F24	84.1(3)
N4	Pb1	O2	121.55(11)		F26	P4	F25	90.4(2)
N4	Pb1	N2	65.28(10)		C2	O4	Pb1	107.4(3)
N4	Pb1	O3	71.13(10)		C3	O4	Pb1	112.7(3)
N4	Pb1	N3	77.12(11)		C3	O4	C2	113.6(4)
N4	Pb1	O4	78.68(10)		C20	N4	Pb1	120.3(3)
F1	P1	F3	89.6(2)		C24	N4	Pb1	120.7(3)
F2	P1	F1	90.4(2)		C24	N4	C20	118.6(4)
F2	P1	F3	88.19(19)		O3	C4	C3	108.8(4)
F2	P1	F5	177.7(2)		C34	O5	Pb2	121.4(4)
F4	P1	F1	179.0(2)		C34	O5	C35	114.7(5)
F4	P1	F2	90.0(2)		C35	O5	Pb2	114.7(3)
F4	P1	F3	89.5(2)		C31	N5	C30	108.3(5)
F4	P1	F5	90.3(2)		C43	N5	C30	111.9(5)
F5	P1	F1	89.3(2)		C43	N5	C31	110.5(5)
F5	P1	F3	89.5(2)		O3	C5	C6	108.8(4)
F6	P1	F1	90.9(2)		C32	O6	C33	113.6(5)
F6	P1	F2	91.7(2)		C25	N6	Pb2	110.9(3)
F6	P1	F3	179.4(2)		C36	N6	Pb2	105.1(3)

F6	P1	F4	89.9(2)		C36	N6	C25	110.0(5)
F6	P1	F5	90.7(2)		C36	N6	C37	110.6(5)
C11	O1	C10	112.9(4)		C37	N6	Pb2	112.3(3)
C1	N1	Pb1	110.1(3)		C37	N6	C25	108.0(4)
C1	N1	C12	107.6(4)		C5	C6	N2	116.0(4)
C12	N1	Pb1	110.4(3)		C29	O7	C28	112.1(4)
C13	N1	Pb1	107.1(2)		C38	N7	Pb2	122.1(3)
C13	N1	C1	109.7(4)		C38	N7	C42	118.3(5)
C13	N1	C12	112.0(4)		C42	N7	Pb2	119.1(4)
N1	C1	C2	112.7(4)		N2	C7	C8	113.4(4)
N6	Pb2	O5	65.55(13)		C26	O8	Pb2	114.6(3)
N7	Pb2	O5	70.86(12)		C26	O8	C27	111.7(4)
N7	Pb2	N6	65.44(13)		C27	O8	Pb2	118.3(3)
N7	Pb2	O8	118.74(13)		C44	N8	Pb2	124.2(3)
O8	Pb2	O5	115.56(12)		C44	N8	C48	116.9(4)
O8	Pb2	N6	64.71(13)		C48	N8	Pb2	118.1(3)
N8	Pb2	O5	147.57(12)		O2	C8	C7	107.0(4)
N8	Pb2	N6	99.98(12)		O2	C9	C10	108.0(4)
N8	Pb2	N7	76.73(12)		O1	C10	C9	109.5(4)
N8	Pb2	O8	79.15(12)		O1	C11	C12	108.6(4)
F7	P2	F8	90.0(3)		N1	C12	C11	115.4(4)
F7	P2	F9	92.5(4)		P3	F13	F14	59.9(4)
F7	P2	F10	176.6(4)		N1	C13	C14	114.7(4)
F7	P2	F11	88.7(3)		N3	C14	C13	118.2(4)
F7	P2	F12	86.9(4)		N3	C14	C15	121.4(4)
F9	P2	F8	86.4(3)		C15	C14	C13	120.2(4)
F9	P2	F10	88.6(4)		C16	C15	C14	120.1(5)
F9	P2	F11	96.8(4)		P3	F16	F17	56.9(5)
F10	P2	F8	86.8(3)		C15	C16	C17	119.1(5)
F10	P2	F11	94.4(3)		P3	F14	F13	56.1(4)
F11	P2	F8	176.5(3)		P3	F17	F16	57.4(4)
F12	P2	F8	90.6(3)		P3	F17	F20	53.6(3)
F12	P2	F9	176.9(4)		F16	F17	F20	92.1(7)
F12	P2	F10	91.9(4)		C16	C17	C18	118.2(5)
F12	P2	F11	86.2(3)		P3	F15	F20	53.4(4)
C8	O2	Pb1	108.9(3)		N3	C18	C17	123.6(4)

C8	O2	C9	113.5(4)		N2	C19	C20	114.8(4)
C9	O2	Pb1	112.2(3)		P3	F20	F17	53.4(4)
C6	N2	Pb1	107.8(2)		P3	F20	F15	58.6(5)
C7	N2	Pb1	111.1(3)		N4	C20	C19	118.3(4)
C7	N2	C6	108.6(3)		N4	C20	C21	121.1(4)
C19	N2	Pb1	108.7(2)		C21	C20	C19	120.6(4)
C19	N2	C6	111.3(4)		C22	C21	C20	119.4(5)
C19	N2	C7	109.5(4)		C21	C22	C23	119.5(4)
O4	C2	C1	107.2(4)		C24	C23	C22	118.2(5)
F13	P3	F16	165.1(7)		N4	C24	C23	123.2(4)
F13	P3	F14	64.1(6)		C26	C25	N6	114.2(5)
F13	P3	F18	78.8(8)		O8	C26	C25	107.5(5)
F13	P3	F15	103.1(6)		O8	C27	C28	108.3(5)
F13	P3	F19	89.6(4)		O7	C28	C27	107.9(5)
F13	P3	F20	82.4(5)		O7	C29	C30	107.0(5)
F16	P3	F14	103.7(8)		N5	C30	C29	115.4(5)
F16	P3	F18	107.4(7)		N5	C31	C32	113.1(5)
F16	P3	F15	75.0(5)		O6	C32	C31	109.5(5)
F16	P3	F19	80.0(5)		O6	C33	C34	108.9(5)
F17	P3	F13	127.7(9)		O5	C34	C33	108.5(5)
F17	P3	F16	65.7(7)		O5	C35	C36	109.4(5)
F17	P3	F14	166.4(9)		N6	C36	C35	115.4(5)
F17	P3	F19	103.7(6)		N6	C37	C38	115.1(5)
F17	P3	F20	73.1(5)		N7	C38	C37	119.1(5)
F18	P3	F15	163.0(8)		N7	C38	C39	121.7(6)
F19	P3	F14	81.7(5)		C39	C38	C37	119.0(6)
F19	P3	F18	71.5(6)		C40	C39	C38	118.9(7)
F19	P3	F15	125.1(8)		C41	C40	C39	120.0(6)
F20	P3	F16	109.8(6)		C42	C41	C40	118.0(7)
F20	P3	F14	104.5(5)		N7	C42	C41	123.0(7)
F20	P3	F18	95.8(7)		N5	C43	C44	116.4(4)
F20	P3	F15	68.0(7)		N8	C44	C43	117.7(5)
F20	P3	F19	166.2(7)		N8	C44	C45	121.8(5)
C4	O3	Pb1	120.0(3)		C45	C44	C43	120.4(5)
C4	O3	C5	113.3(4)		C46	C45	C44	118.0(6)
C5	O3	Pb1	114.5(2)		C47	C46	C45	121.3(6)

C14	N3	Pb1	120.5(3)		C46	C47	C48	117.5(6)
C18	N3	Pb1	121.6(3)		N8	C48	C47	124.4(5)

Crystal data and structure refinement for Crystal structure $[Pb(Cyclen)]^{2+}$

Identification code	Crystal structure Pb-Cyclen
Empirical formula	$C_{50}H_{101}Cl_{12}O_{49}Pb_6N_{25}$
Formula weight	3505.09
Temperature/K	296(2)
Crystal system	monoclinic
Space group	$P2_1/n$
a/Å	14.708(2)
b/Å	25.675(3)
c/Å	28.280(4)
α/°	90
β/°	100.767(5)
γ/°	90
Volume/Å^3	10491(2)
Z	4
ρ_{calc}g/cm^3	2.219
μ/mm^{-1}	9.999
F(000)	6656.0
Crystal size/mm^3	0.511 × 0.352 × 0.321
Radiation	MoKα (λ = 0.71073)
2Θ range for data collection/°	2.924 to 56.624
Index ranges	-19 ≤ h ≤ 19, -34 ≤ k ≤ 34, -37 ≤ l ≤ 37
Reflections collected	185054
Independent reflections	26100 [R_{int} = 0.0721, R_{sigma} = 0.0549]
Data/restraints/parameters	26100/3230/1329
Goodness-of-fit on F^2	1.024
Final R indexes [I>=2σ (I)]	R_1 = 0.0532, wR_2 = 0.1439
Final R indexes [all data]	R_1 = 0.0796, wR_2 = 0.1638
Largest diff. peak/hole / e Å^{-3}	1.99/-2.59

Bond Lengths for Crystal structure $[Pb(Cyclen)]^{2+}$						
Atom	**Atom**	**Length/Å**		**Atom**	**Atom**	**Length/Å**
N101	C25	1.78(5)		N8	C11	1.523(15)
N101	C26	1.17(5)		Cl9	O33	1.385(9)
N101	C27	1.49(5)		Cl9	O34	1.386(9)
N17	Pb4	2.471(10)		Cl9	O35	1.376(11)
N17	C26	1.75(2)		Cl9	O36	1.375(11)
N17	C27	1.294(18)		N9	C9	1.498(13)
Pb1	N2	2.497(9)		N9	C16	1.416(12)
Pb1	N3	2.509(8)		C9	C10	1.488(17)
Pb1	N4	2.502(8)		Cl10	O37	1.442(12)
Pb1	N5	2.531(9)		Cl10	O38	1.391(9)
Cl1	O1	1.433(9)		Cl10	O39	1.388(8)
Cl1	O2	1.400(10)		Cl10	O40	1.347(14)
Cl1	O3	1.439(9)		Cl10	O101	1.44(3)
Cl1	O4	1.404(9)		N10	C22	1.366(17)
N1	C50	1.16(3)		N10	C23	1.556(19)
C1	N2	1.46(2)		C101	N11	1.879(15)
C1	C2	1.42(2)		C101	N12	1.443(13)
Pb2	N6	2.507(8)		C101	C20	1.222(12)
Pb2	N7	2.530(8)		Cl11	O41	1.361(10)
Pb2	N8	2.535(8)		Cl11	O42	1.413(16)
Pb2	N9	2.499(7)		Cl11	O43	1.345(10)
Cl2	O5	1.385(14)		Cl11	O44	1.353(11)
Cl2	O6	1.362(16)		N11	C20	1.423(16)
Cl2	O7	1.286(15)		N11	C21	1.552(16)
Cl2	O8	1.41(2)		C11	C12	1.485(19)
N2	C8	1.39(2)		Cl12	O45	1.393(9)
C2	N3	1.389(16)		Cl12	O46	1.329(9)
Pb3	N10	2.538(10)		Cl12	O47	1.437(13)
Pb3	C101	2.805(11)		Cl12	O48	1.391(11)
Pb3	N11	2.471(8)		N12	C18	1.413(15)
Pb3	N12	2.492(9)		N13	C17	1.566(19)
Pb3	N13	2.511(10)		N13	C24	1.387(18)
Cl3	O9	1.397(11)		C13	C14	1.430(18)
Cl3	O10	1.341(13)		N14	C28	1.579(15)
Cl3	O11	1.356(10)		N14	C29	1.39(2)
Cl3	O12	1.343(11)		N15	C30	1.63(2)

N3	C3	1.457(16)		N15	C31	1.38(2)
C3	C4	1.351(19)		C15	C16	1.486(15)
Pb4	N14	2.527(11)		N16	C25	1.356(19)
Pb4	N15	2.515(10)		N16	C32	1.519(19)
Pb4	N16	2.461(9)		C17	C18	1.466(19)
Cl4	O13	1.404(12)		N18	C42	1.410(16)
Cl4	O14	1.236(15)		N18	C43	1.605(17)
Cl4	O15	1.440(15)		N19	C44	1.427(16)
Cl4	O16	1.416(15)		N19	C45	1.514(18)
N4	C4	1.439(15)		N20	C46	1.442(17)
N4	C5	1.477(16)		N20	C47	1.54(2)
Pb5	N22	2.499(10)		N21	C41	1.578(17)
Pb5	N23	2.516(9)		N21	C48	1.378(19)
Pb5	N24	2.450(9)		C21	C22	1.44(2)
Pb5	N25	2.475(9)		N22	C34	1.66(2)
Cl5	O17	1.421(7)		N22	C35	1.27(2)
Cl5	O18	1.417(9)		N23	C33	1.392(18)
Cl5	O19	1.369(9)		N23	C40	1.618(18)
Cl5	O20	1.412(9)		C23	C24	1.49(2)
N5	C6	1.379(19)		N24	C38	1.699(18)
N5	C7	1.511(19)		N24	C39	1.368(17)
C5	C6	1.39(2)		N25	C36	1.80(2)
Pb6	N18	2.522(8)		N25	C37	1.305(17)
Pb6	N19	2.526(9)		C25	C26	1.23(2)
Pb6	N20	2.505(9)		N26	C28	1.16(6)
Pb6	N21	2.511(9)		N26	C29	1.47(6)
Cl6	O21	1.302(12)		N27	C36	1.18(6)
Cl6	O22	1.373(9)		N27	C37	1.47(6)
Cl6	O23	1.344(14)		C27	C28	1.37(2)
Cl6	O24	1.378(9)		C29	C30	1.33(2)
N6	C13	1.439(14)		C31	C32	1.283(16)
N6	C15	1.497(13)		C33	C34	1.36(2)
Cl7	O25	1.380(12)		C33	N38	1.76(7)
Cl7	O26	1.302(12)		C34	N38	1.24(7)
Cl7	O27	1.310(16)		C35	C36	1.33(2)
Cl7	O28	1.284(13)		C35	N38	1.54(7)
N7	C12	1.425(16)		O37	O40	1.79(3)
N7	C14	1.532(17)		C37	C38	1.38(2)

C7	C8	1.41(2)		C39	C40	1.45(2)
Cl8	O29	1.401(10)		C41	C42	1.41(2)
Cl8	O30	1.423(11)		C43	C44	1.373(19)
Cl8	O31	1.409(10)		C45	C46	1.38(2)
Cl8	O32	1.406(10)		C47	C48	1.41(2)
N8	C10	1.451(14)		C49	C50	1.42(3)

Bond Angles for Crystal structure $[Pb(Cyclen)]^{2+}$								
Atom	**Atom**	**Atom**	**Angle/°**		**Atom**	**Atom**	**Atom**	**Angle/°**
C26	N101	C25	44(2)		O38	Cl10	O37	106.8(8)
C26	N101	C27	145(4)		O38	Cl10	O101	100.5(16)
C27	N101	C25	142(2)		O39	Cl10	O37	104.1(8)
C26	N17	Pb4	101.4(7)		O39	Cl10	O38	114.9(6)
C27	N17	Pb4	118.3(10)		O39	Cl10	O101	92.7(17)
C27	N17	C26	112.5(11)		O40	Cl10	O37	80.0(12)
N2	Pb1	N3	70.2(3)		O40	Cl10	O38	117.7(8)
N2	Pb1	N4	107.9(3)		O40	Cl10	O39	123.2(8)
N2	Pb1	N5	70.4(4)		O101	Cl10	O37	137(2)
N3	Pb1	N5	109.1(3)		C22	N10	Pb3	112.8(8)
N4	Pb1	N3	70.4(3)		C22	N10	C23	115.0(12)
N4	Pb1	N5	69.2(3)		C23	N10	Pb3	104.1(8)
O1	Cl1	O3	109.4(7)		N8	C10	C9	109.4(10)
O2	Cl1	O1	107.6(7)		N11	C101	Pb3	59.9(4)
O2	Cl1	O3	111.7(7)		N12	C101	Pb3	62.5(5)
O2	Cl1	O4	111.2(7)		N12	C101	N11	119.9(9)
O4	Cl1	O1	106.3(7)		C20	C101	Pb3	104.8(10)
O4	Cl1	O3	110.4(7)		C20	C101	N11	49.2(8)
C2	C1	N2	117.1(12)		C20	C101	N12	141.9(11)
N6	Pb2	N7	70.3(3)		O41	Cl11	O42	104.5(11)
N6	Pb2	N8	108.4(3)		O43	Cl11	O41	115.6(9)
N7	Pb2	N8	69.5(3)		O43	Cl11	O42	98.8(13)
N9	Pb2	N6	70.0(3)		O43	Cl11	O44	113.4(9)
N9	Pb2	N7	108.0(3)		O44	Cl11	O41	114.5(8)
N9	Pb2	N8	69.8(3)		O44	Cl11	O42	108.0(13)
O5	Cl2	O8	99.8(15)		C101	N11	Pb3	79.0(4)
O6	Cl2	O5	107.5(13)		C20	N11	Pb3	115.1(7)
O6	Cl2	O8	100.4(13)		C20	N11	C101	40.6(6)
O7	Cl2	O5	103.7(11)		C20	N11	C21	110.2(9)
O7	Cl2	O6	124.5(17)		C21	N11	Pb3	109.7(7)
O7	Cl2	O8	118.2(18)		C21	N11	C101	144.3(8)
C1	N2	Pb1	110.5(8)		C12	C11	N8	112.8(9)
C8	N2	Pb1	114.7(10)		O45	Cl12	O47	99.4(8)
C8	N2	C1	112.5(13)		O46	Cl12	O45	119.1(7)
N3	C2	C1	119.3(12)		O46	Cl12	O47	99.2(10)
N10	Pb3	C101	97.5(3)		O46	Cl12	O48	114.7(8)

N11	Pb3	N10	69.8(3)		O48	Cl12	O45	116.7(7)
N11	Pb3	C101	41.1(3)		O48	Cl12	O47	102.5(10)
N11	Pb3	N12	71.0(3)		C101	N12	Pb3	86.6(6)
N11	Pb3	N13	109.0(3)		C18	N12	Pb3	115.4(8)
N12	Pb3	N10	109.1(3)		C18	N12	C101	119.6(9)
N12	Pb3	C101	30.9(3)		N7	C12	C11	110.2(11)
N12	Pb3	N13	70.2(4)		C17	N13	Pb3	107.8(7)
N13	Pb3	N10	70.3(4)		C24	N13	Pb3	115.3(10)
N13	Pb3	C101	91.7(3)		C24	N13	C17	109.5(11)
O10	Cl3	O9	101.5(12)		C14	C13	N6	113.1(11)
O10	Cl3	O11	103.3(9)		C28	N14	Pb4	103.5(8)
O10	Cl3	O12	101.7(12)		C29	N14	Pb4	112.8(11)
O11	Cl3	O9	116.5(8)		C29	N14	C28	118.6(15)
O12	Cl3	O9	108.4(9)		C13	C14	N7	114.0(9)
O12	Cl3	O11	121.9(9)		C30	N15	Pb4	102.8(9)
C2	N3	Pb1	113.0(8)		C31	N15	Pb4	113.7(9)
C2	N3	C3	114.6(12)		C31	N15	C30	121.6(15)
C3	N3	Pb1	109.4(7)		C16	C15	N6	110.3(8)
C4	C3	N3	120.0(11)		C25	N16	Pb4	115.6(9)
N17	Pb4	N14	67.6(5)		C25	N16	C32	110.7(14)
N17	Pb4	N15	108.6(3)		C32	N16	Pb4	107.7(9)
N15	Pb4	N14	70.9(4)		N9	C16	C15	111.6(9)
N16	Pb4	N17	70.6(4)		C18	C17	N13	112.0(10)
N16	Pb4	N14	107.4(4)		C42	N18	Pb6	113.8(8)
N16	Pb4	N15	70.1(4)		C42	N18	C43	113.0(11)
O13	Cl4	O15	102.6(10)		C43	N18	Pb6	105.2(7)
O13	Cl4	O16	110.3(10)		N12	C18	C17	111.1(12)
O14	Cl4	O13	112.5(12)		C44	N19	Pb6	111.4(8)
O14	Cl4	O15	106.2(15)		C44	N19	C45	114.1(11)
O14	Cl4	O16	121.6(15)		C45	N19	Pb6	107.2(8)
O16	Cl4	O15	101.2(10)		C46	N20	Pb6	113.2(9)
C4	N4	Pb1	112.0(7)		C46	N20	C47	110.6(12)
C4	N4	C5	110.7(12)		C47	N20	Pb6	107.9(8)
C5	N4	Pb1	112.9(8)		C101	C20	N11	90.2(10)
C3	C4	N4	118.6(13)		C41	N21	Pb6	104.1(7)
N22	Pb5	N23	70.5(4)		C48	N21	Pb6	111.2(9)
N24	Pb5	N22	109.7(3)		C48	N21	C41	117.2(13)
N24	Pb5	N23	69.6(4)		C22	C21	N11	111.9(11)

N24	Pb5	N25	70.1(4)		C34	N22	Pb5	102.1(8)
N25	Pb5	N22	71.6(4)		C35	N22	Pb5	116.9(11)
N25	Pb5	N23	108.9(3)		C35	N22	C34	118.8(13)
O18	Cl5	O17	110.3(5)		N10	C22	C21	114.6(13)
O19	Cl5	O17	111.1(6)		C33	N23	Pb5	112.5(9)
O19	Cl5	O18	109.0(8)		C33	N23	C40	117.0(13)
O19	Cl5	O20	110.3(9)		C40	N23	Pb5	104.4(8)
O20	Cl5	O17	109.3(6)		C24	C23	N10	114.2(11)
O20	Cl5	O18	106.6(7)		C38	N24	Pb5	104.3(7)
C6	N5	Pb1	113.9(8)		C39	N24	Pb5	120.1(9)
C6	N5	C7	113.7(13)		C39	N24	C38	107.4(12)
C7	N5	Pb1	107.9(9)		N13	C24	C23	106.5(12)
C6	C5	N4	117.4(12)		C36	N25	Pb5	101.5(7)
N18	Pb6	N19	70.8(3)		C37	N25	Pb5	117.4(9)
N20	Pb6	N18	109.2(3)		C37	N25	C36	109.1(12)
N20	Pb6	N19	68.7(4)		N16	C25	N101	118.0(16)
N20	Pb6	N21	70.9(4)		C26	C25	N101	40.9(13)
N21	Pb6	N18	70.5(3)		C26	C25	N16	113.6(15)
N21	Pb6	N19	108.4(3)		C28	N26	C29	153(4)
O21	Cl6	O22	113.6(10)		N101	C26	C25	96(2)
O21	Cl6	O23	105.1(15)		C25	C26	N17	112.5(13)
O21	Cl6	O24	110.0(9)		C36	N27	C37	147(4)
O22	Cl6	O24	113.0(7)		N17	C27	C28	108.4(15)
O23	Cl6	O22	105.3(10)		C28	C27	N101	155(2)
O23	Cl6	O24	109.4(12)		N26	C28	C27	102(2)
C13	N6	Pb2	113.9(7)		C27	C28	N14	112.5(11)
C13	N6	C15	116.6(9)		C30	C29	N14	112.8(18)
C15	N6	Pb2	108.5(6)		C30	C29	N26	154(2)
N5	C6	C5	121.1(14)		C29	C30	N15	115.5(13)
O26	Cl7	O25	118.6(11)		C32	C31	N15	118.7(15)
O26	Cl7	O27	107.0(13)		C31	C32	N16	123.2(14)
O27	Cl7	O25	109.9(12)		N23	C33	N38	122(2)
O28	Cl7	O25	108.2(10)		C34	C33	N23	109.7(14)
O28	Cl7	O26	118.6(14)		C34	C33	N38	45(2)
O28	Cl7	O27	90.8(14)		C33	C34	N22	109.8(13)
C12	N7	Pb2	114.5(7)		N38	C34	C33	85(3)
C12	N7	C14	112.7(11)		N22	C35	C36	115.7(16)
C14	N7	Pb2	107.2(7)		C36	C35	N38	157(2)

C8	C7	N5	118.1(13)		N27	C36	C35	104(3)
O29	Cl8	O30	106.6(8)		C35	C36	N25	111.8(11)
O29	Cl8	O31	107.9(8)		Cl10	O37	O40	47.7(7)
O29	Cl8	O32	111.6(7)		N25	C37	C38	108.4(15)
O31	Cl8	O30	108.3(8)		C38	C37	N27	161(2)
O32	Cl8	O30	113.2(8)		C34	N38	C33	51(3)
O32	Cl8	O31	109.0(7)		C34	N38	C35	132(5)
C10	N8	Pb2	113.2(6)		C35	N38	C33	141(3)
C10	N8	C11	112.1(10)		C37	C38	N24	112.0(11)
C11	N8	Pb2	108.7(7)		N24	C39	C40	106.4(13)
N2	C8	C7	116.5(14)		C39	C40	N23	114.1(12)
O33	Cl9	O34	112.9(7)		Cl10	O40	O37	52.3(8)
O35	Cl9	O33	107.6(8)		C42	C41	N21	114.2(11)
O35	Cl9	O34	111.1(8)		C41	C42	N18	109.9(13)
O36	Cl9	O33	111.9(8)		C44	C43	N18	113.0(11)
O36	Cl9	O34	113.3(8)		C43	C44	N19	111.9(12)
O36	Cl9	O35	99.1(10)		C46	C45	N19	112.5(11)
C9	N9	Pb2	109.0(6)		C45	C46	N20	110.4(13)
C16	N9	Pb2	112.7(6)		C48	C47	N20	113.1(12)
C16	N9	C9	114.3(9)		N21	C48	C47	116.9(16)
C10	C9	N9	112.5(9)		N1	C50	C49	177(3)

Crystal data and structure refinement for Crystal structure $[Pb(N_4O_2)]^{2+}$

Identification code	Crystal structure Pb-N4O2 done
Empirical formula	$C_{24}H_{48.59}N_8O_{20}ICl_4Pb_2$
Formula weight	1325.47
Temperature/K	298(2)
Crystal system	monoclinic
Space group	$P2_1$
a/Å	9.896(2)
b/Å	14.168(3)
c/Å	15.939(3)
α/°	90
β/°	103.823(7)
γ/°	90
Volume/Å^3	2170.0(8)
Z	2
ρ_{calc}g/cm^3	2.029
μ/mm^{-1}	8.076
F(000)	1281.0
Crystal size/mm^3	0.677 × 0.637 × 0.276
Radiation	MoKα (λ = 0.71073)
2Θ range for data collection/°	3.898 to 60.998
Index ranges	-14 ≤ h ≤ 14, -20 ≤ k ≤ 20, -22 ≤ l ≤ 22
Reflections collected	25158
Independent reflections	13203 [R_{int} = 0.0297, R_{sigma} = 0.0488]
Data/restraints/parameters	13203/617/589
Goodness-of-fit on F^2	1.073
Final R indexes [I>=2σ (I)]	R_1 = 0.0407, wR_2 = 0.1075
Final R indexes [all data]	R_1 = 0.0528, wR_2 = 0.1143
Largest diff. peak/hole / e Å^{-3}	0.66/-1.01
Flack parameter	0.484(3)

Bond Lengths for Crystal structure $[Pb(N_4O_2)]^{2+}$						
Atom	**Atom**	**Length/Å**		Atom	Atom	**Length/Å**
Pb1	N1	2.578(12)		Cl4	O7	1.414(14)
Pb1	N2	2.635(12)		Cl4	O8	1.35(3)
Pb1	N3	2.632(14)		Cl4	O9	1.37(2)
Pb1	N4	2.551(11)		Cl4	O16	1.42(2)
Cl1	O4	1.386(14)		Cl4	O22	1.43(4)
Cl1	O6	1.31(4)		Cl4	O21	1.39(3)
Cl1	O5	1.23(3)		Cl4	O23	1.36(3)
Cl1	O15	1.46(3)		N4	C10	1.466(18)
Cl1	O25	1.48(3)		N4	C11	1.477(17)
Cl1	O26	1.41(4)		N5	C22	1.38(2)
Cl1	O24	1.41(3)		N5	C24	1.400(19)
O1	Cl2	1.37(2)		C5	C6	1.28(4)
N1	C4	1.51(5)		N6	C13	1.469(18)
N1	C5	1.47(3)		N6	C23	1.484(17)
N1	C25	1.48(3)		C6	O18	1.37(3)
C1	C2	1.53(2)		N7	C16	1.409(18)
C1	O17	1.433(19)		N7	C17	1.420(17)
Pb2	N5	2.606(11)		C7	C8	1.36(3)
Pb2	N6	2.565(10)		C7	O18	1.42(2)
Pb2	N7	2.634(9)		N8	C18	1.479(18)
Pb2	N8	2.561(11)		N8	C19	1.45(2)
Pb2	O19	2.739(10)		C9	C10	1.52(2)
Cl2	O2	1.346(16)		C11	C12	1.50(2)
Cl2	O10	1.381(19)		C12	O17	1.441(17)
Cl2	O11	1.402(15)		C13	C14	1.51(2)
N2	C2	1.443(19)		C14	O19	1.463(18)
N2	C3	1.51(2)		C15	C16	1.51(2)
Cl3	O3	1.404(13)		C15	O19	1.488(18)
Cl3	O12	1.347(16)		C17	C18	1.51(2)
Cl3	O13	1.435(16)		C19	C20	1.50(2)
Cl3	O14	1.393(19)		O20	C20	1.47(2)
N3	C8	1.36(2)		O20	C21	1.49(2)
N3	C9	1.47(2)		C21	C22	1.39(3)
C3	C4	1.27(4)		C23	C24	1.44(2)
C3	C25	1.43(4)				

Bond Angles for Crystal structure $[Pb(N_4O_2)]^{2+}$							
Atom	**Atom**	**Atom**	**Angle/°**	**Atom**	**Atom**	**Atom**	**Angle/°**
N1	Pb1	N2	67.6(4)	O7	Cl4	O16	110.4(16)
N1	Pb1	N3	80.8(6)	O7	Cl4	O22	110(2)
N3	Pb1	N2	140.3(6)	O8	Cl4	O7	106.9(16)
N4	Pb1	N1	93.3(4)	O8	Cl4	O9	112(2)
N4	Pb1	N2	90.2(4)	O8	Cl4	O16	111(2)
N4	Pb1	N3	67.6(4)	O9	Cl4	O7	112.6(16)
O4	Cl1	O15	101.9(19)	O9	Cl4	O16	104(2)
O4	Cl1	O25	109.3(14)	O21	Cl4	O7	109(2)
O4	Cl1	O26	123(3)	O21	Cl4	O22	99(3)
O4	Cl1	O24	113.4(18)	O23	Cl4	O7	115.9(18)
O6	Cl1	O4	101(2)	O23	Cl4	O22	108(3)
O6	Cl1	O15	113(3)	O23	Cl4	O21	113(3)
O5	Cl1	O4	111(3)	C10	N4	Pb1	112.3(8)
O5	Cl1	O6	112(4)	C10	N4	C11	114.9(12)
O5	Cl1	O15	117(4)	C11	N4	Pb1	106.2(8)
O26	Cl1	O25	97(3)	C3	C4	N1	123(3)
O24	Cl1	O25	107(3)	C22	N5	Pb2	117.4(12)
O24	Cl1	O26	105(3)	C22	N5	C24	120.6(12)
C4	N1	Pb1	105.4(17)	C24	N5	Pb2	116.1(9)
C5	N1	Pb1	111.1(13)	C6	C5	N1	126(2)
C5	N1	C4	138(2)	C13	N6	Pb2	108.4(7)
C5	N1	C25	104.9(19)	C13	N6	C23	111.3(13)
C25	N1	Pb1	110.8(11)	C23	N6	Pb2	114.9(8)
O17	C1	C2	111.2(11)	C5	C6	O18	121(2)
N5	Pb2	N7	142.6(4)	C16	N7	Pb2	123.4(8)
N5	Pb2	O19	122.3(4)	C16	N7	C17	114.0(11)
N6	Pb2	N5	64.5(4)	C17	N7	Pb2	118.0(8)
N6	Pb2	N7	89.6(3)	C8	C7	O18	112.8(14)
N6	Pb2	O19	66.9(3)	C18	N8	Pb2	108.5(8)
N7	Pb2	O19	62.5(3)	C19	N8	Pb2	112.9(9)
N8	Pb2	N5	86.1(5)	C19	N8	C18	112.0(13)
N8	Pb2	N6	85.1(4)	C7	C8	N3	122.9(19)
N8	Pb2	N7	64.0(4)	N3	C9	C10	105.4(14)
N8	Pb2	O19	118.6(3)	N4	C10	C9	111.4(12)
O1	Cl2	O10	105.4(13)	N4	C11	C12	112.1(13)
O1	Cl2	O11	112.1(14)	O17	C12	C11	108.2(12)

O2	Cl2	O1	111.4(17)		N6	C13	C14	110.2(12)
O2	Cl2	O10	108.6(19)		O19	C14	C13	111.2(12)
O2	Cl2	O11	111.9(12)		O19	C15	C16	111.6(11)
O10	Cl2	O11	107.1(14)		N7	C16	C15	109.0(11)
C2	N2	Pb1	118.1(9)		C1	O17	C12	114.9(12)
C2	N2	C3	111.6(14)		N7	C17	C18	109.0(11)
C3	N2	Pb1	111.5(9)		C6	O18	C7	117.8(18)
N2	C2	C1	109.0(13)		N8	C18	C17	109.0(11)
O3	Cl3	O13	108.5(12)		C14	O19	Pb2	110.2(8)
O12	Cl3	O3	110.6(12)		C14	O19	C15	114.0(12)
O12	Cl3	O13	110.2(14)		C15	O19	Pb2	110.4(8)
O12	Cl3	O14	111.4(17)		N8	C19	C20	112.5(14)
O14	Cl3	O3	111.2(16)		C20	O20	C21	112.7(17)
O14	Cl3	O13	104.8(15)		O20	C20	C19	113.2(13)
C8	N3	Pb1	112.5(13)		C22	C21	O20	117.2(16)
C8	N3	C9	123.4(17)		N5	C22	C21	114.1(16)
C9	N3	Pb1	108.3(10)		C24	C23	N6	113.5(12)
C4	C3	N2	116(2)		N5	C24	C23	108.8(13)
C25	C3	N2	109.7(18)		C3	C25	N1	114(2)

Crystal data and structure refinement for Crystal structure $[Pb(N_2O_4)]^{2+}$

Identification code	$[Pb(N_2O_4)]^{2+}$
Empirical formula	$C_{12}H_{26}Cl_2N_2O_{12}Pb$
Formula weight	668.44
Temperature/K	296(2)
Crystal system	monoclinic
Space group	$P2_1/c$
a/Å	8.4156(12)
b/Å	12.799(2)
c/Å	10.8318(16)
α /°	90
β /°	110.135(5)
γ /°	90
Volume/Å^3	1095.4(3)
Z	2
ρ_{calc}g/cm^3	2.027
μ /mm^{-1}	8.004
F(000)	648.0
Crystal size/mm^3	0.921 × 0.279 × 0.068
Radiation	MoKα (λ = 0.71073)
2Θ range for data collection/°	5.116 to 60.972
Index ranges	-11 ≤ h ≤ 12, -18 ≤ k ≤ 18, -15 ≤ l ≤ 15
Reflections collected	12994
Independent reflections	3327 [R_{int} = 0.0300, R_{sigma} = 0.0274]
Data/restraints/parameters	3327/48/174
Goodness-of-fit on F^2	1.056
Final R indexes [I>=2σ (I)]	R_1 = 0.0211, wR_2 = 0.0516
Final R indexes [all data]	R_1 = 0.0341, wR_2 = 0.0572
Largest diff. peak/hole / e Å^{-3}	0.45/-0.75

Bond Lengths for Crystal structure $[Pb(N_2O_4)]^{2+}$						
Atom	Atom	Length/Å		Atom	Atom	Length/Å
N1	Pb1	2.743(3)		Pb1	O4	2.719(6)
N1	C3	1.484(6)		Pb1	O4[1]	2.719(6)
N1	C4	1.456(5)		Pb1	O12	2.575(14)
Cl1	O4	1.414(5)		Pb1	O12[1]	2.575(14)
Cl1	O5	1.397(6)		O1	C1	1.433(4)
Cl1	O6	1.414(11)		O1	C2	1.421(5)
Cl1	O7	1.366(5)		O3	C5	1.423(4)
Cl1	O9	1.414(13)		O3	C6	1.415(5)
Cl1	O10	1.325(8)		C1	C6[1]	1.481(6)
Cl1	O12	1.426(11)		C2	C3	1.474(6)

[1]1-X,1-Y,1-Z

Bond Angles for Crystal structure $[Pb(N_2O_4)]^{2+}$								
Atom	**Atom**	**Atom**	**Angle/°**		**Atom**	**Atom**	**Atom**	**Angle/°**
C3	N1	Pb1	113.1(2)		O4[1]	Pb1	N1	91.6(2)
C4	N1	Pb1	112.9(2)		O4[1]	Pb1	N1[1]	88.4(2)
C4	N1	C3	111.6(3)		O4	Pb1	N1	88.4(2)
O5	Cl1	O4	107.4(7)		O4[1]	Pb1	O4	180.0
O5	Cl1	O6	109.8(6)		O12[1]	Pb1	N1	98.2(3)
O6	Cl1	O4	110.4(7)		O12	Pb1	N1	81.8(3)
O7	Cl1	O4	105.8(4)		C2	O1	C1	113.5(3)
O7	Cl1	O5	109.5(5)		C6	O3	C5	111.6(3)
O7	Cl1	O6	113.6(6)		Cl1	O4	Pb1	106.3(3)
O9	Cl1	O12	100.8(10)		Cl1	O12	Pb1	113.1(7)
O10	Cl1	O9	113.6(10)		O1	C1	C6[1]	108.0(3)
O10	Cl1	O12	103.2(10)		O1	C2	C3	108.4(3)
O11	Cl1	O9	105.5(13)		C2	C3	N1	110.3(3)
O11	Cl1	O10	115.3(13)		N1	C4	C5	111.0(3)
O11	Cl1	O12	117.8(14)		O3	C5	C4	107.8(3)
N1	Pb1	N1[1]	180.00(13)		O3	C6	C1[1]	107.0(3)
O4	Pb1	N1[1]	91.6(2)					

[1]1-X,1-Y,1-Z

Potentiometric Titrations

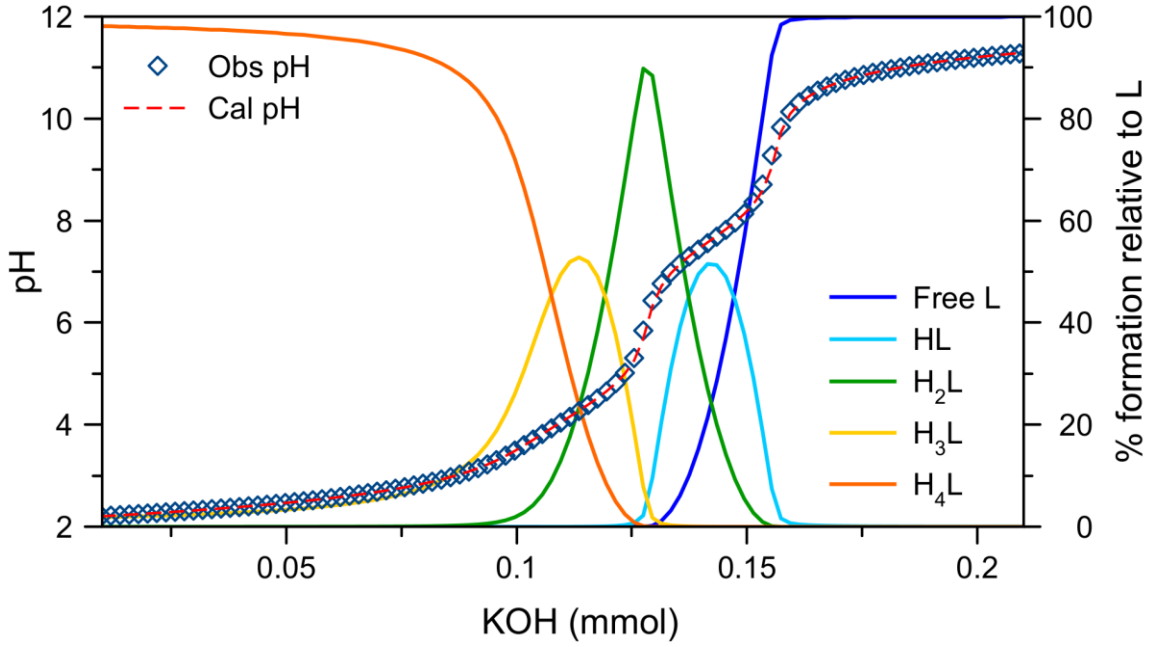

Figure B.20. Representative pH-potentiometric titration plot for protonation constant determination of Crown-4Py ([L] = 0.9 mM; *I* = 0.1 M KCl).

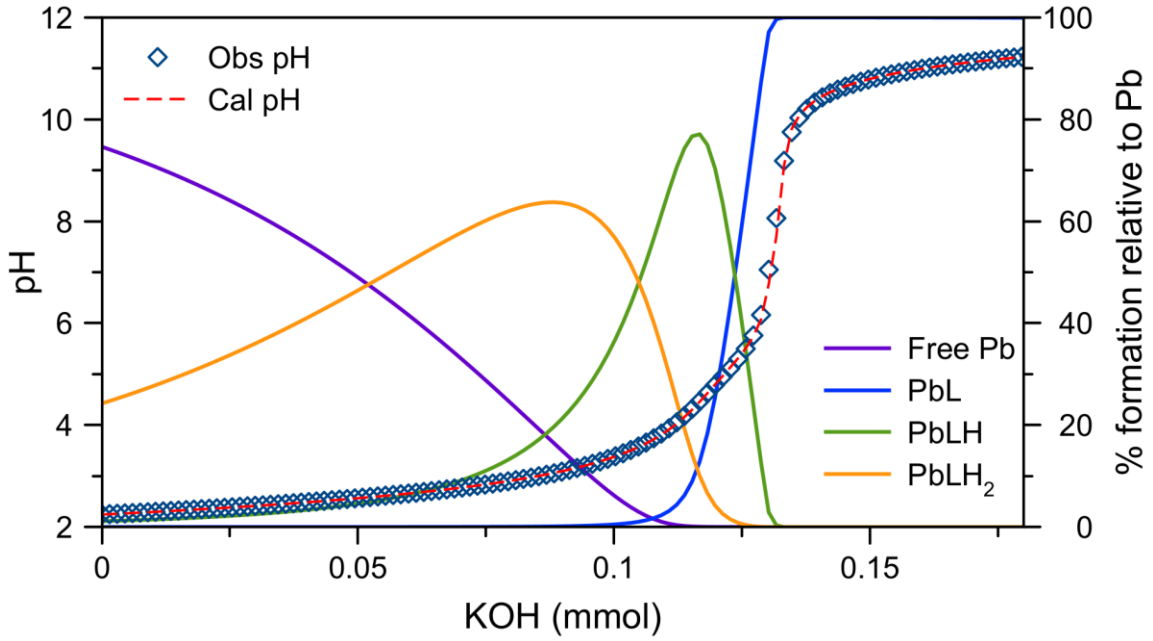

Figure B.21. Representative pH-potentiometric titration plot for stability constant determination of Pb(II)-Crown-4Py system ([M]= 0.8 mM, [L] = 0.9 mM; *I* = 0.1 M KCl).

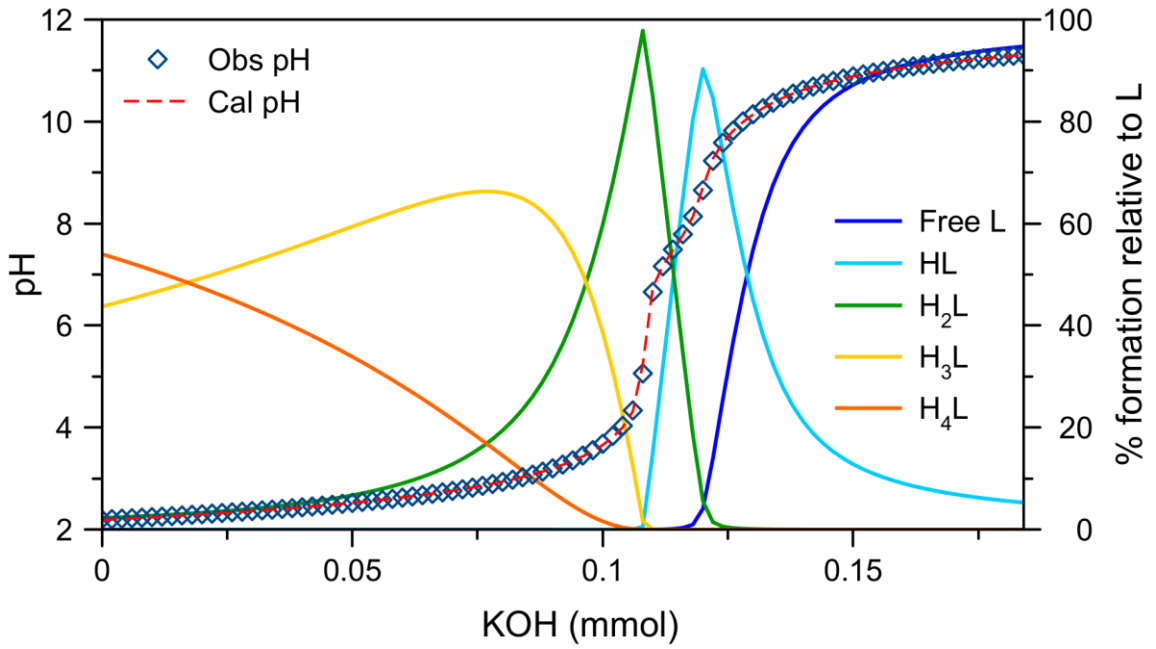

Figure B.22. Representative pH-potentiometric titration plot for protonation constant determination of Cyclen-4Py ([L] = 0.9 mM; *I* = 0.1 M KCl).

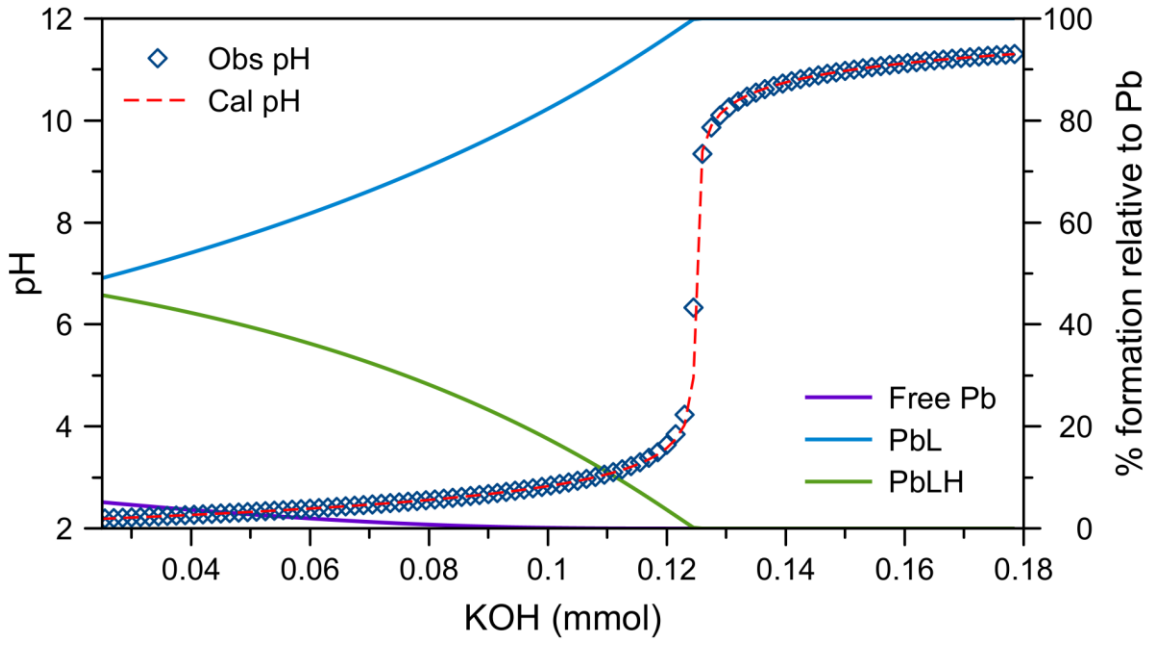

Figure B.23. Representative pH-potentiometric titration plot for stability constant determination of Pb(II)-Cyclen-4Py system ([M]= 0.8 mM, [L] = 0.9 mM; *I* = 0.1 M KCl).

Appendix C.

Supplementary Information for Chapter 4

Synthesis

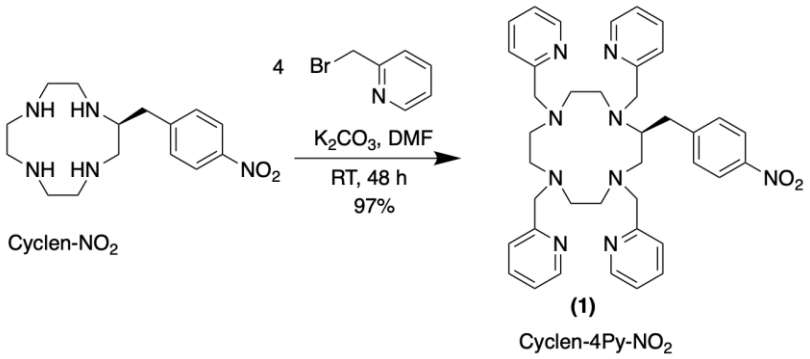

Scheme C.1. Synthesis of Cyclen-4Py-NO_2.

*(S)-2-(4-nitrobenzyl)-1,4,7,10-tetrakis(pyridin-2-ylmethyl)-1,4,7,10-tetraazacyclododecane (**1**)* (*S*)-2-(4-nitrobenzyl)-1,4,7,10-tetraazacyclododecane (15.0 mg, 48.8 μmol, 1 equiv.) was dissolved in 3 mL of anhydrous DMF. To this solution, K_2CO_3 (168.2 mg, 1.22 mmol, 25 equiv.) was added and stirred before the addition of a solution of 2-(bromomethyl) pyridine hydrobromide (61.6 mg, 243.5 μmol, 5 equiv.) dissolved in 2 mL of anhydrous DMF. The reaction was stirred at room temperature for 48 hours. Upon completion, the K_2CO_3 was filtered off and the filtrate was collected and the solvent removed by rotary evaporation. The crude product was redissolved in dichloromethane (15 mL) and washed with saturated $NaHCO_3$ (3 x 15 mL) until the aqueous phase was no longer pink in colour. The organic layers were combined, dried with anhydrous sodium sulphate, and the solvent removed by rotary evaporation to yield the product as a yellow oil (31.72 mg, 47.2 μmol, 97%). The purity of the product was confirmed using reverse-phase semipreparative high-performance liquid chromatography (HPLC) using a Phenomenex Luna C18 (250 x 100 mm) column at 3 mL/min with the following method: A: H_2O with 0.1% TFA, B: Acetonitrile (CH_3CN/ACN) with 0.1% TFA; 0 - 90 % B over 18 minutes. The retention time of the product was 10.2 minutes. ^{1}H NMR (400 MHz, methanol-d_4): δ 8.48 (d, J = 4.8 Hz, 1H), δ 8.45 (d, J = 4.6 Hz, 1 H), δ 8.33 (br. s, 1 H), δ 8.20 (s, 1H), δ (8.18 (s, 1H), δ 7.99 (br. s, 1H), 7.89 – 7.66 (m, 4 H), δ 7.69 – 7.16 (m, 10

H), δ 4.70 – 3.99 (m, 9 H), δ 3.99 – 3.74 (m, 5 H), δ 3.72 – 3.31 (m, 6 H), δ 3.22 – 2.72 (m, 5 H). ^{13}C NMR (101 MHz, methanol-d_4) shift, shift, shift. HR-ESI-MS: Calculated for $C_{39}H_{46}N_9O_2$ ([M + H]$^+$) = 672.3769, found = 672.3772.

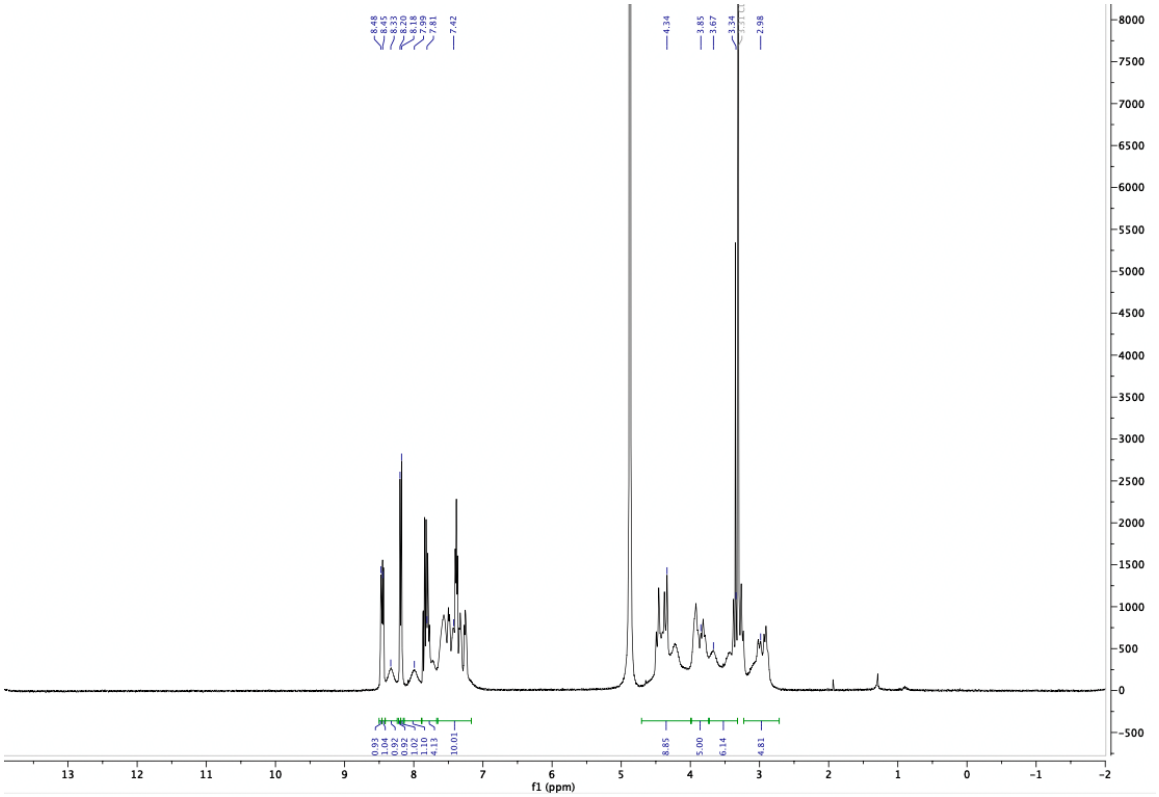

Figure C.1. ^{1}H NMR spectrum of Cyclen-4Py-NO_2 (400 MHz, MeOD, 25 ºC)

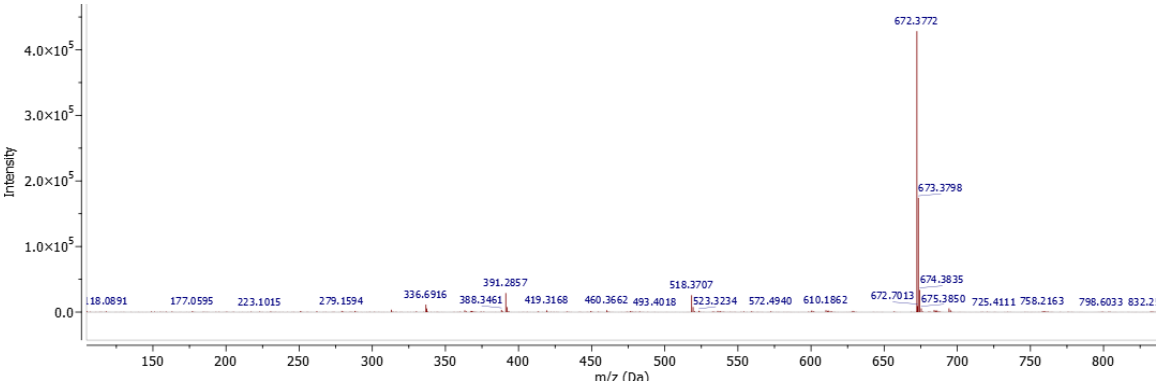

Figure C.2. Mass spectrum of Cyclen-4Py-NO_2.
(m/z calculated [M+H]$^+$ = 672.3769, found [M+H]$^+$ =672.3772).

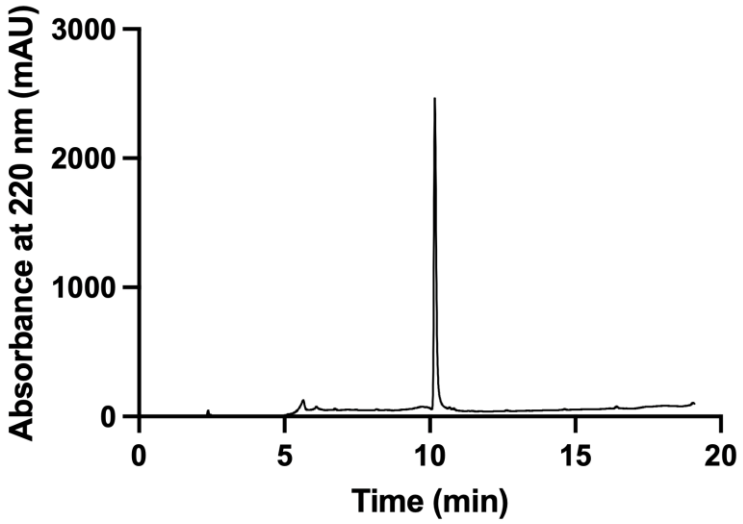

Figure C.3. UV (220 nm absorbance) HPLC chromatogram of Cyclen-4Py-NO_2.
A: H_2O with 0.1% TFA, B: Acetonitrile (CH_3CN/ACN) with 0.1% TFA; 0 - 90 % B over 18 minutes. The retention time of the product was 10.2 minutes.

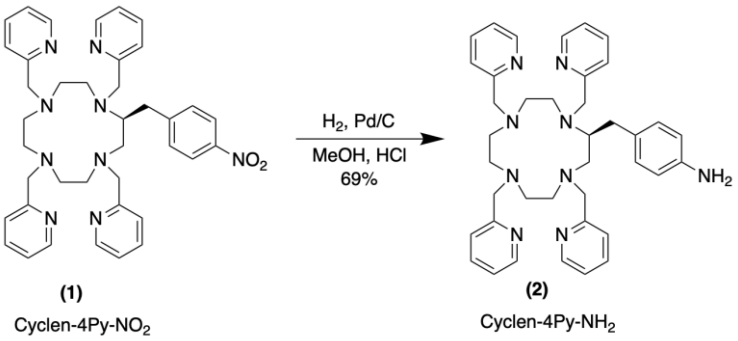

Scheme C.2. Synthesis of Cyclen-4Py-NH_2.

(S)-4-((1,4,7,10-tetrakis(pyridin-2-ylmethyl)-1,4,7,10-tetraazacyclododecan-2-yl)methyl)aniline (***2***). Cyclen-4Py-NO_2 (15.1 mg, 22.4 μmol, 1 equiv.) was dissolved in 1 mL of anhydrous methanol. Pd/C (10% wt, 1.1 mg, 0.05 equiv.) was added to the solution alongside 7 μL of 6 M HCl, which helped increase the rate of the reaction. The reaction was stirred at room temperature under a hydrogen atmosphere for 1.5 hours. The reaction mixture was filtered and washed with methanol. The filtrate was concentrated by rotary evaporation and the crude product was further purified using reverse-phase semipreparative high-performance liquid chromatography (HPLC) using a Phenomenex Luna C18 (250 x 100 mm) column at 3 mL/min with the following method: A: H_2O with 0.1% TFA, B: Acetonitrile (CH_3CN/ACN) with 0.1% TFA; 0 - 13 min 0 to 45.5% B, 13 – 16 min 45.5 - 0 % B. The retention time of the product was 9.7 minutes. These fractions were

collected and lyophilized to yield a yellow oil (9.9 mg, 15.4 μmol, 69%). ^{1}H NMR (500 MHz, D_2O): δ 8.59 (d, J = 5.5 Hz, 1H), 8.52 (d, J = 5.3 Hz, 1H), δ 8.46 – 8.15 (m, 2H), δ 8.08 – 7.99 (m, 2H), δ 7.99 – 7.81 (m, 3H), δ 7.76 (d, J = 7.9 Hz, 1 H), δ 7.70 – 7.49 (m, 5H), δ 7.37 (s, 5H), δ 4.62 (d, J = 15.7 Hz, 1 H), δ 4.55 – 3.91 (m, 7H), δ 3.90 – 3.52 (m, 8 H), δ 3.46 (d, J = 13.6 Hz, 1H), δ 3.40 – 2.66 (m, 8H). HR-ESI-MS: Calculated for $C_{39}H_{48}N_9$ ($[M + H]^+$) = 642.4027, found = 642.4026.

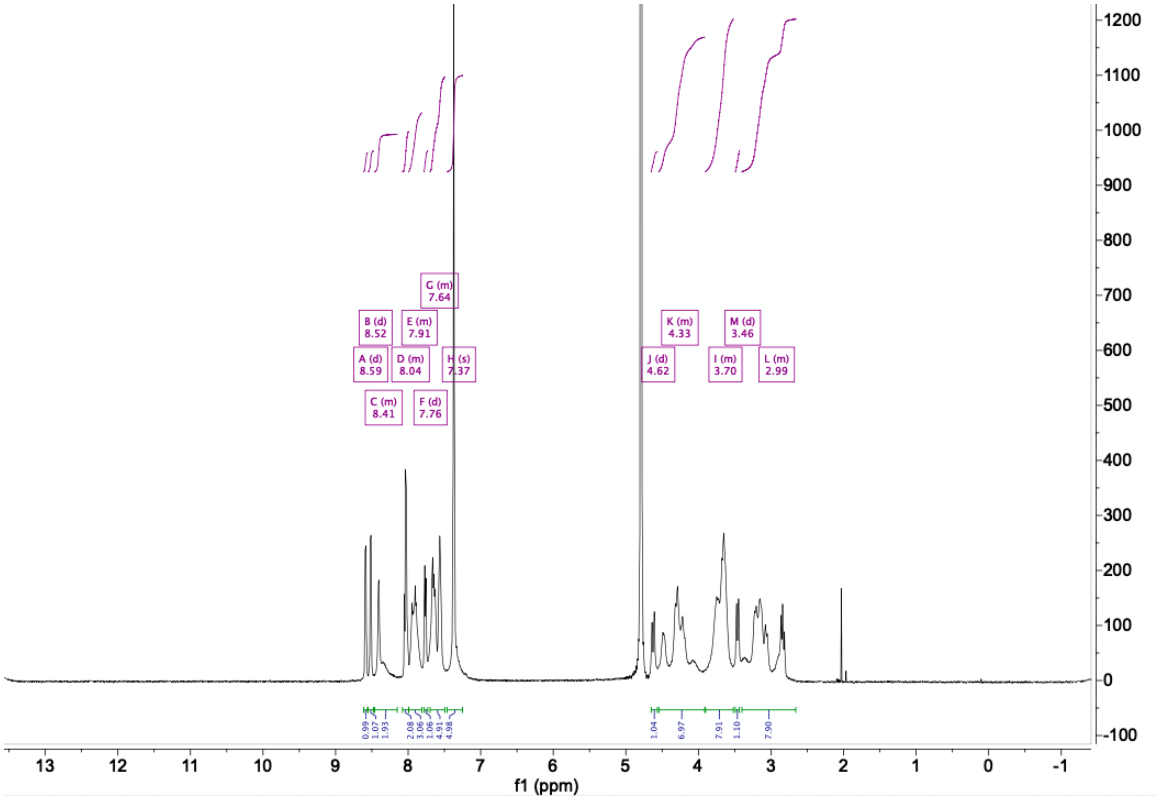

Figure S4. ^{1}H NMR spectrum of Cyclen-4Py-NH_2 (500 MHz, D_2O, 25 °C)

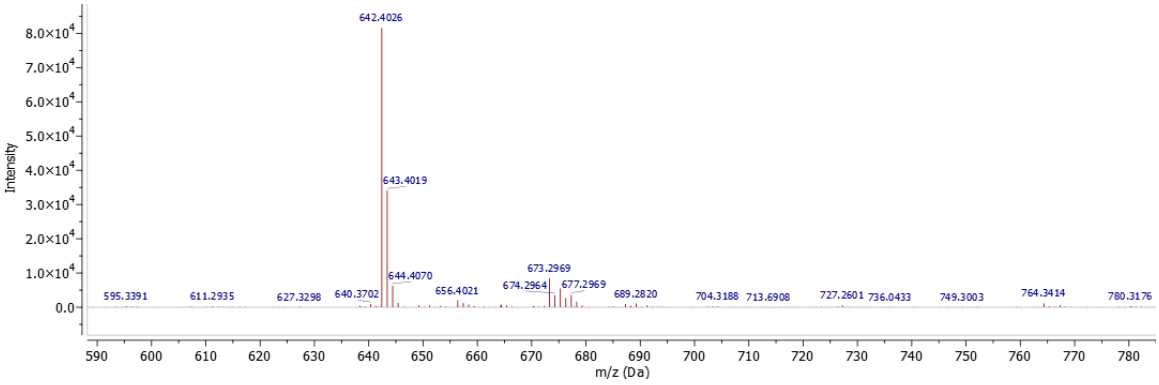

Figure C.5. Mass spectrum of Cyclen-4Py-NH_2.
(m/z calculated $[M+H]^+$ = 642.4027, found $[M+H]^+$ = 642.4026).

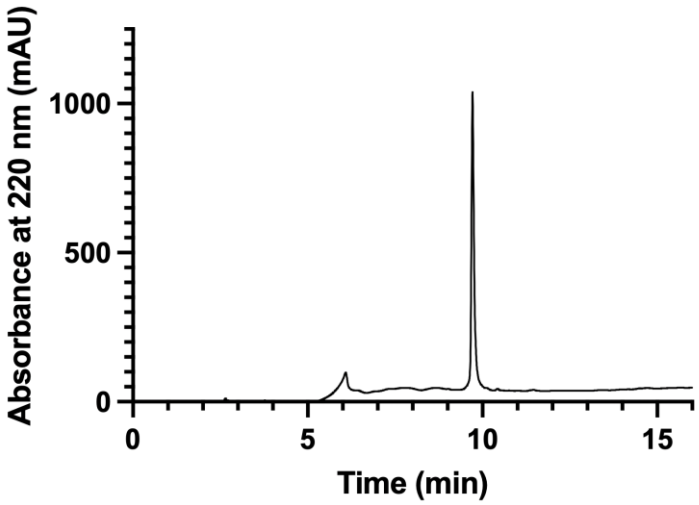

Figure C.6. UV (220 nm absorbance) HPLC chromatogram of Cyclen-4Py-NH_2.
A: H_2O with 0.1% TFA, B: Acetonitrile (CH_3CN/ACN) with 0.1% TFA; 0 - 13 min 0 to 45.5% B, 13 – 16 min 45.5 - 0 % B. The retention time of the product was 9.7 minutes.

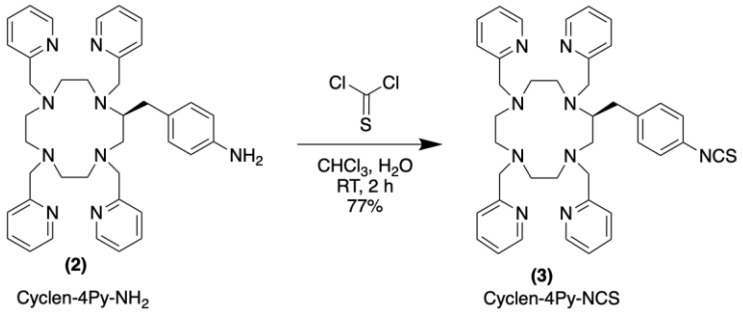

Scheme C.3. Synthesis of Cyclen-4Py-NCS.

(S)-2-(4-isothiocyanatobenzyl)-1,4,7,10-tetrakis(pyridin-2-ylmethyl)-1,4,7,10-tetraazacyclododecane (***3***). Cyclen-4Py-NH_2 (2) (31.8 mg, 49.5 μmol, 1 equiv.) was dissolved in 0.8 mL of deionized water. Thiophosgene (5.2 μL, 68.1 μmol, 1.4 equiv.) in $CHCl_3$ (95 μL) was added to the solution and stirred at room temperature for 2 hours. The aqueous layer was removed and the product was extracted from the $CHCl_3$ layer with water (1 mL x 3). The combined aqueous layers were lyophilized, and the crude was used without further purification due to concerns over its stability (26.0 mg, 77%). HR-ESI-MS: Calculated for $C_{40}H_{46}N_9S$ ($[M + H]^+$) = 684.3591, found = 684.3586.

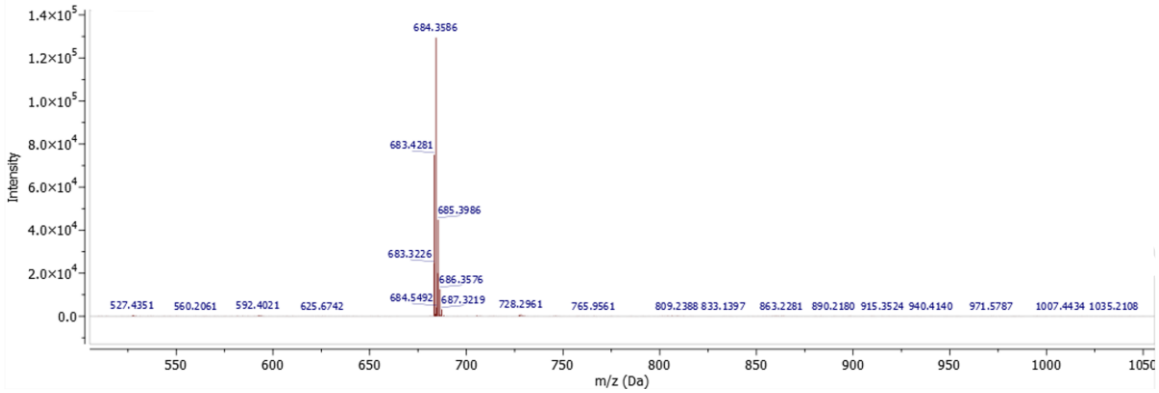

Figure C.7. Mass spectrum of Cyclen-4Py-NCS.
(m/z calculted $[M+H]^+$ = 684.3591, found = $[M+H]^+$ = 684.3586).

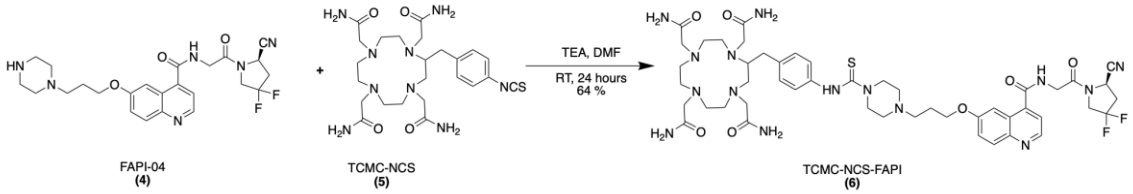

Scheme C.4. Synthesis of TCMC-NCS-FAPI.

FAPI-04 (9.57 mg, 19.7 μmol, 1 equiv.), which was synthesized and purified as previously described[335,336], was dissolved in 1.5 mL of anhydrous DMF. TEA (137 μL, 0.98 mmol, 50 equiv.) and TCMC-NCS (13.6 mg, 19.7 μmol, 1 equiv.) were added and the reaction was stirred at room temperature for 24 hours. The solvent was removed by evaporation and the crude product was purified by reverse phase HPLC with a Phenomenex Luna C18 (250 x 100 mm) column at 3 mL/min with the following method: A: H_2O with 0.1% TFA, B: Acetonitrile (CH_3CN/ACN) with 0.1% TFA; 0 –100 % B over 20 minutes. The retention time of the product was 10.3 minutes. These fractions were collected and lyophilized to yield a white solid (13.1 mg, 64%). The TFA content was found to be 46.7 ± 2.1% by mass (n = 3). HR-ESI-MS: Calculated for $C_{48}H_{66}F_2N_{15}O_7S$ ($[M + H]^+$) = 1034.4953, found = 1034.4923.

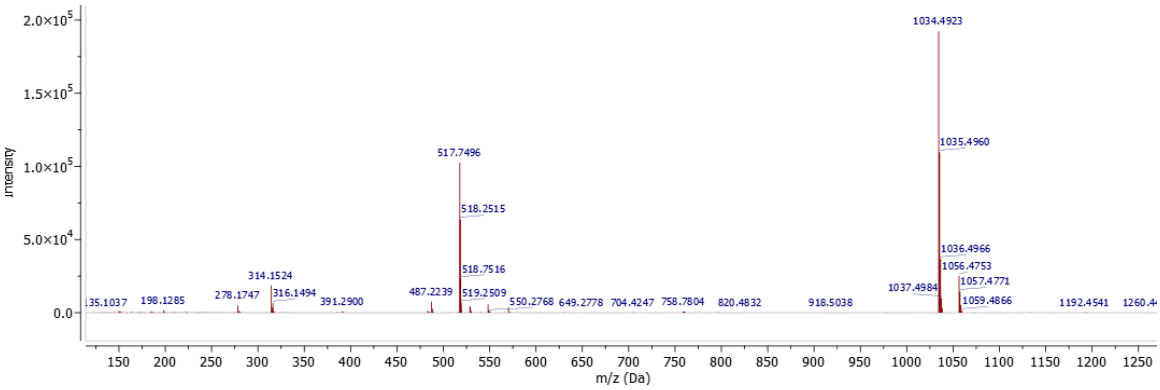

Figure C.8. Mass spectrum of TCMC-NCS-FAPI.
(m/z calculated $[M+H]^+$ = 1034.4953, found $[M+H]^+$ = 1034.4923)

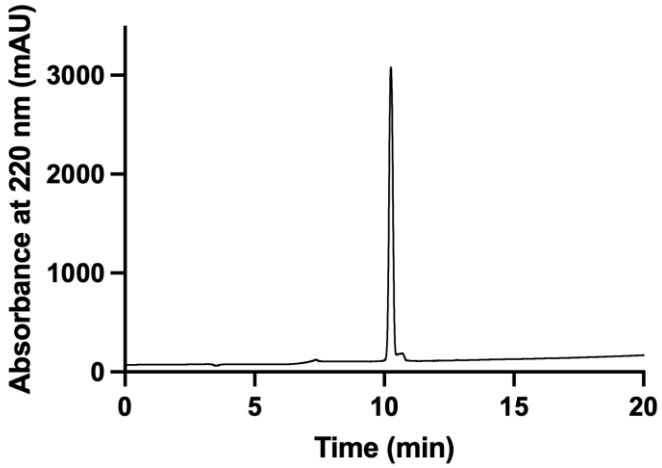

Figure C.9. UV (220 nm absorbance) HPLC chromatogram of TCMC-NCS-FAPI.
A: H_2O with 0.1% TFA, B: Acetonitrile (CH_3CN/ACN) with 0.1% TFA; 0 –100 % B over 20 minutes. The retention time of the product was 10.3 minutes.

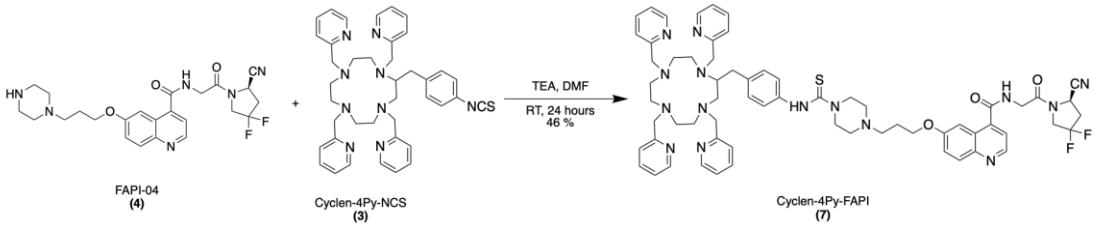

Scheme C.5. Synthesis of Cyclen-4Py-FAPI.

FAPI-04 (2.1 mg, 4.3 μmol, 1 equiv.) was dissolved in 600 mL of anhydrous DMF. TEA (89 μL, 0.64 mmol, 150 equiv.) and Cyclen-4Py-NCS (2.5 mg, 4.3 μmol, 1 equiv.) were added and the reaction was stirred at room temperature for 24 hours. The solvent was removed by evaporation and the crude product was purified by reverse phase HPLC

with a Phenomenex Luna C18 (250 x 100 mm) column at 3 mL/min with the following method: A: H_2O with 0.1% TFA, B: Acetonitrile (CH_3CN/ACN) with 0.1% TFA; 0 – 70 % B over 20 minutes. The retention time of the product was 11.3 minutes. These fractions were collected and lyophilized to yield a pale yellow solid (4.1 mg, 46%). The TFA content was found to be 57.0 ± 3.7% by mass (n = 3). HR-ESI-MS: Calculated for $C_{64}H_{74}F_2N_{15}O_3S$ ([M + H]$^+$) = 1170.5782, found = 1170.5647.

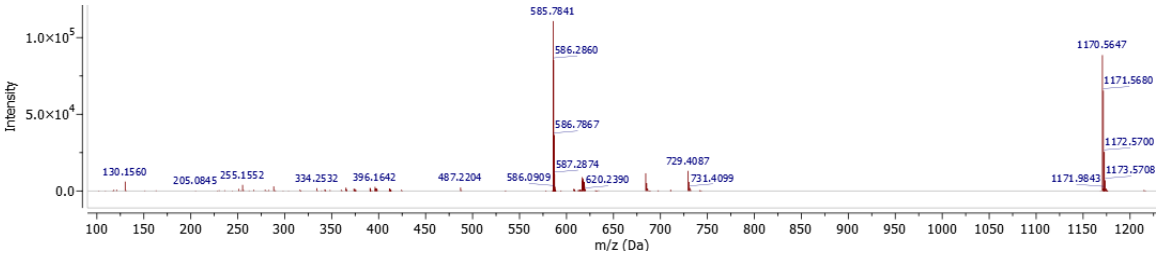

Figure C.10. Mass spectrum of Cyclen-4Py-FAPI.
(m/z calculated [M+H]$^+$ = 1170.5782, found [M+H]$^+$ = 1170.5647)

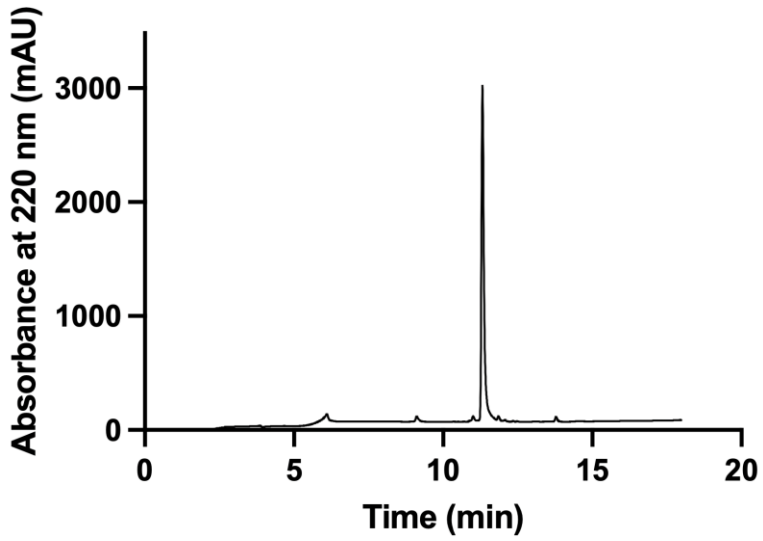

Figure C.11. UV (220 nm absorbance) HPLC chromatogram of Cyclen-4Py-FAPI.
A: H_2O with 0.1% TFA, B: Acetonitrile (CH_3CN/ACN) with 0.1% TFA; 0 – 70 % B over 20 minutes. The retention time of the product was 11.3 minutes.

Scheme C.6. Synthesis of Crypt-FAPI.

FAPI-04 (6.6 mg, 13.6 μmol, 1.1 equiv.) was dissolved in 600 mL of anhydrous DMF. TEA (250 μL, 1.8 mmol, 142 equiv.) and Crypt-NCS (7.0 mg, 12.6 μmol, 1 equiv.), whose synthesis and purification have been described elsewhere[251], were added and the reaction was stirred at room temperature for 24 hours. The solvent was removed by evaporation and the crude product was purified by reverse phase HPLC with a Phenomenex Luna C18 (250 x 100 mm) column at 3 mL/min with the following method: A: H_2O with 0.1% TFA, B: Acetonitrile (CH_3CN/ACN) with 0.1% TFA; 0 – 70 % B over 20 minutes. The retention time of the product was 11.8 minutes. These fractions were collected and lyophilized to yield a white solid (3.7 mg, 28%). The TFA content was found to be 39.3 ± 1.0% by mass (n = 3). HR-ESI-MS: Calculated for $C_{51}H_{72}F_2N_9O_{10}S$ ($[M + H]^+$) = 1040.5085, found = 1040.4955.

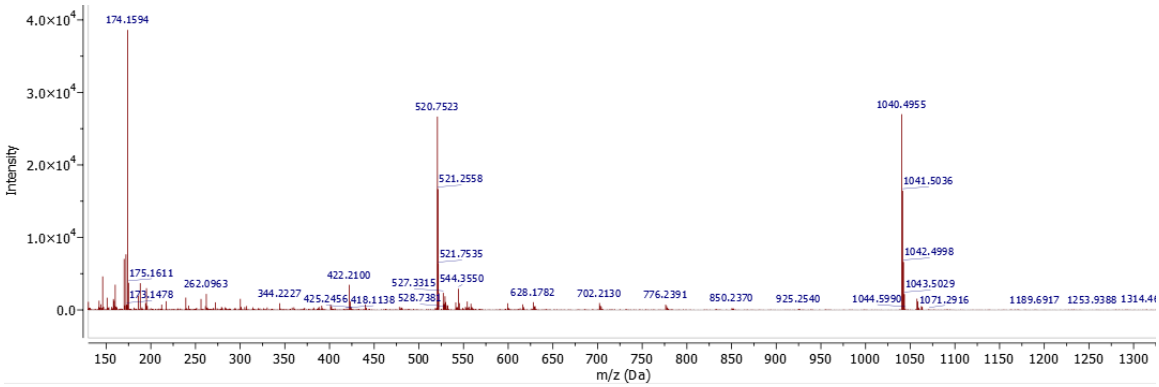

Figure C.12. Mass spectrum of Crypt-FAPI.
(m/z calculated $[M+H]^+$ = 1040.5085, found $[M+H]^+$ = 1040.4955)

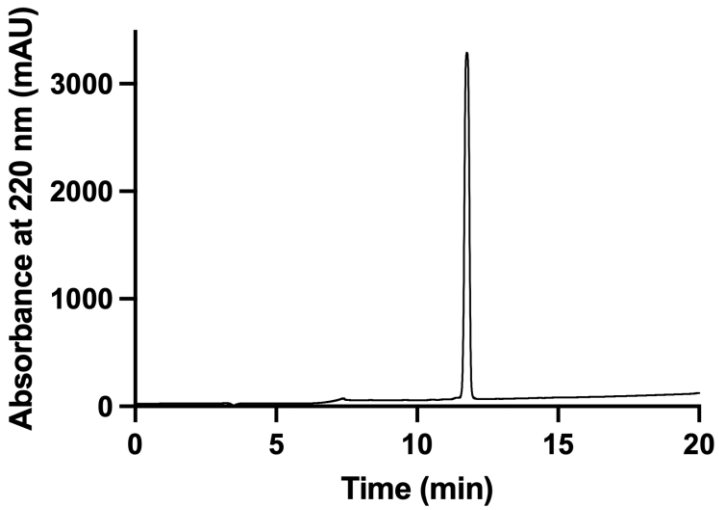

Figure C.13. UV (220 nm absorbance) HPLC chromatogram of Crypt-FAPI.
A: H_2O with 0.1% TFA, B: Acetonitrile (CH_3CN/ACN) with 0.1% TFA; 0 – 70 % B over 20 minutes at 3 mL/min. The retention time of the product was 11.8 minutes.

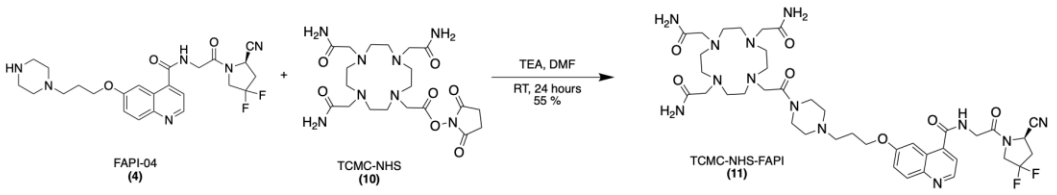

Scheme C.7. Synthesis of TCMC-NHS-FAPI.

FAPI-04 (5.39 mg, 11.7 μmol, 1 equiv.) was dissolved in 0.6 mL of anhydrous DMF. TEA (250 μL, 1.8 mmol, 162 equiv.) and TCMC-NHS (6.1 mg, 12.2 μmol, 1.1 equiv.) were added. Due to the insolubility of TCMC-NHS in solvent, 100 μL of water was added so that the reaction mixture became clear and was then stirred at room temperature for 24 hours. The solvent was removed by evaporation and the crude product was purified by reverse phase HPLC with a Phenomenex Luna C18 (250 x 100 mm) column at 3 mL/min with the following method: A: H_2O with 0.1% TFA, B: Acetonitrile (CH_3CN/ACN) with 0.1% TFA; 0 –100 % B over 20 minutes. The retention time of the product was 9.5 minutes. These fractions were collected and lyophilized to yield a white solid (5.8 mg, 55%). The TFA content was found to be 41.3 ± 3.6 % (n = 3) by mass. HR-ESI-MS: Calculated for $C_{40}H_{58}F_2N_{13}O_7$ ($[M + H]^+$) = 870.4545, found = 870.4570.

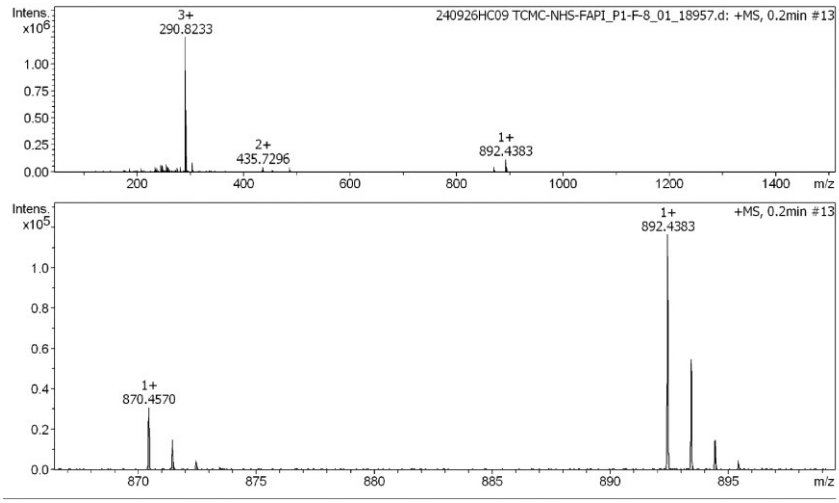

Figure C.14. Mass spectrum of TCMC-NHS-FAPI.
(m/z calculated $[M+H]^+$ = 870.4545, $[M+Na]^+$ = 892.4364, found $[M+H]^+$ = 870.4570, $[M+Na]^+$ = 892.4383).

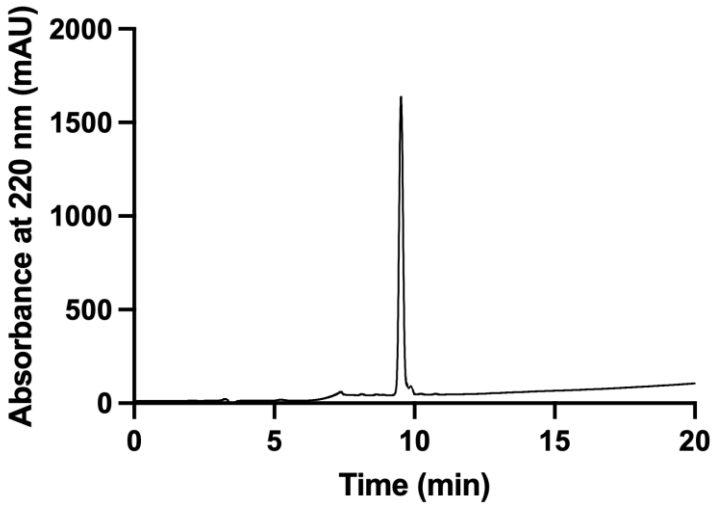

Figure C.15. UV (220 nm absorbance) HPLC chromatogram of TCMC-NHS-FAPI.
A: H_2O with 0.1% TFA, B: Acetonitrile (CH_3CN/ACN) with 0.1% TFA; 0 –100 % B over 20 minutes at 3 mL/min. The retention time of the product was 9.5 minutes.

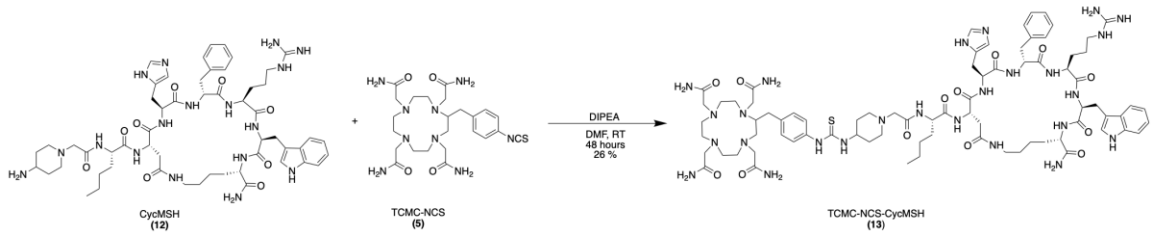

Scheme C.8. Synthesis of TCMC-NCS-CycMSH.

CycMSH (8.0 mg, 7.1 μmol, 1 equiv.), which was synthesized and purified as previously described[327], was dissolved in 0.5 mL of anhydrous DMF. DIPEA (50 μL, 0.28 mmol, 40 equiv.) and TCMC-NCS (4.9 mg, 7.1 μmol, 1 equiv.) were added and the reaction stirred at room temperature for 48 hours. The solvent was removed by evaporation and the crude product was purified by reverse phase HPLC with a Phenomenex Luna C18 (250 x 100 mm) column at 3 mL/min with the following method: A: H_2O with 0.1% TFA, B: Acetonitrile (CH_3CN/ACN) with 0.1% TFA; 0−5 min 10% B; 5−16 min 10−40% B, 16−20 min 10% B. The fraction at 12.8 minutes was collected and lyophilized to yield TCMC-NCS-CycMSH as a white solid (3.1 mg, 26%). The TFA content was found to be 44.8 ± 0.9 % (n = 3) by mass. HR-ESI-MS: Calculated for $C_{79}H_{118}N_{26}O_{13}S$ ($[M + 2H]^+$) = 835.9580, found = 835.9800.

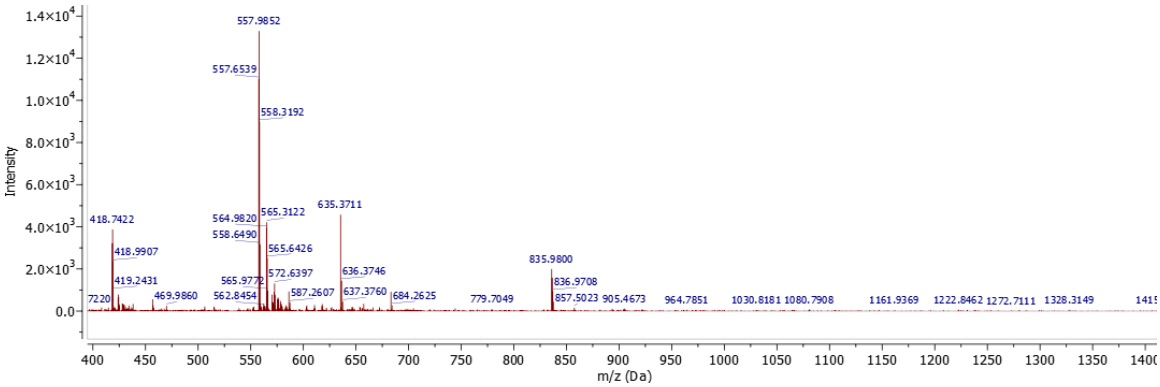

Figure C.16. Mass spectrum of TCMC-NCS-CycMSH.
(m/z calculated $[M+2H]^{2+}$ =835.9580, found $[M+2H]^{2+}$ =835.9800)

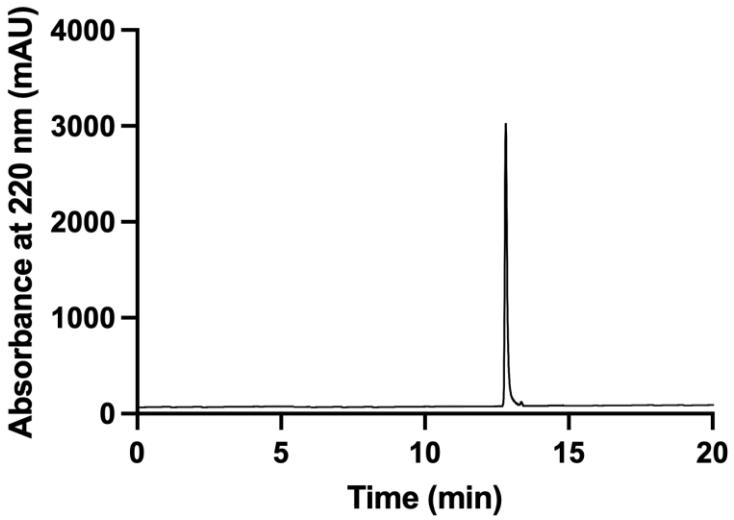

Figure C.17. UV (220 nm absorbance) HPLC chromatogram of TCMC-NCS-CycMSH.
A: H_2O with 0.1% TFA, B: Acetonitrile (CH_3CN/ACN) with 0.1% TFA; 0−5 min 10% B; 5−16 min 10−40% B, 16−20 min 10% B at 3 mL/min. The retention time of the product was 12.8 minutes.

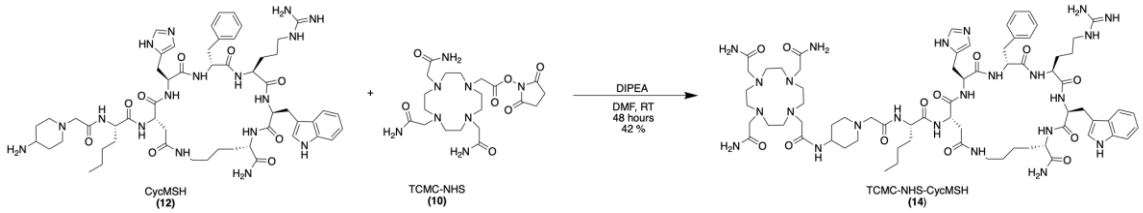

Scheme C.9. Synthesis of TCMC-NHS-CycMSH.

CycMSH (3.0 mg, 2.7 μmol, 1 equiv.), which was synthesized and purified as previously described[327], was dissolved in 0.5 mL of anhydrous DMF. DIPEA (14 μL, 8.0 μmol, 30 equiv.) and TCMC-NHS (2.0 mg, 4.0 μmol, 1.5 equiv.) were added and the reaction stirred at room temperature for 48 hours. The solvent was removed by

evaporation and the crude product was purified by reverse phase HPLC with a Phenomenex Luna C18 (250 x 100 mm) column at 3 mL/min with the following method: A: H_2O with 0.1% TFA, B: Acetonitrile (CH_3CN/ACN) with 0.1% TFA; 0-100% B over 20 min. The fraction at 9.0 minutes was collected and lyophilized to yield TCMC-NHS-CycMSH as a white solid (4.0 mg, 42%). The TFA content was found to be 42.0 $\pm$ 1.9 % (n = 3) by mass. HR-ESI-MS: Calculated for $C_{71}H_{109}N_{24}O_{13}$ ($[M + 2H]^{2+}$) = 753.4337, found = 753.4339.

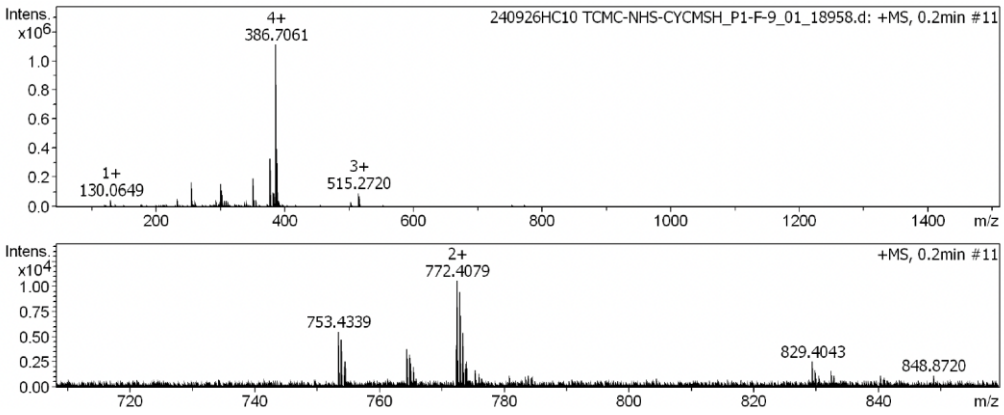

Figure C.18. Mass spectrum of TCMC-NHS-CycMSH
(m/z calculated $[M+2H]^{2+}$ = 753.4337, found $[M+2H]^{2+}$ = 753.4339)

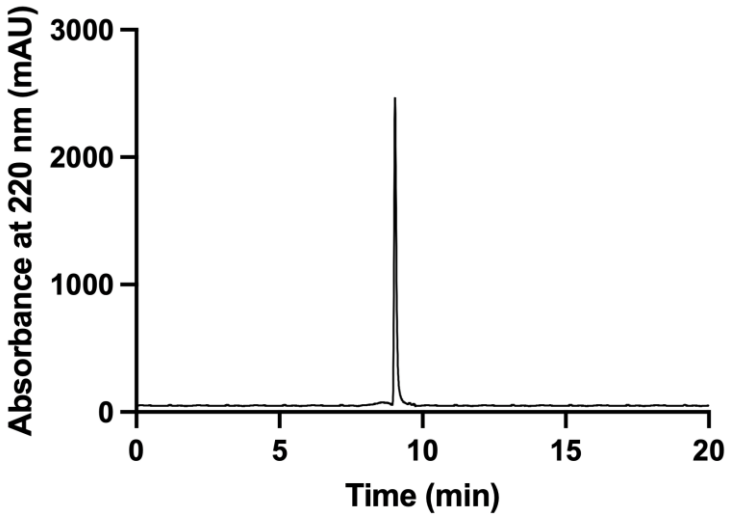

Figure C.19. UV (220 nm absorbance) HPLC chromatogram of TCMC-NHS-CycMSH.
A: H_2O with 0.1% TFA, B: Acetonitrile (CH_3CN/ACN) with 0.1% TFA; 0-100% B over 20 min at 3 mL/min. The retention time of the product was 9.0 minutes.

Radiolabeling

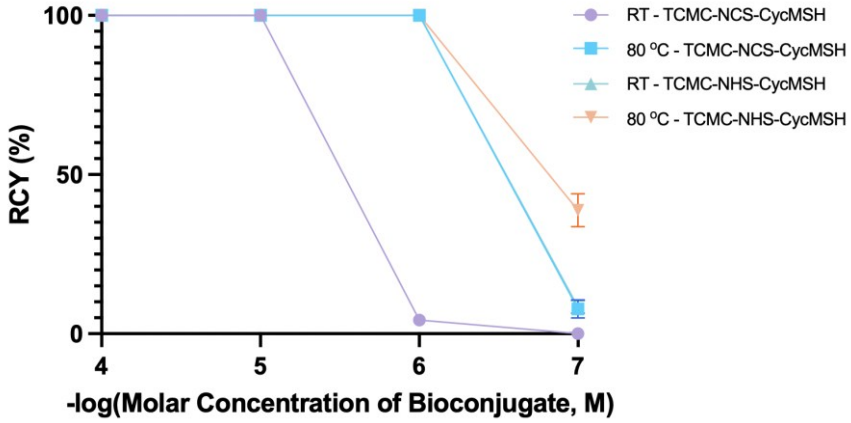

Figure C.20. ^{203}Pb (200 kBq, 0.1 M NH_4OAc, pH 7) radiolabeling results of CycMSH bioconjugates at 60 minutes.

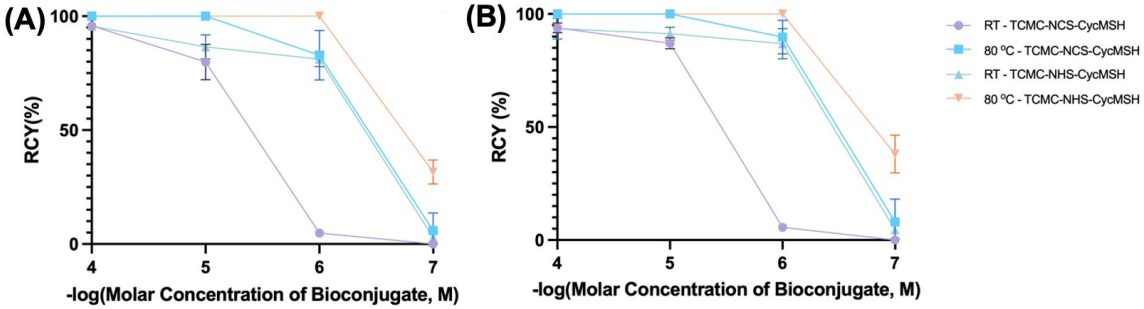

Figure C.21. ^{212}Pb (200 kBq, 0.1 M NH_4OAc, pH 7) radiolabeling results of CycMSH bioconjugates at (A) 30 and (B) 60 minutes.

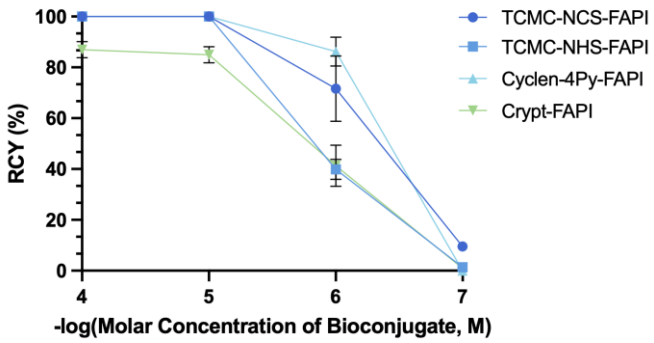

Figure C.22. ^{203}Pb (200 kBq, 0.1 M NH_4OAc, pH 7) radiolabeling results of FAPI bioconjugates at room temperature at 60 minutes.

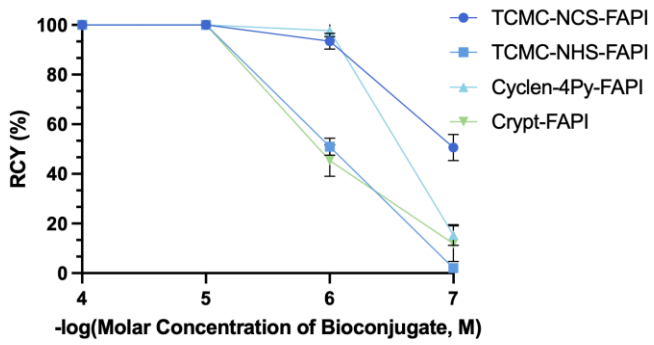

Figure C.23. ^{203}Pb (200 kBq, 0.1 M NH_4OAc, pH 7) radiolabeling results at 80 °C at 60 minutes.

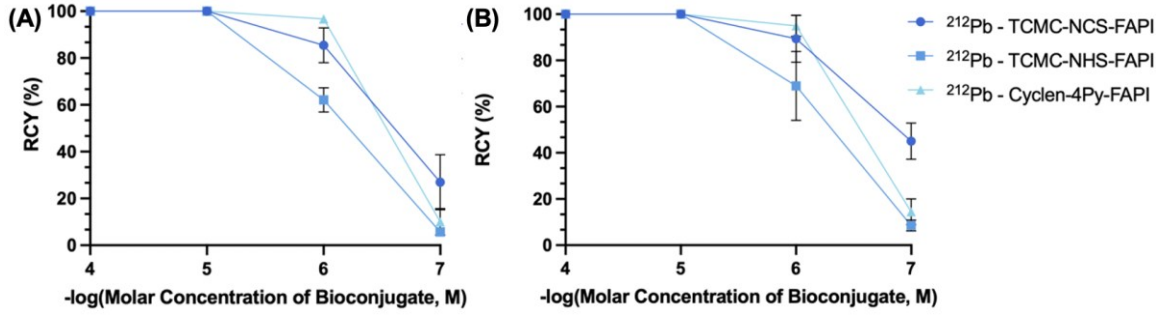

Figure C.24. ^{212}Pb (200 kBq, 0.1 M NH_4OAc, pH 7) radiolabeling results of FAPI bioconjugates at room temperature at (A) 30 minutes and (B) 60 minutes.

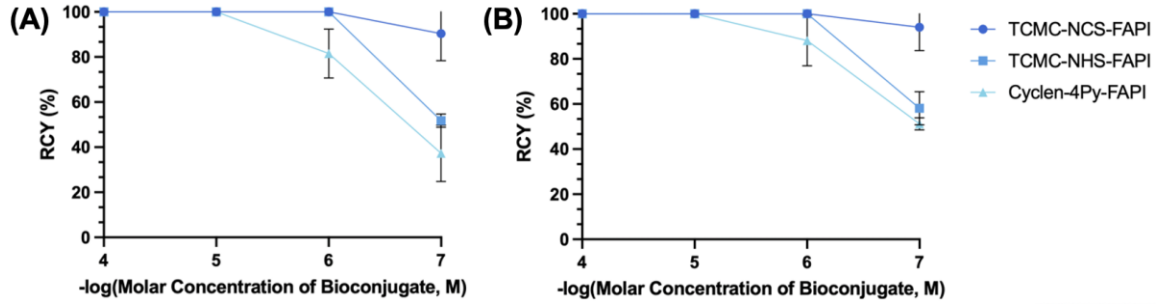

Figure C.25. ^{212}Pb (200 kBq, 0.1 M NH_4OAc, pH 7) radiolabeling results of FAPI bioconjugates at 80 °C at (A) 30 minutes and (B) 60 minutes.

Table C.1. Summary of ^{203}Pb Radiolabeling Results

Bioconjugate	Concentration (M)	Temperature	Average RCY at 30 min (%)	Average RCY at 60 min (%)
TCMC-NCS-CycMSH	10^{-4}	RT	100 ± 0	100 ± 0
		80 °C	100 ± 0	100 ± 0
	10^{-5}	RT	100 ± 0	100 ± 0
		80 °C	100 ± 0	100 ± 0
	10^{-6}	RT	4.3 ± 0.6	2.6 ± 1.5
		80 °C	100 ± 0	100 ± 0
	10^{-7}	RT	0 ± 0	0 ± 0
		80 °C	7.8 ± 2.9	16.4 ± 3.2
TCMC-NHS-CycMSH	10^{-4}	RT	100 ± 0	100 ± 0
		80 °C	100 ± 0	100 ± 0
	10^{-5}	RT	100 ± 0	100 ± 0
		80 °C	100 ± 0	100 ± 0
	10^{-6}	RT	100 ± 0	100 ± 0
		80 °C	100 ± 0	100 ± 0
	10^{-7}	RT	8.5 ± 2.0	12.0 ± 5.8
		80 °C	38.8 ± 5.2	39.6 ± 9.6
TCMC-NCS-FAPI	10^{-4}	RT	100 ± 0	100 ± 0
		80 °C	100 ± 0	100 ± 0
	10^{-5}	RT	100 ± 0	100 ± 0
		80 °C	100 ± 0	100 ± 0
	10^{-6}	RT	65.8 ± 10.2	71.6 ± 12.9
		80 °C	91.8 ± 3.1	93.5 ± 3.2
	10^{-7}	RT	8.2 ± 2.4	9.5 ± 1.4
		80 °C	41.8 ± 2.1	50.6 ± 5.3
TCMC-NHS-FAPI	10^{-4}	RT	100 ± 0	100 ± 0
		80 °C	100 ± 0	100 ± 0
	10^{-5}	RT	100 ± 0	100 ± 0
		80 °C	100 ± 0	100 ± 0
	10^{-6}	RT	33.9 ± 1.3	39.9 ± 4.0
		80 °C	31.6 ± 3.1	51.0 ± 3.5
	10^{-7}	RT	3.3 ± 1.0	1.4 ± 1.2
		80 °C	5.4 ± 1.8	2.0 ± 1.3
Cyclen-4Py-FAPI	10^{-4}	RT	100 ± 0	100 ± 0
		80 °C	100 ± 0	100 ± 0
	10^{-5}	RT	100 ± 0	100 ± 0
		80 °C	100 ± 0	100 ± 0
	10^{-6}	RT	74.8 ± 10.5	86.2 ± 5.7

		80 °C	96.0 ± 3.3	97.7 ± 2.4
	10^{-7}	RT	0 ± 0	0 ± 0
		80 °C	15.7 ± 3.2	15.4 ± 4.2
Crypt-FAPI	10^{-4}	RT	86.9 ± 1.9	86.9 ± 3.1
		80 °C	100 ± 0	100 ± 0
	10^{-5}	RT	83.0 ± 1.5	85.0 ± 3.2
		80 °C	100 ± 0	100 ± 0
	10^{-6}	RT	39.3 ± 7.0	41.3 ± 8.1
		80 °C	45.7 ± 6.5	45.4 ± 6.3
	10^{-7}	RT	0 ± 0	1.0 ± 0.1
		80 °C	6.5 ± 4.4	11.9 ± 7.1

Table C.2. Summary of ^{212}Pb Radiolabeling Results.

Bioconjugate	Concentration (M)	Temperature	Average RCY at 30 min (%)	Average RCY at 60 min (%)
TCMC-NCS-CycMSH	10^{-4}	RT	95.8 ± 1.8	93.9 ± 2.2
		80 °C	100 ± 0	100 ± 0
	10^{-5}	RT	79.9 ± 7.8	87.1 ± 2.4
		80 °C	100 ± 0	100 ± 0
	10^{-6}	RT	4.8 ± 0.2	5.6 ± 0.4
		80 °C	82.9 ± 10.9	89.8 ± 7.4
	10^{-7}	RT	0 ± 0	0 ± 0
		80 °C	5.9 ± 3.8	8.0 ± 4.1
TCMC-NHS-CycMSH	10^{-4}	RT	95.6 ± 1.6	93.5 ± 4.6
		80 °C	100 ± 0	100 ± 0
	10^{-5}	RT	86.5 ± 5.3	91.3 ± 2.9
		80 °C	100 ± 0	100 ± 0
	10^{-6}	RT	81.1 ± 3.2	86.8 ± 6.7
		80 °C	100 ± 0	100 ± 0
	10^{-7}	RT	2.9 ± 2.6	4.5 ± 3.9
		80 °C	31.6 ± 5.3	38.1 ± 8.4
TCMC-NCS-FAPI	10^{-4}	RT	100 ± 0	100 ± 0
		80 °C	100 ± 0	100 ± 0
	10^{-5}	RT	100 ± 0	100 ± 0
		80 °C	100 ± 0	100 ± 0
	10^{-6}	RT	85.8 ± 7.5	89.4 ± 10.2
		80 °C	100 ± 0	100 ± 0
	10^{-7}	RT	27.0 ± 11.8	45.1 ± 7.8
		80 °C	90.4 ± 12.0	94.0 ± 10.3

TCMC-NHS-FAPI	10^{-4}	RT	100 ± 0	100 ± 0
		80 °C	100 ± 0	100 ± 0
	10^{-5}	RT	100 ± 0	100 ± 0
		80 °C	100 ± 0	100 ± 0
	10^{-6}	RT	62.1 ± 5.1	68.9 ± 15.0
		80 °C	100 ± 0	100 ± 0
	10^{-7}	RT	5.7 ± 0.4	8.6 ± 2.3
		80 °C	51.8 ± 3.0	58.1 ± 7.4
Cyclen-4Py-FAPI	10^{-4}	RT	100 ± 0	100 ± 0
		80 °C	100 ± 0	100 ± 0
	10^{-5}	RT	100 ± 0	100 ± 0
		80 °C	100 ± 0	100 ± 0
	10^{-6}	RT	96.7 ± 1.6	95.0 ± 4.5
		80 °C	81.6 ± 10.8	88.1 ± 11.2
	10^{-7}	RT	10.0 ± 5.7	14.4 ± 5.6
		80 °C	37.3 ± 12.5	51.2 ± 2.7

In Vivo Studies

Table C.3. Apparent molar activities achieved for each bioconjugate complex used in this study.

Tracer	Isotope	Imaging Apparent Molar Activity (MBq/nmol)	Biodistribution Apparent Molar Activity (MBq/nmol)
TCMC-NCS-CycMSH	^{203}Pb	163.9	15.0
	^{212}Pb	N/A	16.5
TCMC-NHS-CycMSH	^{203}Pb	232.5	11.3
	^{212}Pb	N/A	6.09
TCMC-NCS-FAPI	^{203}Pb	60.1	3.51
	^{212}Pb	N/A	1.73
TCMC-NHS-FAPI	^{203}Pb	42.7	1.90
	^{203}Pb-blocking	0.2	0.05
	^{212}Pb	N/A	2.15
Crypt-FAPI	^{203}Pb	38.5	1.30
Cyc-4Py-FAPI	^{203}Pb	56.3	0.91

Table C.4. Full biodistribution results (% IA/g) of CycMSH bioconjugates or free, unchelated ^{203}Pb in B16F10 tumour-bearing male C57BLJ/6 mice at 2 hours post injection (n = 4).

Organ	$[^{203}Pb][Pb(TCMC\text{-}NCS\text{-}CycMSH)]^{2+}$	$[^{212}Pb][Pb(TCMC\text{-}NCS\text{-}CycMSH)]^{2+}$	$[^{203}Pb][Pb(TCMC\text{-}NHS\text{-}CycMSH)]^{2+}$	$[^{212}Pb][Pb(TCMC\text{-}NHS\text{-}CycMSH)]^{2+}$	Free ^{203}Pb
Blood	0.35 ± 0.23	0.45 ± 0.08	0.73 ± 0.17	0.23 ± 0.06	3.54 ± 1.29
Urine	107.83 ± 72.25	191.65 ± 35.15	33.69 ± 5.78	22.72 ± 8.66	63.85 ± 37.82
Feces	0.54 ± 0.24	0.53 ± 0.18	0.60 ± 0.61	0.40 ± 0.28	0.61 ± 0.23
Brain	0.04 ±0.02	0.07 ± 0.03	0.08 ± 0.05	0.06 ± 0.04	0.16 ± 0.03
Tumour	1.93 ± 1.28	1.10 ± 0.60	9.75 ± 2.09	11.33 ± 1.34	2.26 ± 0.78
Tail	1.43 ± 0.64	2.34 ± 0.66	2.35 ± 0.58	1.55 ± 0.07	3.67 ± 0.43
Bladder	5.51 ± 4.94	21.40 ± 17.89	5.96 ± 2.43	1.38 ± 0.30	12.72 ± 8.38
Muscle	0.07 ± 0.06	0.18 ± 0.03	0.13 ± 0.03	0.14 ± 0.02	0.11 ± 0.01
Bone	1.32 ± 0.80	2.36 ± 0.17	1.54 ± 0.29	0.79 ± 0.05	8.36 ± 1.23
Pancreas	0.42 ± 0.29	0.33 ± 0.06	0.44 ± 0.15	0.15 ± 0.05	2.37 ± 0.55
Spleen	3.66 ± 2.65	8.87 ± 2.11	1.90 ± 0.25	2.29 ± 1.01	2.90 ± 1.41
Kidneys	5.58 ± 3.56	9.93 ± 1.97	13.89 ± 2.84	7.11 ± 1.96	39.91 ± 8.14
Liver	22.78 ± 3.76	28.06 ± 3.48	7.48 ± 0.85	7.85 ± 1.17	8.07 ± 1.52
Heart	0.43 ± 0.21	0.71 ± 0.29	0.31 ± 0.08	0.27 ± 0.04	0.62 ± 0.20
Lungs	2.09 ± 0.68	7.14 ± 2.74	1.03 ± 0.07	0.65 ± 0.15	2.14 ± 1.67

Stomach	0.45 ± 0.23	0.73 ± 0.28	1.60 ± 0.43	1.18 ± 0.25	1.31 ± 0.27
Large intestine	0.95 ± 0.87	0.70 ± 0.10	0.76 ± 0.15	0.59 ± 0.16	1.91 ± 0.35
Small intestine	1.04 ± 0.58	1.14 ± 0.26	0.86 ± 0.17	0.64 ± 0.12	1.62 ± 0.43

Table C.5. Full biodistribution results (% IA/g ± SD) of TCMC-NCS/NHS-FAPI bioconjugates in HEK293t:hFAP tumour-bearing NRG male mice at 1 hour post injection (n = 4).

Organ	$[^{203}Pb][Pb(TCMC\text{-}NCS\text{-}FAPI)]^{2+}$	$[^{212}Pb][Pb(TCMC\text{-}NCS\text{-}FAPI)]^{2+}$	$[^{203}Pb][Pb(TCMC\text{-}NHS\text{-}FAPI)]^{2+}$	$[^{212}Pb][Pb(TCMC\text{-}NHS\text{-}FAPI)]^{2+}$	$[^{203}Pb][Pb(TCMC\text{-}NHS\text{-}FAPI)]^{2+}$ Blocked
Blood	2.42 ± 0.71	1.74 ± 0.36	1.56 ± 0.16	0.97 ± 0.10	0.49 ± 0.21
Urine	312.52 ± 164.27	231.10 ± 99.49	291.34 ± 114.41	254.27 ± 41.92	662.82 ± 485.91
Feces	0.35 ± 0.26	0.16 ± 0.07	0.31 ± 0.26	0.10 ± 0.03	0.19 ± 0.15
Brain	0.08 ± 0.03	0.07 ± 0.02	0.07 ± 0.02	0.06 ± 0.01	0.02 ± 0.02
Tumour	1.68 ± 0.26	2.09 ± 0.59	8.62 ± 1.32	7.63 ± 0.35	1.22 ± 0.22
Tail	2.78 ± 0.79	1.77 ± 0.42	3.64 ± 1.11	2.68 ± 0.40	1.76 ± 1.32
Bladder	8.11 ± 7.22	7.59 ± 5.34	16.48 ± 14.49	1.58 ± 0.43	3.57 ± 3.30
Muscle	1.05 ± 0.23	0.92 ± 0.19	0.86 ± 0.26	0.59 ± 0.04	0.13 ± 0.02
Bone	2.13 ± 0.69	1.88 ± 0.29	2.54 ± 0.57	2.37 ± 0.32	0.41 ± 0.10
Pancreas	1.32 ± 0.33	1.44 ± 0.50	0.97 ± 0.23	0.53 ± 0.15	0.17 ± 0.04

Spleen	1.00 ± 0.42	0.80 ± 0.26	1.07 ± 0.47	0.81 ± 0.15	0.29 ± 0.11
Kidneys	7.31 ± 1.80	3.79 ± 0.85	4.46 ± 0.32	5.33 ± 1.12	2.79 ± 0.61
Liver	1.73 ± 0.41	1.21 ± 0.36	1.02 ± 0.11	0.57 ± 0.06	0.47 ± 0.16
Heart	1.15 ± 0.25	0.92 ± 0.25	0.96 ± 0.49	0.47 ± 0.06	0.23 ± 0.07
Lungs	1.79 ± 0.59	1.22 ± 0.40	1.32 ± 0.22	0.90 ± 0.06	0.61 ± 0.30
Stomach	0.87 ± 0.44	0.98 ± 0.31	0.93 ± 0.22	0.64 ± 0.06	0.35 ± 0.17
Large intestine	2.16 ± 0.77	2.24 ± 0.82	1.89 ± 0.60	1.17 ± 0.13	0.57 ± 0.21
Small intestine	2.43 ± 0.65	1.99 ± 0.31	1.49 ± 0.28	0.88 ± 0.06	0.35 ± 0.17

Table C.6. Full biodistribution results (% IA/g ± SD) of Crypt-FAPI and Cyclen-4Py-FAPI bioconjugates in HEK293t:hFAP tumour-bearing NRG male mice at 1 hour post injection (n = 4).

Organ	$[^{203}Pb][Pb(Crypt\text{-}FAPI)]^{2+}$	$[^{212}Pb][Pb(Cyclen\text{-}4Py\text{-}FAPI)]^{2+}$
Blood	4.23 ± 1.15	2.36 ± 1.66
Urine	36.52 ± 12.21	84.13 ± 41.62
Feces	0.41 ± 0.25	0.18 ± 0.18
Brain	0.12 ± 0.04	0.95 ± 0.74
Tumour	1.69 ± 0.70	1.61 ± 0.93
Tail	3.19 ± 0.82	5.30 ± 2.70

Bladder	1.32 ± 0.85	4.33 ± 2.34
Muscle	0.25 ± 0.03	0.59 ± 0.28
Bone	5.04 ± 0.76	1.90 ± 0.88
Pancreas	2.13 ± 1.01	0.36 ± 0.18
Spleen	3.26 ± 1.92	3.26 ± 0.73
Kidneys	43.75 ± 5.86	8.44 ± 4.27
Liver	14.46 ± 3.27	31.42 ± 1.02
Heart	0.49 ± 0.35	0.95 ± 0.74
Lungs	3.82 ± 1.30	2.64 ± 1.05
Stomach	1.01 ± 0.42	1.18 ± 0.70
Large intestine	1.58 ± 0.17	1.73 ± 0.92
Small intestine	1.59 ± 0.39	2.71 ± 1.95